

2003

# Hydrogeological investigations of backfilled surface coal mine sites

Faramarz Doulati Ardejani  
*University of Wollongong*

---

## Recommended Citation

Ardejani, Faramarz Doulati, Hydrogeological investigations of backfilled surface coal mine sites, Doctor of Philosophy thesis, Faculty of Engineering, University of Wollongong, 2003. <http://ro.uow.edu.au/theses/1829>

## **NOTE**

This online version of the thesis may have different page formatting and pagination from the paper copy held in the University of Wollongong Library.

## **UNIVERSITY OF WOLLONGONG**

### **COPYRIGHT WARNING**

You may print or download ONE copy of this document for the purpose of your own research or study. The University does not authorise you to copy, communicate or otherwise make available electronically to any other person any copyright material contained on this site. You are reminded of the following:

Copyright owners are entitled to take legal action against persons who infringe their copyright. A reproduction of material that is protected by copyright may be a copyright infringement. A court may impose penalties and award damages in relation to offences and infringements relating to copyright material. Higher penalties may apply, and higher damages may be awarded, for offences and infringements involving the conversion of material into digital or electronic form.

**HYDROGEOLOGICAL INVESTIGATIONS OF  
BACKFILLED SURFACE COAL MINE SITES**

A thesis submitted in fulfilment of the  
requirements for the award of the degree

**DOCTOR OF PHILOSOPHY**

from

**UNIVERSITY OF WOLLONGONG**



by

**FARAMARZ DOULATI ARDEJANI**

**(B.Sc., M.Sc. Mining Engineering)**

**Faculty of Engineering**

**Mining Engineering Division**

February 2003

**IN THE NAME OF GOD**

This thesis is dedicated to my dear parents;

My father: Behroz Doulati  
My mother: Shams Hoshmand

and my dear family

My wife: Ameneh Eisa Pour  
My daughter: Shaghayegh Doulati

For their love, support and patience

## AFFIRMATION

I hereby certify that the work presented in the thesis entitled “Hydrogeological Investigations of Backfilled Surface Coal Mine sites” for fulfilment of the requirements for the award of the degree of Doctor of Philosophy, submitted in the Faculty of Engineering, Division of Mining Engineering, University of Wollongong, is my own work carried out under the supervision of Prof. R. N. Singh and A/Prof. E. Y. Baafi. The thesis contains no material previously published or written by another person except where due reference is made through the text.

The following papers based on this research have been published:

**Doulati Ardejani F.**, Singh R.N. and Baafi E.Y. (2002). A numerical finite volume model for prediction of pollution potential of open cut mine backfill. 6th Annual Environmental Engineering Research Event 2002 conference, Blackheath NSW, Australia, ISBN: 0-9580158-1-3. *Poster presentation of this paper in the conference won the peer voted award for “Excellence in environmental research”.*

**Doulati Ardejani F.**, Singh R.N., Baafi E.Y. and Porter I. (2003). A finite element model to: 1. Predict groundwater inflow to surface mining excavations. *Journal of the International Mine Water Association (IMWA)*, 22 (1), pp.31-38.

**Doulati Ardejani F.**, Singh R.N., Baafi E.Y. and Porter I. (2003). A finite element model to: 2. Simulate groundwater rebound problems in backfilled open cut mines. *Journal of the International Mine Water Association (IMWA)*, 22 (1), pp.39-44.

The following paper has been accepted for publication:

**Doulati Ardejani, F.**, Singh, R.N. and Baafi, E.Y. (2003). Numerical modelling of ion-exchanging solute transport in groundwater systems. *The PHOENICS Journal: Computational Fluid Dynamics & its applications*, CHAM, UK.

**Faramarz Doulati Ardejani**

## ACKNOWLEDGMENTS

The author would like to express his sincere gratitude to Professor R. N. Singh, Head of the Mining Engineering Discipline and A/Prof. E. Y. Baafi for their supervision, encouragement, guidance and inspiration provided during the course of this research. The author would also like to express his sincere thanks to them for provision of the computer and software facilities.

The author also wishes to express his sincere thanks for helpful contributions made by the following professionals during the period of this study.

I wish to express my deep appreciation to Dr. Joe Shonhardt, Senior Visiting Fellow in Mining Engineers for his helpful comments and proof reading of the thesis. I would also like to thank to Dr. P. B. Kosasih, Associate Fellow for his proof revising of the finite volume discretised equations and Dr. Ajit Godbole, Research Fellow for his helpful comments during using PHOENICS software. The author is also grateful to Dr. Dan Jaynes for his valuable comments and his contribution in providing input data for the model developed in this research.

I wish to appreciate to Mr. Des Jamieson, Mr. Peter Turner and Mrs. Leonie McIntyre, ITS staffs for their contributions in providing computer facilities. The assistance provided by the Faculty of Engineering, University of Wollongong is also appreciated.

The author would also like to acknowledge with sincere appreciation, the financial support of the Ministry of Science, Research and Technology of the Islamic Republic of Iran and the University of Shahrood.

Most importantly, the author would like to express his sincere thanks to all members of his family particularly his wife, Ameneh and his daughter, Shaghayegh, for their support and encouragement over the period of this research. The author also wishes to thank his parents and members of his family in Iran for their patience and continuous encouragement throughout the stay in Australia.

Thanks are also due to Mr. H. Daniali, a fellow PhD student, for his valuable assistance for solving computer-related problems and to Mr. F. Sereshki and other friends for their assistance throughout the project.

## ABSTRACT

Australia is one of the major coal producing countries in the world. Coal mine abandonment, groundwater rebound due to cessation of dewatering and associated pollution problems are a cause of serious concern throughout the world, and in particular, in Australia. Coal mining often leads to major environmental pollution problems when pyritic mineral is associated with the coal. The oxidation of pyrite usually generates acid mine drainage (AMD). The generation of AMD containing  $Fe^{++}$ ,  $Fe^{+++}$ ,  $SO_4^{--}$  and  $H^+$  is a source of great concern and can contaminate water resources.

Prediction of groundwater inflow into a mining excavation is important for the design of an effective dewatering system during the feasibility stage of a surface mining operation. A two-dimensional numerical finite element model called SEEP/W has been used for predicting the inflow of water into a surface mine working. The SEEP/W is a 32-bit graphical software that operates on the PC under Microsoft Windows 95, 98, Me, NT, 2000, and XP operating systems. This model has a capability to simulate saturated/unsaturated flow conditions and to calculate the height of the seepage faces of the mining excavation taking into account the hydraulic conductivities and the water content as a function of pore water pressure.

The SEEP/W model with some modifications has also been used to predict the groundwater rebound within backfilled open cut mines. This model has the ability to simulate groundwater flow problems in partially saturated porous media. Flexibility in the model is achieved by assigning different boundary conditions to the model. The results of the model of groundwater rebound are presented and compared with those obtained from analytical solutions, using the existing numerical model as well as with

the field monitored data observed in the UK. This model calculates realistic results that can be used by mine operators and environmental engineers to control the quality of mine drainage in a backfilled open cut mine operation.

A two-dimensional numerical finite volume model using PHOENICS as a computational fluid dynamic (CFD) package has been developed to simulate the transport of oxygen and long-term oxidation of pyrite as well as transport of oxidation products from a backfilled open cut coal mine. Gaseous diffusion was considered to be the principal mechanism for the transport of oxygen through the spoil. It was assumed that both oxygen and ferric iron produced by bacterially mediated oxidation of ferrous iron participate in the oxidation of pyrite. The pyrite oxidation reaction is based on the shrinking-core model. The model takes into account the effects of both surface reaction kinetics and the rate of oxidant diffusion into the particle. The model also assumes the particles have spherical shape and considers the rate of pyrite oxidation to be first order with respect to oxidant concentration and pyrite surface area. Complexation of ferric iron is assumed to take place within the spoil solution. The model can take into account the role of sulphate reduction bacteria governed by Monod type kinetics. The model also incorporates acid neutralisation reactions, linear and equilibrium-controlled ion exchange reactions as well as the effects of precipitation of ferric iron. In this present model, chemical and bacterial oxidation of  $Fe^{2+}$ , pyrite oxidation by oxygen and ferric iron, oxygen diffusion and bacterial sulphate reduction are relatively slow and assumed to be kinetically controlled but ion exchange and complexation reactions as well as precipitation reactions are fast and these are assumed to be equilibrium controlled reactions. Comparisons were made with published numerical modelling results and close agreement was achieved.

It was found that for the development of inflow and post-mining rebound models, a study of the hydrogeological characteristics of spoil is important. A comprehensive model of pyrite oxidation in the backfilled site of an open cut mine should not ignore the role of iron-oxidising bacteria. In the absence of bacteria, oxygen is the only important oxidiser of pyrite and the oxidation rate is highly dependent on the effective diffusion coefficient.

Although the oxidation of pyrite in the presence of air and bacteria is unavoidable, the numerical model developed here provides useful tool for assessing the effectiveness of a rehabilitation strategy to reduce pollutant production within oxidising pyritic material.

## TABLE OF CONTENTS

AFFIRMATION .....	i
ACKNOWLEDGMENT .....	ii
ABSTRACT .....	iii
TABLE OF CONTENTS .....	vi
LIST OF FIGURES .....	xvi
LIST OF TABLES .....	xxi
LIST OF SYMBOLS AND ABBREVIATIONS .....	xxiii

### **CHAPTER ONE: GROUNDWATER PROBLEMS ASSOCIATED WITH ABANDONED OPEN CUT COAL MINES**

1.1 Introduction .....	1
1.2 Surface mining methods .....	2
1.2.1 Surface mining operations .....	2
1.2.2 Basic factors in selecting the mining methods .....	5
1.2.3 Effective parameters in selecting the strip mining methods .....	5
1.3 Removal of the overburden .....	5
1.4 Back fill replacement methods .....	6
1.4.1 Dragline methods .....	6
1.4.2 Shovel and truck operations .....	7
1.4.3 Ripper and scraper operations .....	8
1.5 Water inflow into a surface mine .....	8
1.6. Environmental impacts of surface mining operations .....	9
1.7 Groundwater rebound .....	10
1.7.1 Groundwater rebound and pollution problem .....	12
1.8 Surface mine dewatering .....	12
1.8.1 Passive dewatering method .....	13
1.8.2 Advance (Active) dewatering technique .....	13
1.9 Review of research associated with groundwater modelling in open cut mining ....	15
1.9.1 Inflow models .....	15

1.9.2 Rebound models .....	20
1.9.3 Pyrite oxidation and acid leaching models .....	23
1.10 Need for further research .....	26
1.11 Research objectives .....	27
1.12 Research approach and program .....	30
1.12.1 Research approach .....	30
1.12.2 Research program .....	33
1.13 Conclusions .....	35

## **CHAPTER TWO: MINE WATER QUALITY CHARACTERISATION AND THE POLLUTION PROBLEM**

2.1 Introduction .....	38
2.2 Mine water chemistry .....	39
2.3 Water pollutants .....	40
2.3.1 General consideration .....	40
2.3.2 Mine water pollutants .....	40
2.4 Mine water characteristic .....	40
2.4.1 Physical parameters .....	42
(a) Temperature .....	42
(b) pH .....	42
(c) Turbidity .....	43
(d) Electrical conductivity (EC) .....	43
(e) Dissolved components and solubility .....	44
(f) Dissolved salts and suspended solids .....	44
(g) Hardness .....	45
2.4.2 Chemical parameters .....	45
(a) Chlorides .....	45
(b) Sulphates .....	45
(c) Nitrogen .....	46
(d) Alkalinity .....	47
(e) Acidity .....	48
2.5 Acid mine drainage (AMD) or acid rock drainage (ARD) .....	48

2.5.1	General consideration .....	48
2.5.2	Acid mine drainage (AMD) .....	49
2.5.3	Oxidation reactions and acid generation .....	50
2.5.4	The role of the buffering minerals .....	53
2.5.5	Impacts of acid mine drainage on the receiving environment .....	54
2.5.6	Heavy metals .....	55
2.6	Acid mine drainage neutralisation methods .....	56
2.6.1	Introduction .....	56
2.6.2	Acid mine drainage neutralising agents .....	57
2.6.3	Active treatment systems .....	58
2.6.4	Passive treatment systems .....	58
2.6.5	Passive anoxic limestone drains ( <i>PALD</i> ) .....	59
2.6.6	Open limestone channels .....	60
2.6.7	Wetland systems for acid mine drainage treatment .....	61
	(a) Aerobic wetland systems .....	64
	(b) Anaerobic wetland systems .....	65
	(c) Manganese and Aluminium removal .....	66
2.7	Conclusions .....	67

### **CHAPTER THREE: ANALYTICAL METHODS OF PREDICTION OF GROUNDWATER INFLOW TO OPEN CUT COAL MINES**

3.1	Introduction .....	69
3.2	Sources of water inflow in surface mines .....	70
3.2.1	Water inflow from direct precipitation, surface water and run-off .....	70
3.2.2	Groundwater inflow .....	71
3.3	Types of inflow .....	72
3.4	Prediction of groundwater inflow rate into surface mining excavation .....	76
3.5	Aquifer type, its characteristics, flow regime and mining excavation .....	77
3.6	Idealised hydrogeological profiles related to surface mining .....	78
3.6.1	One-regime flow to a surface mining excavation .....	78
3.6.2	Two-regimes flow into a surface mining excavation .....	79
3.6.3	Three-regimes flow of groundwater to the surface mining excavation .....	80

3.7 Analytical methods for calculation of surface mining excavation inflow rate .....	80
3.7.1 Equivalent well approach (EWA) .....	81
(a) Analytical groundwater inflow models based on EWA .....	82
(b) Limitations of equivalent well approach .....	95
3.7.2 Two-Dimensional Flow Approach .....	96
(a) Modified two-dimensional flow approach .....	101
(b) Limitations of two-dimensional flow equations .....	105
3.8 Limitations of analytical approaches .....	105
3.9 Conclusions .....	106

## **CHAPTER FOUR: A FINITE ELEMENT MODEL FOR GROUNDWATER INFLOW AND REBOUND PREDICTION IN OPEN CUT MINES**

4.1 Introduction .....	108
4.2 Types of models .....	109
4.2.1 Numerical methods .....	110
4.2.2 Finite difference method (FD) .....	111
4.2.3 Finite element method (FE).....	113
4.2.4 Finite volume method (FV) .....	114
4.3 General considerations about SEEP/W .....	114
4.3.1 Applications .....	114
4.3.2 Formulation .....	115
4.4 Groundwater flow models .....	116
4.4.1 General considerations .....	116
4.4.2 Hydrogeological characteristics of backfilled open cut mines .....	118
(a) Lithology of the spoil .....	119
(b) The method of mining and topography .....	119
(c) Effects of spoil age .....	119
4.4.3 Hydraulic parameters of surface mine spoil .....	120
(a) Permeability and transmissivity .....	120
(b) Porosity .....	121
(c) Groundwater velocity .....	122

4.4.4 The flow equation .....	122
4.5 Governing equation for formulation of SEEP/W .....	124
4.6 Boundary conditions .....	127
4.7 Galerkin approximation procedure .....	129
4.7.1 Finite element discretisation .....	130
4.8 Time integration technique .....	133
4.9 Conclusions .....	134

## **CHAPTER FIVE: GROUNDWATER INFLOW MODEL MODIFICATION AND VERIFICATION**

5.1 Introduction .....	136
5.2 Capabilities of the present model .....	137
5.3 Inflow model .....	138
5.4 Model verification .....	140
5.4.1 Problem 1- Development of seepage face in a porous media .....	140
5.4.2 Problem 2- Steady state, unconfined, radial flow to circular pit .....	142
5.4.3 Problem 3- Transient, radial flow to a fully penetrating well in a leaky aquifer .....	144
5.4.4 Problem 4- Steady state, unconfined, radial flow to surface mining excavation .....	146
5.4.5 Problem 5- Transient, radial inflow to a mining pit .....	149
5.4.6 Problem 6- Prediction of groundwater inflow to an open cut mine .....	153
5.5 Conclusions .....	158

## **CHAPTER SIX: PREDICTION OF GROUNDWATER REBOUND IN OPEN CUT MINING**

6.1 Introduction .....	161
6.2 Groundwater rebound model .....	161
6.3 Model verification .....	164
6.3.1 Problem 1- Dewatering simulation in a confined infinite aquifer .....	164
6.3.2 Problem 2-Simulation of groundwater recovery in an idealised pit .....	168

6.3.3 Problem 3-Modelling of groundwater rebound in an open cut mine site ..	170
(a) Axisymmetric model .....	172
(b) Two-dimensional model .....	173
6.3.4 Problem 4-Groundwater rebound simulation at backfilled site 'A' in the East Midlands area, UK .....	175
(a) General consideration .....	175
(b) Site topography, geology and backfill characteristics .....	175
(c) Instrumentation patterns .....	179
(d) Evaluation of field monitored groundwater rebound .....	181
(e) Analytical equation for the rise of groundwater level .....	181
(f) Finite element analysis and results .....	182
(f.1) Modelling performance and prediction (Profile A–A') .....	182
(f.2) Modelling performance and prediction (Profile B–B') .....	186
(g) Sensitivity analysis .....	192
6.4 Error analysis .....	194
6.5 Conclusions .....	195

**CHAPTER SEVEN: APPLICATION OF COMPUTATIONAL FLUID  
DYNAMICS (CFD) TO GROUNDWATER FLOW AND POLLUTANT  
TRANSPORT PROBLEMS**

7.1 Introduction .....	197
7.2 Computational fluid dynamics .....	199
7.3 PHOENICS modules .....	201
7.3.1 SATELLITE .....	201
7.3.2 EARTH .....	203
7.3.3 GROUND.....	203
7.3.4 PHOTON .....	204
7.3.5 AUTO PLOT .....	204
7.4 General stages of a CFD analysis .....	204
7.5 Finite volume method .....	206
7.6 Introduction to PHOENICS .....	207
7.6.1 PHOENICS governing equation .....	208

7.6.2 PHOENICS setting .....	209
7.7 Implementation of boundary conditions and source terms in PHOENICS .....	210
7.8 PIL commands for sources and boundary conditions .....	211
7.8.1 Initial-value patches .....	213
7.8.2 Sources and boundary condition patches .....	213
7.9 The finite volume discretisation .....	213
7.9.1 Finite volume discretisation of groundwater flow .....	213
7.9.2 Finite volume discretisation of transport equation .....	218
7.9.3 The upwind differencing scheme .....	221
7.10 Solution method by PHOENICS .....	224
7.11 Conclusions .....	225

**CHAPTER EIGHT: A NUMERICAL FINITE VOLUME MODEL FOR PYRITE OXIDATION AND OXYGEN TRANSPORT WITHIN SPOILS OF AN OPEN CUT COAL MINE**

8.1 Introduction .....	228
8.2 Pyrite oxidation and oxygen transport model description .....	229
8.2.1 Conceptual model .....	229
8.2.2 Pyrite oxidation model .....	231
(a) Calculation of pyritic surface area per unit volume of particle .....	233
(b) Reaction skin depth .....	234
8.2.3 Finite volume discretisation of pyrite oxidation model .....	236
8.2.4 Oxygen transport model .....	237
8.2.5 Development of mathematical expressions for oxygen consumption terms .....	240
8.2.6 Boundary conditions for oxygen transport model .....	243
8.3 Enthalpy (temperature) transport model .....	244
8.3.1 Enthalpy model .....	244
8.3.2 Calculation of enthalpies .....	245
8.3.3 Boundary conditions assigned for enthalpy model .....	246
8.4 One-dimensional modelling settings and input data .....	246

8.5 Modelling results .....	249
8.6 Conclusions .....	261

## **CHAPTER NINE: TRANSPORTATION OF PYRITE OXIDATION PRODUCTS THROUGH GROUNDWATER FLOW SYSTEMS**

9.1 Introduction .....	263
9.2 Transport equation .....	264
9.3 Boundary and initial conditions .....	265
9.4 Analytical models .....	266
9.5 Reaction on solid surfaces .....	267
9.5.1 Ion exchange reactions .....	269
9.6 PHOENICS setting for ion exchange reactions .....	270
9.6.1 Additional source terms due to the non-linear quaternary heterovalent ion exchange reaction .....	272
9.7 Model verification .....	273
9.7.1 One-dimensional advection-dispersion with linear ion-exchange reaction transport model .....	273
9.7.2 Nonlinear ion exchange model verification .....	275
(a) Verification of the ion-exchanging reactive transport model with field data .....	275
(b) Leaching of a sodic soil - binary heterovalent ion exchange .....	278
(c) Ternary, 1:1:1 ion exchange .....	279
(d) Quaternary heterovalent ion exchange problem .....	282
9.8 Other chemical reactions .....	284
9.9 Two-dimensional simulation .....	285
9.9.1 Modelling setting and input data .....	285
9.9.2 Two-dimensional simulation results .....	288
(a) Case 2D-1, without ion-exchange process, no acid neutralisation, no bacteria are present .....	288
(b) Case 2D-2, without ion-exchange process, incorporating acid neutralisation, bacteria are present .....	296
(c) Case 2D-3, Incorporating ion-exchange process, without acid neutralisation process, bacteria are absence .....	302

9.10 Conclusions .....	304
 <b>CHAPTER TEN: GENERAL CONCLUSIONS AND RECOMMENDATIONS</b>	
10.1 Summary .....	307
10.2 General Conclusions .....	310
10.3 Capabilities of inflow and post-mining rebound models .....	313
10.4 Capabilities of pyrite oxidation and solute transport model using finite volume method .....	314
10.5 Modelling studies and evaluation of the results.....	315
10.6 Recommendation for further research .....	317
 <b>REFERENCES</b> .....	 320
 <b>APPENDICES</b>	
<b>APPENDIX A</b> .....	334
Finite element discretisation of the groundwater flow equation	
 <b>APPENDIX B</b> .....	 343
Derivation of the pyrite oxidation model based on a shrinking core model	
 <b>APPENDIX C</b> .....	 351
A review of pyrite oxidation models	
 <b>APPENDIX D</b> .....	 384
Mass transport mechanisms	
 <b>APPENDIX E</b> .....	 391
Chemical reactions and the law of mass action	
 <b>APPENDIX F</b> .....	 394
The complement of the error function	

<b>APPENDIX G</b> .....	396
Derivation of the operational partial differential equations for different cases of ion-exchange reactions	
<b>APPENDIX H</b> .....	413
Acid neutralisation reactions	
<b>APPENDIX I</b> .....	417
Mineral precipitation and dissolution reactions	
<b>APPENDIX J</b> .....	421
Ferric iron complexation reactions	
<b>APPENDIX K</b> .....	428
The role of bacteria	
<b>APPENDIX L</b>	
Q1 file (soft copy)	
<b>APPENDIX M</b>	
Modified GROUND subroutine (soft copy)	

## LIST OF FIGURES

Figure	Page
1.1 Diagrammatic plan of a typical strip coal mining operations .....	3
1.2 A typical open pit mine with rail haulage .....	4
1.3 Diagrammatic illustration of surface mining operation using dragline .....	7
1.4 Schematic diagram showing shovel and truck operation system .....	8
1.5 Various sources of water inflow to a surface mine .....	9
1.6 The stages of groundwater rebound .....	11
1.7 Sump pumping .....	13
1.8 Advance Dewatering methods in different surface mining situations .....	14
1.9 A flowchart of the modelling approach .....	29
1.10 Structure of chapters in the thesis .....	31
2.1 Mine water Pollutants .....	41
2.2 Passive anoxic limestone drains .....	59
2.3 Open limestone channels for mine drainage treatment .....	60
2.4 Schematic diagram of a typical engineered wetland .....	63
2.5 Schematic diagram of aerobic and anaerobic wetland cells .....	64
3.1 Catchment hydrological cycle .....	71
3.2 Passive flow through a cylinder in a homogenous aquifer .....	73
3.3 Passive flow through a highly conductive cylinder .....	73
3.4 Inflow variation as a Gaussian distribution .....	74
3.5 Inflow increases with time .....	74
3.6 Constant inflow with time .....	75
3.7 Decreasing inflow with time .....	75
3.8 Mixed inflow behaviour .....	76
3.9 Laminar and Turbulent flow behaviours .....	77
3.10 One regime flow into a surface mining excavation .....	79
3.11 One regime flow into a surface mining excavation .....	79
3.12 Two regime flow into a surface mining excavation .....	80

3.13	Three regime flow into a surface mining excavation .....	81
3.14	A schematic diagram of radial flow towards a pumping well .....	83
3.15	Groundwater inflow to a pit .....	93
3.16	Values of the integral $G(x/H, \tau)$ for given values of $\tau$ and $x/H$ .....	98
3.17	Prediction of groundwater inflows into an excavation .....	100
3.18	Schematic diagram for inflow from an aquifer incised by surface mining excavation .....	101
4.1	Schematic representations of numerical finite element and finite difference grids for simulating an aquifer system .....	112
4.2	Schematic diagram showing different types of boundary conditions .....	127
4.3	Quadrilateral element: Local coordinates- $(\eta, \xi)$ , Global coordinates- $(x, y)$ ...	131
5.1	Groundwater inflow problem observed in an open cut coal mine, Singleton, Australia .....	137
5.2	Flowchart of groundwater inflow into a surface mine .....	139
5.3	Conceptual model of radial inflow to a surface mining excavation .....	140
5.4	Finite element grid for development of the seepage face.....	141
5.5	Finite element grid for prediction of radial flow to a circular pit, velocity vectors and water table .....	143
5.6	Comparison of analytical and numerical solutions for drawdowns under transient conditions in a leaky aquifer .....	146
5.7	Axisymmetric model, fully penetrating, vertical walls .....	147
5.8	Axisymmetric model, partially penetrating, vertical walls .....	148
5.9	Finite element grid, fully penetrating, non-vertical walls .....	149
5.10	Finite element grid, partially penetrating, non-vertical walls .....	149
5.11	Comparison of an analytical Jacob-Lohman solution and a numerical method for pit inflow prediction .....	151
5.12	The effects of the anisotropy ratio on the height of the seepage face .....	152
5.13	Finite element grid for prediction of inflow to an open cut mine .....	156
5.14	Comparison of analytical and numerical methods for the prediction of water inflow to an open cut mine .....	158
6.1	Groundwater rebound problem observed in an open cut coal mine, Singleton, Australia .....	162
6.2	Flowchart of groundwater rebound simulation in an open cut mine .....	163

6.3	Finite element representation of the dewatering problem .....	165
6.4	Comparison of drawdown predicted by numerical method and calculated value by the theis method at the well axis .....	166
6.5	Comparison of analytical and numerical residual drawdown as a function of time .....	167
6.6	Modified hydraulic conductivity functions of aquifer and excavated rocks .....	169
6.7	Comparison of finite element models for prediction of groundwater rebound in an idealised pit .....	170
6.8	Location map of Horsley site .....	171
6.9	Finite element representation of the axisymmetric problem .....	172
6.10	Comparison of numerical model and field data for prediction of water table rebound at the Horsley backfilled site in the UK (axisymmetric analysis) .....	173
6.11	Finite element representation of two-dimensional problem .....	173
6.12	Comparison of numerical model and field data for prediction of water table rebound at the Horsley backfilled site in the UK (two-dimensional analysis) ..	174
6.13	A typical geological section of the excavated material at the site 'A' in the East Midlands area .....	176
6.14	Site characteristics and instrument stations .....	177
6.15	Illustration of pre-mining geological profile A-A' .....	178
6.16	Illustration of pre-mining geological profile B-B' .....	178
6.17	Instrumentation scheme, Section A-A' .....	179
6.18	Instrumentation scheme, Section B-B' .....	180
6.19	Finite element mesh, Section A-A' .....	183
6.20	Water table before groundwater rebound, the position of instruments was also illustrated .....	183
6.21	Water recovery patterns after 10, 21, 32, 43, 50, 70, 110 and 120 days ceasing of pumping .....	185
6.22	Comparison of measured values, analytical solutions and model predictions for groundwater rebound process at instrumentation stations, Section A-A' .....	187
6.23	Finite element mesh, Section B-B' .....	188
6.24	Water table before rebound process, and the position of instrumentation stations .....	188
6.25	Modified conductivity function assigned in aquifer and backfill .....	189

6.26	Water recovery patterns after 10, 21, 32, 43, 50, 70, 84 and 110 days ceasing of pumping .....	191
6.27	Comparison of measured values, analytical solutions and model predictions for groundwater rebound process at instrumentation stations, Section B–B' .....	193
6.28	Sensitivity analysis for rainfall values .....	194
7.1	The procedure of solution in PHOENICS .....	202
7.2	Main stages in CFD simulation process .....	205
7.3	A part of two-dimensional grid and a control volume .....	214
7.4	Control volume for the two-dimensional situation .....	218
8.1	Conceptual model of pyrite oxidation and subsequent transport of oxidation products in backfilled open cut mines.....	230
8.2	One-dimensional grid and velocity vectors .....	248
8.3	Comparison of the POLS modelling results (dots) with the finite volume simulated results (solid lines) for oxygen mole fraction as a function of depth for 5-year period for cases 1, 3 and 4.....	250
8.4	The results of the finite volume model for the relative oxygen concentration versus depth over 27-year period for different diffusion coefficients .....	252
8.5	Comparison of the POLS results (dots) with the PHOENICS results (solid lines) for the pyrite consumed vs. time over entire spoil column for Cases 1 and 3 ....	253
8.6	PHOENICS results for $Fe^{2+}$ vs. time at the outlet of the profile for Cases 1 and 3 .....	253
8.7	PHOENICS results for $pH$ vs. time at the outlet of the profile for Cases 1 and 3 .....	254
8.8	Comparison of the POLS results (dots) with the PHOENICS results (solid lines) for the ratio of $Fe^{3+}$ to $Fe^{2+}$ in the outlet of spoil column in the presence and absence of bacteria .....	255
8.9	Comparison of the POLS results (dots) with the PHOENICS results (solid lines) for the pyrite oxidised vs. time over entire spoil column for Cases 2 and 4 .....	256
8.10	Ferrous iron concentration vs. depth for a 5-year simulation .....	257
8.11	Ferric iron concentration as a function of depth over a 5 year period .....	258
8.12	$pH$ as a function of depth over a 5 year period .....	259
8.13	$SO_4^{2-}$ concentration as a function of depth over a 5 year period .....	260
8.14	Total iron leaching rate vs. time in the water leaving the spoil profile for cases	

3 and 4 .....	260
9.1 Comparison of numerical modelling and analytical solution for one-dimensional advection-dispersion with linear ion-exchange transport of $Na^+$ and $Cl^-$ .....	274
9.2 Comparison of the field observations and simulation results for breakthrough curves of $Ca^{2+}$ and $Mg^{2+}$ .....	277
9.3 Changes in concentration profiles due to the leaching of a sodic soil .....	280
9.4 Concentration profiles due to 14.6 days of leaching of a soil with ternary, 1:1:1, non-linear ion exchange, comparison with published data .....	282
9.5 Concentration profiles of leaching of a soil with 1:2:2:2 exchange .....	284
9.6 Two-dimensional simulation cross-section: (a) finite volume grid; (b) hydraulic head and the segment of the spoil where oxidation reactions take place; (c) velocity vectors .....	287
9.7 Oxygen concentration after 5 years of simulation .....	289
9.8 2-D simulation results after 5 years: (a) oxygen concentration; (b) pyrite fraction remaining; (c) pyrite fraction oxidised .....	290
9.9 Temperature rise after: (a) 5 years; (b) 10 years of the simulation .....	291
9.10 $pH$ after: (a) 5 years; (b) 10 years of simulation .....	292
9.11 $SO_4^{2-}$ concentrations after: (a) 5; (b) 10 years of simulation .....	293
9.12 $Fe^{3+}$ after 5 years of simulation: (a) without precipitation reaction; (b) including precipitation reaction .....	294
9.13 $Fe^{3+}$ after 10 years of simulation: (a) without precipitation reaction; (b) including precipitation reaction .....	295
9.14 $Fe^{2+}$ concentration after: (a) 5 years; (b) 10 years of simulation .....	296
9.15 Oxygen concentration after 5 years of simulation .....	297
9.16 $Fe^{2+}$ after 5 years of simulation .....	297
9.17 $Fe^{2+}$ after 10 years of simulation .....	298
9.18 $pH$ after: (a) 5 years; (b) 10 years of simulation .....	299
9.19 $Fe^{3+}$ concentration after: (a) 5 years; (b) 10 years (without precipitation reaction); (c) 10 years (including precipitation reaction) of simulation .....	300
9.20 $SO_4^{2-}$ concentration after: (a) 5 years; (b) 10 years of simulation .....	301
9.21 Evolution of $Fe^{2+}$ concentrations at: (a) 2.5; (b) 5; and (c) 10 years of simulation .....	303

## LIST OF TABLES

<b>Table</b>	<b>Page</b>
1.1 Research activities and schedule .....	34
2.1 A list of metal sulphide minerals can be affected by T. Ferrooxidans .....	52
3.1 Analytical equations for surface mine inflow prediction based on equivalent well approach .....	84
3.2 Values of $K_0(r/B)$ - Hantush 1956 well function .....	85
3.3 Theis well function $W(u)$ .....	86
3.4 Jacob-Lohman well function .....	86
3.5 Values of Hantush 1956 well function for leaky aquifer, $W(u, r/B)$ .....	87
3.6 Values of $Y = \int_0^\infty \exp(-\tau \lambda \tanh \lambda) d\lambda$ .....	98
3.7 Dimensionless drawdown for given values of dimensionless distance, $x/R$ ...	100
4.1 Ranges of hydraulic conductivity and transmissivity from five reclaimed surface coal mine sites in Western Pennsylvania and Northern West Virginia .....	120
4.2 The local coordinates of nodal points .....	131
5.1 Comparison of results of numerical models in relation to physical model .....	141
5.2 Comparison of results of numerical models for prediction of the inflow and the height of the seepage in a circular pit .....	144
5.3 Comparison of results of numerical model and analytical solutions .....	148
6.1 Instrumentation details .....	180
6.2 Calculated error in related to measured values .....	194
7.1 A comparison of a number of common commercial CFD codes .....	200
8.1 Parameters used for simulation .....	247
8.2 Influx and background chemistry .....	247
8.3 A summary of the conditions maintained for the test cases used in this study .....	248
9.1 Settings in the Q1-file and GROUND subroutine for linear ion exchange reactions .....	271
9.2 Settings in the Q1-file to activate each source term, with CO and VAL referring to the corresponding coefficient and value settings within PHOENICS .....	272
9.3 Selectivity coefficients, initial and source concentrations for a ternary heterovalent ion exchange problem.....	277

9.4	Ion exchange parameters for a binary heterovalent exchange reaction .....	279
9.5	Ion exchange reaction parameters for a ternary homovalent exchange .....	281
9.6	Ion exchange reaction parameters for a quaternary heterovalent ion exchange problem .....	283
9.7	Source and background concentrations of aqueous components used for two- dimensional simulations .....	285
9.8	Illustration of the specific conditions for two-dimensional simulation cases .....	288

## LIST OF SYMBOLS AND ABBREVIATIONS

### SYMBOLS

$1 - D$	: one-dimensional	
$2 - D$	: two-dimensional	
$3 - D$	: three-dimensional	
$A$	: circular area of the pit by level	89
$A$	: cross-sectional area of the control volume face in x-direction	215
$A_F$	: particle surface area per millilitre spoil water	
$A_T$	: increase in the acidity term	
$A'$	: cross-sectional area of the control volume face in y-direction	
$a$	: unreacted radius of a particle of spoil	353, 363
$a$	: a dummy variable	97
$a_{Fe^{3+}}, a_{Fe^{2+}}$	: activities of ferric and ferrous iron respectively	
$a_{Py}^{rock}$	: surface area of pyrite per unit volume of waste rock	374
$a_{Sulf}^R$	: surface area of sulphide mineral per unit volume of waste	
$apor(x)$	: air-filled porosity of the tailings	
$aporos$	: air-filled porosity of the spoil	
$(aq)$	: aqueous phase	
$B$	: leakage factor	85, 145
$B$	: mole of pyrite consumed in pyrite-oxygen reaction per heat generated	245
$b$	: an empirical constant is used to calculate the unsaturated hydraulic conductivity	123
$b$	: stoichiometric ratio between pyrite and oxidant	233, 343, 358
$b$	: thickness of the confined aquifer	72, 85, 104, 145, 276
$b, m$	: empirical coefficients (0.16 and -1 respectively)	432
$B'$	: mole of pyrite consumed in pyrite- $Fe^{3+}$ reaction per heat generated	
$b'$	: thickness of the semi-confining layer (aquitard)	85, 145
$b'$	: stoichiometric ratio for $Fe^{2+}$ and oxygen	241
$C$	: contaminant concentration	385

$C$	: oxygen concentration in the gas phase	367
$C$	: heat capacity for the total dump (subscript T), the liquid (subscript $l$ ) and gas (subscript $g$ ) phase of the dump	354
$\{C\}$	: flux vector	
$C_i$	: concentration of $i^{th}$ dissolved species	
$C_{init}$	: initial concentration	
$C_{influx}$	: influx concentration of $i^{th}$ dissolved species	
$C_{i_{init}}$	: initial concentration of $i^{th}$ dissolved species	
$C_m$	: concentration of $m^{th}$ aqueous species	393
$C_0$	: source concentration	267
$C_0$	: concentration of oxygen at the surface	368
$C_0$	: oxidant concentration at fragment surface	358
$C_{O_2}$	: oxygen concentration at the particle surface	
$C_{[Ox]}$	: oxidant concentration in the water surrounding the particle	
$C_P$	: specific heat capacity of the spoil	245
$C_P, C_E, \text{ and } C_W$	: solute concentration in nodal points $P, E, \text{ and } W$ respectively	220
$C_T$	: total concentration of pore fluid species	
$C(x, t)$	: solute concentration at any point and time;	
$C_{T_{influx}}$	: influx total concentration of the aqueous species	
$C_{T_{init}}$	: initial total concentration of the aqueous species	
$C_{Fe^{3+}}$	: ferric iron concentration at the particle surface	
$C_{tw}$	: slope of the water storage curve	
$cv$	: control volume	
$C_Z$	: concentration of oxygen at the depth, $z$ , where the oxidation occurs	
$\bar{C}$	: sorbed component	
$\bar{C}_{fh}$	: amount of precipitated ferrihydrite per bulk volume of solids	
$\bar{C}_i$	: concentration of the species $i$ on the solid phase	
$\bar{C}_i^*$	: equivalent mole fraction of species $i$ in the sorbed phase	

$C_P^0$	: old value of $C$ at nodal point $P$	
$C_P^1$	: new value of $C_P$ at time $t + \Delta t$	
$\bar{C}_T$	: cation exchange capacity ( $CEC$ ) of the medium	
$Co_\phi$	: coefficient of a source term in linear form	
$C_w$	: heat capacity of water	
$\frac{\partial C}{\partial t}$	: change in concentration with time	
$\frac{\partial C}{\partial x}$	: concentration gradient which is negative in the direction of diffusion	
$D$	: integration domain	
$d$	: depth of the pit lake	
$D^*$	: an effective diffusion coefficient for an ion	
$D_1$	: effective diffusion coefficient of oxygen within the pore space of the dump	362
$D_1$	: diffusion coefficient	385
$D_1(x)$	: diffusion coefficient for the porous materials	377
$D_2$	: diffusion coefficient of oxygen for the oxidised coating surrounding the unoxidised core of the particles (water phase)	363, 378
$D_{b(O_2,CO_2)}, D_{b(O_2,N_2)}$	: binary diffusion coefficients for gas pairs of $O_2, CO_2$ and $O_2, N_2$	
$D_C$	: effective diffusion coefficient of oxidant in water	
$D_{dif}$	: molecular diffusion coefficient	
$D_e$	: effective diffusion coefficient for oxygen within pore space of spoil	
$D_{e[Ox]}$	: diffusion coefficient of oxidant within a particle	
$D_{jk}$	: hydrodynamic dispersion tensor	
$D_L$ and $D_T$	: longitudinal and transverse dispersion coefficients	
$D_m$	: mechanical dispersion	
$D_O$	: effective diffusion coefficient of $O_2$ in an $O_2, CO_2, N_2$ atmosphere	
$D_{Py}$	: density of pyrite	
$D_S$	: diffusion coefficient for sulphate ion	
$D_w$	: diffusion rate of oxygen in water	

$D_x$	: hydrodynamic dispersion coefficient in $x$ direction	
$D_{x_w}, D_{x_e}$	: interface diffusion coefficients at west and east faces of a control volume	
$D'_{OX}$	: diffusion coefficient of ferric ions in water	
$E_i$	: percent error	
$E_{M'}$	: energy per mole of electrons oxidised used by the bacterial population	
$E_{\max}$	: maximum percent error	
$\overline{E_s}$	: maximum potential flux of infiltration or evaporation	
$erf$	: error function	
$erfc$	: complimentary error function	
$F$	: mass flux of contaminant per unit area per unit time	
$F_1$	: advection flux	
$f$	: a weighting factor used in finite volume discretisation method	219
$f$	: stoichiometric coefficient that relates degradation of organic carbon to consumption of sulphate	433
$f(x)$	: a geometric factor depending on the fraction of pyrite remaining, $X$ (0 to 1)	373
$F_{O_2}$	: mole fraction of oxygen in atmosphere	
$Fe^{2+}$	: ferrous iron concentration	
$Fe^{3+}$	: ferric iron concentration	
$FPY$	: moles of pyrite leached per mole of sulphide copper leached	
$fracsulf(x)$	: fraction of sulphur in the tailings materials	
$G$	: volumetric rate of oxygen consumption by the oxygen-pyrite reaction	367
$G$	: concentration of organic carbon	431
$G_A$	: an empirical constant that defines the buffer system	
$G_{NS}$	: initial copper nonsulphide grade of dump	
$G_{Py}$	: pyrite fraction in a particle	
$G_S$	: initial copper sulphide grade of dump	
$H$	: a hydrogen ion	423

$H$	: height of the dump	355
$H$	: artesian head measured from top of confined aquifer	103
$H$ or $H_0$	: initial water table elevation or saturated thickness of aquifer (pre-mining potentiometric surface elevation)	85, 88, 89, 91, 97, 99, 153
$H$	: total head	125
$h$	: potentiometric surface elevation at a specific point	89
$h$	: hydraulic head	85, 123, 124, 128
$h$	: head at any local coordinate	339
$h$	: residual drawdown	166
$h$	: height of water table above impervious base of aquifer	103
$\{h\}$	: vector of heads at the nodes	
$h_A$	: prescribed hydraulic head at the portion A of the flow boundary	
$H_{Gen}^+$	: $H^+$ generated through chemical reactions	
$h_i(t)$	: hydraulic head at node $i$	
$h_l$	: minimum hydraulic head allowed under the prevailing soil conditions	
$h_0$	: initial hydraulic head or initial water table elevation	128, 150
$h_0$	: initial water table elevation above the base of zone A	94
$h_0$	: hydraulic drawdown along the pit bottom	95
$h_{(0)}$	: initial water level	
$h_p$	: water table elevation at excavation (pit) face	153
$h_p$	: saturated thickness above the base of zone A at $r_p$	94
$H^+$	: actual increase of hydrogen ion in solution	
$h_{(t)}$	: water level rise at time $t$	
$h_w$	: water table elevation at excavation face	
$I$	: ionic strength	393
$I$	: regional hydraulic gradient	72
$J$	: total (convection plus diffusion) fluxes	
$[J]$	: Jacobian matrix	
$J_D$	: diffusive flux of oxygen in the gas phase	
$K$	: thermal conductivity	245

$K$	: stability constant	422
$K$	: permeability of the aquifer	72, 85, 88,89, 97, 99, 144, 153, 166
$K$	: first order rate constant	367
$K$	: oxidant required for leaching a unit volume of waste particle	353
$K$	: solubility product of amorphous ferrihydrite	419
$k$	: time-dependent first-order rate parameter	432
$K'$	: permeability of the semi-confining layer	
$K_1, K_2$	: reaction constants for chemical oxidation of ferrous iron	241
$*K_1, K_1, K_2$	: stability constants for $Fe^{3+}$ complexes	425
$k_{AVE}$	: average permeability of the waste dump	
$K_B$	: first-order reaction rate coefficient for bacterial oxidation of $Fe^{2+}$	
$K_d$	: distribution coefficient	
$K_{eq} (K)$	: equilibrium constant	
$K_f$	: forward rate constant	
$K_h$	: horizontal permeability coefficient	
$K_{h1}$	: horizontal permeability of aquifer within zone A (pit walls)	
$K_{h2}$	: horizontal hydraulic conductivity for zone B (pit bottom)	
$K_i$	: equilibrium constant	392
$K_{ij}$	: component of the hydraulic conductivity tensor	
$K_j^i$	: a constant	
$K_i^j$	: ion exchange selectivity coefficient	
$K_0 (r / B)$	: Hantush & Jacob well function for steady state leaky aquifer	
$K_{[Ox]}$	: surface reaction rate constant	
$k_{OX}$	: first order rate constant for the oxidation of pyrite	374
$K_{OX}$	: overall volumetric kinetic constant	373
$K_r$	: reverse rate constant	
$K_S$	: first-order surface reaction rate constant	344, 359
$K_S$	: saturated hydraulic conductivity	123

$K_S$	: concentration at which rate of reduction is half of maximum reduction rate	434
$K_{sp}$	: solubility product which is an equilibrium constant specific to a solid	
$K_T$	: thermal conductivity of the dump	
$K_v$	: vertical permeability coefficient	
$K_{v_2}$	: vertical conductivity for zone B (pit bottom)	
$K_x, K_y$	: hydraulic conductivities	
$K_{x_{aq}}$	: horizontal hydraulic conductivity of aquifer	
$K_{x_{b,f}}$	: horizontal hydraulic conductivity of backfilled site	
$K_{x_w}, K_{x_e}, K_{y_s}, K_{y_n}$	: interface hydraulic conductivities	
$K_{y_{aq}}$	: vertical hydraulic conductivity of aquifer	
$K_{y_{b,f}}$	: vertical hydraulic conductivity of backfilled site	
$K(\theta)$	: unsaturated hydraulic conductivity	
$L$	: height of the dump	362
$L$	: a differential operator defined in the flow region	334
$L$	: a ligand	423
$L$	: length of the spoil profile	243
$l$	: one-half thickness of a thin plate fragment	
$l_x, l_y$	: direction cosines of the normal to the boundary	
$M$	: any metal	
$M^{2+}$	: a divalent heavy metal	
$m$	: thickness of the confined aquifer	
$m_2$	: anisotropy parameter	
$m_w$	: slope of moisture characteristic curve	
$N$	: number of layers of dump	
$n$	: recharge coefficient	85
$n$	: porosity of the medium	374, 388, 127
$n$	: total number of nodes in the problem domain	334
$n$	: valence of the ion	270
$n_a$	: air-filled porosity of the spoil	

$N_{aq}$	: total number of aqueous species	
$N_B$	: amount of $B$ within a particle	
$n_c$	: number of dissolved species participating in the ion exchange reactions	
$N_{CO_2}$ and $N_{O_2}$	: molar fluxes for $CO_2$ and $O_2$	
$N_i$	: a vector of interpolating shape functions	
$n_i$	: outward unit vector normal to the boundary where the outward flux is $-V$	
$N_i(x, y)$	: shape functions or basis functions	
$[O_2]^g$	: concentration of oxygen in gas phase of dump	
$[\overline{O_2}]^g$	: normalised concentration of oxygen in gas phase of dump	
$[O_2]_{STP}^g$	: oxygen concentration in atmosphere under standard conditions	
$[OX]$	: oxidant concentration ( $Fe^{+++}$ ) in leaching solution	
$P$	: atmospheric pressure	
$P_1$	: porosity of the dump	362
$P_1, P_2, \dots$	: valences	
$P_e$	: non-dimensional cell Peclet number	
$Q$	: groundwater inflow	85, 90
$Q$	: groundwater inflow to an open pit in an unconfined aquifer	88
$Q$	: water inflow rate to a pit	89, 150
$Q$	: rate of injected water into well at source point	276
$Q$	: dewatering rate	145, 166
$Q$	: boundary flux	125
$q$	: inflow per unit length of excavation	99, 153
$q$	: water flux	130, 337
$q^*$	: volumetric consumption of oxygen from the pore space of the dump	
$q(x, t)$	: volumetric oxygen consumption term due to pyrite-oxygen reaction	
$Q_1$	: inflow from the pit walls	
$Q_2$	: inflow rate from pit bottom	

$Q_A$	: consumption term for oxygen by bacteria while oxidising ferrous iron	
$q_a$	: inflow on the highwall face per unit length of excavation	
$Q_{Ar}$	: flux of oxidant $A$ through surface of particle when radius is $r$	
$Q_{Arc}$	: flux of oxidant $A$ through reaction surface	
$Q_{AS}$	: flux of oxidant $A$ through outside of particle	
$Q_C$	: oxygen consumption rate due to chemical oxidation of ferrous iron	
$Q_{gw_{pi}}$	: passive inflow component	
$Q_{j\_l}$	: inflow calculated using Jacob & Lohman equation	
$Q_{model}$	: inflow calculated using numerical model	
$Q_O$	: oxygen consumption term	360
$Q_{O_2}, Q_{CO_2}, Q_{N_2}$	: mole fractions of $O_2, CO_2,$ and $N_2$ in gas	
$Q_P$	: rate of oxygen consumption by the oxygen-pyrite reaction	
$q_j$	: vector components of the pore fluid specific discharge	
$q_{re}$	: surface recharge	
$Q_t$	: total inflow rate	
$q_x, q_y$	: component of the rate of flow of water through a porous media	
$q_{x_e}, q_{x_w}$	: interface pore fluid specific discharge at east and west faces of a control volume	
$R$	: a residual or error	335
$R$	: gas constant	238, 359
$R$	: radius of influence	85, 88, 89, 99
$R$	: particle radius	233, 374
$r$	: well radius	166
$r$	: equivalent radius	82, 85
$r$	: distance between injection well and the observation well	276
$r$	: mass produced or consumed per unit volume per unit time	389
$R^*$	: radius of the particle	
$R^*(x^*, t^*)$	: location of the reaction front within particles of the dump	
$r^*$	: radial distance within a particle	

$R_a$	: average rate of elongation of the pit	
$r_b$	: radius of the pit base	
$R_C$	: length of the depressed part of the confined aquifer	
$r_{(CO_2, O_2)}$	: molar flux ratio for gas pair of $CO_2$ and $O_2$	
$r_c^*(x)$	: radius of the reaction front or the radius of the unreacted core	
$R_{Cu}, R_{O_2}$ and $R_A$	: rate of leaching of copper, the rate of oxygen consumption, and the rate of heat generation, respectively	
$R_f$	: retardation factor	
$r_i$	: volume fraction of phase $i$	
$R_O$	: overall rate of reaction	
$r_0$	: reduced radius of the open pit by level	88
$r_0$	: radius of influence	93
$r_p$	: radius of the pit at the desired level	72, 89, 93
$r_s$	: rate of mass sorption	
$R_{uc}$	: interval in which aquifer is unconfined	
$r_w$	: well radius	
$S$	: storage coefficient	85, 90, 103, 145, 150
$S$	: sinks and sources representing the changes in aqueous component concentrations	265
$S$	: sulphate concentration	433
$S$	: surface area per unit volume of particle	367
$S$	: drawdown in the aquifer	88, 89
$s$	: drawdown in the aquifer ( $m$ )	85
( $s$ )	: solid phase	417
$s, n$	: south and north side faces of a control volume	214
$S_{bc_i}$	: boundary conditions	
$\bar{S}$	: average value of source $S$ over the control volume	
$S_1$	: coefficient of storage during recovery	
$S_B$	: oxygen sink term due to iron-oxidising bacteria	

$S_C$	: oxygen consumption term caused by chemical oxidation of ferrous iron	
$S_{K_{Py-O_2}}$	: volumetric oxygen consumption term by the pyrite oxidation reaction	
$S_{K_{Fe^{2+}-O_2}}$	: volumetric oxygen consumption term by the chemical oxidation of ferrous iron	
$S_{K_{B-O_2}}$	: volumetric oxygen consumption term by bacteria	
$S_0$	: concentration of $SO_4$	
$S_P$	: oxygen sink term due to direct oxidation of pyrite by oxygen	
$S_y$	: specific yield	
$S_{\phi_i}$	: source rate of variable $\phi_i$	
$T$	: transmissivity of aquifer	85, 90, 97, 103, 144, 150, 153
$T$	: absolute temperature	238, 359, 429
$T$	: temperature ( $^{\circ}C$ )	244
$t$	: time	153, 209, 232, 245, 264, 267
$t$	: elapsed time	90
$t$	: time interval at which water level rise from $h_{(0)}$ to $h_{(t)}$	182
$t$	: time since the water table was instantaneously lowered to the specified level	150
$t$	: time since pumping started	166
$t^*$	: time	
$t_1$	: time since pumping stopped	
$t_a$	: time period during which the pit is elongating	
$t_C$	: total time required for full leaching of pyrite where the chemical reactions were the rate controlling process	
$t_D$	: total time required for complete oxidation of pyrite within a fragment when the diffusion processes control the oxidation rate	
$T_L$	: linear transmissivity	
$T_R^L$	: tortuosity of diffusion pathways	
$T_T$	: turbulent transmissivity	

$temp$	: temperature ( ° K )	
$u$	: oxygen concentration in the spoil pore space	
$u^*$	: oxygen concentration within the pore space of the dump	
$U_A^*$	: oxygen concentration in the pore space of the tailings	
$u_{j_i}$	: velocity component in the $x_j$ direction	
$u_{O_2}$	: oxygen concentration within the pore space of spoil	
$U_w$	: matric potential	
$U_w^*$	: oxygen concentration in the water film surrounding the particle	
$u_w$	: pore-water pressure	
$u_{x,w}$	: water velocity	
$-V$	: outward fluid flux	128
$v$	: pore-water flow velocity (linear velocity)	
$Val_\phi$	: value of a source term in linear form	
$V_d (v_d)$	: Darcy velocity	
$V_g$	: Darcy air velocity through the dump	
$V_l$	: Darcy velocity for the liquid phase	
$v(r^*, x^*, t^*)$	: concentration of oxygen within a particle of the dump	
$V_x$	: x-direction velocity	
$v_x$ and $v_y$	: average linear velocities in the $x$ and $y$ directions	
$v_{x_j}$	: linear groundwater velocity, is a vector with components $v_x$ and $v_y$	
$v_x nC, v_y nC$	: advection fluxes in $x$ and $y$ directions	
$W$	: recharge or discharge per unit volume (source or sink term)	123
$W$	: distributed recharge flux	93
$W$	: width of the mine	82
$w$	: pore water velocity	433
$w, e$	: west and east side faces of a control volume	
$W_i$	: weighting functions over domain D	
$W(u)$	: Theis well function	
$W(u, r / B)$	: Hantush well function	

$W(\lambda)$	: Jacob & Lohman well function	
$\overline{W}$	: average value of source $W$ over the control volume	
$X$	: fraction of pyrite remaining in a particle	232, 358
$X$	: clay mineral	415
$x$	: distance in the x-direction	266
$x$	: any metal ligand	58
$x^*$	: vertical coordinate	
$x_1, x_2, \dots; y_1, y_2, \dots$	: nodal coordinates	
$x_i$	: measured water level	
$X_s^i$	: fraction of sulphide copper remaining in the $i^{\text{th}}$ layer of the dump	
$x_j$	: Cartesian coordinates	
$\{X\}, \{Y\}$	: global x-y coordinates of the element nodes	
$x, y, z$	: coordinates	
$X_P$	: fraction of pyrite remaining in nodal point $P$ inside a control volume	
$X_P^0$	: old value of $X_P$	
$X_s$	: fraction of initial sulphide copper remaining in the dump after some leaching	
$X_T$	: temperature kinetic factor	
$X_{wO}$	: kinetic factor of oxygen in the liquid phase	
$Y$	: mine length	
$y$	: elevation	
$Y_0$	: mole fraction of oxygen in gas	
$Y_p$	: maximum length of the pit	
$Z$	: elevation	124
$z$	: depth	433
$z$	: depth of the dump	354
$Z_i$	: depth	
$Z_m$	: charge of aqueous species $m$	
$\Delta h$	: drawdown	

$\Delta h_c$	: confined aquifer drawdown	
$\Delta h_{uc}$	: unconfined aquifer drawdown	
$\Delta l'$	: water film thickness	
$\Delta P$	: pressure drop across the dump	
$\Delta t$	: time step	
$\Delta v$	: volume	
$\Delta x$	: distance between faces $w$ and $e$ of a control volume	
$\Delta x_i$	: difference between measured water level and predicted water level	
$\Delta y$	: distance between faces $s$ and $n$	
$\alpha$	: surface area of pyrite per unit volume of fragment	359
$\alpha$	: hydrogeological characteristics of the basin	182
$\alpha$	: dispersivity	385
$\alpha$	: a dimensionless parameter	91
$\alpha_{i,m}$	: stoichiometric coefficient of dissolved species $m$ in species $i$	
$\alpha_L$	: longitudinal dispersivity	
$\alpha_T$	: transverse dispersivity	
$\alpha_{Py}^{rock}$	: surface area of pyrite per unit volume of particle	
$\beta$	: ratio of solid volume to water volume	434
$\beta$	: boundary of the problem domain	336
$\beta$	: constant value is used to calculate the error function	394
$^*\beta_2, ^*\beta_3, ^*\beta_4, ^*\beta_{22}$	: stability constants for $Fe^{3+}$ complexes	425
$\delta$	: reaction skin depth	
$\delta_x$	: cell width	
$\delta_{xWP}, \delta_{xPE}$	: distances between the nodes $W$ and $P$ , and between nodes $P$ and $E$	
$\delta_{ySP}, \delta_{yPN}$	: distances between the nodes $S$ and $P$ , and between nodes $P$ and $N$	
$\varepsilon$	: mass of oxygen used per mass of sulphur in the oxidation reaction	
$\theta$	: volumetric water content	
$\theta_n$	: antecedent water content	
$\theta_S$	: saturated water content	
$\gamma$	: dimensionless discharge	99

$\gamma$	: conversion factor between the oxygen concentrations in the gas and water phases	235
$\gamma_{Fe^{3+}}$ , $\gamma_{Fe^{2+}}$ , and $\gamma_{H^+}$	: activity coefficients for $Fe^{3+}$ , $Fe^{2+}$ , and $H^+$ respectively	
$\gamma_m$	: activity coefficient	
$\gamma_w$	: unit weight of water	
$\eta$	: conversion factor accounts the number of electrons released by organic carbon decay to those electrons actually used in sulphate reduction process	
$(\eta, \xi)$	: local coordinates	
$\rho$	: density of the total dump (subscript T), the liquid (subscript l) and gas (subscript g) phase of the dump	
$\rho_B$	: molar density of $B$ in the solid	
$\rho_b$	: bulk density	
$\sigma_f$	: molar density of pyrite within the fragment	
$\rho_i$	: PHOENICS-term for density of phase $i$	
$\rho_{Prctl}$	: particle density	
$\rho_{Py}$	: molar density of pyrite in the particle	
$\rho_R$	: density of waste materials	
$\rho_S$	: molar density of pyrite in spoil	240
$\rho_S$	: density of sulphur in the dump	364
$\rho_{OX}^{air}$	: oxygen concentration in the air	
$\rho_{Py}^{rock}$	: density of pyrite within the blocks	
$\rho_w$	: density of water in the spoil	
$\phi$	: porosity	240, 265, 276
$\phi$	: inter-block porosity of the dump	352
$\phi_a$	: air-filled porosity of the spoil	
$\phi_i$	: any of the dependent variables of phase $i$	
$\phi_R^L$	: porosity of waste particles	
$\phi_w$	: water-filled porosity	

$\Gamma_{\phi_i}$	: diffusive exchange coefficient for solved variable $\phi$ in phase $i$	
$\lambda$	: reaction skin depth	
$\sigma_a$	: molar density of air	
$\tau$	: dimensionless time	99
$\tau$	: tortuosity of diffusion passage way	238, 360
$\tau_c$	: time for complete oxidation of pyrite if the oxidation reaction is controlled by surface reaction	
$\tau_D$	: time required for full oxidation of pyrite in diffusion controlled reaction	
$\omega$	: an empirical constant is used to calculate the effective diffusion coefficient for a ion	
$\mu_g$	: viscosity of air	
$\nu$	: number of particles per unit volume of the dump	
$\delta$	: effective thickness of the fragment in which pyrite is oxidised	
[ ]	: activities in solution	392

## ABBREVIATIONS

<i>A.O.D</i>	: above ordinance datum
<i>AMD</i>	: acid mine drainage
<i>ARD</i>	: acid rock drainage
b. c.	: boundary condition
<i>CEC</i>	: cation exchange capacity
<i>CFD</i>	: computational fluid dynamic
<i>CHAM</i>	: concentration heat and momentum Ltd
<i>C.T.E (Cte)</i>	: constant
<i>EC</i>	: electrical Conductivity
<i>EWA</i>	: equivalent well approach
<i>FD</i>	: finite difference
<i>FE</i>	: finite element
<i>FV</i>	: finite volume
<i>IAP</i>	: ion activity product
<i>Ligand</i>	: atoms or groups bound to a central atom in a polyatomic molecular entity are called ligands.
<i>MREMP</i>	: mine rehabilitation and environmental management plan
<i>Oxd</i>	: oxidant
<i>PALD</i>	: passive anoxic limestone drains
<i>PHOENICS</i>	: a general-purpose CFD package developed by CHAM (2000) which can be used for simulation of fluid flow, heat transfer, mass transfer and associated chemical reactions
<i>pH</i>	: negative logarithm of the hydrogen ion concentration in a solution
<i>PIL</i>	: PHOENICS input language

<i>POLS</i>	: a computer program for acid mine drainage simulation developed by Jaynes et al. (1984a, b)	
<i>SEEP/W</i>	: a finite element commercial software developed by Geo-slope International Ltd. (Geo-slope International Ltd., 2002) which can be used for simulation of seepage problems.	
<i>SI</i>	: saturation index	
<i>SS</i>	: suspended solids	
<i>TDS</i>	: total dissolved solids	
<i>TSS</i>	: total soluble salts	
<i>tiny</i>	: a very small real number	
[ ]	: concentration operator	419
[[ <i>M</i> , <i>N</i> ]]	: a operator defined as the greater of <i>M</i> and <i>N</i> , by implying the upwind scheme	

## **CHAPTER ONE**

# **GROUNDWATER PROBLEMS ASSOCIATED WITH ABANDONED OPEN CUT COALMINES**

## **CHAPTER ONE**

### **GROUNDWATER PROBLEMS ASSOCIATED WITH ABANDONED OPEN CUT COALMINES**

#### **1.1 Introduction**

The depletion of shallower deposits has led to a considerable increase in the economic working depth of open cut coalmines. As a consequence many surface coalmine operations are now being carried out below the groundwater table. This in effect can create a number of water related problems affecting the design and economic viability of the mining operations. Groundwater inflow from the surrounding strata towards the mining excavation will require installation of large scale dewatering facilities to lower the water table and create an extensive and prolonged cone of depression. Coalmine abandonment, cessation of dewatering, groundwater rebound and associated pollution issues are considered to be a serious problem in mining throughout the world. If the effects and magnitude of a water related problem can be identified in advance of mining, appropriate water management strategies to minimise the socio-economic and environmental impact of mine dewatering often can be efficiently incorporated into the mine plan. To design an effective drainage scheme for a surface mine, prediction of water inflow into a mine excavation during the feasibility stage of a large surface mining operation is a major task.

Dewatering of surface mines during mining operations causes a considerable hydrological stress on the regional groundwater flow system around the mine. Therefore, in many open cut mining sites when mining is completed and the dewatering operations have ceased, the water table will return to its equilibrium level as was prior

to the commencement of the mining operation. Groundwater covers the spoil containing oxidised pyrite and other oxidation products and may be contaminated. Hence, prediction of the post mining water table elevation within the mine spoil is an important consideration for the addition of alkaline material and for applying special handling techniques for neutralising purposes. In addition, it has now become mandatory in NSW to develop a Mine Rehabilitation and Environmental Management Plan (MREMP) during the design stage of an open cut mining operation.

This chapter contains brief reviews of the methods of surface coal mining, groundwater inflow and post-mining groundwater rebound problems and associated environmental pollution problems in open cut coalmines.

## **1.2 Surface mining methods**

Australia is one of the largest producers of coal and is currently known as one of the greatest coal exporting countries in the world. Historically, surface mining operations in Australia are competing not only with other mining methods internationally but also domestically. Underground mining operations are considered to be another competitor. Nearly all of the horizontal and shallow deposits have been extracted during the last two decades and new surface mining methods must be used to extract deeper coal deposits. It is well recognised that the deeper mines involve more complicated geological conditions and are faced with more difficult geotechnical and hydrogeological problems, often involving multi-seam operations.

### **1.2.1 Surface mining operations**

The major surface mining operation methods can be briefly classified as:

### (a) Strip mining

This mining method is used in extracting relatively horizontal deposits in which the overburden and the deposit are relatively thin. In this technique surface material is removed to expose a coal seam or a mineral deposit. The removed overburden materials are then placed into the void created by the previous mining operation, employing a walking dragline, stripping shovel or a bucket wheel excavator with a boom stacker. When a dragline is used for stripping overburden, the dragline bucket is dragged up the face of the highwall until it is filled with the overburden and hoisted up clear of the bench. The dragline upper structure is then rotated through 90 degrees and the overburden is then dumped into the space left by the previous strip. Thus the ore body or coal seam is exposed which is then extracted by a truck and shovel operation. Figure 1.1 shows a diagrammatic plan of a typical strip mine. The strip mine shown here has two inclines plus haul road access at each end of the cut. Highwall access to the drilling and dragline operation is illustrated at intervals of 450 metres. This interval is selected so as to be equal to the power cable lengths to make the handling easier. The mining operation is extended from the right to the left side. The position of the dragline, loading shovel, spoil piles and highwalls can be easily identified in Figure 1.1.

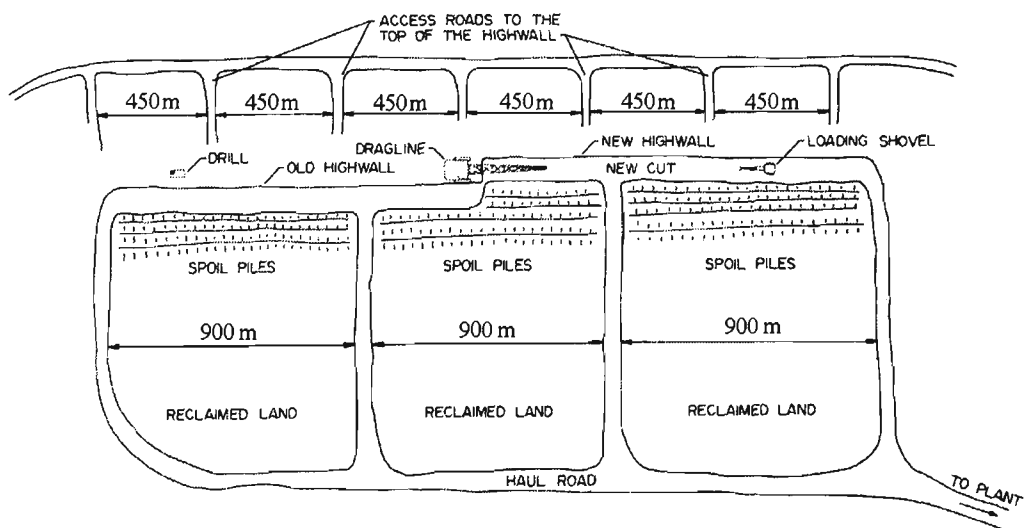


Figure 1.1. Diagrammatic plan of a typical strip coal mining operations  
(after Bucyrus-Erie Co., 1977).

### **(b) Lateral- advance, multi- bench mining technique**

This method is used where the deposit is relatively horizontal and the overburden is too thick to allow direct casting. The overburden materials are transported round the excavation and backfilled in the void left by former mining operations using round-the-pit conveyors, rails or trucks (Atkinson, 1976).

### **(c) Conical open pit mining operation**

The term open pit mining is traditionally applied to metalliferous mining where multiple benches are employed to extract the ore deposits at depth. This term is sometimes used for all non-dragline operations in Australian coalmines (Kukla et al., 1986). The method is usually employed for mining irregular deposits, pipes, stock works and steeply inclined stratified deposits (Atkinson, 1976). Open pit mining (Figure 1.2) has seen a little change in size over time, but the mine design system has not changed considerably (Atkinson, 1982). The pit is often excavated by truck/shovel operations. In deep pits inclined or vertical skip haulage is usually employed from selected levels (Atkinson, 1976).

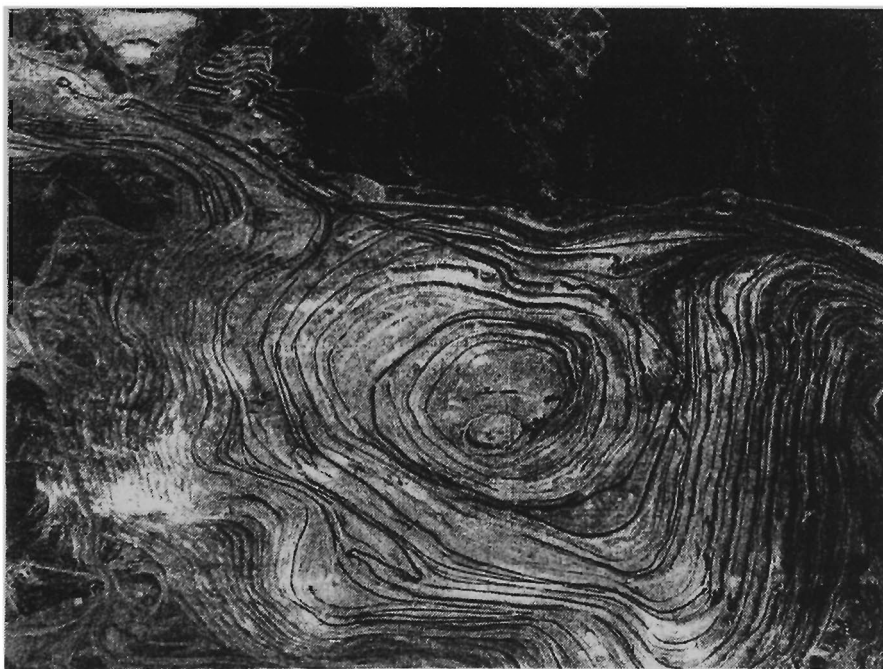


Figure 1.2. A typical open pit mine with rail haulage (after Kennedy, 1990).

### **1.2.2 Basic factors in selecting the mining methods**

The major parameters that control the choice of mining technique between open cut mining and underground operations are:

- a) Cost of mining
- b) Recovery of ore deposits and
- c) Dilution

In a surface mining operation, mining cost mainly consists of the cost of removing the waste materials including overburden and waste in the pit slopes. The ratio of waste material to ore is an important factor in determining the mining costs and then in selecting the mining methods (Soderberg and Rausch, 1968).

### **1.2.3 Effective parameters in selecting the strip mining methods**

The following factors must be evaluated before selection of open cut methods:

- 1) The size and the geometry of the ore deposit
- 2) The nature of the overburden
- 3) The significance of hydrogeological aspects of the formations.
- 4) The significance of geological structures such as folds, faults and shear zones
- 5) Consideration of the chemical and physical conditions of the overburden

In the selection of the stripping method primary parameters such as the type of overburden material, size of project, volume per day and kind of power system at the mine site must exactly be considered (Moolick, and O'Neill, 1968).

## **1.3 Removal of the overburden**

The overburden has to be removed to expose the ore body. Different type of machines can be used for overburden removal. In nearly all of the main strip mines in Australia, draglines have been used as the most suitable machine for overburden removal. Of

course, in many cases depending on special conditions, other stripping equipment such as scrapers, trucks, or bucket wheel excavators have been employed (Isles et al., 1986).

#### **1.4 Back fill replacement methods**

Removed overburden materials are commonly placed into the mine void. This technique is called back filling of waste materials (Reed, 1986). Generally back filling techniques are carried out by one of three different methods or a combination of these methods (Reed et al., 1987):

- 1) Dragline methods
- 2) Shovel and truck operations
- 3) Ripper and scraper techniques

##### **1.4.1 Dragline methods**

In Australia, especially in N.S.W since 1980 there has been an important growth in the use of dragline operations rather than other surface mining methods. In the past two decades, the walking dragline has become the preferred machine for overburden removal in surface coalmines in Australia, because of deeper digging capability, flexibility in operation and relatively lower operating costs (Atkinson, 1982). In many of Australian strip mines, draglines are encountering different geological conditions than those in other mining areas of the world. Many dragline operations in Australia are employing innovative digging techniques to overcome these more complicated geological conditions and to improve the machines capabilities to maximise the reach and dump height. Due to the presence of thicker overburden most Australian strip mines have wider pits, typically 60- 80 m, for the purpose of reducing rehandle and to avoid both spoil and high wall failures.

Draglines normally sit on top of the overburden bench while stripping overburden to expose the coal seam and cast the overburden directly into the void created by the former cut without using an auxiliary haulage system (Moolick and O'Neill, 1968). For a detailed discussion of dragline operations the readers are referred to Bucyrus-Erie Company (1977) and Mirabediny (1998). Figure 1.1 on page 3 shows the plan view of a surface mining method using a dragline operation system while Figure 1.3 shows a cross section of a typical dragline operation. It illustrates the position of the dragline sitting on the highwall for maximum reach, it also shows the shape and size of the proposed cut (cut A), and the shape and size of the resulting spoil pile (spoil A). Thus, a dragline digs and removes the overburden and places it on a spoil pile A (Figure 1.3).

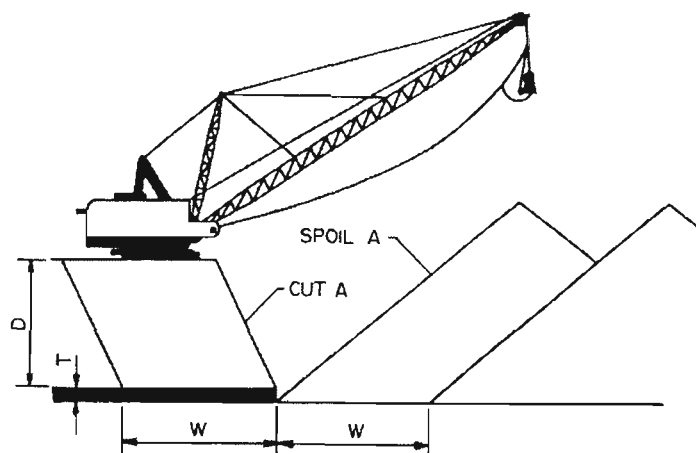


Figure 1.3. Diagrammatic illustration of surface mining operation using dragline,  $D$ , is the overburden depth,  $T$ , is coal thickness and  $W$  is the pit width (after Bucyrus-Erie Company, 1977).

#### 1.4.2 Shovel and truck operations

In this system waste material is generally loaded into trucks by excavating shovels (see Figure 1.4). It is then transported out of the pit and is finally dumped in a temporary spoil heap or end-tipped over the edge of the advancing loose wall (Reed et al., 1987). In Australia, especially in the many mine sites of N.S.W where the dragline usually operates in the lower sequence of the mine, these methods are generally employed to

remove upper over-burden and inter-burden horizons. This kind of operation has been used where the strip mines have become deeper and in more complex geological conditions (Isles et al., 1986).

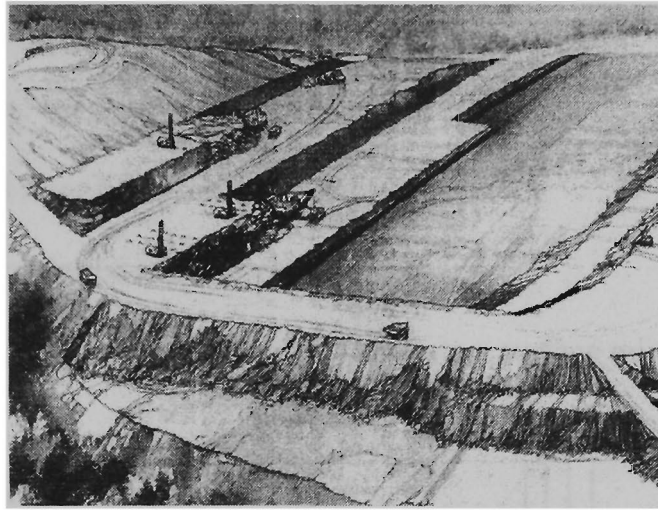


Figure 1.4. Schematic diagram showing shovel and truck operation system (after Kennedy, 1990).

#### **1.4.3 Ripper and scraper operations**

Scrapers have been used in a few strip mining operations for stripping and exposing the ore deposit. They are generally used in conjunction with draglines for pre-stripping in deeper areas and in the vicinity of haulage ramps. Hence, the dragline's stripping efficiency is significantly increased (Isles et al., 1986).

#### **1.5 Water inflow into a surface mine**

Estimation of water inflow into a surface mining operation is a most important task in designing the mine drainage system (Singh and Reed, 1987). Furthermore the prediction of water inflow is a necessary aspect of assessing the long-term hydrological impact and provides useful information for environmental studies (Naugle and Atkinson, 1993). The water inflow sources into a surface mining operation are given as follows (Reed, 1986):

- a) Water inflow due to atmospheric precipitation and percolation through the backfill in a surface mine.
- b) Water inflow from underground aquifers and mineral beds.
- c) Water inflow due to geological structure including discontinuities such as folds, faults and shear zones.
- d) Inflow through pit floor heave and/or piping
- e) Inflow through abandoned mine workings.

Figure 1.5 shows various sources of water inflow into a surface mine:

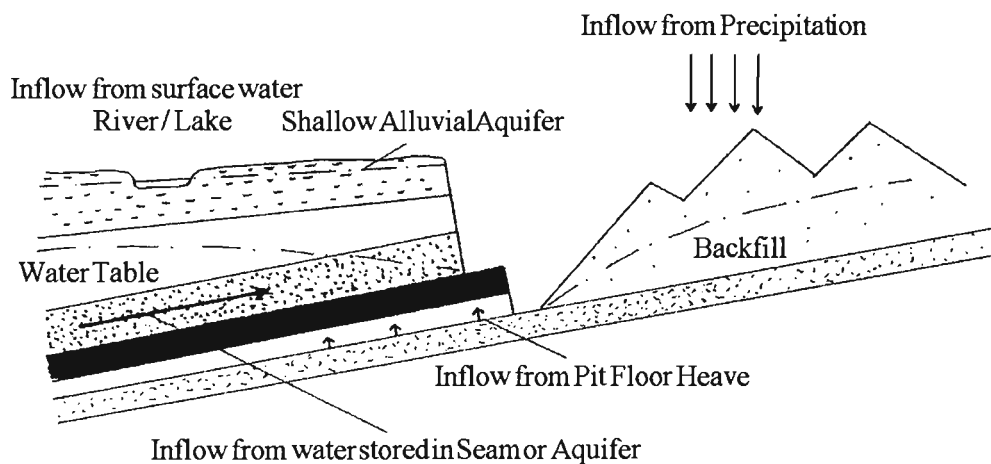


Figure 1.5. Various sources of water inflow to a surface mine (after Reed, 1986).

## 1.6. Environmental impacts of surface mining operations

Different methods of surface mining operations generate wastes that can affect surface and groundwater quality. Surface runoff from strip mines with a high concentration of dissolved minerals may discharge directly into surface streams or rivers and chemically pollute them (Stiefel and Busch, 1983). The removal of overburden to expose an underlying ore deposit changes not only the natural shape and state of layers but also affects the whole ecological balance of the site (Reed, 1986). Not all surface mining wastes are detrimental to the groundwater and surface water. However, there are some contaminants in mine wastes that are considered to be beneficial for these water

resources. The following factors play a basic role in determining the extent of pollution in surface mining area:

- a) Type of mine waste
- b) Location of waste materials
- c) Climatic conditions
- d) Restoration method
- e) Condition of foundation
- f) Regulatory requirement (Bohnet and Kunze, 1990)

The problem due to surface strip mining operations may be considered with respect to the surface environmental problems as outlined below:

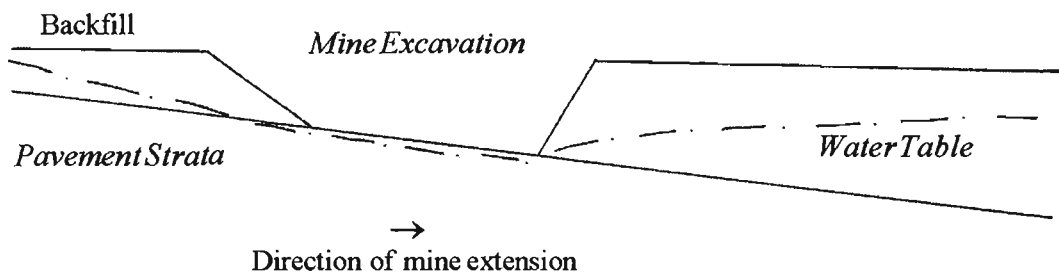
- a) Degradation of land
- b) Groundwater and surface water pollution
- c) Air pollution
- d) Vibrations due to blasting
- e) Noise pollution (Reed, 1986)

However, many regulations for controlling these environmental impacts already exist.

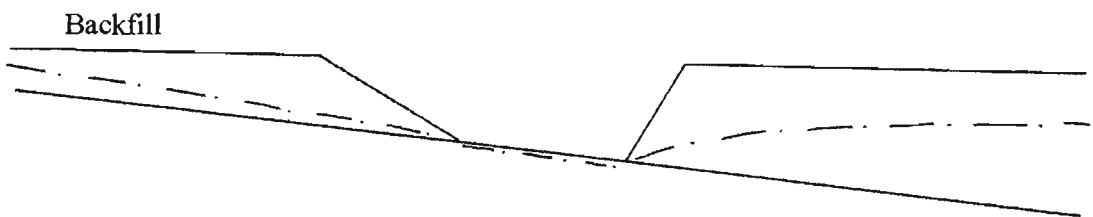
The present author considers in this thesis groundwater inflow, rebound and subsequent pollution problems in a backfilled open cut mine site.

### **1.7 Groundwater rebound**

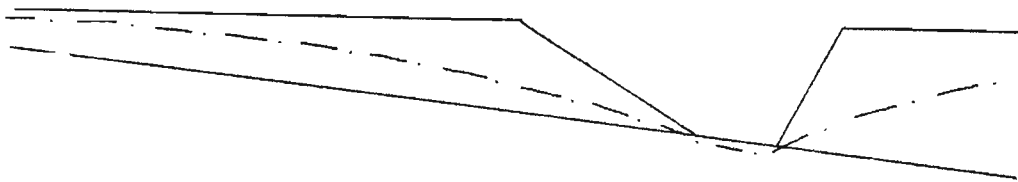
Dewatering of strip mines during mining operations causes a considerable hydrologic stress on the regional hydrologic system. (Naugle and Atkinson, 1993). Therefore, once pumping has stopped and the mine has been backfilled, the water level will return to its equilibrium position or original level prior to mining operations. Figure 1.6 shows a general sequence of groundwater rebound.



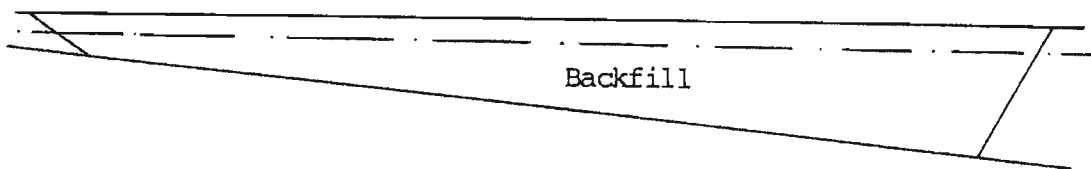
1) Advancing down-dip surface mine. Groundwater table depressed by dewatering.



2) Groundwater rebounds within backfill as mining operation progresses.



3) Mining operation approaches completion, water table recovering through backfill.



4) Groundwater rebounds to its equilibrium level after mine closure.

Figure 1.6. The stages of groundwater rebound (after Reed and Singh, 1986).

### **1.7.1 Groundwater rebound and pollution problem**

As already mentioned, many of the opencast mining operations, once they are completed and dewatering has ceased the water table will then return to its initial levels. Where the groundwater covers backfill materials containing pyrite, it becomes contaminated. In many cases the process of groundwater recovery results in springs which may contain ferruginous and acidic water (Norton, 1983). In addition to backfill materials, topography, climate, geological discontinuities and the level of groundwater below the ground surface may affect the amount of groundwater contamination (Bohnet and Kunze, 1990). Backfill wastes show more porosity and high permeability hence groundwater can easily pass through them and become contaminated. Opencast backfill after dumping becomes weathered and is susceptible to oxidation because oxygen can easily flow through the voids of the fill material. Therefore, there is no doubt that pyritic minerals in the wastes will decompose to contribute to groundwater contaminants (Norton, 1983).

### **1.8 Surface mine dewatering**

Dewatering is an effective method for controlling water flow entering a surface mining excavation. Once a surface mine intersects the initial groundwater table, groundwater flow occurs towards the excavation, hence dewatering is necessary. The dewatering process produces a cone of depression in the vicinity of the mining excavation and reduces the hydraulic gradient in the aquifers, increases the slope stability and controls mine excavation flooding (Nghah, 1985). A hydrogeological investigation of the mine site is necessary to design an appropriate dewatering technique. Collection of hydrogeological data such as the coefficient of permeability, storage coefficient and previous groundwater flow regime are all main factors in designing appropriate

dewatering techniques (Singh, 1998). There are various dewatering techniques for surface mines. In general, these methods may be divided into two groups:

### 1.8.1 Passive dewatering method

In this method a sump is excavated at the bottom of the mining excavation and the groundwater is generally allowed to enter the sump, from where it is eventually pumped to the surface. In this passive technique a submersible or a skid-mounted centrifugal pump using a diesel engine or electric motor is usually employed (Figure 1.7). This method can be used for many mines where small amounts of groundwater are expected and for controlling surface runoff and direct precipitation entering the pit (Norton, 1983).

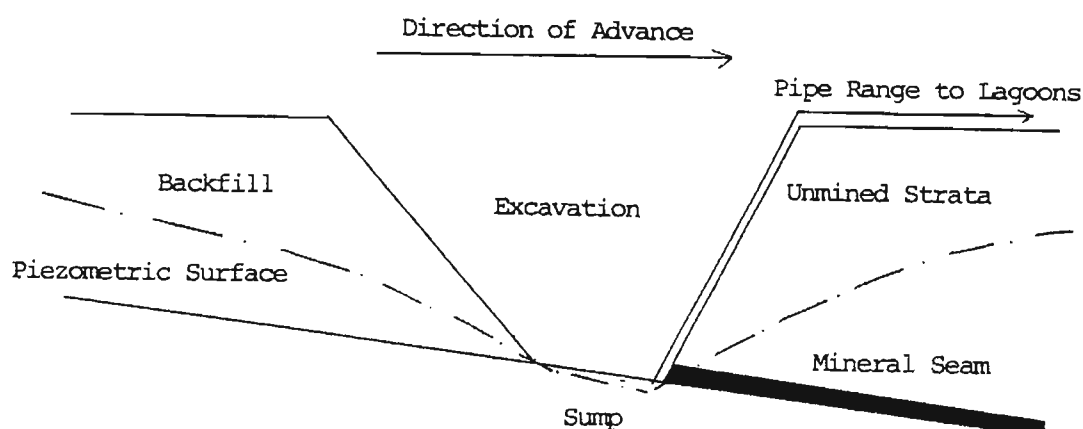
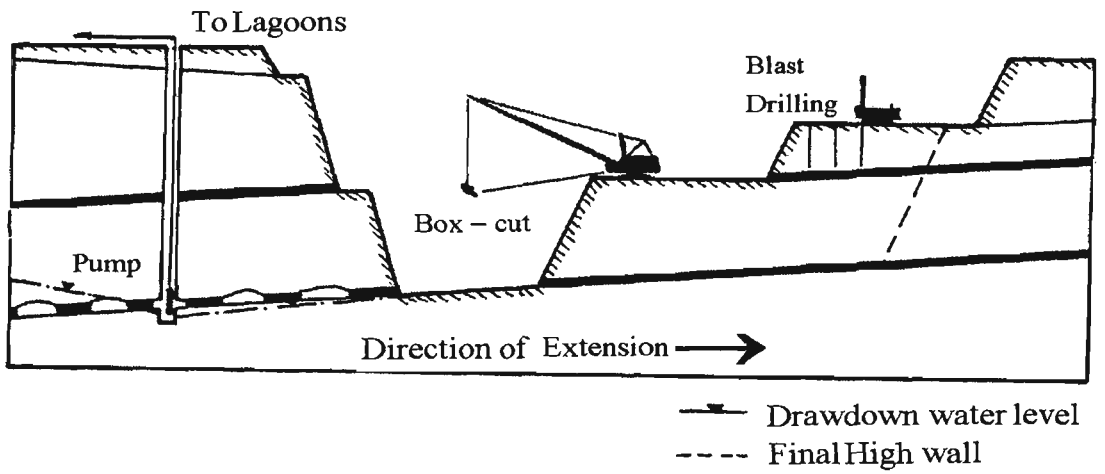


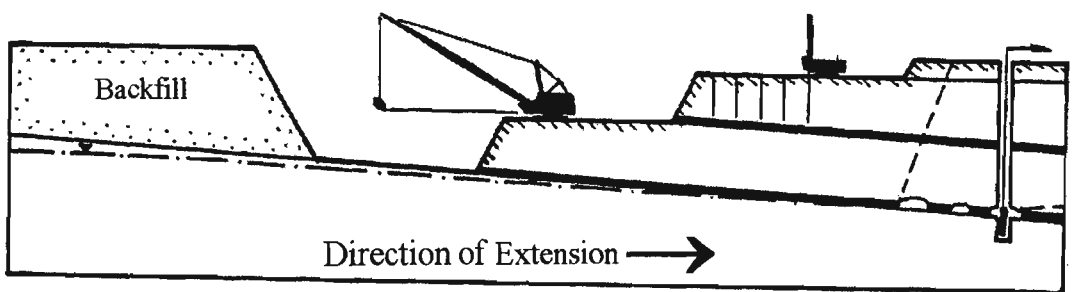
Figure 1.7. Sump pumping (after Reed, 1986).

### 1.8.2 Advance (Active) dewatering technique

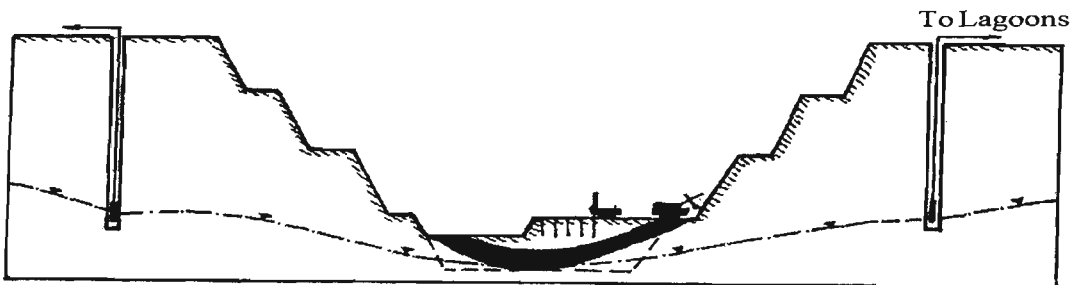
In this technique electrical submersible pumps are installed in vertical boreholes drilled within the geological formations around the perimeter of the mining excavation (Norton, 1983). The crucial task of the technique is to maintain the water table draw down in advance of the mine excavation level. This technique is successfully used in surface mine sites where a large amount of groundwater inflow into the excavation is expected (Figure 1.8).



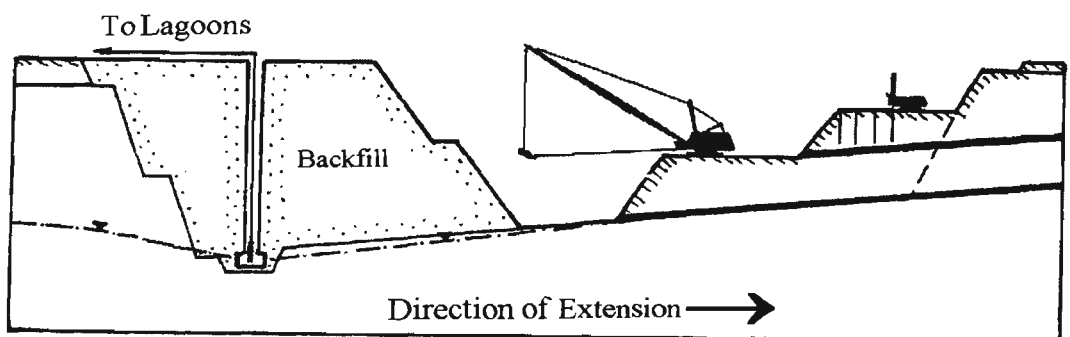
(a) Box-cut and retreat (up-dip) mining



(b) Shallow down-dip mining



(c) Open pit mining



(d) Up-dip mining, pump installed in backfilled box-cut area

Figure 1.8. Advance Dewatering methods in different surface mining situations (after Norton, 1983).

## **1.9 Review of research associated with groundwater modelling in open cut mining**

The inflow prediction models are characterised as follows:

### **(i) Analytical model**

- Equivalent well approach model (Singh and Atkins, 1984; Singh and Atkins, 1985a; Singh and Atkins, 1985b; Singh et al., 1985; Vandersluis et al., 1995; and Lewis, 1999)
- Two dimensional model (McWhorter, 1981)

### **(ii) Numerical model (Azrag et al., 1998)**

### **(iii) Combined models**

- Combined numerical and analytical model (Hanna et al., 1994)
- Combined two-dimensional and equivalent well approach model (Singh and Reed, 1987)

It may be noted that these models for prediction of inflow rate into the surface mining excavations range from a simple analytical solution to relatively complex numerical models.

### **1.9.1 Inflow models**

Singh et al. (1985) presented the appropriate simple analytical equations for prediction of inflow under various flow regimes and different aquifer conditions. These equations are based on the equivalent well approach. However, these analytical solutions are based on some assumptions, and special boundary conditions limit their applicability in different mining situations and they are not as versatile as numerical methods which deal with complex mining situations. Furthermore, the equivalent well approach

assumes that the mining excavation is a large diameter well. This assumption is not reliably applicable to surface mining operations with relatively complex geometry.

Singh and Reed (1987) reported several two-dimensional analytical solutions for predicting groundwater inflow into a surface mine excavation. Based on this approach, the inflow regime is essentially assumed to be two-dimensional. These equations assume linear flow far from the mine, and take into consideration that in the close proximity of the mining excavation the assumption of linear flow is not valid and the vertical component of the flow is more dominant. Incorporating this situation into analytical solutions make them more reliable and applicable for predicting inflow quantity into a surface mine excavation. These equations, however, are not appropriate for all mining situations and under some specific conditions such as those near the seepage plane and in the region of a vertical impervious boundary the simplified flow assumptions can predict unrealistic results.

Rubio and Lorca (1993) categorised different types of inflow behaviour into mine workings in different parts of the world as follows:

- (a) Constant rate of inflow
- (b) Rate of inflow following a Gaussian distribution
- (c) Rate of inflow increasing with time as the mine extends
- (d) Rate of inflow decreasing with time as the finite source aquifer dries up
- (e) A mine displaying mixed rates of inflow

This is described in details in Chapter 3, Section 3.3 on Page 72.

Lewis (1999) presented an analytical equation based on well hydraulics for estimation of steady state inflow rate to an open pit mine. Lewis (1999) suggested that a limitation of analytical solutions derived from well hydraulics for groundwater inflow is to assume an initially flat potentiometric surface for the aquifers. These equations do not take into account the passive component of groundwater inflow. Incorporating the passive component of inflow is very important for an accurate prediction of the inflow quantities into a mining excavation in order to design an appropriate dewatering system. An equation was developed to take into account the passive inflow to an ideal fully penetrating pit in a uniform flow field. The analytical equation presented by Lewis (1999), however, is unable to predict the transient groundwater inflow into a surface mining excavation.

Vandersluis et al (1995) presented an analytical equation for estimation of horizontal groundwater inflow rate into a pit in an unconfined aquifer. This equation calculates the inflow using large well equations based on the Dupuit assumptions for lateral, radial steady state flow into a fully penetrating well. This equation is only applicable in arid and semi-arid areas where precipitation is generally limited and water inflow to a pit is normally controlled by the horizontal groundwater inflow rates.

Hofedank (1979) presented an analytical equation previously developed by Hantush and Jacob to calculate groundwater leakage to a lignite opencast mine. This equation was based on an analogy between an assumed circular pit and a large diameter well. The equation assumes that the pit fully penetrates an aquifer. The aquifer has an infinite areal extent and transmissivity and storativity are assumed to be uniform. Brown (1979) also used this equation for prediction of inflow to underground oil shale mines.

McWhorter (1981) applied the concept of the steady state flow approach to develop an analytical equation for the prediction of groundwater inflow to a surface mine excavation from a confined aquifer. This method assumes that the variation of piezometric head with time corresponds to the steady state instantaneous draw down affected by a particular rate of groundwater inflow to the excavation. It was also noted that incising the confined aquifer during mining causes the aquifer to become unconfined near the excavated face while remote from the mine the aquifer remains confined. Considering that the confined aquifer will become unconfined near the mining excavation, it is necessary to assume that the storage coefficient applied to the unconfined zone of the aquifer is much greater than that which is used in the confined zone. The advantage of this method is that it takes into account the effect of time and face advance on the predicted inflow quantities. However, the predicted inflow would be much larger in the initial stages of mining because the entire pit is not established instantaneously. Furthermore, this approach assumes that flow occurs only in planes normal to the long axis of the advancing pit while the actual flow in the plan view will be two-dimensional. Moreover, the discharge to the pit through the ends is not considered in this method and it is assumed that the length to width ratio is large.

Most analytical solutions do not directly account for the amount of inflow taking place through the bottom of the mining excavation. Although the analytical solutions developed by Marinelli and Niccoli (2000) take into account the upward flow through the bottom of the mining excavation; however, the solutions assume an equivalent porous medium and are based on many simplifying assumptions. Hence their analytical solutions are not appropriate for all hydrogeological situations.

On the other hand, numerical models are powerful tools used to simulate all aquifer conditions and to provide a more realistic representation of the interaction between groundwater systems and mining excavations. Many numerical models are limited in their ability to represent the variable height of the seepage faces and cannot easily model various aquifer conditions such as saturated/unsaturated flow, confined/unconfined flow and non-linear hydraulic characteristics of the porous medium. Hanna et al (1994) developed a three-dimensional finite element groundwater model for prediction of groundwater inflow but it has been limited to an idealised open pit. Azrag et al. (1998) developed a finite element code called MINEDW. This particular code includes subroutines to calculate the height of the seepage face in a pit wall, simulate faults, model pit infilling and to predict groundwater inflow to underground drifts. However, this particular code has not been developed for simulation of groundwater inflow problems in backfilled open cut mines.

In order to overcome some of the limitations of the existing models, there is a need to develop a new numerical inflow prediction model for open cut mines dealing with the following characteristics:

- (a) Saturated/unsaturated flow conditions
- (b) Confined/unconfined aquifer systems
- (c) Steady state/transient conditions

This model should be able to specify different boundary conditions. Furthermore, the excavation of a surface mine should be easily simulated by removing elements and nodes. Moreover, the model should have the capability to calculate the height of the

seepage faces of the mining excavation taking into account the hydraulic conductivities and the water content as a function of pore water pressure.

### **1.9.2 Rebound models**

Prediction of the post-mining groundwater rebound is also noted to be an important task in order to control the quality of mine drainage in a backfilled open cut mine operation. Numerical groundwater flow models can provide an approach to simulate groundwater rebound after cessation of mining operations.

#### **(a) Rebound models for backfilled sites**

Many research workers have carried out research in relation to groundwater rebound problems in open cut coalmines (Henton, 1981; Norton, 1983; Reed, 1986; Reed and Singh, 1986; and Davis and Zabolotney, 1996).

Problems of groundwater rebound after the cessation of mining activities and the subsequent effects on the quality of ground and surface water have been highlighted by Henton (1981). It was concluded that the real source of the pollution problem is not with the pumped mine waters but with the natural discharges that occur when a coalmine has been abandoned and the groundwater is allowed to rebound to its equilibrium level.

Norton (1983) and Reed (1986) observed groundwater rebound and monitored settlement at the Horsley backfilled site located about 15 kilometres to the west of Newcastle-upon-Tyne in Northumberland and a shallow backfilled site in the East Midlands area at Nottingham, both located in the United Kingdom. It was proved that a

major factor of opencast backfill settlement is due to the recovery of groundwater when the mining operation has ceased. Groundwater rebound is, however, the main cause of ground and surface water pollution. It was suggested that the most obvious method of minimising groundwater pollution is to seal the backfill material by inundation and therefore prevent access of air to the backfill void material.

Davis and Zabolotney (1996) developed a groundwater flow model to simulate the post-mining recharge rate from precipitation at the Belle Ayr surface coalmine. The model predicted a post-mining recharge rate of 0.05 metres per year exceeding the pre-mining recharge rate to aquifers at the Belle Ayr Mine which was about 0.04 metres per year due to the lowered permeabilities of backfill materials. A sensitivity analysis showed that transmissivity was the most sensitive parameter affecting the modelling results.

#### (b) Pit lake refilling models

The formation of lakes in abandoned open pit mines and the simulation of the post-mining filling of pit lakes has become an important topic to many modelers, including Naugle and Atkinson (1993); Vandersluis et al. (1995) and Shevenell (2000).

Naugle and Atkinson (1993) developed a numerical groundwater model predicting the post mining filling of open pit mines. The calculations were based on the planned pit-dewatering activities and the available geological and hydrological data. The model was first verified with analytical solutions for a simplified hydrological problem and then applied to a more complex case. The results indicated that the pit lake would recover to about 99% of the pre-mining groundwater level after approximately 75 years. Although the numerical model cost-effectively and successfully simulated post-mining recovery, it has been limited to open pit mines.

Vandersluis et al. (1995) predicted the rate at which a pit lake forms and the groundwater rises to its equilibrium level after the cessation of mining using a simple analytical method and a spreadsheet program. The model takes into consideration inflow to the lake by direct precipitation on the lake surface, surface runoff from the pit watershed, and horizontal groundwater inflow from bedrock as well as outflow from the lake which occurs by means of evaporation and seepage. Outflow by seepage only occurs when the pit lake surface level approaches its pre-mining equilibrium level.

Shevenell (2000) used an analytical model to estimate the rate of pit lake filling and groundwater fluxes into the lake with particular reference to the Getchell Mine, Nevada, USA. An analytical spreadsheet method was used for the modelling of pit lake filling. A volume-stage relationship was computed for the filling calculations. Based on this analytical model, it was concluded that an assumed decreasing net rate of inflow into a pit lake may be realistic in pit lake simulation.

It may be noted that the simulation of pit lake refilling is not a subject of this thesis.

Problems concerning groundwater flow in partially saturated porous media are relatively difficult to model for cases involving highly nonlinear ground characteristics. In particular, it is difficult to assign to the model the highly sensitive behavior of unsaturated field variables such as hydraulic conductivity, specific storage and atmospheric boundary conditions associated with the seepage face, infiltration and evaporation. Predicting the configuration of the ground water table and the height of the seepage face in surface mine high walls for slope stability analysis is also very important. Estimating the groundwater rebound in backfilled open cut mines is amongst the more complex problems encountered in mining operations.

Due to the limitations of the most common groundwater flow codes used in dealing with these problems, more work is needed to develop a numerical model incorporating saturated/unsaturated and confined/unconfined flow conditions in order to predict post mining groundwater rebound within the spoil of an open cut mine.

### **1.9.3 Pyrite oxidation and acid leaching models**

Acid mine drainage is probably the worst of the environmental problems and clearly poses a serious unfavourable impacts for receiving waters (Gray, 1998). Acid generation from some abandoned coalmines has caused great concern in the UK and acid drainage discharged from abandoned mines has been the main cause of freshwater pollution in central Scotland (Norton, 1983). Furthermore acid mine drainage at inactive mine waste areas in North America (Walter et al., 1994a, b) and from abandoned coal strip mines in the humid eastern United States (Jaynes et al., 1984a, b) has again been a serious problem. Acid mine drainage is also a serious problem in Australia, at central western and north eastern regions of Tasmania, Captain's Flat and the Hunter Valley of New South Wales and Rum Jungle in the Northern Territory (Davis, 1983). Simulation of long-term pyrite oxidation and the transportation of oxidation products provides useful information which can be used for the design of efficient remediation programs.

Although considerable effort has been made to model the pyritic oxidation and other sulphide minerals, the focus is mainly on the oxidation of pyrite and the generation of acidic leachate from waste rock dumps (Cathles and Apps, 1975; Cathles, 1979; Davis, 1983; Davis and Ritchie, 1986a; Davis et al., 1986b; Lefebvre and Gelinas, 1995). Further work by Elberling et al. (1994); Walter et al. (1994a); Walter et al. (1994b); Bridwell and Travis (1995); and Wunderly et al. (1996) is related to mine tailings discharge and is not relevant to the oxidation and transportation processes occurring in

abandoned open cut coalmines. However, there is little work reported in the literature quantifying the mechanisms that control the rate of pyrite oxidation and the subsequent leaching of the reaction products from open cut mines (Rogowski et al., 1977; Jaynes et al., 1984a,b). Hence there is a need to develop a model describing the long-term oxidation of pyrite and taking into consideration the physical and chemical transport processes involved in the migration of dissolved chemical species discharged from an open cut coalmine source into an aquifer.

Cathles and Apps (1975) described a one-dimensional model for oxidation and leaching processes which considers temperature dependence, oxygen balance and air convection effects. However, the model assumes air convection to be the main mechanism of oxygen transport through the dump in order to oxidise ferrous iron in the presence of iron oxidising bacteria. The leaching process takes place through the action of both chemical and diffusion controlled processes in which the sulphides are oxidised primarily by ferric ions. Such conditions may present a reasonable assumption for the mechanism occurring in coarse copper-waste dumps but they cannot be easily applied to open cut mine sites where the oxidation process is mainly controlled by gaseous diffusion of oxygen and the bacterial oxidation processes are not considered dominant.

Jaynes et al. (1984a, b) presented a model for pyrite oxidation and the subsequent leaching of the oxidation products from reclaimed open cut coalmines. Direct molecular oxygen oxidation and ferric iron oxidation were included in the model and it was assumed that pyrite oxidation is controlled by first order kinetics and the rate of diffusion of oxidant into the reaction particle. A one dimensional diffusion model was developed to supply oxygen into the reclaimed profile. Ferric iron was assumed to be produced by both the chemical and bacterial catalysed oxidation of ferrous iron.

Activity of the iron oxidising bacteria is controlled by the energy available from the ferrous-ferric oxidation reaction and from the energy substrate and the deviation of the bacterial environment. The complexation and precipitation of ferric iron and the reaction between  $H^+$  and the spoil matrix were included in the model. However, because of the one-dimensional nature of the model it was assumed that the oxidation products were removed from the reclaimed open cut mine by percolating surface water and the role of groundwater to transport the oxidation products was neglected. Furthermore, the interaction between the solid phase and dissolved species was not included.

Davis and Ritchie (1986a) and Davis et al. (1986b) developed a one-dimensional mathematical model for pyrite oxidation in waste rock dumps where diffusion of oxygen to the reaction sites is the rate-limiting factor. The modelling was carried out in a two-stage approach: first, the diffusion of oxygen into the pore space of the dump, and second, a shrinking core model to describe the diffusion of oxygen into the individual particles through the oxidised coating that forms around the unreacted core of the particles. The model is widely accepted and used. However, the role of bacteria in the oxidation of pyrite and subsequent transport of the oxidation products was not included.

There is therefore a need to develop a numerical model to predict long-term pyrite oxidation and the subsequent transport of the oxidation products from abandoned backfilled open cut coalmines. The model should incorporate complexation and precipitation reactions for ferric iron. A transient, advection, dispersion and molecular diffusion model, which includes the chemical reactions necessary for accurate calculation of the removal of the oxidation products, should be also developed. The model should take into consideration the linear and equilibrium ion exchange processes

for the main ions. The model should also be capable of taking into account the role of iron oxidising bacteria as well as sulphate reduction bacteria.

### **1.10 Need for further research**

The literature review thus far has indicated that the groundwater pollution problem associated with open cut coal mining has not been completely solved. In order to solve the pollution problem the aspects of groundwater inflow and groundwater rebound into the backfill material has to be considered before modelling groundwater pollution problems in open cut coal mining.

The main problem here lies with the formation of acidic water produced by oxidation of pyritic minerals present in coalmine spoil. This acidic water readily dissolves heavy metals producing salt and metal ion contamination of the receiving water. The effects of contaminated waters from such mining operations on the environment is a matter of grave concern. If other metal sulphides are associated with the pyrite, heavy metal transportation and contamination will result in long-term environmental pollution (Davis, 1983) due to the presence of dissolved salts of metals such as copper, manganese, and zinc. Although the oxidation of pyrite and its long-term effects on receiving water bodies continues after abandonment of mining operations, the best cost-effective management strategies are required in order to minimise the impact of the long-term acid and metal leaching problems.

There is therefore a need to understand and quantify the amount of groundwater inflow into an open cut mine during the mining operations, groundwater rebound when the mining operation has ceased and quantification of the processes involved in pyrite oxidation and related chemical reactions, subsequent metal solubilisation and

transportation. Mining engineers must find the best way for identifying, quantifying and understanding the mechanisms involved in the generation of pollutant materials and solute transport in the subsurface environment. Numerical contaminant transport models are valuable tools in assessing changes in groundwater quality after mine closure. A numerical model enables the prediction of future events. It may indicate which factors in a real system are most important from a sensitivity point of view. A model can help to design, optimise and predict the performance of field remediation and land reclamation programs. This research addresses the above problems and therefore the main objectives of this research are formulated in the following section.

### **1.11 Research objectives**

The objective of this research was to investigate hydrogeological systems affected by backfilled open cut coal mining operations. The amount of pollutants produced in a backfilled site can be reduced by using efficient reclamation techniques after cessation of mining operations. However, the assessment and development of best reclamation and management techniques in order to minimise the effect of mining on the hydrogeology of the area is a long-term and expensive procedure. The development of a numerical model that describes groundwater pollution potential and leaching from backfilled sites would facilitate the development of a mine rehabilitation and environmental management plan during the design stage of an open cut mining operation. In order to achieve this goal, the purpose of thesis is to develop the following three numerical models.

**(1) Inflow model:** The prediction of groundwater inflow into a mining excavation is very important for the design of an effective dewatering system during the mine

planning stage. Use of a numerical finite element model is required for predicting inflow of water into a surface mine workings. A two-dimensional numerical package, called SEEP/W has been used which has the capability to simulate saturated/unsaturated flow conditions and to allow calculation of the height of the seepage faces of the mining excavation taking into account the permeabilities and the water content as a function of pore water pressure.

**(2) Groundwater rebound model:** The two-dimensional numerical finite element model SEEP/W was also modified to predict the groundwater rebound within backfilled open cut mines after cessation of mining operations. This package has the ability to simulate groundwater flow problems in partially saturated porous media. This model calculates realistic results that can be used by mine operators and environmental engineers to control the mine drainage quality more efficiently and allows the design of mine drainage pollution prevention schemes for a backfilled open cut mining operation.

**(3) Long-term pyrite oxidation and subsequent transport model:** The primary objective of this thesis was to develop a numerical finite volume model (FV) using PHOENICS, as a CFD (Computational fluid dynamics) code to predict pollution potential with particular reference to the long-term oxidation of pyrite and transport of the oxidation products through groundwater flow systems contaminated by acid mine drainage (AMD) as a consequence of mining operations.

To validate the models presented in this thesis and in order to assess each model's accuracy, reference is often made to the field data monitored by Norton (1983) and Reed (1986) at the Horsley backfilled site located about 15 kilometres to the west of

Newcastle-upon-Tyne in Northumberland and the backfilled site 'A' in the East Midlands area near Nottingham, both located in the United Kingdom. The models of long-term pyrite oxidation and subsequent transport of oxidation products have been mainly verified using published analytical and numerical models. Sensitivity analyses of the models are also presented to assess and indicate how changes in some of the main input data for the models can affect the models predictions. A schematic diagram of the modelling approach is presented in Figure 1.9.

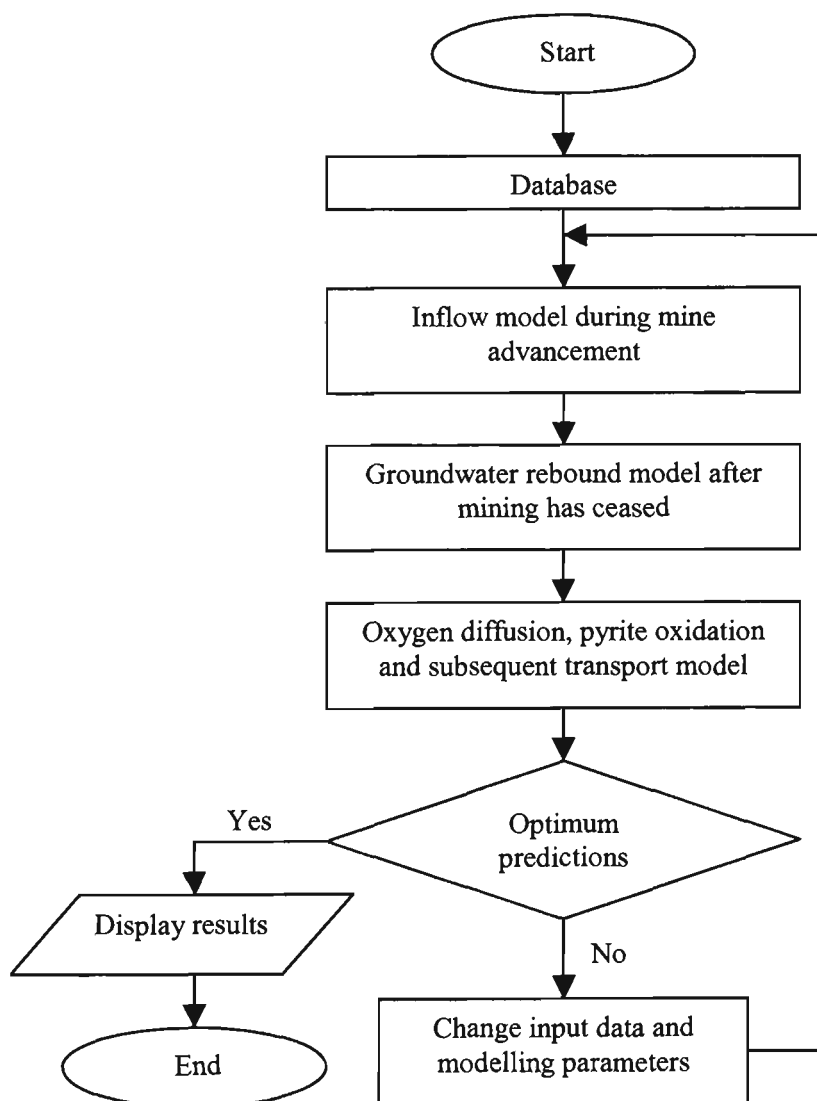


Figure 1.9. A flowchart of the modelling approach.

## **1.12 Research approach and program**

### **1.12.1 Research approach**

This thesis is presented in ten chapters. The flowchart of the arrangement of the thesis is shown in Figure 1.10.

- Chapter 1 presents the general purpose of the research, different types of surface mining methods and their impact on the environment, and also highlights the water inflow, groundwater rebound and pollution problems associated with open cut mining. The main aim of the first chapter is to show how the pollution problems arise in a backfilled site of an open cut mine.
- Chapter 2 includes physico-chemical characteristics of mine drainage. This chapter focuses on oxidation reactions and acid mine drainage generation and also discusses the effects of the relevant factors on the rate of pyrite oxidation. A summary of the different methods of acid mine treatment systems is also presented.
- Chapter 3 deals with a brief review of the analytical methods of prediction of groundwater inflow into open cut mines, including methods based on the equivalent well approach and the two-dimensional flow approach.
- Chapter 4 describes a two-dimensional finite element model used to simulate groundwater inflow and rebound within spoils of an open cut mine, taking into consideration the Galerkin approximation method for discretisation of the groundwater flow equation. Prior to modelling, a short description of the SEEP/W package, its features, applications and formulation is given. This chapter also includes the hydrogeological characteristics of the spoil.

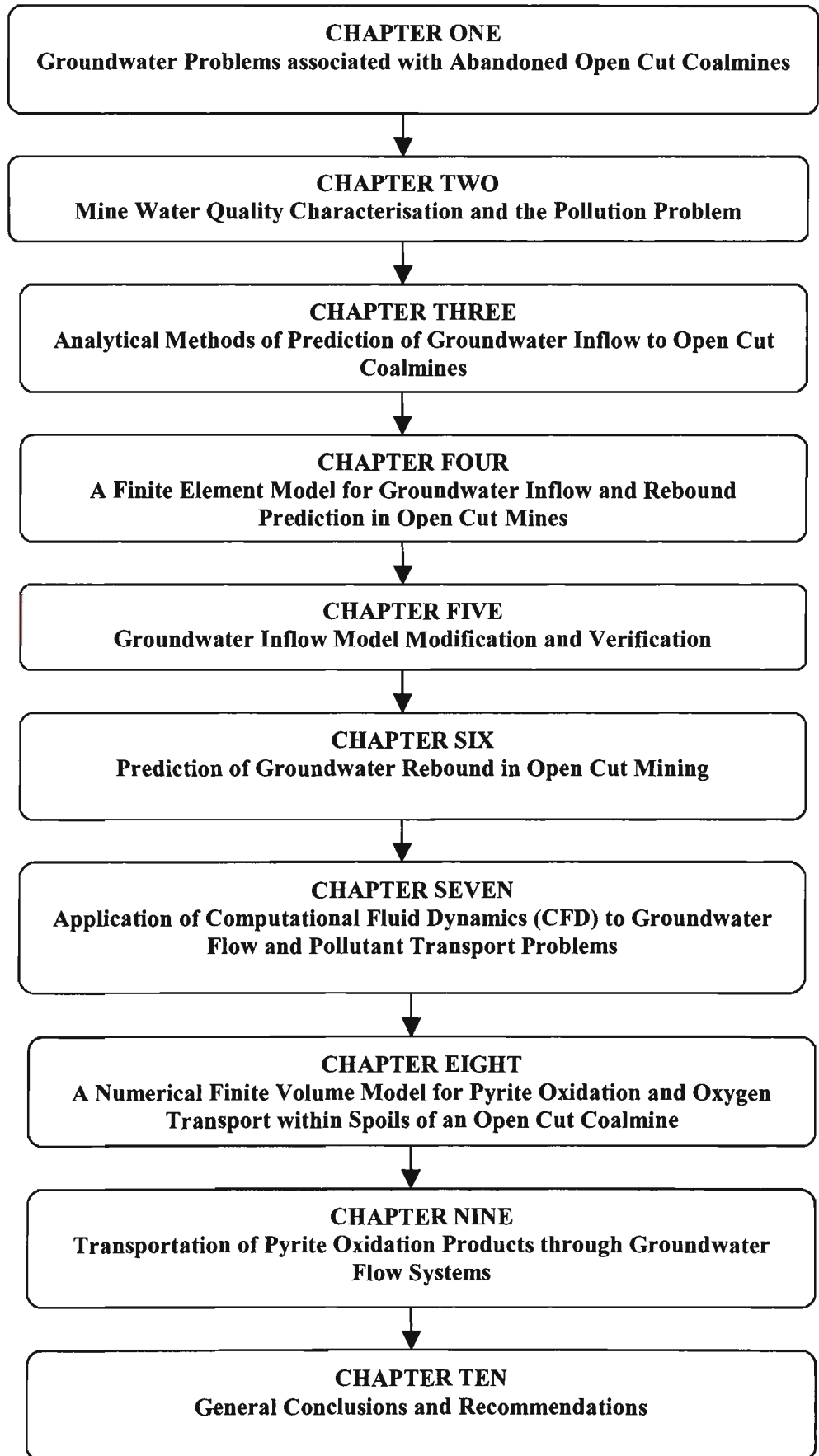


Figure 1.10. Structure of chapters in the thesis.

- Chapter 5 deals with the validation of the numerical modelling results for groundwater inflow. It presents the results of the analytical solutions and the previous numerical simulation results. A comparison is made with the present modelling results, which shows that the model is a reliable predictor of groundwater inflow into an open cut mine. Six problems have been selected for the verification of the model. Capabilities of the present model and inflow model development and specification of boundary conditions are also given.
- Chapter 6 gives a brief description of the finite element technique applied to groundwater rebound model application. The model is verified using analytical equations, published numerical models and the monitored field data observed by Norton (1983) and Reed (1986) at backfilled sites in the United Kingdom and the results are presented.
- Chapter 7 describes the general features of computational fluid dynamic (CFD) analysis, with particular reference to the fundamentals of the finite volume method (FV). This chapter covers a brief description of the features and application of PHOENICS as a CFD code. This chapter also provides basic information about finite volume discretisation of the governing differential equations of groundwater flow and contaminant transport.
- Chapter 8 illustrates a conceptual model for pyrite oxidation processes taking place in an abandoned backfilled open cut coalmine and details a two-dimensional finite volume model (FV) for the oxygen transport, heat transfer and pyrite oxidation processes. This chapter also gives the results of one-dimensional simulations of the pyrite oxidation and the pollutant transport in backfilled open cut coalmines. The results of the present model and comparisons

with a published model show that the model, based on the finite volume method and using PHOENICS as a CFD code is a reliable tool for assessing and predicting long-term oxidation of pyrite and acid generation within the spoil of an open cut mine.

- Chapter 9 gives the governing solute transport equation. It also contains the results of two-dimensional simulations of the subsequent transport of the oxidation products through the groundwater flow system.
- Chapter 10 summarises the results and principal conclusions of the research work presented in this thesis together with the suggestions for further research.
- Appendix A contains the finite element discretisation of the groundwater flow equation. Appendix B gives the derivation of the pyrite oxidation model based on a shrinking core model. A review of the existing pyrite oxidation models are provided in Appendix C. The physical and the chemical processes of the mass transport phenomenon are given in Appendices D through K. The Q1 file in PHOENICS input language and the GROUND subroutine in FORTRAN language are given in appendices L and M respectively.

### **1.12.2 Research program**

This research work has been divided into eight distinct phases extending over a period of one session each as shown in Table 1.1.

In the first phase of this research a literature survey of the mining operations, associated pollution problems and a review of numerical methods was carried out. The second

phase dealt with the evaluation of different numerical codes. A finite element code called SEEP/W was selected to simulate groundwater inflow and post-mining rebound

Table 1.1. Research activities and schedule.

TASK	2000		2001		2002	
	$S_1^*$	$S_2^{**}$	$S_1$	$S_2$	$S_1$	$S_2$
<p><b>Phase 1:</b> Literature Survey of the mining operations and associated pollution problems and other related investigations and a review of numerical methods.</p> <p><b>Phase 2:</b> Evaluation of different numerical codes, selecting a finite element (FE) code (SEEP/W) for inflow and rebound models and a finite volume (FV) code (PHOENICS) for pyrite oxidation and subsequent transport of oxidation products.</p> <p><b>Phase 3:</b> Development of groundwater inflow and rebound modelling algorithms, evaluation of groundwater model with dewatering problems in confined, unconfined and leaky aquifers.</p> <p><b>Phase 4:</b> Development of a FV model for oxygen transport and pyrite oxidation. Evaluation of the physical processes and chemical reactions involved in transport mechanism.</p> <p><b>Phase 5:</b> Verification of inflow and post-mining rebound models with analytical and previous numerical models for groundwater inflow to surface mine excavations, development of seepage face in a surface mine, groundwater inflow to an open cut coalmine and groundwater rebound in an idealised pit.</p> <p><b>Phase 6:</b> Development of a FV model for contaminant transport with taking into account physical processes (advection and diffusion), and chemical reactions.</p> <p><b>Phase 7:</b> Further validation of groundwater rebound modelling with monitored field data and verification of pyrite oxidation, oxygen transport and subsequent transport models.</p> <p><b>Phase 8:</b> Thesis Preparation            Outline            Draft one            Subsequent drafts            Submission of final thesis</p>						

problems. A numerical finite volume package, PHOENICS, was selected to model pollution problems associated with open cut coalmines. The third phase was involved with the development of groundwater inflow and rebound models, mesh generation and specification of boundary conditions. The main aim of this phase was to run the selected finite element program for assessing aquifer related problems. The groundwater model was validated using dewatering problems in confined, unconfined and leaky aquifers. The fourth phase included the development of a finite volume model for transport of oxygen through spoils of an open cut mine and a model for pyrite oxidation based on a shrinking-core model. The physical processes involved in the transport mechanism were also evaluated. In phase five, the models developed for groundwater inflow into the mining excavation and post-mining rebound were verified using existing analytical and numerical models. In this phase the modelling was carried out mainly on groundwater inflow into a circular pit and surface mining excavation, development of a seepage face into a surface mine, groundwater inflow into an open cut coalmine and groundwater rebound in an idealised pit. The sixth phase was to develop a finite volume model for transport of the oxidation products through the groundwater flow system. Modelling includes physical processes (dispersion, molecular diffusion and advection), and chemical reactions taking place during the transport of the oxidation products such as bacterially catalysed reactions, ion exchange, acid neutralisation, complexation and precipitation reactions. The seventh phase was carried out to further validate groundwater rebound modelling with monitored field data and to verify pyrite oxidation, oxygen transport and subsequent transport models.

### **1.13 Conclusions**

In this chapter, the methods of surface mining, groundwater inflow, post-mining groundwater rebound problems and associated environmental pollution problems in

open cut coalmines were briefly reviewed. The generation of pollution may commence during the operational phase of mining and it will continue long after the closure if there is no action taken to prevent it. Prediction of inflow and post-mining groundwater rebound are important intermediate steps in evaluating the pollution problem. Simulation of the long-term pyrite oxidation and subsequent transport of the oxidation products are noted to be the final step. The estimation of any pollution occurrences can help in the design of a more efficient remediation program and this is considered to be a main step for the preparation of the mine rehabilitation programme.

## **CHAPTER TWO**

# **MINE WATER QUALITY CHARACTERISATION AND THE POLLUTION PROBLEM**

## CHAPTER TWO

### MINE WATER QUALITY CHARACTERISATION AND THE POLLUTION PROBLEM

#### 2.1 Introduction

Mining operations invariably disturb the balance of the existing geo-water systems which may have a long-term environmental impact due to the mineral operations. Surface mining operations often leave land in a condition unsuitable for further use. The post-mining mine drainage condition has been identified as one of the pollutants. When the rebound of the water table commences after ceasing of dewatering operations, mine water pollution may occur depending upon the conditions of the surrounding ground and backfill materials. The major problems like acid mine drainage (AMD) and heavy metal pollution are considered to be the most serious water pollution problems in mining areas. Such drainages containing iron sulphates and other components can affect the quality of the receiving water bodies (National Coal Board, 1982).

Open cut mining results in the generation of large amounts of waste materials creating overburden dumps which lead to various environmental impacts including water pollution which is considered to be one of the more serious impacts. The quality of drainage water depends on various factors such as geology of the strata, hydrogeological characteristics and mining parameters that can vary considerably from one mine site to another. In many mines waste water has poor quality due to the generation of acid mine drainage that produces problems of transporting suspended solids and dissolving heavy metals (Rubio and Lorca, 1993). AMD and heavy metals

are thus the most important sources of water pollution especially after cessation of mining activities that lead to long-term environmental effects. This chapter discusses:

- Mine water chemistry
- Physical and chemical parameters
- Acid mine drainage and relevant chemical reactions

Mine water quality and quantity data are required in analysing and evaluating simulation results. Mine water quality and quantity monitoring programs will provide necessary data for exact calibration of the numerical models (Ricca and Schultz, 1979).

## **2.2 Mine water chemistry**

The nature and state of mine water varies considerably from one site to another. In different mine sites, the quality of mine water can be classified as alkaline, acidic and ferruginous or that containing dissolved metal. Therefore, the impacts of these waters can be different. There is no doubt that to consider the nature of such water is a basic task in dealing with and controlling the mine water drainages from different mines.

Coalmine discharge pollution is generally due to the oxidation of pyrite. In coalmines pyrite is generally found in either the coal layers or in mudstones with a marine origin. When pyritic minerals are exposed to air, rapid oxidation of such minerals occurs however, which produces acidic drainage (Ricca and Schultz, 1979; Atkins and Pooley, 1982; and Pentreath, 1994). Such water drainage particularly in the presence of pyrite poses a number of problems and has a detrimental effect on surface and groundwater aquifers and soils (Atkins and Pooley, 1982; Rubio and Del Olmo, 1995; and Adam et al., 1997).

## **2.3 Water pollutants**

### **2.3.1 General consideration**

As water is a good solvent, the possible sources of water pollutants are nearly countless. There is no doubt that the sources and causes of such pollution associated with human activities are numerous. The most important sources of water pollution are untreated sewage, domestic wastes, industrial effluent, industrial solid wastes, municipal wastes, agricultural wastes, mining operations, nuclear wastes, oil-field brines and gasoline and other leaks from storage tanks. Study of mine water pollution is the major concern of this thesis.

### **2.3.2 Mine water pollutants**

In open cut mining operations, huge amounts of waste drainage can be produced. Such waste has harmful effects on water quality. The major water pollutants associated with both open cut and underground mining activities, however, may be classified as shown in Figure 2.1:

In the four pollutant groups illustrated in Figure 2.1, radiological pollutants are associated with uranium mines.

## **2.4 Mine water characteristics**

A basic study of the different aspects of mine water chemistry is necessary for any researcher who deals with pollution problems related to mining wastes. Furthermore, knowledge of mine drainage quality helps in the design of a mine rehabilitation program. A short description of the physical and chemical parameters of mine water quality is considered below:

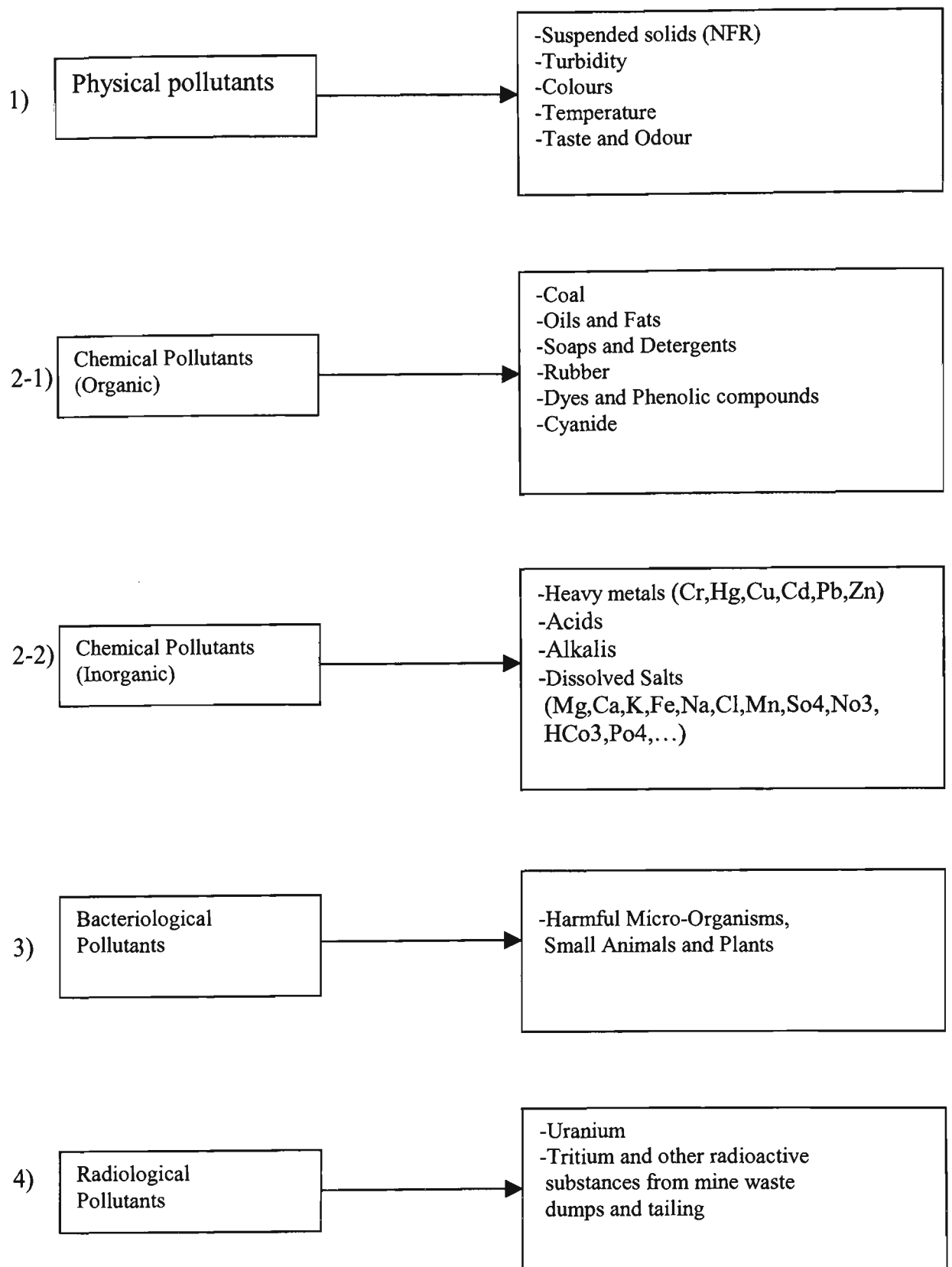


Figure 2.1. Mine water pollutants (Singh, 1998).

## 2.4.1 Physical parameters

### (a) Temperature

The pollution due to temperature is not normally a problem in mining sites. However, the temperature of the water may be an important factor in controlling the biochemical activity. According to Malouf and Prater (1961), temperature has an important effect on the rate of the bacterial oxidation of ferrous to ferric iron. The model developed by Cathles (1979) takes into account the role of temperature on the rate of bacterial leaching of sulphide minerals. Hoth et al. (1998) noted that a contaminant transport model in isothermal conditions cannot cover the complexity of the processes and reactions in such areas. McNab and Narasimhan (1994) emphasised that a reactive transport model including both inorganic geochemistry and degradation reactions may provide the most important primary data in understanding the behaviour of complex environments. Merrington and Alloway (1993) reported that the oxidation of pyrite is an exothermic reaction and it is necessary to take into consideration the effect of temperature in development of model for prediction of pollution potential in spoil of any open cut coalmine where the biological activity determines the amount of pollutants discharged from the mine spoil.

### (b) *pH*

The symbol *pH* is generally expressed as the negative logarithm of the hydrogen ion concentration in a solution. Therefore,

$$pH = -\log_{10} [H^+] \quad (2.1)$$

Its values range between 0 and 14. A *pH* of 7 shows neutrality and a *pH* less than 7 indicates acidity, and also a *pH* with higher values denotes alkalinity.

The solubility of metals in aqueous phases depends upon the *pH*. According to Malouf and Prater (1961), the iron oxidising bacteria are only active in acidic environments having a *pH* of between 2 and 3.5. Furthermore, low *pH* prevents precipitation of ferric iron from the aqueous system. Schnaitman et al. (1969) noted that the bacterial iron oxidation is *pH*-dependent and that optimum range of *pH* is 2.5 to 3.8. The higher values of *pH* cause precipitation of metal oxides, whereas, its low values inducing solubility of the species. The acceptable values of *pH* from any surface mine range between 6.0 and 9.0 (Stiefel and Busch, 1983).

### **(c) Turbidity**

Turbidity is a measure of the concentration of very small size particles in the water. This parameter may be used to estimate the level of suspended solids in a sample (Stiefel and Busch, 1983). The value of turbidity is calculated based on the light absorption property of a suspension of fine solids.

### **(d) Electrical conductivity (EC)**

Conductivity is the measure of the capability of a liquid phase to conduct electricity. This parameter is related to the concentration of dissolved inorganic solids in the aqueous system. Therefore, quantity of these solids in mine drainage can be calculated by use of conductivity measurements. The following equations between electrical conductivity (*EC*), total dissolved solids (*TDS*) and total soluble salts (*TSS*) are generally applied to Australian surface waters.

$$TDS = 0.952 TSS \quad (2.2)$$

$$TSS = 0.65 EC \quad (2.3)$$

Electrical conductivity is measured in situ and is recorded in terms of micro ohms ( $\mu\text{s}$ ). *EC* is a function of temperature hence its value has to be adjusted or corrected to  $25^\circ\text{C}$  (Stiefel and Busch, 1983).

#### **(e) Dissolved components and solubility**

The measure of solid materials dissolved in water may vary from very small amounts to the maximum dissolvable quantity. The highest concentration is called the solubility for the solute in the liquid. If an aqueous phase contains the maximum amount, is said to be saturated with regard to that solute material.

The basic factor affecting solubility is temperature. The solubility of the majority of solid materials increases with a rise in temperature. Dissociation is considered to be another phenomenon that may happen when a solid dissolves in water. In this case, an ionic solid dissolves and breaks down into its primary or individual ions.

In a typical water sample  $\text{Na}^+$ ,  $\text{K}^+$ ,  $\text{Ca}^{2+}$ ,  $\text{Mg}^{2+}$ ,  $\text{Cl}^-$ ,  $\text{SO}_4^{2-}$ ,  $\text{HCO}_3^-$  and  $\text{CO}_3^{2-}$  are the major ions (Freeze and Cherry, 1979) and  $\text{NO}_3^-$ ,  $\text{F}^-$ ,  $\text{Br}^-$ ,  $\text{Si}^{2+}$ ,  $\text{Ba}^{2+}$ ,  $\text{Fe}^{2+}$ ,  $\text{Li}^+$ ,  $\text{B}^{3+}$  and  $\text{PO}_4^{3-}$  are other minor ions existing in solution (Hounslow, 1995).

#### **(f) Dissolved salts and suspended solids**

Dissolved salts and suspended solids are the common types of pollutants associated with mining operations. Especially, dissolved salts contribute to the most important problem in the environment.

Suspended solids (*SS*) such as coal fines, silts and other small solid particles are the usual type of material in suspended state or undissolved solids in a typical water sample. *TDS* is the dissolved solids content of a water sample. The sum of the suspended solids

and dissolved solids is called the total solids in a typical water sample (Stiefel and Busch, 1983; and Hounslow, 1995).

#### **(g) Hardness**

Hardness is basically the sum of the calcium and magnesium concentration in the water (Hounslow, 1995). It is denoted in terms of *mg/l* of calcium carbonate ( $CaCO_3$ ) (Stiefel and Busch, 1983). Although other metals such as strontium, iron, manganese and some heavy metals are present and can be determined but, especially in fresh water, these are negligible in comparison with calcium and magnesium.

### **2.4.2 Chemical parameters**

#### **(a) Chlorides**

Halite ( $NaCl$ ) is normally present in salty water resources affected by sea water (Shaw, 1983). Hounslow (1995) explained that halite, due to seepage from the sea and from hot springs are the common sources of the chloride. It is naturally found in water bodies in low concentrations depending on the geological layers in contact with the water.

Chlorides in high quantities have an unfavourable impact on metallic water handling systems due to corrosion and it can also accelerate corrosion difficulties in pipe systems.

#### **(b) Sulphates**

Sources of sulphates are pyrite ( $FeS_2$ ), gypsum ( $CaSO_4 \cdot 2H_2O$ ) and anhydrite ( $CaSO_4$ ). Under some special conditions, high concentrations of sulphate may be generated from organic sulphur compounds (Hounslow, 1995). Sulphates in AMD are generated by the rapid oxidation of pyrite under atmospheric conditions. In such

conditions the sulphidic minerals are oxidised and AMD is generated by releasing iron (Arkesteyn, 1980; Atkins and Pooly, 1982; and Xavier, 1990).

Sulphate reduction is a bacterial reaction (Atkins and Pooly, 1982). In this process the oxygen in  $SO_4^{2-}$  ion is consumed by bacteria to oxidise organic matter to  $CO_2$ .  $H_2S$  as a by-product is formed. The relevant equation for sulphate reduction is (Hounslow, 1995):



The indicator (guideline) concentration of sulphates for drinking water is 400  $mg/l$  (quoted in Singh, 1998). Stiefel and Busch (1983) suggested that sulphate values in surface water resources be limited to concentrations of less than 250  $mg/l$ .

### (c) Nitrogen

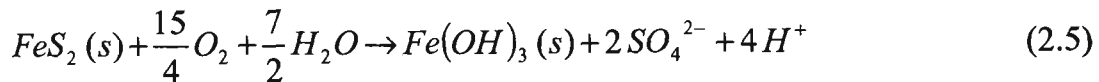
Nitrogen can be found in water in the forms of organic compounds generated by domestic wastes, as ammonia ( $NH_3$ ) and in other oxidised forms such as nitrates and nitrites (Shaw, 1983). Concentrations of organic forms of nitrogen are typically low in groundwater except where groundwater aquifers are affected by sewage and agricultural effluents.

Ammonia in water has its origin in rainwater, domestic sewage, and industrial wastes. Quantities of ammonia in uncontaminated groundwater and surface waters are generally less than 50  $\mu g N/l$ . High concentrations of ammonia may occur in waste disposal leaching zones. Nitrates in water may come from rainwater, industrial wastes, domestic wastes and organic origin (Department of Resources and Energy, 1983).

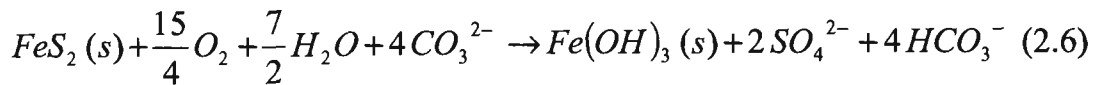
#### (d) Alkalinity

The alkalinity of a liquid sample is defined as the measure of the ability of a solution to react with acid or neutralise it (Hounslow, 1995). Alkalinity in a solution is due to bicarbonate ( $HCO_3^-$ ), carbonate ( $CO_3^{2-}$ ), hydroxide ions and weak acid salts. It is determined by neutralisation (titration) with a standard solution of sulphuric acid to a  $pH = 8.3$  for the alkalinity of hydroxide and carbonate and to a  $pH = 4.5$  for the total alkalinity (Stiefel and Busch, 1983).

In mine drainage, if sufficient alkalinity and carbonate minerals are present, the rate of pyrite oxidation and  $pH$  reduction will be decreased (Hummel et al., 1985; Blowes et al., 1994; and Vandersluis et al., 1995). In alkaline mine waters, the oxidation of pyrite is expressed by the following reaction:



The presence of carbonate in buffered waters in sufficient concentrations will cause the  $pH$  value to be neutral. In such environments, the total oxidation reaction is described by:



Hence, the rate of acid generation is nearly equal to acid consumption and the  $pH$  has a neutral value.

Alkalinity is generally expressed as the equivalent value of  $CaCO_3$  in  $meq/l CaCO_3$ :

$$meq/l CaCO_3 = \frac{mg/l CaCO_3}{\text{The equivalent weight of } CaCO_3 (50)} \quad (2.7)$$

### **(e) Acidity**

The acidity of a liquid phase is defined as the capacity of a liquid to neutralise a strong base such as  $NaOH$ . It is generally determined by titrating a known volume of water with a strong base. The most important sources of acidity are acid rain and AMD due to the oxidation of sulphide minerals in metal and coalmines. The significance of AMD is related to the pollution problems that will be discussed in this chapter. Acidity in mine drainage is also caused by the dissolution of carbon dioxide ( $CO_2$ ) in water. Acidity is reported in terms of an equivalent value of calcium carbonate, generally in mg/l  $CaCO_3$  (Stiefel and Busch, 1983).

## **2.5 Acid mine drainage (AMD) or acid rock drainage (ARD)**

### **2.5.1 General consideration**

Mining operations are often one of the most important causes of surface and groundwater pollution. These activities produce poor water quality and pose many environmental problems. Among the problems associated with mining activities, AMD is the more important and it is considered to be a major cause of water pollution contributing high concentrations of iron,  $SO_4^{2-}$  and acidity to receiving waters (Williams, 1975; Erickson et al., 1982; and Chen et al., 1999).

As a consequence of mining operations, sulphide minerals especially pyrite are oxidised into sulphuric acid. The resulting acid containing dissolved minerals and metals is released into surface and groundwater where it may cause soil and water pollution (Atkins and Pooley, 1982; Merrington and Alloway, 1993; and Fang, 1997).

Although the oxidation process of pyrite and other metal sulphide minerals in the presence of air is often unavoidable, studies of the geochemistry of ore minerals and

waste materials, hydrological aspects, and the mine plan can help in the design of the mining operations to minimise the various effects on the environment during the activities. Environmental damage, as a result of AMD, due to poor management during the planning, development, operation and closure of mining activities and incorrect understanding of AMD in the past (Environment Australia, 1997), has often occurred.

The effects of AMD may remain for long times after mine closure, hence careful environmental management is a necessary task during mining operations and a basic mine closure strategy has to be developed to prevent the subsequent generation of AMD.

### **2.5.2 Acid mine drainage (AMD)**

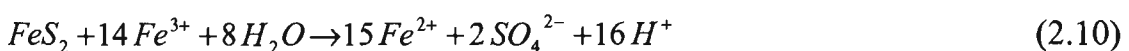
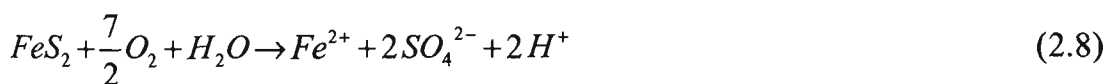
Acid mine drainage is probably the worst environmental problem caused by mining operations, with negative impacts on surface and groundwater quality. Many types of mining sites, such as coal mining, metalliferous mining, backfilled opencast mining, quarries as well as tailings dams and overburden waste materials contain iron sulphide minerals, in particular pyrite ( $FeS_2$ ). The oxidation of iron sulphide minerals, especially pyrite, by oxygen and water particularly in the presence of certain bacteria cause AMD (Singer and Stumm, 1970; Williams, 1975; Atkins and Pooley, 1982; Norton, 1992; Saharan et al., 1995; Adam et al., 1997; Environment Australia, 1997 and Modis et al., 1998).

AMD is produced when sulphide minerals are exposed to the atmosphere (Atkins and Pooley, 1982; and Toit et al., 1998). Therefore, AMD not only occurs due to mining operations, it may take place in sites of out-cropping pyrite minerals. Such occurrences have previously been used as an important key for the exploration of ore deposits (Saharan et al., 1995; and Environment Australia, 1997).

AMD is often characterised by high concentrations of *Fe*, high sulphate and low *pH* (Williams, 1975; Gray, 1998 and Toit et al., 1998). In addition to iron and sulphate, other metal concentrations such as aluminium (*Al*), manganese (*Mn*) and total dissolved solids are present and precipitation of many secondary minerals such as gypsum or ferric hydroxy-sulphates may occur. According to Williams (1975) and Gray (1998), depending on the geology of the host rock of the ore deposit and depending upon the materials contacted, a variety of metals with elevated concentrations may be present. Adam et al (1997) emphasised that acidic water contains many metallic ions such as *Fe*, *Cu*, *Zn* and *As*. These metals are considered to be a potential source of surface and groundwater contamination. Stokstand (1998) reported that AMD can leach and transport other metallic contaminants depending on the host rock geology. These may include arsenic, asbestos, cadmium, copper, iron, lead, mercury, sulphur and zinc. These metals are transported into waterways and finally pollute surface and groundwater.

### 2.5.3 Oxidation reactions and acid generation

AMD results at mine sites from the oxidation of certain sulphide minerals (Atkins and Pooley, 1982) in particular pyrite. The overall stoichiometric reactions describing the oxidation of pyrite and leaching generation are given as:



Pyrite oxidation can be initiated with direct oxidation of pyrite by  $O_2$  (Reaction 2.8), forming  $Fe^{2+}$ ,  $SO_4^{-2}$  and  $H^+$  (Singer and Stumm, 1970; Williams et al., 1979; Guedes et al., 1986; Herbert Jr., 1994; Bridwell and Travis, 1995).  $Fe^{2+}$  released by pyrite oxidation is converted to  $Fe^{3+}$  (Reaction 2.9) (Rogowski, et al., 1977). Reaction 2.9 is the only important source of  $Fe^{3+}$  in strip mine site (Jaynes et al., 1984a). Oxidation of  $Fe^{2+}$  to  $Fe^{3+}$  is slow under low  $pH$  values of natural acidic systems such as strip mine spoil. However it may be catalysed by the bacteria *Thiobacillus ferrooxidans* (Singer and Stumm, 1970; Hoffmann et al., 1981; and Xavier, 1990).  $Fe^{3+}$  produced by the oxidation of ferrous iron, may react with pyrite (Reaction 2.10) to produce additional  $Fe^{2+}$ ,  $SO_4^{-2}$  and  $H^+$  (Singer and Stumm, 1970). It has been suggested that oxidation of pyrite by  $Fe^{3+}$  is important only when bacteria are present (Jaynes et al., 1984a, b).  $Fe^{3+}$  may be hydrolysed and precipitated as amorphous ferric hydroxide (Reaction 2.11). In the presence of sulphate reduction bacteria, sulphate is reduced (Reaction 2.12) to sulphide, neutralising  $pH$  and consuming sulphate (Atkins and Pooley, 1982; Rose and Cravotta III, 1998; and Drury, 2000).

According to Williams (1975) and Hellier (1998), the oxidation reaction in solution is increased by  $Fe^{3+}$  instead of  $O_2$  as an oxidising agent. If the acidity falls below  $pH = 3.5$  and ratio of  $\frac{Fe^{3+}}{Fe^{2+}}$  becomes large, in this case,  $Fe^{3+}$  plays a basic role in oxidising the  $FeS_2$ .

The following factors determine the rate of pyrite oxidation and acid production (Malouf and Prater, 1961; Saharan et al., 1995):

- The form of sulphur mineral

- Grain size of the rock containing pyrite
- The concentrations of oxygen and temperature
- *pH* and *Eh* conditions
- The quantity of sulphur
- Catalytic effects and the availability of certain bacteria

The various metal sulphide minerals oxidised by *Thiobacillus Ferrooxidans* can be found in Xavier (1990); Robins (1991); Nordstrom and Southam (1997); Rose and Cravotta III (1998):

Table 2.1. A list of metal sulphide minerals which can be affected by *T. Ferrooxidans*

<u>Sulphide mineral</u>	<u>Chemical formula</u>
Arsenopyrite	$FeS_2 \cdot FeAs_2$
Bornite	$Cu_5FeS_4$
Chalcocite	$Cu_2S$
Chalcopyrite	$CuFeS_2$
Covellite	$CuS$
Enargite	$3Cu_2S \cdot As_2S_5$
Galena	$PbS$
Marcasite	$FeS_2$
Millerite	$NiS$
Molybdenite	$MoS_2$
Orpiment	$As_2S_3$
Pyrite	$FeS_2$
Sphalerite	$ZnS$

#### 2.5.4 The role of the buffering minerals

Although the presence of pyrite and other sulphide minerals has an important role in the generation of AMD, this is not a sufficient condition. If the sulphide minerals are not reactive or if a great quantity of alkaline minerals, which act as buffering materials, are present, the AMD will be neutralised (Williams, 1975; Blowes, et al., 1994; and Saharan et al., 1995).

Studies made by Blowes, et al. (1994); Vandersluis et al. (1995) and Bowell et al. (1998) confirmed the role of carbonate minerals as buffering  $H^+$  in decreasing the rate of pyrite oxidation and generation in mine drainage. Bowell et al (1998) emphasised that buffering minerals such as carbonates cause acid–neutralisation reactions. According to Williams (1975) lime, limestone, and soda ash can neutralise acid mine drainage to  $pH$  6.5 to 8 and iron to less than 7.0 ppm. Acid neutralisation reactions are often accompanied by the precipitation of metal-hydroxides, hydroxy-sulphates and oxyhydroxide minerals. The maximum rate of pyrite oxidation takes place from  $pH = 2.4$  to  $pH = 3.6$ . At low  $pH$ ,  $Fe^{3+}$  appears as an oxidant agent while at  $pH$  values greater than 3.5 ferric iron precipitates as ferric hydroxide  $Fe(OH)_3$ . It was reported that at  $pH$  below 4 secondary minerals may produce Jarosite. This mineral plays a basic role in maintaining acidity long after pyrite and other sulphide minerals have been consumed. Many other factors such as materials, mine site topography, and climate conditions (particularly rainfall and temperature) affect the rate of pyrite oxidation and acid generation, the potential for transporting oxidation products into the receiving environments and the consumption of resultant materials (Environment Australia, 1997).

### **2.5.5 Impacts of acid mine drainage on the receiving environment**

AMD is an overall problem influencing receiving water in many mining sites. Acid drainage contributes high concentrations of metals such as manganese, aluminum and iron which pollutes both surface and groundwater aquifers. In a 1993 hydrogeological investigation and hydrogeochemical analysis of water samples affected by AMD, Ezeigbo and Ezeanyim described their findings concerning the effects of AMD water on surface and groundwater pollution. The authors expressed the view that the cause of death of aquatic life is due to acidic drainage channeled into receiving waters. Further, this water infiltrates into groundwater aquifers and pollutes them. Other research agrees with the effect of acidic drainage in pollution of surface water bodies and groundwater aquifers have a detrimental effect on receiving environment. Rubio and Lorca (1993) emphasised that acidic waters in mining activities produce a number problems. Amongst the major problems, the environmental problem is very important.

AMD with low *pH*, high salinity, high concentrations of heavy metals and sulphate, causes soil acidity and salinity, the death of vegetation, increase in the rate of erosion, and detrimental impacts on aquatic biota in receiving water ways. However, AMD clearly poses a number of serious problems for the receiving environment. These are as follows:

- Negative impact on mine water quality contributing to corrosion problems for mine equipment.
- Disturbing the aquatic ecosystem in downstream environments caused by low *pH* and high concentrations of dissolved heavy metals, threatening aquatic life and contributing to health hazards for human beings and other creatures, death of fish particularly salmon and trout species, depletion of numbers of free swimming and benthic aquatic organisms.

- Groundwater pollution due to infiltration of acid drainage into the aquifers.
- Surface water pollution is considered to be another most important problem associated with acidic drainage. This acidic water containing high values of metals and dissolved sulphates when neutralised with fresh water streams, causes the precipitation of iron hydroxide that decolourises the water and destroys the natural beauty of rivers. Furthermore, this drainage makes surface waters fishless resulting from covering the river bed with precipitated iron hydroxides (Atkins and Pooley, 1982; Pentreath, 1994; Saharan et al., 1995; Environment Australia, 1997; and Singh, 1998).

### **2.5.6 Heavy metals**

Drainage from many metal sulphide mines including abandoned mines, may contain elevated concentrations of iron, manganese, zinc, copper, arsenic, cadmium and lead (Robb and Robinson, 1995). Heavy metals are known to be toxic to aquatic organisms and human life (Stiefel and Busch, 1983).

Most metals at higher concentrations pose detrimental impacts to fish, any other aquatic life and human beings as well as destroying the stream ecology. In environmental geochemical studies carried out in India, Govil et al., (1999), described their findings concerning the effects of heavy metals on environmental pollution. The authors pointed out that heavy metals accumulate between soil particles and contribute to a long term environmental hazard. Furthermore, many heavy metals at elevated concentrations are considered to be toxic and affect plant life adversely.

Xavier (1990) focussed mainly on the role of particular microorganisms in the dissolution and precipitation of specific metals. The author also discussed the metal solubility and mobility in acidic drainage environments as being influenced by several

factors such as *pH*, *Fe* and *Mn* concentrations, redox potential and organic matter. The author believed that changes of oxidation reduction potential and *pH* conditions by microbial activities have a basic role in the mobilisation of metals in acid mine drainage.

## **2. 6 Acid mine drainage neutralisation methods**

### **2.6.1 Introduction**

The acid drainages from surface coalmines with high concentrations of heavy metals contribute environmental pollution. The neutralisation and prevention of acid drainage is a necessary task for mining industries at areas where AMD takes place (Environment Australia, 1997). In such sites remediation methods and chemical treatment facilities will be necessary before acidic drainage can be discharged into the receiving waters (Williams, 1975). Although temporary remediation may reduce the acidic water effects on the environment, however active and/or passive treatment systems will be necessary for exact amelioration of AMD (Robb & Robinson, 1995). Because active treatment systems often produce a contaminated effluent and need additional treatment facilities, therefore such systems are generally expensive.

Constructed wetlands are often effective, low-maintenance and inexpensive treatment systems for AMD (Perry and Kleinmann, 1991; Norton, 1992). Such systems are successful in removing metals from AMD. However, wetlands are not always reliable during all seasons of the year for water quality improvement (Skousen, 2000).

The main aim of treatment systems is to remove contaminants such as iron and manganese from mine drainage and raise the *pH*. Such treated mine effluents can then be directed into the receiving waters.

## 2.6.2 Acid mine drainage neutralising agents

Many research and experimental works have been carried out to find the most efficient and appropriate chemical materials for neutralising the AMD. The most common method for AMD treatment is to use the alkaline reagents. Mining companies use limestone ( $CaCO_3$ ), hydrated lime (calcium hydroxide,  $Ca(OH)_2$ ), sodium hydroxide (caustic soda,  $NaOH$ ), sodium carbonate, magnesium oxide (caustic magnesia) or ammonia to treat AMD (Williams, 1975; Skousen, 2000; and Environment Australia, 1997). Rogowski et al. (1977) and Singh (1998) have also mentioned certain clays and silicates as acid neutralising agents.

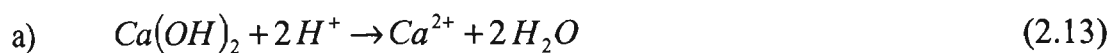
Many coalmines in the eastern United States and other parts of the world use alkaline agents to treat AMD. These chemical materials remove iron and other pollutants. The treated water can then be discharged into the rivers (Skousen, 2000). Diz (1998) reported chemical treatment strategies which have commonly been employed at active mining operations. In these systems, sodium hydroxide ( $NaOH$ ) or lime ( $CaO$ ) is used to increase the  $pH$  value. Skousen (2000) emphasised that the residual materials after the process of treatment of AMD must be considered for each chemical agent.

According to Williams (1975) and Tsukamoto and Miller (1999), lime precipitation is the most common agent for acid neutralisation. The advantages of lime treatment systems are neutralising acidity, removal of iron and aluminium salts and the reduction in sulphate concentration. But this procedure generates large amounts of gypsum sludge contaminated by heavy metals. Furthermore this treatment process is also expensive. Pearce and Ries (1982) have outlined the common cost-effective chemical treatment methods for AMD. They have also mentioned other treatment methods such as sodium treatment, microbial inhibition, electro dialysis, ion exchange and foam separation.

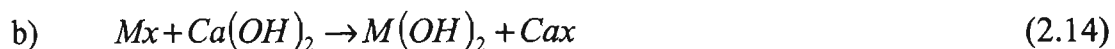
### 2.6.3 Active treatment systems

In this method, a chemical, in particular an alkaline material such as calcium hydroxide ( $CaCO_3$ ), sodium hydroxide ( $NaOH$ ) or magnesium hydroxide ( $Mg(OH)_2$ ) is generally added to increase the  $pH$  value of acid drainage and allowing the precipitation of metals as insoluble hydroxides. The relevant neutralisation and metal precipitation reactions between alkaline and AMD are as follows:

The neutralisation of acidity:



The generation of metal hydroxide:



where,

$M$  = any metal;

$x$  = any metal ligand such as sulphate.

This process produces large values of sludge creating numerous environmental problems. Furthermore, the cost of initial equipment and building is relatively high (Pearce and Ries, 1982; Robb and Robinson, 1995; and Saharan et al., 1995).

### 2.6.4 Passive treatment systems

Passive treatment techniques employ similar processes which are used in the active remediation method but with a different operational methodology. In this method alkalinity is added into the acidic drainage to increase  $pH$  value. These systems are appropriate for the treatment of low acidity drainage in particular in areas where the flow is relatively low (Robb and Robinson, 1995; and Environment Australia, 1997).

Passive methods have been applied to treat acid drainage independently hence the cost of maintenance is relatively low. Such cost-effective treatment methods are basically required in areas such as abandoned mines where mining companies do not accept the responsibility of the environmental problems due to acidic drainage (Skousen, 2000).

### 2.6.5 Passive anoxic limestone drains (PALD)

A method is known as anoxic limestone drains have been developed for pre-treatment of acid drainage, in which acid drainage is generally passed through a drain including crushed limestone under anoxic conditions for avoiding the precipitation of metal hydroxides within the drain and on the limestone gravels (Figure 2.2).



Figure 2.2. Passive anoxic limestone drains (Skousen, 2002).

The reaction between the mine drainage and the surface of the limestone raises the alkalinity:



Subsequent aeration and ponding of the discharge from the drain causes precipitation of metal hydroxides in the settling pond (Environment Australia, 1997; Robb and Robinson, 1995). According to Diz (1998), a successful treatment of AMD using anoxic limestone drains can be achieved if these methods are combined with natural or constructed wetlands. PALD method can effectively be applied in sites where the

concentrations of dissolved oxygen and aluminum in acid drainage is low and the iron is present in the form of ferrous iron ( $Fe^{2+}$ ). These conditions ensure that the PALD approach is best-suited and a cost-effective method in treating AMD (Skousen, 2000). After removing the iron by employing an aerobic wetland, an anaerobic wetland system can then be employed to remove the remaining metals such as zinc, copper, cadmium, lead and mercury (Robb and Robinson, 1995).

### 2.6.6 Open limestone channels

This approach is an important method in ameliorating or treating AMD. These systems are constructed by covering the streambed with high quality of limestone (Figure 2.3) (Diz, 1998; and Skousen, 2000). The limestone dumped in the streambed is effective in neutralising the acidity of the mine drainage but basically the limestone is eventually covered with iron oxy-hydroxides in sites where the water is not anoxic. However, results obtained from sites have clearly demonstrated that acidity and metal contents removal are improved 25% when flowing through coated limestone (Skousen, 2000).



Figure 2.3. Open limestone channels for mine drainage treatment (Skousen, 2002).

In an investigation with both passive and active treatment methods, Hamilton et al. (1999) used a passive treatment system to ameliorate AMD at the abandoned Wheal Jane mine in Cornwall, in the UK. They employed a pilot passive treatment plant

including three individual systems. Each system consists of five aerobic reed beds, an anaerobic cell and an aerobic rock filter. For two of them however, a pre-treatment system was also constructed. Those readers who require more information about the system are referred to Hamilton et al. (1999).

Norton (1995) also reported on the pollution problem due to high concentrations of toxic metals such as cadmium, arsenic, iron, zinc and lead in the abandoned Wheal Jane mine due to the groundwater rebound after the closure. He emphasised that a cost-effective passive treatment system is an important approach to overcome the long-term pollution problem in abandoned mines.

#### **2.6.7 Wetland systems for acid mine drainage treatment**

Wetlands are considered to be the alternative low-cost, low-maintenance passive systems for the treatment of AMD (Kleinmann, 1990). Wetland systems can be effectively combined with other methods such as passive anoxic limestone drains, as a final stage for acid mine treatment (Environment Australia, 1997). Wetlands are not only successfully used for acid mine treatment but also they are more economic than chemical treatment systems (Kleinmann, 1990). A wetland is a chemically complex system and many physical, chemical and biological processes occur within the wetlands including adsorption, ion exchange, bacterial and abiotic oxidation, bioaccumulation, sedimentation, neutralisation, sulphate reduction and carbonate minerals formation (Kleinmann, 1990). Although many of these processes taking place in a wetland environment are not fully understood, they have been shown to be effective in metal removal, in particular iron, and in the raising of *pH* as well as sulphate reduction. It should be noted that large amounts of sludge are not produced as metallic precipitation in the wetland substrate, common in chemical neutralisation methods. Another

advantage of constructed wetlands is the long-term sedimentation and immobilisation of metals (Kleinmann, 1990; and Saharan et al., 1995).

Wetland systems have encountered many difficulties in treatment of large flows, in land areas available for large wetlands (Environment Australia, 1997) and also where the efficiency of metal removal is reduced due to evapotranspiration in warmer climate conditions. A typical design of an engineered wetland is shown in Figure 2.4. A constructed wetland usually consists of a series of shallow pits to easily control the flow of mine drainage. These pits are filled with organic substrate and planted with *Typha*. The mine drainage then is channelled into the pits as illustrated in Figure 2.4. A 15 cm layer of alkaline material such as limestone gravels or phosphate is laid on top of the compacted base in order to accelerate the process by initially increasing the *pH*. A 14 to 45 cm thick un-compacted layer of an organic substrate is placed on top of the crushed limestone layer. This organic substrate includes spent mushroom compost, a waste product of mushroom farming, well digested sewage sludge, peat, and chicken manure. The floor of wetlands is designed to be horizontal or may have a small gradient (up to 3%) from the inflow to the out flow of the system (Kleinmann, 1990; and Norton, 1992).

American Forests (1992) emphasised that wetlands should be constructed both large enough and flat enough to contain the mine drainage at least for 12 hours. Typically a constructed wetland system generally includes a series of shallow cells for easier flow control. These cells are covered with a special plant is known *Typha* and are flooded with AMD (Kleinmann, 1990). Most wetlands are usually constructed to be rather small and the average size is around 1 hectare. Kleinmann (1990) presented a suitable guide to sizing of wetlands based on iron loading and *pH* of acidic drainage:

- If the  $pH$  of the mine drainage is equal to 6.0 or above, the area in square metres needed is equivalent to the iron loading in  $gr/day$  divided by 10.
- If the  $pH$  of drainage ranges from 4.0 to 5.0 then the wetland area required is equivalent to the iron loading multiplied by the coefficient (2/10).
- For  $pH$  values below 4, the area required is equivalent to the iron loading divided by 2.

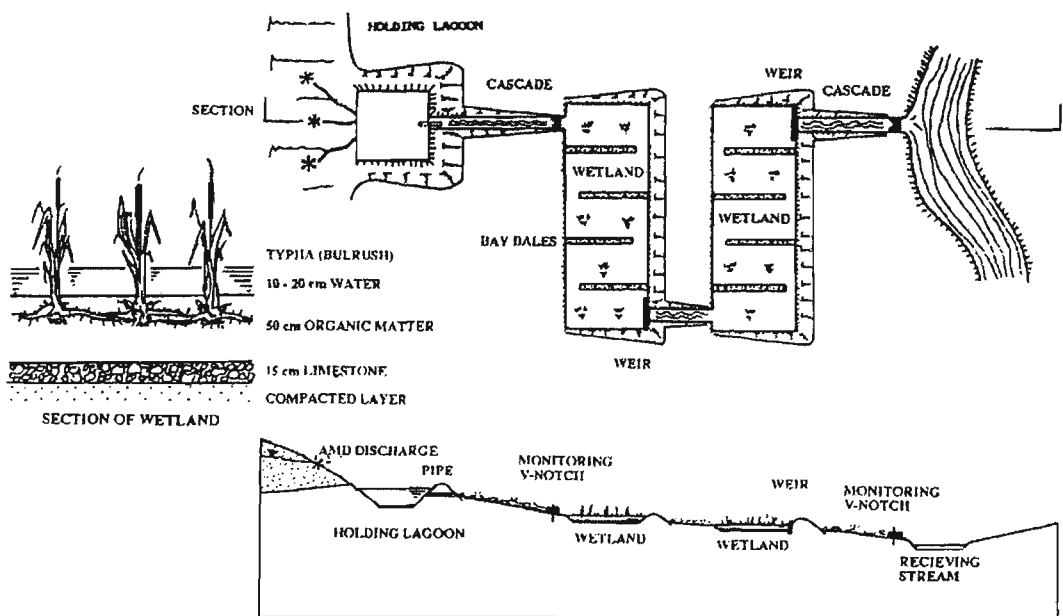


Figure 2.4. Schematic diagram of a typical engineered wetland (quoted in Norton, 1992).

Two kinds of constructed wetland systems have been reported by Saharan et al. (1995) and Skousen (2002). These are aerobic and anaerobic wetland systems. According to Skousen (2002), in aerobic wetlands, acid mine drainage treatment is dominated by processes in the shallow surface layer while in anaerobic wetlands, by the chemical interactions taking place within the organic substrate. Figure 2.5 shows both types of wetlands.

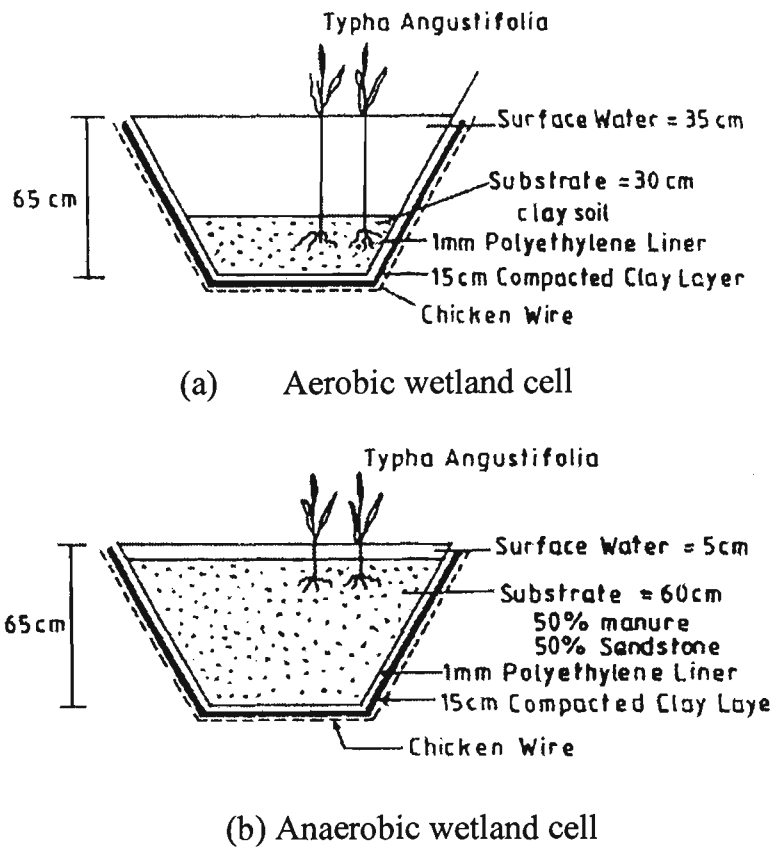


Figure 2.5. Schematic diagram of aerobic and anaerobic wetland cells (quoted in Saharan et al., 1995).

### (a) Aerobic wetland systems

Aerobic wetland systems are constructed to promote the oxidation process. They are designed to be relatively shallow with a depth of 30 cm, planted, and where the surface flow is predominant. In the wetland system, ferrous iron is changed to ferric iron, a hydrolysis reaction occurs which forces the precipitation of ferric hydroxide or ferric oxy hydroxide. The chemical reactions involved are as follows:



or,



As a result the oxidation reaction causes iron removal in the aerobic wetland. These reactions, however, will increase the acidity and the  $pH$  value will be reduced. Lower

values of  $pH$  can then reduce the rate of the oxidation process and plants growing in the aerobic cells, may be affected by the low  $pH$ .

It should be noted that alkalinity could be added to the aerobic wetland systems to raise the  $pH$  value and ensure the optimum rate of iron removal. Alkalinity required to aerobic treatment systems can be provided by the following ways:

- Plant species such as reeds (i.e. *Typha Latifolias* and *Phragmites Australis*) are encouraged to grow in the aerobic systems. The growing reeds can pass oxygen through the organic materials that will generate carbon dioxide. Acidity may be neutralised finally by dissolving the gas in the mine drainage.
- The use of anoxic limestone drainage is considered to be another approach in providing alkalinity in the aerobic systems (Robb and Robinson, 1995).

#### **(b) Anaerobic wetland systems**

Anaerobic cells are designed with a thicker organic substrate consisting of organic materials such as hay, manure, peat moss or mushroom compost (Skousen, 2002; Saharan et al., 1995).

Bacterial sulphate reduction in the anaerobic systems of the organic materials is considered to be the most important approach for metal removal in wetland cells. In this approach, the metallic sulphates in mine drainage are reduced to sulphides that generate an insoluble precipitate within the organic materials. This reaction also improves water quality and increases the  $pH$  value (Kleinmann, 1990; and Norton, 1992).

Although bacterial oxidation processes are not considered to be an effective way to remove the most toxic and heavy metals, the hydrogen sulphide released by bacterial sulphate reduction can react with many heavy metals to generate insoluble sulphide

precipitates. This may be an appropriate approach for treatment of mine drainage contaminated with many toxic metals (Kleinmann, 1990).

The bacterial sulphate reduction processes are well documented by many research investigators (Silver, 1989; Rose and Cravotta III, 1998; and Drury, 2000) and will be discussed in Appendix K. According to Silver (1989), under anaerobic conditions, sulphate-reducing bacteria will effectively reduce sulphate. Sulphides formed may combine with heavy metals to cause their precipitation. Castro et al. (1999) employed sulphate reduction bacteria in improving water quality in a pit lake contaminated with high concentrations of sulphate, iron and arsenic. They used varying amounts of organic waste products from a potato-processing plant and composted steer manure under anoxic conditions. Sulphate reduction caused the formation of sulphide. The concentrations of iron, sulphate and arsenic were dramatically reduced and approached zero levels, and finally the *pH* value approached neutrality.

In a 1998 research program at the Nickel Rim mine near Sudbury, Ontario, Canada, Herbert et al. described a method for the passive treatment of groundwater affected by acid drainage. They employed a permeable reactive barrier consisting of a mixture of municipal waste, leaf compost and wood chips. The organic material raises sulphate reduction. Hydrogen sulphide as a by-product of sulphate reduction may then complex with aqueous  $Fe^{2+}$  and finally precipitate as iron sulphide. This study mainly demonstrated the formation and accumulation of iron sulphide minerals in the reactive materials.

### **(c) Manganese and Aluminium removal**

The aerobic wetland cells employed for iron removal do not considerably remove the manganese content by oxidation especially in the case of lower *pH* values. Manganese

however may be removed under anaerobic conditions. Robb and Robinson (1995) believed that a separate passive anaerobic system is required to remove manganese under alkaline conditions by the following reactions:

For  $pH > 6.0$ :



Under  $pH > 10.6$  manganese hydroxide can precipitate:



According to Robb and Robinson (1995), aluminium may be removed in an anoxic Slurry pond as aluminium hydroxide under high values of  $pH$  and alkalinity and in the presence of some sulphate reduction bacteria:



## 2.7 Conclusions

This chapter reviewed water pollutants, mine water characteristics, the chemistry of pyrite oxidation and acid mine drainage (AMD) generation and AMD characteristics, and the effects of AMD on the environment. It also briefly reviewed acid mine drainage neutralisation methods. It is concluded that among the problems associated with open cut coal mining operations, AMD is highlighted to be a dominant problem affecting receiving water bodies and wild life. It contributes to high concentrations of iron, sulphate and acidity in the surrounding environment. A study of mine water quality and quantity data is required in order to verify a numerical model describing long-term pyrite oxidation and the subsequent transportation of the oxidation products.

## **CHAPTER THREE**

### **ANALYTICAL METHODS OF PREDICTION OF GROUNDWATER INFLOW TO OPEN CUT COALMINES**

## CHAPTER THREE

### ANALYTICAL METHODS OF PREDICTION OF GROUNDWATER INFLOW TO OPEN CUT COALMINES

#### 3.1 Introduction

The large surface mining excavations which are currently carried out below the water table can create a number of water related problems affecting the operational efficiency and economic viability of the mining operation. This water inflow from the surrounding strata towards the mining excavation requires installation of dewatering facilities to keep the mine workings dry and create an extensive and prolonged cone of depression. In order to design an effective drainage scheme for a surface mine, prediction of water inflow into a mining excavation during the feasibility stage of the operation is a major task (Singh et al., 1985). An effective drainage scheme will necessarily allow mining to be carried out in dry conditions and improve the slope stability, reduce oxidation of sulphide minerals and reduction of corrosion of mining plant and equipment.

An essential tool for the prediction of groundwater inflow into mining operations is the use of a mathematical model. The inflow models range from simple analytical solutions to relatively complex numerical models. Mine feasibility and environmental evaluations can benefit from the use of simple analytical methods to predict groundwater inflow, as a preliminary estimation of potential groundwater inflow, when there is not sufficient time and hydrogeological data available to validate and justify the use of a numerical model.

In this chapter, therefore, possible sources of water inflow into surface mines are presented and idealised hydrogeological profiles of various surface mining operations

are described. Also described are the analytical methods available for the prediction of water inflow into a surface mining excavation including two-dimensional flow equations for different aquifers under both steady-state and transient flow conditions.

### **3.2 Sources of water inflow in surface mines**

For prediction of the groundwater rebound process, it is necessary to consider the various sources of water inflow and outflow. The most important portion of water entering a mining excavation may originate from a variety of sources listed as follows (Singh and Reed, 1987):

- Water from direct precipitation and surface run-off
- Horizontal or vertical inflow of groundwater from aquifers, bed rock or alluvium

#### **3.2.1 Water inflow from direct precipitation, surface water and run-off**

Water originating from surface precipitation may enter into a surface mining excavation directly as rainfall or indirectly as surface run-off or floodwater during unexpected rainfall. Although water from precipitation and run-off is small in comparison with the groundwater inflow, in some situations, however, these sources of inflow should not be ignored and are considered in any model for simulation of groundwater rebound and water quality models (reported in Lewis, 1999). According to Lewis (1999) for pit water-quality modelling, run-off is often considered as the sum of two constituents:

- The run-off from the pit high wall often contains high concentrations of metals leached from oxidised pit wall geological formations and rocks. This portion of run-off is often assumed to be 50 % to 100 % of direct precipitation.
- The run-off from the remaining pit catchment area with low quantities of metals and dissolved materials which is assumed to be 10 % to 20 % of direct precipitation.

Direct precipitation can be measured directly or can be estimated indirectly from regional flow data or surface-water flow models. Figure 3.1 shows a hypothetical surface mining catchment area.

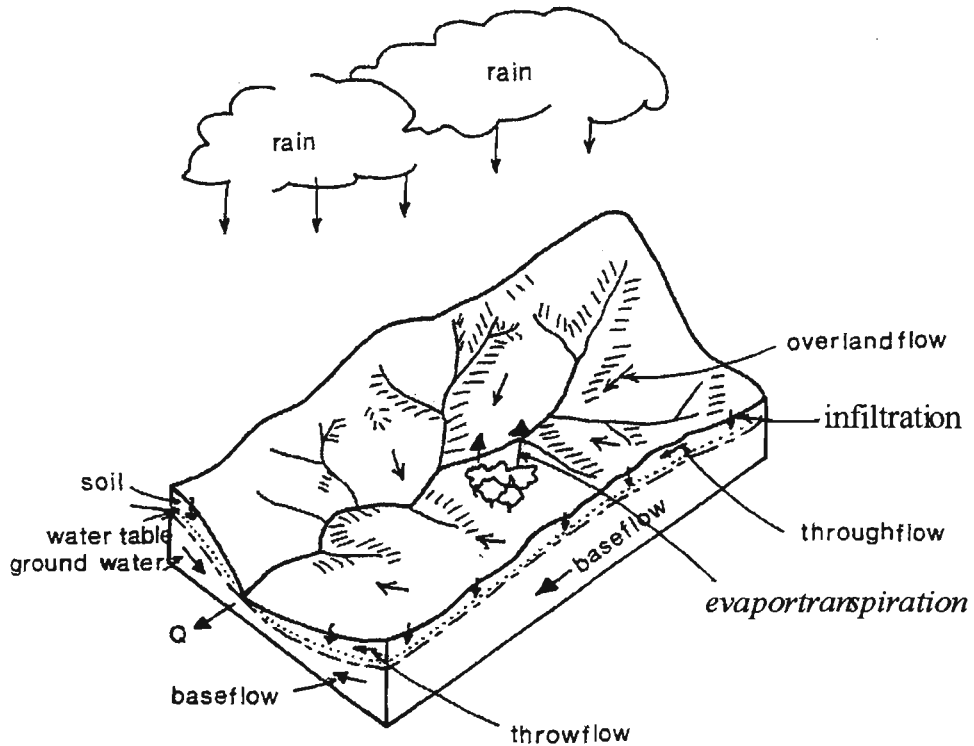


Figure 3.1. Catchment hydrological cycle (after Singh and Reed, 1987).

### 3.2.2 Groundwater inflow

Groundwater inflow from aquifers is basically much greater than other inflow sources and, therefore, has the most important influence on the groundwater rebound process in open cut mines. It is often essential to be able to predict the nature and amount of this component of inflow. Water inflow from aquifers to an excavation consists of the following components:

- The inflow resulting from the drawdown of the initial potentiometric surface provided by dewatering and evaporation (McWhorter, 1981).
- The passive inflow. This component of groundwater inflow is often the result of an initial slope of water table or piezometric surface.

It was well recognised that a limitation of analytical solutions derived from well hydraulics for prediction of groundwater inflow is to assume an initially flat surface of potentiometric for aquifers. These equations do not take into account the passive component of groundwater inflow. The following equation incorporates the passive inflow to an ideal fully penetrating pit in a uniform flow field (Lewis, 1999) (Figures 3.2 and 3.3).

$$Q_{gw_{pi}} = \frac{2KbI(r_b + r_p)}{\cos\beta} \quad (3.1)$$

where,

$Q_{gw_{pi}}$  = passive inflow component ( $m^3 / s$ );

$K$  = aquifer permeability ( $m/s$ );

$b$  = aquifer thickness ( $m$ );

$I$  = regional hydraulic gradient;

$r_b$  = radius of the pit base ( $m$ );

$r_p$  = radius of the pit surface( $m$ ).

### 3.3 Types of inflow

The amount of water inflow to mine activities can be categorised into the following types (Rubio and Lorca, 1993):

- Rate of inflow following a Gaussian distribution.

This type of inflow can occur in the case of a large water inrush. The initial inflow rate increases dramatically for a short period of time and then decreases gradually with time finally it reaches to a certain steady-state flow (Figure 3.4).

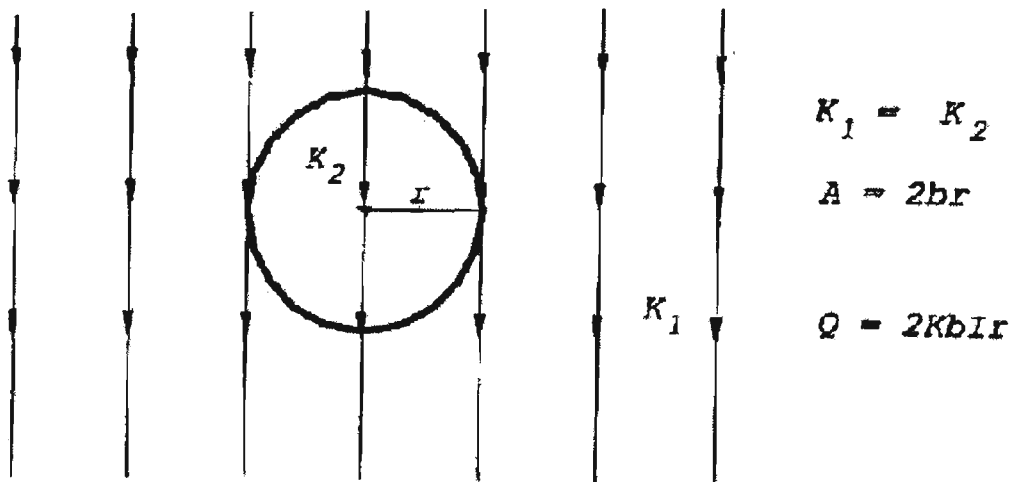


Figure 3.2. Passive flow through a cylinder in a homogenous aquifer (quoted in Lewis, 1999).

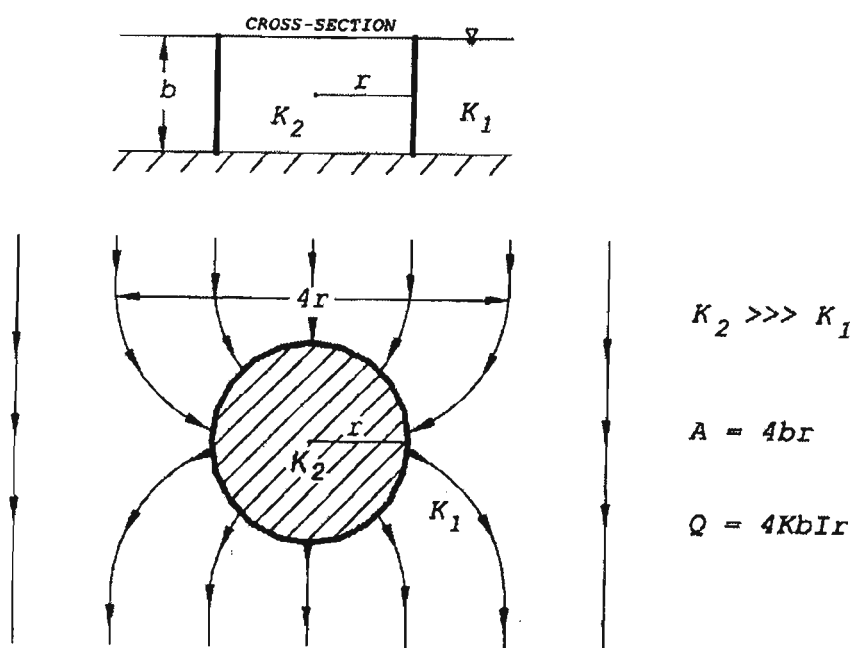


Figure 3.3. Passive flow through a highly conductive cylinder (quoted in Lewis, 1999).

This type of inflow variation is a typical behaviour in heterogeneous environments. It normally occurs when the water inflow takes place in conjunction with an intensive surface run-off, water coming from the impermeable base layer of aquifer or in the presence of big channels in a heterogeneous aquifer.

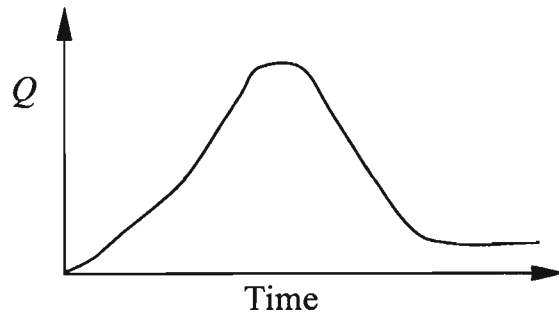


Figure 3.4. Inflow variation as a Gaussian distribution.

- Rate of inflow increasing with time as the mine extends.

This type of inflow behaviour is common in both surface mining excavations and underground mining. Water coming to the mining excavation shows a gradual raise in level with time and this is mainly a result of increasing mining excavation depth and surface area (Figure 3.5).

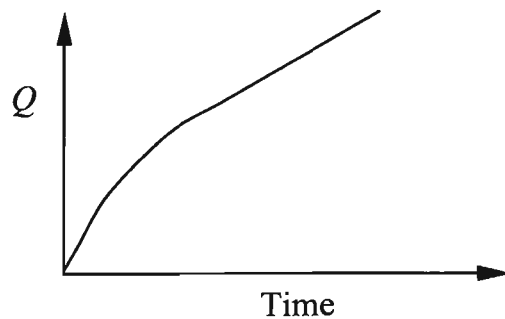


Figure 3.5. Inflow increases with time.

- Constant rate of inflow.

In this type of inflow, the inflow rate nearly remains constant for long time (Figure 3.6). This behaviour can occur in a multiplayer aquifer system in which the intermediate aquitard layer with a relatively low permeability has a leaking effect. Typical problems associated with this behaviour have been well exemplified by Rubio and Lorca (1993).

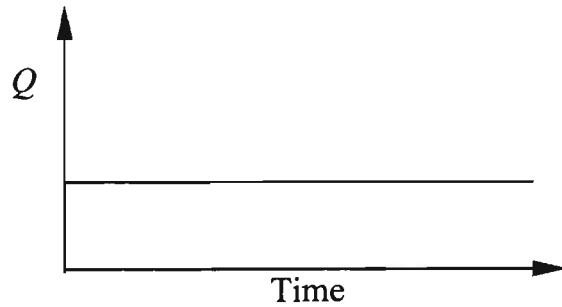


Figure 3.6. Constant inflow with time.

- Rate of inflow decreasing with time as the finite source aquifer dries up.

In many cases, water inflow decreases with time (Figure 3.7). This behaviour is typical in the case of unsteady or time dependent flow regime with a constant drawdown pumping in a vertical well.

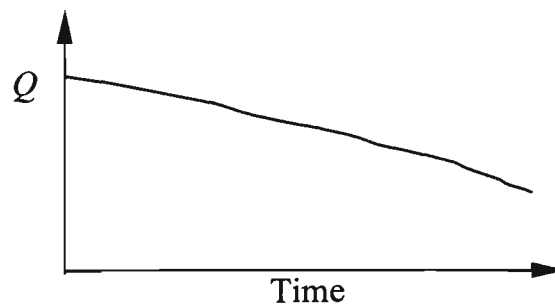


Figure 3.7. Decreasing inflow with time.

- Mixed rates of inflow.

This type of inflow behaviour is characterised as a combination of the various inflow shapes previously described (Figure 3.8). Inflow problem in the underground zinc mine of Vazante in Minas Gerais, Brazil, is a typical example showing mixed inflow behaviour described by Rubio and Lorca (1993). As Figure 3.8 shows, inflow increases with time until equilibrium is achieved then it remains constant with time.

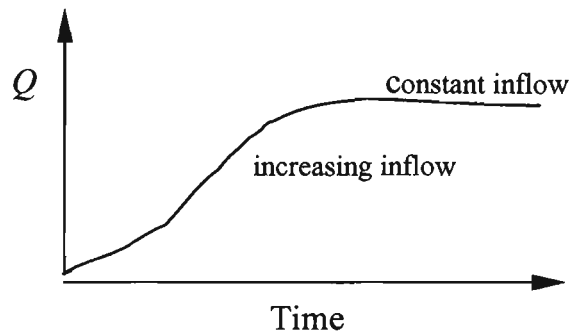


Figure 3.8. Mixed inflow behaviour.

Although considerable work has been carried out to describe the above mentioned inflow behaviours, no attempt has been made to present analytical equations describing different modes of inflow.

### 3.4 Prediction of groundwater inflow rate into surface mining excavation

An accurate prediction of the inflow quantities into mining excavation is necessary for the following purposes:

- To design an appropriate dewatering system in new mining works (Singh et al., 1985)
- For economic, safety and environmental purposes (Venburg, 1979)

Singh and Atkins (1985b) reported that an accurate prediction of groundwater inflow is also necessary and important in many existing mines where mining is carried out under large bodies of water in aquifers or under sea conditions.

Groundwater inflow rate into a mining excavation can be predicted by using one of the following techniques:

- Analytical methods
- Numerical methods

In the present work a two-dimensional finite element groundwater package, SEEP/W was modified to predict groundwater inflow to an open cut coal mining excavation as

well as prediction of post-mining groundwater rebound after cessation of dewatering. Before describing the numerical technique used in this work and the simulation results, a critical review of current simple analytical approaches is necessitated especially as some of these analytical solutions are used to validate the numerical results.

### 3.5 Aquifer type, its characteristics, flow regime and mining excavation

The complexity of the relationship between the type of aquifer, the hydraulic characteristic of porous media, flow regimes and the geometry of surface mining excavations often cause difficulties in predicting mine water inflow rate. The flow regime varies with the type of flow medium. In unconsolidated sediments, the flow regime is linear. Linear flow is slow and flow lines remain in the general vector direction of overall groundwater flow (Figure 3.9a). Darcy's law is therefore valid. By contrast, in rock environments where fractures and faults provide the conductivity of the medium, or in mine spoils where large voids may present, the flow type is obviously non-linear or turbulent (Figure 3.9b). Non-Darcy equations therefore govern flow of water in these mediums (Rogowski et al., 1977; Singh and Reed, 1987).

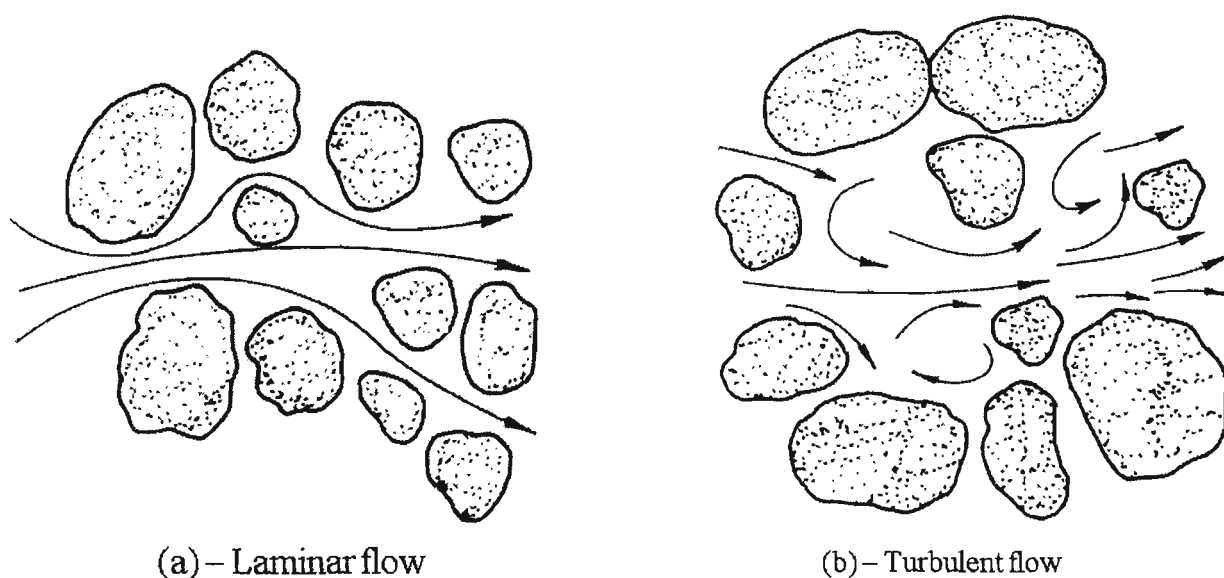


Figure 3.9. Laminar and Turbulent flow behaviours.

According to Dudgeon (1985) the non-Darcy flow can cause considerable reductions in groundwater inflow into an open pit mines in fractured rocks with high permeability due to significant non-Darcy head losses at long distances from the pit excavation boundary. He has developed a numerical finite element model to predict non-Darcy flow to an open-pit mine in a well fractured limestone medium. His measurements of inflows into two surface mines in carbonate aquifers in Australia have provided necessary data identifying the presence of non-Darcy flow. Near the mine, because the vertical component of flow is considerable and the hydraulic gradient is also high, therefore linear equations are not valid.

In the present research a Darcy flow assumption was applied to the simulation of groundwater inflow, groundwater rebound after ceasing mining and leaching of the pyrite oxidation products from an open cut coalmine.

### **3.6 Idealised hydrogeological profiles related to surface mining**

The most commonly encountered origins of sub-surface water flow to surface mining are given below:

#### **3.6.1 One-regime flow to a surface mining excavation**

This usually occurs in one of the following two cases:

- 1) Ore deposit acts as an aquifer underlain by an impervious layer. In this case, water inflow takes place into the mine (Figure 3.10). Advanced dewatering operation is most commonly used to avoid pit flooding. For sedimentary deposits, water flow generally occurs horizontally and the flow regime is assumed to be laminar at points far from the mining excavation face (Singh et al., 1985).

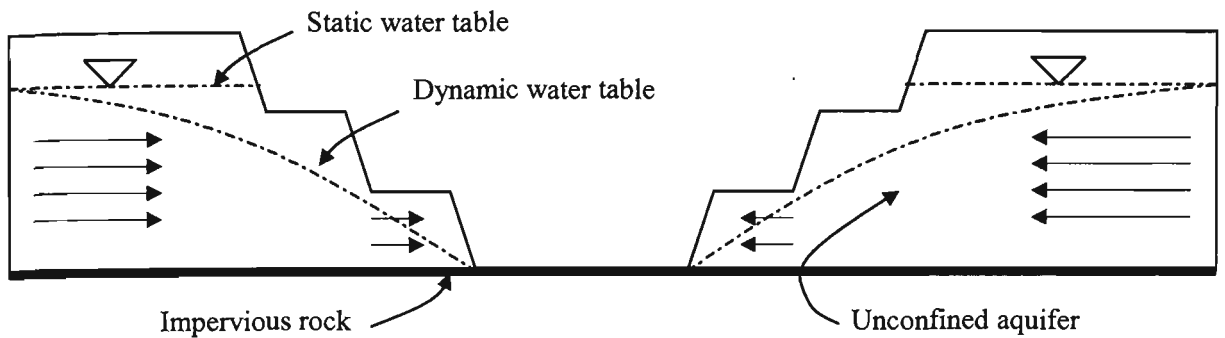


Figure 3.10. One regime flow into a surface mining excavation (quoted in Singh et al., 1985).

2) One regime flow can also occur where the mineral deposit is located above a confined aquifer. As the overburden materials and the mineral deposit are extracted during the mining operation, the impervious bed may break and water with high pressure is now allowed to flow into the mining excavation. In this case, inflow to the mine generally occurs in the vertical direction (Figure 3.11).

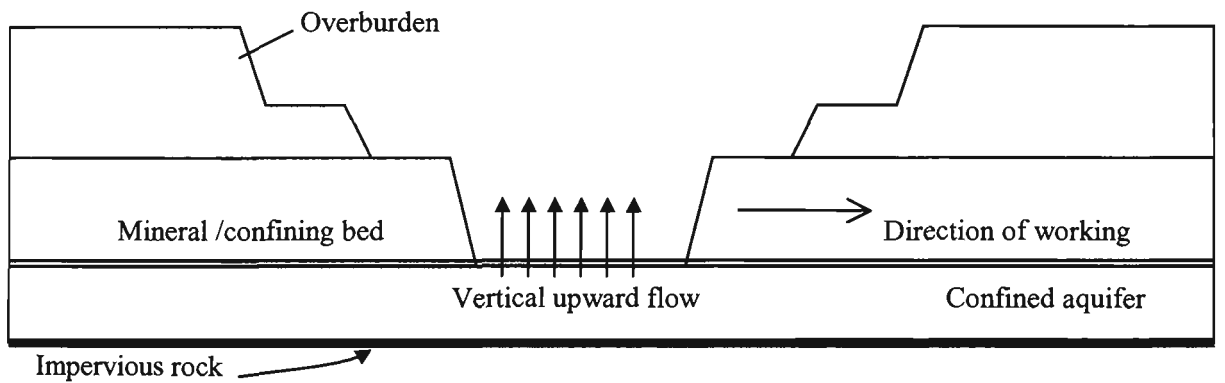


Figure 3.11. One regime flow into a surface mining excavation (quoted in Singh et al., 1985).

### 3.6.2 Two-regimes flow into a surface mining excavation

This case normally occurs where mining is carried out in an unconfined aquifer overlain by an alluvial deposit that maintains its own water table. Figure 3.12 shows this situation. Horizontal inflow to the mining excavation takes place from the unconfined aquifer which in turn receives vertical recharge from the alluvial sediment. The rate of

expansion of the cone of depression controls the size of the vertical recharge area in the overlying alluvial series contributing to the groundwater inflow into the mining excavation (Singh et al., 1985).

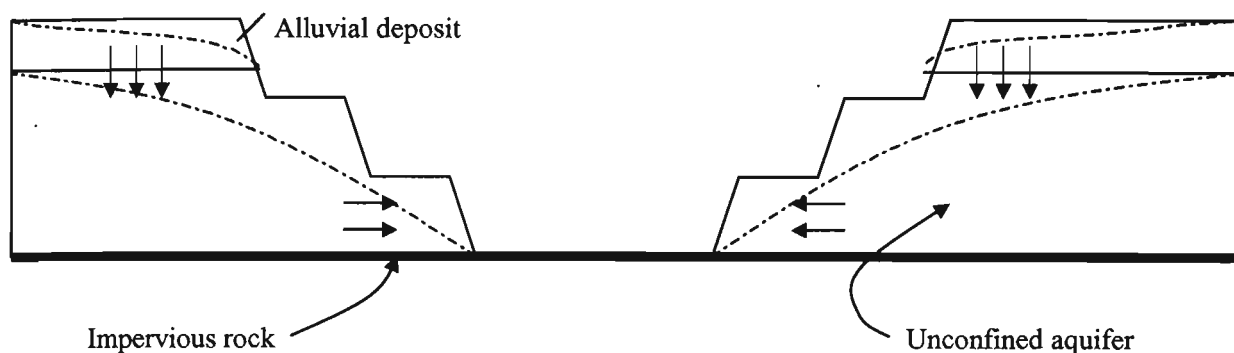


Figure 3.12. Two regime flow into a surface mining excavation (quoted in Singh et al., 1985).

### 3.6.3 Three-regime flow of groundwater to the surface mining excavation

In this situation, the process of mining may occur in a water table aquifer overlain by an alluvial sequence and underlain by a confined aquifer as illustrated in Figure 3.13. In such situations the flow regimes can be complicated due to horizontal flows from the alluvial deposit, horizontal flows occurring from the unconfined aquifer as well as vertical downwards recharge from the overlying alluvial aquifer to the unconfined aquifer and vertical upwards flow from the confined aquifer into the mining excavation. In this situation, mine extension will release the pressures of overburden layers on the confined aquifer and the confining layer splits and finally upward inflow from floor beds occurs.

### 3.7 Analytical methods for calculation of surface mining excavation inflow rate

Analytical approaches can be economically used to predict mine inflow rates during the initial stages of mine planning. This method is typically based on a simple mathematical equation.

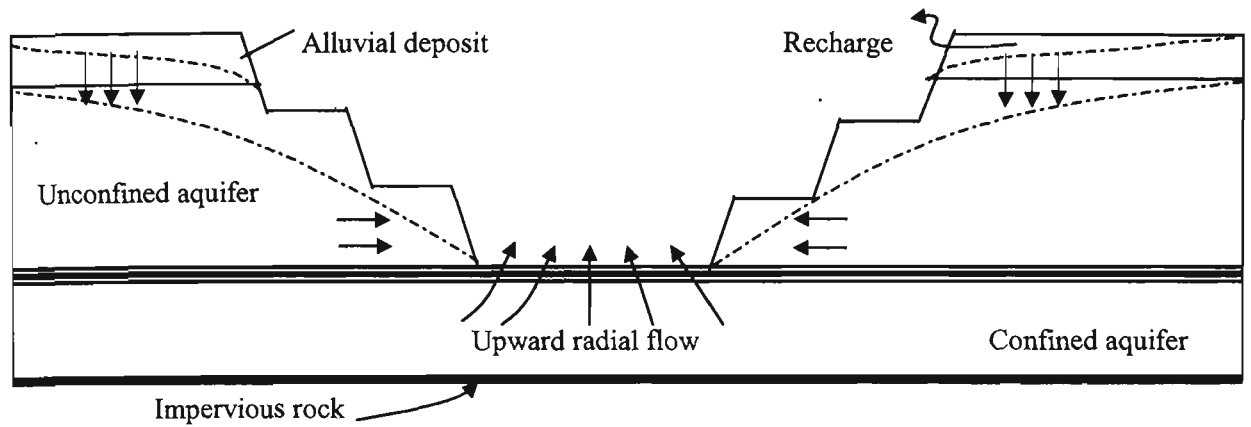


Figure 3.13. Three regime flow into a surface mining excavation  
(quoted in Singh et al., 1985).

In order to use an analytical equation, some assumptions are usually necessary to predict groundwater inflow. For instance, most analytical approaches assume that the aquifer media is homogenous and isotropic (Wang and Anderson, 1982). The analytical methods for prediction of mine water inflow are based on drawdown theory and are broadly classified into the following groups:

### 3.7.1 Equivalent well approach (EWA)

Based on this approach pumping in a surface mine is carried out using an imaginary fully penetrating well in the entire saturated thickness of an idealised aquifer. The water table or piezometric surface is lowered to below the mining excavation horizon at the mine wall by a constant pumping rate. The uniform pumping changes the hydraulic balance and establishes a difference in water level within and outside of the well as a cone of depression develops radially outward from the dewatering well (Walton, 1970). The outer boundary of the cone of depression describes the area of well influence (Todd, 1959). Because of this differential head, a three dimensional radial flow of water takes place towards the pit or surface mining excavation in order to provide the required equilibrium condition.

For development of the appropriate equation in this method, knowledge of the following aquifer characteristics is required:

- Transmissivity ( $T$ )
- Permeability or hydraulic conductivity ( $K$ )
- Storativity ( $S$ )
- Leakage factor for leaky aquifer ( $B$ ) and
- Mine geometry

EWA assumes that the mining excavation is as a large diameter well. Where, most open cut mining excavations have a nearly square or rectangle shape, hence an equivalent radius for the imaginary well can be properly calculated using the equation given by (quoted in Singh et al., 1985, Singh and Reed, 1987).

$$r = \left( \frac{2}{\pi} \right) (Y.W)^{\frac{1}{2}} \quad (3.2)$$

where,

$r$  = equivalent radius (m);

$Y$  = mine length (m);

$W$  = width of the mine (m).

Figure 3.14 shows the concept of equivalent well approach for prediction of water inflow into a surface mining excavation.

#### **(a) Analytical groundwater inflow models based on EWA**

Considerable effort has been placed into the development of analytical methods for modelling of surface mine inflows. Analytical equations for prediction of water inflow to surface mining excavations are presented in Singh and Atkins (1984); Singh et al. (1985); Singh and Reed (1987); Hanna et al. (1994); Vandersluis et al. (1995); Lewis (1999); and Marinelli and Niccoli (2000).

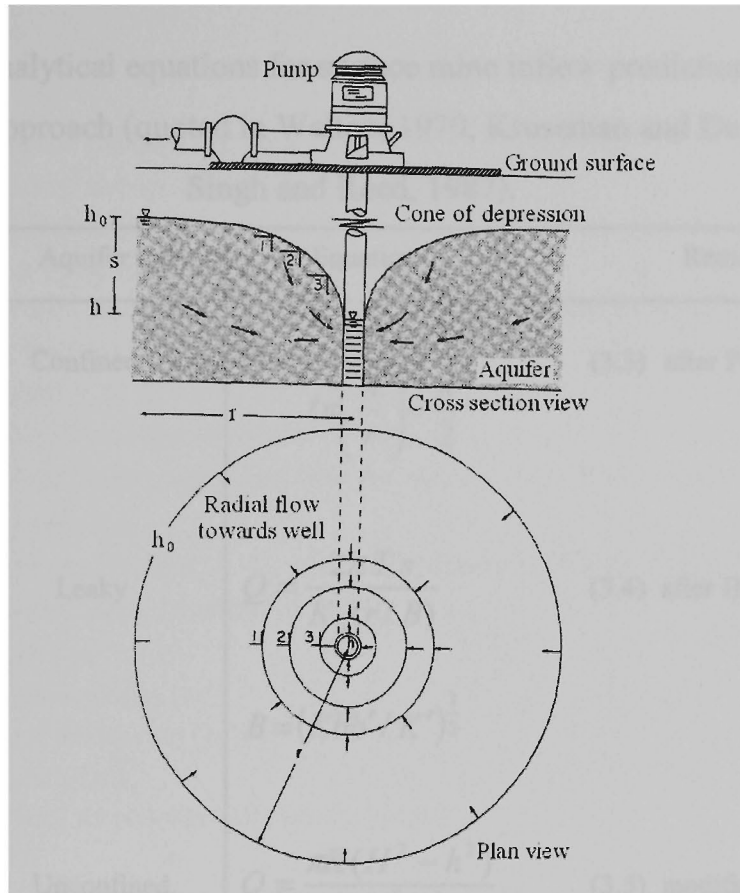


Figure 3.14. A schematic diagram of radial flow towards a pumping well (quoted in Watson and Burnett, 1993).

The analytical equations presented in the above mentioned technical papers can be used to predict groundwater inflow into surface mining excavations with particular sets of boundary conditions and some specific assumptions that limit their applicability in solving many real problems in different mining situations.

Table 3.1 outlines the appropriate simple analytical equations for prediction of inflow rates under various flow regimes and different aquifers (Walton, 1970; Kruseman and De Ridder, 1979; Singh and Reed, 1987). Tables 3.2, 3.3, 3.4 and 3.5 illustrate Hantush 1956 well function, Theis well function, Jacob & Lohman well function and values of  $W(u, r/B)$  respectively (Walton, 1970).

Table 3.1. Analytical equations for surface mine inflow prediction based on equivalent well approach (quoted in Walton, 1970; Kruseman and De Ridder, 1979; Singh and Reed, 1987).

Flow regime	Aquifer type	Equation	Remarks
Linear, Steady state	Confined	$Q = \frac{2\pi T s}{\ln\left(\frac{R}{r}\right) - \frac{n}{2}}$	(3.3) after Peterson (1957)
Linear, Steady state	Leaky	$Q = \frac{2\pi T s}{K_0(r/B)}$ $B = (Kbb'/K')^{\frac{1}{2}}$	(3.4) after Hantush (1956)
Linear, Steady state	Unconfined	$Q = \frac{\pi K(H^2 - h^2)}{\ln\left(\frac{R}{r}\right)}$	(3.5) modified Dupuit's Eq.
Linear, Transient state	Leaky	$Q = \frac{4\pi T s}{W(u, r/B)}$ $u = r^2 S / 4T t$	(3.6) after Hantush (1956)
Linear, Transient state	Confined	$Q = 2\pi T s W(\lambda)$	(3.7) after Jacob-Lohman
		$Q = 4\pi T s W(u)$	(3.8) Theis curve fitting
Linear, Transient state	Unconfined	as for confined aquifer (Kruseman and De Ridder, 1979) $s$ is replaced by: $s_1 = s - (s^2 / 2H)$	
Non-linear, Steady state	Confined	$s = Q \ln(R/r) / 2\pi T_L + Q^2 (R-r) / 4\pi^2 T_T^2 R r$ (3.9)	
Non-linear, Transient state	Confined	$s = Q r W(u) / 2\pi T_L + Q^2 (R-r) / 4\pi^2 T_T^2 R r$ (3.10)	

where,

- $b$  = thickness of the aquifer ( $m$ );
- $b'$  = thickness of the aquitard ( $m$ );
- $B$  = leakage factor ( $m$ );
- $h$  = head at a specific point ( $m$ );
- $H$  = initial water table elevation or saturated thickness of aquifer above mining footwall ( $m$ );
- $K$  = permeability of the aquifer ( $m/s$ );
- $K'$  = permeability of the aquitard ( $m/s$ );
- $K_0(r/B)$  = Hantush & Jacob well function for steady state leaky aquifer (dimensionless);
- $n$  = recharge coefficient,  $n = 1$ , for completely recharge system,  $n = 0$  without recharge (dimensionless);
- $Q$  = flow rate ( $m^3/s$ );
- $r$  = equivalent radius ( $m$ );
- $R$  = radius of influence ( $m$ );
- $s$  = drawdown ( $m$ );
- $S$  = coefficient of storage (dimensionless);
- $t$  = time ( $s$ );
- $T$  = transmissivity of the aquifer ( $m^2/s$ );
- $T_L$  = linear transmissivity ( $m^2/s$ );
- $T_T$  = turbulent transmissivity, ( $m^2/s$ );
- $W(u)$  = Theis well function (dimensionless);
- $W(u, r/B)$  = Hantush well function (dimensionless);
- $W(\lambda)$  = Jacob & Lohman well function (dimensionless).

Table 3.2. Values of  $K_0(r/B)$ - Hantush 1956 well function (quoted in Walton, 1970).

N	$r/B = N \times 10^{-3}$	$N \times 10^{-2}$	$N \times 10^{-1}$	N
1.0	7.0237	4.7212	2.4271	0.4210
1.5	6.6182	4.3159	2.0300	0.2138
2.0	6.3305	4.0285	1.7527	0.1139
2.5	6.1074	3.8056	1.5415	0.0623
3.0	5.9251	3.6235	1.3725	0.0347
3.5	5.7709	3.4697	1.2327	0.0196
4.0	5.6374	3.3365	1.1145	0.0112
4.5	5.5196	3.2192	1.0129	0.0064
5.0	5.4143	3.1142	0.9244	0.0037
5.5	5.3190	3.0195	0.8466	
6.0	5.2320	2.9329	0.7775	0.0012
6.5	5.1520	2.8534	0.7159	
7.0	5.0779	2.7798	0.6605	0.0004
7.5	5.0089	2.7114	0.6106	
8.0	4.9443	2.6475	0.5653	
8.5	4.8837	2.5875	0.5242	
9.0	4.8266	2.5310	0.4867	
9.5	4.7725	2.4776	0.4524	

Table 3.3. Theis well function  $W(u)$  (quoted in Walton, 1970).

N	$\mu$ or $\mu_{xy}$							
	$N \times 10^{-14}$	$N \times 10^{-12}$	$N \times 10^{-10}$	$N \times 10^{-8}$	$N \times 10^{-6}$	$N \times 10^{-4}$	$N \times 10^{-2}$	N
1.0	31.6590	27.0538	22.4486	17.8435	13.2383	8.6332	4.0379	0.21940
2.0	30.9658	26.3607	21.7555	17.1503	12.5451	7.9402	3.3547	0.04890
3.0	30.5604	25.9552	21.3500	16.7449	12.1397	7.5348	2.9591	0.01305
4.0	30.2727	25.6675	21.0623	16.4572	11.8520	7.2472	2.6813	0.003779
5.0	30.0495	25.4444	20.8392	16.2340	11.6280	7.0242	2.4679	0.001148
6.0	29.8672	25.2620	20.6569	16.0517	11.4465	6.8420	2.2953	0.0003601
7.0	29.7131	25.1079	20.5027	15.8976	11.2924	6.6879	2.1508	0.0001155
8.0	29.5795	24.9744	20.3692	15.7640	11.1589	6.5545	2.0269	0.0000376
9.0	29.4618	24.8566	20.2514	15.6462	11.0411	6.4368	1.9187	0.0000124

Table 3.4. Jacob-Lohman well function (quoted in Walton, 1970).

N	$\lambda$								
	$N \times 10^{-4}$	$N \times 10^{-2}$		$N \times 10^2$	$N \times 10^4$	$N \times 10^6$	$N \times 10^8$	$N \times 10^{10}$	$N \times 10^{12}$
1	56.9	6.13	0.985	0.346	0.1964	0.1360	0.1037	0.0838	0.0764
2	40.4	4.47	0.803	0.311	0.1841	0.1299	0.1002	0.0814	0.0744
3	33.1	3.74	0.719	0.294	0.1777	0.1266	0.0982	0.0801	0.0733
4	28.7	3.30	0.667	0.212	0.1733	0.1244	0.0968	0.0792	0.0726
5	25.7	3.00	0.630	0.274	0.1701	0.1227	0.0958	0.0785	0.0720
6	23.5	2.78	0.602	0.268	0.1675	0.1213	0.0950	0.0779	0.0716
7	21.8	2.60	0.580	0.263	0.1654	0.1202	0.0943	0.0774	0.0712
8	20.4	2.46	0.562	0.258	0.1636	0.1192	0.0937	0.0770	0.0709
9	19.3	2.35	0.547	0.254	0.1621	0.1184	0.0932	0.0767	0.0706
10	18.3	2.25	0.534	0.251	0.1608	0.1177	0.0927	0.0764	0.0704

Table 3.5. Values of Hantush 1956 well function for leaky aquifer,  $W(u, r/B)$   
 (quoted in Walton, 1970; Watson and Burnett, 1993).

r/B	0.004	0.008	0.01	0.02	0.04	0.06	0.08	0.10	0.20	0.40	0.60	0.80	1.000	2.000	4.0000
0	11.3	9.89	9.44	8.06	6.67	5.87	5.29	4.85	3.51	2.23	1.55	1.13	0.842	0.228	0.0223
$2 \times 10^{-6}$	11.2	9.89	9.44	8.06	6.67	5.87	5.29	4.85	3.51	2.23	1.55	1.13	0.842	0.228	0.0223
$4 \times 10^{-6}$	11.1	9.88	9.44	8.06	6.67	5.87	5.29	4.85	3.51	2.23	1.55	1.13	0.842	0.228	0.0223
$6 \times 10^{-6}$	10.9	9.87	9.44	8.06	6.67	5.87	5.29	4.85	3.51	2.23	1.55	1.13	0.842	0.228	0.0223
$8 \times 10^{-6}$	10.7	9.84	9.43	8.06	6.67	5.87	5.29	4.85	3.51	2.23	1.55	1.13	0.842	0.228	0.0223
$1 \times 10^{-5}$	10.6	9.80	9.42	8.06	6.67	5.87	5.29	4.85	3.51	2.23	1.55	1.13	0.842	0.228	0.0223
$2 \times 10^{-5}$	10.1	9.58	9.30	8.06	6.67	5.87	5.29	4.85	3.51	2.23	1.55	1.13	0.842	0.228	0.0223
$4 \times 10^{-5}$	9.45	9.19	9.01	8.03	6.67	5.87	5.29	4.85	3.51	2.23	1.55	1.13	0.842	0.228	0.0223
$6 \times 10^{-5}$	9.08	8.89	8.77	7.98	6.67	5.87	5.29	4.85	3.51	2.23	1.55	1.13	0.842	0.228	0.0223
$8 \times 10^{-5}$	8.81	8.67	8.57	7.91	6.67	5.87	5.29	4.85	3.51	2.23	1.55	1.13	0.842	0.228	0.0223
0.0001	8.59	8.48	8.40	7.84	6.67	5.87	5.29	4.85	3.51	2.23	1.55	1.13	0.842	0.228	0.0223
0.0002	7.92	7.86	7.82	7.50	6.62	5.86	5.29	4.85	3.51	2.23	1.55	1.13	0.842	0.228	0.0223
0.0004	7.24	7.21	7.19	7.01	6.45	5.83	5.29	4.85	3.51	2.23	1.55	1.13	0.842	0.228	0.0223
0.0006	6.84	6.82	6.80	6.68	6.27	5.77	5.27	4.85	3.51	2.23	1.55	1.13	0.842	0.228	0.0223
0.0008	6.55	6.53	6.52	6.43	6.11	5.69	5.25	4.84	3.51	2.23	1.55	1.13	0.842	0.228	0.0223
0.0010	6.33	6.32	6.31	6.23	5.97	5.61	5.21	4.83	3.51	2.23	1.55	1.13	0.842	0.228	0.0223
0.0020	5.64	5.63	5.63	5.59	5.45	5.24	4.98	4.71	3.50	2.23	1.55	1.13	0.842	0.228	0.0223
0.0040	4.95	4.94	4.94	4.92	4.85	4.74	4.59	4.42	3.48	2.23	1.55	1.13	0.842	0.228	0.0223
0.0060	4.54	4.54	4.54	4.53	4.48	4.41	4.30	4.18	3.43	2.23	1.55	1.13	0.842	0.228	0.0223
0.0080	4.26	4.26	4.26	4.25	4.21	4.15	4.08	3.98	3.36	2.23	1.55	1.13	0.842	0.228	0.0223
0.0100	4.04	4.04	4.04	4.03	4.00	3.95	3.89	3.81	3.29	2.23	1.55	1.13	0.842	0.228	0.0223
0.0200	3.35	3.35	3.35	3.35	3.34	3.31	3.28	3.24	2.95	2.18	1.55	1.13	0.842	0.228	0.0223
0.0400	2.68	2.68	2.68	2.68	2.67	2.66	2.65	2.63	2.48	2.02	1.52	1.13	0.842	0.228	0.0223
0.0600	2.30	2.30	2.30	2.29	2.29	2.28	2.27	2.26	2.17	1.85	1.46	1.11	0.839	0.228	0.0223
0.0800	2.03	2.03	2.03	2.03	2.02	2.02	2.01	2.00	1.94	1.69	1.39	1.08	0.832	0.228	0.0223
0.1000	1.82	1.82	1.82	1.82	1.82	1.82	1.81	1.80	1.75	1.56	1.31	1.05	0.819	0.228	0.0223
0.2000	1.22	1.22	1.22	1.22	1.22	1.22	1.22	1.22	1.19	1.11	1.00	0.86	0.715	0.227	0.0223
0.4000	0.70	0.70	0.70	0.70	0.70	0.70	0.70	0.70	0.69	0.67	0.62	0.57	0.502	0.210	0.0223
0.6000	0.45	0.45	0.45	0.45	0.45	0.45	0.45	0.45	0.45	0.44	0.42	0.39	0.354	0.177	0.0222
0.8000	0.31	0.31	0.31	0.31	0.31	0.31	0.31	0.31	0.31	0.30	0.30	0.27	0.254	0.144	0.0218
1.0000	0.22	0.22	0.22	0.22	0.22	0.22	0.22	0.22	0.22	0.21	0.21	0.20	0.185	0.114	0.0207
2.0000	0.05	0.05	0.05	0.05	0.05	0.05	0.05	0.05	0.05	0.05	0.05	0.05	0.044	0.034	0.0110
4.0000	0.00	0.00	0.00	0.00	0.00	0.00	0.00	0.00	0.00	0.00	0.00	0.00	0.004	0.003	0.0016
6.0000	0.00	0.00	0.00	0.00	0.00	0.00	0.00	0.00	0.00	0.00	0.00	0.00	0.000	0.000	0.0002
8.0000	0.00	0.00	0.00	0.00	0.00	0.00	0.00	0.00	0.00	0.00	0.00	0.00	0.000	0.000	0.0000

In arid and semi-arid areas where precipitation is generally limited and water inflow to a pit is normally controlled by horizontal groundwater inflow, Vandersluis et al. (1995) used the following analytical equation for estimation of the horizontal groundwater inflow rate to a pit in an unconfined aquifer. This equation is used to calculate inflow using large well equations based on the Dupuit assumptions for lateral, radial steady state flow to a fully penetrating well in an aquifer.

$$Q = \frac{1.366 K(2H - S)S}{\log(R + r_0) - \log r_0} \quad (3.11)$$

where,

$Q$  = groundwater inflow to an open pit in an unconfined aquifer ( $m^3 / day$ );

$K$  = permeability ( $m / day$ );

$H$  = potentiometric surface or initial water table elevation ( $m$ );

$S$  = drawdown in the aquifer ( $m$ );

$R$  = radius of influence;

$r_0$  = reduced radius of the open pit by level ( $m$ ).

The radius of influence can be estimated using the following equation:

$$R = 575 S(HK)^{0.5} \quad (3.12)$$

where,

$R$  = radius of influence ( $m$ );

$S$  = drawdown ( $m$ );

$K$  = permeability of aquifer ( $m / s$ );

$H$  = pre-mining potentiometric surface elevation.

The reduced radius of the open pit mine can then be calculated using the following expression:

$$r_0 = \left( \frac{A}{\pi} \right)^{\frac{1}{2}} \quad (3.13)$$

where,

$A$  = circular area of the pit by level ( $m^2$ ).

The following analytical equation based on well hydraulics can be used for estimation of steady state inflow rate to an open pit mine. This equation was derived from Thiem-Dupuit equation and can be applied for unconfined aquifer (Todd, 1959; Kruseman and De Ridder, 1979).

$$Q = \frac{\pi K (H^2 - h^2)}{\ln \left( \frac{R}{r_p} \right)} \quad (3.14)$$

where,

$Q$  = water inflow rate to a pit ( $m^3 / s$ );

$K$  = aquifer permeability ( $m / s$ );

$H$  = pre-mining potentiometric surface elevation ( $m$ );

$h$  = potentiometric surface elevation at a specific point ( $m$ );

$R$  = radius of influence ( $m$ );

$r_p$  = radius of the pit at the desired level ( $m$ ).

The radius of influence can be calculated using the following equation:

$$R = 575 S (HK)^{0.5} \quad (3.15)$$

where,

$S$  = drawdown ( $m$ ).

The following equation developed by Jacob - Lohman has been used for prediction of groundwater inflow to a surface mine pit (Kruseman and De Ridder, 1979; and Hanna et al., 1994). This analytical equation describes the transient decrease in groundwater inflow to a fully penetrating well in an idealised confined aquifer with this assumption that the drawdown in the well is instantaneously imposed and maintained at a constant elevation. This equation assumes that the well fully penetrates an aquifer. The aquifer has an infinite arial extent and transmissivity and storativity are assumed to be uniform.

The analytical equation is as follows:

$$Q = \frac{4\pi T \Delta h}{\ln \left( \frac{2.25 T t}{r_w^2 S} \right)} \quad (3.16)$$

where,

$Q$  = groundwater inflow ( $m^3 / day$ );

$T$  = transmissivity of the aquifer ( $m^2 / day$ );

$\Delta h$  = drawdown ( $m$ );

$t$  = elapsed time ( $days$ );

$r_w$  = radius of the well ( $m$ );

$S$  = storage coefficient of aquifer (dimensionless).

Based on above equation if transmissivity, storage coefficient, drawdown and well radius are assumed to be constant, the calculated inflow to the well will decrease with increasing logarithm of time.

According to Hanna et al. (1994), this solution can only be applied if the value of the dimensionless parameter,  $\alpha$  is greater than about 0.01.  $\alpha$  is defined as:

$$\alpha = \frac{Tt}{r_w^2 S} \quad (3.17)$$

Equation 3.16 is used to estimate passive inflow to an advancing open pit mine based on an analogy between an assumed circular pit and a large diameter well. For this case  $r_w$  will be the equivalent radius of pit ( $r_p$ ) and  $\Delta h$  is the difference between the elevation of the pre-mining potentiometric surface level and the elevation of the bottom of the pit at a given stage of mining.

For applying Equation 3.16 for pit inflow simulation, the assumption should be made that the pit is excavated instantaneously during each stage of mining and drawdown also takes place instantaneously.

It should be noted that the Equation 3.16 can be used for confined aquifers. To apply the equation in an unconfined or water table aquifer, the following correction should be applied to convert the unconfined aquifer drawdown,  $\Delta h_{uc}$  to the equivalent confined aquifer drawdown,  $\Delta h_c$  (Kruseman and De Ridder, 1979):

$$\Delta h_c = \Delta h_{uc} - \frac{\Delta h_{uc}^2}{2H} \quad (3.18)$$

where,

$\Delta h_c$  = confined aquifer drawdown (  $m$  );

$\Delta h_{uc}$  = unconfined aquifer drawdown (  $m$  );

$H$  = initial water table elevation (  $m$  ).

Combining Equations 3.16 and 3.18 yields:

$$Q = \frac{4\pi T(\Delta h - \frac{\Delta h^2}{2H})}{\ln\left(\frac{2.25Tt}{r_p^2 S}\right)} \quad (3.19)$$

Equation 3.19 can be used for prediction of inflow into a pit in unconfined aquifers.

Marinelli and Niccoli (2000) presented an analytical model for prediction of the groundwater inflow to a mining excavation. As in the case of most analytical solutions, they are based on some assumptions and the solutions are not applicable for all mining situations. The analytical method takes into account:

- The effect of decreasing saturated thickness near the pit walls
- The effect of distributed recharge flux and
- The effect of upward groundwater inflow through the pit excavation bottom

This analytical solution is based on the following assumptions:

- The saturated thickness of aquifer will decrease with lowering the water table
- The component of inflow occurring through the pit bottom is incorporated
- The aquifer is semi-infinite below the pit hence there is no no-flow boundary condition at depth.
- The flow type is steady state
- The pit walls are assumed as a right circular cylinder
- Groundwater flow is horizontal
- The pre-mining water table is assumed as horizontal
- Surface infiltration is considered as uniform distributed recharge

Based on analytical solution described by Marinelli and Niccoli (2000), the flow region is divided into two zones as shown in Figure 3.15:

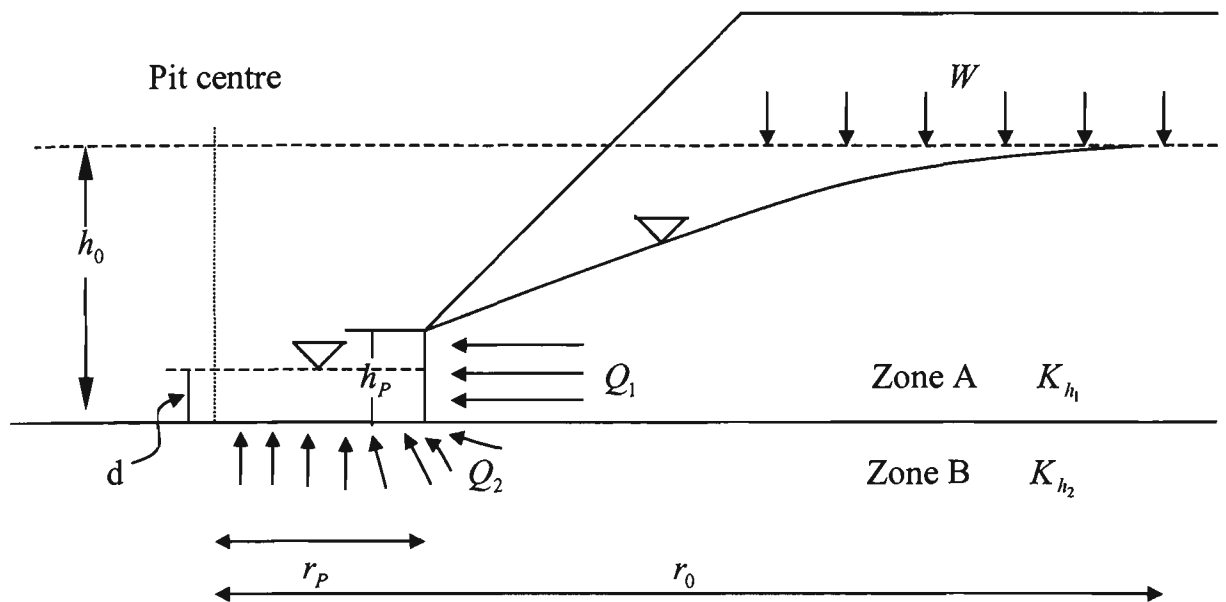


Figure 3.15. Groundwater inflow to a pit (quoted in Marinelli and Niccoli, 2000).

- Zone A, contains that above the pit base and considers the groundwater inflow occurring through the pit walls.
- Zone B, exists below the pit bottom and represents the upward inflow through the pit bottom.

The pit inflow rate from zone A is calculated by:

$$Q_1 = W\pi(r_0^2 - r_p^2) \quad (3.20)$$

where,

$Q_1$  = inflow from the pit walls;

$W$  = distributed recharge flux;

$r_p$  = effective pit radius;

$r_0$  = radius of influence.

The radius of influence ( $r_0$ ) can be calculated using the following equation:

$$h_0 = \left( h_p^2 + \frac{W}{K_{h1}} \left[ r_0^2 \ln \left( \frac{r_0}{r_p} \right) - \left( \frac{r_0^2 - r_p^2}{2} \right) \right] \right)^{\frac{1}{2}} \quad (3.21)$$

where,

$h_0$  = initial water table elevation above the base of zone A;

$h_p$  = saturated thickness above the base of zone A at  $r_p$  ;

$K_{h1}$  = horizontal permeability of aquifer within zone A.

In this solution  $W$ ,  $K_{h1}$ ,  $r_p$ ,  $h_p$  and  $h_0$  are given as input data and  $r_0$  is then calculated from Equation 3.21 by iteration procedure.  $Q_1$  is finally computed using Equation 3.20. The inflow component for zone B is based on steady state flow to one side of a circular disk sink of constant and uniform drawdown, in which the sink denotes the bottom of the pit. The solution is based on the following assumptions:

- Hydraulic head is initially uniform for the entire zone B. Initial head is equal to the initial water table elevation in zone A.
- Hydraulic head is constant for the disk sink and it is equal to the pit lake water surface elevation.
- In the case of complete dewatering, the head of the disk sink is equal to the elevation of the pit bottom.
- Water flow to the disk sink is three-dimensional and axially symmetric.
- The aquifer within zone B is anisotropic and the principal coordinate directions for permeability are horizontal and vertical.

The steady state inflow from zone B is calculated from the following equations:

$$Q_2 = 4r_p \left( \frac{K_{h_2}}{m_2} \right) (h_0 - d) \quad (3.22)$$

and

$$m_2 = \sqrt{\frac{K_{h_2}}{K_{v_2}}} \quad (3.23)$$

where,

$Q_2$  = pit inflow rate from zone B;

$K_{h_2}$  = horizontal hydraulic conductivity for zone B;

$K_{v_2}$  = vertical conductivity for zone B;

$m_2$  = anisotropy parameter;

$d$  = depth of the pit lake;

$h_0$  = hydraulic drawdown along the pit bottom.

The total inflow rate ( $Q_i$ ) to pit is finally calculated from:

$$Q_i = Q_1 + Q_2 \quad (3.24)$$

### **(b) Limitations of equivalent well approach**

Equivalent well approach is based on drawdown theory. The reliability of this method and its results depend to the following assumptions of drawdown theory. It should be mentioned that, in real mining situations, these assumptions are rarely met hence obtained results using equivalent well approach are only approximate results.

- The aquifer has an infinite horizontal extend.
- The aquifer is homogeneous and isotropic with respect to its hydrogeological characteristics.
- The aquifer has a uniform thickness over the mine radius of influence.

- The pre-mining water table or potentiometric surface is approximately horizontal over the area influenced by surface mining excavation.
- The pumping rate is constant with time.
- The imaginary well penetrates the entire aquifer.
- The groundwater flow towards the well is horizontal and flow of water occurs from the entire thickness of the aquifer.
- Water removed from storage is discharged instantaneously with decline of head.

### **3.7.2 Two-dimensional flow approach**

Several two-dimensional analytical solutions for predicting the steady state and time dependent drawdown in a surface mining excavation have been reported (Freeze and Cherry, 1979; McWhorter, 1981; Singh et al., 1985; Ngah, 1985; Singh and Reed, 1987).

Based on this approach, when a surface mining activity is carried out below the water table, groundwater flows from the incised aquifer into the mining excavation. Flow regime is essentially assumed to be two-dimensional. Far from the mine, flow is linear but near the mining excavation the linear flow assumption is not valid and the vertical component of the flow is important. This situation makes an exact analytical solution using the equivalent well method very approximate (Singh and Reed, 1987).

These equations are simple to use for estimating inflows and drawdown for different situations. These solutions provide approximate results that are sufficiently accurate for practical purposes. These approaches, however, are not appropriate for all mining situations and under some specific conditions such as near the seepage plane and in the

region of the vertical impervious boundary the simplified flow assumptions can predict unrealistic results (Singh and Reed, 1987).

The following is a quick and easy analytical transient solution for estimating drawdown and inflow rate to a surface mining excavation (Singh et al., 1985). The drawdown at a distance  $x$  from the mining excavation at a time  $t$  is given by the following equation:

$$D = (H - h_w) [1 - G(x/H, \tau)] \quad (3.25)$$

and inflow rate into the excavation per unit length of excavation is given as follows:

$$q = \left( \frac{4T}{\pi H} \right) (H - h_w) \int_0^\infty \exp(\tau \lambda \operatorname{Tanh} \lambda) d\lambda \quad (3.26)$$

where,

$H$  = initial water table elevation (  $m$  );

$h_w$  = water table elevation at excavation face (  $m$  );

$T$  = transmissivity of the aquifer (  $m^2 / day$  ).

$$\tau = \left( \frac{K}{S_y H} \right) t \quad (3.27)$$

$$\lambda = aH \quad (3.28)$$

$a$  = dummy variable which vanishes in integration;

$K$  = permeability of the aquifer (  $m / day$  );

$S_y$  = specific yield (unit less);

$t$  = time (  $day$  ).

Table 3.6 gives the values of  $\int_0^\infty \exp(-\tau \lambda \operatorname{Tanh} \lambda) d\lambda$  for a given  $t$  and Figure 3.16

gives  $G(x/H, \tau)$  for given values of  $\tau$  and  $x/H$ .

It should be noted that the above equation however assumes large time increments and that there is a uniform rate of flow at the outlet or outflow region.

Table 3.6. Values of  $Y = \int_0^\infty \exp(-\tau \lambda \tanh \lambda) d\lambda$  (quoted in Singh et al., 1985).

$\tau$ :	0.001	0.002	0.003	0.004	0.005	0.006	0.007	0.008	0.009	0.010	0.025	0.050
Y:	999.9	500.0	333.3	250.0	200.0	166.7	142.9	125.0	111.1	100.0	40.00	20.00
$\tau$ :	0.100	0.250	0.500	1.0	2.0	4.0	6.0	8.0	10.0	20.0	30.0	40.0
Y:	10.04	4.081	2.133	1.188	0.723	0.474	0.379	0.326	0.291	0.201	0.164	0.141
$\tau$ :	60.0	80.0	100.0	200.0	300.0	400.0	500.0	600.0	700.0	800.0	900.0	1000
Y:	0.115	0.099	0.089	0.063	0.051	0.044	0.040	0.036	0.034	0.031	0.030	0.028

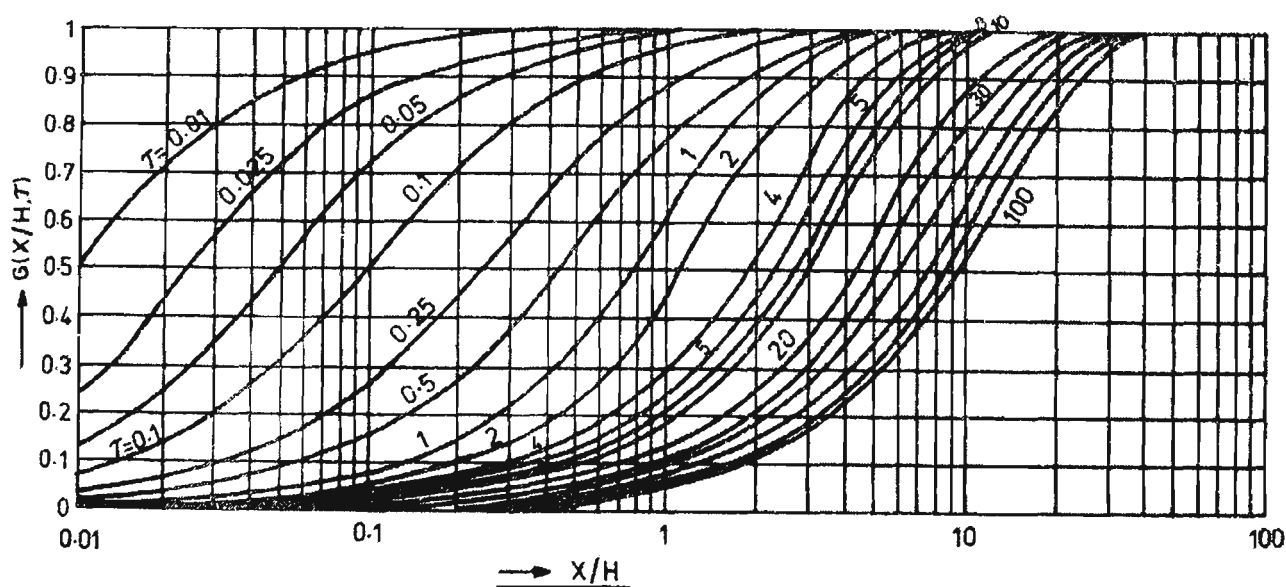


Figure 3.16. Values of the integral  $G(x/H, \tau)$  for given values of  $\tau$  and  $x/H$  (quoted in Singh et al., 1985).

For a finite aquifer the two-dimensional transient groundwater inflow into an excavation can be predicted from the following equation (Freeze and Cherry, 1979; Singh et al., 1985; Domenico and Schwartz, 1990):

$$q = \frac{H^2 K}{S_y R} \gamma \quad (3.29)$$

$$\tau = \frac{KH}{S_y R^2} t \quad (3.30)$$

where,

$\tau$  = dimensionless time or the time constant for a basin calculated from prior knowledge of  $K$ ,  $H$  and  $S_y$ ;

$\gamma$  = dimensionless discharge;

$R$  = radius of influence ( $m$ );

$t$  = time (days);

$S_y$  = specific yield (unit less);

$K$  = permeability ( $m / day$ );

$H$  = initial water table elevation ( $m$ );

$q$  = flow rate into the excavation per unit length of excavation ( $m^2 / day$ ).

Figure 3.17a illustrates the geometry of the two-dimensional vertical cross section of the problem. The relationship between the dimensionless discharge  $\gamma$  and the dimensionless time  $\tau$  is given in Figure 3.17b. The dimensionless drawdown for given values of dimensionless distance ( $x/R$ ) is shown in Table 3.7.

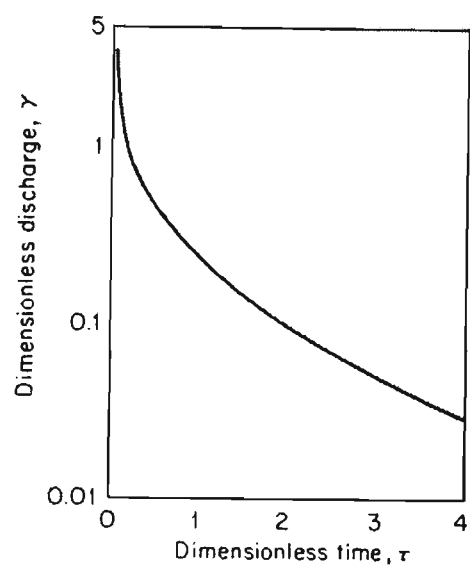
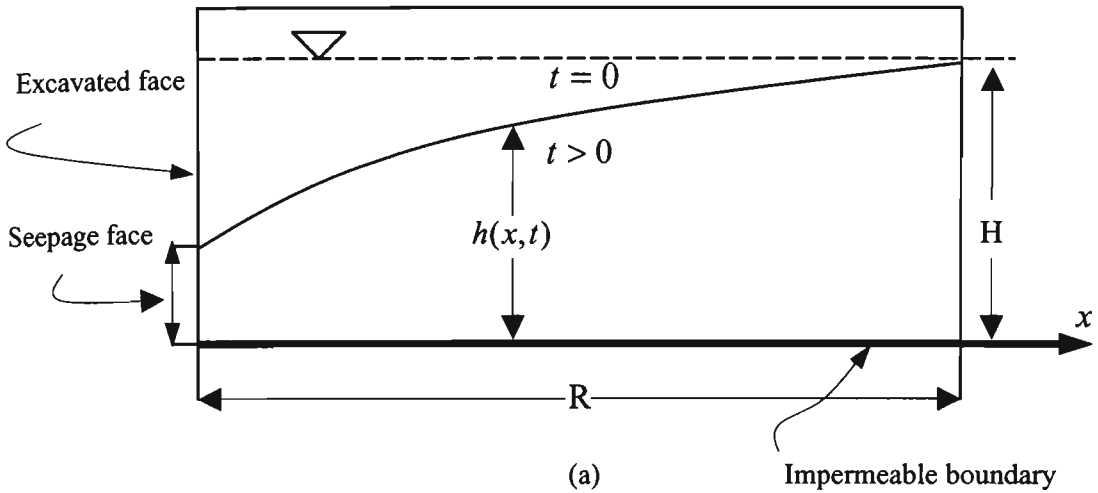


Figure 3.17. Prediction of groundwater inflows into an excavation (quoted in Freeze and Cherry, 1979).

Table 3.7. Dimensionless drawdown for given values of dimensionless distance,  $x/R$  (quoted in Singh et al., 1985).

$\tau$	$x/R$	0	0.25	0.5	0.75	1.0
5	0.025	0.095	0.1335	0.1500	0.1775	
2.5	0.045	0.1557	0.2150	0.2500	0.2500	
1.0	0.0875	0.2950	0.4050	0.4550	0.5000	
0.5	0.1125	0.4250	0.5700	0.6450	0.6950	
0.25	0.1750	0.5315	0.7075	0.8200	0.8500	
0.10	0.1825	0.6750	0.8650	0.9350	0.9550	
0.05	0.2875	0.7750	0.9200	0.9700	1.0000	
0.025	0.4000	0.8625	0.9550	1.050	1.0375	

**(a) Modified two-dimensional flow approach**

McWhorter (1981) applied the concept of a successive steady state flow approach to predict water inflow into a surface mining excavation from a confined aquifer incised by mining activity as shown in Figure 3.18. In this method there is an assumption that the variation of piezometric head with time corresponds to the steady state instantaneous drawdown affected by a particular rate of groundwater inflow to the excavation.

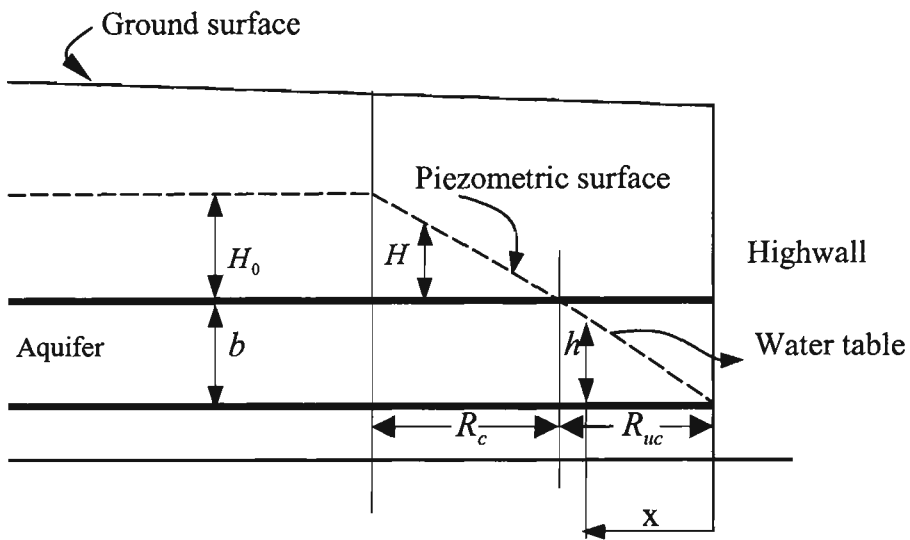


Figure 3.18. Schematic diagram for inflow from an aquifer incised by surface mining excavation (after McWhorter, 1981).

It was noted that incising the confined aquifer during mining causes the aquifer to become unconfined near the excavated face while remote from the mine the aquifer remains confined. Consideration of the fact that the confined aquifer will become unconfined near the mining excavation is necessary because the storage coefficient applied in the unconfined zone of the aquifer is much greater than that which is used in the confined zone.

In this approach, it is assumed that the length of the excavation increases linearly with time at an average rate of advancement equal to  $R_a$  then,

$$R_a = \frac{Y_p}{t_a} \quad (3.31)$$

where,

$R_a$  = average rate of elongation of the pit (*m / day*);

$Y_p$  = maximum length of the pit (*m*);

$t_a$  = time period during which the pit is elongating (*day*).

The rate of groundwater inflow on the highwall face per unit length of cut is given as follows (McWhorter, 1981):

$$q_a = At^{\frac{1}{2}} \quad (3.32)$$

and

$$R_{uc} = \frac{Tb}{2q} \quad (3.33)$$

$$R_c = \frac{TH_0}{q} \quad (3.34)$$

$$A = \frac{1}{2} \left( \sqrt{\frac{S_y Tb^2}{3} + STH_0^2 + STH_0 b} \right) \quad (3.35)$$

Equation 3.32 can be modified to estimate groundwater inflow into a mining excavation where the length of the excavation increases with time by taking into account the flow from different increments of exposed face.

The total inflow into the pit from one side of the excavation is given as follows:

$$Q = 2R_a A \sqrt{t} \quad t \leq \frac{Y_p}{R_a} \quad (3.36)$$

Equation 3.36 calculates the total inflow into the pit after time  $t$  at which the pit ceases to elongate. The inflow rate when mine extension has ceased is given below:

$$Q = 2R_a A \left( \sqrt{t} - \sqrt{t - \frac{Y_p}{R_a}} \right), \quad t \geq \frac{Y_p}{R_a} \quad (3.37)$$

Equation 3.37 shows that the inflow to the pit decreases sharply once the maximum length of pit has been established.

The total inflow to the mine from both sides of the excavation is obtained as follows:

$$Q = 4R_a A \sqrt{t}, \quad t \leq \frac{Y_p}{R_a} \quad (3.38)$$

$$Q = 4R_a A \left( \sqrt{t} - \sqrt{t - \frac{Y_p}{R_a}} \right), \quad t \geq \frac{Y_p}{R_a} \quad (3.39)$$

The distances  $R_{uc}$  and  $R_c$  are given as follows:

$$R_{uc} = \frac{Tb}{2A} \sqrt{t - \frac{Y_p}{R_a}} \quad (3.40)$$

and

$$R_c = \frac{TH_0}{A} \sqrt{t - \frac{Y_p}{R_a}} \quad (3.41)$$

where,

$h$  = height of water table above impervious base of aquifer;

$H$  = artesian head measured from top of confined aquifer;

$K$  = permeability of the aquifer;

$S_y$  = apparent specific yield;

$S$  = storage coefficient;

$T$  = transmissivity;

$t$  = time;

$R_{uc}$  = interval in which aquifer is unconfined;

$R_c$  = length of the depressed part of the confined aquifer;

$b$  = thickness of the confined aquifer;

$R_a$  = average rate of extension of the pit;

$Y_p$  = maximum length of the pit;

$\frac{Y_p}{R_a}$  = time period during which the pit is elongating.

It is noted that for an unconfined aquifer the parameter  $H_0$  is equal to zero in all of the equations mentioned above. In particular, the parameter  $A$  will reduce to the following equations:

$$A = \left( \frac{S_y T b^2}{12} \right)^{\frac{1}{2}} = \frac{b}{2} \sqrt{\frac{S_y T}{3}} \quad (3.42)$$

The advantage of this method is that it takes into consideration the effect of time and face advance on the predicted inflow quantity. However, the predicted inflow would be much larger, particularly in the initial stages of mining because the entire pit is not established instantaneously. Furthermore, this approach assumes that flow occurs only in planes normal to the long axis of the advancing pit while the actual flow in plan view will be two-dimensional. Moreover, the discharge to the pit through the ends of the excavation is not considered in this method and it is assumed that the length to width ratio is large.

### **(b) Limitations of two-dimensional flow equations**

The following assumptions are necessary in two-dimensional approaches for predicting groundwater inflow to the surface mining excavation which limit their applicability in many mining situations.

- The mining excavation is made instantaneously
- Drawdown in the mining excavation is assumed to be instantaneous along the entire length of exposed face. This assumption results in over-prediction of the quantity of inflow into a mining excavation.
- An aquifer is not entirely confined. Part of the aquifer near the exposed face becomes unconfined while remote from the excavated face the aquifer remains confined. McWhorter (1981) considered this situation in his modified two-dimensional inflow model.
- Two-dimensional flow approaches do not take into account the amount of inflow taking place through the ends of the excavation. In the two-dimensional formulae, it is assumed that the ratio of the length to width is always large.

### **3.8 Limitations of analytical approaches**

- The analytical solutions assume that the flow to a surface mining excavation occurs from an idealised aquifer. While inflow to a real pit is remarkably more complex than that assumed by analytical methods.
- Groundwater inflow into a surface mining excavation is usually three-dimensional hence lateral flow does not occur only through the sides of the mining excavation.
- The saturated thickness of the aquifer decreases towards the surface mining excavation due to drawdown hence transmissivity of the aquifer will decrease towards the excavation.

- There is anisotropy in the aquifer, therefore horizontal permeability ( $K_h$ ) is not equal to vertical permeability ( $K_v$ ).
- There are heterogeneities in the aquifer such as faults, dykes and changes in lithology.

Each of the above mentioned deviations from the idealised conditions implicit in the analytical approaches result in over prediction of the amount of inflow to a mining excavation.

### **3.9 Conclusions**

Simple analytical equations derived from groundwater theories have been reviewed. Their suitability for prediction and quantification of water inflow into surface mining excavations have been evaluated. The analytical equations are divided into two major groups on the basis of assumptions made. The equivalent well approach assumes that the surface mining excavation as a large diameter well and inflow into the excavation is calculated by the use of drawdown theory. The two-dimensional method takes into consideration the idealised pit geometry for calculation of inflow rate. The method also considers inflow resulting from different increments of exposed face as the length of the pit increases with time as mining operation extends. Although analytical solutions provide quick estimates of groundwater inflow for use in a field situation, in particular, during the initial stages of mine development, they are, however, based on some specific assumptions that limit their applicability in many mining situations. A numerical model provides a powerful tool to simulate all aquifer conditions and gives a more realistic representation of the interaction between hydrogeological conditions and mining operations.

## **CHAPTER FOUR**

### **A FINITE ELEMENT MODEL FOR GROUNDWATER INFLOW AND REBOUND PREDICTION IN OPEN CUT MINES**

## CHAPTER FOUR

### A FINITE ELEMENT MODEL FOR GROUNDWATER INFLOW AND REBOUND PREDICTION IN OPEN CUT MINES

#### 4.1 Introduction

Analytical solutions of groundwater inflow regimes are based on some idealised assumptions and simplified boundary conditions that limit their applicability to different mining situations. However, analytical approaches are not as versatile as numerical methods in simulating complex aquifer conditions and complex mine geometry. Numerical models provide a more realistic approach in evaluating interaction between groundwater systems and mining. Furthermore, numerical models are more reliable in predicting groundwater inflow into mining excavations than analytical approaches.

An accurate mine inflow prediction is an essential task for designing appropriate dewatering systems. Numerical groundwater flow models can be used by mining operators to predict the quantity of inflow to mines and to evaluate the effects of mining on local and regional water bodies. While simple analytical approaches are commonly used during the initial stages of mine development, numerical models for estimating mine inflow rates may be required at advanced stages of mine planning. Numerical models are relatively inexpensive and versatile to implement, and when there is sufficient time and hydrogeological data, the numerical approach is the only method that can predict realistic inflow rates. A numerical method is also able to predict the post-mining groundwater rebound within backfilled open cut mines.

According to Naugle and Atkinson (1993) a detailed numerical groundwater model is a powerful tool for the following purposes:

- Evaluating complex geology near the surface mine
- Assessing the impact of active mine dewatering
- Estimating the long-term impacts of post-mining rebound

Many previous commercial numerical based computer packages were limited in their ability to calculate the height of the seepage faces, to predict groundwater inflow, post-mining rebound and to be applicable for various aquifer conditions. In this thesis, SEEP/W (Geo-slope International Ltd., 2002) which is a two-dimensional axis-symmetric finite element package was used to simulate mine water inflow and post-mining rebound processes.

#### **4.2 Types of models**

A model is a representation of what occurs in a real system. The main objective of modelling is to increase understanding of processes that are occurring within a real system, and to predict how the system will behave in the future. Models can help to design, optimise and predict performance of field remediation strategies. Models can be used to evaluate the effects of uncertainty in mining, geology, hydrogeology, and chemistry on the ability to predict an outcome. There are different types of models as follows:

(a) Conceptual models, which describe qualitatively the processes occurring within a real system.

(b) Physical models, which have been considerably used for the better understanding of real problems in particular in studies of hydrogeological problems. Physical models may provide scope for systematically varying any selected parameters in order to generate qualitative simulations or imitations of the problem (Edwards et al., 1995). The main problems associated with physical models are that they are very costly.

Furthermore these models are limited in their applications to simple hydrogeological problems (Watson and Burnett, 1993).

(c) Mathematical models. Once a conceptual model has been developed for the problem in hand, mathematical models may be used to quantify the behaviour of the system. This method involves developing or adopting a mathematical equation. The appropriate equations are then solved analytically if possible or numerically using an appropriate algorithm or computer code for the selected variable, which defines the system under study.

#### **4.2.1 Numerical methods**

Numerical models, particularly the finite element method are extensively used for modelling the groundwater flow in a complex aquifer system, the finite element method, in particular the Galerkin approach has been known as a strong and powerful numerical technique for this purpose (Rabbani and Warner, 1994).

Numerical modelling methods are used to solve mathematical models of groundwater flow using computers. Development and improvement in numerical approaches as well as the rapid growth of computers and software now make it possible to deal with very complicated flow problems in underground flow systems (Hromadka II, 1992). A mathematical model consists of a set of partial differential equations that are recognised to govern the groundwater flow in the subsurface. The reliability of predictions made by a mathematical groundwater model depends on how well such a model can approximate the real field situation. Because the real field situations are very complicated, some simplifications are necessary in order to model groundwater flow. To deal with more complicated field situations, it is necessary to solve governing equations approximately for groundwater flow using numerical methods (Wang and Anderson, 1982).

Numerical simulations of groundwater flow have been widely carried out for a number of years to help in aquifer management. Among these studies are work by Pinder and Frind (1972); Neuman (1972); Pinder et al., (1973); Desai (1974); Neuman (1974); Gray and Pinder (1974); Grove (1977); Frind and Verge (1978); Freeze and Cherry (1979); Huyakorn et al. (1986); and Rabbani (1994). Some numerical models have also been used to predict groundwater inflow into surface and underground mines and to estimate the post mining filling rate of pit lakes. Amongst this research, work presented by Rogowski and Weinrich (1981); Williams et al. (1986); Naugle and Atkinson (1993); Hanna et al. (1994); Davis and Zabolotney (1996); and Azrag et al (1998) are all noteworthy. The different numerical methods used in this research work are given below:

#### **4.2.2 Finite difference method (FD)**

The finite difference method is the most common numerical method for solving differential equations. This method describes the unknown variable  $\phi$  by the use of point samples at the nodal points of a grid of co-ordinate lines. Truncated Taylor series expansions are often used to generate finite difference approximations of derivatives of unknown variable in terms of point samples of  $\phi$  at each grid point and its immediate neighbours. Those derivatives appearing in the governing equations are replaced by finite differences to yield an algebraic equation for the values of  $\phi$  at each grid point.

The finite difference method is easily used because the derivatives in the partial differential equations governing groundwater flow are easily approximated (Williams et al., 1986). In modelling of non-uniform and anisotropic aquifer systems (Figure 4.1.b), the FD method, however, is not always easy to apply (Neuman, 1974). One of the disadvantages of the finite difference model is that it is necessary to apply a rectangular

system of node points. This limitation makes difficulty in dealing with a mesh to irregular boundaries in aquifer systems (Williams et al., 1986).

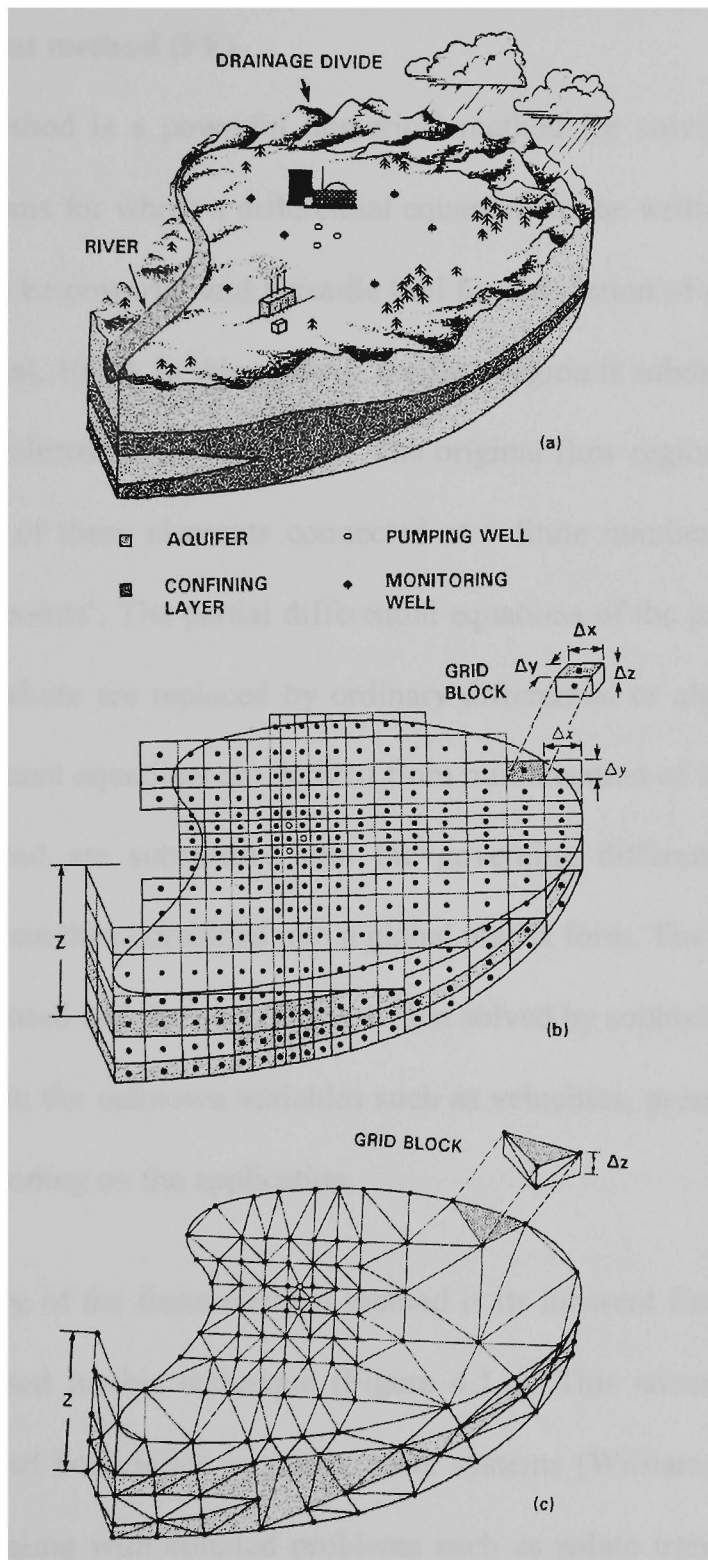


Figure 4.1. Schematic representations of numerical finite element and finite difference grids for simulating an aquifer system. (a) A map view of the aquifer illustrating well field, observation wells and aquifer boundaries. (b) Finite difference mesh with block-centred nodes. (c) Finite element grid with triangular elements where  $\Delta Z$  is the aquifer thickness (Wang and Anderson, 1982; Watson and Burnett, 1993).

In this thesis, a finite difference approximation scheme was used for time integration of the governing equations of groundwater flow (see Section 4.9).

#### **4.2.3 Finite element method (FE)**

Finite element method is a powerful numerical method for solving a wide range of engineering problems for which a differential equation can be written. This method has been considered to be powerful and versatile tool for simulation of groundwater flow in porous media (Desai, 1974). In this method, the flow region is subdivided into a number of small regions, referred to as 'elements'. The original flow region is then considered as an assemblage of these elements connected at a finite number of joints called as 'nodes' or 'nodal points'. The partial differential equations of the problem covering the flow region as a whole are replaced by ordinary differential or algebraic equations in each element. Element equations are derived from minimisation of the residual left after a trial solution, and are substituted into the governing differential equations. The element equations are then combined into a global matrix form. The necessary boundary conditions are imposed and the equations are then solved by sophisticated mathematical techniques to obtain the unknown variables such as velocities, pressure, temperature or concentration depending on the application.

The great advantage of the finite element method is its inherent flexibility in the shape of the elements used in this technique (Figure 4.1.c). This advantage facilitates the simulation of curved boundaries in groundwater systems (Williams et al., 1986). It is also flexible in dealing with coupled problems such as solute transport, or in solving moving boundary problems such as a moving water table (Wang and Anderson, 1982). The finite element method is known to be more efficient than the finite difference method in dealing with difficulties arising from the non-linear nature of boundary

conditions along the seepage faces. But non-linear boundary conditions along the seepage faces can be easily simulated with the symmetric nature of the finite element matrix (Neuman, 1974). However, finite element models are generally more difficult to formulate than finite difference models. Finite element solutions require more computing time than finite difference methods.

In this thesis, the finite element method was used for the simulation of the groundwater inflow and the prediction of the post mining rebound related to an open cut coalmine.

#### **4.2.4 Finite volume method (FV)**

The finite volume method is a numerical technique for solving the governing equations of fluid flow and mass transport. In this thesis, the finite volume method was used to predict the long term pyrite oxidation and the subsequent transportation of the oxidation products from a backfilled open cut coalmine. This method is presented in Chapter 7.

### **4.3 General considerations about SEEP/W**

SEEP/W is a finite element commercial software developed by Geo-slope Inc. (Geo-slope International Ltd., 2002) which can be used to simulate both simple and highly complex seepage problems because of its comprehensive formulation nature. SEEP/W may also be used in the analysis of geotechnical, civil, hydrogeological and mining engineering problems. SEEP/W is a 32-bit graphical software product that operates under Microsoft Windows 95, 98, Me, NT, 2000, and Windows XP (Geo-slope International Ltd., 2002).

#### **4.3.1 Applications**

SEEP/W is a general seepage analysis program that simulates both saturated and unsaturated flow. The ability of software to model unsaturated flow allows SEEP/W to

handle a wider range of practical problems than other seepage softwares. It should be mentioned that consideration of unsaturated flow in groundwater modelling is important for obtaining realistic results. The program permits analysis of seepage as a function of time, precipitation infiltration, migration of a wetting front, steady state or transient flow, and confined or unconfined flow. For unconfined flow, SEEP/W discretises the entire flow domain into a finite element mesh. After achieving a converged solution, the zero-water pressure contour within the mesh is considered as the phreatic surface or water table.

Another most important feature of SEEP/W is transient or time dependence seepage analysis. The software can account for the drainage of water from soil pores, or water filling soil pores, and the changes in hydraulic conductivity or permeability that occur in a transient seepage flow system. One of the great features and capabilities of SEEP/W is the definition of the permeability and volumetric water content as a function of pore-water pressure in saturated-unsaturated flow systems. Furthermore, SEEP/W also supports heterogeneous hydraulic properties such as hydraulic conductivity and storage in an isotropic and heterogeneous flow system.

#### **4.3.2 Formulation**

The package SEEP/W is designed to analyse both saturated and unsaturated flow. The flow in unsaturated soil follows Darcy's law in a similar manner to groundwater flow in saturated soil. The flow is proportional to the coefficient of permeability and the hydraulic gradient. The main difference between saturated and unsaturated flow is that in an unsaturated porous media, the hydraulic conductivity varies greatly with changes in pore-water pressure, while in a saturated soil the hydraulic conductivity is insensitive to the pore-water pressure. For saturated-unsaturated analysis, the relationship between

hydraulic conductivity and pore-water pressure (known as a conductivity function) must be defined for each medium. The variation of hydraulic conductivity with pore-water pressure makes the governing finite element equations non-linear, hence an iterative process is required to solve the equation. The ability of the soil to store water must be defined by a soil-water characteristic curve. This typical curve indicates the relationship between water content and pore-water pressure.

For steady state analysis, the amount of water entering and leaving an elemental soil volume is the same hence the soil-water characteristic function is not required. SEEP/W is formulated for both triangular and quadrilateral elements. The simplest elements are three-noded triangular and four-noded quadrilateral elements. Higher-order elements can also be used by definition of nodes at the midpoints of the element sides. SEEP/W uses Gaussian numerical integration to formulate the elemental characteristic matrices. The integration involves sampling the element characteristics at selected points and summing the sampled values. Therefore, it is possible to use a different material property at each sampled point with the result that the material properties, such as the hydraulic conductivity, can vary throughout the element.

This software is also designed to handle transient boundary conditions. One of the most important features of this package is modification and improving boundary conditions in response to simulated results (Geo-slope International Ltd., 2002).

## **4.4 Groundwater flow models**

### **4.4.1 General considerations**

Predicting groundwater inflow and post mining rebound involves flow of water in both soil and rock. Furthermore, a study of the flow of water in underground systems is a necessary task for a better understanding of the transport of the contaminant because a

transport process occurs in the flow system. The interaction between the groundwater system and mining operations is noted to be another important consideration. In recent years, groundwater modelling has received greater attention from hydrogeologists, scientists, and environmental and mining engineers.

Predicting inflow into an open cut mine during mine extensions and estimating the groundwater rebound at backfilled open cut mines are among the more complex problems encountered in mining operations. Predictions of the configuration of the groundwater table and the height of the seepage face in surface mine high walls for slope stability analyses are also very important. Problems concerning groundwater flow in partially saturated porous media are relatively difficult to model for cases involving highly nonlinear ground characteristics. In particular, it is difficult to assign to the model the highly sensitive behaviour of unsaturated field variables such as hydraulic conductivity, specific storage and atmospheric boundary conditions associated with the seepage face, infiltration and evaporation.

Due to the limitations of the most common groundwater flow codes in dealing with these problems, a two-dimensional finite element model called SEEP/W (Geo-slope International Ltd., 2002) has been used in order to predict groundwater inflow into a surface mining excavation and post-mining groundwater rebound within the spoil of an open cut mine. This model incorporates both the saturated and unsaturated flow conditions. It is also able to predict the configuration and geometry of the water table and the height of the seepage face in a surface mining excavation.

#### **4.4.2 Hydrogeological characteristics of backfilled open cut mines**

A study of hydrogeological characteristics of surface mine spoil is a necessary task in predicting mine drainage quality efficiently. According to Hawkins (1995) studies of mine spoil assumed that groundwater flow in surface backfilled mines was a porous media flow system, similar to groundwater flow through unconsolidated sediments. Recent field work on surface mine spoil indicated that this assumption is not completely valid. Hawkins (1998) noted that based on the physical observation and field testing in the backfill groundwater flow regime of a surface mine in Central West Virginia, has shown as pseudo karst, where the groundwater flows through large voids. Pseudo karst hydraulic characteristics are similar to those observed in some carbonate karst.

Subsequent research carried out by Hawkins and Aljoe (1990) illustrated that mine spoil exhibits characteristics of both porous medium and double-porosity aquifers. Under steady-state conditions, spoil behaves as a porous medium and this is a key factor in the development of a model for the movement of oxidation products through backfilled materials. Although large voids within the backfill significantly influence the groundwater flow regime, groundwater velocity and hydraulic properties of the medium are controlled by the lower hydraulic conductivity zones within the backfill. Field monitoring and testing by Hawkins (1998) indicated that groundwater could easily move through large voids. However, these voids are not always well interconnected across a mine site. Hence, a diffusion process of groundwater flow through the interstices of the small grains between the voids may play a significant role on the overall site hydrology. The following factors can affect the hydraulic characteristics of surface mine spoil:

### **(a) Lithology of the spoil**

Lithology of the spoil can influence the permeability in reclaimed surface mines. Analysis of spoil hydraulic conductivity, performed by Hawkins (1995) in different surface mines indicated that lithologic content of the spoil directly affects the hydraulic properties of the site. The highest hydraulic conductivity was obtained from the sites with the highest percentage of sandstone. Sandstone-rich spoil zones yield larger fragments that promote the formation of large voids. Shales, on the other hand, tend to break into smaller fragments during mining and create smaller voids. Furthermore, they easily weather and break down to silt and clay-sized grains, which further decrease the permeability of the spoil.

### **(b) The method of mining and topography**

The location of haul roads across the backfill can affect the hydraulic properties of spoil (Hawkins, 1998). Spoil underlying haul roads is highly compacted due to the traffic of vehicles and heavy equipment so that the hydraulic conductivity of spoil under the haul road decreases. Topography influences groundwater flow in surface mine spoil, since groundwater can move based on the difference of hydraulic gradient and topography directly influences the hydraulic gradient.

### **(c) Effects of spoil age**

The age of the spoil is noted to be another factor influencing its hydraulic properties. As the age of the spoil increases, the hydraulic conductivity also increases, because the interconnection between the voids will improve with time (Hawkins, 1998).

### 4.4.3 Hydraulic parameters of surface mine spoil

#### (a) Permeability and transmissivity

Determining the hydraulic characteristics of surface mine spoil, in particular permeability, is very important. Because the hydraulic conductivity and other hydrological data can be used to predict the post mining groundwater rebound within the spoil. This is subsequently important for mine drainage pollution prevention. These hydraulic properties are necessary for prediction of mine drainage. These data can be used to calculate groundwater velocity, and water table fluctuation within different zones in the backfilled sites. Hawkins (1995) analysed data from five reclaimed surface coalmines in Western Pennsylvania and Northern West Virginia and observed that hydraulic conductivity values of the mine spoil vary from  $1.2 \times 10^{-5}$  to  $1.4 \times 10^{-4} \text{ m/s}$  which are from 0.83 to 2.65 orders of magnitude higher than that of the adjacent unmined strata,  $3.8 \times 10^{-8}$  to  $4.1 \times 10^{-6} \text{ m/s}$ . Table 4.1 outlines his findings:

Table 4.1. Ranges of hydraulic conductivity and transmissivity from five reclaimed surface coalmine sites in Western Pennsylvania and Northern West Virginia (Hawkins, 1995).

Hydraulic parameters	Site identification				
	1	2	3	4	5
Spoil permeability ( $m/s$ )	$1.4 \times 10^{-4}$	$2.8 \times 10^{-5}$	$1.2 \times 10^{-5}$	$1.2 \times 10^{-4}$	$1.3 \times 10^{-5}$
Strata permeability ( $m/s$ )	$3.1 \times 10^{-7}$	$4.1 \times 10^{-6}$	$7.1 \times 10^{-8}$	$2.0 \times 10^{-6}$	$3.8 \times 10^{-8}$
Spoil transmissivity ( $m^2/s$ )	$5.9 \times 10^{-4}$	$1.1 \times 10^{-4}$	$3.1 \times 10^{-5}$	$1.2 \times 10^{-4}$	$7.8 \times 10^{-6}$
Strata transmissivity ( $m^2/s$ )	$2.5 \times 10^{-6}$	$3.2 \times 10^{-5}$	$4.6 \times 10^{-7}$	$9.3 \times 10^{-6}$	$4.9 \times 10^{-8}$
Spoil saturated thickness ( $m$ )	4.35	4.03	1.88	1.53	0.72
Strata saturated thickness ( $m$ )	7.86	7.75	6.49	4.78	1.28

Based on Table 4.1, the geometric mean of the permeability of the spoil ( $3.75 \times 10^{-5} \text{ m/s}$ ) was over 2 orders of magnitude greater than that of the unmined strata ( $3.69 \times 10^{-7} \text{ m/s}$ ). In other words, mine spoil tends to be approximately 100 times more conductive than unmined strata. Furthermore, present numerical modelling of groundwater rebound within open cut mine spoil indicated that the effective hydraulic conductivity of the spoil was about 2 orders of magnitude higher than that of the unmined aquifer.

### **(b) Porosity**

Porosity determination in a backfilled open cut mine is noted to be another important factor in accurately predicting mine drainage quality. However, estimation of porosity is not an easy task. Based on aquifer tests, porosity values for the mine spoil in Western Pennsylvania and Northern West Virginia were determined to be between 13.8 % to 16.4 % (Hawkins, 1995). Hawkins (1998) reported laboratory porosities of 25 % to 36 % for surface mine spoils from Eastern and Western Kentucky and laboratory-measured values of porosities of 41 % to 48 % with an average of 44 % from Eastern Ohio spoil.

Hawkins (1998) also noted that for unconfined conditions, the estimated storage coefficient was equal to the effective porosity. Effective porosities for a reclaimed surface mine in Upshur County, West Virginia were found as between 14 % and 16 %. Davis and Zabolotney (1996) reported an effective porosity of 3 % for confined coal aquifer at the Belle Ayr mine. Porosity values for undisturbed coal strata are significantly lower than those determined for spoils. Hawkins (1995) reported that porosity values for coal strata range from 0.8 % to 9.4 % with an average of 3.9 %.

### (c) Groundwater velocity

Determination of groundwater velocity in a spoil site is important for prediction of mine drainage; hence it should be determined based on field-testing. Groundwater velocity in a spoil site was considerable greater than that observed from undisturbed strata. The following parameters can affect on groundwater velocities:

- The rate of recharge
- The effective porosity
- Permeability
- Head differential

Hawkins (1998) reported a groundwater velocity range of  $1.2 \times 10^{-5}$  to  $4.9 \times 10^{-5} \text{ m/s}$  for backfill of a reclaimed surface mine in Central West Virginia, a groundwater velocity range of  $2.7 \times 10^{-3}$  to  $4.3 \times 10^{-3} \text{ m/s}$  for a surface mine spoil in Eastern Kentucky and a groundwater velocity of  $2.0 \times 10^{-5} \text{ m/s}$  for a surface mine spoil in Eastern Ohio.

#### 4.4.4 The flow equation

Groundwater flow under the influence of hydraulic gradients is caused by differences in hydraulic head. In unsaturated flow, the hydraulic conductivity is not constant and is dependent on water content ( $\theta$ ). Reddi and Inyang (2000) have listed common empirical functions for unsaturated hydraulic conductivity. These functions,  $K(\theta)$  describe the variation of hydraulic conductivity with either moisture (water) content ( $\theta$ ) or matric potential of water. Green and Clothier (1994) used a power-law function for the hydraulic conductivity of unsaturated soil in Equation 4.1:

$$K(\theta) = K_s \left( \frac{\theta - \theta_n}{\theta_s - \theta_n} \right)^b \quad (4.1)$$

where,

$K_s$  = saturated hydraulic conductivity ( $m/s$ );

$b$  = empirical constant;

$\theta$  = volumetric water content;

$\theta_s$  and  $\theta_n$  = saturated and antecedent water contents, respectively.

The flow of water through unsaturated soil and porous rock for specific water content is governed by Darcy's law:

$$q_x = -K_x(\theta) \frac{\partial h}{\partial x} \quad (4.2)$$

$$q_y = -K_y(\theta) \frac{\partial h}{\partial y} \quad (4.3)$$

where,

$q_x$  and  $q_y$  = components of the rate of flow of water through a porous media in the x and y directions, respectively;

$K_x$  and  $K_y$  = components of the hydraulic conductivity tensor;

$h$  = hydraulic head.

By coupling the continuity equation and Darcy's law, the two-dimensional governing equation for groundwater flow in unsaturated porous media can be expressed as follows (Freeze and Cherry, 1979):

$$\frac{\partial}{\partial x} \left( K_x \frac{\partial h}{\partial x} \right) + \frac{\partial}{\partial y} \left( K_y \frac{\partial h}{\partial y} \right) = \frac{\partial \theta}{\partial t} - W \quad (4.4)$$

where,

$W$  = recharge or discharge rate per unit volume ( $T^{-1}$ )

A change in moisture content ( $\theta$ ) may be related to a change in pore-water pressure by the following equation (Freeze and Cherry, 1979):

$$\frac{\partial \theta}{\partial t} = C_{uw} \frac{\partial U_w}{\partial t} \quad (4.5)$$

where,

$C_{uw}$  = slope of the water storage curve;

$U_w$  = matric potential and is defined as:

$$U_w = h - Z \quad (4.6)$$

and where

$h$  = total hydraulic head;

$Z$  = elevation.

Equation 4.6 reduces to

$$\frac{\partial U_w}{\partial t} = \frac{\partial h}{\partial t} \quad (4.7)$$

In Equation 4.6 the elevation  $Z$  is a constant, hence, the derivative of  $Z$  with respect to time is zero and combining Equations 4.5 and 4.7 gives:

$$\frac{\partial \theta}{\partial t} = C_{uw} \frac{\partial h}{\partial t} \quad (4.8)$$

Equation 4.8 can be substituted into Equation 4.4 and leads the following governing differential equation for two-dimensional, saturated-unsaturated flow of groundwater (Freeze and Cherry, 1979):

$$\frac{\partial}{\partial x} \left( K_x \frac{\partial h}{\partial x} \right) + \frac{\partial}{\partial y} \left( K_y \frac{\partial h}{\partial y} \right) = C_{uw} \frac{\partial h}{\partial t} - W \quad (4.9)$$

#### 4.5 Governing equation for formulation of SEEP/W

For all SEEP/W simulations, the flow equation must be expressed in the following general form (Geo-slope International Ltd., 2002):

$$\frac{\partial}{\partial x} \left( K_x \frac{\partial H}{\partial x} \right) + \frac{\partial}{\partial y} \left( K_y \frac{\partial H}{\partial y} \right) + Q = \frac{\partial \theta}{\partial t} \quad (4.10)$$

where,

$H$  = total head;

$K_x$  = hydraulic conductivity in the x-direction;

$K_y$  = hydraulic conductivity in the y-direction;

$Q$  = boundary flux;

$\theta$  = volumetric water content;

$t$  = time.

Equation 4.10 means that the difference between the rate of flow entering and leaving a control volume at a point in time is equal to the change in the volumetric water content.

SEEP/W assumes that a change in volumetric water content can be related to a change in pore-water pressure by the following equation:

$$\partial \theta = m_w \partial u_w \quad (4.11)$$

where,

$\partial \theta$  = change in volumetric water content;

$\partial u_w$  = change in pore-water pressure;

$m_w$  = equivalent to the slope of moisture characteristic curve.

The total head is given by:

$$H = \frac{u_w}{\gamma_w} + y \quad (4.12)$$

where,

$u_w$  = pore-water pressure;

$\gamma_w$  = unit weight of water;

$y$  = elevation.

Rearranging Equation 4.12 in terms of  $u_w$  and substituting it into Equation 4.11 reduces to:

$$\partial\theta = m_w \gamma_w \partial(H - y) \quad (4.13)$$

Substituting Equation 4.13 into Equation 4.10 leads to the following equation:

$$\frac{\partial}{\partial x} \left( K_x \frac{\partial H}{\partial x} \right) + \frac{\partial}{\partial y} \left( K_y \frac{\partial H}{\partial y} \right) + Q = m_w \gamma_w \frac{\partial(H - y)}{\partial t} \quad (4.14)$$

Since the elevation  $y$  is a constant, the derivative of  $y$  with respect to time will be zero, giving the following governing differential equation used in the formulation of SEEP/W (Geo-slope International Ltd., 2002).

$$\frac{\partial}{\partial x} \left( K_x \frac{\partial H}{\partial x} \right) + \frac{\partial}{\partial y} \left( K_y \frac{\partial H}{\partial y} \right) + Q = m_w \gamma_w \frac{\partial H}{\partial t} \quad (4.15)$$

Equations 4.9 and 4.15 are similar. In this thesis, Equation 4.9 was used to predict groundwater inflows into open cut mines as well as prediction of groundwater rebound after mine closure.

Under steady state conditions, the water flux entering and leaving a control volume is the same at all times. Hence, the transient term in right hand side of the Equation 4.9 is eliminated and the equation reduces to the governing equation for two-dimensional steady state groundwater flow defined by Equation 4.16:

$$\frac{\partial}{\partial x} \left( K_x \frac{\partial h}{\partial x} \right) + \frac{\partial}{\partial y} \left( K_y \frac{\partial h}{\partial y} \right) + W = 0 \quad (4.16)$$

The average linear velocity is used in the mass transport equation is commonly defined as the specific discharge divided by porosity (Freeze and Cherry, 1979; and Krabbenhoft et al., 1990) and is given by Equations 4.17 and 4.18:

$$V_x = -\frac{K_x}{n} \frac{\partial h}{\partial x} \quad (4.17)$$

$$V_y = -\frac{K_y}{n} \frac{\partial h}{\partial y} \quad (4.18)$$

where,

$n$  = effective porosity.

#### 4.6 Boundary conditions

The solution of Equation 4.9 requires specification of both the initial and boundary conditions in order to constrain the problem and make solutions unique. Various workers have used different boundary conditions for various solutions as discussed below (see Figure 4.2):

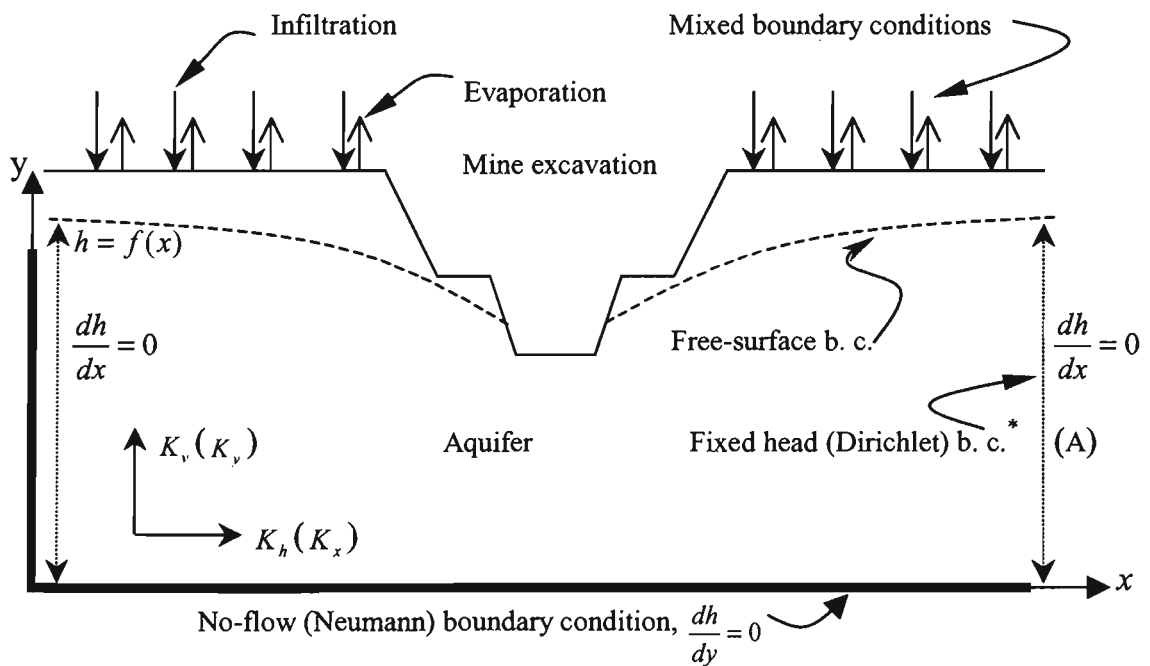


Figure 4.2. Schematic diagram showing different types of boundary conditions.

1) The first is the Dirichlet or fixed head boundary condition,

where,

$$h(x_i, 0) = h_0(x_i) \quad (4.19)$$

\* boundary condition

and

$$h(x_i, t) = h_A \text{ on } A \quad (4.20)$$

where,

$h_0$  = initial hydraulic head;

$h_A$  = prescribed hydraulic head at the portion A (Figure 4.2) of the flow boundary.

2) The flux boundary or Neumann boundary condition is defined as:

$$v_d n_i = k_{ij} \frac{dh}{dx_j} n_i = -V \quad (4.21)$$

where,

$K_{ij}$  = component of the hydraulic conductivity tensor;

$x_j$  = Cartesian direction;

$h$  = hydraulic head;

$-V$  = outward fluid flux;

$v_d$  = Darcy velocity;

$n_i$  = outward unit vector normal to the boundary where the prescribed outward flux

is  $-V$ .

The base of the flow region is assumed to be impermeable (or a no-flow boundary).

3) Mixed boundary conditions

For some boundaries such as soil-air interfaces where evaporation or infiltration occurs, conditions may change from a prescribed flux type boundary to a prescribed head type and vice versa. According to Frind and Verge (1978) and Huyakorn et al. (1986), boundary fluxes along infiltration and evaporation boundaries are subject to the following requirements:

$$|v_i n_i| \leq \overline{E_s} \quad (4.22)$$

$h_i \leq h \leq 0$  for infiltration

$h \leq h_i$  for evaporation

where

$\overline{E_s}$  = maximum potential flux of infiltration or evaporation under the prevailing atmospheric conditions;

$h_i$  = minimum hydraulic head allowed under the prevailing soil conditions.

In Figure 4.2, a free surface boundary condition is considered along the water table where the pressure (along the water table) is atmospheric and the hydraulic head ( $h$ ) is a function of  $x$  only  $h = f(x)$ .

#### 4.7 Galerkin approximation procedure

To solve the Equation 4.9 by the finite element method, the Galerkin approximation approach is used. Galerkin approach is a weighted residual method in which the governing differential equation is substituted by an approximate solution. For a detailed discussion of the application of the Galerkin approach in groundwater flow, see Pinder and Frind (1972); Pinder et al. (1973); Pinder (1973); Neuman (1974); Pickens and Lennox (1976); Gray and Pinder (1974); and Rabbani (1994).

Using the Galerkin approach, the general finite element equation for groundwater flow (Equation 4.9) can be written in a matrix form (Pinder and Frind, 1972). More details of the finite element integration of the flow equation are given in Appendix A.

$$[A] \{h\} + [B] \left\{ \frac{dh}{dt} \right\} + \{C\} = 0 \quad (4.23)$$

where  $[A]$  and  $[B]$  are  $n$  by  $n$  matrices in which

$$A_{ij} = \iint_D \left[ K_x \frac{dN_i}{dx} \frac{dN_j}{dx} + K_y \frac{dN_i}{dy} \frac{dN_j}{dy} \right] dx dy \quad (4.24)$$

$$B_{ij} = \iint_D C_{uw} N_i N_j dx dy \quad (4.25)$$

and  $\{C\}$  is the flux vector in which

$$C_i = -\iint_D W N_i dx dy - \int_{\beta} N_i \sum_{j=1}^n \left[ K_x \frac{dN_j}{dx} l_x + K_y \frac{dN_j}{dy} l_y \right] h_j d\beta \quad (4.26)$$

The last term in Equation 4.26 incorporates the Neumann boundary condition in the form

$$\int_{\beta} N_i q d\beta \quad (4.27)$$

where,

$q$  = flux of water and can be expressed as

$$q = K \frac{dh}{dn} \quad (4.28)$$

This term is formed only when the groundwater flux is nonzero along the edge of a boundary element.

Equation 4.23 is the general finite element equation for a transient groundwater flow in porous media. For a steady-state flow, the head is independent of time and consequently Equation 4.23 can be reduced to:

$$[A]\{h\} + \{C\} = 0 \quad (4.29)$$

#### 4.7.1 Finite element discretisation

The suitability of the Galerkin approach for computer applications depends on the choice of basis functions. In this thesis, the cross-section of the flow domain is divided into quadrilateral elements. The main objective of this discretisation process is to divide

the system into a suitable number and arrangement of elements so that the realistic solution can be adequately approximated.

The integrals that appear in the matrices of Equation 4.23 must be evaluated using numerical methods. A Gaussian quadrature scheme can be used to perform integrations (Pinder and Frind, 1972; Wang and Anderson, 1982).

An exact solution can be obtained using this scheme (Pinder, 1973). Integrations are carried out in the local coordinate system  $(\eta, \xi)$ , with limits of integration between  $-1$  and  $+1$  and then transformed to the corresponding global coordinates system  $(x, y)$  (Figure 4.3). The local coordinates for each of the nodes are given in Table 4.2:

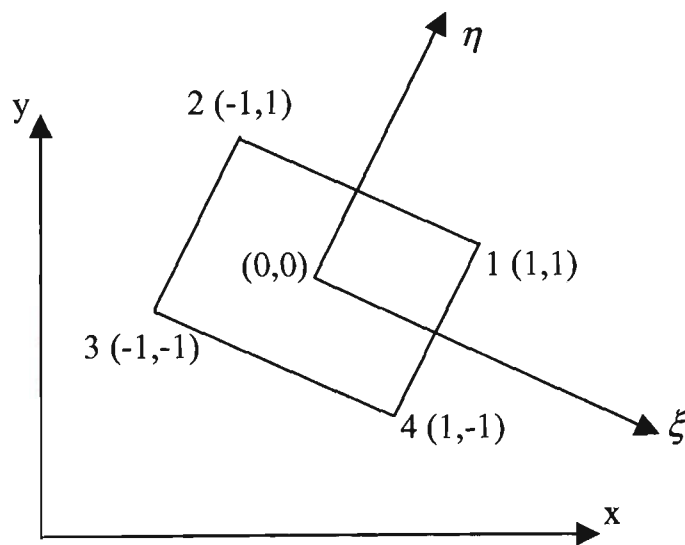


Figure 4.3. Quadrilateral element: Local coordinates-  $(\eta, \xi)$ , Global coordinates-  $(x, y)$  (Pinder and Frind, 1972).

Table 4.2. The local coordinates of nodal points.

Element type	Node	$\xi$	$\eta$
Quadrilateral	1	+1	+1
	2	-1	+1
	3	-1	-1
	4	+1	-1

The x and y coordinates anywhere in the element are related to the local coordinates and to the x-y coordinates of the nodes by the following equations:

$$x = N_i \{X\} \quad (4.30)$$

$$y = N_i \{Y\} \quad (4.31)$$

or

$$x = N_1 x_1 + N_2 x_2 + N_3 x_3 + N_4 x_4 \quad (4.32)$$

$$y = N_1 y_1 + N_2 y_2 + N_3 y_3 + N_4 y_4 \quad (4.33)$$

where,

$N_i$  = a vector of interpolating shape functions;

$\{X\}$  and  $\{Y\}$  = global x-y coordinates of the element nodes.

Therefore, once a set of local coordinates  $(\xi, \eta)$  have been specified, the corresponding global coordinates can be obtained by the Equations 4.30 and 4.31.

The following relationship (Equation 4.34) is required to perform the necessary integrations in the local coordinate rather than global coordinate system (Pinder and Frind, 1972):

$$\partial x \partial y = \det[J] \partial \eta \partial \xi \quad (4.34)$$

where  $[J]$  is the Jacobian matrix and is defined as follows:

$$[J] = \begin{bmatrix} \frac{\partial x}{\partial \xi} & \frac{\partial y}{\partial \xi} \\ \frac{\partial x}{\partial \eta} & \frac{\partial y}{\partial \eta} \end{bmatrix} \quad (4.35)$$

The limits of integration must be changed to  $-1$  and  $+1$  by applying the above transformations Equation 4.24 for example can be rewritten as:

$$A_{ij} = \int_{-1}^1 \int_{-1}^1 \left[ K_x \frac{\partial N_i}{\partial x} \frac{\partial N_j}{\partial x} + K_y \frac{\partial N_i}{\partial y} \frac{\partial N_j}{\partial y} \right] \det[J] \partial\eta \partial\xi \quad (4.36)$$

Similar forms are developed for the Equations 4.25 and 4.26 and given in Equations 4.37 and 4.38:

$$B_{ij} = \int_{-1}^1 \int_{-1}^1 C_{uvw} N_i N_j \det[J] \partial\eta \partial\xi \quad (4.37)$$

and

$$C_i = - \int_{-1}^1 \int_{-1}^1 W N_i \det[J] \partial\eta \partial\xi - \int_{\beta} N_i \sum_{j=1}^n \left[ K_x \frac{dN_j}{dx} l_x + K_y \frac{dN_j}{dy} l_y \right] h_j d\beta \quad (4.38)$$

#### 4.8 Time integration technique

Equation 4.23 is a first-order matrix differential equation. To solve for the undetermined coefficients,  $h_i$ , ( $i=1,2,\dots,n$ ), a finite difference approximation scheme can be introduced into Equation 4.23. Pinder (1973) found that the backward difference scheme provided a more accurate groundwater flow solution than a Crank-Nicholson centered scheme in time approach.

Using this approach yields the following relationship:

$$[A]\{h\}_{t+\Delta t} + [B] \frac{\{h\}_{t+\Delta t} - \{h\}_t}{\Delta t} = -\{C\} \quad (4.39)$$

Equation 4.39 can be rearranged to form:

$$\left( [A] + \frac{[B]}{\Delta t} \right) \{h\}_{t+\Delta t} = \frac{[B]}{\Delta t} \{h\}_t - \{C\} \quad (4.40)$$

At  $t=0$ ,  $\{h\}_0$  is known because of the prescribed initial conditions. Given appropriate initial and boundary conditions, the hydraulic head,  $h$  is obtained from Equation 4.40. The error related to this approximation approach can be reduced by setting the appropriate time step.

In this study, the finite element method using Galerkin approximation approach was used to simulate groundwater inflow into open cut surface mining and post mining rebound process. A modelling approach using the SEEP/W package and simulation results is given in Chapters 5 and 6.

#### **4.9 Conclusions**

In this chapter a two-dimensional model has been presented to simulate groundwater inflow and rebound within the spoil of an open cut mine. A Galerkin approximation method was used to discretise the groundwater flow equations using the SEEP/W package and its features, and the capabilities and formulation method are described. A short discussion of the hydrogeological characteristics of open cut mine spoil was also included.

## **CHAPTER FIVE**

### **GROUNDWATER INFLOW MODEL MODIFICATION AND VERIFICATION**

## CHAPTER FIVE

### GROUNDWATER INFLOW MODEL MODIFICATION AND VERIFICATION

#### 5.1 Introduction

The inflow model using SEEP/W for simulating groundwater inflow to open cut mines has the following main features:

It

- Takes into account the amount of inflow occurs through the excavation bottom
- Predicts the height of the seepage face in excavation highwall
- Takes into consideration saturated/unsaturated flow conditions
- Incorporates confined/unconfined aquifer conditions
- Simulates aquifer heterogeneities
- Predicts water table position in unconfined aquifer

and

- Incorporates different boundary conditions

In this chapter an algorithm for the simulation of groundwater inflow to an open cut mine is outlined. The capabilities and features of the SEEP/W finite element model are briefly reviewed and finally modelling performance and verification are given in six different mining related problems.

Figure 5.1 presents a realistic mine water problem observed in a backfilled open cut coalmine, in the Hunter Valley region, Australia.

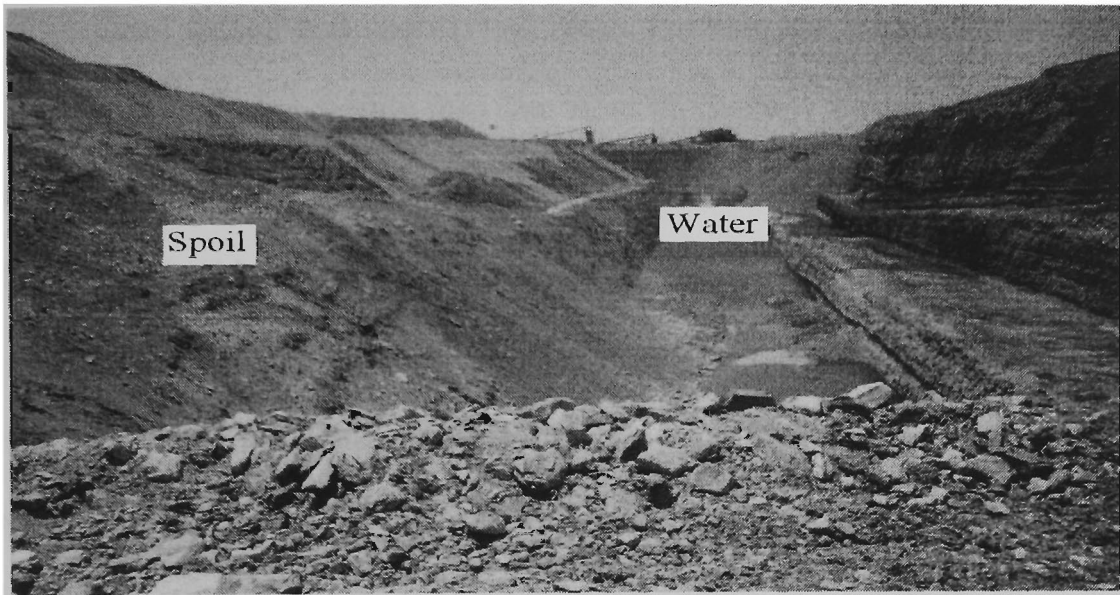


Figure 5.1. Groundwater inflow problem observed in an open cut coalmine, Singleton, Australia.

## 5.2 Capabilities of the SEEP/W model

The SEEP/W model can simulate both saturated and unsaturated flow. The ability of the model to assume unsaturated flow condition allows it to solve a wider range of problems than some other codes and obtain realistic inflow results. The model is able to simulate seepage faces on highwalls predicting the configuration of the phreatic surface and height of the seepage face on the highwalls of a surface mining excavation, thus providing the necessary information for slope stability analysis. One of the important features and capabilities of the SEEP/W model is the definition of hydraulic conductivity and volumetric water content as a function of pore-water pressure in saturated-unsaturated flow systems. The model simulates heterogeneous hydraulic properties such as hydraulic conductivity and storage in an isotropic and heterogeneous flow system. Therefore, a conductivity function, which defines the relationship between hydraulic conductivity and pore-water pressure, can be defined for each material. This feature of the model is very important in simulation of groundwater inflow in backfilled open cut mines where the hydraulic characteristics of the spoil are different from those

of the un-mined aquifer and unexcavated rocks. Furthermore, the horizontal hydraulic conductivity differs considerably than that from the vertical hydraulic conductivity in heterogeneous systems. The model can take into consideration transient boundary conditions and is able to modify boundary conditions in response to predicted results. The model can also simulate unconfined flow problems by assuming the zero pore-water pressure contours within the flow domain in order to represent the water table. Although many numerical models are now used to predict groundwater inflow to a surface mining excavation they are limited in their ability to quantify the more detailed problems by taking the above mentioned features and relationships into account. The present finite element model was developed with a view to overcoming most existing modelling problems.

### **5.3 Inflow model**

In order to simulate an inflow model, it was necessary to construct an initial condition representing the pre-mining situation. Pre-mining groundwater table elevation data, rainfall data, geological and hydraulic characteristics of aquifer were used to establish the initial conditions for the inflow model. A steady-state simulation was performed using the initial and boundary conditions to represent the pre-mining groundwater system. This initial condition was then used to simulate groundwater inflow during mine advancement. A head boundary condition was assigned at the outer boundary of the model. An infinite boundary condition was also assigned at the outer boundary of aquifer in order to simulate an infinite, homogenous aquifer extending away from the mining excavation. The bottom of the model was considered to be impermeable hence a no-flow boundary condition was maintained at the bottom or lower boundary of the model. A constant head was specified at the radius of the surface mine equal to the elevations of pit depth at various stages of the mining operation. A rectangular mesh

was then constructed for the model. A flowchart representing the steps of groundwater inflow simulation are shown in Figure 5.2. Figure 5.3 shows a conceptual model of the problem.

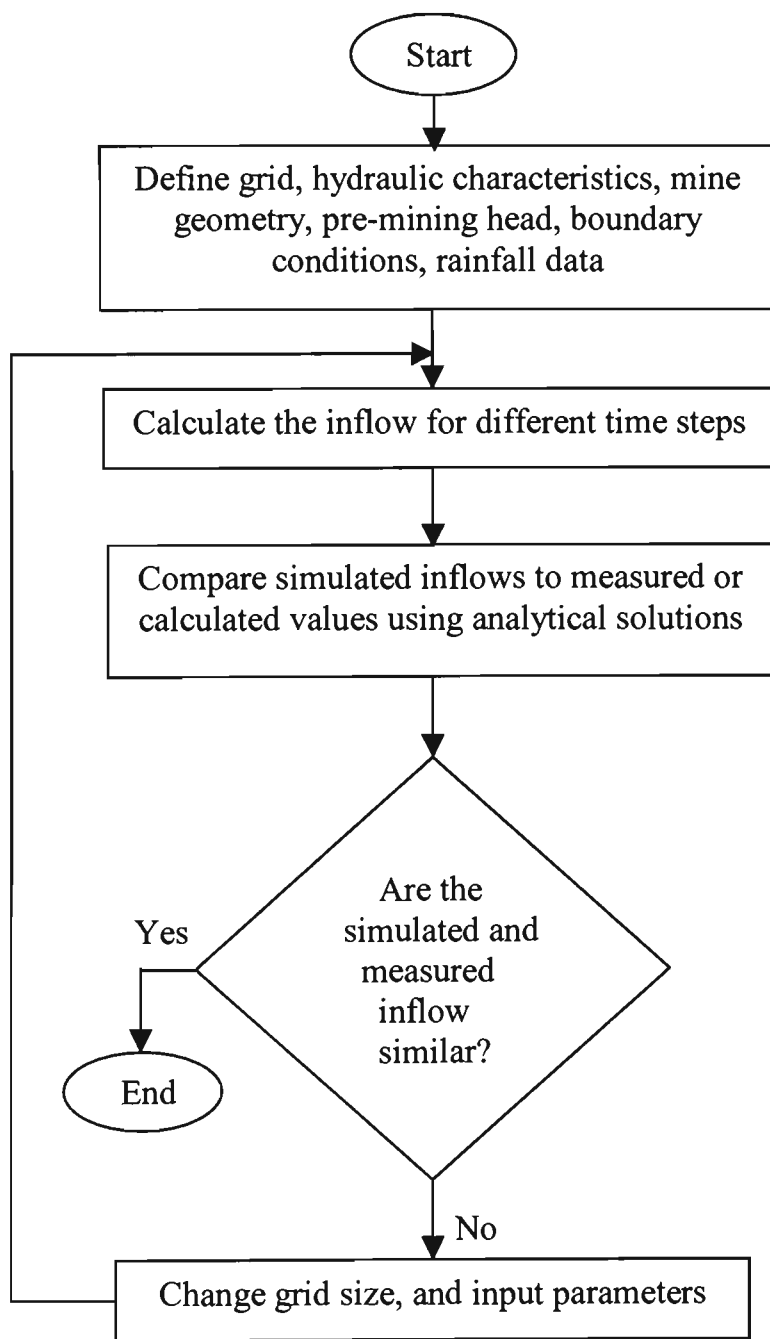


Figure 5.2. Flowchart of groundwater inflow into a surface mine.

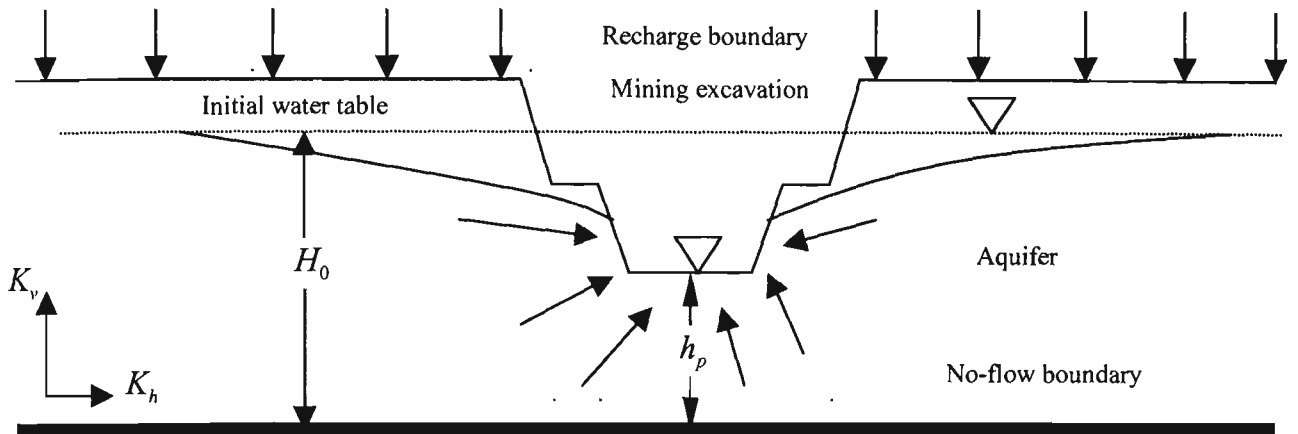


Figure 5.3. Conceptual model of radial inflow to a surface mining excavation.

## 5.4 Model verification

Six problems are described to verify finite element modelling of groundwater inflow.

### 5.4.1 Problem 1- Development of the seepage face in porous media

In this example, results from the present numerical model are compared to those from a numerical finite element model, MINEDW, and a physical model developed by Azrag et al., (1998). In that example, a 15-degree, pie-shaped finite element model consisting of 561 nodes, 640 elements, and 10 layers each 0.15 m thick was developed. A constant head of 1.22 m was assigned at the outer boundary of the model at a radial distance of 1.95 m. A constant head of 0.3 m was maintained in the well. The permeability was about  $4.63 \times 10^{-3} \text{ m/s}$  (400m/day), and the radius of well was 0.12 m.

A finite element model consisting of 336 nodes, 300 elements and 15 layers having a thickness of about 0.105 m was constructed (Figure 5.4). A comparison of the height of the seepage and the inflow rate predicted by the present finite element model and those calculated by the MINEDW model (developed by Azrag et al., 1998) and those

measured in the laboratory by Hall (reported by Azrag et al., 1998) are presented in Table 5.1.

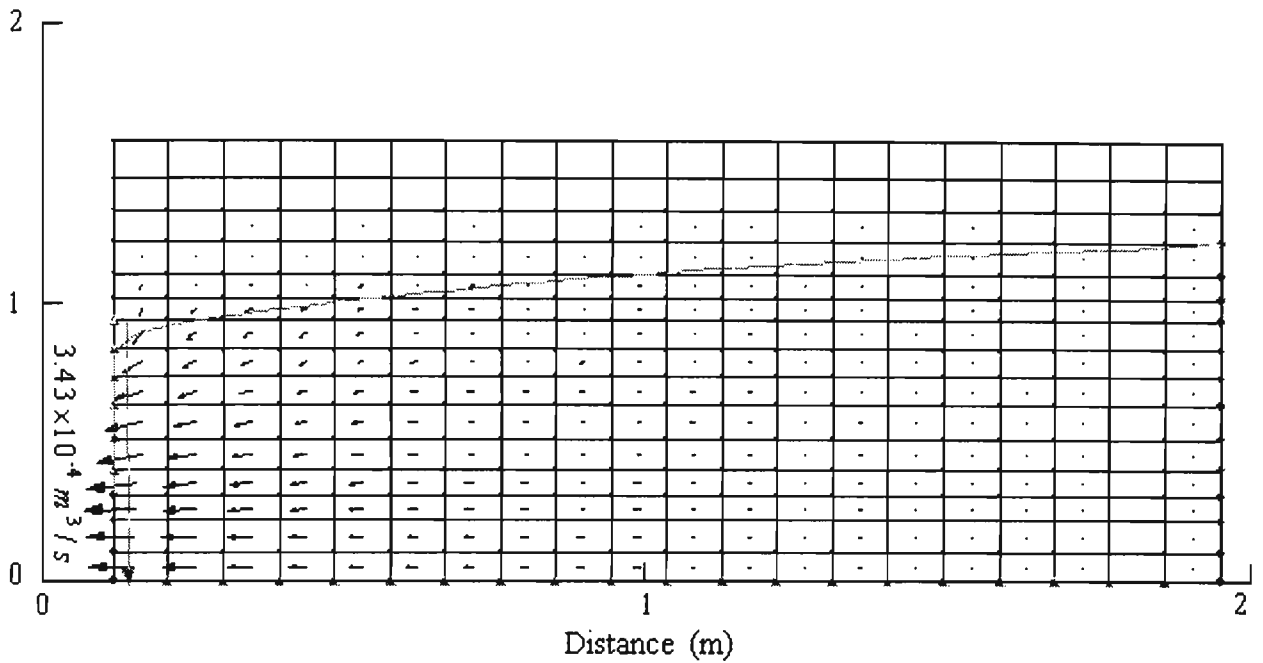


Figure 5.4. Finite element grid for the problem.

**Table 5.1.** Comparison of results of numerical models in relation to physical model by Hall.

	The inflow ( $Q$ ) ( $m^3 / s$ )	The height of the seepage $L(m)$	% error in related to physical model	
			$Q$	$L$
Physical model	$3.45 \times 10^{-4}$	0.54	---	---
MINEDW model	$3.40 \times 10^{-4}$	0.49	1.45	9.3
SEEP/W model	$3.43 \times 10^{-4}$	0.53	0.58	1.85

#### 5.4.2 Problem 2- Steady state, unconfined, radial flow to circular pit

In this second example, results of the SEEP/W finite element model are compared to those from a finite element model, MINEDW, a finite difference code, MODFLOW and a physical model reported by Azrag, et al. (1998). The main objective in dealing with the problem was to validate the capabilities of MINEDW for saturated/unsaturated flow, prediction of the inflow into a circular pit as well as prediction of the height of the seepage face.

Azrag, et al. (1998) constructed a 90-degree circular grid mesh consisting of 2312 nodes and 16 layers representing a total thickness of 1.2 m for an unconfined aquifer. The radial distance of the outer boundary was 2.4 m. The partially penetrating circular pit had a radius of 0.59 m. A hydraulic conductivity of  $0.06 \text{ m/s}$  was assigned for the unconfined aquifer. To show the effects of the partially penetrating pit, the authors removed the uppermost 12 layers of elements within the radius of the circular pit. Constant heads of 1.09 m and 0.835 m were maintained at the outer boundary of the model and at the pit floor respectively. The values of 0.065 m and  $2.54 \times 10^{-2} \text{ m}^3 / \text{s}$  were predicted for the height of the seepage and the rate of inflow under steady-state condition. The results were favourably comparable with the measured height of the seepage face of 0.045 m and the inflow rate of  $2.54 \times 10^{-2} \text{ m}^3 / \text{s}$  obtained from the physical model described in Azrag, et al. (1998).

For further validation of the model, Azrag, et al. (1998) also constructed a finite difference grid consisting of 42 rows and 42 columns of cells with an equal size of 0.059 m and 16 layers for a total of 28224 cells. For the simulation, MODFLOW, a finite difference code was utilised. The cells located inside the circular pit were inactive. The finite difference model was then run under steady-state conditions. The

MODFLOW-based model predicted an inflow rate of  $4.16 \times 10^{-2} \text{ m}^3 / \text{s}$  about 60 % greater than that observed in the physical model and predicted from the MINEDW-based model. The code did not predict the height of the seepage.

A finite element model consisting of 365 nodes, 328 rectangular elements and 12 layers was constructed (Figure 5.5). Constant heads of 1.09 m and 0.835 m were assigned at the outer boundary and at the pit floor respectively. A no-flow boundary condition was maintained at bottom of the model. The model was then run under steady-state conditions.

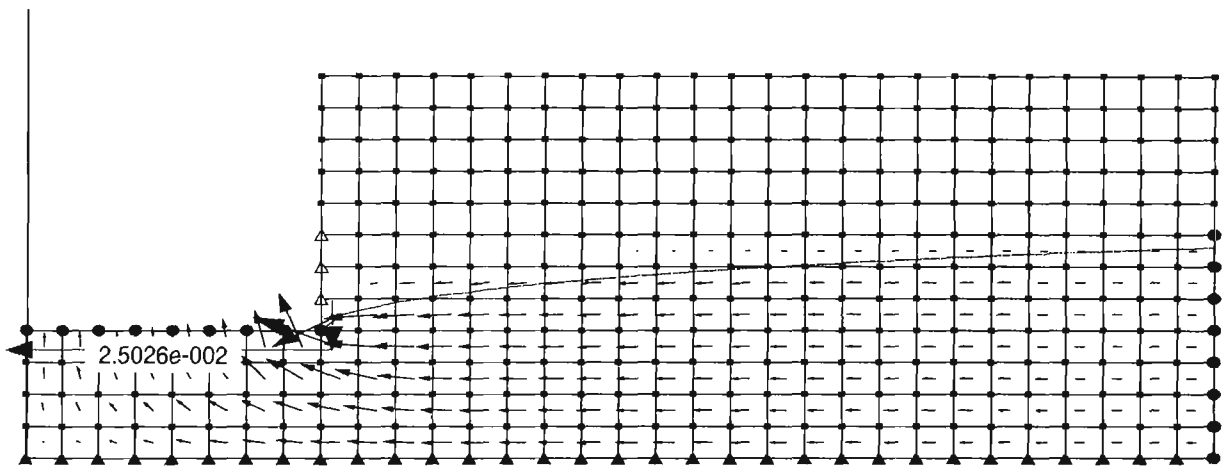


Figure 5.5. Finite element grid for the problem, velocity vectors and water table.

The predictions for the inflow rate and the height of the seepage were  $2.50 \times 10^{-2} \text{ m}^3 / \text{s}$  and 0 respectively. A close agreement was obtained between the SEEP/W model and MINEDW-based model as well as the physical model presented by Azrag et al. (1998) for inflow. However, the SEEP/W model did not predict the height of the seepage face. The following table outlines the values for inflow and the height of seepage predicted with different models.

Table 5.2. Comparison of results of the SEEP/W model and those presented in Azrag et al. (1998) for prediction of the inflow and the height of the seepage in a circular pit.

	The inflow rate	The height of the seepage
	( $m^3 / s$ )	( $m$ )
Physical model	$2.54 \times 10^{-2}$	0.045
MODFLOW model	$4.16 \times 10^{-2}$	-----
MINEDW model	$2.54 \times 10^{-2}$	0.065
SEEP/W model	$2.50 \times 10^{-2}$	-----

### 5.4.3 Problem 3- Transient, radial flow to a fully penetrating well in a leaky aquifer

The main objective of this third problem was to calibrate the finite element model for the simulation of the dewatering analysis. The following (Hantush 1956) analytical solution presented for a leaky aquifer (Walton, 1970; Freeze and Cherry, 1979; Watson and Burnett, 1993) was used for validation of the numerical model:

$$Q = \frac{4\pi T\Delta h}{W(u, r/B)} \quad (5.1)$$

$$u = \frac{r^2 S}{4Tt} \quad (5.2)$$

$$B = \sqrt{\frac{(Kbb')}{K'}} \quad (5.3)$$

where,

$K$  = permeability of the aquifer ( $m / s$ );

$T$  = transmissivity of the aquifer ( $m^2 / s$ );

$Q$  = dewatering rate ( $m^3 / s$ );

$b$  = thickness of the aquifer ( $m$ );

$K'$  = permeability of the semi-confining layer ( $m / s$ );

$t$  = time ( $s$ );

$b'$  = thickness of the semi-confining layer ( $m$ );

$S$  = storativity of the aquifer (dimensionless);

$B$  = leakage factor (dimensionless);

$W(u, r / B)$  = well function for a leaky aquifer.

On the basis of a dewatering test performed on a leaky-confined aquifer (Worked example 17-2, Watson and Burnett, 1993), the following input data are given:

The hydraulic conductivity of the aquifer  $6.12 \text{ m/day}$ , storativity of the aquifer 0.001, the hydraulic conductivity of the semi confining layer  $0.0025 \text{ m/day}$ , storativity of the semi confining layer 0, the thickness of the aquifer 15.7 m, the thickness of the semi confining layer 3.2 m, the dewatering rate  $475 \text{ m}^3 / \text{day}$ , and elapsed time 1 day.

The main aim of the problem is to calculate drawdowns at increasing distances from the dewatering well in order to determine the cone of depression after one day of dewatering testing.

To solve the problem numerically, a finite element grid consisting of 11205 nodes and 2800 eight-nodded rectangular elements and 2 layers was constructed. The lowermost layer representing the aquifer had a 15.7 m thickness. The uppermost layer which represents the semi- confining layer had a thickness of 3.2 m. Hydraulic conductivities of  $6.12 \text{ m/day}$  and  $0.0025 \text{ m/day}$  were assigned at the aquifer and at the semi-confining layer respectively. The initial conditions were modelled by running a steady-state

simulation. The total head at the two ends of the model was assigned as an arbitrary value of 25 m. Hence a uniform total head distribution of 25 m was generated throughout the entire aquifer. The file for this part of the simulation was named *LEAKYAQUIFER2\_I.SEP*. For simulation of dewatering, a constant head of 25 m was assigned at the outer boundary of the model. A no-flow boundary condition was maintained at the bottom of the model representing an impermeable layer. A flux boundary condition was assigned near the dewatering well in order to specify a flux equal to the amount of dewatering rate. Storativities of 0.001 and 0 were specified at the aquifer and semi confining layer respectively. The model was then run by calling file *LEAKYAQUIFER2\_I.SEP* as the initial conditions. The file for this part of the simulation was named *LEAKYAQUIFER2.SEP*.

The comparison of the drawdowns predicted by the SEEP/W model and those calculated using the analytical solution are shown in Figure 5.6.

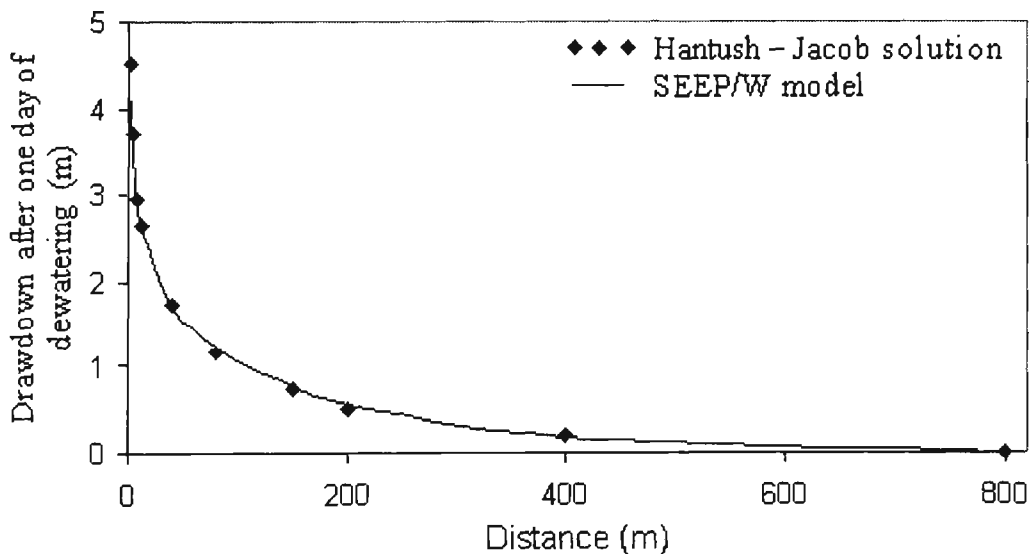


Figure 5.6. Comparison of analytical and numerical solutions for drawdowns under transient conditions in a leaky aquifer.

#### 5.4.4 Problem 4- Steady state, unconfined, radial flow to surface mining excavation

To perform an inflow simulation for an open pit mine at an unconfined aquifer under transient conditions, the following simple model was developed for steady-state

conditions and compared with Dupuit's analytical equation quoted in Singh et al. (1985) and Vandersluis et al. (1995) in order to calibrate the model developed for transient flow conditions. The simple model assumes that a steady state, radial flow to a surface mining excavation takes place in an unconfined aquifer. The following data were used for the simulation:

Hydraulic conductivity of the aquifer =  $4.3 \times 10^{-6} \text{ m/s}$

Equivalent mine radius = 160 m

Thickness of aquifer = 500 m

The radius of influence = 2000 m

Head of the outer boundary = 500 m

Head at the mining excavation = 150 m

The following four different simulations were performed for calibration purposes:

**Case 1:**

In Case 1 was performed for a fully penetrating pit with vertical walls (Figure 5.7); the simulated inflow was compared to those calculated using analytical equations outlined in Table 5.3 and close agreement was achieved. The finite element model consisted of 7171 nodes, 7000 rectangular elements and 70 layers.

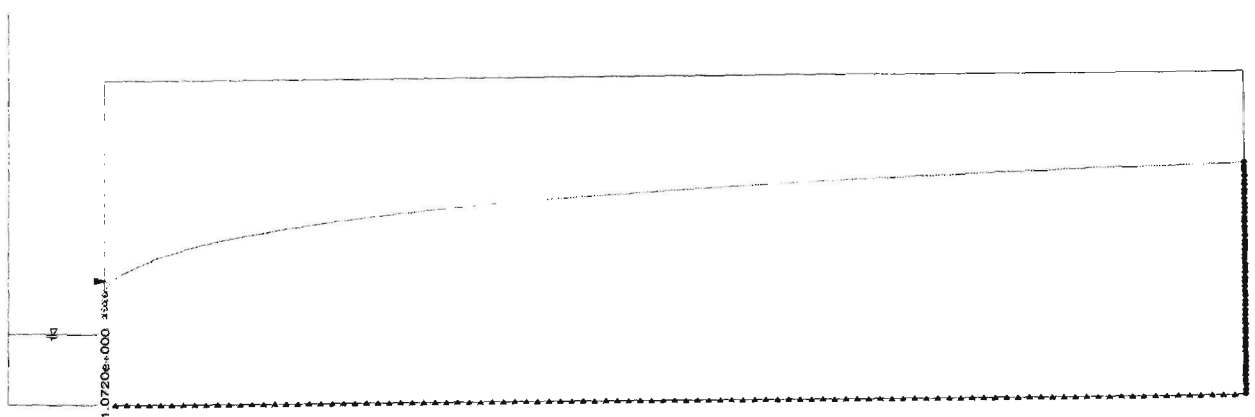


Figure 5.7. Axisymmetric model, fully penetrating, vertical walls.

Table 5.3. Comparison of results of numerical model and analytical solutions.

	The inflow ( $m^3 / s$ )	The height of the seepage ( $m$ )
Analytical solutions:		
Equation 3.5 (Chapter 3, Page 84)	1.217	---
Equation 3.11(Chapter 3, Page 88)	1.182	---
SEEP/W model	1.070	104

**Case 2:**

In Case 2, modelling was performed for a partially penetrating pit with vertical walls in an unconfined aquifer. The values of  $1.159 \text{ m}^3 / s$  and  $80 \text{ m}$  were obtained for the inflow and the height of the seepage respectively (Figure 5.8).

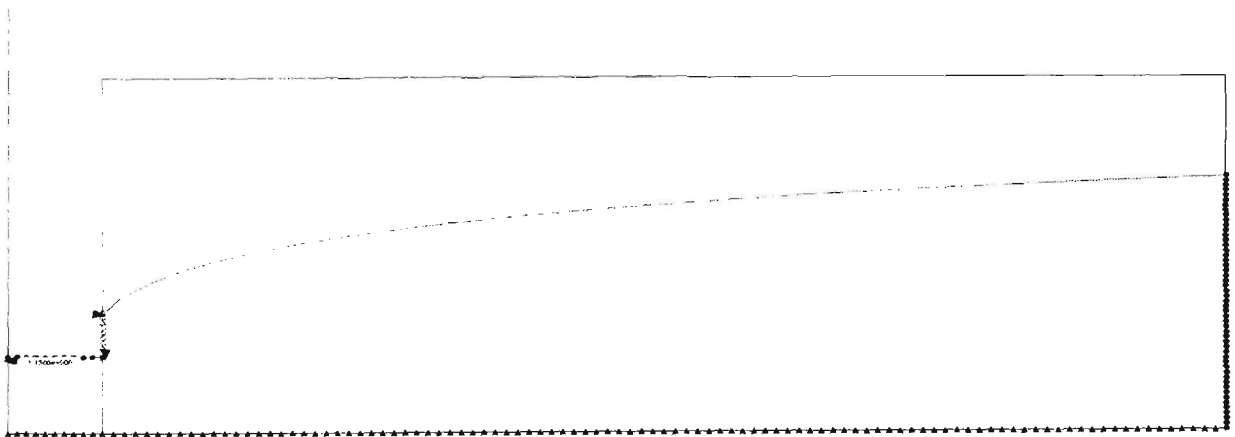


Figure 5.8. Axisymmetric model, partially penetrating, vertical walls.

**Case 3:**

In Case 3, a fully penetrating pit with non-vertical walls was selected for the simulation. The calculated inflow and the height of the seepage face were  $1.43 \text{ m}^3 / s$  and  $90 \text{ m}$  (Figure 5.9).

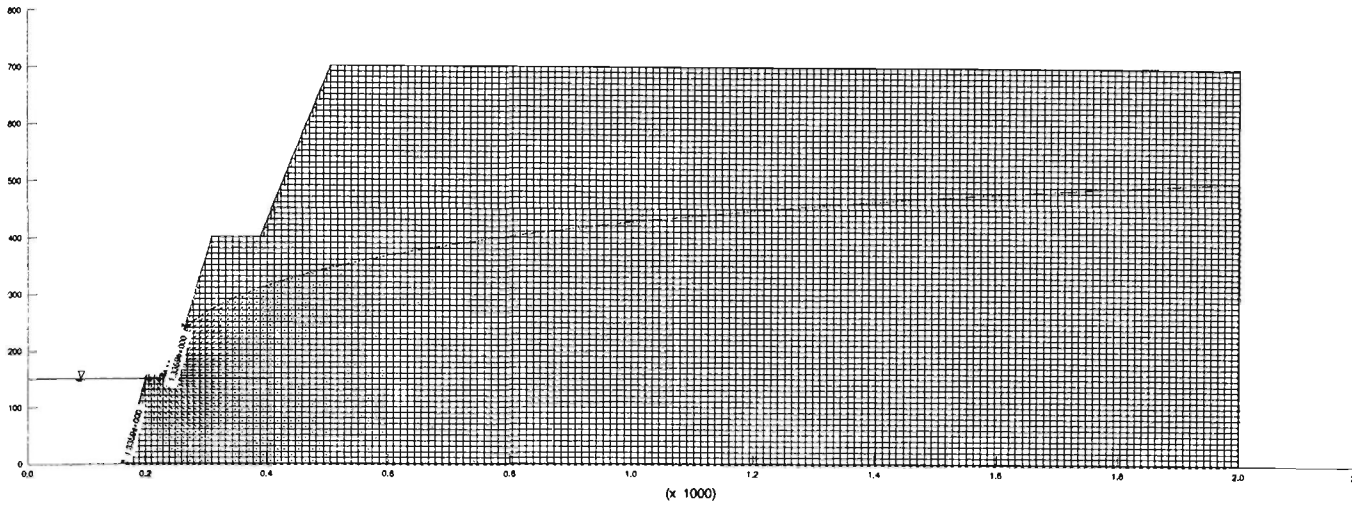


Figure 5.9. Finite element grid, fully penetrating, non-vertical walls.

**Case 4:**

In this problem, a partially penetrating pit with non-vertical walls in an unconfined aquifer was considered. The predicted inflow and the height of the seepage face were  $1.095 \text{ m}^3 / \text{s}$ , and  $150 \text{ m}$  respectively (Figure 5.10).

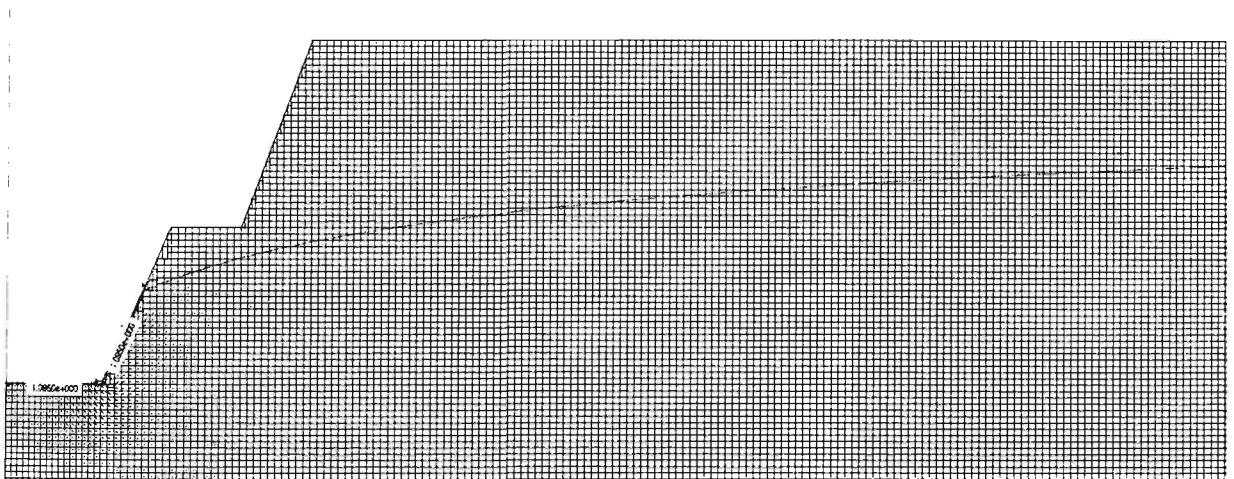


Figure 5.10. Finite element grid, partially penetrating, non-vertical walls.

**5.4.5 Problem 5 - Transient, radial inflow to a mining pit**

In this fifth problem, results from the SEEP/W model are compared to those from the Jacob and Lohman analytical equation (Kruseman and De Ridder, 1979; and Hanna et al., 1994). This equation is based on lateral, radial flow to a fully penetrating circular pit

in an idealised confined aquifer. One of the most important features of the SEEP/W model is to predict inflow to a partially penetrating pit from an unconfined aquifer. The model is able to determine the height of the seepage face developed around a surface mine. The Jacob-Lohman equation for confined aquifer is given as follows:

$$Q = \frac{4\pi T \Delta h}{\ln\left(\frac{2.25 T t}{r_w^2 S}\right)} \quad (5.4)$$

where,

$T$  = transmissivity ( $m^2 / s$ );

$\Delta h$  = drawdown ( $m$ );

$t$  = time since the water table was instantaneously lowered to the specified level ( $s$ );

$r_w$  = radius of the well ( $m$ );

$S$  = storativity of aquifer (dimensionless);

$Q$  = inflow ( $m^3 / s$ ).

As mentioned in Chapter 3, the Jacob-Lohman equation can be used for a confined aquifer. To use Equation 5.4 in an unconfined aquifer, the following correction should be applied to convert unconfined aquifer drawdown  $\Delta h_{uc}$  to equivalent confined aquifer drawdown  $\Delta h_c$  (Kruseman and De Ridder, 1979).

$$\Delta h_c = \Delta h_{uc} - \frac{\Delta h_{uc}^2}{2h_0} \quad (5.5)$$

where,

$\Delta h_c$  = drawdown in confined aquifer ( $m$ );

$\Delta h_{uc}$  = drawdown in unconfined aquifer ( $m$ );

$h_0$  = initial water table elevation ( $m$ ).

An axisymmetric finite element analysis was performed using a grid constructed with 446301 nodes, 8750 elements and 50 bedding planes of total 500 m thickness. The rectangular grid had a total length of 2000 m. The hydraulic conductivity of  $4.3 \times 10^{-6} \text{ m/s}$  and a specific yield of 0.001 were assigned to the aquifer. A constant head of 500 m was assigned at the outer boundary of the model. The bottom of the model was presumed to be impermeable hence a no-flow boundary condition was maintained at the bottom of the model. The advance of the pit was simulated by assigning a constant head at the radius of the pit corresponding to specified pit depths at various stages of the mining operation. It was assumed that the hypothetical mining operation used to compare the results of numerical simulation to those obtained from the Jacob-Lohman equation was an idealised cylindrical pit (with a radius of 150m) that advanced 20 m every six months for a maximum duration of four years (Hanna et al., 1994). A series of calculations was made using the numerical model and the Jacob-Lohman equation to estimate inflow from an unconfined aquifer to a circular pit for which the anisotropy ratio of horizontal ( $K_h$ ) and vertical ( $K_v$ ) hydraulic conductivities ( $K_h/K_v$ ) were varied.

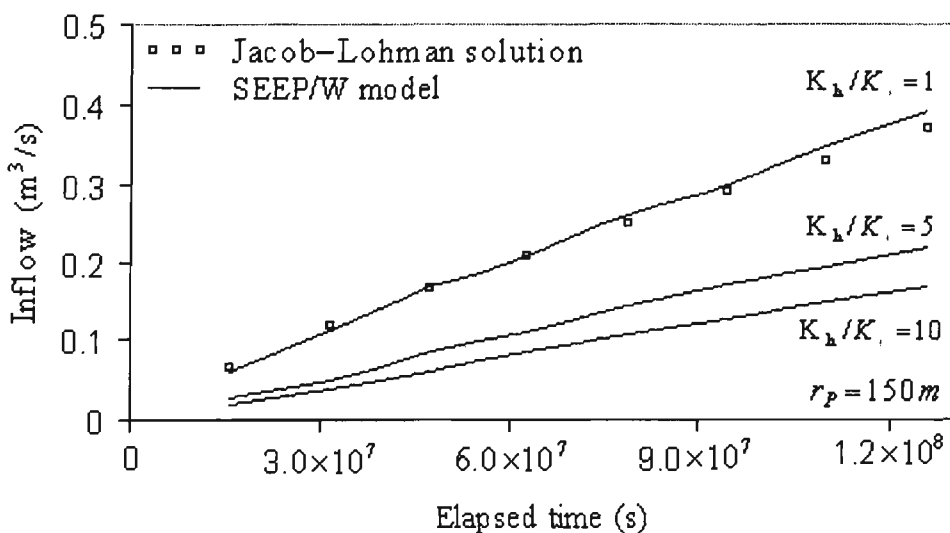


Figure 5.11. Comparison of an analytical Jacob-Lohman solution and a numerical method for pit inflow prediction.

It was found that differences in the results of the two methods were most sensitive to this anisotropy ratio. As it is shown in Figure 5.11, with an anisotropy ratio of 1 ( $K_h/K_v=1$ ) the predicted inflows using the numerical model are similar to those calculated using the Jacob-Lohman equation. The slight overestimation of inflow by the numerical model is due to the fact that the Jacob-Lohman solution does not account for bottom inflow (Hanna et al., 1994) while it can be predicted by the numerical model. As indicated in Figure 5.11, the predicted inflows are slightly under-estimated with respect to an increase in the anisotropy ratio.

The anisotropy ratio determines the height of the seepage face and the relative amount of inflow through the bottom of the pit in the numerical model. To see the relation between the anisotropy ratio and the height of the seepage face, constant heads of 500 m and 340 m were specified at the outer boundary and the bottom of the pit at a radius of 150 m. Figure 5.12 shows the height of the seepage face at various anisotropy ratios at an elapsed time of 4 years. As indicated in Figure 5.12 a decreasing anisotropy ratio (or increasing the  $K_h/K_v$ ) will result in reduction of the height of the seepage face.

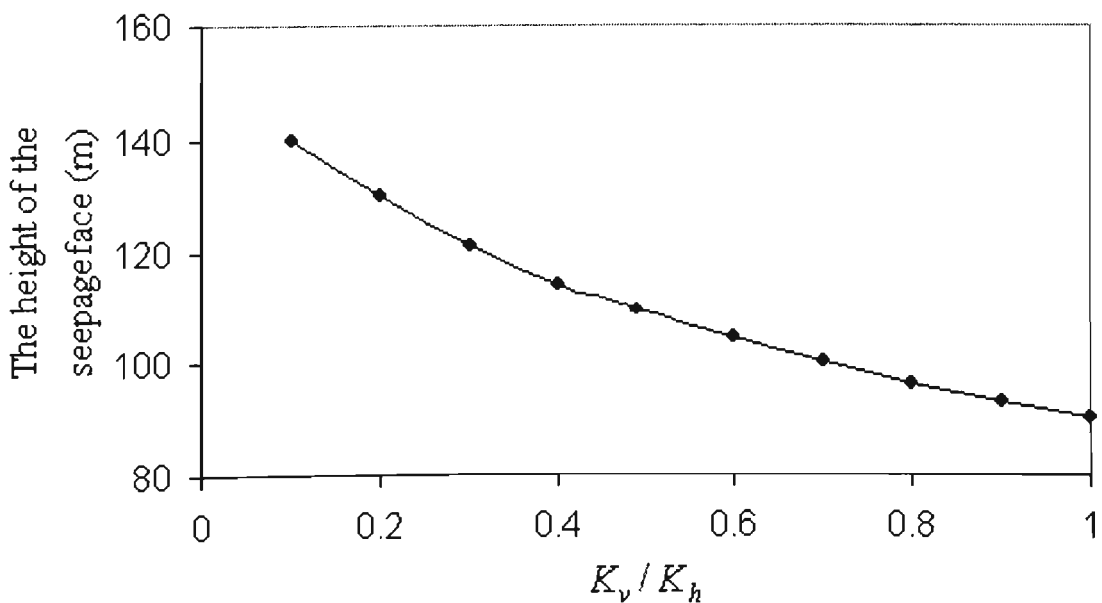


Figure 5.12. The effects of the anisotropy ratio on the height of the seepage face,  $H_o = 500m$ ,  $r_p = 150m$ ,  $h_p = 340m$ , elapsed time = 4 years.

#### 5.4.6 Problem 6 - Prediction of groundwater inflow to an open cut mine

The main aim of this sixth problem was to present the capability of the SEEP/W finite element model for prediction of groundwater inflow to an open cut mine from an unconfined aquifer. In this case, the results of the simulation were compared to those obtained from two analytical solutions.

The first analytical solution has been given by Singh et al. (1985). The equation determines the inflow to a surface mining excavation using Laplace type formulation. The method is two- dimensional and is a quick and easy method of estimation of inflow as a function of time. The equation is given as follows:

$$q = \left( \frac{4T}{\pi H_0} \right) (H_0 - h_p) \int_0^{\infty} \exp(-\tau \lambda \operatorname{Tanh} \lambda) d\lambda \quad (5.6)$$

where,

$$\tau = \left( \frac{K}{S_y H_0} \right) t \quad (5.7)$$

where,

$q$  = inflow rate into the excavation per unit length of excavation;

$T$  = transmissivity of the aquifer;

$H_0$  = original elevation of water table;

$h_p$  = water table elevation at excavation face;

$S_y$  = specific yield;

$K$  = hydraulic conductivity;

$t$  = time.

However, this analytical solution assumes large time increments and that at the outflow region a uniform flow is established.

The second analytical solution was presented by McWhorter (1981). The rate of inflow on the highwall face per unit length of excavation is given as follows:

$$q_a = At^{-\frac{1}{2}} \quad (5.8)$$

where,

$$A = \frac{1}{2} \left( \sqrt{\frac{S_y T b^2}{3} + STH_0^2 + STH_0 b} \right) \quad (5.9)$$

Equation 5.8 can be modified to calculate inflow to an open cut mining excavation where the length of the excavation increases as a function of time. The total inflow to the excavation from two sides can be calculated using the following equations:

$$Q = 4R_a A \sqrt{t} \quad , \quad t \leq \frac{Y_p}{R_a} \quad (5.10)$$

where,

$R_a$  = average rate of elongation of the excavation ( $m$ );

$Y_p$  = maximum length of the pit ( $m$ );

$\frac{Y_p}{R_a}$  = time period during which the excavation is advancing ( $days$ ).

This equation calculates the total inflow after time  $t$  at which the mining excavation ceases to elongate.

The inflow from both sides of the excavation after elongation has ceased is given by the following equation:

$$Q = 4R_a A \left( \sqrt{t} - \sqrt{t - \frac{Y_p}{R_a}} \right), \quad t \geq \frac{Y_p}{R_a} \quad (5.11)$$

The advantage of this method is that it takes into consideration the effect of time and face advance on the predicted inflow quantity. However, the predicted inflow would be much larger, particularly at small time intervals because the entire pit is not established instantaneously. Furthermore, this approach assumes that flow occurs only in planes normal to the long axis of the advancing pit while the actual flow in plan view will be two-dimensional. Moreover, the discharge to the pit through the ends of the excavation was not incorporated in this method and it is assumed that the length to width ratio is large.

To compare inflow predicted by the finite element model to those calculated with analytical solutions, the following problem was considered. The objective is to estimate inflow to a surface coalmine from an unconfined aquifer perched above the coal seam (McWhorter, 1981). The inflow to the first cut of the mine was considered in this example. The saturated thickness of aquifer, transmissivity and specific yield were 18 m,  $0.93 \text{ m}^2 / \text{day}$  and 0.05 respectively. The production rate of coal was  $3.62 \times 10^5 \text{ m}^3 / \text{yr}$  from cuts with 30 m in width penetrating a coal seam of average thickness of 2.09 m. The average rate of advance of the excavation was  $15.8 \text{ m} / \text{day}$ . The excavation had a maximum length of 915 m. The problem was first solved analytically using equations used by Singh et al. (1985) and McWhorter (1981).

To predict inflow to a surface mining excavation numerically, a two-dimensional finite element grid consisting of 1078 nodes, 950 elements and 19 layers was constructed (Figure 5.13).

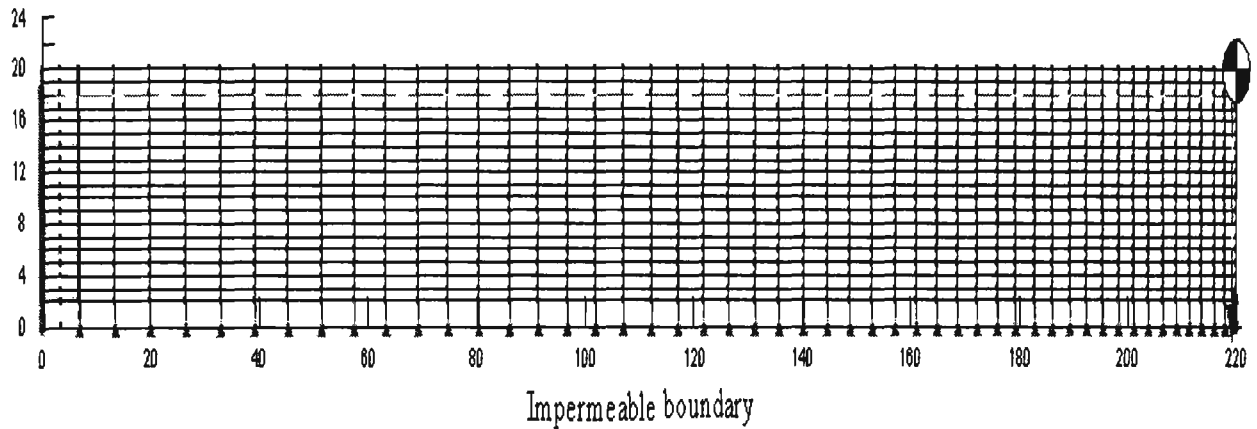


Figure 5.13. Finite element grid for prediction of inflow to an open cut mine.

The grid spacing increases from the outer boundary to the pit. A constant head of 18 m was assigned at the outer boundary while the head in the mining excavation was maintained at about 2 m. Hydraulic conductivity of  $5.17 \times 10^{-2}$  m/day and a specific yield of 0.05 were specified for the model. Time steps of 10 days were considered for the simulation. However, a slight change was made on time step of 6 to take into account the time at which the excavation ceased to elongate. Hence, time step 6 was specified as 58 days rather than 60 days.

A no-flow boundary condition was maintained at the bottom of the model. An infinite boundary condition was specified at the outer boundary of the model to allow consideration of an aquifer extended far from the mining excavation.

A steady-state simulation was carried out to establish an initial condition for the model. Constant heads of 18 m were assigned at the two ends of the aquifer. After specifying the hydraulic conductivity, the model was run in order to generate a uniform total head

distribution of 18 m throughout the entire aquifer. The file for this steady-state simulation representing the pre-mining situation was named *STRIPMINE1\_I.SEP*.

In the second stage of simulation, a constant head of about 2 m was assigned at the mining excavation. By calling the initial condition (*STRIPMINE1\_I.SEP*) and by specifying a specific yield of 0.05, the modelling of the inflow was performed in which the length of the excavation increased until the maximum length of excavation was made at time step six ( $t = 58$  days). During each time step inflow to the excavation was predicted. The model for this second phase of simulation was named *STRIPMINE1.SEP*.

In the third part of the simulation, a length of 916 m (maximum length of excavation) was assigned for the model. A constant head of 18 m was removed at the outer boundary of the model. The predictions obtained for time step six of the second phase of the simulation (*STRIPMINE1\_I.H06*) was called an initial condition for predicting inflows for time intervals of greater than 58 days. However slight modifications were made on the hydraulic characteristics of the aquifer, in particular, during the final phase of inflow simulation in order to predict reasonable inflows in comparison with inflows calculated using analytical methods. The inflows calculated using analytical solutions were compared with those predicted by the finite element model in Figure 5.14.

As Figure 5.14 shows that analytical and numerical methods represent approximately a similar trend for inflow rate as a function of time. Inflow increases with time during elongation of excavation ( $t \leq 58$  days). Inflow decreases sharply after elongation has ceased ( $t \geq 58$  days).

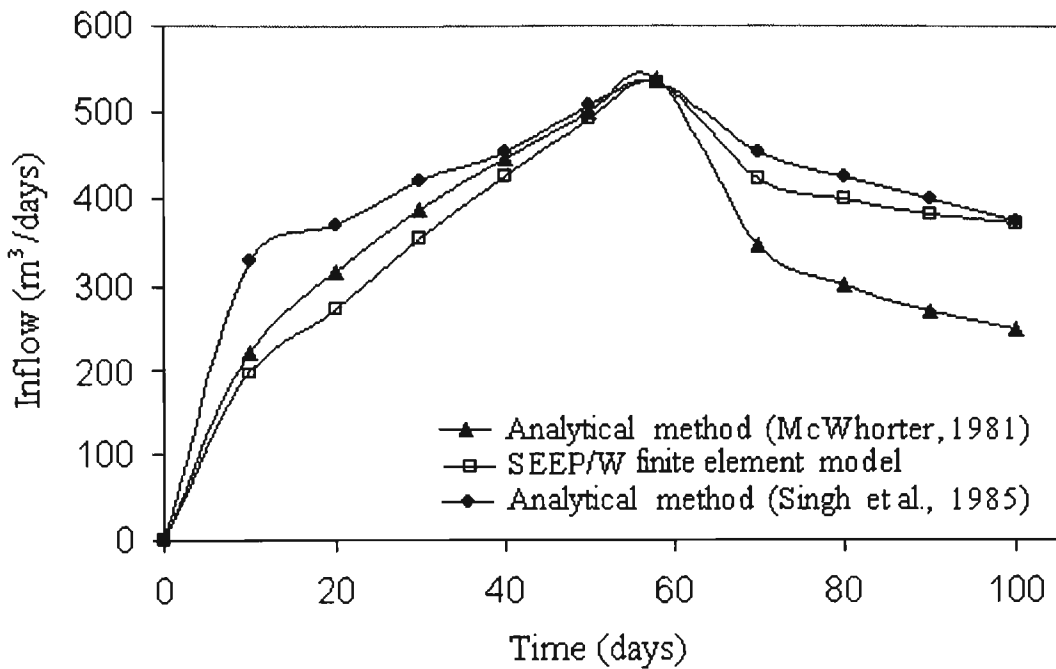


Figure 5.14. Comparison of analytical and numerical methods for the prediction of water inflow to an open cut mine.

McWhorter (1981) noted that the inflow to the excavation decreases sharply once the maximum elongation has made. However, both the numerical method and the analytical solution presented by Singh et al. (1985) do not follow this trend. During pit elongation, relatively slight differences are seen between the results of the numerical model and the analytical solution presented by McWhorter (1981). Analytical solution of Singh et al. (1985) overestimated inflow for initial time steps during mine advancement.

## 5.5 Conclusions

In this chapter, a numerical groundwater model called SEEP/W has been used to predict groundwater inflow into surface mines. This model has the capability to simulate saturated/unsaturated flow conditions and to calculate the height of the seepage faces of the excavation, taking into account the hydraulic conductivities and the water content as a function of pore water pressure. The model was evaluated by comparing the output from the SEEP/W model with the results obtained from analytical solutions developed by McWhorter (1981) and Singh et al. (1985) and a published numerical model. It was

found that during pit elongation, inflow values predicted by the model were relatively similar to those calculated using the analytical model developed by McWhorter (1981). The results of the inflow simulation can provide significant information for designing mine dewatering systems and storage facilities.

## **CHAPTER SIX**

### **PREDICTION OF GROUNDWATER REBOUND IN OPEN CUT MINING**

## CHAPTER SIX

### PREDICTION OF GROUNDWATER REBOUND IN OPEN CUT MINING

#### 6.1 Introduction

Mine abandonment leading to groundwater rebound due to cessation of dewatering and associated pollution issues is considered to be a serious problem associated with open cut coal mining. If the effects and magnitude of a water-related problem can be properly identified in advance of mining, appropriate water management strategies can be undertaken to minimise the socio-economic and environmental impacts of mine dewatering. Prediction of groundwater rebound is an important aspect in assessing the long-term impact of mining on local and regional hydrologic systems and the controlling of pollution problems related to the mine drainage.

In this chapter an algorithm for the simulation of post-mining groundwater rebound is presented. SEEP/W, a two-dimensional finite element package has been used in order to predict post-mining groundwater rebound within the spoil of an open cut mine. The model was validated by comparing the output from an existing model and the results obtained from analytical solutions, as well as field monitored data, and close agreement with these was achieved. Figure 6.1 shows a representation of a groundwater rebound problem observed in an open cut coalmine in Australia.

#### 6.2 Groundwater rebound model

The final predictions of groundwater elevations calculated during the mine dewatering modelling were employed to predict groundwater rebound after mining.

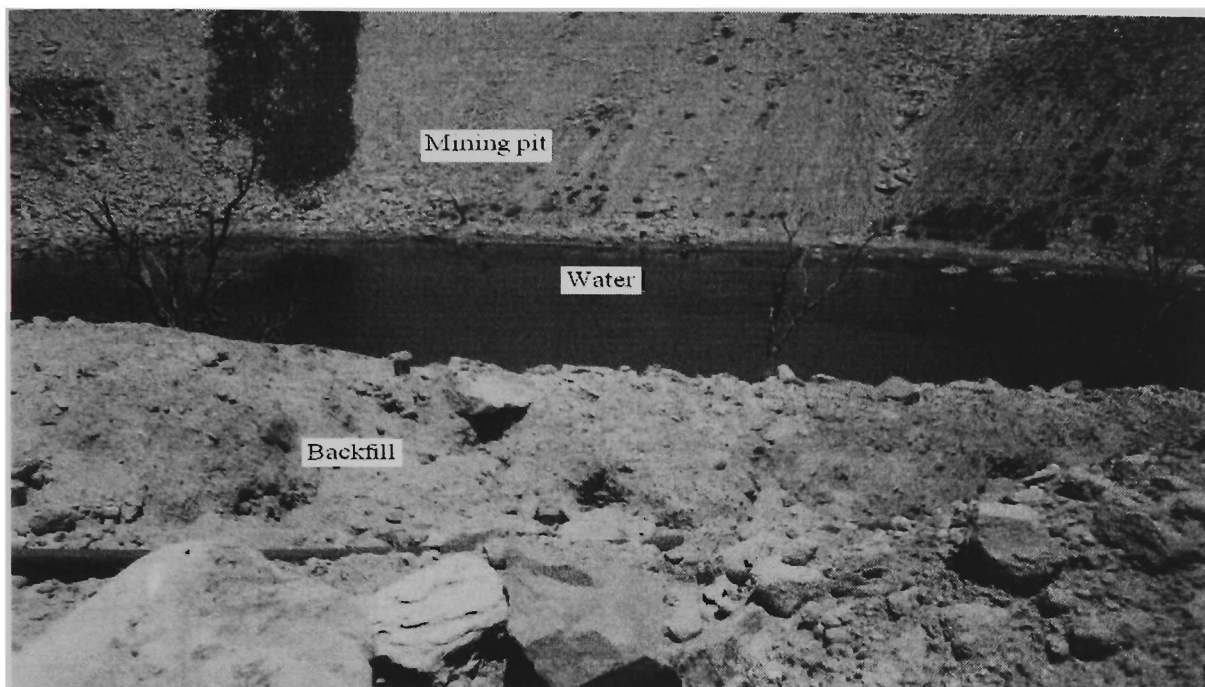


Figure 6.1. Groundwater rebound problem observed in an open cut coalmine, Singleton, Australia.

For transient simulation of groundwater rebound within spoil, it was necessary to assign new hydraulic characteristics to those parts of the model elements that represented excavated rock as well as backfilled materials. A finite hydraulic conductivity value was assigned to the part of the model that represents excavated rocks and spoil (Naugle and Atkinson, 1993). Hence, the predicted groundwater elevations were different in the spoil at the edges and the centre of the excavation. To reduce the error in the predicted water table elevations within the spoil and the pit, the permeability was modified to a value that would minimise the differences of water table levels. The hydraulic conductivity of backfilled material was assigned about two orders of magnitude greater than that of the unmined strata. The following aquifer characteristics were the main input parameters for the model:

- Initial potentiometric heads and rainfall data
- Saturated thickness

- Hydraulic conductivity and transmissivity
- Specific yield and porosity

A flowchart in Figure 6.2 summarises the groundwater rebound modelling procedure in an open cut mine.

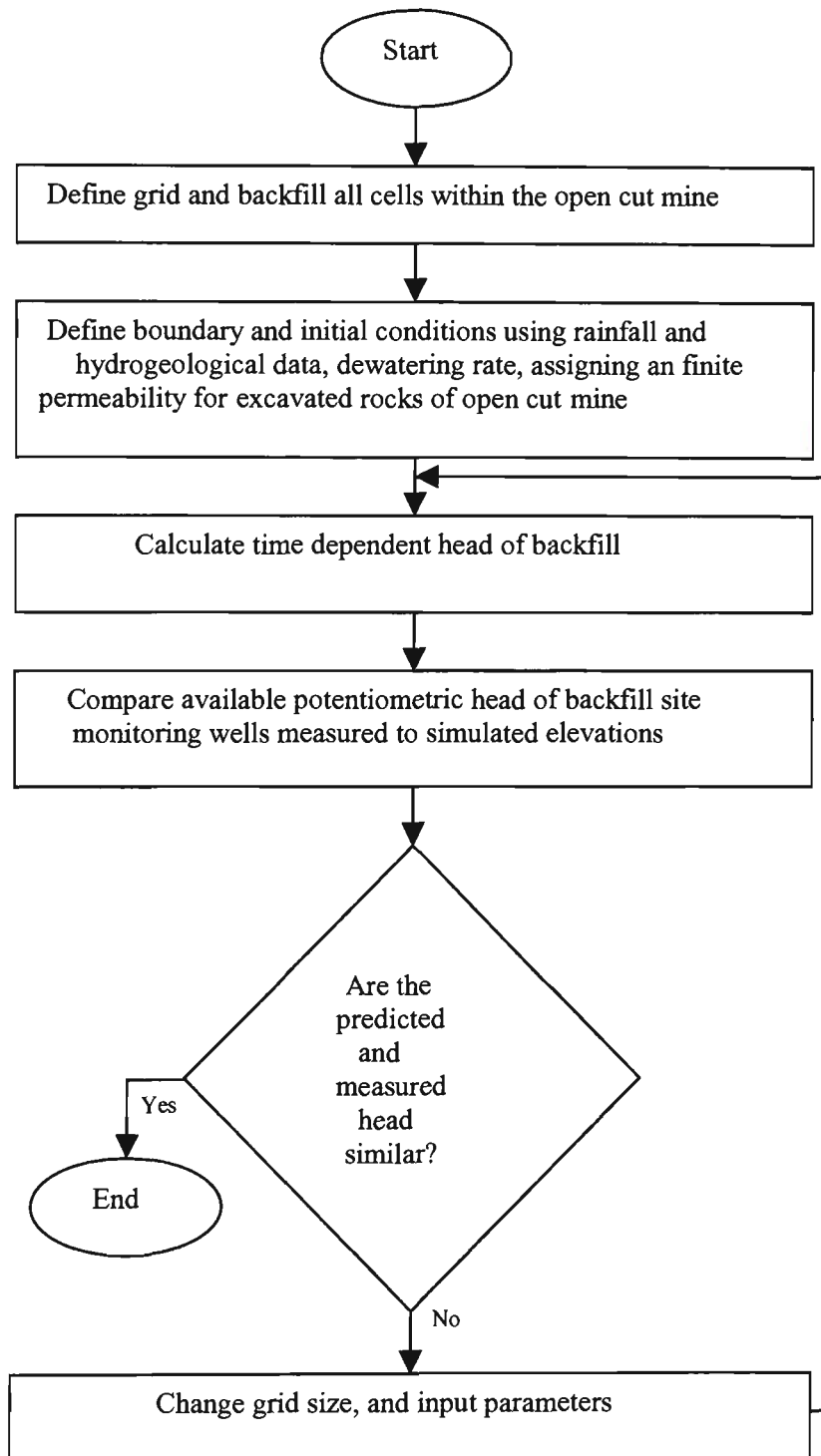


Figure 6.2. Flowchart of groundwater rebound simulation in an open cut mine.

### 6.3 Model verification

The following four problems are described to verify the numerical modelling of groundwater rebound after mining:

#### 6.3.1 Problem 1- Dewatering simulation in a confined infinite aquifer

This first problem is modelled to compare the results of a dewatering test in a confined infinite aquifer under transient conditions using an analytical solution incorporating the Theis equation (Walton, 1970) with the numerical model. The recovery period has also been taken into consideration in this example. An axisymmetric analysis was used to simulate radial flow to a well. The total hydraulic head in the aquifer was taken as 15 m. The aquifer had a hydraulic conductivity of  $2.0 \times 10^{-3} \text{ m/s}$  and a storativity of 0.06. The dewatering rate was  $0.12 \text{ m}^3/\text{s}$  and the well radius was 0.15 m. The first part of the simulation was mostly taken from SEEP/W user's manual (Geo-slope International Ltd., 2002).

To solve the problem numerically, a finite element grid was constructed with 126 nodes and 45 elements in a single layer 5 m thick. The rectangular grid consisted of eight-noded elements with an infinite element at the right end of the model. The length of the grid was 45 m. Figure 6.3 shows the finite element grid for the problem where 11 time steps were used for the simulation. From time steps 1 to 7, an increment of 10 seconds and an expansion factor of 2 up to a maximum increment size of 900 seconds were used. The increment size was changed for the remaining time steps. A steady-state simulation was performed to establish initial conditions. The head at the two ends of the aquifer was set as 15 m. This will construct a uniform total head distribution of 15 m throughout the aquifer. The model for this part of the analysis was named *WPA\_I.SEP*.

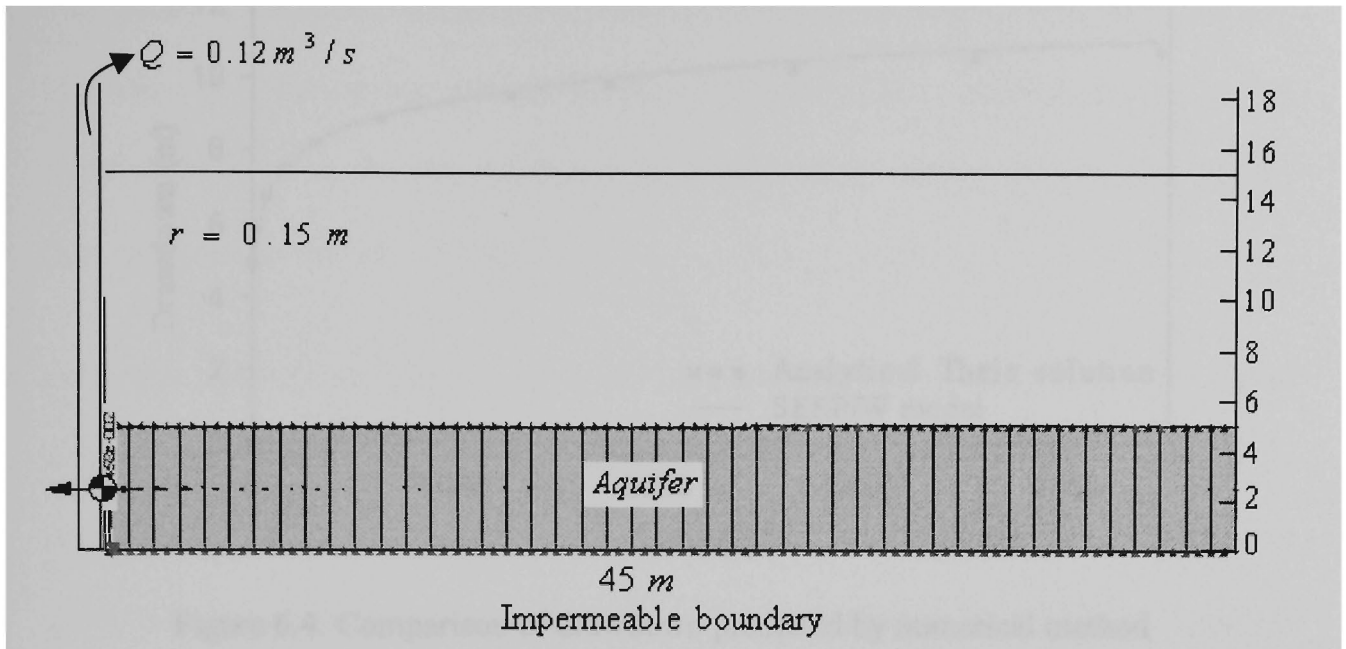


Figure 6.3. Finite element representation of the problem.

For the transient analysis (model *WPA.SEP*), the model *WPA\_I.SEP* was used as the initial condition. The following boundary conditions were considered for transient simulation:

- No-flow boundary conditions at the upper and lower boundaries of the aquifer.
- A head boundary at the right side of the model.
- A flux boundary at the left side next to the dewatering well.

The drawdowns calculated by analytical solution were compared with those predicted by the numerical model in Figure 6.4 showing an error of 0.42 %.

During model calibration, sensitivity analyses were performed to consider the parameters most affecting the simulation results. Transmissivity and storage coefficient appeared to be the most sensitive of the input parameters. Davis and Zabolotney (1996) have reported the same results during the sensitivity analyses of groundwater modelling for the determination of post mining recharge rates at the Belle Ayr mine.

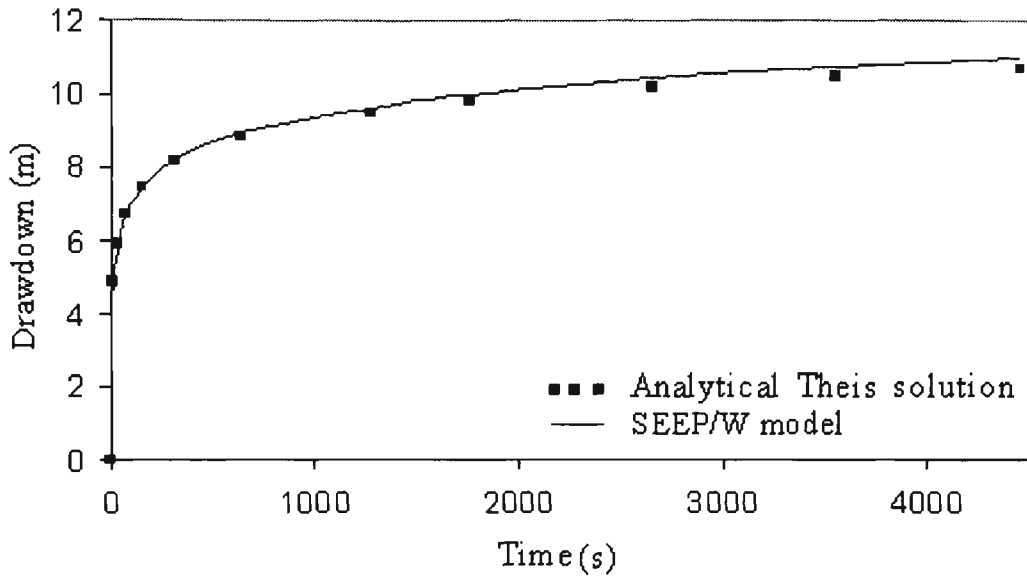


Figure 6.4. Comparison of drawdown predicted by numerical method and calculated values by the Theis method at the well axis.

An analytical solution was used to compute the recovery of a well after dewatering has stopped. This analytical solution has been presented by Theis (Kruseman and De Ridder, 1979). The equation calculating the residual drawdown during the recovery period is given by:

$$h = \frac{Q}{4\pi K m} \left\{ \ln\left(\frac{4Kmt}{r^2 S}\right) - \ln\left(\frac{4Kmt_1}{r^2 S_1}\right) \right\} \quad (6.1)$$

where,

$t_1$  = time since pumping stopped (s) ;

$S_1$  = coefficient of storage during recovery;

$m$  = thickness of the aquifer (m) ;

$S$  = coefficient of storage during pumping;

$r$  = radius of the pumped well (m) ;

$t$  = time since pumping started (s) ;

$Q$  = dewatering rate ( $m^3 / s$ ) ;

$K$  = permeability of the aquifer (m/s) ;

$h$  = residual drawdown or rebound (m) .

This equation assumes that the rate of recharge  $Q$  is constant and equal to the mean rate of discharge  $Q$  during dewatering. This means that drawdown variations resulting from slight differences in the rate of discharge do not occur during the recovery period (Kruseman and De Ridder, 1979).

The Theis recovery method also assumes that conditions and assumptions of the Jacob method must be satisfied. The final predictions of groundwater elevations calculated during the well dewatering simulations (file *WPA11.SEP*) were used as the initial conditions for transient simulation of the recovery period. The following boundary conditions were set for transient simulation of the recovery period:

- No-flow boundary conditions for the upper and lower boundaries of aquifer
- Head boundary conditions at the right side of the model (outer boundary)

Based on the sensitivity analysis made of the hydraulic characteristics of the aquifer, a close agreement was achieved between the analytical results and the numerical predictions of the residual drawdown for a permeability of  $2.0 \times 10^{-3}$  m/s and a storage coefficient of 0.05 (Figure 6.5).

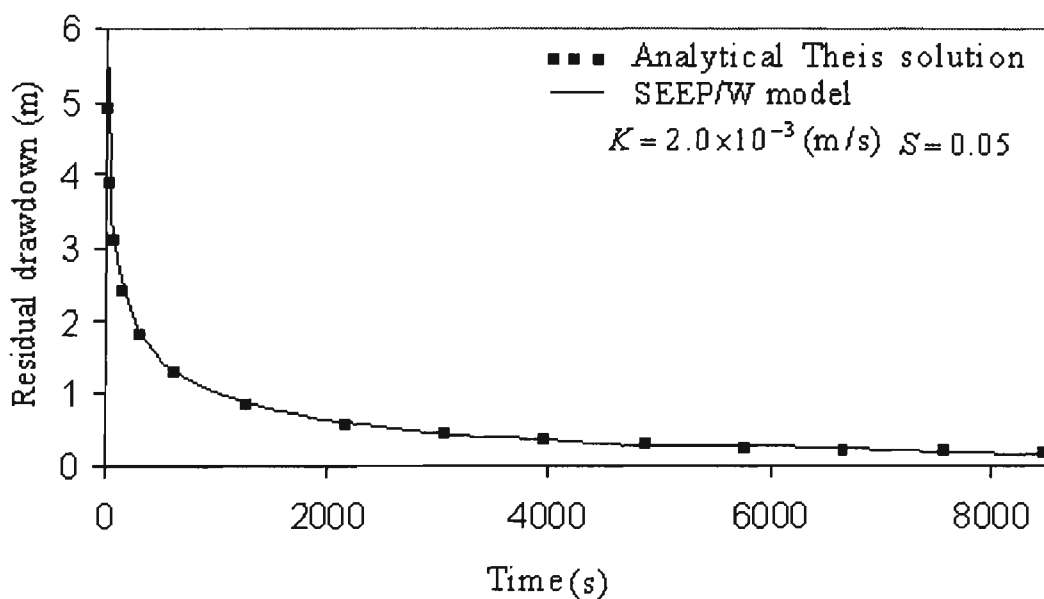


Figure 6.5. Comparison of analytical and numerical residual drawdown as a function of time (calculated error 3.58 %).

### 6.3.2 Problem 2 - Simulation of groundwater recovery in an idealised pit

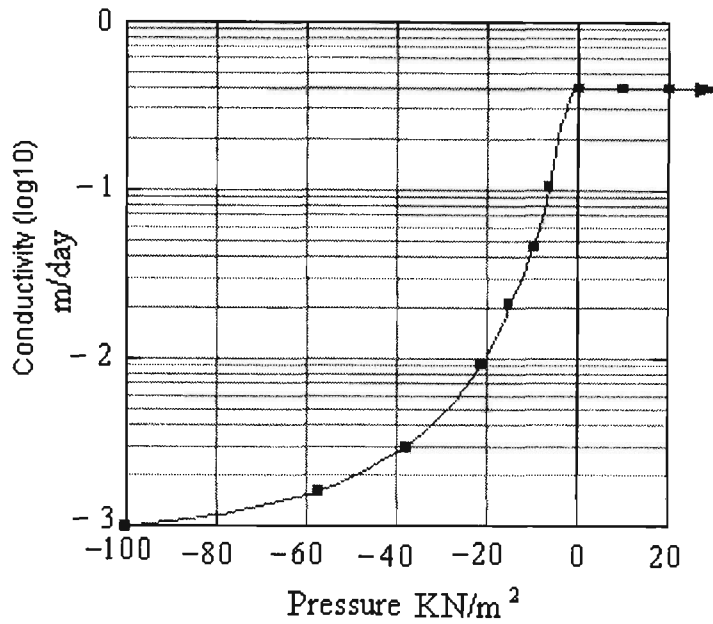
In this second problem, results from the present finite element model are compared to those from a numerical finite element modelling of groundwater recovery in an open pit after mining (Naugle and Atkinson, 1993). From the numerical model developed by Naugle and Atkinson (1993), only the recovery period of the first example was selected for evaluation of the SEEP/W finite element model. In that problem, pit radius, transmissivity and specific storage were 150 m,  $120 \text{ m}^2 / \text{day}$  and 0.001 respectively.

A finite element axisymmetric grid consisting of 2501 nodes, 2400 elements, and 40 layers each 10 m thick was constructed. A finer grid was designed near the pit while the grid was coarse at the far end from the pit (the grid spacing increases from the pit to the outer boundary).

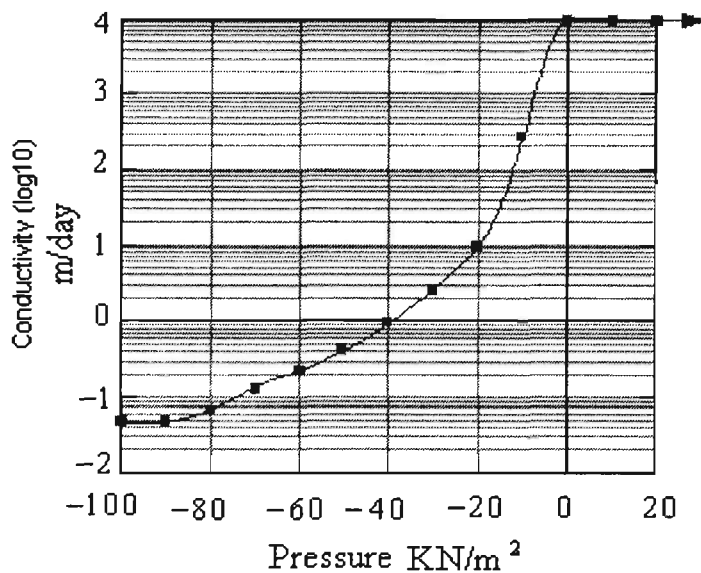
A constant head of 300 m was maintained at the outer boundary while the head in the pit was adjusted to 50 m. A no-flow boundary condition was maintained at the lower boundary of the aquifer.

A model representing the final stage of dewatering was simulated incorporating the boundary conditions. This file was named *POST\_I.SEP*. The second phase of simulation concentrated on the post-mining effects on the hydrologic system. The final estimates of groundwater elevations (*POST\_I.SEP*) were used in predicting the post-mining recovery of groundwater. This second phase of the groundwater recovery model was named *POST.SEP*.

Figure 6.6 shows the modified conductivity functions assigned to the aquifer and excavated rock. A conductivity function defines the relationship between pore-water pressure and hydraulic conductivity values (Geo-slope International Ltd., 2002).



(a) Aquifer conductivity



(b) Conductivity of the excavated rock

Figure 6.6. Modified hydraulic conductivity functions of  
(a) aquifer and (b) excavated rocks.

The results of numerical simulation were then compared to the published numerical finite element model developed by Naugle and Atkinson (1993). The agreement was very good. A comparison of the results for the recovery period is presented in Figure 6.7. The difference between the results of the SEEP/W model and those presented by

Naugle and Atkinson (1993) is 6.85 % and this can be attributed to the hydraulic conductivity values assigned to the excavated rocks and the errors occurring during the digitisation of the groundwater recovery curve.

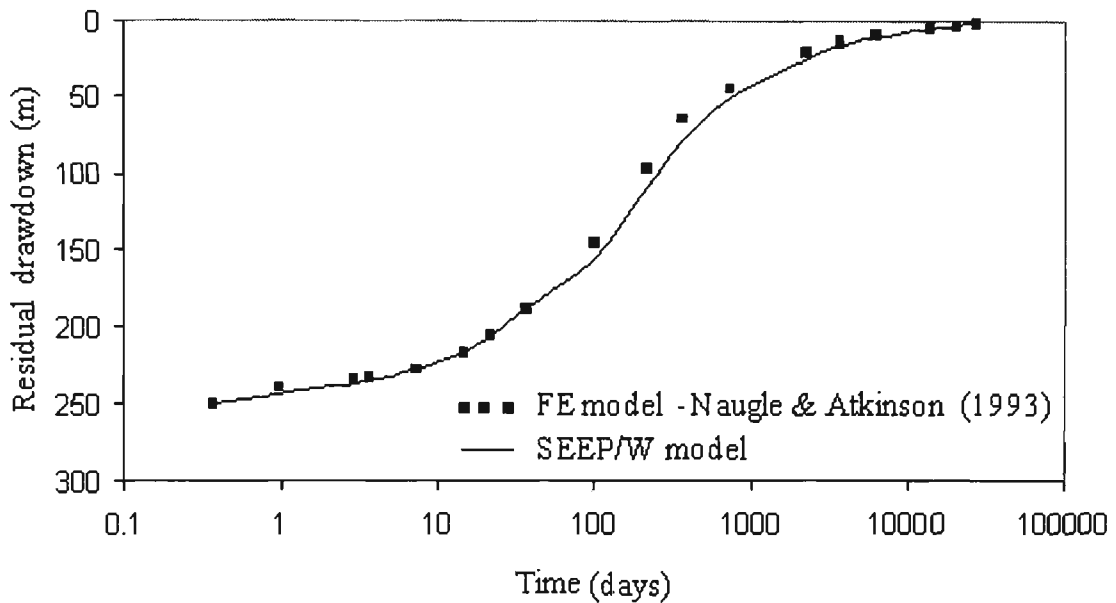


Figure 6.7. Comparison of the SEEP/W finite element model and finite element model developed by Naugle & Atkinson (1993) for prediction of groundwater rebound in an idealised pit.

### 6.3.3 Problem 3 -Modelling of groundwater rebound in an open cut mine site

The main objective of this third problem was to further validate the finite element model with the monitored field data. For this purpose, the observations made by Norton (1983) at the Horsley backfilled site in the United Kingdom were used. The Horsley site is located about 15 kilometres to the West of Newcastle-upon-Tyne in Northumberland (Figure 6.8). The mining operation was carried out between the years 1961 and 1970. From a geological point of view, the site was located in a complicated geological structure in the Coal Measures strata. Approximately 370,000 tonnes of coal was extracted from the mining excavation with a maximum depth of 63 m. The strata were the normal Coal Measure sequence with about 30 % arenaceous deposits. The site was

very wet with artesian water (the piezometric elevation was high). Advance dewatering was used to prevent inflows to the mine excavation. The working head for the pump was 72 m and the pump had a working capacity of  $42\text{ l/s}$ . The Horsley site was backfilled in 1970 and dewatering continued until 1974. The hydraulic conductivity of the spoil was assessed to be greater than  $10^{-4}\text{ m/s}$ .

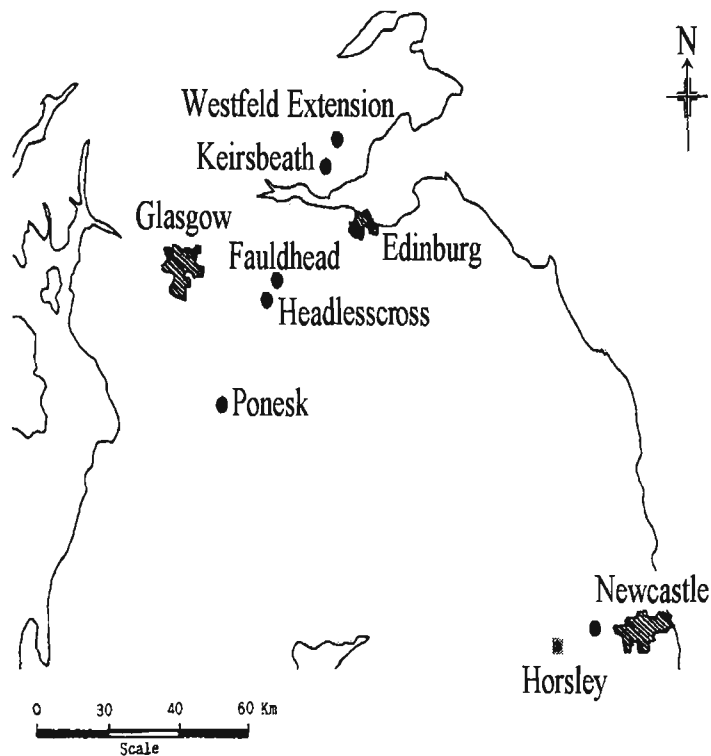


Figure 6.8. Location map of Horsley site (after Norton, 1983).

For the simulation, both two-dimensional and axisymmetric analyses were used. For the axisymmetric analysis, a grid consisting of 1776 nodes, 1679 elements, and 23 layers of different thickness was constructed. The grid spacing increases to the outer boundary (Figure 6.9). Constant heads of 48 m and 4.8 m were assigned at the backfill and at the model boundary in order to construct an initial condition (File *MAXISYM\_I.SEP*). A sensitivity analysis was performed to evaluate the parameters most sensitive to the simulation results. It was found that the transmissivity and the storage coefficient appeared to be the most sensitive of the remaining parameters.

**(a) Axisymmetric model**

For an axisymmetric analysis, an average precipitation of  $4.65 \times 10^{-8} \text{ m/s}$  (Norton, 1983) was assigned at upper boundary of the model.

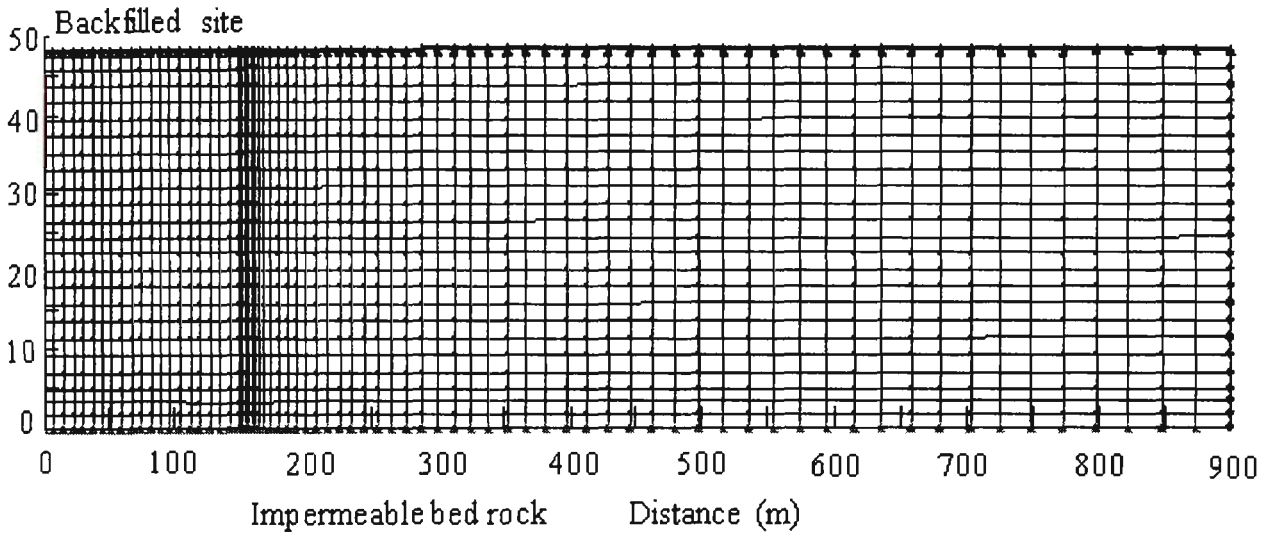


Figure 6.9. Finite element representation of the axisymmetric problem.

The saturated hydraulic conductivities of  $9.5 \times 10^{-6} \text{ m/s}$  and  $4.0 \times 10^{-3} \text{ m/s}$  were assigned at the aquifer and at the backfilled site respectively. The first time step was selected at 2 months, after that time steps of 6 months were assigned. Storage coefficients of 0.0055 and 0.0065 were considered at the aquifer and at the backfilled site respectively. Figure 6.10 shows the predicted and measured values of residual drawdown at the backfilled site as a function of time.

Figure 6.10 indicates that for the period 0-500 days the model slightly overestimates the residual drawdown while for the period 500 to 1000 days slightly underestimates the amount of rebound. It is estimated that the average error in calculation of the rebound by the model is 2.19 %.

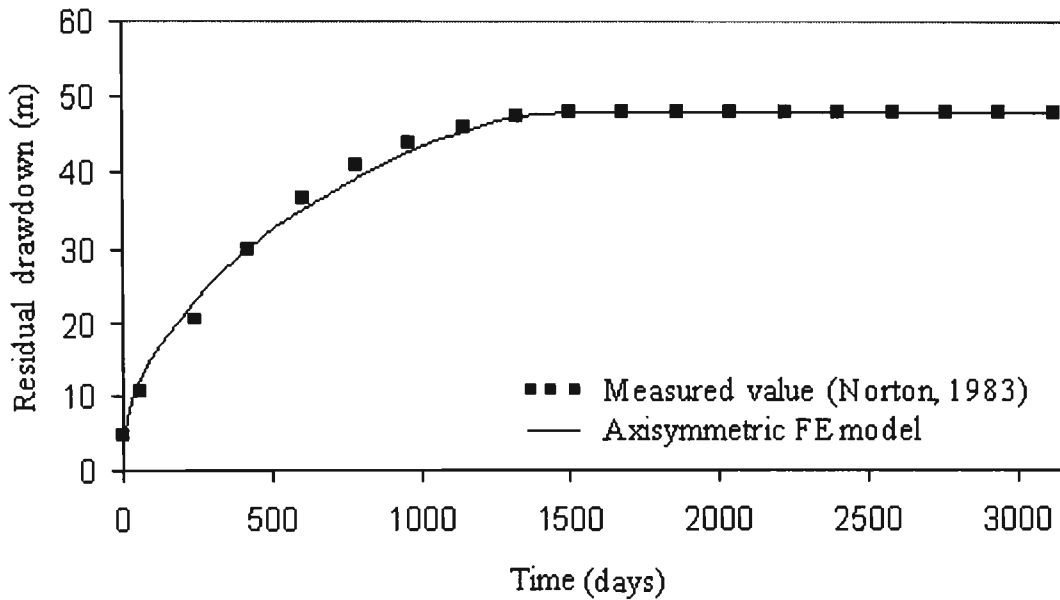


Figure 6.10. Comparison of numerical model and field data (from Norton, 1983) for prediction of water table rebound at the Horsley backfilled site in the UK.

**(b) Two-dimensional model**

For the two-dimensional simulation, a finite element grid consisting of 3381 nodes, 3200 elements and 20 layers was designed. A finer grid was constructed around the open cut as well as the boundary between the aquifer and the spoil (Figure 6.11).

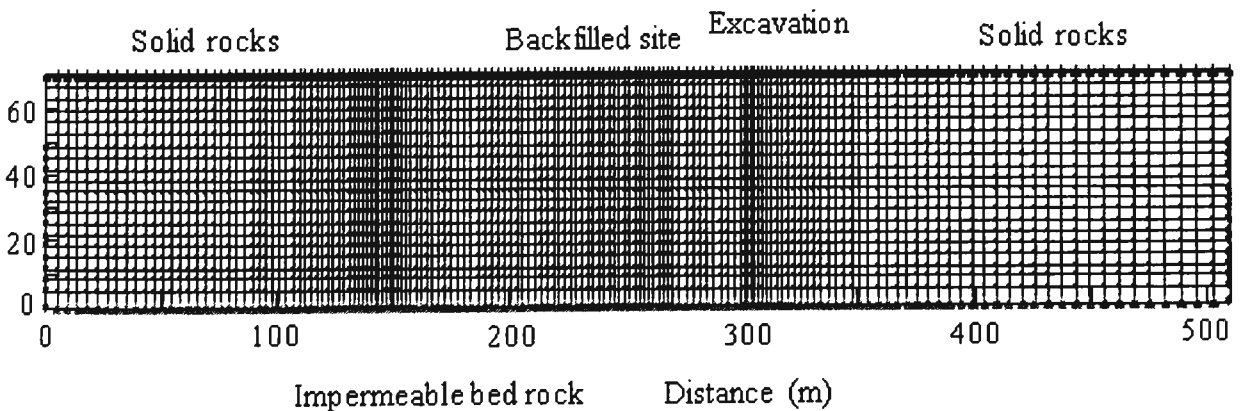


Figure 6.11. Finite element representation of two-dimensional problem.

In order to establish an initial condition for the model, constant heads of 48 m were assigned at the outer boundaries of the aquifer. The corresponding head of 4.8 m was

assigned at the backfill site. An impermeable layer was simulated by assigning a no-flow boundary condition at the lower boundary of the model. A two-dimensional model was then performed and named *SM2D\_I.SEP*. In this simulation, hydraulic conductivities of  $1.0 \times 10^{-6} \text{ m/s}$ ,  $1.0 \times 10^{-4} \text{ m/s}$  and  $4.0 \times 10^{-3} \text{ m/s}$  were assigned to the aquifer, backfill and excavated rock respectively. The hydraulic conductivity of excavated rock was equivalent to the original hydraulic conductivity of the aquifer multiplied by 4000 in order to minimise the errors occurring during the prediction of groundwater table elevations.

The anisotropy ratios of 1.25 and 1 were used as input parameters for the aquifer and spoil respectively. An average precipitation of  $1.0 \times 10^{-10} \text{ m/s}$  and a storage coefficient of 0.001 were assigned in the model. The comparison of the residual drawdown predicted by the two-dimensional finite element model and those observed at the Horsley site (Norton, 1983) are shown in Figure 6.12.

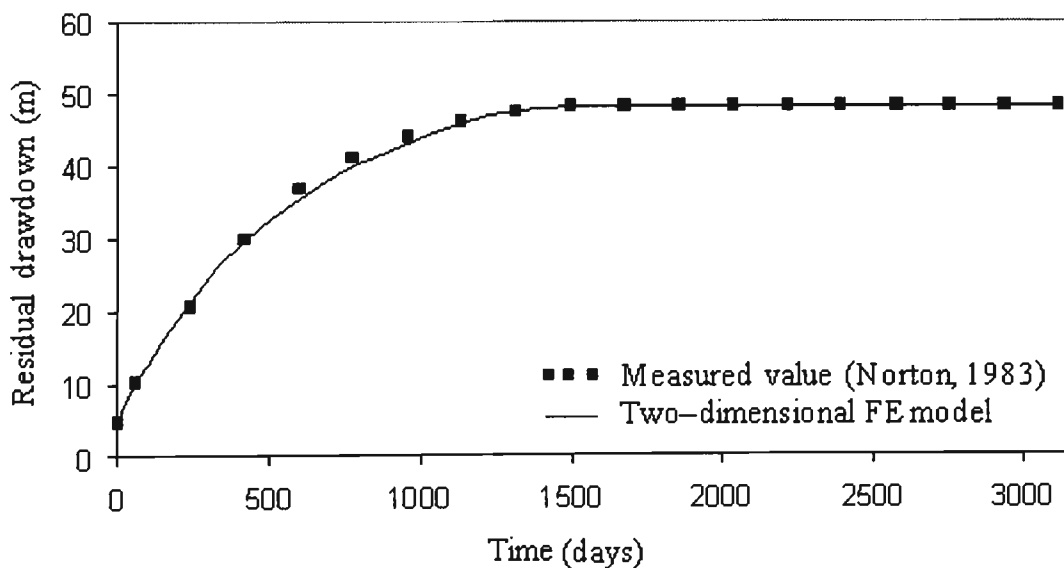


Figure 6.12. Comparison of numerical model and field data (Norton 1983) for prediction of water table rebound at the Horsley backfilled site in the UK.

As Figure 6.12 shows, the model under-estimates the rebound for a period 500-1000 days and the average error in predicted values are within 0.82 % of the measured values.

### **6.3.4 Problem 4-Groundwater rebound simulation at backfilled site 'A' in the East Midlands area, UK**

#### **(a) General consideration**

In this problem, results from the numerical finite element model are verified with the monitored field data. For this verification purpose, the observation made by Reed (1986) on a shallow backfilled site, called truck & shovel site 'A' in the East Midlands area in the UK were used. The site was relatively small in size with 0.9 hectares, 6 coal seams, at an overburden to coal ratio of 10:1. The mining operations extended down-dip from the coal outcrop to maximum depth of 31 metres, the average depth of excavation on the site was 17 metres. The mining operation was carried out over a period of 2 years by truck and shovel methods. The mining void was backfilled by dump trucks tipping over the edge of the loose wall. Scrapers were employed to regrade the overburden levels and to replace soils. The average rate of coal production was 1000 tonnes per week.

#### **(b) Site topography, geology and backfill characteristics**

The pre-mining land surface was essentially flat, lying at a level of 46 to 47 metres above ordinance datum (A.O.D). The site was bounded on the eastern and southern sides by railway lines. Figure 6.13 presents a typical geological section of the excavated materials over the site. Figure 6.14 illustrates the layout of the site with respect to site boundaries, areas of excavation and position of monitoring instruments and Figures 6.15 and 6.16 show the pre-mining geological profiles.

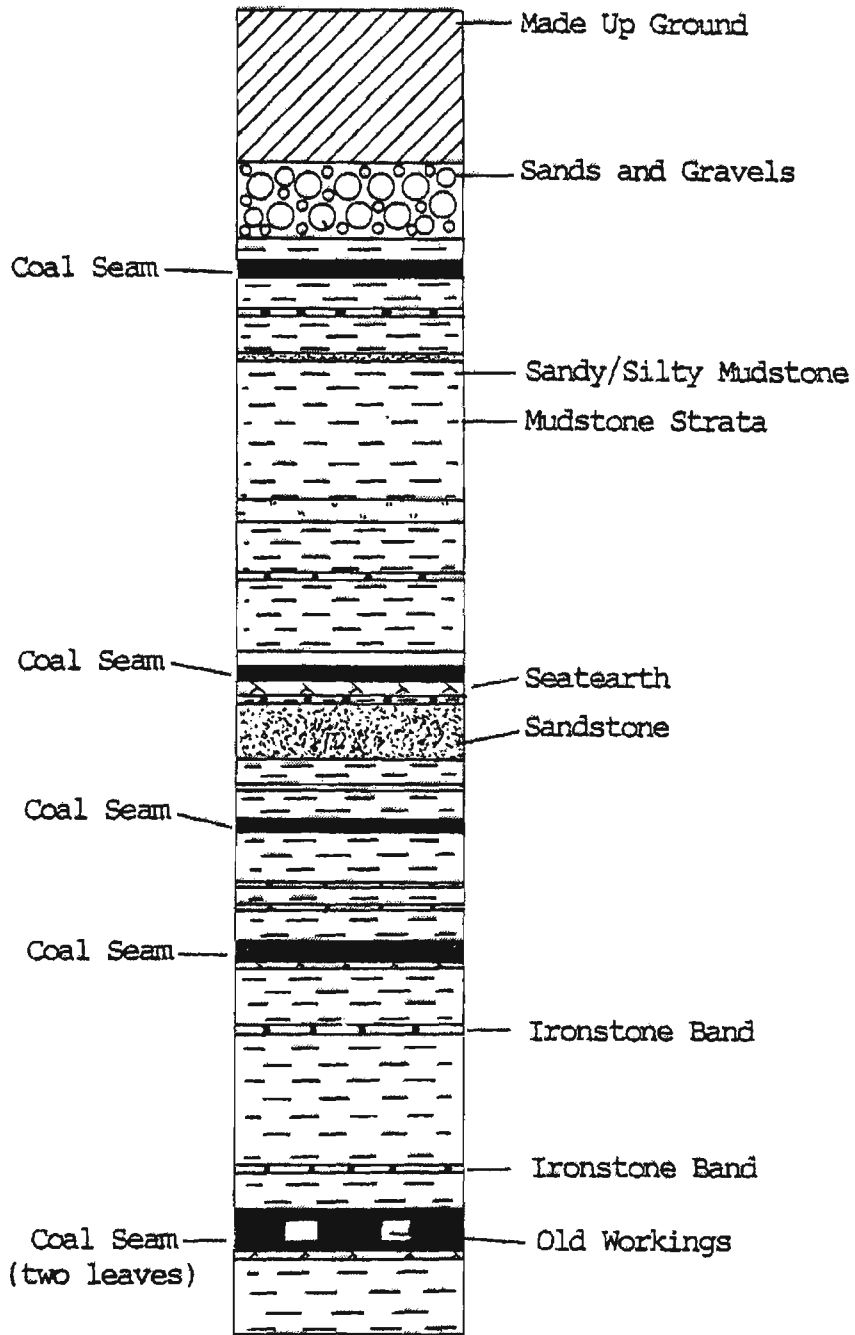


Figure. 6.13. A typical geological section of the excavated material, total depth of section is 44 m (after Reed, 1986).

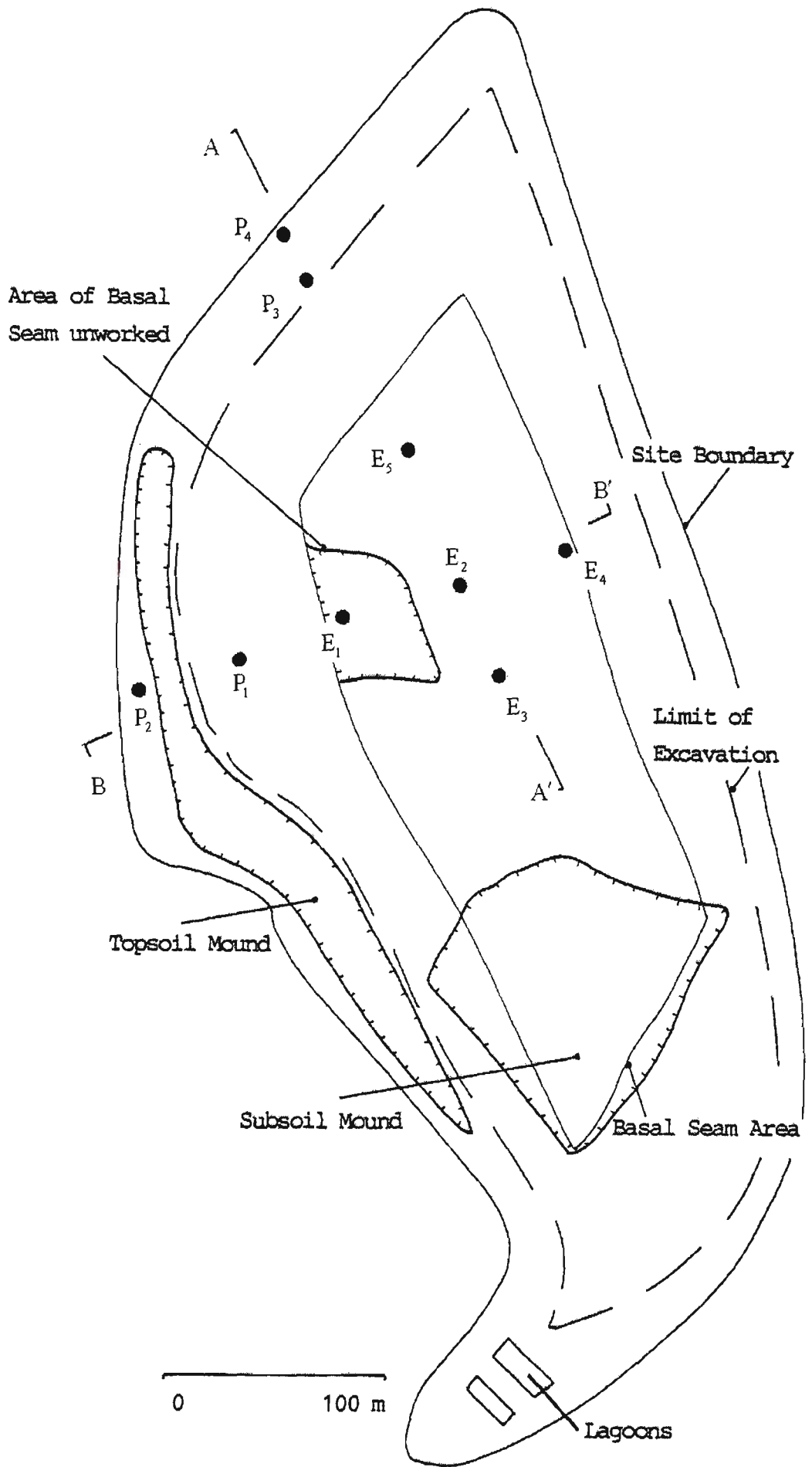


Figure 6.14. Site characteristics and instrument stations (after Reed, 1986).

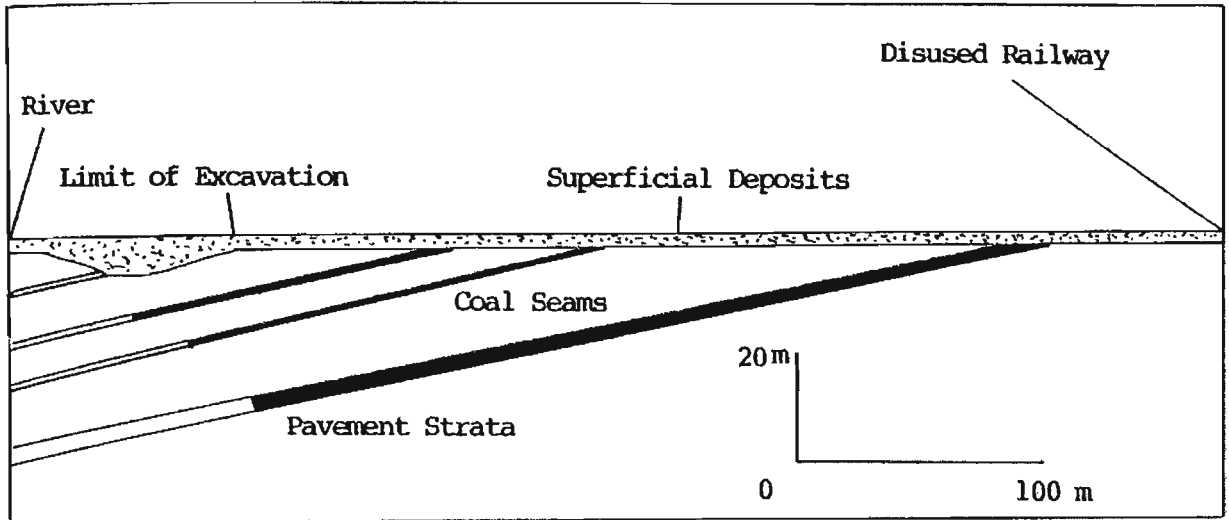


Figure. 6.15. Illustration of pre-mining geological profile A-A' (after Reed, 1986).

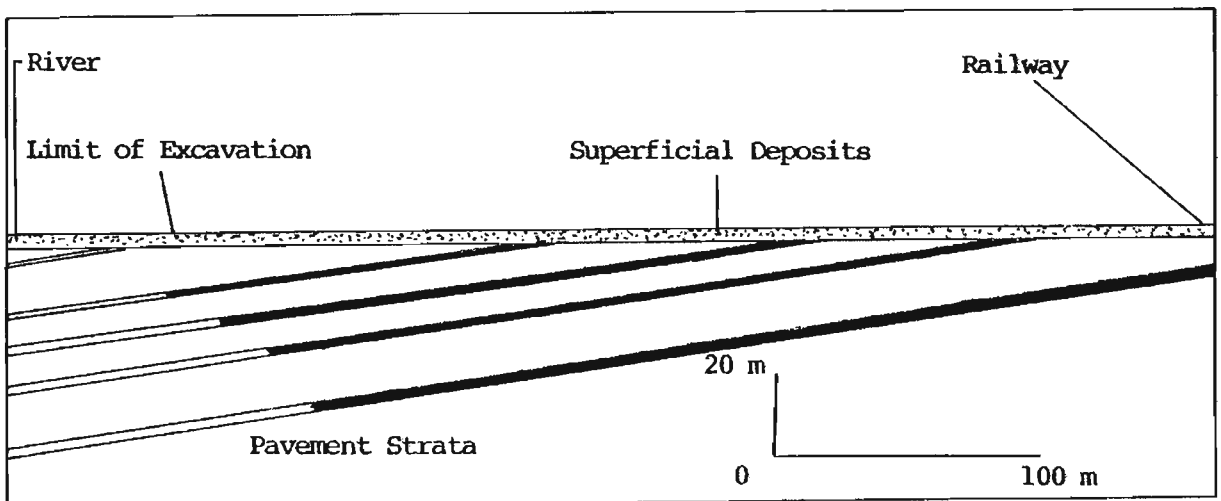


Figure. 6.16. Illustration of pre-mining geological profile B-B' (after Reed, 1986).

Overburden and inter-burden strata consisted of mainly mudstone rocks together with occasional bands of silty or sandy material. Alluvial deposits covered the entire area of the site to a depth of approximately 3 to 4 metres, which increased to 9 metres in the north-western part where a buried river channel laid. These deposits mainly contained 0 to 2 metres of sands and gravels overlain by clay layers.

During the life of the mining operation 2,200 litres per minute were dewatered from the void using sump pumping techniques. The backfill is identified to have an uniform

composition over the area of the site. The backfill was mainly mudstone (70 %), containing 12 % alluvial deposits. The rest of the spoil consisted of sandstones, siltstones and seatearths.

**(c) Instrumentation patterns**

The instrumentation was commenced as soon as the overburden restored to its final level, prior to the replacement of the soils in order to minimise the time gap between installation of the instrumentation and the cessation of dewatering. The instrumentation scheme contained five magnetic extensometers/ piezometers ( $E_1, E_2, \dots, E_5$ ) in two profiles across the mine, and four piezometers ( $P_1, P_2, \dots, P_4$ ) in the unmined strata, two at one end of each profile (see Figure 6.14). The piezometers were installed to monitor water levels in the solid strata and the rate of the water rebound process. Furthermore, the magnetic extensometers /piezometers were installed in the backfilled site in order to monitor the groundwater rebound through the backfill as well as measuring the settlement within the backfill. All bore holes were then backfilled on installation with a weak bentonite grout. As Figure 6.14 shows one of the two profiles was directed along the strike of the mine and the second was down-dip. Figures 6.17 and 6.18 illustrate cross-sections of the backfill site along the profiles A–A’ and B–B’. The instrumentation scheme is also shown.

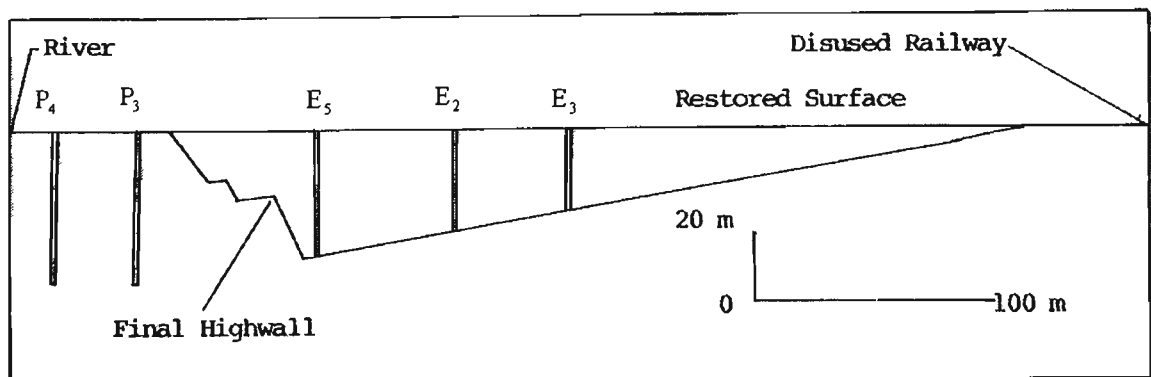


Figure. 6.17. Instrumentation scheme for section A–A’ (after Reed, 1986).

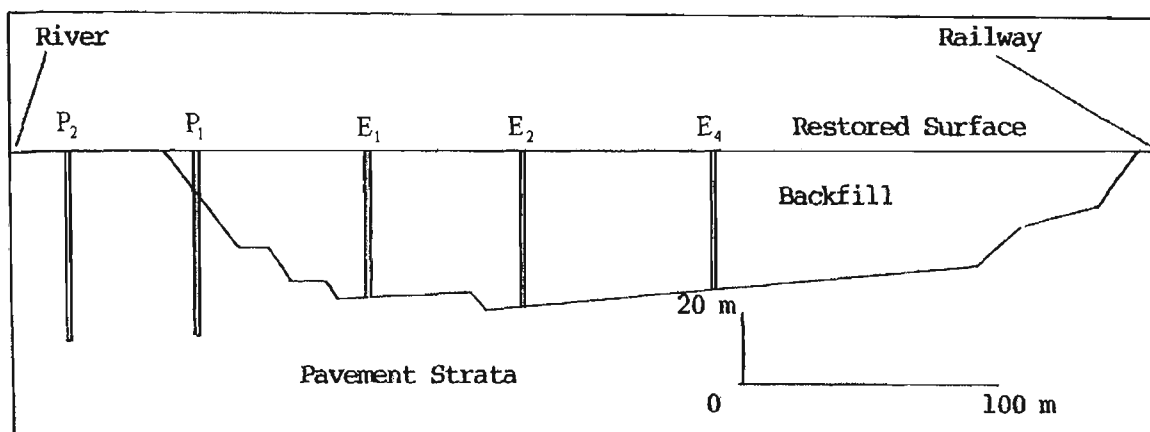


Figure. 6.18. Instrumentation scheme for section B-B' (after Reed, 1986).

Table 6.1 outlines the initial surface levels and depths of each instrument and gives the individual magnet positions.

Table 6.1. Instrumentation details (after Reed, 1986).

Extensometer	Fill depth (m)	Surface level (m A.O.D)	Magnet positions (Depth metres)					
E <sub>1</sub>	20.56	45.48	20.5	17.5	13.8	8.70	3.80	1.90
E <sub>2</sub>	23.90	44.98	23.3	22.7	18.5	13.4	7.80	2.70
E <sub>3</sub>	22.70	45.67	21.9	17.8	15.3	11.7	7.50	2.80
E <sub>4</sub>	21.40	45.04	20.4	16.9	13.0	10.3	6.40	2.50
E <sub>5</sub>	25.40	45.40	24.7	19.4	15.7	10.8	6.00	2.20
Piezometers	Depth							
P <sub>1</sub>	33.60	45.51						
P <sub>2</sub>	33.60	47.22						
P <sub>3</sub>	33.60	48.94						
P <sub>4</sub>	33.20	48.27						

Drilling of the boreholes and installation of the instruments were completed within three weeks. Reed (1986) reported that several technical and mechanical delays were encountered.

#### **(d) Evaluation of field monitored groundwater rebound**

Groundwater levels were monitored by Reed (1986) at a depth of 11 m below the restored surface mine site. His observations were as follows:

"The flood level recovered to the surface of the backfilled site within 120 days. As the groundwater rebound is a continuous process and observations commenced 48 days after the cessation of dewatering, therefore there were 48 lost days. In that time period prior to monitoring, groundwater levels in the site were measured from 24 m below the restored surface to 15 m, a recovery of 9 metres. During the first 48 days of monitoring groundwater levels rose by a further 9 m, and in the second similar period by 5 m. Therefore, within 144 days from the termination of dewatering, groundwater recovered 23 m. Water levels initially showed the expected trends of a drawdown curve lowering towards the final void area. The highest initial groundwater level was monitored on instrumentation point  $E_3$ , the one furthest from the final void. Water levels in instruments  $E_1$  and  $E_2$  were observed to be the same whilst those in  $E_4$  were slightly lower. Slight rebound was monitored on instrument  $E_3$  for the first 15 days. Water levels in all instrumentation points then rose uniformly from day 15 to 50. Between days 50 to 70, an abnormal rainfall was reported which flooded areas of the restored surface, particularly around instruments  $E_2$  and  $E_4$ . 110 days after the commencement of monitoring groundwater levels in the fill of  $E_3$  stood above the restored levels of  $E_2$ . Finally by day 120, the surface became flooded." (after Reed, 1986).

#### **(e) Analytical equation for the rise of groundwater level**

The rise of the water level may be approximately calculated using the following equation (Mittel and Singh, 1993):

$$h_{(t)} = h_0 e^{-\alpha t} \quad (6.2)$$

where,

$h_{(t)}$  = water level rise at time  $t$  (m);

$h_{(0)}$  = initial water level (m);

$\alpha$  = hydrogeological characteristics of the basin (%);

$t$  = time interval at which water level rise from  $h_{(0)}$  to  $h_{(t)}$ .

The main objective of using analytical Equation 6.2 was to further evaluate and assess the model simulation results and to find the appropriate ranges for  $\alpha$ , applicable to backfilled open cut coalmines. If this is achieved, this analytical equation with the modified  $\alpha$  describing the hydrogeological characteristics of the site can produce a reasonable preliminary estimate of the groundwater rebound process within the backfill. It was found that  $\alpha$  predominantly ranges from about 0.9 to 3.5 at the backfill site.

## **(f) Finite element analysis and results**

### **(f.1) Modelling performance and prediction (Profile A–A')**

A finite element grid consisting of 4903 nodes and 4557 elements was constructed (see Figure 6.19). The problem domain was divided as rectangular elements, while triangular elements were used near the boundaries of backfill and unmined strata. A finer mesh was constructed at boundaries where a rapid change of hydraulic conductivities is seen. The following boundary conditions were assigned to the model:

- A no-flow boundary condition at the lower boundary of the aquifer
- An infinite boundary condition at two ends of the model
- A recharge boundary condition at upper boundary in order to take into consideration net rate of precipitation

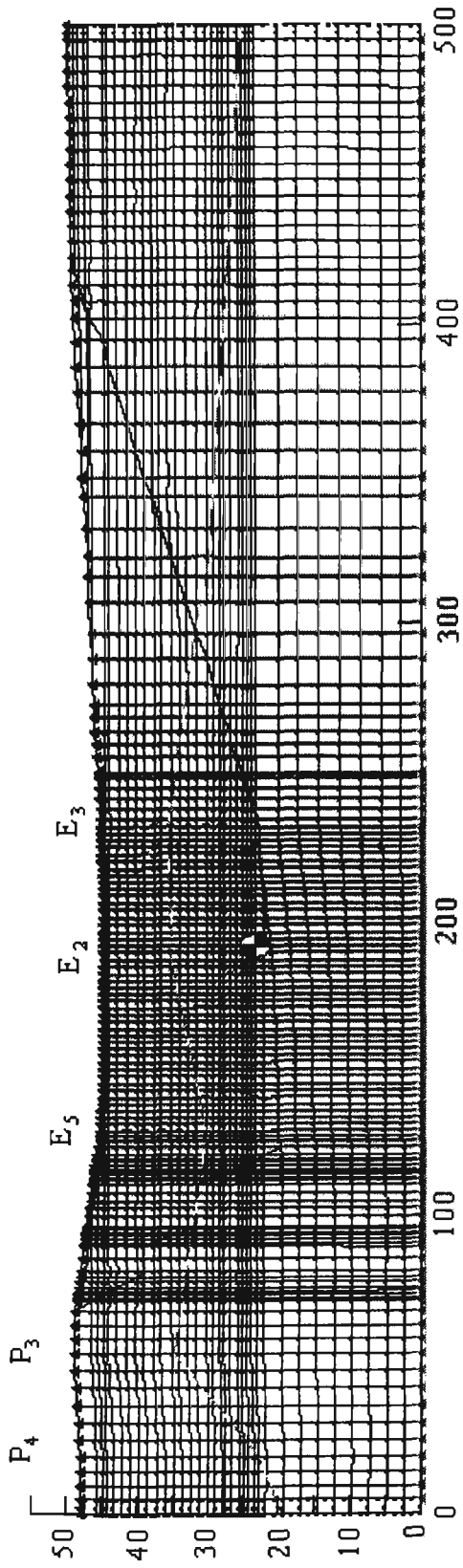


Figure 6.19. Finite element grid (Section A - A').

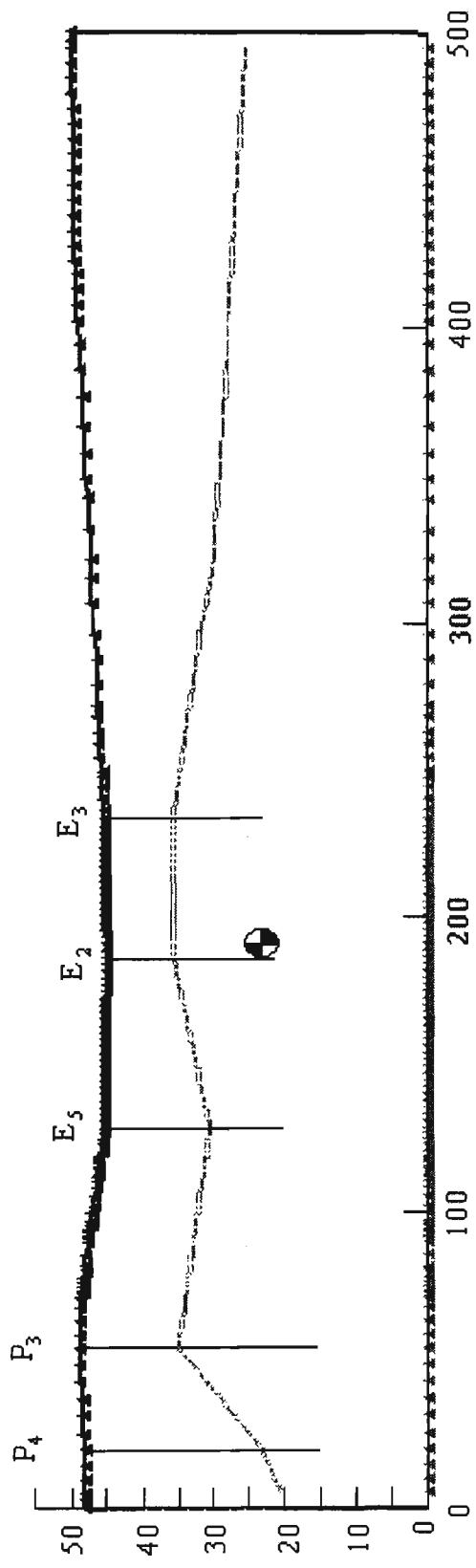


Figure 6.20. Water table before groundwater rebound, the position of instruments was also illustrated (Section A - A').

The initial water table was established from water levels recorded in the instrumentation points (Figure 6.20). These water levels should be used as an initial condition for the transient simulations of the post-mining rebound.

The saturated hydraulic conductivities of  $9 \times 10^{-5} \text{ m/s}$  and  $6.4 \times 10^{-6} \text{ m/s}$  were assigned to the backfill and the unmined aquifer respectively. A saturated water content of 0.35 was assumed in this model based on measured values (Rogowski and Weinrich, 1981). An average precipitation of  $3 \times 10^{-8} \text{ m/s}$  was maintained for the model. However, because of the abnormal precipitation rate between days 50 to 70, this value needed to be increased to  $5 \times 10^{-8} \text{ m/s}$ .

After specification of all initial and boundary conditions, the transient simulation was performed and groundwater was then allowed to rebound. The simulation was carried out in three distinct phases:

- 1) Groundwater was allowed to rebound until day 50. The model for this part of the simulation was called *SITEA\_S\_A\_A*.
- 2) Between days 50 to 70, because of an abnormal rainfall, the recharge value was changed to  $5 \times 10^{-8} \text{ m/s}$  and the model was then run using *SITEA\_S\_A\_A* as an initial condition and finally it was named *SITEA\_S\_A\_A\_1*.
- 3) The transient simulation was eventually completed with a reduction in the recharge value to  $2.7 \times 10^{-8} \text{ m/s}$ . The model for this phase of the simulation was known as *SITEA\_S\_A\_A\_2*.

Figure 6.21 shows the groundwater rebound patterns within 120 days after the cessation of dewatering. It indicates a rapid rate of groundwater recovery in the backfill because the hydraulic conductivities of the spoil are much larger than those of the unexcavated

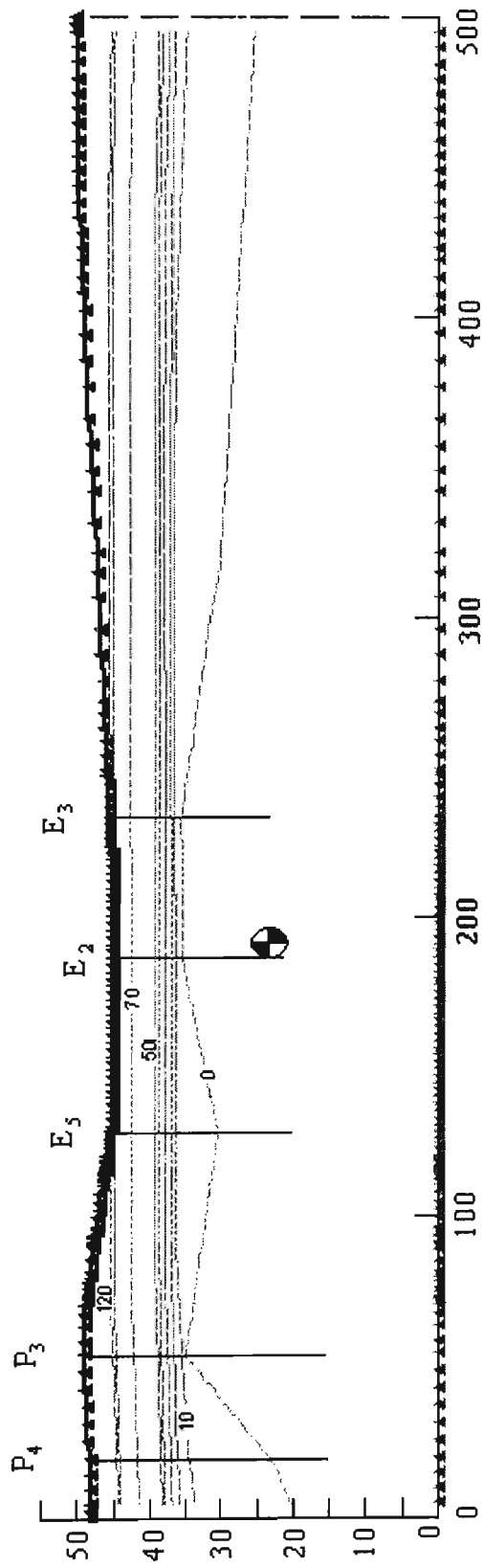


Figure 6.21 . Water recovery patterns after 10, 21, 32, 43, 50, 70, 110, and 120 days ceasing of pumping.

aquifer. Modelling predictions verified the field observations that the surface of the backfill was flooded after 120 days following cessation of pumping.

Comparisons were made over each time period between the simulated groundwater levels and the actual water levels measured at the site as well as the groundwater rebound predictions using the analytical Equation 6.2 (Figure 6.22).

Figure 6.22 indicates that for the period 50 to 110 days both the analytical equation and the model slightly underestimated the groundwater levels. For the period 0-50 days, close agreement was achieved between the three methods at instrumentation point  $E_2$  in the backfill area. Although the model simulated groundwater levels at this point were in agreement with the analytical solution for the period 0-50 days, but a slight overestimation appeared. Similarly, the model slightly over predicted the water levels at point  $E_5$  over the backfill and  $P_4$  at the unexcavated aquifer within the period 0-50 days, while at instrumentation point  $P_3$  located in solid strata, the model slightly underestimated the rebound process.

#### **(f.2) Modelling performance and prediction (Profile B–B')**

To evaluate the groundwater rebound process within the backfill site, the simulation was also performed along the section B–B'.

A finite element model consisting of 3466 grid points and 3311 elements was constructed. The model was mainly divided into rectangular elements. Triangular elements were also used for those parts of the flow system representing the boundaries of the backfill and unmined strata. The proposed model is a rectangular shape of 700 m length and 50 m width. Figure 6.23 shows a finite element mesh applied to the problem.

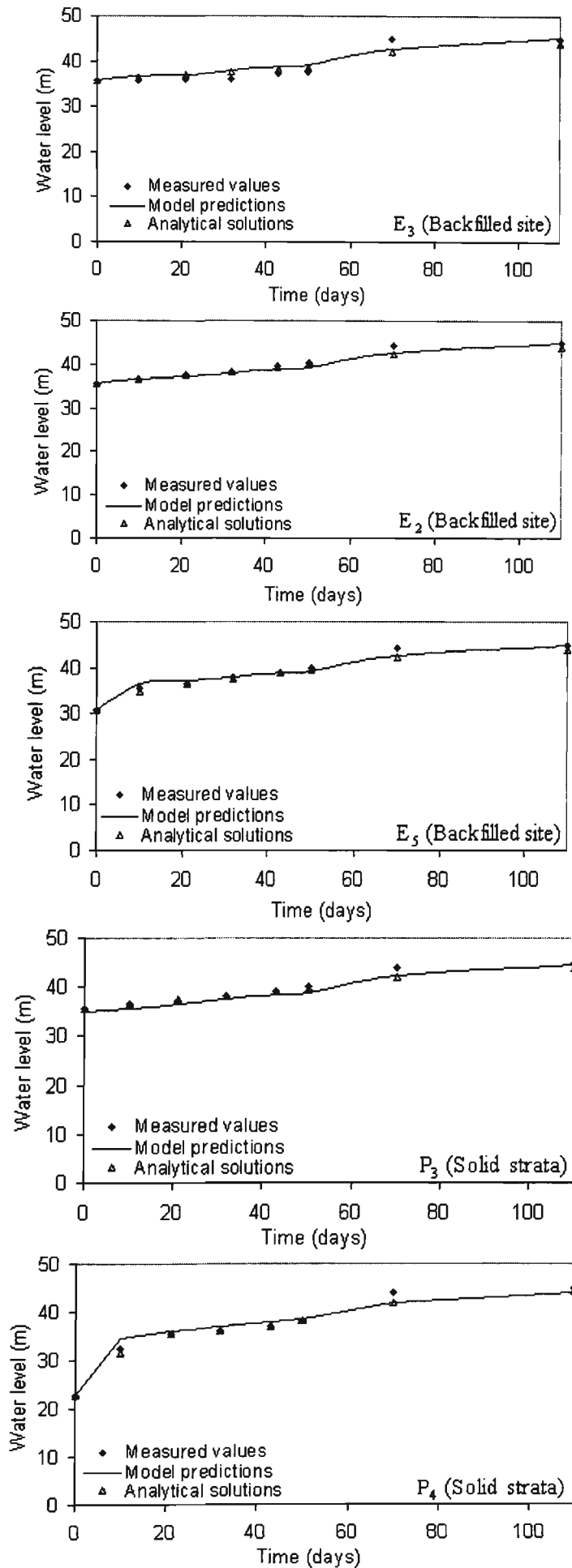


Figure 6.22. Comparison of measured values, analytical solutions and model predictions for groundwater rebound process at instrumentation stations (Section A–A').

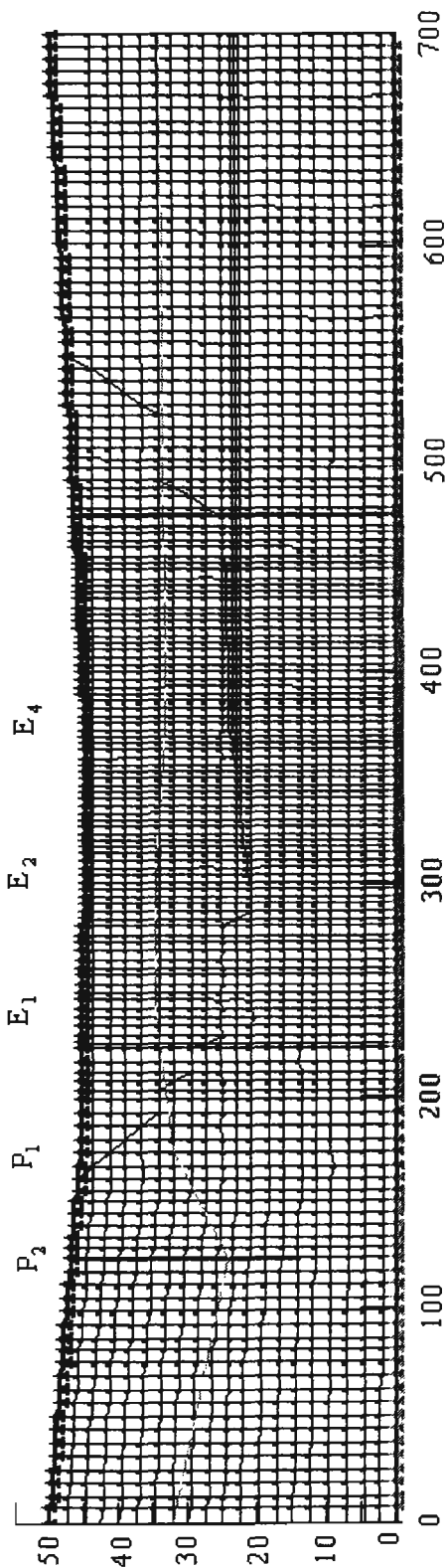


Figure 6.23. Finite element mesh (Section B-B').

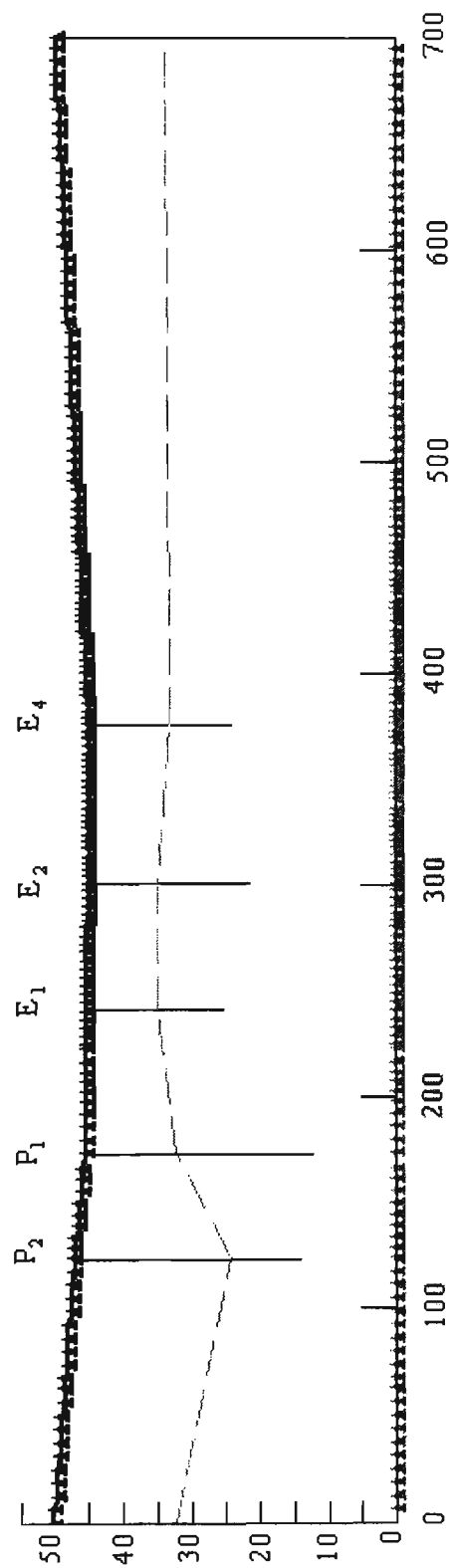


Figure 6.24. Water table before groundwater rebound process, and the position of instrumentation stations (Section B-B').

A no-flow boundary condition was maintained at the lower boundary of the model. An average precipitation of  $3 \times 10^{-8} \text{ m/s}$  was assigned to the upper boundary of the model. No change was made in this value over a period of 0-50 days while the value was changed to  $5 \times 10^{-8} \text{ m/s}$  within the time period of 50-70 days to take into account the abnormal rainfall which took place during this period. The value of  $3 \times 10^{-8} \text{ m/s}$  was again maintained over the period of 70-84 days. After that it was, however, reduced to  $1 \times 10^{-8} \text{ m/s}$  for better representation of the real system. Considerable attempt was made to adjust the initial water table in backfill and unmined strata using field data monitored at instrumentation points (Figure 6.24).

This water level represents the lowest groundwater table maintained by the use of the dewatering operation in order to prevent its interference with mining works. As previously mentioned this initial water level was used as an initial condition for the transient groundwater rebound simulation. Figure 6.25 shows the hydraulic conductivities as a function of pore-water pressure assigned to the backfill and unmined strata.

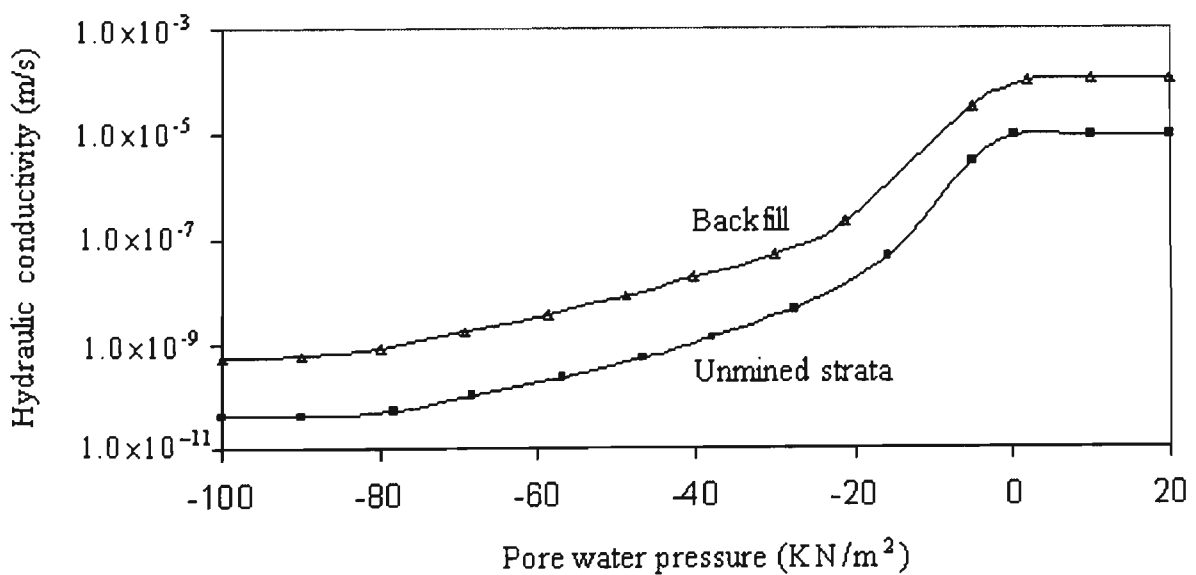


Figure 6.25. Modified conductivity function assigned in aquifer and backfill.

As Figure 6.25 shows, the saturated hydraulic conductivities were  $9 \times 10^{-5} \text{ m/s}$  and  $8.5 \times 10^{-6} \text{ m/s}$  for the backfill and the solid strata respectively. However, slight modification was made on the hydraulic conductivity function of backfill in order to take into consideration the settlement which took place in the backfill as the groundwater level rose within the backfill. Therefore the saturated hydraulic conductivity of the backfill was changed from  $9 \times 10^{-5} \text{ m/s}$  to  $1 \times 10^{-5} \text{ m/s}$  in the final stage of rebound process.

The transient simulation of post-mining rebound was then performed in four stages as given below:

The first stage takes into account groundwater recovery over a period of 0-50 days. The model for this part of the simulation was named *SITEA\_S\_B\_B*. The second, third and the fourth phases simulate groundwater rebound over time periods of 50-70, 70-84, and 84-120 days respectively. The models for these three distinct stages were named *SITEA\_S\_B\_B\_1*, *SITEA\_S\_B\_B\_2*, and *SITEA\_S\_B\_B\_3* respectively.

It should be noted that the simulated values made in each phase were used as an initial boundary condition for the next stage simulation. Figure 6.26 illustrates the simulated water levels at different time steps.

The groundwater levels measured at the site were compared with those predicted by the use of the finite element model and those calculated using the analytical Equation 6.2 (Figure 6.27).

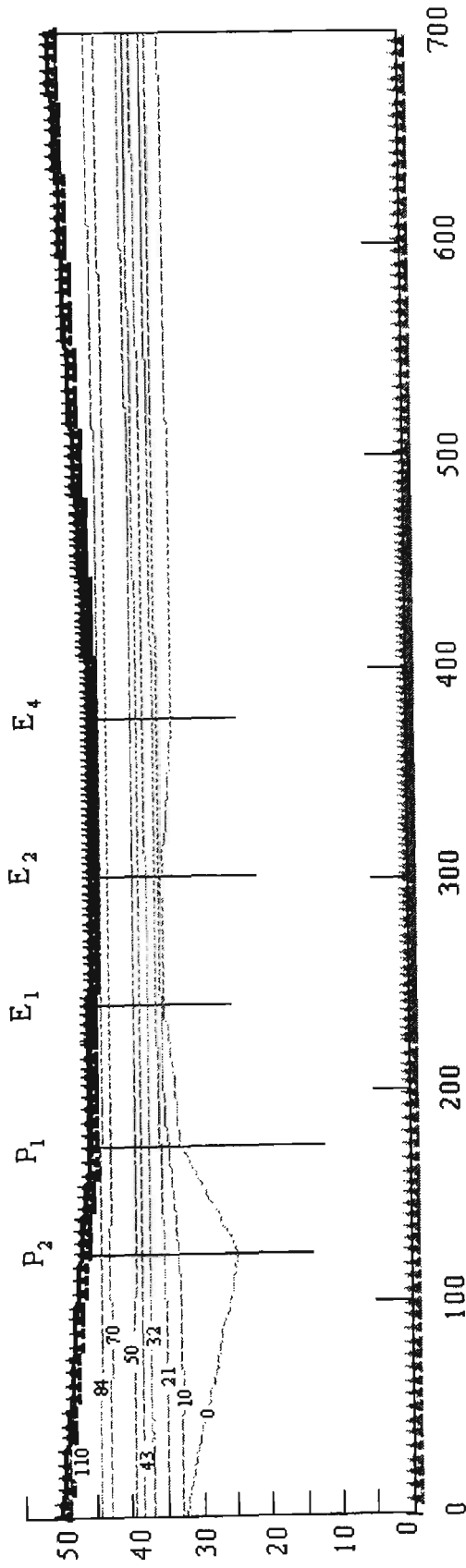


Figure 6.26. Water recovery patterns after 10, 21, 32, 43, 50, 70, 84 , and 110 days ceasing of pumping.

As Figure 6.27 shows, both analytical and numerical methods predicted approximately similar water levels at instrumentation points  $E_1$ ,  $E_2$ , and  $E_4$  and close agreement was achieved with the measured values. However, both the analytical and the numerical methods underestimated water levels over the period 50-70 days. After this time period, the model-simulated water levels were similar to those monitored at the site while the analytical equation slightly underestimated the water levels. At point  $E_1$ , the model slightly underestimated the water levels in comparison to the analytical prediction and the field monitored water levels. A close agreement was achieved between the analytical predictions of water levels and the measured values at point  $P_1$  but the model overestimated the water levels at this point. On the other hand, at point  $P_2$  over unmined strata, a close agreement was achieved between the simulated values and the field-measured values while the analytical equation slightly underestimated the water levels.

#### **(g) Sensitivity analysis**

A sensitivity analysis was carried out to assess which parameters most affected the simulation results. A time period of 0-50 days after cessation of the dewatering operation was selected for the performance of the analysis. It was found that although the modelling results can be highly affected by the hydraulic conductivities and storativities, rainfall values appeared to be the most sensitive characteristic (Figure 6.28).

Based on the sensitivity analysis, annual precipitation of  $2 \times 10^{-8} - 3 \times 10^{-8} \text{ m/s}$  was selected for the simulation. This range is almost identical with the average annual rainfall (600-800 *mm/yr*) quoted by National Coal Board (1982) for this area.

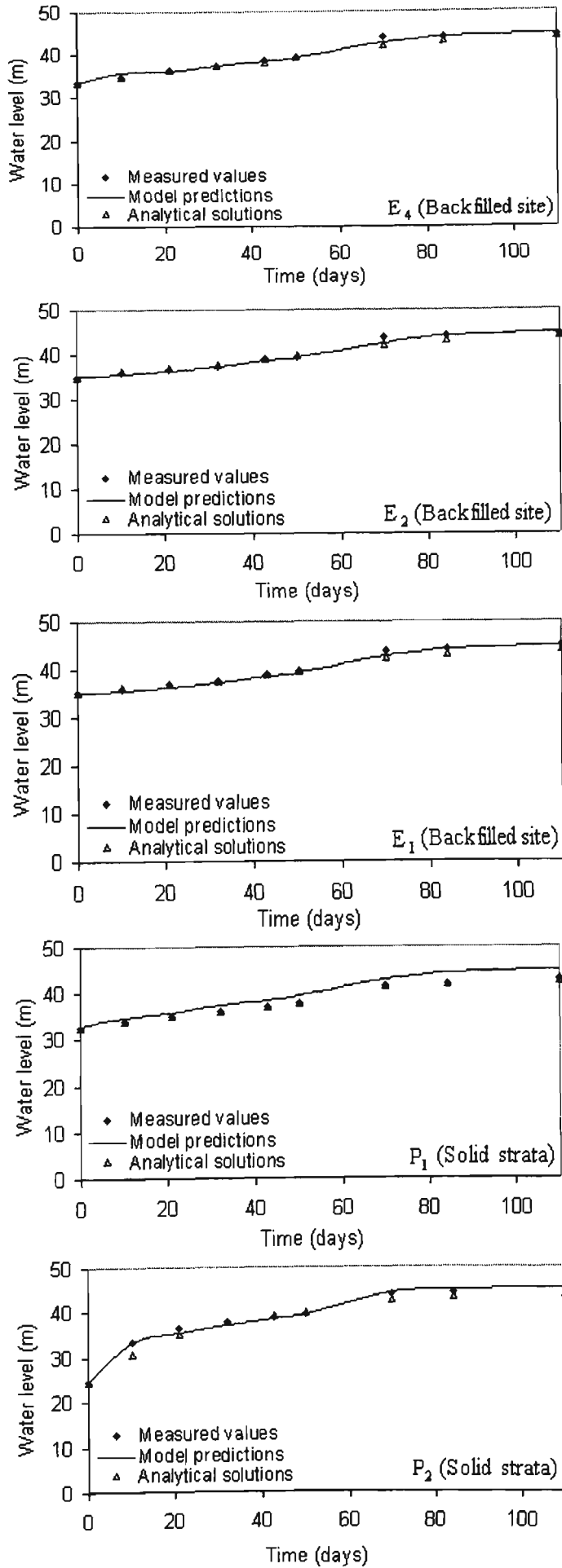


Figure 6.27. Comparison of measured values, analytical solutions and model predictions for groundwater rebound process at instrumentation stations (Section B-B').

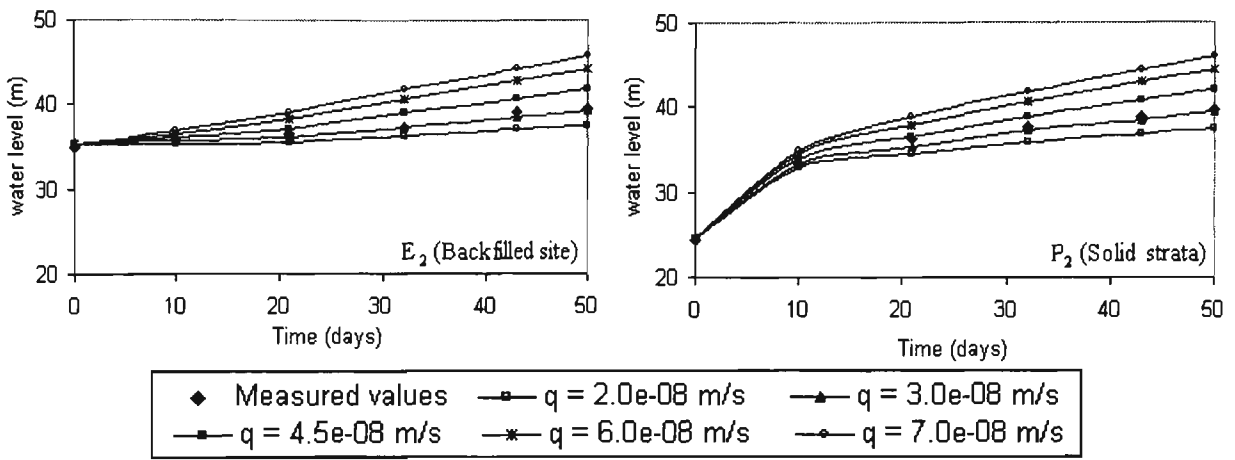


Figure 6.28. Sensitivity analysis for rainfall values.

#### 6.4 Error analysis

Table 6.2 illustrates the maximum percent error for prediction of the groundwater rebound by the model at different instrumentation points using the following equation (quoted in Hughson and Codell, 2001). For error calculation, the results of the present numerical simulation were compared with the field-monitored data.

$$E_i = \left( \left| \frac{\Delta x_i}{x_i} \right| \times 100\% \right) \quad (6.3)$$

The maximum percent error in each instrumentation point is reduced to:

$$E_{\max} = \max(E_i) \quad (6.4)$$

where,

$E_i$  = percent error (%);

$E_{\max}$  = maximum percent error (%);

$\Delta x_i$  = difference between measured water level and predicted water level ( $m$ )

$x_i$  = measured water level ( $m$ ).

Table 6.2. Calculated error in related to measured values.

Instrumentation Point	E <sub>1</sub>	E <sub>2</sub>	E <sub>3</sub>	E <sub>4</sub>	E <sub>5</sub>	P <sub>1</sub>	P <sub>2</sub>	P <sub>3</sub>	P <sub>4</sub>
Maximum Error (%)	3.09	3.68	4.92	3.10	3.67	5.33	2.80	4.03	6.61

The transient groundwater rebound simulations showed that the groundwater rebound process is very quick at the early stages after termination of the dewatering operation, where a significant proportion of the fill settlement can be observed at these times.

Comparison of the results obtained with the three methods for simulation of post-mining groundwater rebound yields values for the hydrogeological characteristic coefficient in the range of 0.9 to 3.5. These values can produce a reasonable preliminary estimate of the groundwater rebound within the backfill of an open cut mine.

## **6.5 Conclusions**

A numerical two-dimensional groundwater model has been presented in this chapter. The model utilised a suite of SEEP/W libraries together with modified permeability functions to simulate groundwater rebound process within a backfilled open cut mine. The model was evaluated by comparing the output from an existing model and the results obtained from analytical solutions as well as field monitored data. The results indicated a close agreement with an existing numerical model and the analytical solution as well as measured data. The results obtained from the simulation of the post-mining groundwater rebound can be used by environmental groups and mine operators for the following purposes:

- Design of mine drainage pollution prevention schemes
- Providing useful information related to the settlement of backfill mass, which is particularly important for the further use and development of abandoned mine land

## **CHAPTER SEVEN**

### **APPLICATION OF COMPUTATIONAL FLUID DYNAMICS (CFD) TO GROUNDWATER FLOW AND POLLUTANT TRANSPORT PROBLEMS**

## CHAPTER SEVEN

### APPLICATION OF COMPUTATIONAL FLUID DYNAMICS (CFD) TO GROUNDWATER FLOW AND POLLUTANT TRANSPORT PROBLEMS

#### 7.1 Introduction

Many environmental problems associated with the mining industry involve the understanding and analysis of fluid or gas flow, typical examples include groundwater flow, transport of contaminants, heat transfer, explosions, fire development and dust movements. Both experimental work and numerical models can provide the necessary information for solution of any particular problem. The long-term pyrite oxidation and transportation of the oxidation products are noted to be the most important problems that can be modelled in order to predict the transport of the contaminants through groundwater flow systems, to interpret the geochemistry and achieve a better understanding of the processes involved.

The use of computational fluid dynamics (CFD) to simulate flow problems has risen dramatically in the past two decades and become a fairly well established discipline shared by a number of engineering and science branches. Associated with the widespread availability of high performance and advanced computers and computational methods, CFD is rapidly becoming accepted as a cost-effective design and predictive tool. Numerical solution methods may be used for CFD analysis for the simulation of fluid flow and heat and mass transport problems when it is expressed in terms of partial differential equations. Recent improvement of CFD codes enables researchers to visualise easily the local

velocity, temperature, concentrations of solutes and pressure fields in a domain by means of graphic facilities (Edwards et al., 1995).

Computational fluid dynamic is a very powerful tool and applicable to a wide range of industrial and non-industrial areas, including aerodynamics of aircraft, automotive, pollution control, power plant, turbo machinery, electrical and electronic engineering, civil engineering, hydrology and oceanography, meteorology and medical science (Versteeg and Malalasekera, 1995).

Computational fluid dynamic has been recently used in many applications relating to environmental studies as a way of estimating impacts and developing control strategies for the long-term impacts of mining on the environment and many other activities. The low response time and cost associated with the simulations compared to experiments are the main benefits provided that adequate accuracy may be obtained by the computer model.

Some researchers used the finite element method to solve the partial differential equations for modelling of solute transport through groundwater flow systems (eg Pinder, 1973; Pickens and Lennox, 1976; Rabbani and Warner, 1994; and Wunderly et al., 1996). Green and Clothier (1994) used the PHOENICS-code incorporating the finite volume method to simulate water and solutes transport into unsaturated soils. Edwards et al. (1995) have noted the applicability of the CFD analysis in mine safety and health problems such as methane control, gas or coal outbursts, dust suppression and explosions. Balusu (1993) developed a numerical model using a CFD code, FIDAP, to simulate airflow patterns and the respirable dust concentration at a longwall face in underground coalmines.

The analysis of contaminant transport in groundwater systems using finite volume techniques have been carried out by Putti et al. (1990) and Binning and Celia (1996).

In the present work attention has been focussed on numerical simulation of oxygen transport, pyrite oxidation within the spoil of an open cut mine and the subsequent transport of the oxidation products through the groundwater flow system. To achieve these objectives the PHOENICS (CHAM, 2000) as a CFD package was used to model the problem at hand.

## **7.2 Computational fluid dynamics**

Computational fluid dynamics or CFD is defined as the analysis of systems involving fluid flow, heat and mass transfer and associated phenomena such as chemical reactions using computer-based simulation. To predict the way in which a fluid will flow for a given situation, a mathematical analysis of the fluid flow has to be made to formulate the governing equations of flow, and the CFD code enables users to calculate numerical solutions to these equations. To produce a solution, these equations have to be transformed into numerical analogues using discretisation techniques such as finite difference, finite element and finite volume.

CFD codes are now widely available commercially, each with its own particular set of features to deal with fluid flow problems. Edwards et al. (1995) has given a comparison of some commercial CFD codes (Table 7.1).

As Table 7.1 shows the application of the PHOENICS package in the mining industry was not known. In this thesis, it was found that PHOENICS is a capable package for simulating any mining related problems.

Table 7.1. A comparison of a number of common commercial CFD codes  
(after Edwards et al., 1995).

<b>Features</b>	<b>FLUENT</b>	<b>PHOENICS</b>	<b>FLOW3D</b>	<b>FIDAP</b>
Discretisation methods	Finite volume	Finite volume	Finite volume	Finite volume
Compressible flow modelling	Provided	Provided	Provided	Ideal gas law with user defined equation of state (V7.0)
Multiphase flow modelling	Provided	Provided	Provided	Provided
Free surface capability	Not Provided	Provided	Limited	Provided
Mesh generation	Unstructured mesh	Structured mesh, interactive mesh generation, body fitted coordinates, Cartesian/cylindrical	Structured mesh, Cartesian/cylindrical option, rotating co-ordinates, multi-block BFC	Unstructured
Combustion modelling	Combustion/Chemical reaction	Combustion/Chemical reaction	Combustion/Chemical reaction	Surface Chemical reactions
Code expandability	Cannot add FORTRAN subroutines directly, need full source code	User supplied FORTRAN subroutines can be added	User supplied FORTRAN subroutines can be added	User supplied FORTRAN subroutines can be added
Target application	General purpose	General purpose	General purpose	General purpose
application	Chemical and process engineering; heat transfer options; gas cleaning; fire research; pollution control; architectural design.	Heating and ventilation; fire engineering; geophysical studies; pollution control; electronics cooling; heat transfer, oil industry.	Combustion and fire modelling; aerodynamics; off-shore safety; mechanical engineering; heat transfer	Automotive; electronics and semiconductors; chemicals; aerospace/defence; machinery/appliances
Mining application	Yes	unknown	Yes	Yes
Vendor	Fluent Europe Sheffield, UK	CHAM London, UK	CFDS AEA Technology Oxford, UK	FLUID DYNAMICS INTERNATIONAL Evanston, IL, USA

In general, a flow analysis with CFD codes can be divided into three main phases:

- Pre-processing phase includes the input of a flow problem to a CFD package using an operator-friendly interface and the subsequent transformation of this input data into an appropriate form for use by the solver. This phase mainly consists of the definition of the geometry of the problem of interest, mesh generation, specification of physical

properties of the fluid and appropriate boundary conditions. An unknown flow variable such as velocity, pressure, and temperature is solved at nodes inside each cell. The accuracy of a CFD solution is governed by the number of cells in the grid. The accuracy is improved by increasing the number of cells. Optimal meshes are often non-uniform. A finer mesh is constructed in areas where large variations occur from point to point and a coarser grid is used in regions with relatively little change (Versteeg and Malalasekera, 1995).

- Simulation phase including solution of the governing equation for the unknown flow variable.
- Post-processing phase including domain geometry and grid display, vector plots, surface plots, x-y graphs, line and shaded contour plots and animation for dynamic result display.

### **7.3 PHOENICS modules**

The PHOENICS program has a few different modules to perform all these three phases of flow analysis, namely SATELLITE, EARTH, and post-processing facilities including VR VIEWER, PHOTON, AUTO PLOT, and RESULT (CHAM, 2000). Figure 7.1 shows the solution performance in the PHOENICS package.

#### **7.3.1 SATELLITE**

The SATELLITE is the pre-processing part of PHOENICS where input data is read and prepared for calculation. The program is coded in PIL (PHOENICS Input Language) and saved in a Q1 file (see Appendix L).

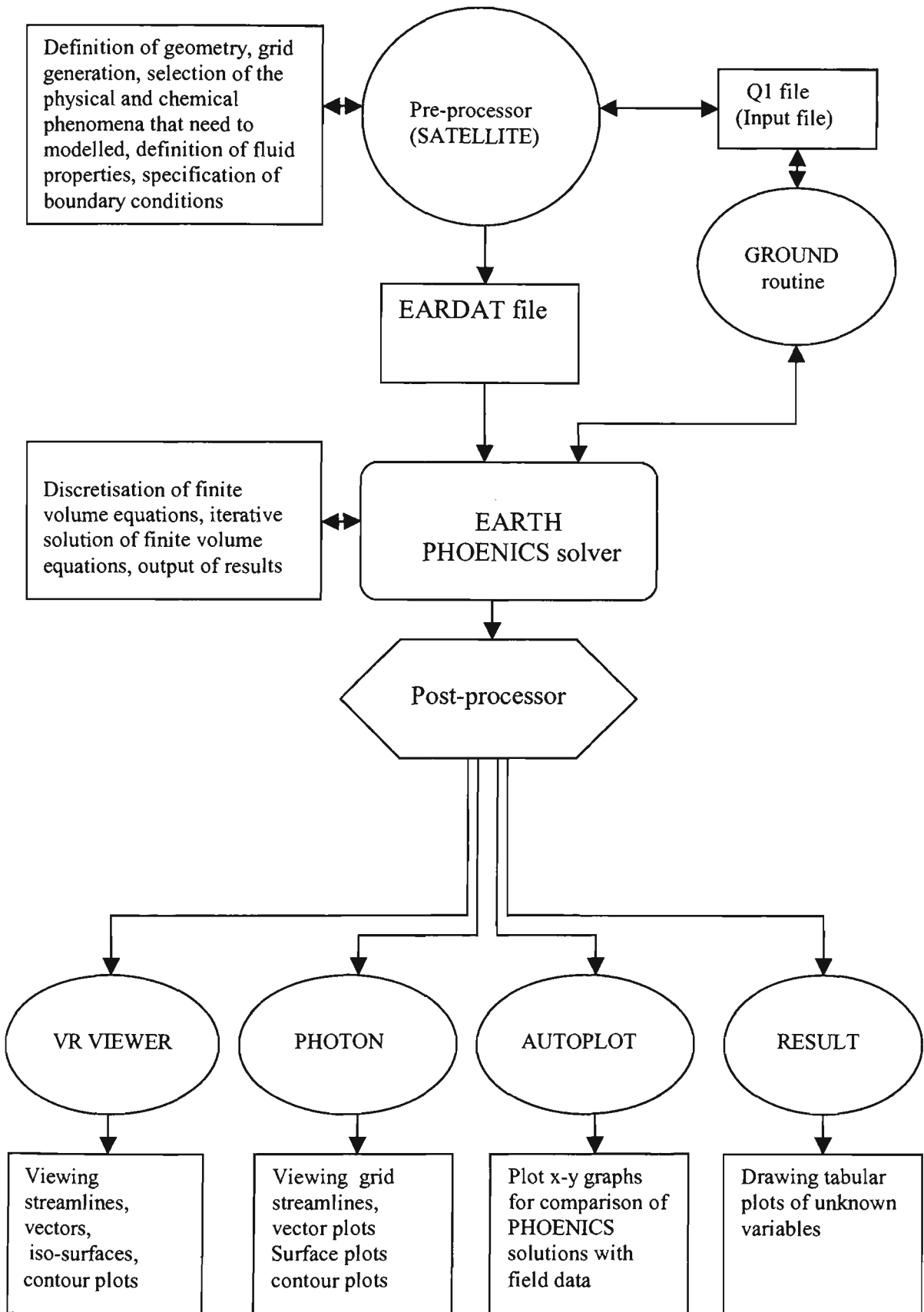


Figure 7.1. The procedure of solution in PHOENICS (CHAM, 2000).

Therefore SATELLITE is an interpreter, and from instructions provided by the user it creates a data file called EARDAT, containing instructions which can subsequently be understood by the PHOENICS solver, EARTH (Spalding, 1981). Most of the settings containing definitions of the geometry, mesh generation, specification of boundary conditions and definition of the fluid properties are made in the Q1 file. Supplementary coding is added through GROUND routine in FORTRAN language for all the non-standard computations.

### **7.3.2 EARTH**

EARTH is the main program of the PHOENICS package. The simulation phase or solution of governing equations is carried out by EARTH. It reads the EARDAT file generated by SATELLITE and executes the corresponding computations. EARTH then creates an output file called RESULT and also another file called PHI which can be interpreted and read by the display modules PHOTON and AUTOPLOT. EARTH turns to GROUND for further data settings and feature-adding purposes.

### **7.3.3 GROUND**

GROUND is a FORTRAN subroutine which forms part of the PHOENICS solver module, EARTH. GROUND is supplied as a structured set of GOTO's and statement labels, between which coding sequences can be inserted. It is subdivided into 24 groups in the same manner as in the Q1 file, to make implementation easier. It performs no function unless the user inserts some coding in the spaces provided. After inserting any new coding sequence, GROUND must be re-compiled and the EARTH program re-linked. One of the most important features of this research work is the development of extra coding which is then inserted in the empty GROUND routine (see Appendix M).

### **7.3.4 PHOTON**

PHOTON is a part of PHOENICS, as a post-processor, which can be used to display the results of fluid flow simulations generated by PHOENICS. PHOTON reads the PHI file produced by EARTH, and in response to instructions provided by user, represents the computed grid and the flow pattern graphically. PHOTON enables user to draw a grid, or grid outlines over the whole or parts of the domain, and vector and contour plots for scalar variables such as temperature, concentration as well as many other types of plots.

### **7.3.5 AUTO PLOT**

AUTO PLOT is the second graphics program of the PHOENICS code. It can access data from PHI file and also from user created files. AUTO PLOT can plot x-y graphs from many files simultaneously. This allows easy comparison of PHOENICS simulation results with experimental or analytical results. It is an interactive program which allows adjustment of the scaling and position of the plots. The data can be manipulated in a number of ways, such as subtracting or adding constants, multiplying or dividing by constants, raising to power, taking logs and anti-logs, and many other features.

## **7.4 General stages of a CFD analysis**

To produce a CFD simulation, a number of key steps should be followed in order to generate an exact picture of a particular problem. Figure 7.2 shows the main steps for a CFD analysis.

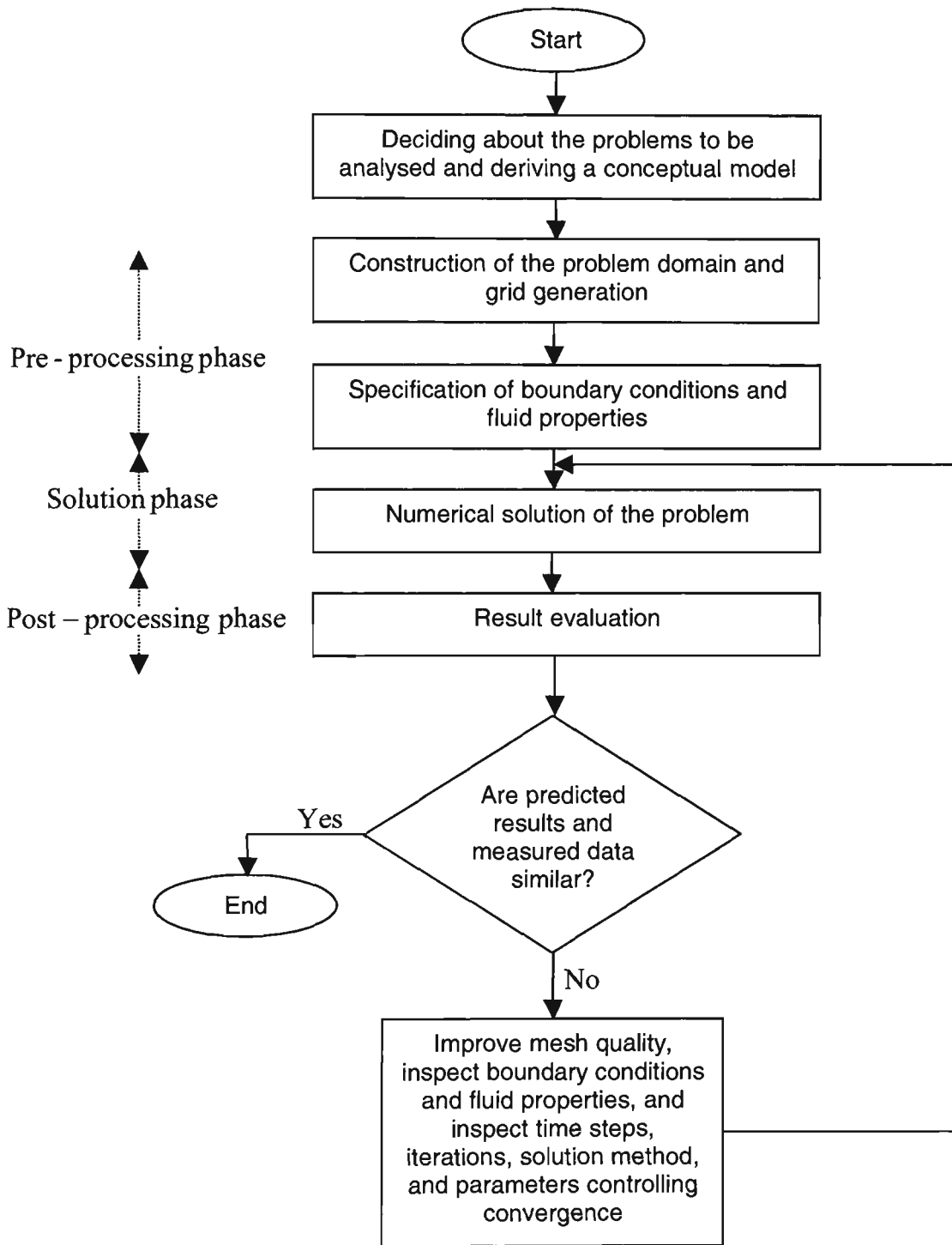


Figure 7.2. Main stages in CFD simulation process.

## 7.5 Finite volume method

Although the finite element method is mainly used for the simulation of the contaminant transport problems through groundwater flow systems, finite volume techniques have also been used by many researchers for the solution of groundwater flow and solute transport governing equations in saturated and unsaturated flow systems (see Putti et al., 1990; Green and Clothier, 1994; Binning and Celia, 1996; and Svensson, 1997).

The finite volume method is a numerical technique for solving governing equations of fluid flow and mass transport that calculates the values of the conserved variables averaged across the control volume. The calculation domain is broken down into a set of control volumes such that there is one control volume surrounding each grid point. The partial differential equation is integrated over each control volume. The resulting discretisation equation containing the values of a variable  $\phi$  for grid points involves the substitution of a variety of finite-difference-type approximations for the different terms in the integrated equation representing flow and transport processes such as convection, diffusion and source terms. The integral equations are therefore, converted into a system of algebraic equations. The algebraic equations obtained in this manner are then solved iteratively.

The basic principles and concepts of the finite volume formulation are very simple and easier to understand by engineers than other numerical techniques. One advantage of the finite volume method over finite difference methods is that a structured grid is not required although a structured mesh can also be utilised. Furthermore, the finite volume method is noted to be superior to other numerical methods due to the fact that boundary conditions can be applied non-invasively because the values of the conserved variables are located

within the control volumes, and not at nodes or surfaces. Finite volume methods are particularly useful in dealing with coarse non-uniform grids.

The conservation of any flow variable  $\phi$  within a control volume is expressed as a balance equation between the various processes causing an increased or decreased value of  $\phi$  (Versteeg and Malalasekera, 1995).

$$\left( \begin{array}{l} \text{Net flux of } \phi \text{ due to} \\ \text{convection and diffusion} \\ \text{into the control volume} \end{array} \right) \pm \left( \begin{array}{l} \text{Rate of production or} \\ \text{consumption of } \phi \\ \text{inside the control volume} \end{array} \right) = \left( \begin{array}{l} \text{Rate of change of } \phi \\ \text{in the control volume} \\ \text{with respect to time} \end{array} \right) \quad (7.1)$$

The quantities being balanced are the dependent variables such as the mass of a chemical species, energy, momentum and turbulence quantities.

CFD packages such as PHOENICS, FLUENT, FLOW3D and STAR-CD contain discretisation techniques appropriate for dealing with the main transport processes such as convection (i.e. transport due to fluid flow), diffusion (i.e. random motion of molecules) as well as for the source terms (i.e. chemical reaction for energy or chemical species) and the rate of change of  $\phi$  with time (i.e. accumulation within a cell).

## 7.6 Introduction to PHOENICS

In recent years a number of commercial CFD packages have become available. PHOENICS is a general-purpose CFD package which can be used for simulation of fluid flow, heat transfer, mass transfer and associated chemical reactions as well as stress analysis in solids. Using PHOENICS, material properties, geometries and boundary conditions can be easily incorporated. It has been continuously marketed, used and developed since 1981 and still

possesses many features and capabilities not yet adopted by later competitors such as the parabolic option, simultaneous solid-stress analysis, the multi-fluid turbulence model and many other features (CHAM, 2000).

PHOENICS can be used to model many engineering, environmental and architecture and building science problems such as heating and ventilation, fire engineering, pollution control, electronics cooling, heat and mass transfer, nuclear power industry, oil industry and many other problems.

The simulations are based on the finite volume method which can be conducted on various scales. These simulations are mathematical deductions from established physical principles. These principles and theoretical basis of this computational technique are set out in publications such as those of Patankar (1980) and Versteeg and Malalasekera (1995).

### 7.6.1 PHOENICS governing equation

For all PHOENICS simulations, the differential equation solved by PHOENICS has the following general form (CHAM, 2000):

$$\frac{\partial}{\partial t}(r_i \rho_i \phi_i) + \frac{\partial}{\partial x_j} \left( r_i \rho_i u_{j_i} \phi_i - r_i \Gamma_{\phi_i} \frac{\partial \phi_i}{\partial x_j} \right) = r_i S_{\phi_i} \quad (7.2)$$

In the differential equation given above, the functions of  $\frac{\partial}{\partial t}(r_i \rho_i \phi_i)$ ,  $r_i \rho_i u_{j_i} \phi_i$ ,  $r_i \Gamma_{\phi_i} \frac{\partial \phi_i}{\partial x_j}$  and  $r_i S_{\phi_i}$  are represented as the transient, convection, diffusion and source terms, respectively.

where,

$\phi_i$  = any of the dependent variables of phase  $i$  ;

$t$  = time;

$r_i$  = volume fraction of phase  $i$  ;

$\rho_i$  = PHOENICS-term for density of phase  $i$  ;

$u_{j_i}$  = velocity component in the  $x_j$  direction;

$\Gamma_{\phi}$  = diffusive exchange coefficient for  $\phi$  in phase  $i$  ;

$S_{\phi}$  = source rate of  $\phi$  .

In the case of a single-phase problem, the volume fraction  $r_i$  is omitted from the equations;

therefore the general governing equation reduces:

$$\frac{\partial}{\partial t}(\rho\phi) + \frac{\partial}{\partial x_j} \left( \rho u_j \phi - \Gamma_{\phi} \frac{\partial \phi}{\partial x_j} \right) = S_{\phi} \quad (7.3)$$

In this thesis  $\rho$  is set equal to 1.0.

### 7.6.2 PHOENICS setting

All settings are coded in PIL (PHOENICS Input Language), and saved in a Q1-file (see Appendix L) with calls to the GROUND routine for all non-standard computations. The necessary coding is supplied through GROUND in FORTRAN language. It is subdivided into groups in the same manner as in the Q1-file to make implementation easier. One of the most important features of this study is the extra coding developed for inclusion in the GROUND file. The complete GROUND routine is given in Appendix M.

## 7.7 Implementation of boundary conditions and source terms in PHOENICS

Differential equations governing the pyrite oxidation process, oxygen transport, contaminant transport and heat transfer need to be supplemented by boundary conditions before they can be solved. Furthermore, these differential equations contain additional source terms which should be calculated during each iteration using the FORTRAN routine located in GROUP13 of GROUND (Appendix M). In the governing general differential equation solved by PHOENICS, boundary conditions and source terms appear at the right hand side:

$$\frac{\partial}{\partial t}(\rho\phi) + \frac{\partial}{\partial x_j} \left( \rho u_j \phi - \Gamma_\phi \frac{\partial \phi}{\partial x_j} \right) = S_{\phi_1} + S_{\phi_2} + \dots + S_{bc_1} + S_{bc_2} + \dots \quad (7.4)$$

where,

$S_{\phi_i}$  = source terms such as rate of heat generation due to the pyrite oxidation reaction or the oxygen consumption term associated with chemical oxidation of ferrous iron;

$S_{bc_i}$  = different boundary conditions which may be presented only in certain regions of the calculation domain.

Boundary conditions and source terms have to be cast into a linearised format before they can be handled by PHOENICS (CHAM, 2000):

$$S = Co_\phi (Val_\phi - \phi) \quad (7.5)$$

The finite volume discretisation of the PHOENICS governing differential equation yields the following algebraic equation for each cell  $P$  in the calculation domain.

$$a_P \phi_P = \sum_{N,S,E,W,H,L,T} a_K \phi_K + \sum_{Patches} Co_\phi (Val_\phi - \phi_P) \quad (7.6)$$

where,

$Co_\phi$  = coefficient;

$Val_\phi$  = value.

It should be noted that  $Co_\phi Val_\phi$  is added to the numerator, and  $Co_\phi$  is incorporated to the denominator. This makes the solution easier.

$$\phi_P = \frac{\sum a_K \phi_K + \sum Co_\phi Val_\phi}{a_P + \sum Co_\phi} \quad (7.7)$$

If  $Co_\phi$  is set to a large value, this will set  $\phi$  equal to  $Val_\phi$ .

$$\phi_P = Val_\phi \quad (7.8)$$

If  $Co_\phi$  is set to a small value and dividing  $Val_\phi$  with the same value, this places  $Val_\phi$  on the right hand side of the  $\phi$  equation.

$$\phi_P = \frac{\sum a_K \phi_K + tiny \frac{Source}{tiny}}{a_P + tiny} \quad (7.9)$$

or

$$\phi_P = \frac{\sum a_K \phi_K + Source}{a_P} \quad (7.10)$$

where,

$tiny$  = a very small real number, defaulted to  $1.0 \times 10^{-20}$  which is used in the PHOENICS solver, EARTH, to guard against division by zero.

## 7.8 PIL commands for sources and boundary conditions

The PHOENICS SATELLITE accepts the user's specifications of sources and boundary conditions in terms of a 'Coefficient' ( $Co_\phi$ ) and a 'Value' ( $Val_\phi$ ) through a command

named *COVAL*. Another command called *PATCH* is used to define sections of the simulation domain over which the initial values of variables in question are to be set, sources and boundary conditions are to be specified, and the convection or diffusion terms in differential equations of variables to be modified, and also profile, contour or tabular plots of variables to be printed. The *PATCH* command has 10 elements, namely:

*PATCH* (Patch name, TYPE, first IX, last IX, first IY, last IY, first IZ, last IZ, first time step, last time step)

The *PATCH* name is unique and may be up to 8 characters long. *TYPE* is the second element of *PATCH* command as a geometrical multiplier. *CELL*, *VOLUME*, *PHASEM*, *NORTH*, *EAST*, ... are examples of *PATCH TYPES*. The last eight elements are termed as *PATCH* domain and time limits.

*CAVAL* is the command used for specifying coefficients and values of sources of dependent variables. *COVAL* has four arguments:

- (a) Name of *PATCH* in question (same name assigned by command *PATCH*)
- (b) Variable in question
- (c) Coefficient
- (d) Value

The *COVAL* command has the following format:

*COVAL* (Name, Variable, Coefficient, Value)

The coefficient and value can be set as real numbers, but certain names are also recognised, such as *FIXVAL*, *FIXFLU*, *FIXP*, *ONLYMS*, *OPPVAL*, *GRND*, *GRND1*, ..., *GRND10* for coefficients and *SAME*, *GRND*, *GRND1*, ..., *GRND10* for values.

### 7.8.1 Initial-value patches

The initial value patches are used in group 11 of the Q1 file for specifying initial boundary conditions. This *PATCH* mainly has the following format:

*PATCH* (*Name*, *INIVAL*, *IXF*, *IXL*, *IYF*, *IYL*, *IZF*, *IZL*, 1, 1)

*COVAL* (*Name*, *Variable*, *Coefficient*, *Value*)

It should be noted that two elements are always 1 because the initial values can be set only at time step 1.

### 7.8.2 Sources and boundary condition patches

Sources and boundary condition patches are used in group 13 to define the areas or volumes over which boundary conditions or special sources or sinks are to be set by means of *COVAL* command. When a *GRND<sub>i</sub>* flag is set in a *COVAL* command as coefficient or value, a particular section of group 13 of the GROUND routine is visited by the EARTH solver. EARTH expects the corresponding coefficient or value to be set in that section. Particular coding for any special source or boundary condition can be inserted by the user in that section.

## 7.9 The finite volume discretisation

### 7.9.1 Finite volume discretisation of groundwater flow

The governing equation for two-dimensional groundwater flow under steady state conditions can be rewritten as (see Chapter 4, Equation 4.16)

$$\frac{\partial}{\partial x} \left( K_x \frac{\partial h}{\partial x} \right) + \frac{\partial}{\partial y} \left( K_y \frac{\partial h}{\partial y} \right) + W = 0 \quad (7.11)$$

The first step in developing a finite volume method is to divide the domain into discrete control volumes. A portion of a two-dimensional grid used for the discretisation is illustrated in Figure 7.3.

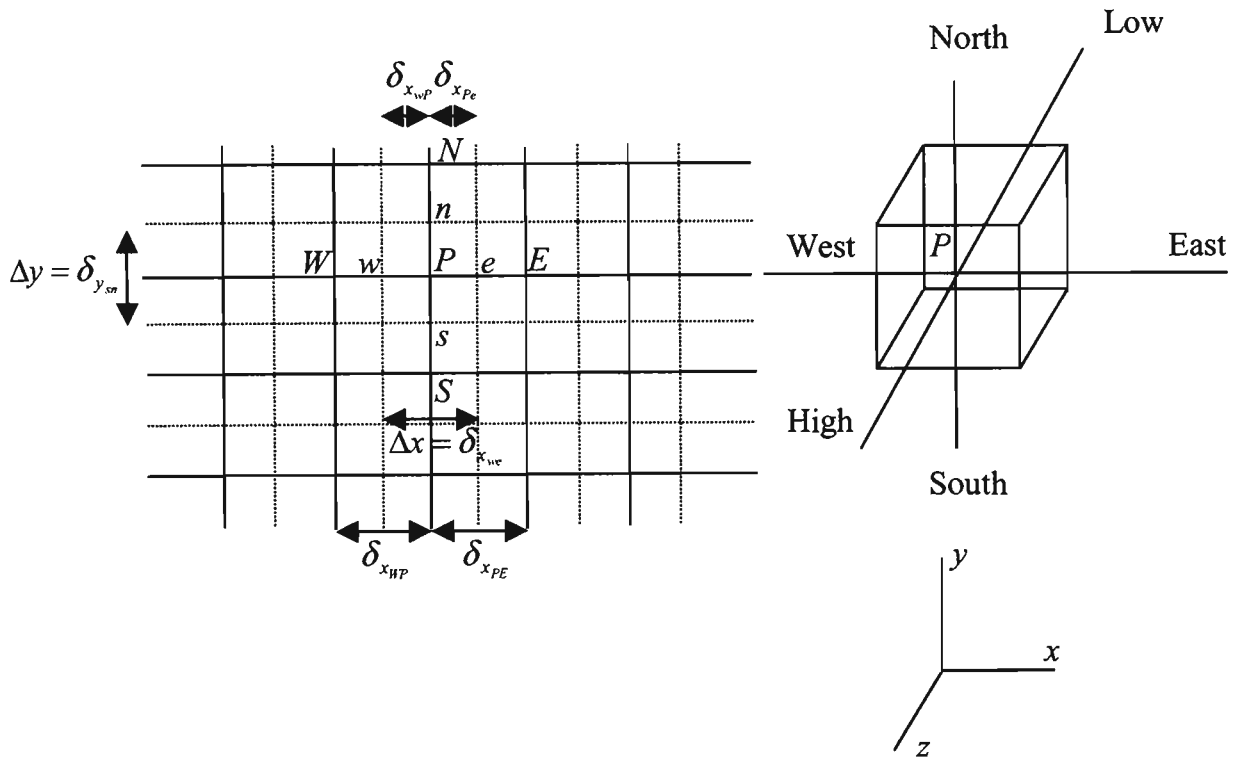


Figure 7.3. A part of two-dimensional grid and a control volume.

The faces of the control volume are positioned mid-way between adjacent nodes. Therefore, each node is surrounded by a control volume. For a nodal point  $P$ , points ' $W$ ' and ' $E$ ' (denoting west and east) are its  $x$ -direction neighbours, while ' $S$ ' and ' $N$ ' (denoting south and north) are the  $y$ -direction neighbours. Its thickness in the  $z$  direction is assumed to be unity. The west and east side faces of the control volume are referred to by ' $w$ ' and ' $e$ ', while the south and north side faces are referred to by ' $s$ ' and ' $n$ '. The distances between the nodes  $W$  and  $P$ , and between nodes  $P$  and  $E$  are identified by  $\delta_{x_{WP}}$  and  $\delta_{x_{PE}}$  respectively, while the distances between the nodes  $S$  and  $P$ , and between

nodes  $P$  and  $N$  are identified by  $\delta_{x_{sp}}$  and  $\delta_{x_{pn}}$  respectively.  $\Delta x$  is the distance between faces  $w$  and  $e$ , and  $\Delta y$  is the distance between faces  $s$  and  $n$ . The governing equation of groundwater flow is now integrated over the control volume (shown in Figure 7.3) to yield a discretised equation at its nodal point  $P$ . This gives:

$$\int_{\Delta v} \frac{\partial}{\partial x} \left( K_x \frac{\partial h}{\partial x} \right) dx dy + \int_{\Delta v} \frac{\partial}{\partial y} \left( K_y \frac{\partial h}{\partial y} \right) dx dy + \int_{\Delta v} W dv = 0 \quad (7.12)$$

$$\left( K_x A \frac{\partial h}{\partial x} \right)_e - \left( K_x A \frac{\partial h}{\partial x} \right)_w + \left( K_y A' \frac{\partial h}{\partial y} \right)_n - \left( K_y A' \frac{\partial h}{\partial y} \right)_s + \overline{W} dv = 0 \quad (7.13)$$

where,

$A$  = cross-sectional area of the control volume face in x-direction;

$A'$  = cross-sectional area of the control volume face in y-direction;

$\Delta v$  = volume;

$\overline{W}$  = average value of source  $W$  over the control volume.

Appropriate forms of the discretised equations are obtained by estimation of the interface

hydraulic conductivities  $K_x$  and  $K_y$ , and the gradients  $\frac{\partial h}{\partial x}$  and  $\frac{\partial h}{\partial y}$  at east, west, north and

south using the nodal values of  $K$  and  $h$ . To estimate the gradients (and hence fluxes) at the faces of the control volume an approximate distribution of properties between nodal points is used. A central-difference approximation is noted to be the obvious and the simplest way to calculate the interface values of hydraulic conductivities and the gradients.

Using this method, in a uniform grid the interface values for  $K_{x_w}$ ,  $K_{x_e}$ ,  $K_{y_s}$  and  $K_{y_n}$  are given below:

$$K_{x_w} = \frac{K_{x_w} + K_{x_p}}{2} \quad (7.14)$$

$$K_{x_e} = \frac{K_{x_p} + K_{x_E}}{2} \quad (7.15)$$

$$K_{y_s} = \frac{K_{y_s} + K_{y_p}}{2} \quad (7.16)$$

$$K_{y_n} = \frac{K_{y_p} + K_{y_N}}{2} \quad (7.17)$$

and the flux terms at the control volume faces are calculated as

$$\left( K_x A \frac{\partial h}{\partial x} \right)_w = K_{x_w} A_w \left( \frac{h_p - h_w}{\delta_{x_{wp}}} \right) \quad (7.18)$$

$$\left( K_x A \frac{\partial h}{\partial x} \right)_e = K_{x_e} A_e \left( \frac{h_E - h_p}{\delta_{x_{pe}}} \right) \quad (7.19)$$

$$\left( K_y A' \frac{\partial h}{\partial y} \right)_s = K_{y_s} A'_s \left( \frac{h_p - h_s}{\delta_{y_{sp}}} \right) \quad (7.20)$$

$$\left( K_y A' \frac{\partial h}{\partial y} \right)_n = K_{y_n} A'_n \left( \frac{h_N - h_p}{\delta_{y_{pn}}} \right) \quad (7.21)$$

It should be noted that  $A_e = A_w = \Delta y \times 1$  and  $A'_n = A'_s = \Delta x \times 1$

Substitution of Equations 7.18, 7.19, 7.20, and 7.21 into Equation 7.13 gives:

$$K_{x_e} A_e \left( \frac{h_E - h_p}{\delta_{x_{pe}}} \right) - K_{x_w} A_w \left( \frac{h_p - h_w}{\delta_{x_{wp}}} \right) + K_{y_n} A'_n \left( \frac{h_N - h_p}{\delta_{y_{pn}}} \right) - K_{y_s} A'_s \left( \frac{h_p - h_s}{\delta_{y_{sp}}} \right) + \bar{W} \Delta v = 0 \quad (7.22)$$

Equation 7.22 is now rearranged as:

$$\left( \frac{K_{x_e} A_e}{\delta_{x_{PE}}} + \frac{K_{x_w} A_w}{\delta_{x_{WP}}} + \frac{K_{y_n} A'_n}{\delta_{y_{PN}}} + \frac{K_{y_s} A'_s}{\delta_{y_{SP}}} \right) h_P = \frac{K_{x_e} A_e}{\delta_{x_{PE}}} h_E + \frac{K_{x_w} A_w}{\delta_{x_{WP}}} h_W + \frac{K_{y_n} A'_n}{\delta_{y_{PN}}} h_N + \frac{K_{y_s} A'_s}{\delta_{y_{SP}}} h_S + \overline{W} \Delta v \quad (7.23)$$

The discretisation Equation 7.23 can be cast to the following form:

$$a_P h_P = a_E h_E + a_W h_W + a_N h_N + a_S h_S + b \quad (7.24)$$

where,

$$a_E = \frac{K_{x_e} \Delta y}{\delta_{x_{PE}}} \quad (7.25)$$

$$a_W = \frac{K_{x_w} \Delta y}{\delta_{x_{WP}}} \quad (7.26)$$

$$a_N = \frac{K_{y_n} \Delta x}{\delta_{y_{PN}}} \quad (7.27)$$

$$a_S = \frac{K_{y_s} \Delta x}{\delta_{y_{SP}}} \quad (7.28)$$

$$a_P = a_E + a_W + a_N + a_S \quad (7.29)$$

$$b = \overline{W} \Delta x \Delta y = \text{Source term} \quad (7.30)$$

Thus the distribution of the variable  $h$  in a given two-dimensional situation is obtained using discretised equations of the form of Equation 7.24 at each nodal point of the subdivided domain. The discretised Equation 7.24 can be cast to

$$a_P h_P = \sum a_{nb} h_{nb} + b \quad (7.31)$$

and

$$a_P = \sum a_{nb} \quad (7.32)$$

Where the subscript *nb* presents a neighbour and the sign  $\sum$  indicates that the summation is to be taken over all the neighbours.

### 7.9.2 Finite volume discretisation of transport equation

In the case of a two-dimensional situation, the governing transport equation can be generally written as (see Chapter 9, Section 9.2, Page 264):

$$\frac{\partial}{\partial t}(\phi C) = \frac{\partial}{\partial x} \left( D_x \frac{\partial C}{\partial x} \right) + \frac{\partial}{\partial y} \left( D_y \frac{\partial C}{\partial y} \right) - \frac{\partial}{\partial x} (q_x C) - \frac{\partial}{\partial y} (q_y C) + S \quad (7.33)$$

Integration of the transport Equation 7.33 over the control volume shown in Figure 7.4 and over a time interval from  $t$  to  $t + \Delta t$  gives:

$$\begin{aligned} \phi \int_t^{t+\Delta t} \int_{CV} \frac{\partial C}{\partial t} dv dt &= \int_t^{t+\Delta t} \int_{CV} \frac{\partial}{\partial x} \left( D_x \frac{\partial C}{\partial x} \right) dv dt + \int_t^{t+\Delta t} \int_{CV} \frac{\partial}{\partial y} \left( D_y \frac{\partial C}{\partial y} \right) dv dt - \int_t^{t+\Delta t} \int_{CV} \frac{\partial}{\partial x} (q_x C) dv dt \\ &- \int_t^{t+\Delta t} \int_{CV} \frac{\partial}{\partial y} (q_y C) dv dt + \int_t^{t+\Delta t} \int_{CV} S dv dt \end{aligned} \quad (7.34)$$

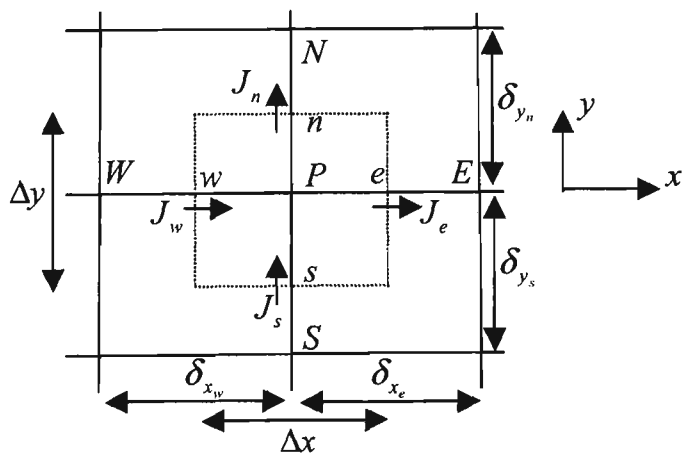


Figure 7.4. Control volume for the two-dimensional situation.

$J$  is the total (convection plus diffusion) fluxes.

Equation 7.34 reduces to:

$$\begin{aligned} \phi(C_P - C_P^0)\Delta x \Delta y = & \int_t^{t+\Delta t} \left( \frac{D_{x_e} \Delta y (C_E - C_P)}{\delta_{x_e}} - \frac{D_{x_w} \Delta y (C_P - C_W)}{\delta_{x_w}} \right) dt + \\ & \int_t^{t+\Delta t} \left( \frac{D_{y_n} \Delta x (C_N - C_P)}{\delta_{y_n}} - \frac{D_{y_s} \Delta x (C_P - C_S)}{\delta_{y_s}} \right) dt - \int_t^{t+\Delta t} [(q_x C)_e \Delta y - (q_x C)_w \Delta y] dt - \\ & \int_t^{t+\Delta t} [(q_y C)_n \Delta x - (q_y C)_s \Delta x] dt + \int_t^{t+\Delta t} \bar{S} \Delta x \Delta y \end{aligned} \quad (7.35)$$

Consider the following integration over a time interval from  $t$  to  $t + \Delta t$ :

$$\int_t^{t+\Delta t} C_P dt = [f C_P^1 + (1-f)C_P^0] \Delta t \quad (7.36)$$

where,

$f$  = a weighting factor between 0 and 1. For the fully implicit scheme (see Patankar, 1980),  $f$  is assumed to be 1 and Equation 7.36 reduces to:

$$\int_t^{t+\Delta t} C_P dt = C_P^1 = C_P \quad (7.37)$$

where,

$C_P^1$  = 'new' value of  $C_P$  at time  $t + \Delta t$ .

Using this concept, Equation 7.35 can be written as:

$$\begin{aligned} \frac{\phi(C_P - C_P^0)\Delta x \Delta y}{\Delta t} = & \frac{D_{x_e} \Delta y (C_E - C_P)}{\delta_{x_e}} - \frac{D_{x_w} \Delta y (C_P - C_W)}{\delta_{x_w}} + \\ & \frac{D_{y_n} \Delta x (C_N - C_P)}{\delta_{y_n}} - \frac{D_{y_s} \Delta x (C_P - C_S)}{\delta_{y_s}} - (q_x C)_e \Delta y + (q_x C)_w \Delta y - \\ & (q_y C)_n \Delta x + (q_y C)_s \Delta x + \bar{S} \Delta x \Delta y \end{aligned} \quad (7.38)$$

where,

$C_P^0$  = 'old' value of  $C_P$ , the value at the beginning of the time step. In Equation 7.38 the superscript 1 representing the new values of  $C_P, C_E, C_W, C_N$  and  $C_S$  was dropped.

If the central-difference approximation is also used for the convection term, Equation 7.38 can be written:

$$\begin{aligned} \frac{\phi(C_P - C_P^0)\Delta x \Delta y}{\Delta t} = & \frac{D_{x_e} \Delta y (C_E - C_P)}{\delta_{x_e}} - \frac{D_{x_w} \Delta y (C_P - C_W)}{\delta_{x_w}} + \\ & \frac{D_{y_n} \Delta x (C_N - C_P)}{\delta_{y_n}} - \frac{D_{y_s} \Delta x (C_P - C_S)}{\delta_{y_s}} - \frac{1}{2} q_{x_e} \Delta y (C_E + C_P) + \frac{1}{2} q_{x_w} \Delta y (C_P + C_W) - \\ & \frac{1}{2} q_{y_n} \Delta x (C_N + C_P) + \frac{1}{2} q_{y_s} \Delta x (C_P + C_S) + \bar{S} \Delta x \Delta y \end{aligned} \quad (7.39)$$

The discretisation equation reduces:

$$a_P C_P = a_E C_E + a_W C_W + a_N C_N + a_S C_S + b \quad (7.40)$$

where,

$$a_E = \frac{D_{x_e} \Delta y}{\delta_{x_e}} - \frac{1}{2} q_{x_e} \Delta y \quad (7.41)$$

$$a_W = \frac{D_{x_w} \Delta y}{\delta_{x_w}} + \frac{1}{2} q_{x_w} \Delta y \quad (7.42)$$

$$a_N = \frac{D_{y_n} \Delta x}{\delta_{y_n}} - \frac{1}{2} q_{y_n} \Delta x \quad (7.43)$$

$$a_S = \frac{D_{y_s} \Delta x}{\delta_{y_s}} - \frac{1}{2} q_{y_s} \Delta x \quad (7.44)$$

$$a_p^0 = \phi \frac{\Delta x \Delta y}{\Delta t} \quad (7.45)$$

$$b = \bar{S} \Delta x \Delta y + a_p^0 C_p^0 \quad (7.46)$$

$$a_p = a_E + a_W + a_N + a_S + a_p^0 + q_{x_e} \Delta y - q_{x_w} \Delta y + q_{y_n} \Delta x - q_{y_s} \Delta x \quad (7.47)$$

### 7.9.3 The upwind differencing scheme

The central differencing scheme does not identify the flow direction or the strength of convection relative to diffusion in particular when the Peclet number ( $P_e$ ) is high.

The non-dimensional cell Peclet number is defined as a measure of the relative strengths of convection and diffusion (Patankar, 1980):

$$P_e = \frac{\text{convection}}{\text{diffusion}} = \frac{q_x}{\Gamma / \delta_x} \quad (7.48)$$

where,

$\delta_x$  = cell width.

For no convection and only pure diffusion  $P_e = 0$  and for no diffusion and pure convection

$P_e \rightarrow \infty$ .

The central-differencing scheme assumes that the convected property  $\phi_w$  at the west interface is the average of  $\phi_W$  and  $\phi_P$  and the convected property  $\phi_e$  at the east interface is the average of  $\phi_E$  and  $\phi_P$ . For a strong convective flow from west to east for example, this assumption is inappropriate because the west interface receives much stronger influencing from node  $W$  than from node  $P$ .

To overcome this weak point arising during discretisation of convection term, the upwind differencing scheme may be used for large Peclet numbers ( $P_e \geq 2$ ) (Versteeg and Malalasekera, 1995).

According to the upwind-differencing scheme, the discretisation of the diffusion term in the transport equation remains unchanged, but the convected value of a property at a cell face is taken to be equal to the value of property at the upstream node. Thus,

$$\phi_w = \phi_W \quad \text{if} \quad q_x > 0 \quad (7.49)$$

$$\phi_w = \phi_P \quad \text{if} \quad q_x < 0$$

and

$$\phi_e = \phi_P \quad \text{if} \quad q_x > 0 \quad (7.50)$$

$$\phi_e = \phi_E \quad \text{if} \quad q_x < 0$$

In this thesis an upwind-differencing scheme was used for discretisation of the convection term using the *PIL* command  $DIFCUT=0.0$ . Furthermore, this scheme was also used to calculate those source terms dependant on velocities.

To apply the upwind scheme for a two-dimensional case, the following new operator is defined (Patankar, 1980) to rearrange the conditional statements 7.49 and 7.50 to more compactly statements. If  $[[M, N]]$  is defined as the greater of  $M$  and  $N$ , by implying the upwind scheme,

$$q_{x_w} C_w = C_W [[q_{x_w} \Delta y, 0]] - C_P [[q_{x_w} \Delta y, 0]] \quad (7.51)$$

$$q_{x_e} C_e = C_P [[q_{x_e} \Delta y, 0]] - C_E [[-q_{x_e} \Delta y, 0]] \quad (7.52)$$

When the convection term in Equation 7.38 is replaced by this concept, the following equation is obtained:

$$\begin{aligned} \frac{\phi(C_P - C_P^0)\Delta x \Delta y}{\Delta t} = & \frac{D_{x_e} \Delta y (C_E - C_P)}{\delta_{x_e}} - \frac{D_{x_w} \Delta y (C_P - C_W)}{\delta_{x_w}} + \\ & \frac{D_{y_n} \Delta x (C_N - C_P)}{\delta_{y_n}} - \frac{D_{y_s} \Delta x (C_P - C_S)}{\delta_{y_s}} - C_P [[q_{x_e} \Delta y, 0]] + C_E [[-q_{x_e} \Delta y, 0]] + \\ & C_W [[q_{x_w} \Delta y, 0]] - C_P [[-q_{x_w} \Delta y, 0]] - C_P [[q_{y_n} \Delta x, 0]] + C_N [[-q_{y_n} \Delta x, 0]] + \\ & C_S [[q_{y_s} \Delta x, 0]] - C_P [[-q_{y_s} \Delta x, 0]] + \bar{S} \Delta x \Delta y \end{aligned} \quad (7.53)$$

The discretisation equation becomes:

$$a_P C_P = a_E C_E + a_W C_W + a_N C_N + a_S C_S + b \quad (7.54)$$

where,

$$a_E = \frac{D_{x_e} \Delta y}{\delta_{x_e}} + [[-q_{x_e} \Delta y, 0]] \quad (7.55)$$

$$a_W = \frac{D_{x_w} \Delta y}{\delta_{x_w}} + [[q_{x_w} \Delta y, 0]] \quad (7.56)$$

$$a_N = \frac{D_{y_n} \Delta x}{\delta_{y_n}} + [[-q_{y_n} \Delta x, 0]] \quad (7.57)$$

$$a_S = \frac{D_{y_s} \Delta x}{\delta_{y_s}} + [[q_{y_s} \Delta x, 0]] \quad (7.58)$$

$$a_P^0 = \phi \frac{\Delta x \Delta y}{\Delta t} \quad (7.59)$$

$$b = \bar{S} \Delta x \Delta y + a_P^0 C_P^0 \quad (7.60)$$

$$a_P = a_E + a_W + a_N + a_S + a_P^0 \quad (7.61)$$



5. Use explicit formulation for time-dependent flows?
6. Use harmonic averaging of diffusion coefficients?

The defaulted setting of *SOLUTN* command for PHOENICS is:

*SOLUTN*( $\phi$ , N, N, N, N, N, N)

These only imply the explicit formulation for transient flows.

Point-by-point method is recommended when the governing equations of solved variables contain strong non-linear terms. Because the rate of change of variable from sweep to sweep is low, this poses some additional stability (CHAM, 2000). The main disadvantage of this method is that its convergence is very slow, in particular when a large number of grid points are involved (Patankar, 1980).

In this thesis, a whole-field method was used for all scalar variables such as enthalpy, concentrations of chemical species and head. This method is always recommended when non-linearities are slight.

## 7.11 Conclusions

The general features of the computational fluid dynamic (CFD) analysis and the fundamentals of the finite volume numerical technique were described. PHOENICS as a CFD package, its features, capabilities and applications were briefly reviewed. Finite volume discretisation of the groundwater flow and transport equations are presented. The basic principles of the finite volume method can be easily understood and it is particularly strong on coarse non-uniform meshes. One important advantage of the finite volume method over other numerical methods is its strong capability in dealing with boundary

conditions and specific source terms. This feature of the finite volume method is very important for acid mine drainage cases associated with production (source term) and consumption (sink term) for many chemical components and the specification of different boundary and initial conditions.

## **CHAPTER EIGHT**

### **A NUMERICAL FINITE VOLUME MODEL FOR PYRITE OXIDATION AND OXYGEN TRANSPORT WITHIN SPOILS OF AN OPEN CUT COALMINE**

## CHAPTER EIGHT

### A NUMERICAL FINITE VOLUME MODEL FOR PYRITE OXIDATION AND OXYGEN TRANSPORT WITHIN SPOILS OF AN OPEN CUT COALMINE

#### 8.1 Introduction

Acidic water emanating from open cut mine sites usually carries various pollutants in dissolved form, which contaminates the groundwater resources. Although considerable effort has been made to model the pyritic oxidation and pollution generation, the focus is mainly on pyrite oxidation and leaching processes in waste rock dumps (Cathles and Apps, 1975; Cathles, 1979; Davis 1983; Davis et al., 1986b; Lefebvre and Gelinas, 1995). Although many research publications are related to mine tailings discharge (Elberling et al., 1994; Walter et al., 1994a, b; Bridwell and Travis, 1995; and Wunderly et al., 1996) they are generally not relevant to abandoned open cut coalmines. However, some research can be found in the literature quantifying the mechanisms that control the rate of pyrite oxidation and the subsequent leaching of the reaction products from open cut mines (Rogowski et al., 1977; and Jaynes et al., 1984a, b). Hence there is a need to develop a model describing the long-term oxidation of pyrite and taking into consideration the physical and chemical transport processes involved in the migration of dissolved chemical species discharged from an open cut coalmine source into an aquifer.

In this chapter a numerical model is presented for prediction of pollution potential with particular focus on the long-term pyrite oxidation and the results of one-dimensional simulations of pollutant transport in backfilled open cut coalmines. The results of two-

dimensional simulations of the subsequent transport of the oxidation products will be described in Chapter 9. The results of this model can help in the design of efficient reclamation techniques in order to minimise the negative impacts of mining operations on surrounding environment.

A number of numerical models of pyrite oxidation have been reported in the literature. These models range from simple coupling of oxygen diffusion through an unsaturated medium to the first order shrinking-core model (Levenspiel, 1972) to complex oxygen diffusion-pyrite oxidation and subsequent reactive transport models. A review of such mathematical models (Appendix C) is useful in the understanding of the long-term pyrite oxidation as well as the physical and chemical transport processes involved in the migration of dissolved chemical species discharged from an open cut coalmine source into an aquifer.

## **8.2 Pyrite oxidation and oxygen transport model description**

### **8.2.1 Conceptual model**

Figure 8.1 shows a conceptual model used in developing the pyrite oxidation and subsequent transport model. A conceptual model is a representation of a real system, describing the processes occurring within the system qualitatively. This model identifies oxygen diffusion, pyrite oxidation in backfilled materials, surface recharge, influx composition, background chemistry of groundwater flow systems, the role of bacteria, chemical reactions and the transport of oxidation products through porous media. The model assumes that the backfilled materials consist of spherical, uniformly sized particles surrounded by a water film. Particles are assumed to have a homogeneous distribution of pyrite within them. Pyrite oxidation occurs at the surface of the pyrite grains contained within the particles. Oxidation reactions and products diffuse through the particle between

the pyrite grains and the spoil solution surrounding the particles (Jaynes et al., 1984a). The oxidation of  $Fe^{2+}$  is catalysed by bacteria, consuming  $O_2$  and  $Fe^{2+}$ , within the particles.

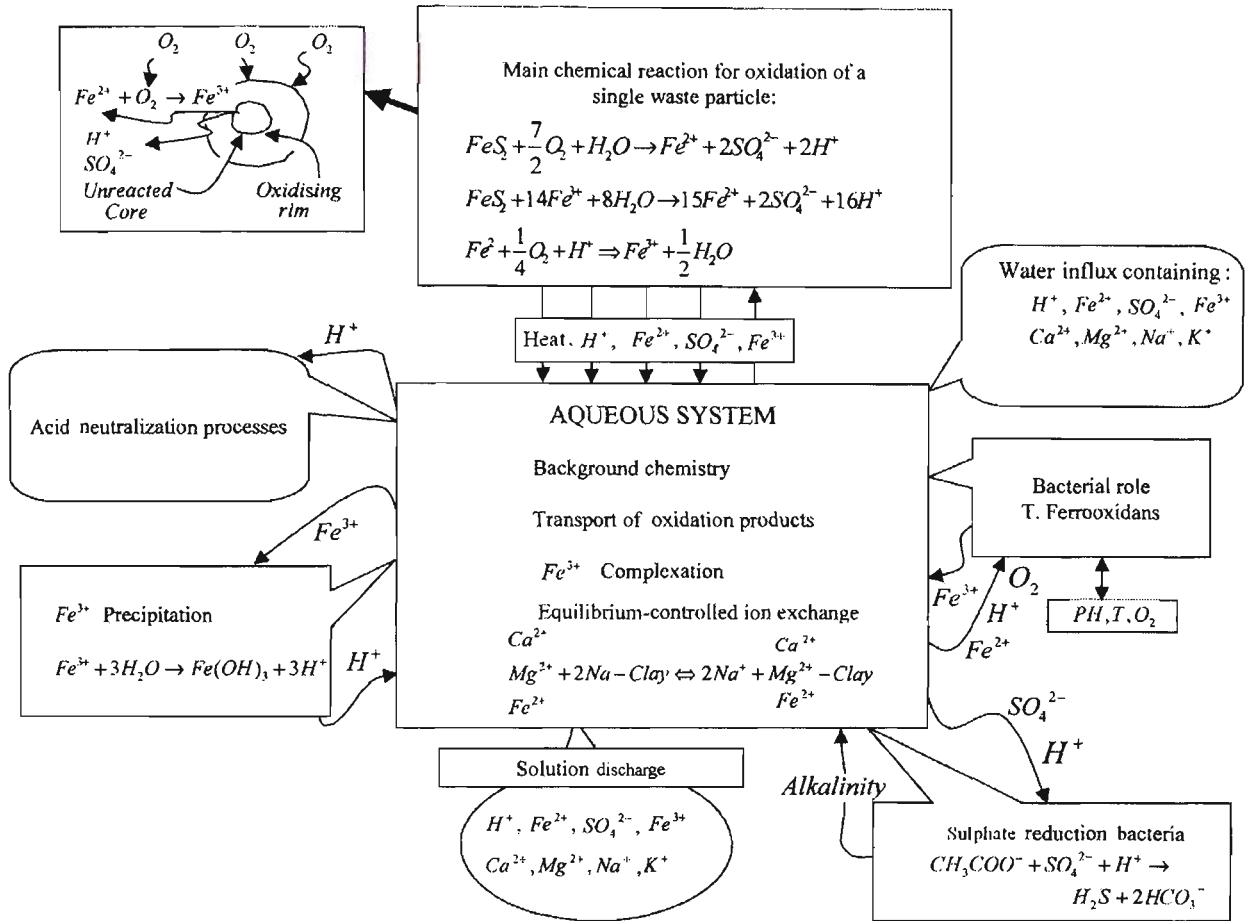


Figure 8.1. Conceptual model of pyrite oxidation and subsequent transport of oxidation products in backfilled open cut mines.

Oxygen diffuses from zones of higher oxygen concentration to zones of lower oxygen concentration through the air-filled pore space in the backfilled materials, with the oxygen in equilibrium with the spoil solution. It was assumed that diffusion is the dominant process supplying oxygen for oxidation reactions. Complexation of ferric iron is assumed to take place within the spoil solution. In the case of sulphate reduction bacteria, the reaction necessary for this was included to take into consideration the consumption of

$SO_4^{2-}$  and  $H^+$ . A reaction between  $H^+$  in solution and the spoil matrix can occur, consuming  $H^+$  from the spoil solution and increasing the  $pH$  (Banks, 1994). Equilibrium-controlled ion exchange is assumed to take place between the solution and solid phases within the spoil solution. It is assumed that ions of  $Fe^{2+}$ ,  $Mg^{2+}$ ,  $Ca^{2+}$ , and  $Na^+$  participate in the ion exchange reaction. Precipitation of  $Fe(OH)_3$  consumes  $Fe^{3+}$  and produces  $H^+$  from the solution. The oxidation products are transported by recharge water and groundwater from the backfilled materials. A kinetically and equilibrium controlled mathematical expression for each of these chemical reactions need to be developed.

In this model, chemical and bacterial oxidation of  $Fe^{2+}$ , pyrite oxidation by oxygen and ferric iron, oxygen diffusion, and bacterial sulphate reduction are relatively slow and assumed to be kinetically controlled but ion exchange and complexation reactions as well as precipitation reactions are fast and assumed to be equilibrium controlled reactions.

### **8.2.2 Pyrite oxidation model**

The oxidation of pyrite is based on the shrinking-core model (Levenspiel, 1972). The model takes into consideration the effects of both surface reaction kinetics and the rate of oxidant diffusion into the particle as was used by Levenspiel (1972); Cathles and Apps (1975); Jaynes et al., (1984a) and Lefebvre and Gelinias, (1995). Assuming that the particles are spherical and noting the pyrite leaching rate to be first order with respect to pyrite surface area and concentration of oxidant, the oxidation rate per unit area of pyrite within a spherical particle can be described by Equation 8.1.

$$\frac{dX}{dt} = \frac{-3X^{\frac{2}{3}}}{6\tau_{D_{|Oxd|}}X^{\frac{1}{3}}\left(1-X^{\frac{1}{3}}\right) + \tau_{C_{|Oxd|}}} \quad (8.1)$$

Details of the integration and steps for the derivation of this model are given in Appendix B.

Equation 8.1 is called a shrinking-core model which describes the leaching of a spherical particle when both chemical reaction and diffusion control the pyrite oxidation rate.

If both oxygen and ferric iron participate in the pyrite oxidation process, Equation 8.1 can be modified as follows:

$$\frac{\partial X}{\partial t} = \frac{-3X^{\frac{2}{3}}}{6\tau_{D_{[O_2]}}X^{\frac{1}{3}}\left(1-X^{\frac{1}{3}}\right) + \tau_{C_{[O_2]}}} + \frac{-3X^{\frac{2}{3}}}{6\tau_{D_{[Fe^{3+}]}}X^{\frac{1}{3}}\left(1-X^{\frac{1}{3}}\right) + \tau_{C_{[Fe^{3+}]}}} \quad (8.2)$$

where,

$X$  = fraction of pyrite remaining within the particle (Kg/Kg);

$t$  = time (s);

$\tau_c$  = total time required for complete oxidation of pyrite within a particle if the oxidation process is only controlled by the decreasing surface area of pyrite (s);

$\tau_D$  = total time required for full oxidation of pyrite within a particle assuming oxidation rate is solely controlled by oxidant diffusion into the particles (s);

$Oxd$  = oxidant.

$\tau_D$  and  $\tau_c$  can be calculated from Equations 8.3 and 8.4 (Levenspiel, 1972).

$$\tau_D = \frac{\rho_{Py} R^2}{6bD_{e[Ox]} C_{[Ox]}} \quad (8.3)$$

$$\tau_c = \frac{\rho_{Py} R}{bK_{[Ox]} \alpha_{Py}^{rock} \lambda C_{[Ox]}} \quad (8.4)$$

where,

$\rho_{Py}$  = density of pyrite in the particle ( $mol / m^3$ );

$R$  = particle radius ( $m$ );

$b$  = stoichiometric ratio of pyrite to oxidant consumption ( $mol/mol$ );

$D_{e[Ox]}$  = effective diffusion coefficient of oxidant in oxidised rim of the particle;

$K_{[Ox]}$  = first-order surface reaction rate constant ( $m/s$ );

$\alpha_{Py}^{rock}$  = surface area of pyrite per unit volume of particle ( $m^{-1}$ );

$\lambda$  = thickness of the particle in which pyrite oxidation occurs (reaction skin depth) ( $m$ );

$C_{[Ox]}$  = concentration of oxidant in the water surrounding the particle ( $mol / m^3$ ).

These Equations were modified to take into account the reaction skin depth and the surface area of pyrite per unit volume of a particle (Cathles and Apps, 1975; Jaynes et al., 1984a; Lefebvre and Galinas, 1995):

**(a) Calculation of pyritic surface area per unit volume of particle ( $\alpha_{Py}^{rock}$ )**

Pyritic surface area per unit volume of particle was determined from the pyrite fraction within a particle. The surface area for sandstone ( $1000 \text{ m}^2 / \text{Kg}$ , as quoted in Jaynes, 1983) was modified by the pyrite fraction, pyrite density and particle density to give the following equation (Jaynes, 1983) :

$$\alpha_{Py}^{rock} = 1000 \times \rho_{Prctl} \left( \frac{G_{Py} \rho_{Prctl}}{D_{Py}} \right)^{\frac{2}{3}} \quad (8.5)$$

where,

$\alpha_{Py}^{rock}$  = surface area of pyrite per unit volume of particle ( $m^{-1}$ );

$\rho_{Prcl}$  = particle density ( $Kg / m^3$ );

$D_{Py}$  = density of pyrite ( $Kg / m^3$ );

$G_{Py}$  = pyrite fraction in a particle ( $Kg/Kg$ ).

For a spoil fragment containing 0.002 pyrite content and the pyrite and particle densities of  $5000 \text{ Kg} / m^3$  and  $2100 \text{ Kg} / m^3$ , Jaynes (1983) calculated  $\alpha_{Py}^{rock}$  equal to  $18700 \text{ m}^{-1}$ . In this thesis, the value of  $\alpha_{Py}^{rock}$  was reduced to  $8000 \text{ m}^{-1}$  (Cathles and Apps, 1975) to take into account spherical particle shapes rather than thin plates fragments as assumed by Jaynes (1983).  $\alpha_{Py}^{rock}$  is recalculated as time progresses to incorporate the reduction in surface area of pyrite.

### (b) Reaction skin depth ( $\lambda$ )

The reaction skin depth is the distance into the particle containing pyrite where pyrite is oxidised. It can be obtained using Equations 8.6 and 8.7 presented by Cathles and Apps (1975) and further modified by Jaynes (1983):

$$\lambda = \frac{1}{\frac{v}{\omega} + \frac{\alpha_{Py}^{rock} K_{[Ox]} (1-X) R}{D_{e[Ox]}}} \quad (8.6)$$

and

$$\omega = \omega_1 \{ \exp(vR) - \exp(vR[1-X]) \} - \omega_2 \{ \exp(-vR) - \exp(-vR[1-X]) \} \quad (8.7)$$

In above equations:

$$v = \sqrt{\frac{K_{[Ox]} \alpha_{Py}^{rock}}{D_{e[Ox]}}} \quad (8.8)$$

$$\omega_1 = \frac{\exp(-2vR)}{\exp\{vR(1-X) - 2vR\} + \exp\{-vR(1-X)\}} \quad (8.9)$$

$$\omega_2 = \frac{1}{\exp\{vR(1-X) - 2vR\} + \exp\{-vR(1-X)\}} \quad (8.10)$$

The oxygen concentration within the pore space of the spoil can be related to its concentration in the liquid phase using Henry's law and the gas law (Davis and Ritchie, 1986a; Wunderly et al., 1996; Lefebvre and Gelinas, 1995):

$$C_{[O_2]} = \gamma u_{O_2} \quad (8.11)$$

where,

$C_{[O_2]}$  = concentration of  $O_2$  in water;

$u_{O_2}$  = oxygen concentration within the pore space of spoil;

$\gamma$  = conversion factor between the oxygen concentrations in the gas and water phases.

According to Jaynes et al. (1984a), for  $\tau_D \gg \tau_C$ , diffusion will be a significant process for controlling the oxidation rate and an oxidised rim depleted of pyrite will form at the surface of the particle and develop inwards. As the oxidised coating develops the rate of pyrite oxidation decreases due to the longer diffusion paths and a shrinking reaction zone (Cathles and Apps, 1975; and Wunderly et al., 1996). For  $\tau_D \ll \tau_C$ , diffusion will not control the oxidation process, and entire the particle will oxidise uniformly (Jaynes et al., 1984a).

The pyrite oxidation process generates sink and source terms for many components as oxidation products. It produces heat, sulphate, iron and acidity. Furthermore, the reaction consumes oxygen and pyrite. These production and consumption terms must be incorporated into the governing equation of each component as sink and source terms.

### 8.2.3 Finite volume discretisation of pyrite oxidation model

After integration of Equation 8.1 in a one-dimensional situation (only in the  $x$  direction, for example), over a control volume and over a time interval  $t$  to  $t + \Delta t$  described in Chapter 7, the discretisation equation reduces to the following expression:

$$a_p X_p = b \quad (8.12)$$

where,

$$a_p = a_p^0 \quad (8.13)$$

$$a_p^0 = \frac{\Delta x}{\Delta t} \quad (8.14)$$

$$b = \bar{S} \Delta x + a_p^0 X_p^0 \quad (8.15)$$

The source term  $\bar{S}$  is given by Equation 8.16 as follows:

$$\bar{S} = \frac{-3 X^{\frac{2}{3}}}{6 \tau_{D_{Oxd}} X^{\frac{1}{3}} \left(1 - X^{\frac{1}{3}}\right) + \tau_{C_{Oxd}}} \quad (8.16)$$

Using Equation 7.5 (Chapter 7, Page 210), the above source term can be linearised as follows:

$$\bar{S} = \frac{-3 X^{\frac{1}{3}}}{6 \tau_{D_{Oxd}} X^{\frac{1}{3}} \left(1 - X^{\frac{1}{3}}\right) + \tau_{C_{Oxd}}} (0.0 - X_p) \quad (8.17)$$

where,

$$Co_{\phi} = \frac{-3X^{\frac{1}{3}}}{6\tau_{D_{Oxd}}X^{\frac{1}{3}}\left(1-X^{\frac{1}{3}}\right) + \tau_{C_{Oxd}}} \quad \text{and} \quad (8.18)$$

$$Val_{\phi} = 0.0 \quad (8.19)$$

With the linearised source term, the discretisation Equation 8.12 reduces to:

$$a_p X_p = b \quad (8.20)$$

where,

$$a_p = a_p^0 - Co_{\phi} \Delta x \quad (8.21)$$

$$a_p^0 = \frac{\Delta x}{\Delta t} \quad (8.22)$$

$$b = Val_{\phi} \Delta x + a_p^0 X_p^0 \quad (8.23)$$

where,

$X_p$  = fraction of pyrite remaining in nodal point  $P$  inside a control volume;

$\bar{S}$  = average value of source  $S$  over the control volume;

$X_p^0$  = old value of  $X_p$ ;

$\Delta x$  = distance between faces  $w$  and  $e$ ;

$\Delta t$  = time step.

#### 8.2.4 Oxygen transport model

Oxygen has an important role in the oxidation of pyrite. Gaseous diffusion was considered to be the principal mechanism of oxygen resupply to the surface mine spoil (Jaynes et al., 1984a). The equation governing oxygen transport into the pore space of the spoil,

incorporating the volumetric oxygen consumption terms, in which air-filled porosity is assumed to be constant over time, can be written as follows (Jaynes et al., 1984a):

$$\phi_a \frac{\partial u}{\partial t} = \frac{\partial}{\partial x_j} \left( D_o \frac{P}{RT\sigma_a} \frac{\phi_a}{\tau} \frac{\partial u}{\partial x_j} \right) + S_{K_{Py-O_2}} + S_{K_{Fe^{2+}-O_2}} + S_{K_{B-O_2}} \quad (8.24)$$

where,

$\phi_a$  = air-filled porosity of the spoil ( $m^3 / m^3$ );

$\sigma_a$  = molar density of air ( $mol / m^3$ );

$u$  = oxygen concentration in the pore space of the spoil ( $mol / m^3$ );

$T$  = temperature (K);

$P$  = atmospheric pressure (101 KPas);

$R$  = gas constant ( $8.31 \times 10^{-3}$  KPas  $m^3$   $mol^{-1}$   $K^{-1}$ );

$\tau$  = tortuosity of diffusion passageway ( $m / m$ );

$x_j$  = Cartesian coordinates (m);

$S_{K_{Py-O_2}}$ ,  $S_{K_{Fe^{2+}-O_2}}$ , and  $S_{K_{B-O_2}}$  = volumetric oxygen consumption terms ( $mol / m^3 s$ ) by the pyrite oxidation reaction, chemical oxidation of ferrous iron and oxygen consumption by bacteria;

$D_o$  = effective diffusion coefficient of  $O_2$  in a mixed  $O_2, CO_2, N_2$  atmosphere ( $m^2 / s$ ) and can be described by the following equation (Jaynes and Rogowski, 1983):

$$D_o = \frac{D_{b(O_2,CO_2)} D_{b(O_2,N_2)}}{D_{b(O_2,N_2)} Q_{CO_2} + D_{b(O_2,CO_2)} Q_{N_2} + r_{(CO_2,O_2)} D_{b(O_2,N_2)} Q_{O_2}} \quad (8.25)$$

where,

$D_{b(O_2,CO_2)}$  and  $D_{b(O_2,N_2)}$  = binary diffusion coefficients for gas pairs of  $O_2, CO_2$  and  $O_2, N_2$  respectively ( $m^2 / s$ );

$Q_{O_2}, Q_{CO_2}$  and  $Q_{N_2}$  = mole fractions of  $O_2, CO_2$ , and  $N_2$  in gas ( $mol / mol$ );

$r_{(CO_2,O_2)}$  = molar flux ratio for gas pair of  $CO_2$  and  $O_2$  and it is equivalent to:

$$r_{(CO_2,O_2)} = \frac{N_{CO_2}}{N_{O_2}} \quad (8.26)$$

where,

$N_{CO_2}$  and  $N_{O_2}$  = molar fluxes for  $CO_2$  and  $O_2$ , respectively.

For a temperature of  $25^\circ C$  and a pressure of  $101 KPa$ , the binary diffusion coefficients are  $0.210 \times 10^{-4}$ ,  $0.166 \times 10^{-4}$  and  $0.166 \times 10^{-4}$  ( $m^2 / s$ ) for  $D_{b(O_2,N_2)}, D_{b(N_2,CO_2)}$ , and  $D_{b(O_2,CO_2)}$  respectively (Jaynes and Rogowski, 1983, Table 1, p.428). For example, with  $Q_{O_2} = 0.21$ ,  $Q_{CO_2} = 0.04$ ,  $Q_{N_2} = 0.75$  and  $r_{(CO_2,O_2)} = 0.5$  the calculated value for effective diffusion coefficient from Equation 8.25, is  $2.25 \times 10^{-5} m^2 / s$ .

If it is assumed that  $P, R, T, \tau, D_o, \sigma_a$ , and  $\phi_a$  are constant, Equation 8.24 can then be reduced to the following equation:

$$\phi_a \frac{\partial u}{\partial t} = D_e \left( \frac{\partial^2 u}{\partial x_j^2} \right) + S_{K_{Py-O_2}} + S_{K_{Fe^{2+}-O_2}} + S_{K_{B-O_2}} \quad (8.27)$$

where,

$D_e$  = effective diffusion coefficient, it may be reduced to:

$$D_e = \frac{P}{RT\sigma_a} \left( \frac{\phi_a}{\tau} \right) D_o \quad (8.28)$$

### 8.2.5 Development of mathematical expressions for oxygen consumption terms

Mathematical expressions for each of the consumption terms in Equation 8.27 need to be developed separately.

(i)  $S_{K_{Py-O_2}}$ . An expression for the rate at which oxygen is consumed due to the oxidation of pyrite,  $S_{K_{Py-O_2}}$ , can be developed from Equation 8.1 by taking into account the molar density of pyrite in spoil ( $\rho_s$ ) and the stoichiometric ratio of pyrite consumption to oxygen consumption ( $b$ ). The expression is given below:

$$S_{K_{Py-O_2}} = \frac{-3(1-\phi)b^{-1}\rho_s X^{\frac{2}{3}}}{6\tau_{D_{O_2}} X^{\frac{1}{3}} \left(1 - X^{\frac{1}{3}}\right) + \tau_{C_{O_2}}} \quad (8.29)$$

where,

$\phi$  = porosity of spoil.

(ii)  $S_{K_{Fe^{2+}-O_2}}$ . The second relationship needs to be developed to take into consideration the rate of consumption of oxygen due to the oxidation of  $Fe^{2+}$ . The rate of  $Fe^{2+}$  oxidation by oxygen is a function of  $pH$ . It is very slow at low  $pH$ . The kinetics of the chemical oxidation of  $Fe^{2+}$  have been previously studied and the necessary rate expression was found. Singer and Stumm (1970) proposed the following rate law:

At constant partial pressure of  $O_2$  and at  $pH$  values greater than 4.5, the rate is:

$$-\frac{\partial[Fe^{2+}]}{\partial t} = K[Fe^{2+}] \frac{u}{u+33.857} [OH^-]^2 \quad (8.30)$$

where,  $K=1.3 \times 10^{12} (l^2 / mol^2 atm s)$

Equation 8.30 reduces to:

$$-\frac{\partial[Fe^{2+}]}{\partial t} = K_1 [Fe^{2+}] \frac{u}{u+33.857} [H^+]^{-2} \quad (8.31)$$

where,  $K_1 = 1.3 \times 10^{-10} \text{ (mol}^2 / (\text{m}^3)^2 \text{ s)}$

At  $pH$  values under 3.5, the rate is independent to  $pH$  and can be described by:

$$-\frac{\partial[Fe^{2+}]}{\partial t} = K_2 [Fe^{2+}] \frac{u}{u+33.857} \quad (8.32)$$

where,  $K_2 = 1.7 \times 10^{-9} \text{ s}^{-1}$ .

The rate of oxygen consumption ( $S_{K_{Fe^{2+}-O_2}}$ , in  $\text{mol/m}^3 \text{ s}$ ) may now calculated by modifying both Equations 8.31 and 8.32 using the stoichiometric ratio of  $Fe^{2+}$  consumption to oxygen consumption ( $b'$ ) and the water-filled porosity ( $\phi_w$ ) (Jaynes et al., 1984a):

$$S_{K_{Fe^{2+}-O_2}} = -\phi_w b'^{-1} [Fe^{2+}] \frac{u}{u+33.857} \left\{ K_1 \left( \frac{1}{[H^+]} \right)^2 + K_2 \right\} \quad (8.33)$$

where,

$[Fe^{2+}]$  and  $[H^+]$  = concentrations of  $Fe^{2+}$  and  $H^+$  ( $\text{mol/m}^3$ ).

(iii) The third sink term,  $S_{K_{B-O_2}}$ , accounts for the rate of oxygen consumption by bacterial activity during oxidation of  $Fe^{2+}$  in the surface mine spoil. Experimental studies showed that the presence of *T. ferrooxidans* increases the rate of  $Fe^{2+}$  oxidation by more than six orders of magnitude (Singer and Stumm, 1970). Jaynes et al. (1984a) applied the following

rate expression for the bacterial oxidation of  $Fe^{2+}$  in an approach similar to the chemical oxidation of  $Fe^{2+}$  :

$$S_{K_B-O_2} = -\phi_W b'^{-1} K_B [Fe^{2+}] \frac{u}{u+33.857} \quad (8.34)$$

where,

$K_B$  = first order reaction rate coefficient for bacterial oxidation of  $Fe^{2+}$  in terms of  $s^{-1}$  that takes into account the bacterial activity in the surface mine spoil. The lower limit of  $K_B$  is 0, when the bacteria are not active. The upper limit is estimated by the following equation:

$$(K_B)_{\max} = \frac{4A_F D_{e[O_2]}}{\Delta l' [Fe^{2+}]} \quad (8.35)$$

where,

$A_F$  = particle surface area per volume of spoil water;

$D_{e[O_2]}$  = diffusion coefficient of oxygen in water;

$\Delta l'$  = water film thickness.

According to Jaynes et al. (1984a), the value of  $K_B$  is calculated between these upper and lower limits from the bacterial activity which depends on the suitable conditions available for the growth of the bacteria.

In this approach, energy available from the environment and inhabitation factors were utilised to compute the activity which determines the  $Fe^{3+}$  production rate. The inhabitation factors considered in the bacterial model were solution  $pH$ , temperature and oxygen concentration. The effects of each inhabitation factor were determined empirically based on experimental work as reported by Jaynes et al. (1984a). It was assumed that the

bacterial activity is in dynamic equilibrium with the environment in which pyrite oxidation takes place, hence the variations of bacterial activity caused by changes in their environment are very fast and bacterial activity is always at the maximum level. Details on the bacterial activity model developed by Jaynes et al. (1984a) are given in Appendix K.

The final equation used to describe oxygen transport combined with consumption terms is given by (modified from Jaynes et al., 1984a):

$$\phi_a \frac{\partial u}{\partial t} = D_e \left( \frac{\partial^2 u}{\partial x_j^2} \right) - \frac{3(1-\phi)b^{-1} \rho_s X^{\frac{2}{3}}}{6 \tau_{D_{O_2}} X^{\frac{1}{3}} \left( 1 - X^{\frac{1}{3}} \right) + \tau_{C_{O_2}}} - \phi_w b'^{-1} [Fe^{2+}] \frac{u}{u + 33.857} \left\{ K_1 \left( \frac{1}{[H^+]} \right)^2 + K_2 \right\} - \phi_w b'^{-1} K_B [Fe^{2+}] \frac{u}{u + 33.857}$$

(8.36)

### 8.2.6 Boundary conditions for oxygen transport model

It was assumed that the oxygen concentration at the spoil surface is the molar concentration of oxygen in air,

$$u(0, t) = u_o = 9 \text{ mol m}^{-3}$$

(8.37)

At the base of the spoil profile a 'zero concentration gradient' boundary condition was specified,

$$\frac{\partial u}{\partial x_j}(L, t) = 0$$

(8.38)

where,

$L$  = length of the spoil profile.

Finally it was further assumed that initially there is no oxygen within the spoil,

$$u(x_j, 0) = 0$$

(8.39)

### 8.3 Enthalpy (temperature) transport model

The temperature may play a significant role in the oxidation reaction rates. The oxidation of pyrite generates heat. The enthalpy of Reaction 2.8 (Chapter 2, Section 2.5.3, Page 50),  $\Delta H_R$ , is approximately  $-1.4 \times 10^6 J$  (Cathles and Apps, 1975) and according to Rose and Cravotta III, (1998)  $-1.49 \times 10^6 J$  at  $25^\circ C$ . Furthermore the enthalpy for Reaction 2.10 (Chapter 2, Section 2.5.3, Page 50) is  $17860 J$ , based on enthalpies in CRC (1998).

Heat transfer in spoil occurs through the following mechanisms:

- (i) conduction in the bulk of the spoil material resulting from temperature gradients
- (ii) advection of fluids (liquid and gas) carrying heat. Heat transfer by advection of gas was neglected. The mechanisms of heat transfer are responsible for heating the centre of the spoil by carrying heat away from the zone of maximum temperature where the oxidation reaction takes place.

#### 8.3.1 Enthalpy model

To model the heat transfer, a simple enthalpy balance is employed using Equation 8.40 (modified from Cathles and Apps, 1975):

$$\rho_b C_p \frac{\partial T}{\partial t} = K_T \left( \frac{\partial^2 T}{\partial x_j^2} \right) - \rho_w C_w u_{x,w} \frac{\partial T}{\partial x_j} + \frac{3(1-\phi)B^{-1} \rho_s X^{\frac{2}{3}}}{6\tau_{D_{O_2}} X^{\frac{1}{3}} \left( 1 - X^{\frac{1}{3}} \right) + \tau_{C_{O_2}}} + \frac{3(1-\phi)B'^{-1} \rho_s X^{\frac{2}{3}}}{6\tau_{D_{Fe^{3+}}} X^{\frac{1}{3}} \left( 1 - X^{\frac{1}{3}} \right) + \tau_{C_{Fe^{3+}}}}$$

(8.40)

where,

$T$  = temperature ( $^\circ C$ );

$\rho_b$  = bulk density of the spoil ( $Kg / m^3$ );

$K$  = thermal conductivity ( $J/m\ ^\circ C S$ );

$C_p$  = specific heat capacity of the spoil ( $J/Kg\ ^\circ C$ );

$t$  = time ( $s$ );

$\rho_w$  = density of water in the spoil ( $Kg/m^3$ );

$u_{x,w}$  = water velocity ( $m/s$ );

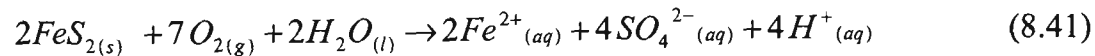
$C_w$  = heat capacity of water ( $J/Kg\ ^\circ C$ );

$B$  = mole of pyrite consumed in pyrite-oxygen reaction per heat generated ( $mol/J$ );

$B'$  = mole of pyrite consumed in pyrite-  $Fe^{3+}$  reaction per heat generated ( $mol/J$ ).

### 8.3.2 Calculation of enthalpies

Rearranging the pyrite-oxygen reaction (Equation 2.8, Page 50) into the following form and using enthalpies (in terms of  $KJ/mol$ ) given in CRC (1998), the enthalpy of the reaction can be estimated as follows:



$$FeS_2(s) = -171.54$$

$$H_2O_{(l)} = -285.83$$

$$Fe^{2+}_{(aq)} = -89.1$$

$$Fe^{3+}_{(aq)} = -48.5$$

$$SO_4^{2-}_{(aq)} = -909.27$$

$$H^+_{(aq)} = 0.0$$

$$O_{2(g)} = 0.0$$

$$\Delta H^\circ = 2\Delta H_f^\circ (Fe^{2+}) + 4\Delta H_f^\circ (SO_4^{2-}) + 4\Delta H_f^\circ (H^+) - 2\Delta H_f^\circ (FeS_2) - 7\Delta H_f^\circ (O_2) - 2\Delta H_f^\circ (H_2O)$$

$$\Delta H^\circ = 2(-89.1) + 4(-909.27) + 4(0.0) - 2(-171.54) - 7(0.0) - 2(-285.83)$$

$$\Delta H^\circ = -2900.54 \text{ KJ/mol}$$

The calculated enthalpy is for the oxidation of 2 moles of pyrites. Hence,  $\Delta H^\circ$  for every mole of pyrite is  $-1450.27 \text{ KJ/mol}$ . The moles of pyrite consumed in the pyrite-oxygen reaction per heat generated,  $B$ , is  $1/1450270 = 6.9 \times 10^{-7} \text{ mol/J}$ .

Using the above enthalpies and but now taking into consideration the pyrite-ferric iron oxidation reaction (Equation 2.10, Page 50), the enthalpy and the moles of pyrite consumed per heat generated,  $B'$ , are:

$$\Delta H^\circ = -17.86 \text{ KJ/mol}, B' = 1/17860 = 5.6 \times 10^{-5} \text{ mol/J}.$$

### 8.3.3 Boundary conditions assigned for enthalpy model

The following boundary conditions were specified for the temperature:

The spoil was initially set at  $15^\circ\text{C}$  as follows:

$$T(x_j, 0) = 15^\circ\text{C} \tag{8.42}$$

The top surface temperature was also fixed at  $15^\circ\text{C}$  using a first-type boundary condition.

### 8.4 One-dimensional modelling settings and input data

In order to evaluate the above model, a one-dimensional simulation was performed using the PHOENICS package. Four cases with different conditions were selected for the simulation. The model input data were taken from Jaynes et al. (1984b) and given in Table 8.1. Influx chemistry and the background history of the water in the profile are listed in Table 8.2.

Table 8.1. Parameters used for simulation (Jaynes et al., 1984b).

Pyrite fraction	0.0025	Kg pyrite/ Kg spoil
Fraction coarse particles containing pyrite	75 %	
The bulk density of spoil	1650	$Kg/m^3$
The porosity of the spoil	0.321	
Water-filled porosity	0.225	
Surface area of pyrite per unit volume of spoil	80 $cm^{-1}$	(Cathles and Apps, 1975)
Radius of particles	2 $cm$	
Diffusion coefficient of oxidant in water	$1.0 \times 10^{-11} m^2/s$	
Molar density of pyrite within particle	23 $mol/m^3$	
First-order rate constant for $Fe^{3+}$	$4.4 \times 10^{-8} m/s$	
First-order rate constant for oxygen	$8.3 \times 10^{-10} m/s$	
Recharge value	0.5 $m/yr$	
constants for chemical oxidation of $Fe^{2+}$ $K_1 = 1.3 \times 10^{-10} (mol^2/(m^3)^2 (s))$ , $K_2 = 1.7 \times 10^{-9} s^{-1}$		

Table 8.2. Influx and background chemistry (Jaynes et al., 1984b).

Aqueous components	concentration ( $mol/m^3$ )
<b>Influx data:</b>	
$Fe^{2+}$	0.0
$Fe^{3+}$	0.0
$SO_4^{2-}$	50
$pH$	5
<b>Background data:</b>	
$Fe^{2+}$	0.5
$Fe^{3+}$	0.0
$SO_4^{2-}$	50
$pH$	5

A spoil profile with a depth of 10 metres was divided into 20 equal size control volumes. Figure 8.2 shows a one-dimensional grid.

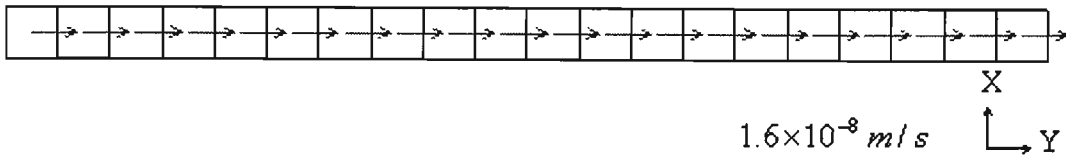


Figure 8.2. One-dimensional grid and velocity vectors.

Jaynes et al. (1984a, b) developed a model called POLS, which is a computer program using the finite difference method for the simulation of the long-term pyrite oxidation and leaching processes in reclaimed strip mines. They used the same cases with the same input data. The results of the finite volume model using PHOENICS were compared and verified with the POLS model results in order to calibrate the accuracy of the model. The specific conditions maintained for four different cases are summarised in Table 8.3.

Table 8.3. A summary of the conditions maintained for the test cases used in this study.

Case	air-filled porosity	Tortuosity	bacteria	$H^+$ - spoil interaction
1	0.09	10	absent	not included
2	0.09	10	present	not included
3	0.18	5	absent	not included
4	0.09	10	present	included

The surface of the spoil was initially specified as a first type boundary condition with the oxygen concentration equal to the atmospheric concentration, 0.21 mole fraction ( $\approx 9 \text{ mol/m}^3$ ). At the base of the spoil column a zero-gradient boundary condition was assigned.

It was further assumed that no oxygen initially exists within the profile. The spoil temperature was 15 °C .

For transport of the oxidation products, the top surface of the spoil was assigned a constant recharge of 0.5 *m / yr* . A hydrodynamic dispersion of  $1.0 \times 10^{-10} \text{ m}^2 / \text{s}$  was used to achieve consistency with the POLS model results. A first-type boundary condition was selected at the top surface of the spoil for the concentration of the oxidation products. An initial boundary condition was specified to describe the distribution of the dissolved ions within the water in the spoil profile. A zero-concentration gradient boundary condition was assumed at the outlet of the profile.

### **8.5 Modelling results**

In the first case no bacteria were allowed to affect the oxidation process. As the simulation progresses, oxygen diffuses through the spoil profile and reacts with pyrite directly. In addition, ferric iron also participates in the pyrite oxidation reaction. In this case, because the chemical oxidation of ferrous iron is the only source of ferric iron, therefore ferric iron has no significant role in pyrite oxidation. Figure 8.3 shows the oxygen concentration versus depth for a time period of 5 years. The oxygen concentration decreases as a curve over the whole profile depth.

In Figure 8.3 a comparison was made for the oxygen concentration between the finite volume model shown as solid lines and the POLS model shown as dots for Cases 1, 3 and 4 and the agreement was close. In Cases 1 and 3, oxygen diffused over entire profile because no bacteria were active to consume the oxygen.

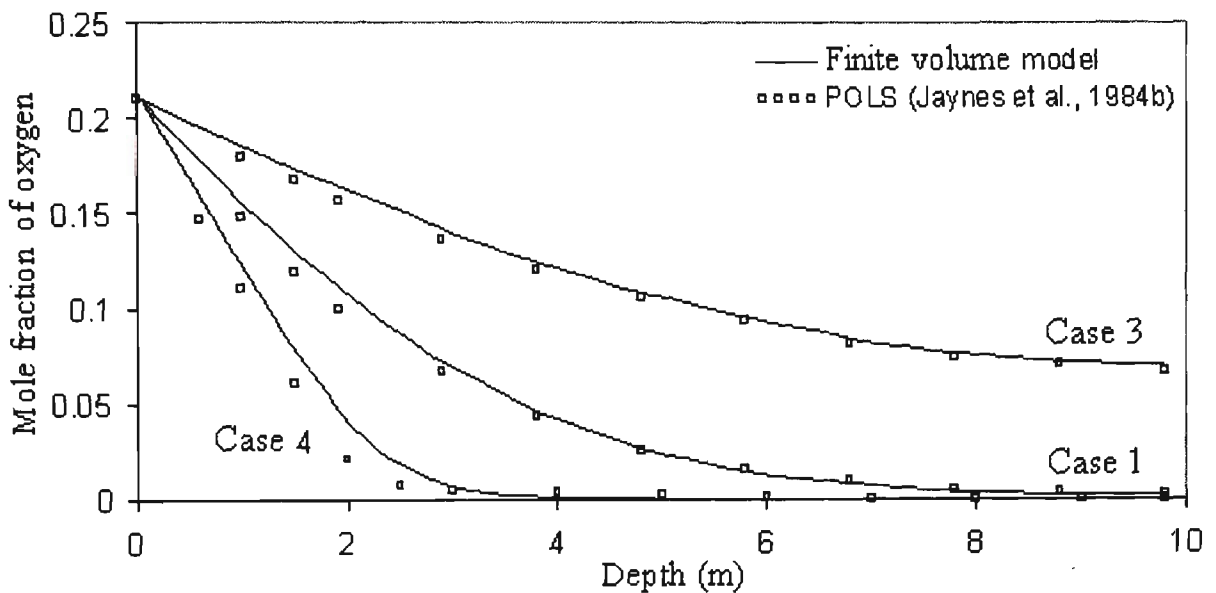
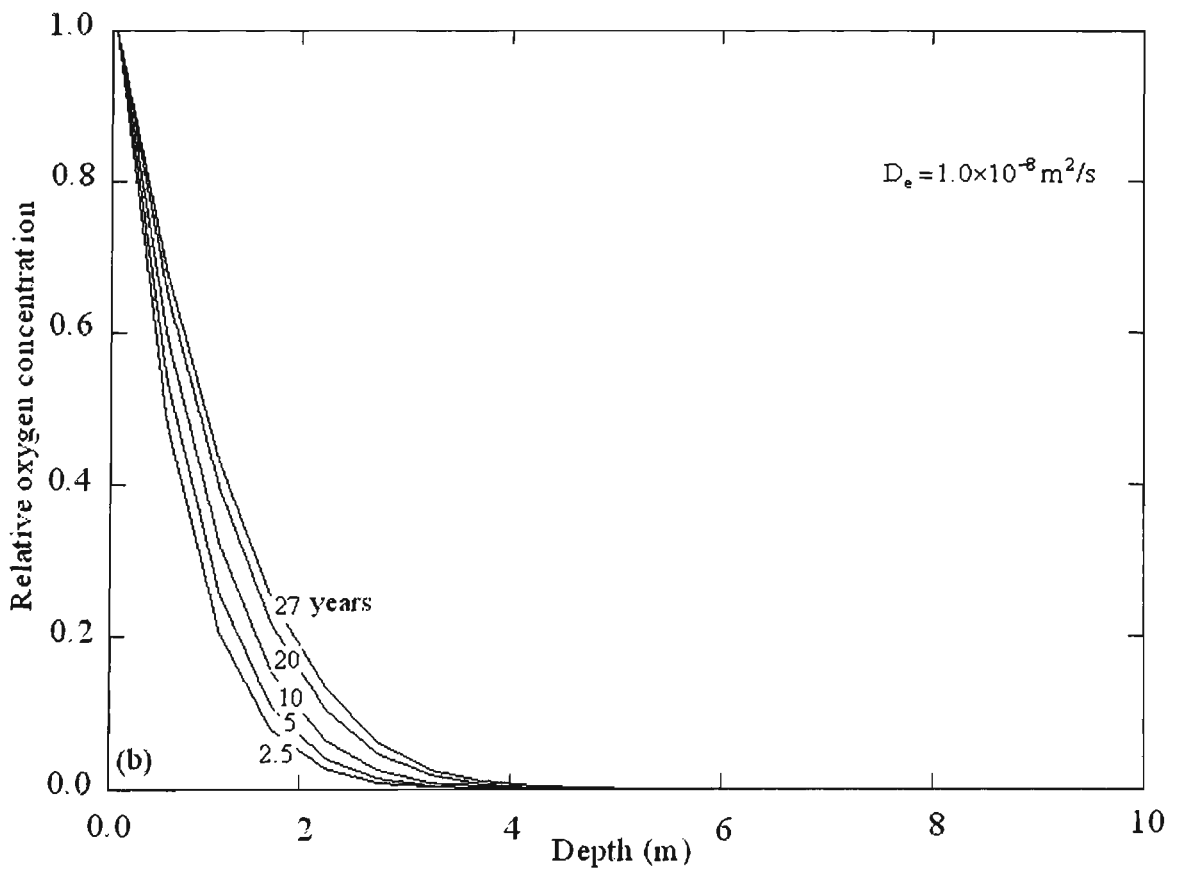
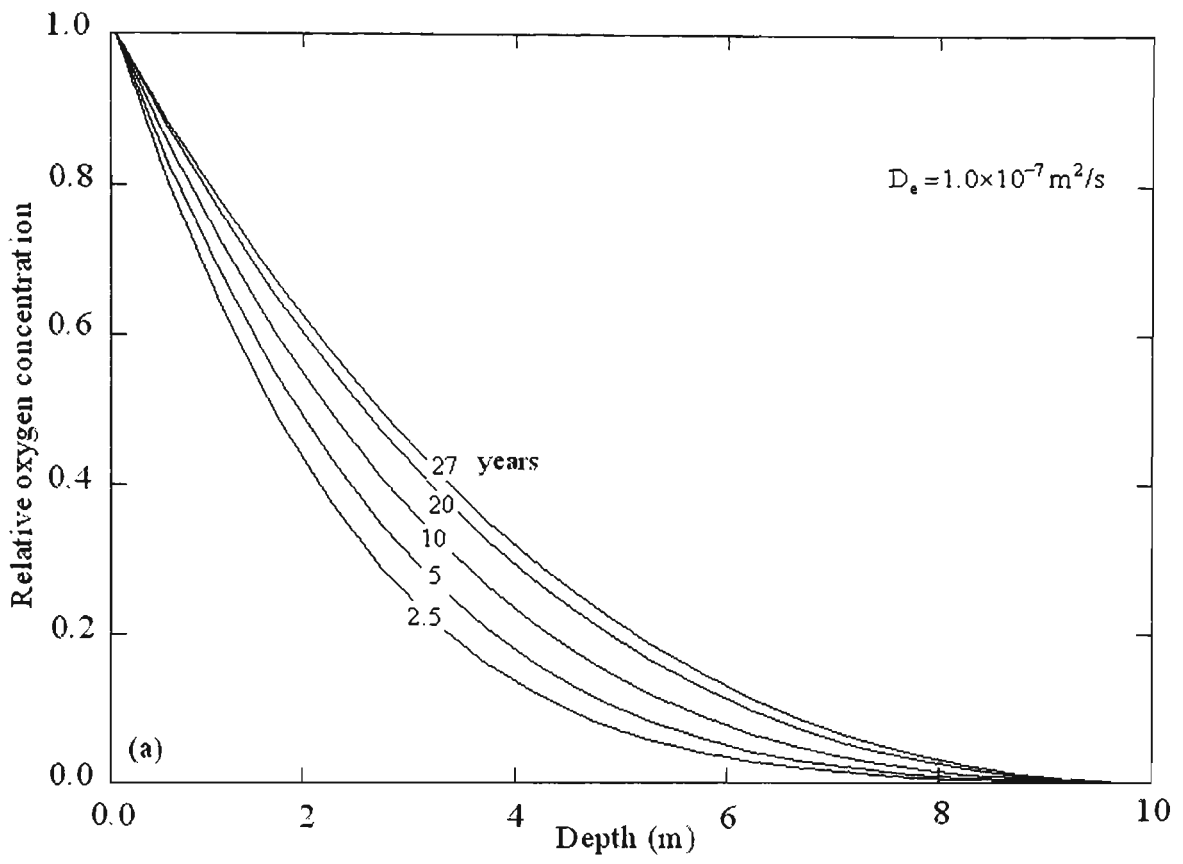


Figure 8.3. Comparison of the POLS modelling results (dots) with the finite volume simulated results (solid lines) for oxygen mole fraction as a function of depth for 5-year period for Cases 1, 3 and 4.

In Case 3 similar to Case 1, bacteria were not active but the effective diffusion coefficient increased by a factor of 4. Increasing the diffusion coefficient caused considerable oxygen concentration to occur in the lower depths and consequently it increased the rate of pyrite oxidation.

The results indicated that the concentration of oxygen is most sensitive to the effective diffusion coefficient (Figure 8.4). Lower diffusion values resulted in steeper gradients and oxygen decreases linearly from the spoil surface to the reaction front.



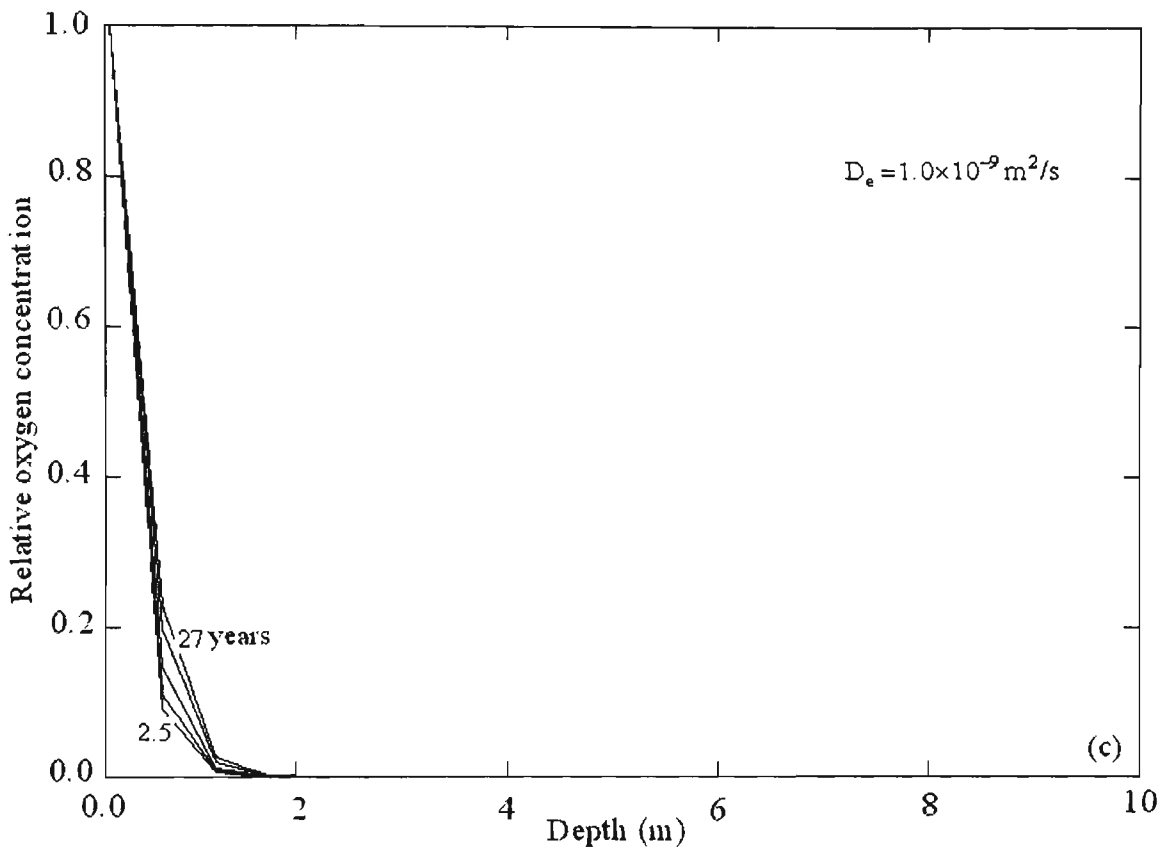


Figure 8.4. The results of the finite volume model for the relative oxygen concentration versus depth over 27-year period for different diffusion coefficients. Effective diffusion coefficient: (a)  $1.0 \times 10^{-7} \text{ m}^2 / \text{s}$  , (b)  $1.0 \times 10^{-8} \text{ m}^2 / \text{s}$  , (c)  $1.0 \times 10^{-9} \text{ m}^2 / \text{s}$

Figure 8.5 illustrates the pyrite fraction oxidised within the entire spoil column versus time. A simulation was performed over a 27-year period. About 20 % of pyrite was consumed in Case 1 after 27 years. It was found that oxygen was the only important factor for the oxidation reaction in this case. Jaynes et al. (1984b) observed that only 22 % of pyrite oxidised after the same time period. The small difference may due to the fact that the POLS model assumed that the fragments were thin plates whereas the finite volume model using PHOENICS assumes that the particles containing pyrite are spherical. It should be noted that the surface area for thin plates is greater than that for spheres.

As Figure 8.5 shows, the oxidation of pyrite increased in Case 3 with an increase in the effective diffusion coefficient for oxygen. In this diagram the PHOENICS results are again shown in solid lines and are compared with the POLS results shown as data points.

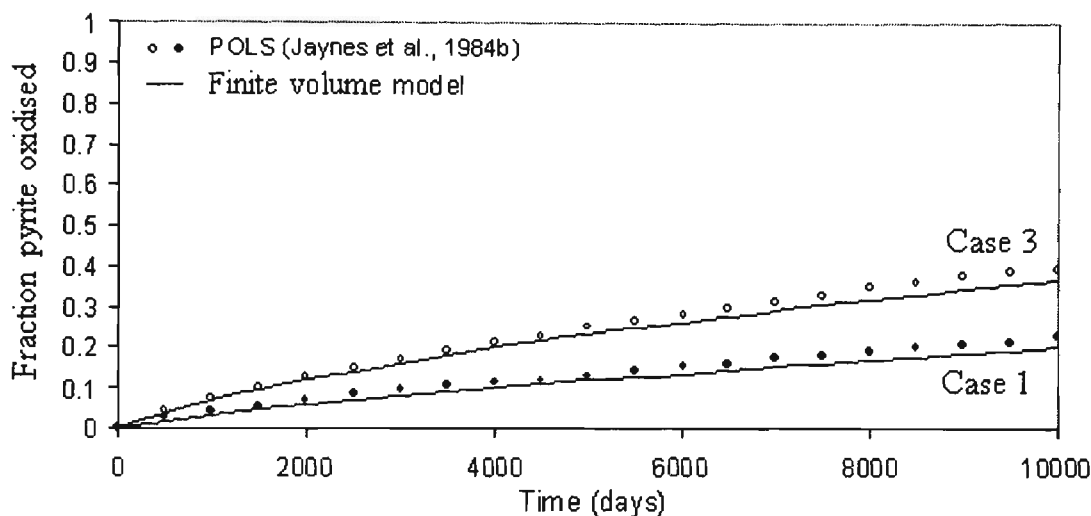


Figure 8.5. Comparison of the POLS results (dots) with the PHOENICS results (solid lines) for the pyrite consumed vs. time over entire spoil column for Cases 1 and 3.

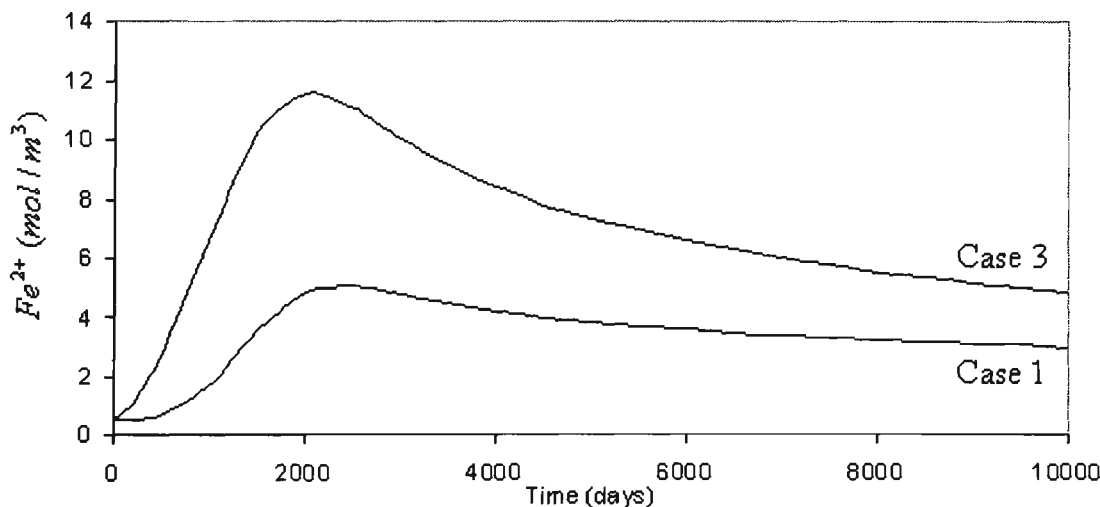


Figure 8.6. PHOENICS results for  $Fe^{2+}$  vs. time at the outlet of the profile for Cases 1 and 3.

Figures 8.6 and 8.7 show the ferrous iron concentration and  $pH$  as a function of time in the outlet of the profile for Cases 1 and 3 respectively. In Case 1 ferrous iron concentration

after 2100 days of the oxidation process increased to  $5 \text{ mol/m}^3$  and  $pH$  decreased to 2.02. After 27 years of simulation, the ferrous iron concentration decreased to  $2.98 \text{ mol/m}^3$ , and the  $pH$  increased to 2.22. These values obtained for the ferrous iron concentration as well as the values for  $pH$  exactly agree with those obtained by POLS model.

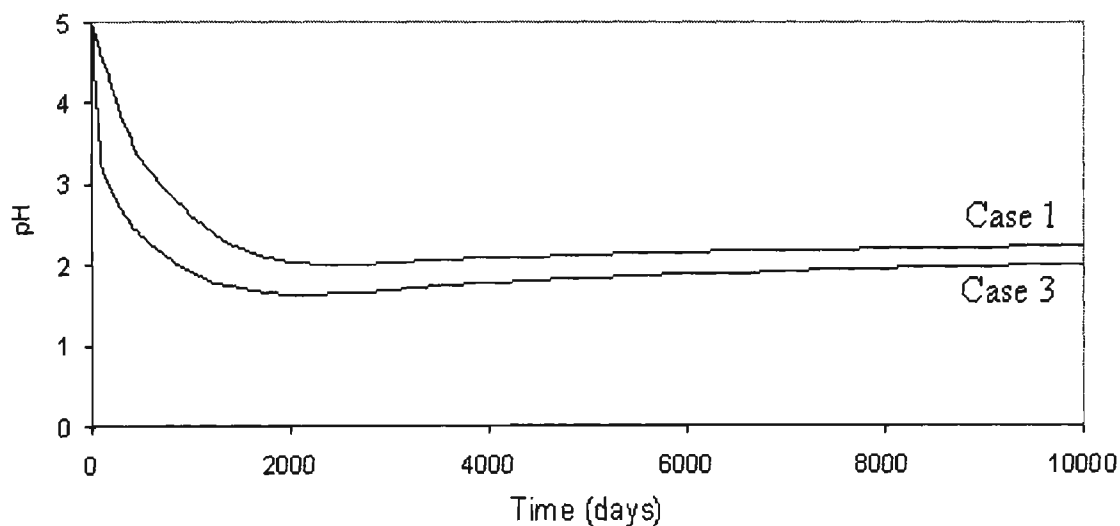


Figure 8.7. PHOENICS results for  $pH$  vs. time at the outlet of the profile for Cases 1 and 3.

In Case 3, the ferrous iron concentration increased to  $11.2$  and  $4.81 \text{ mol/m}^3$  after 2100 and 10000 days of oxidation, and the  $pH$  decreased to 1.65 and 2 after the same time periods. The main reason for the lower values of  $pH$  is that the neutralisation process for  $H^+$  was ignored in these cases.

In Case 2, the same effective diffusion coefficient used in Case 1 was selected but iron-oxidising bacteria were allowed to be active. The bacterial activity model developed by Jaynes et al. (1984a) was used for the simulation.

Figure 8.8 shows the ratio of ferric iron to ferrous iron versus time in the outlet of the spoil profile for Cases 1 and 2. The comparison was made with the POLS model outputs and the

results were in good agreement. As Figure 8.8 shows the iron-oxidising bacteria increased the ferric/ferrous ratio about 100 times in Case 2.

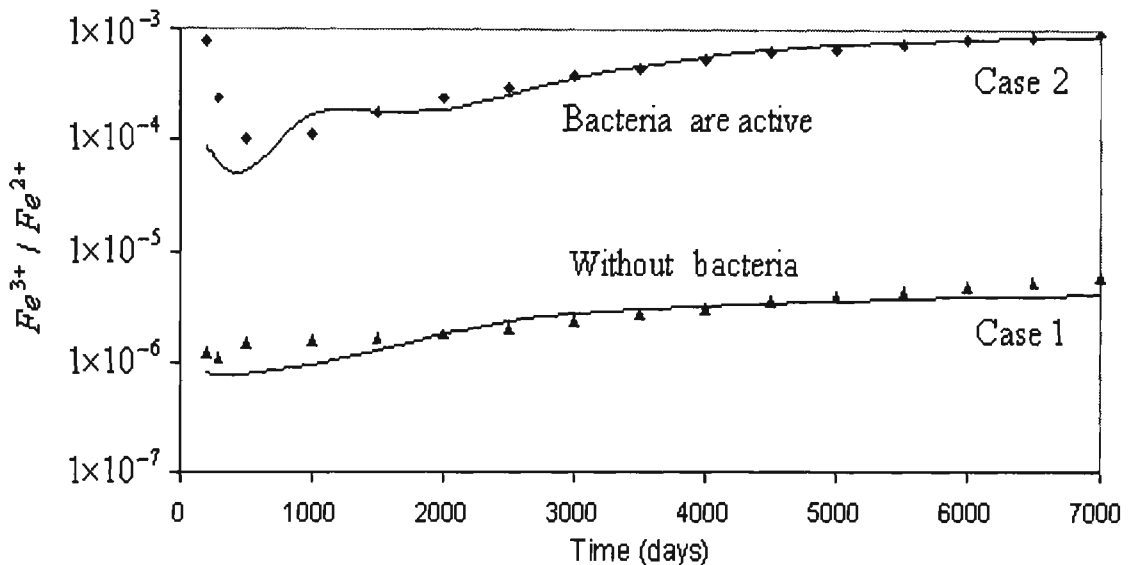


Figure 8.8. Comparison of the POLS results (dots) with the PHOENICS results (solid lines) for the ratio of  $Fe^{3+}$  to  $Fe^{2+}$  in the outlet of spoil column in the presence and absence of bacteria.

As Figure 8.9 shows, no significant change was obtained for the consumption of pyrite in Case 2. The main reason for the small role of bacteria influencing the consumption of pyrite in Case 2 is that just at the beginning of the simulation the  $pH$  in the entire profile decreased sharply below the minimum  $pH$  value required for activity of iron-oxidising bacteria. According to Jaynes et al. (1984a), bacteria have a maximum activity between  $pH$  2.5 and 4.

In Case 4, similar to Case 2, the bacteria were allowed to be present but unlike Case 2 the interaction between  $H^+$  produced by oxidation reactions and spoil was incorporated. In this case the solution  $pH$  was maintained above 2.5. No ferric iron complexation reaction was considered in this case.

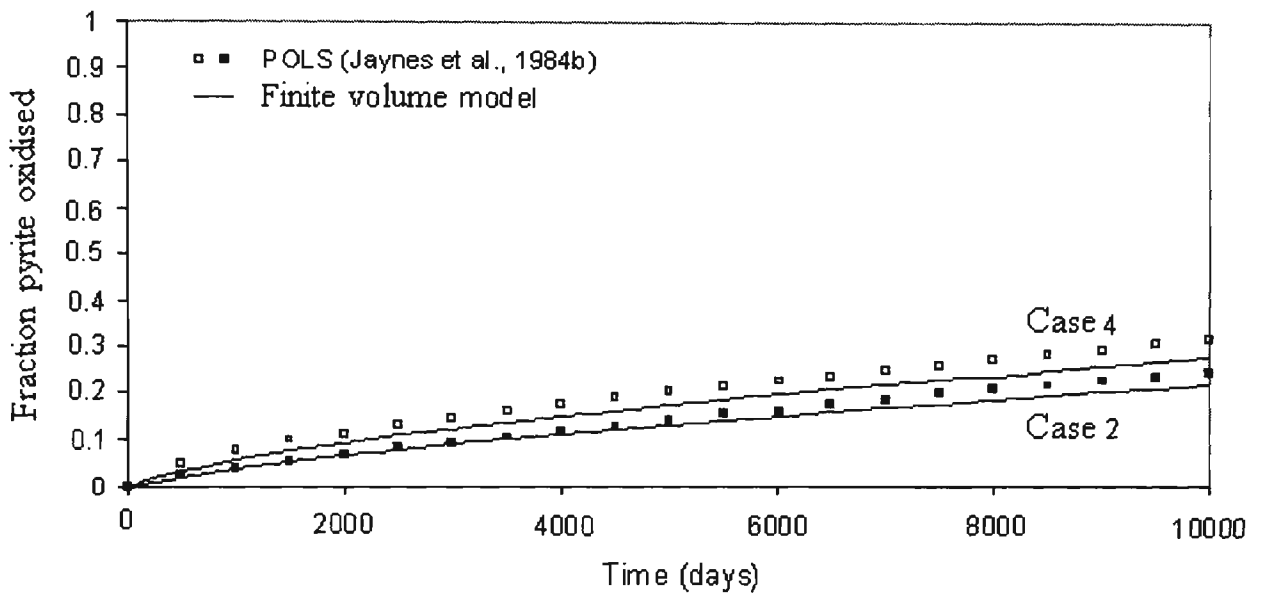


Figure 8.9. Comparison of the POLS results (dots) with the PHOENICS results (solid lines) for the pyrite oxidised vs. time over entire spoil column for Cases 2 and 4.

The  $H^+$ -spoil interaction increased the  $pH$  of the solution. It caused an increase in the bacterial activity therefore more ferric iron was produced. Consequently, the pyrite oxidation rate increased considerably over time (Figure 8.9). As Figure 8.9 shows, about 29 % of the pyrite was oxidised after 10000 days of the simulation. For this time, the POLS model predicted that 30.5 % of pyrite was consumed. The difference between the finite volume modelling predictions and those predicted by the POLS model can be explained in that unlike the POLS model, for Case 4 the ferric complexation reaction was not incorporated in the finite volume model. The complexation reaction increases the ferric concentration. Consequently the rate of pyrite oxidation increases.

The mole fraction of oxygen within the spoil profile versus depth for Case 4 was illustrated in Figure 8.3. Oxygen decreased linearly to a depth of about 1.75 m. Below this depth the oxygen concentration gradually decreased non-linearly, where it reached zero at a depth of approximately 5 m. Bacterial activity was the main reason for this sharp reduction of

oxygen concentration within the surface layers of the spoil profile, which consumed most of the oxygen over this part of the profile.

Figure 8.10 shows the ferrous iron concentration as a function of depth after 5 years of the simulation. For surface layers (up to 2 m) where the concentration of oxygen is high and bacterial activity is significant, ferrous iron concentration increased gradually due to conversion of some ferrous iron to ferric iron by the bacterial action. In the zone between 2 m and 3.5 m where the bacteria have no significant role, the ferrous iron increased linearly. In this zone both oxygen and ferric iron oxidise pyrite and produce ferrous iron. In the zone between 3.5 m and 6.5 m depth the ferrous iron concentration increased at a slower rate because some pyrite still oxidised and produced ferrous iron. For deeper layers (below 6.5 m) where no oxygen and ferric iron are available to oxidise pyrite, the ferrous iron concentration decreased steadily.

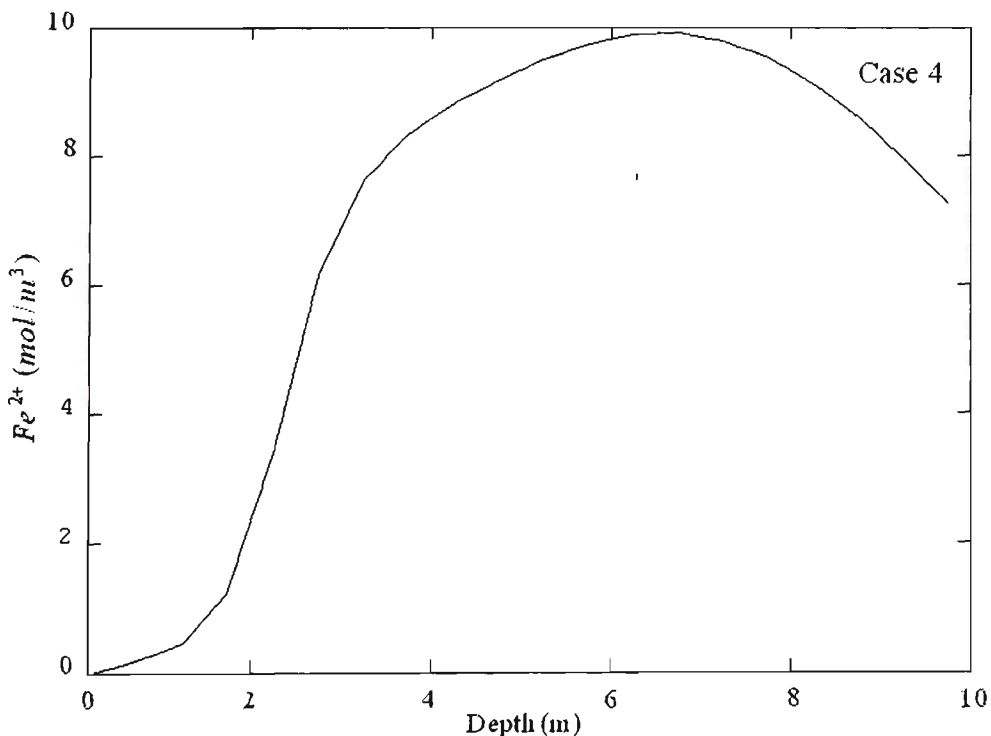


Figure 8.10. Ferrous iron concentration vs. depth for a 5-year simulation.

Figure 8.11 shows the ferric iron concentration versus the depth of the spoil profile after five years of the simulation. The concentration of ferric iron increased sharply in the zone between the spoil surface and depth of 2 m where oxygen is present in the pore space of the spoil and the bacteria are also available. In the zone between 2 m and 3 m depth the ferric concentration decreased rapidly. Below this depth the ferric concentration decreased non-linearly and reached zero to a depth of approximately 5 m because of lower oxygen concentration and less bacterial activity.

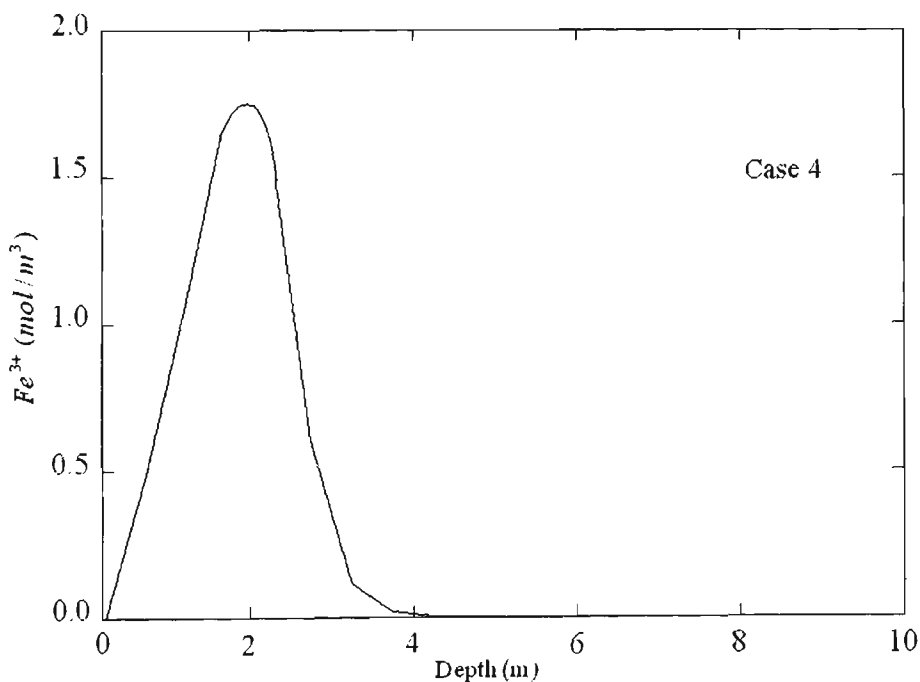


Figure 8.11. Ferric iron concentration as a function of depth over a 5 year period.

Figure 8.12 shows the  $pH$  of the solution as a function of depth over a 5-year simulation. It can be seen that  $pH$  decreased from 5 to about 3.5 in the zone between the spoil surface and depth of 0.5 m where oxygen is readily available. The  $pH$  decreased again at a steady rate from 3.5 to 3 in the zone between 0.5 m and 2.5 m. Because of in this zone oxygen concentration decreased sharply and also some hydrogen ions were consumed due to the bacterial activity. At depths below 2.5 m  $pH$  increased steadily. In Case 1 where the  $H^+$  -

spoil interaction was not incorporated, solution  $pH$  dropped to 2 after 5 years of the simulation. But in Case 4 where the interaction between spoil and  $H^+$  is allowed to take place, the  $pH$  value did not drop below 3 at any point of the spoil profile due to the neutralisation of acid, which in turn enhanced the precipitation and removal of ferric iron from the solution phase.

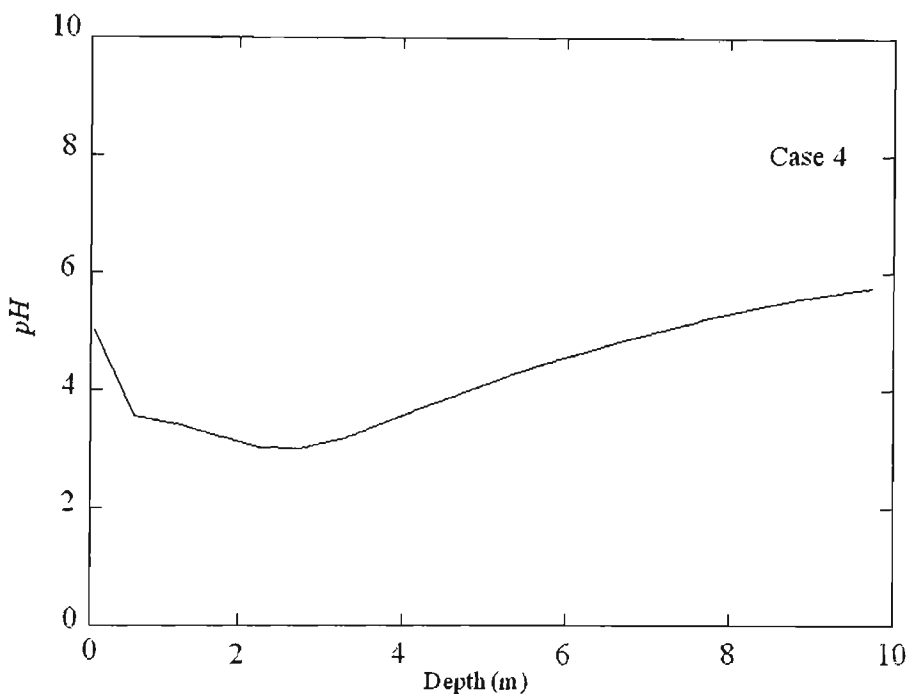


Figure 8.12.  $pH$  as a function of depth over a 5 year period.

Figure 8.13 shows sulphate concentration versus depth after 5 years of the oxidation reaction. As the figure shows the sulphate concentration increases exponentially from  $50 \text{ mol/m}^3$  to about  $56.2 \text{ mol/m}^3$  to a depth of 1.75 m and increases sharply to a depth of 2.75 m. At this depth the sulphate concentration is about  $63 \text{ mol/m}^3$ . Below this depth the sulphate concentration again increases gradually to a depth of 6.5 m, where it reaches about  $70 \text{ mol/m}^3$ . Below this depth it decreases steadily.

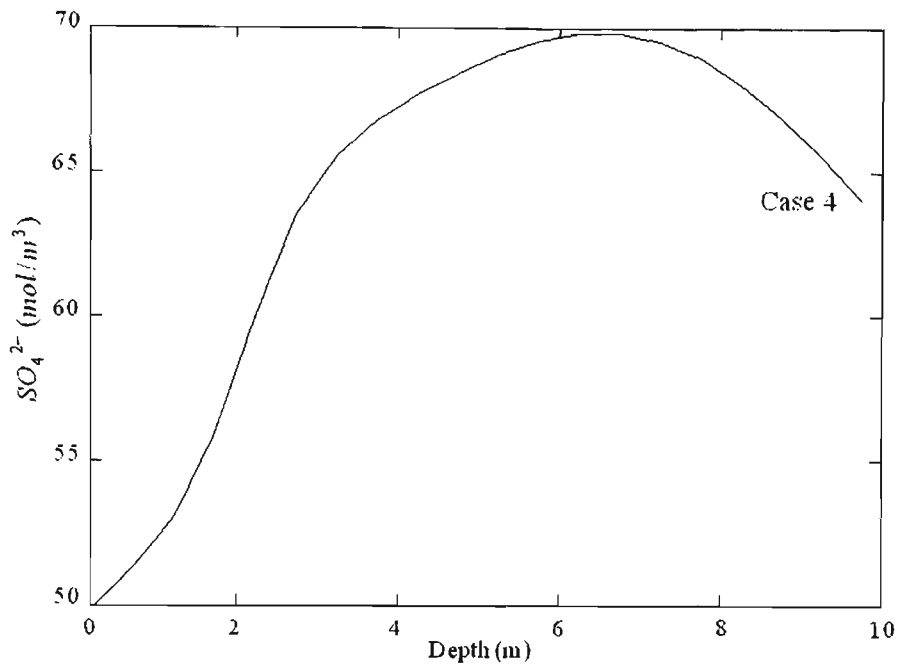


Figure 8.13.  $SO_4^{2-}$  concentration as a function of depth over a 5 year period.

Figure 8.14 shows the total iron-discharging rate as a function of time predicted in the water leaving the spoil profile for Cases 3 and 4. A comparison was made with those results predicted by the POLS model (dots). The iron-leaching rate showed a similar pattern with time for both cases and the maximum rate occurred between 1750 to 2100 days. As Figure 8.14 shows, the leaching rate in Case 3 is greater than in Case 4. This is because in Case 3 the effective diffusion coefficient is four times greater than that in Case 4.

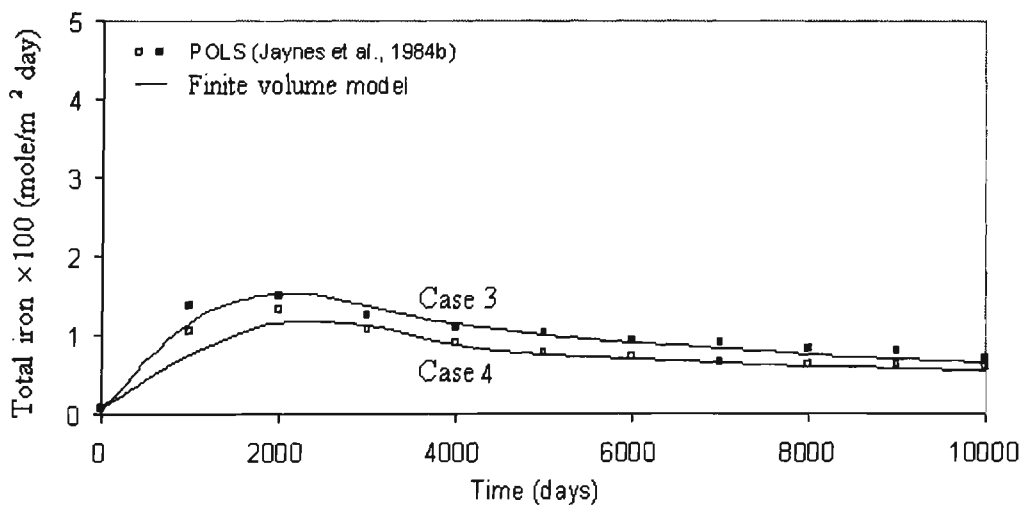


Figure 8.14. Total iron leaching rate vs. time in outlet boundary for Cases 3 and 4.

## 8.6 Conclusions

A numerical model using the PHOENICS package is presented for simulation of long-term pyrite oxidation within the spoil of an open cut coalmine. Oxygen penetrated from the spoil surface to the reaction site by the mechanism of diffusion. The heat transfer was analysed using a simple enthalpy model. In this study the following conclusions were made:

- Gaseous diffusion process is an important source for supplying oxygen to the reaction site.
- Both oxygen and ferric iron produced by bacterially mediated oxidation of ferrous iron participate in the oxidation of pyrite.
- The shrinking-core model can reasonably describe the pyrite oxidation process.
- A comprehensive model of pyrite oxidation and subsequent leaching of pollutants should incorporate the acid neutralisation reaction, ion exchange process as well as the effects of complexation and precipitation reactions for ferric iron.
- It was found that a model of pyrite oxidation in the backfilled site of an open cut mine should take into consideration the role of iron oxidising bacteria.
- In the absence of bacteria, oxygen is the only important oxidant of pyrite and the oxidation rate is highly dependent on the effective diffusion coefficient.
- The model developed here provides a useful tool for evaluating the efficiency of a rehabilitation plan to reduce pollutant potential.
- This model in the future should further consider the role of sulphate reduction bacteria where they are active.

## **CHAPTER NINE**

# **TRANSPORTATION OF PYRITE OXIDATION PRODUCTS THROUGH GROUNDWATER FLOW SYSTEMS**

## CHAPTER NINE

### TRANSPORTATION OF PYRITE OXIDATION PRODUCTS THROUGH GROUNDWATER FLOW SYSTEMS

#### 9.1 Introduction

In studying groundwater pollution, it is important to understand the factors which govern the transport of contaminants contained in groundwater. It is well recognised that these solutes participate in several physical, chemical and biological transformation processes during the course of their movement. These processes should be taken into consideration in the development of the transport models. Knowledge of mass transport in porous media is important in site remediation activities. The processes governing the migration of contaminants can be considered in terms of transport processes and attenuation processes. The transport processes can be mathematically expressed by equations based on flow laws. These equations can be incorporated into a mass balance equation with those processes causing the attenuation of the contaminants. This yields the general governing partial differential equation for contaminant transport. The starting point for any formulation for contaminant transport in porous media is the application of the mass conservation principle. This principle applied to contaminants in a control volume of porous media reduces to:

$$\begin{aligned} &(\text{mass inflow rate}) - (\text{mass outflow rate}) \pm (\text{rate of mass production or consumption}) = \\ &(\text{rate of mass accumulation}) \end{aligned}$$

This conservation equation is described in terms of mass per unit time. There are two major processes for contaminant transport. Advection process is the migration of the

contaminant in the flowing groundwater. Dispersion refers to mixing and spreading of the contaminant within the groundwater system.

The basic mechanisms of mass transport are given in Appendix D.

## 9.2 Transport equation

The basic partial differential equation describing the transport of dissolved species has been presented by several investigators (Rubin and James, 1973; Freeze and Cherry, 1979; Jennings, et al., 1982; and Domenico and Schwartz, 1990). For the aqueous part of component  $i$ , the governing equation is given as:

$$\frac{\partial(\phi C_i)}{\partial t} + \frac{\partial(\rho_b \bar{C}_i)}{\partial t} = \frac{\partial}{\partial x_j} \left( D_{jk} \frac{\partial C_i}{\partial x_k} \right) - \frac{\partial}{\partial x_j} (q_j C_i) + q_{re} C_i \pm S \quad (9.1)$$

$$i = 1, 2, \dots, n_c$$

In the present work  $q_i$ ,  $\phi$ ,  $\rho_b$  and  $D$  are assumed to be constant, hence Equation 9.1 reduces to:

$$\phi \frac{\partial C_i}{\partial t} + \rho_b \frac{\partial \bar{C}_i}{\partial t} = D \frac{\partial^2 C_i}{\partial x_j^2} - q_j \frac{\partial C_i}{\partial x_j} + q_{re} C_i \pm S \quad (9.2)$$

$$i = 1, 2, \dots, n_c$$

where,

$t$  = time (s);

$C_i$  = concentration of dissolved species ( $mol/m^3$ );

$x_j$  = Cartesian coordinates (m);

$\bar{C}_i$  = concentration of the adsorbed form of species  $i$  of dry porous medium ( $mol/Kg$ );

$\rho_b$  = bulk density of the medium ( $Kg/m^3$ );

$D_{jk}$  = hydrodynamic dispersion tensor ( $m^2 / s$ ), which in turn depends on the longitudinal and transverse dispersivities  $\alpha_L$  and  $\alpha_T$  ( $m$ ) and the molecular diffusion coefficient

$D_{dif}$ ;

$q_{re}$  = surface recharge ( $m / s$ );

$S$  = sink and source terms representing the changes in aqueous component concentrations due to the chemical reactions;

$q_j$  = vector components of the pore fluid specific discharge ( $m / s$ ) and it is related to the

pore water velocity by  $v_j = \frac{q_j}{\phi}$ .

where,

$\phi$  = porosity.

A summary of the type of chemical reactions and the law of mass action are given in Appendix E.

### 9.3 Boundary and initial conditions

A complete set of boundary conditions and an initial condition must be specified for each dissolved species to take into account for the effects of the outside of the system.

The following boundary conditions were specified as follows:

#### (i) *Initial condition*

$$C(x,0) = C_{init} \quad x \geq 0$$

An initial condition describes the distribution of a dissolved species within the domain when the simulation begins ( $t = 0$ ).

#### (ii) *The variable flux boundary condition*

In this kind of boundary condition, a constant flux with constant input concentration of the aqueous species can be specified along a boundary as given below:

$$q = C(0, t) = q_{re} C_0, \quad t > 0$$

**(iii) Fixed boundary condition**

A fixed concentration boundary condition may also be specified instead of the flux boundary condition:

$$C(0, t) = C_0, \quad t > 0$$

**(iv) Outflow boundary condition**

Another boundary condition may be specified at the outflow boundary:

$$C(\infty, t) = C_{init}, \quad t \geq 0$$

**9.4 Analytical models**

Analytical models have been shown to be powerful tools for analysing solute transport processes (Domenico and Schwartz, 1990). In cases where a numerical model is not applied, in particular in the early phases of a project when it is often not necessary to use a comprehensive computer model, it may be appropriate to use a mathematical equation (Watson and Burnett, 1993). The solution of Equation 9.2 taking into account the Freundlich isotherm for linear ion exchange is given as follows (Reddi and Inyang, 2000):

$$C(x, t) = C_{init} + \frac{1}{2}(C_0 - C_{init}) \left\{ \operatorname{erfc} \left( \frac{R_f x - V_x t}{2\sqrt{R_f D_x t}} \right) + \exp \left( \frac{V_x x}{D_x} \right) \operatorname{erfc} \left( \frac{R_f x + V_x t}{2\sqrt{R_f D_x t}} \right) \right\} \quad (9.3)$$

where,

$D_x$  = hydrodynamic dispersion coefficient in  $x$  direction ( $m^2 / s$ );

$R_f$  = retardation factor (see section 9.5);

$V_x$  =  $x$ -direction velocity ( $m / s$ );

$x$  = distance in the  $x$ -direction ( $m$ );

$t = \text{time (s)}$ ;

$C_0 = \text{source concentration (mol/m}^3\text{)}$ ;

$C_{ini} = \text{initial concentration (mol/m}^3\text{)}$ ;

$C(x,t) = \text{solute concentration at any point and time (mol/m}^3\text{)}$ .

Equation 9.3 calculates the concentration  $C$ , at distance  $x$ , from the source at concentration  $C_0$ , at the time  $t$ , and at initial concentration  $C_i$ .

In Equation 9.3 'erfc' is referred to the complement of the error function, 'erf' which is given in terms of its argument  $\beta$  (Appendix F).

Equation 9.3 was used to verify the results of the numerical model for one-dimensional advection-dispersion with linear ion-exchange reactions transport of  $Na^+$  and  $Cl^-$  species.

It may be noted that Equation 9.3 can be reduced to Equation 9.4 when the retardation factor  $R_f$  is equal to 1 and the initial concentration is 0 (Fetter, 1988).

$$C(x,t) = \frac{C_0}{2} \left\{ \operatorname{erfc} \left( \frac{x - V_x t}{2\sqrt{D_x t}} \right) + \exp \left( \frac{V_x x}{D_x} \right) \operatorname{erfc} \left( \frac{x + V_x t}{2\sqrt{D_x t}} \right) \right\} \quad (9.4)$$

In this case the dissolved species are non-reactive and distribution coefficient (see Section 9.5) is zero (Reddi and Inyang, 2000).

## 9.5 Reaction on solid surfaces

Reactions between dissolved species and the surfaces of porous medium solids play an important role in the transport processes (Domenico and Schwartz, 1990). Accurate predictions of the transport of sorbing chemical species can be often based on the knowledge of the equilibrium sorption reactions of the solutes. The sorption of mass

from solution is considered to be an important case of a heterogeneous equilibrium reaction (Domenico and Schwartz, 1990). The rate law (Rubin and James, 1973; Valocchi et al., 1981; Domenico and Schwartz, 1990) can be given as follows:

$$r_s = \frac{\partial \bar{C}_i}{\partial t} \quad (9.5)$$

where,

$\bar{C}_i$  = concentration of the species  $i$  in the solid phase.

Taking the linear Freundlich isotherm (for more information, the reader is referred to Grove, 1977; Valocchi et al., 1981; Domenico and Schwartz, 1990; Sheng and Smith, 1997; Reddi and Inyang, 2000) and incorporating it into the transport Equation 9.2 gives:

$$\left(1 + \frac{\rho_b}{\phi} K_d\right) \frac{\partial C_i}{\partial t} = D_x \frac{\partial^2 C_i}{\partial x^2} - v_x \frac{\partial C_i}{\partial x} \quad (9.6)$$

where,

$K_d$  = distribution coefficient (the slope of the linear sorption isotherm).

The quantity in parenthesis on the left-hand side is a constant and is called the Retardation Factor,  $R_f$ . Thus Equation 9.6 becomes:

$$R_f \frac{\partial C_i}{\partial t} = D_x \frac{\partial^2 C_i}{\partial x^2} - v_x \frac{\partial C_i}{\partial x} \quad (9.7)$$

The retardation factor thus describes the average amount of retardation in the transport of the aqueous species relative to the average pore space velocity (Grove, 1977). In other words, the retardation factor causes a decrease in the values of the transport characteristics such as hydrodynamic dispersion coefficient  $D$  and pore water velocity  $v$  (Domenico and Schwartz, 1990).

### 9.5.1 Ion exchange reactions

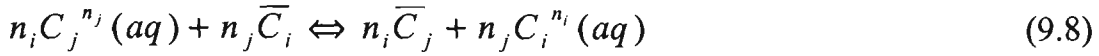
Ion exchange is a special case of competitive sorption which occurs due to the substitution of cations in solids (Reddi and Inyang, 2000). This reaction is due to the electrostatic attraction between charged cations in solution and the surface charge on clay minerals. Clay minerals have an important fixed negative surface charge (Domenico and Schwartz, 1990). Cations binding to the exchange sites balance the negative surface charges of the mineral. These cations may exchange with other cations present in solution. Cation exchange reactions may neutralise the  $pH$  of the solution by the exchange of acidic cations such as  $H^+$  and  $Al^{3+}$  against basic cations such as  $Ca^{2+}$  and  $Mg^{2+}$ .

In this thesis, the method presented for treating ion exchange reactions is similar to that employed by Rubin and James (1973). The ion exchange reaction is controlled by local equilibria. This assumption is applicable only when the ion exchange processes are relatively fast in comparison with the physical transport processes (Rubin and James, 1973; and Jennings et al., 1982).

The accuracy of the model was verified with the analytical solution incorporating a simplified linear sorption. Furthermore, the data from a field test presented by Valocchi et al. (1981) and two of the five computed examples presented by Rubin and James (1973) were used to validate the numerical model for non-linear ion exchange processes. These are exemplified in Case H (Rubin and James, 1973, Fig.5, page1349) and also in the example involving a ternary 1:1:1 exchange (Rubin and James, 1973, Fig.7, page1351). The model was then extended to the case of more complicated equilibrium-controlled ion exchange reactions, when close agreement was achieved between the present model and field measurements as well as those results of the model

presented by Rubin and James (1973). The present model has been implemented in the general-purpose PHOENICS computational fluid dynamic code.

The ion exchange reaction can be written as:



where,

$n$  = valence of the ion;

$\bar{C}$  = sorbed component.

The mass action equation (Fetter, 1988; and Schnoor, 1996) for the above reaction reduces to:

$$K_i^j = \left( \frac{\bar{C}_j}{C_j} \right)^{n_i} \left( \frac{C_i}{\bar{C}_i} \right)^{n_j}, \quad i \neq j \quad i, j = 1, 2, \dots, N \quad (9.9)$$

where,

$K_i^j$  = ion exchange selectivity coefficient, assumed to be constant. In fact,  $K_i^j$  is not constant and is a function of the sorbed phase concentrations (Valocchi, et al., 1981).

The method for derivation of the operational partial differential equations for ion-exchanging transport is given in Appendix G.

## 9.6 PHOENICS setting for ion exchange reactions

This section explains how the PHOENICS package was used to set up the model of ion exchanging solute transport. A one-dimensional grid was constructed for the simulation purpose.

In the case of linear exchange, the diffusion and convection terms are easily identified by comparing Equations 9.7 and the PHOENICS governing equation (Equation 7.3,

Chapter 7, Page 209). A slight modification is necessary for the transient term to change the transport equation to a “PHOENICS equivalent” format. The rearrangement of Equation 9.7 yields the following equation:

$$\frac{\partial C_i}{\partial t} = D_x \frac{\partial^2 C_i}{\partial x^2} - v_x \frac{\partial C_i}{\partial x} + (1 - R_f) \frac{\partial C_i}{\partial t} \quad (9.10)$$

where, terms in  $\partial C_i / \partial t$  have been added to both sides. The last term in Equation 9.10 identifies an additional source term, which was evaluated by FORTRAN 99 subroutines located in GROUP 13 of GROUND. The settings for this source in Q1-file and GROUND subroutine are provided in Table 9.1:

Table 9.1. Settings in the Q1-file and GROUND subroutine for linear ion exchange reactions.

Setting in Q1-file:	
PATCH (C1SOUR ,VOLUME,1,NX,1,NY,1,NZ,1,LSTEP)	
COVAL (C1SOUR ,C1 ,GRND2 ,GRND2 )	
<p>The FORTRAN coding for this source in GROUP 13 of GROUND routine:</p> <p>C--- GROUP 13. Boundary conditions and special sources:</p> <p>C---- SECTION 3 ---- coefficient = GRND2  IF(INDVAR.EQ.C1)THEN  IF(NPATCH.EQ.'C1SOUR')THEN</p> <p>C--- Add source <math>(R_f - 1) (C_{old} - C_p) / \partial t</math></p> <p>C----- COefficient is <math>(R_f - 1) / \partial t</math></p> <p>LOCO = LOF(CO)  DO 13201 IY = IYF, IYL  DO 13201 IX = IXF, IXL  ICELL = IY + (IX-1)*NY</p> <p>C----- <math>R_f = RG(1)</math></p> <p>GRETRD = RG(1)  F(LOCO+ICELL) = (GRETRD-1)/DT</p> <p>13201 CONTINUE  ENDIF  ENDIF  RETURN</p>	<p>C---- SECTION 14 ----- value = GRND2  IF(INDVAR.EQ.C1)THEN  IF(NPATCH.EQ.'C1SOUR')THEN</p> <p>C----- VALue is: <math>C_{old}</math></p> <p>L0VAL = LOF(VAL)  DO 13131 IY = IYF, IYL  DO 13131 IX = IXF, IXL  ICELL = IY + (IX-1)*NY  F(L0VAL+ICELL)= VARYX(OLD(C1))</p> <p>13131 CONTINUE  ENDIF  ENDIF  RETURN</p>

**9.6.1 Additional source terms due to the non-linear quaternary heterovalent ion exchange reaction, i.e.**

$$(n_c = 4, P_1 : P_2 : P_3 : P_4 = 1 : 2 : 2 : 2 \quad C_1 = Na, \quad C_2 = Mg, \quad C_3 = Ca, \quad C_4 = Fe)$$

The transport equations governing non-linear ion exchanging solutes with  $n_c = 4$  and  $P_1 : P_2 : P_3 : P_4 = 1 : 2 : 2 : 2$  contain additional source terms which were calculated during each iteration by FORTRAN 99 code in the GROUND file. Table 9.2 outlines how each source term was activated using settings made in the Q1-file.

Table 9.2. Settings in the Q1-file to activate each source term, with CO and VAL referring to the corresponding coefficient and value settings within PHOENICS.

Solute	Source Term	PHOENICS Variable	PATCH Name	PATCH Type	Coefficient CO	Value VAL
$Na^+$	$(1-\phi) \frac{\partial [Na^+]}{\partial t}$	C19	NAWCEX1	VOLUME	GRND	GRND
	$-\rho \frac{f_{11}}{g_1} \frac{\partial [Na^+]}{\partial t}$		NAF11E2	VOLUME	GRND	GRND
	$\rho \frac{f_{12}}{g_1} \frac{\partial [Mg^{2+}]}{\partial t}$		NAF12E3	VOLUME	FIXFLU	GRND
	$\rho \frac{f_{13}}{g_1} \frac{\partial [Ca^{2+}]}{\partial t}$		NAF13E4	VOLUME	FIXFLU	GRND
	$\rho \frac{f_{14}}{g_1} \frac{\partial [Fe^{2+}]}{\partial t}$		NAF14E5	VOLUME	FIXFLU	GRND
$Mg^{2+}$	$(1-\phi) \frac{\partial [Mg^{2+}]}{\partial t}$	C17	MGWCEX1	VOLUME	GRND	GRND
	$-\rho \frac{f_{22}}{g_2} \frac{\partial [Mg^{2+}]}{\partial t}$		MGF22E2	VOLUME	GRND	GRND
	$\rho \frac{f_{21}}{g_2} \frac{\partial [Na^+]}{\partial t}$		MGF21E3	VOLUME	FIXFLU	GRND
	$\rho \frac{f_{23}}{g_2} \frac{\partial [Ca^{2+}]}{\partial t}$		MGF23E4	VOLUME	FIXFLU	GRND
	$\rho \frac{f_{24}}{g_2} \frac{\partial [Fe^{2+}]}{\partial t}$		MGF24E5	VOLUME	FIXFLU	GRND

Table 9.2. (Continued).

Solute	Source Term	PHOENICS Variable	PATCH Name	PATCH Type	Coefficient CO	Value VAL
$Ca^{2+}$	$(1-\phi)\frac{\partial[Ca^{2+}]}{\partial t}$	C15	CAWCEX1	VOLUME	GRND	GRND
	$-\rho\frac{f_{33}}{g_3}\frac{\partial[Ca^{2+}]}{\partial t}$		CAF33X2	VOLUME	GRND	GRND
	$\rho\frac{f_{31}}{g_3}\frac{\partial[Na^+]}{\partial t}$		CAF31X3	VOLUME	FIXFLU	GRND
	$\rho\frac{f_{32}}{g_3}\frac{\partial[Mg^{2+}]}{\partial t}$		CAF32X4	VOLUME	FIXFLU	GRND
	$\rho\frac{f_{34}}{g_3}\frac{\partial[Fe^{2+}]}{\partial t}$		CAF34X5	VOLUME	FIXFLU	GRND
$Fe^{2+}$	$(1-\phi)\frac{\partial[Fe^{2+}]}{\partial t}$	C1	IR2WCEX1	VOLUME	GRND	GRND
	$-\rho\frac{f_{44}}{g_4}\frac{\partial[Fe^{2+}]}{\partial t}$		IR2F44X2	VOLUME	GRND	GRND
	$\rho\frac{f_{41}}{g_4}\frac{\partial[Na^+]}{\partial t}$		IR2F41X3	VOLUME	FIXFLU	GRND
	$\rho\frac{f_{42}}{g_4}\frac{\partial[Mg^{2+}]}{\partial t}$		IR2F42X4	VOLUME	FIXFLU	GRND
	$\rho\frac{f_{43}}{g_4}\frac{\partial[Ca^{2+}]}{\partial t}$		IR2F43X5	VOLUME	FIXFLU	GRND

## 9.7 Model verification

### 9.7.1 One-dimensional advection-dispersion with linear ion-exchange reaction transport model

The present numerical model of ion-exchange processes has been checked by comparison with analytical solutions for one-dimensional advection-dispersion with the linear ion exchange reaction transport model. In the following example (Parkhurst and Appelo, 2002) a 130 m flow tube contains water with zero initial concentration. The concentration of the displacing solution is 1 *mmol/Kgw* and the pore-water flow

velocity ( $v$ ) is  $4.75 \times 10^{-7} \text{ m/s}$  (15 m/year). The dispersivity ( $\alpha_L$ ) is 5 m, and the effective diffusion coefficient ( $D_{dif}$ ) is  $0 \text{ m}^2/\text{s}$ . The simulation time is 4 years. Two chemical species are considered in the model. The first is  $Cl^-$  with a retardation factor of 1 and the other is  $Na^+$  with a retardation factor of 2.5. The hydrodynamic dispersion coefficient reduces to:  $D_x = D_{dif} + \alpha_L v = 0 + 5 \times 4.75 \times 10^{-7} = 2.4 \times 10^{-6} \text{ m}^2/\text{s}$ .

This example was first solved using analytical Equation 9.3 for both species  $Cl^-$  and  $Na^+$ . To solve the problem numerically, the PHOENICS code was modified to solve Equation 9.7. A one-dimensional coordinate system with a uniform grid spacing consisting of 70 cells was constructed. The  $x$ -direction was used to simulate horizontal flow. Fifteen (15) time steps were assigned for the simulation. A first-type or Dirichlet boundary condition was assigned at the inlet ( $x = 0$ ), i.e.  $C(0, t) = 1 \text{ mmol/Kgw}$ . An initial value of 0 was maintained at  $t = 0$ . A value of 0 was specified at the outlet boundary, i.e.  $C(\infty, t) = 0$

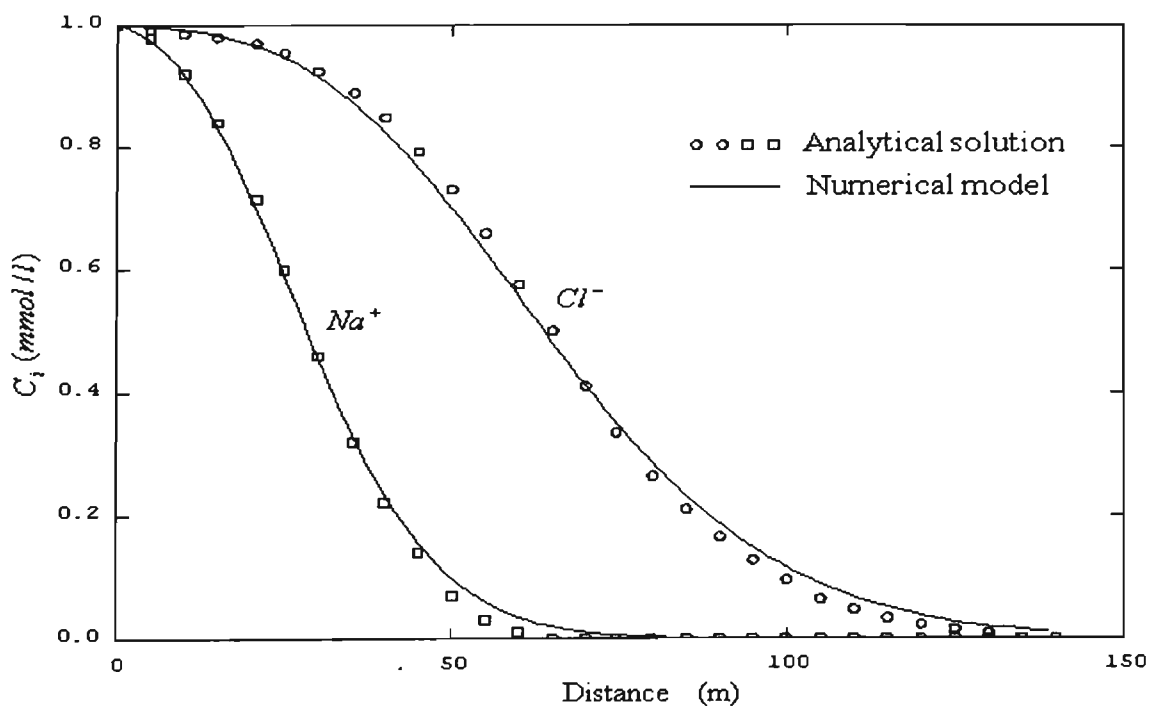


Figure 9.1. Comparison of numerical modelling and analytical solution for one-dimensional advection-dispersion with linear ion-exchange transport of  $Na^+$  and  $Cl^-$ .

Figure 9.1 shows the comparison of the numerical modelling results with those obtained using analytical solutions for one-dimensional advection-dispersion with linear ion-exchange reactions resulting in the transport of species  $Cl^-$  and  $Na^+$ . The close agreement between the simulated and calculated profiles illustrated in Figure 9.1 indicates that PHOENICS can reliably simulate solute transport problems in porous media (average error 12.65 %)

### 9.7.2 Nonlinear ion exchange model verification

Three examples are described below to verify the capabilities of the finite volume modelling of the ion exchange reaction. In the first one, the accuracy of the finite volume model using PHOENICS for the simulation of ternary heterovalent exchange reactions between the ions  $Mg^{2+}$ ,  $Ca^{2+}$ , and  $Na^+$  was assessed using field measurement data presented by Valocchi et al. (1981). The second and third examples are taken from Rubin and James (1973).

The data used for the simulations correspond to those of real systems. In these examples, it was assumed that the flow system is saturated and the water flow is in a steady state. Furthermore, transport of species is influenced by hydrodynamic dispersion as well as by equilibrium-controlled ion exchange. It was also assumed that the ion exchange equilibrium is the only chemical reaction present in the simulations. After verification of the finite volume model with these examples, the model was then extended to the case of the more complex ion exchange of  $Mg^{2+}$ ,  $Ca^{2+}$ ,  $Fe^{2+}$  and  $Na^+$ .

#### (a) Verification of the ion-exchanging reactive transport model with field data

To check the capability of the numerical model using the PHOENICS package to deal with chemically reactive transport phenomena, the model was used to simulate a field

experiment in the Palo Alto Baylands, California involving nonlinear ion exchange reactions. For this simulation field data were taken from Valacchi et al. (1981). In this field problem, a municipal effluent was injected into a shallow alluvial aquifer and the breakthrough curves of the major anions and cations were plotted based on the monitored data at an observation well S23, 16 metres from the injection well. The principal chemical process involved in the transport is the ternary heterovalent ion exchange  $Na^+$ ,  $Ca^{2+}$ , and  $Mg^{2+}$ .

A one-dimensional simulation was performed for this process. A 16 metre horizontal profile was divided into 50 equal sized control volumes. The effluent water was injected at an average rate of  $21 m^3 / hr$  and the aquifer had a thickness of 2 metres. The initial and injection water compositions as well as the selectivity coefficients are listed in Table 9.3. As detailed by Valacchi et al. (1981), the bulk density of the medium was  $1875 g/l$ , the cation exchange capacity was  $0.1 meq/gr$  and the porosity was 25 %. A hydrodynamic dispersion coefficient of  $4 \times 10^{-4} m^2 / s$  was selected. For this simulation, groundwater velocity was calculated using the following equation:

$$v = \frac{Q}{2\pi b \phi r} \quad (9.11)$$

where,

$Q$  = rate of injected water into well at source point ( $m^3 / s$ );

$b$  = thickness of the aquifer ( $m$ );

$\phi$  = porosity (dimensionless);

$r$  = distance between injection well and the observation well ( $m$ ).

Figures 9.2 compare the field and the simulated breakthrough curves for  $Ca^{2+}$  and  $Mg^{2+}$  at well S23. The model predictions some what agree with the field measurements (average error 13.21 %).

Table 9.3. Selectivity coefficients initial and source concentrations for a ternary heterovalent ion exchange problem (Valocchi et al., 1981).

Chemical component	Aqueous concentration in injected well (meq / m <sup>3</sup> )	Initial concentration (meq / m <sup>3</sup> )
<i>Cl</i> <sup>-</sup>	9.03×10 <sup>3</sup>	1.61×10 <sup>5</sup>
<i>Na</i> <sup>+</sup>	9.40×10 <sup>3</sup>	8.66×10 <sup>4</sup>
<i>Mg</i> <sup>2+</sup>	4.94×10 <sup>2</sup>	1.79×10 <sup>4</sup>
<i>Ca</i> <sup>2+</sup>	2.12×10 <sup>3</sup>	1.11×10 <sup>4</sup>

Chemical reaction	Selectivity coefficient
$Mg^{2+} + 2\bar{Na} \leftrightarrow 2Na^+ + \bar{Mg}, \left( \frac{\bar{Na}}{Na^+} \right)^2 \left( \frac{Mg^{2+}}{\bar{Mg}} \right)$	$K_2^1 = 0.33$
$Ca^{2+} + 2\bar{Na} \leftrightarrow 2Na^+ + \bar{Ca}, \left( \frac{\bar{Na}}{Na^+} \right)^2 \left( \frac{Ca^{2+}}{\bar{Ca}} \right)$	$K_3^1 = 0.59$

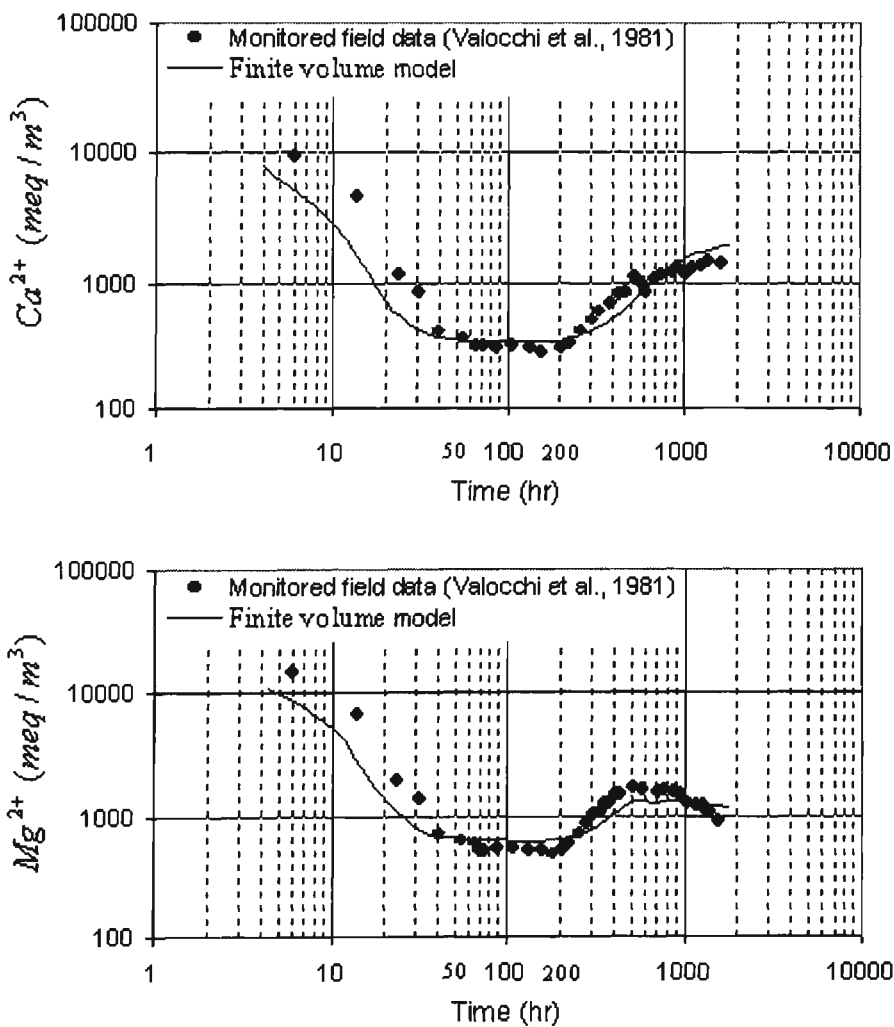


Figure 9.2. Comparison of the field observations (quoted in Valocchi et al., 1981) and simulation results for breakthrough curves of  $Ca^{2+}$  and  $Mg^{2+}$ .

Using Equation 9.11 the groundwater velocity reduces to  $1.16 \times 10^{-4} \text{ m/s}$ . The elapsed times were calculated from the rate of water injection. A longitudinal dispersivity of 1.5  $m$  was selected.

As Figure 9.2 shows from the beginning of the simulation to time about 55 hours,  $Ca^{2+}$  and  $Mg^{2+}$  concentrations decrease because the low concentrations of aqueous species in the injected water displace the high-concentrations in the groundwater. Between times 55 hours and 200 hours the solute concentrations remained to a level concentration. During this time period, the injected water and the solid material of porous medium reached an equilibrium. After that the ion exchange process retards the concentration profiles. Between times 200 and 1000 hours a concentration plateau occurred due to the competitive interactions between the  $Mg^{2+}$  and  $Ca^{2+}$ . Walter et al. (1994a) also used this field data to validate their own model and similar observations were obtained.

#### **(b) Leaching of a sodic soil - binary heterovalent ion exchange**

In the second example, the ion exchange reaction taking place involves two ions of different valence,  $Na^+$  (monovalent,  $P_1 = 1$ ) and  $Ca^{2+}$  (divalent,  $P_2 = 2$ ). The influent contains high concentrations of  $Ca$ , and gypsum is not present in the soil. The initial and the influent concentrations, selectivity coefficient as well as other parameters are provided in Table 9.4.

To solve this example numerically using PHOENICS, a one-dimensional non-uniform grid (power/ratio was equal to 1.4) was constructed with 150 cells. The number of time steps used was 14 and the time-steps were set via a power-law expansion (power was equal to 1.0). The y-direction was used to simulate vertical flow. A total iteration of 500 was assigned to the simulation.

Table 9.4. Ion exchange parameters for a binary heterovalent exchange reaction (after Rubin and James, 1973).

Reaction	Selectivity coefficient
$Ca^{2+} + 2\bar{Na} \Leftrightarrow 2Na^+ + \bar{Ca}$ $K_2^1 = \left( \frac{\bar{Na}}{Na^+} \right)^2 \left( \frac{Ca^{2+}}{\bar{Ca}} \right)$	$K_2^1 = 0.078$
where,  $P_1 : P_2 := 1 : 2$ , Binary exchange $C_1 = Na$ , $C_2 = Ca$ , $\bar{C}_T = 0.434$ $C_{1(inf lux)} = 0.002$ , $C_{2(inf lux)} = 0.0072$ , $C_{T(inf lux)} = 0.0092$ $C_{1(init)} = 0.028$ , $C_{2(init)} = 0.002$ , $C_{T(init)} = 0.03$ $\phi = 0.54$ , $\rho_b = 1.2$ , $q = 1.5855 \times 10^{-7} m/s$ , $D = 1.5855 \times 10^{-8} m^2/s$	

The program was then run for different leaching durations of 14.6, 29.2 and 43.8 days. A comparison of the concentration profiles for the species  $Na^+$  and  $Ca^{2+}$  predicted by the model and those predicted by the Galerkin-finite element model of Rubin and James (1973) are shown in Figure 9.3 (average error 2.28 %).

Figure 9.3 shows that only the upper parts of the  $Na^+$  and  $Ca^{2+}$  profiles are affected significantly by the ion exchange process. These effects are more pronounced with increased elapsed time. The lower parts of these profiles reflect more the original pore water concentration while the effects of influent concentrations are relatively very low.

### (c) Ternary, 1:1:1 ion exchange

The third example involves a ternary  $P_1 : P_2 : P_3 = 1 : 1 : 1$  exchange. In this case the values of  $C_T$  and solute composition in the influent is different from the background porous medium solution. Table 9.5 shows the background and the influent concentrations of the ions involved in the ion exchange reaction, selectivity coefficients and the properties of the system.

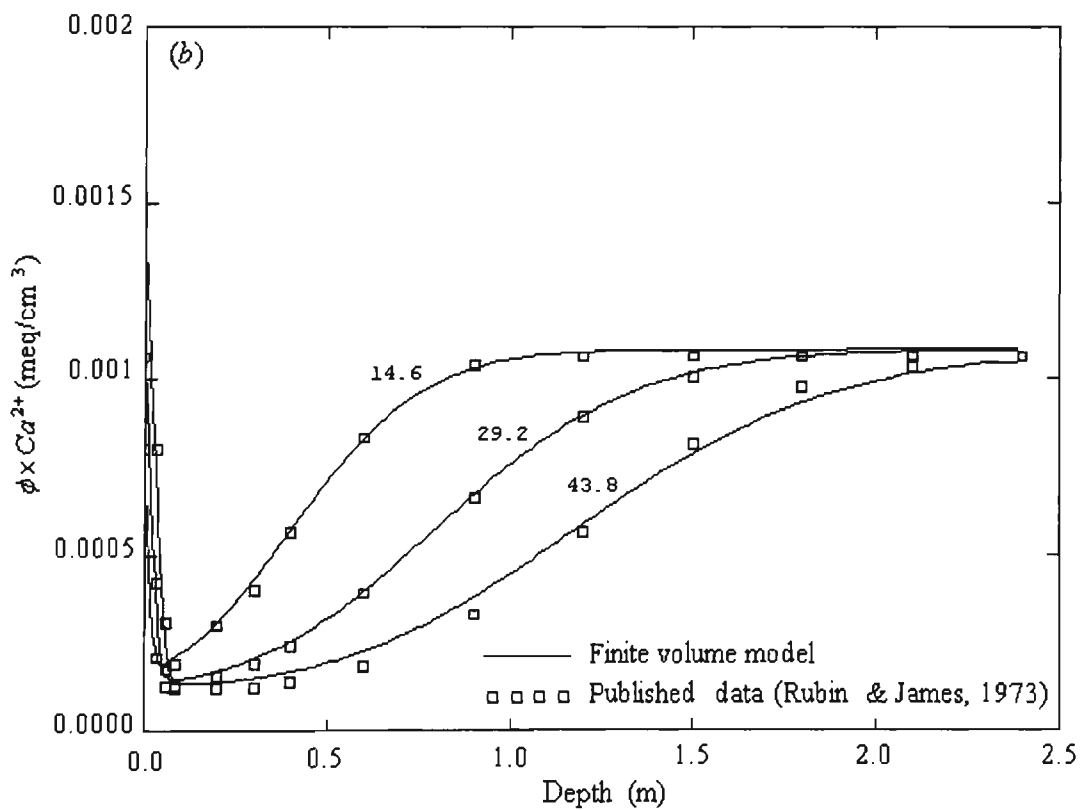
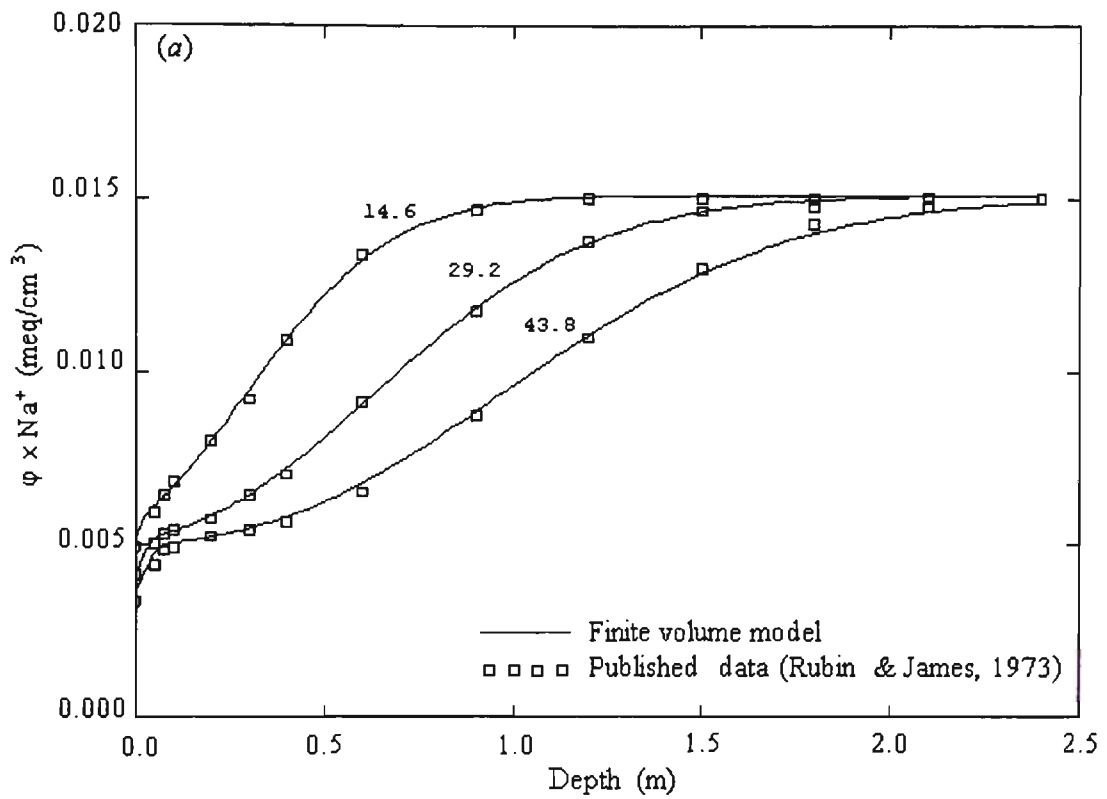


Figure 9.3. Changes in concentration profiles due to the leaching of a sodic soil. The numbers labelling the curves show leaching duration in days, comparison with published data (from Rubin and James, 1973). (a) Profiles for the dissolved sodium ions, (b) profiles for the dissolved calcium ions.

A one-dimensional non-uniform grid (power/ratio was equal to 1.4) was constructed with 150 cells to solve the problem numerically. Fourteen time steps were assigned with a power-law (power was equal to 1.0) distribution. The number of iterations was 500. A whole-field method (CHAM, 2000) was selected for the solution of the problem. Once again the y-direction was used to simulate vertical flow.

Table 9.5. Ion exchange reaction parameters for a ternary homovalent exchange (after Rubin and James, 1973).

Reaction	Selectivity coefficient
$C_2^+ + \bar{C}_1 \Leftrightarrow \bar{C}_2 + C_1^+$	$K_2^1 = 0.2$
$C_3^+ + \bar{C}_1 \Leftrightarrow \bar{C}_3 + C_1^+$	$K_3^1 = 25$
where,	
$\bar{C}_T = 0.026, \quad C_{T(\text{influx})} = 60 \text{ meq/l}, \quad C_{T(\text{init})} = 120 \text{ meq/l}$	
$(C_1/C_T)_{\text{influx}} = 1.0, \quad (C_2/C_T)_{\text{influx}} = 0.0, \quad (C_3/C_T)_{\text{influx}} = 0.0$	
$\frac{C_{1(\text{init})}}{C_{T(\text{influx})}} = 1.2, \quad \frac{C_{2(\text{init})}}{C_{T(\text{influx})}} = 0.6, \quad \frac{C_{3(\text{init})}}{C_{T(\text{influx})}} = 0.2$	
$\phi = 0.54, \quad \rho_b = 1.2, \quad q = 1.5855 \times 10^{-7} \text{ m/s}, \quad D = 1.5855 \times 10^{-8} \text{ m}^2/\text{s}, \quad t = 14.6 \text{ days}$	

Figure 9.4 shows a comparison of the concentration profiles for species  $C_1, C_2$  and  $C_3$  predicted by the finite volume model and those obtained by the finite element model developed by Rubin and James (1973) (average error 2.01 %).

The results predicted by the present model agreed closely with those predicted by the modelling results of Rubin and James (1973), suggesting that the finite volume model using PHOENICS package is able to accurately simulate the physical processes as well as the chemical reactions affecting the transport of the dissolved species.

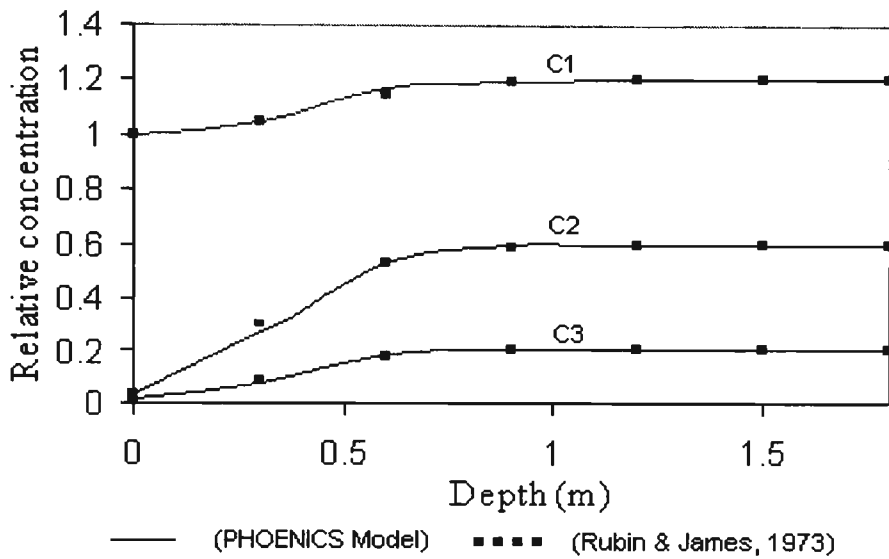


Figure 9.4. Concentration profiles resulting from 14.6 days of leaching of a soil with ternary, 1:1:1, non-linear ion exchange, comparison with published data (from Rubin and James, 1973).

**(d) Quaternary heterovalent ion exchange problem ( $P_1 : P_2 : P_3 : P_4 = 1 : 2 : 2 : 2$ )**

After validation of the finite volume model using analytical solutions, field data as well as a published numerical model, the model is now extended to a more case of a complicated exchange reaction in which species of  $Ca^{2+}$ ,  $Mg^{2+}$ ,  $Fe^{2+}$  and  $Na^+$  are involved in the ion exchange reaction. The background and influent concentrations of solute involved in the ion exchange reaction, selectivity coefficient and physical parameters of medium are given in Table 9.6.

A one-dimensional finite volume grid was constructed with 27 elements to simulate the above problem. The length of the model was 16 m. One hundred time steps with a power law distribution (power =1.5) were considered. A total iteration of 250 was assigned to the simulation. The model was run for different leaching durations of 60, 120, and 200 days. A grid distribution with geometric pressure was used with a

power/ratio of 1. An upwind differencing scheme was considered (see Chapter 7, Section 7.9.3, Page 221).

Table 9.6. Ion exchange reaction parameters for a quaternary heterovalent ion exchange problem (unpublished data).

Chemical reactions	Selectivity Coefficient
$Mg^{2+} + 2\bar{Na} \Leftrightarrow \bar{Mg} + 2Na^+$	$K_2^1 = 0.2$
$Ca^{2+} + 2\bar{Na} \Leftrightarrow \bar{Ca} + 2Na^+$	$K_3^1 = 0.1$
$Fe^{2+} + 2\bar{Na} \Leftrightarrow \bar{Fe} + 2Na^+$	$K_4^1 = 0.5$
<p>where,</p> <p><math>C_1 = Na, C_2 = Mg, C_3 = Ca, C_4 = Fe, \bar{C}_T = 0.1 meq/gr</math></p> <p><math>(C_1/C_T)_{inf lux} = 0.92, (C_2/C_T)_{inf lux} = 0.03, (C_3/C_T)_{inf lux} = 0.0, (C_4/C_T)_{inf lux} = 0.05</math></p> <p><math>\frac{C_{1(init)}}{C_{T(inf lux)}} = 1.05, \frac{C_{2(init)}}{C_{T(inf lux)}} = 0.2, \frac{C_{3(init)}}{C_{T(inf lux)}} = 0.3, \frac{C_{4(init)}}{C_{T(inf lux)}} = 0.45</math></p> <p><math>\phi = 0.35, \rho_b = 1.2 gr/cm^3, q = 1.0 \times 10^{-7} m/s, D = 8.0 \times 10^{-8} m^2/s</math></p>	

The concentration profiles for solutes  $Na^+, Ca^{2+}, Mg^{2+}$  as well as  $Fe^{2+}$  predicted by the finite volume model are shown in Figure 9.5 which shows that only the upper parts of the  $C_1, C_2, C_3$  and  $C_4$  concentration profiles are affected by the exchange reaction. The lower parts of the profiles reflect primarily the mixing between the less concentrated influent and the more concentrated background pore space fluid.

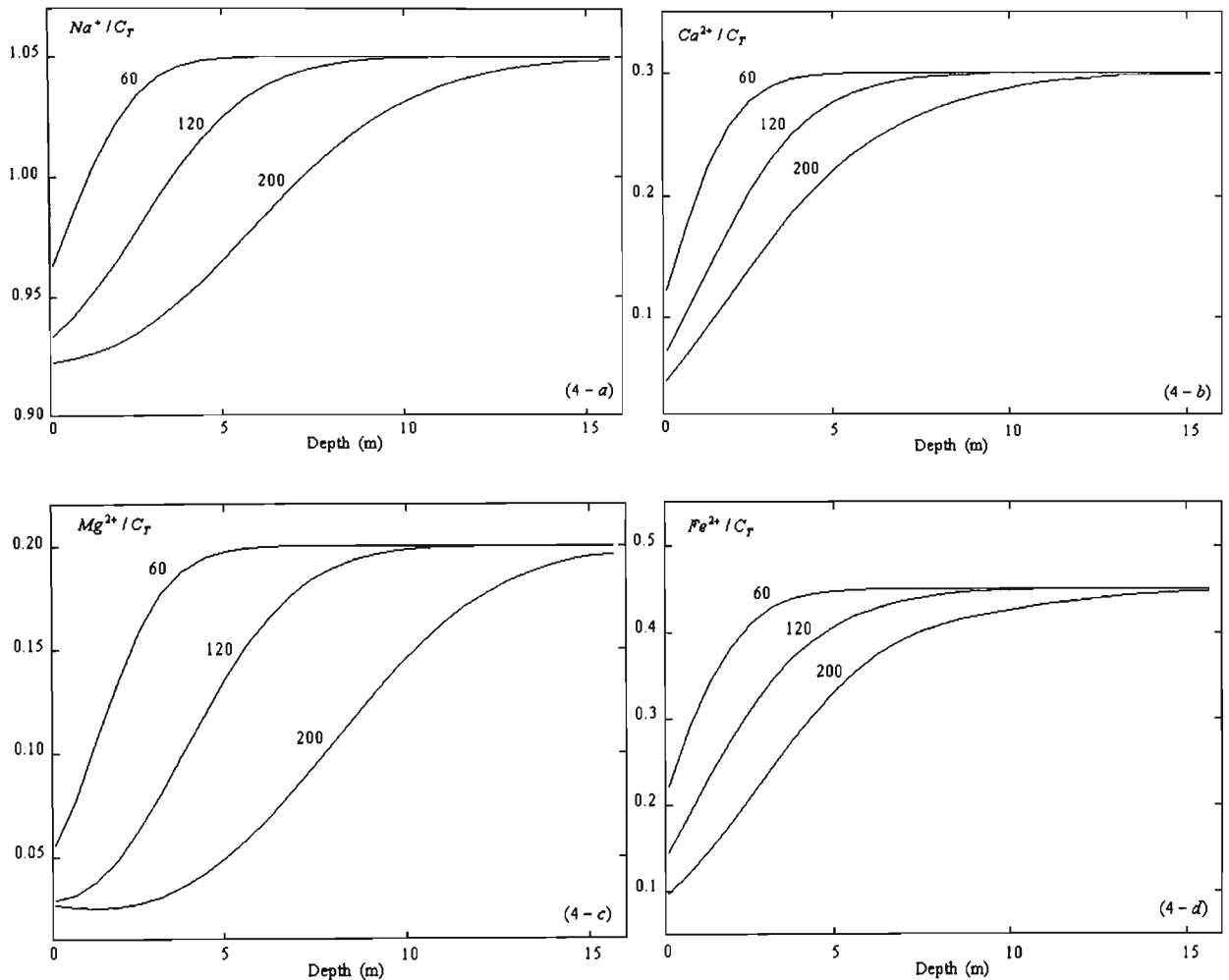


Figure 9.5. Concentration profiles of leaching of a soil with 1:2:2:2 exchange. The numbers labelling the curves show leaching duration in days. (4-a) Profiles for  $Na^+$  ions, (4-b) Profiles for  $Ca^{2+}$  ions, (4-c) Profiles for  $Mg^{2+}$  ions, (4-d) Profiles for  $Fe^{2+}$  ions. Leaching duration is 200 days.

### 9.8 Other chemical reactions

Many other chemical reactions may take place during the transport of the oxidation products through the groundwater flow system. Included in these reactions are the acid neutralisation reaction, precipitation reaction, and complexation reaction. These reactions were incorporated in the present model. A simple empirical model quoted in Jaynes et al. (1984a) was used in order to take into account  $H^+$  neutralisation reactions taking place in open cut coalmine spoil (Appendix H). Ferric iron precipitation and complexation reactions were considered based on the concept of local equilibrium. The modelling methods for these reactions are given in Appendix I and Appendix J

respectively. Finally the role of iron-oxidising bacteria and sulphate reduction bacteria are provided in Appendix K. Although the role of sulphate reduction bacteria was ignored in the present work, the model is capable of simulating this, and the role of such bacteria should be taken into consideration where they are active.

## 9.9 Two-dimensional simulation

### 9.9.1 Modelling setting and input data

Two-dimensional simulations were also performed to demonstrate the capability of the finite volume model for prediction of the long-term pyrite oxidation and transportation of the oxidation products from backfilled open cut coalmines. The input parameters are similar to those input data used for one-dimensional simulation (Table 8.1, Chapter 8, Page 247) but slight modification was made to the influx and background chemistry of the aqueous components. Chemical species considered in the two-dimensional simulations are the same as those in the one-dimensional model with inclusion of  $Mg^{2+}$ ,  $Ca^{2+}$  and  $Na^+$  in order to simulate the non-linear ion-exchange processes. These chemical species with their influx and background concentrations are listed in Table 9.7.

Table 9.7. Source and background concentrations of aqueous components used for two-dimensional simulations.

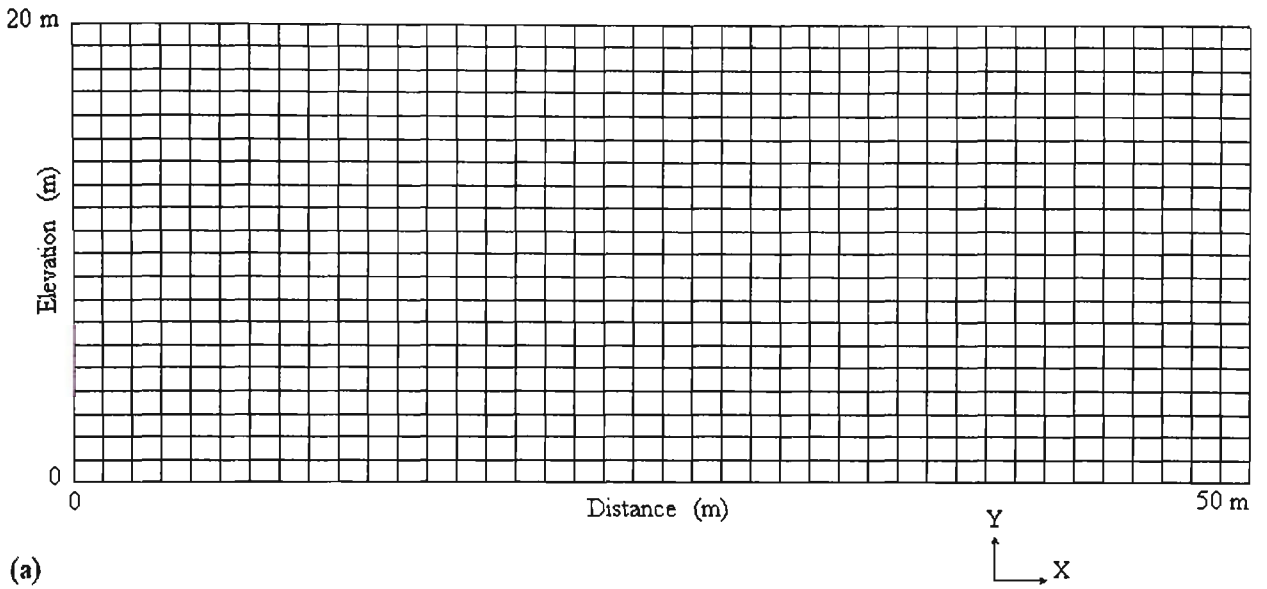
Chemical component	Source concentration <i>mol / m<sup>3</sup></i>	Background concentration <i>mol / m<sup>3</sup></i>
$Fe^{2+}$	$5.00 \times 10^{-1}$	$5.00 \times 10^{-1}$
$Fe^{3+}$	$2.00 \times 10^{-5}$	0
$SO_4^{-2}$	$5.00 \times 10^1$	$5.00 \times 10^1$
$Ca^{2+}$	$2.25 \times 10^{-3}$	$1.64 \times 10^{-3}$
$Mg^{2+}$	$1.24 \times 10^{-3}$	$2.50 \times 10^{-5}$
$Na^+$	$2.50 \times 10^{-1}$	$3.00 \times 10^{-1}$
<i>pH</i>	4	5

The two-dimensional cross-sectional dimensions are 50 m horizontally by 20 m vertically and this domain is discretised into  $40 \times 20$  control volumes of size 1.25 m horizontally  $\times$  1 m vertically. Figure 9.6.a shows the finite volume grid of the problem.

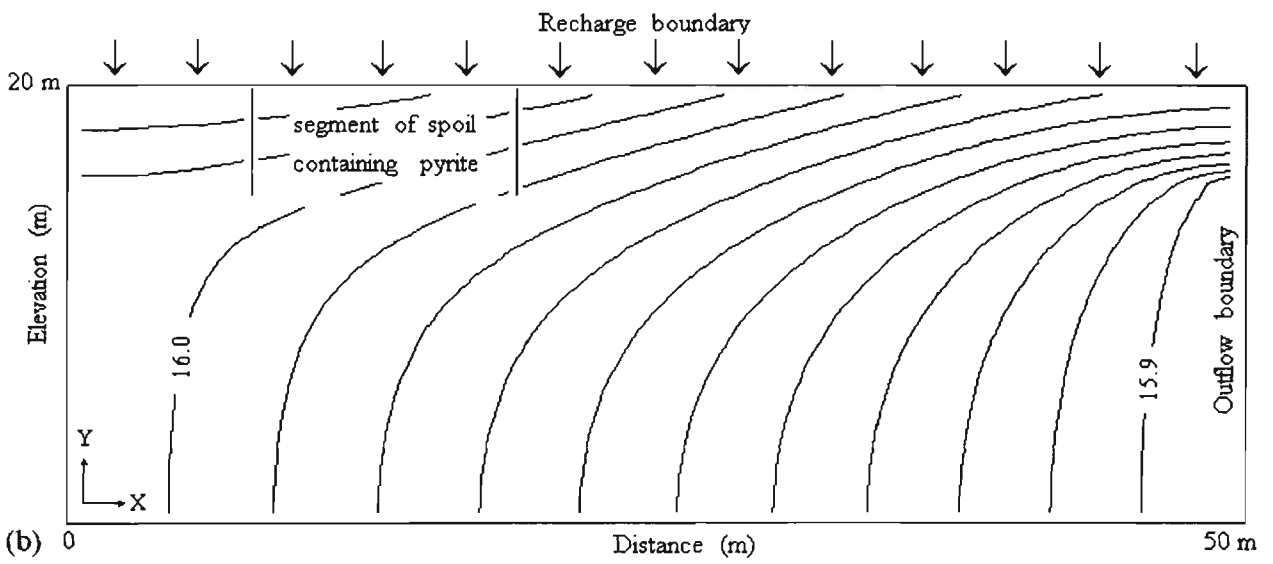
The groundwater flow system was assumed to be steady. The difference head between the left and the right boundaries was maintained at 0.1 m. An average recharge value of  $0.3 \text{ m/yr}$  was considered for the upper boundary (spoil surface). For the simulation it was assumed that reactive pyrite was contained only in a 12.5-m-wide segment of the unsaturated zone of the spoil (Figure 9.6.b).

The upper 4 m of the grid was assumed to be unsaturated and the remainder fully saturated with a constant porosity of 0.321. For simplicity the horizontal component of the velocity was ignored in the unsaturated zone and flow was only assumed to be vertical in this zone. Horizontal and vertical hydraulic conductivities of  $1.50 \times 10^{-5} \text{ m/s}$  and  $1.50 \times 10^{-6} \text{ m/s}$  were used for the simulation. Horizontal and vertical dispersion coefficients of  $7.0 \times 10^{-9} \text{ m}^2 / \text{s}$  and  $5.0 \times 10^{-9} \text{ m}^2 / \text{s}$  were specified for the model. The steady state flow system in terms of velocity vectors is given in Figure 9.6.c.

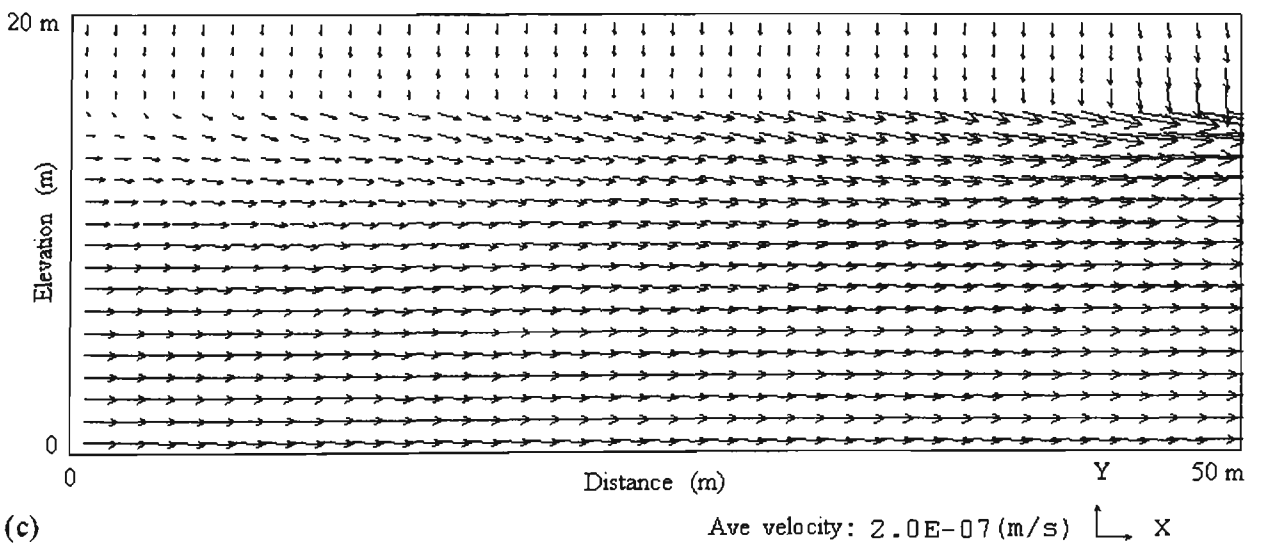
The spoil temperature was assumed constant at  $15 \text{ }^\circ\text{C}$  and the temperature rise due to the oxidation reactions was predicted using an enthalpy balance as described in Chapter 8, Section 8.3.1, Page 244. Three different cases with various specific conditions were selected to perform the two-dimensional simulations. These conditions are listed in Table 9.8. The spoil surface was maintained as a first-type boundary condition for oxygen equal to its atmospheric concentration ( $9 \text{ mol/m}^3 \approx 0.21 \text{ mol/mol}$ ). Both first – type and zero concentration gradient boundary conditions were specified above the water table for the oxygen transport model.



(a)



(b)



(c)

Figure 9.6. Two-dimensional simulation cross-section: (a) finite volume grid; (b) hydraulic head and the segment of the spoil where oxidation reactions take place; (c) velocity vectors.

Table 9.8. Illustration of the specific conditions for two-dimensional simulation cases.

Case	Diffusion coefficient $m^2 / s$	ion-exchange process	bacteria	$H^+$ - spoil interaction
2D-1	$2.0 \times 10^{-7}$	not included	absence	not incorporated
2D-2	$2.0 \times 10^{-7}$	not included	present	incorporated
2D-3	$2.0 \times 10^{-7}$	included	absence	not incorporated

The spoil solution initially contained no oxygen. To avoid non-linearity problems, no ferric complexation reactions were allowed to take place. Ferric precipitation reaction was incorporated for 2-D simulations. An oxidation period of 10000 days ( $\approx 27$  years) was considered for the simulation.

The simulation results for oxygen concentration, temperature, fraction of pyrite remaining and the fraction of pyrite oxidised as well as the results of the aqueous components are given in the form of contour plots. The contours of the oxygen concentrations as well as the aqueous components are in terms of moles per cubic metre ( $mol/m^3$ ), the contours showing the distribution of temperature through the spoil are given in terms of  $^{\circ}C$ . The contours of the fraction of pyrite remaining and the fraction of the pyrite oxidised are in terms of  $kg/kg$  and percent (%) respectively.

### 9.9.2 Two-dimensional simulation results

#### (a) Case 2D-1, without ion-exchange process, no acid neutralisation, no bacteria are present

In first two-dimensional (Case 2D-1) analysis, an effective diffusion coefficient of  $2.0 \times 10^{-7} m^2 / s$  was considered for the oxygen diffusion model. This case was conducted with no acid neutralisation reaction and the role of bacteria in the oxidation

reaction was not taken into account. In this case, chemically produced ferric iron resulting from the oxidation of ferrous iron had no significant role on the pyrite oxidation and oxygen was noted to be the main oxidant for the oxidation processes. Because a fixed boundary value of less than  $0.1 \text{ mol/m}^3$  was maintained for oxygen at the top of the water table, oxygen decreased linearly from the spoil surface to the water table. Figure 9.7 shows the simulation results for oxygen concentrations after 5 years. Oxygen decreased in the segments where the oxidation reactions take place.

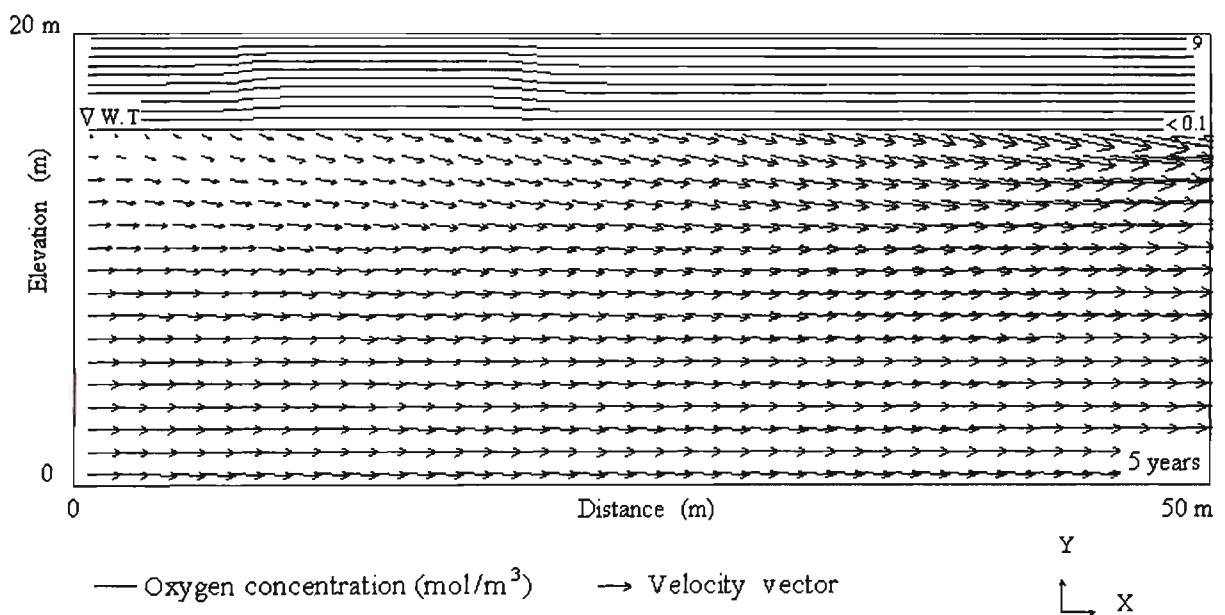
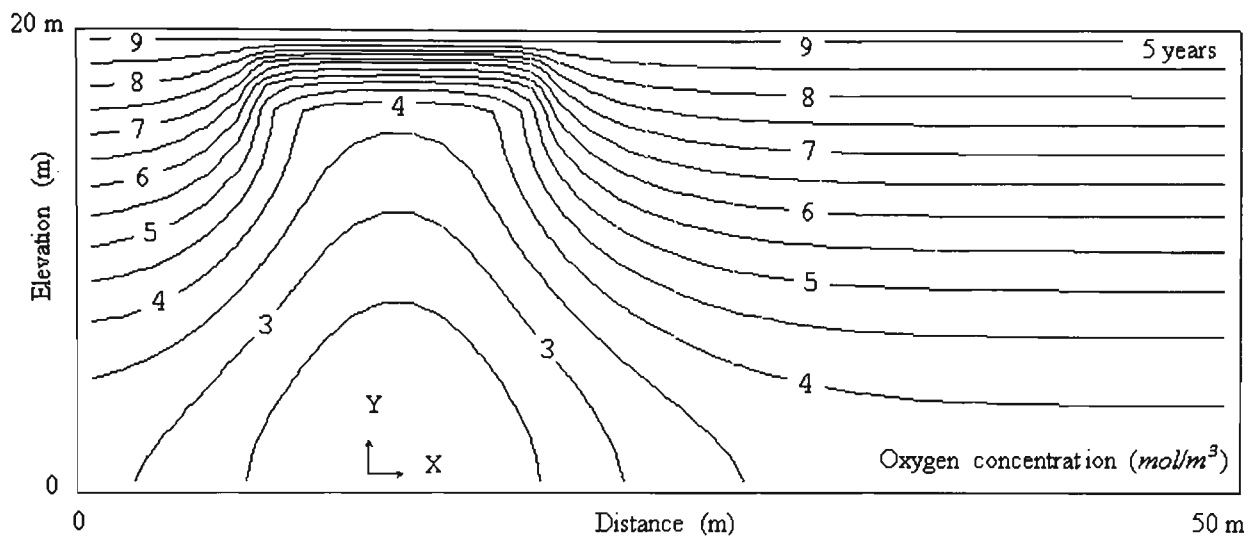


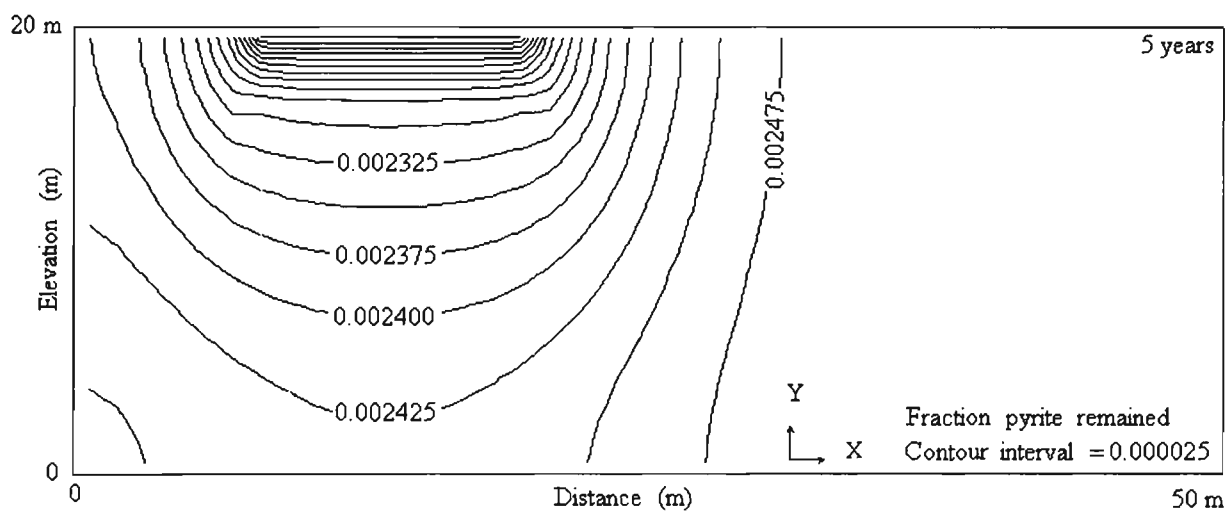
Figure 9.7. Oxygen concentration after 5 years of simulation.

The depletion zone of oxygen due to the chemical oxidation of ferrous iron as well as pyrite oxidation is well illustrated in Figure 9.8.a, where a zero gradient type boundary condition rather than a fixed boundary was specified as a bottom value for the oxygen balance.

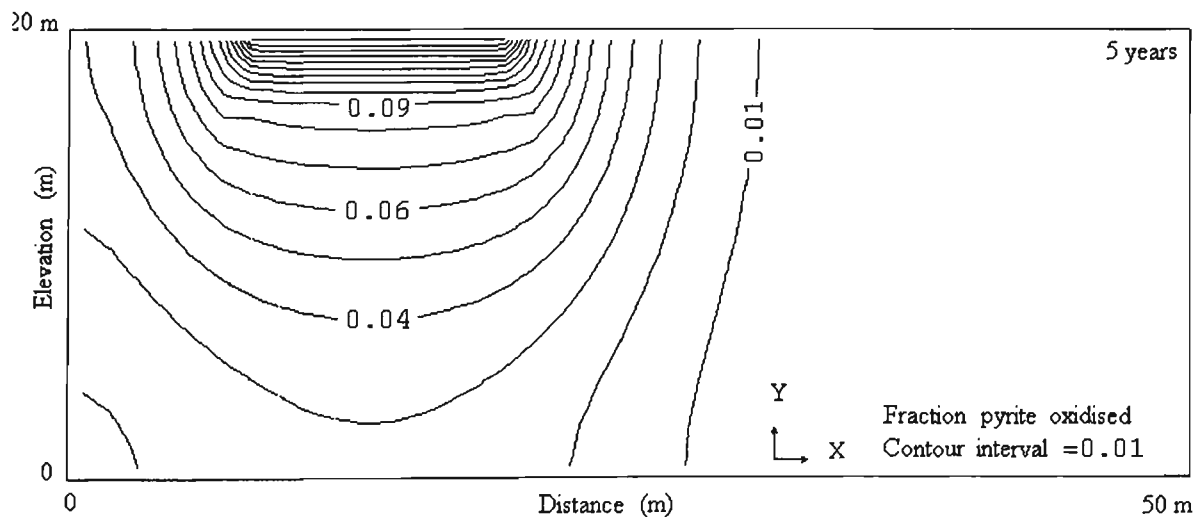
Figures 9.8.b and 9.8.c show the contour plots for the pyrite fraction remaining and the fraction of the pyrite oxidised for a simulation time of 5 years. It was supposed that reactive pyrite was contained only in a 12.5-metre-wide segment of the spoil.



(a)



(b)



(c)

Figure 9.8. 2-D simulation results after 5 years: (a) oxygen concentration; (b) pyrite fraction remaining; (c) pyrite fraction oxidised.

As Figure 9.8.c shows that more than about 15 % of pyrite was oxidised in the section above the water table where the concentration of oxygen is high. In the zone where the oxygen decreased to less than  $3 \text{ mol/m}^3$ , only about 1 % of the pyrite was oxidised.

Figures 9.9.a and 9.9.b show the temperature distribution within the spoil section predicted after 5 and 10 years of simulations, respectively. As these figures show in the zone where the pyrite oxidation reaction takes place, the temperature rose from a background spoil temperature equal to  $15^\circ\text{C}$  to a maximum value of more than  $15.6^\circ\text{C}$ . This maximum temperature decreased to  $15.5^\circ\text{C}$  after 10 years of the simulation. A good correlation between reduction of pyrite oxidation and reduction of temperature by time is shown.

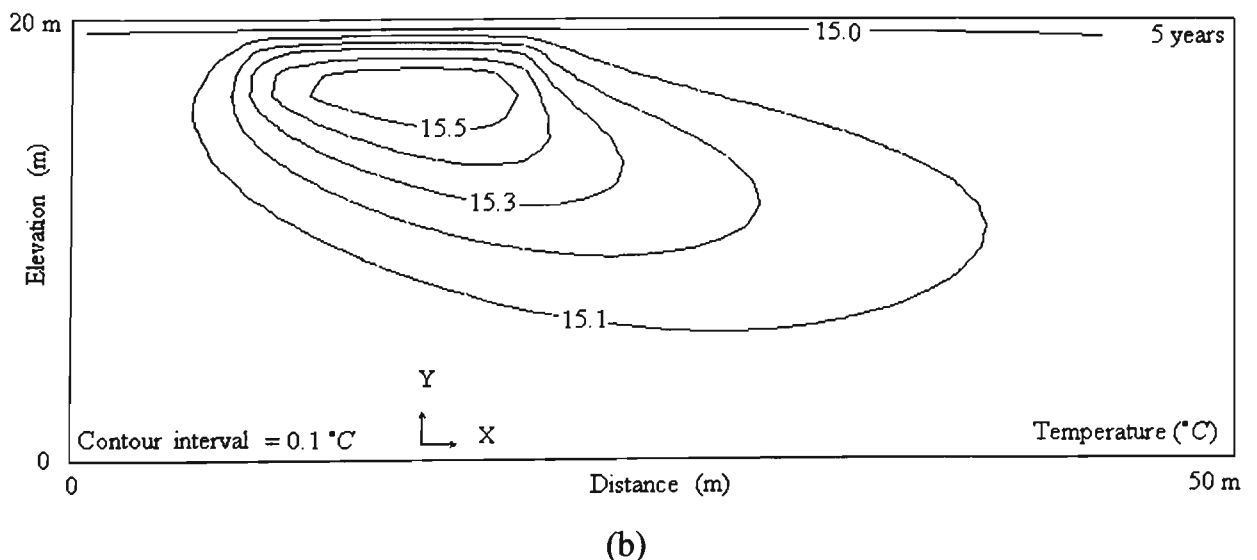
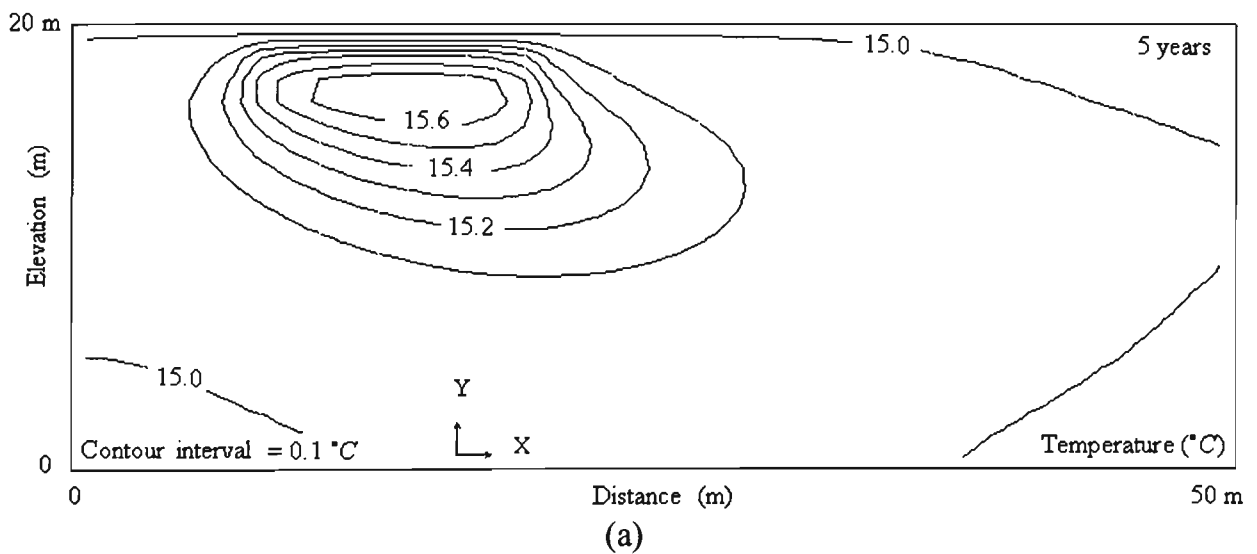
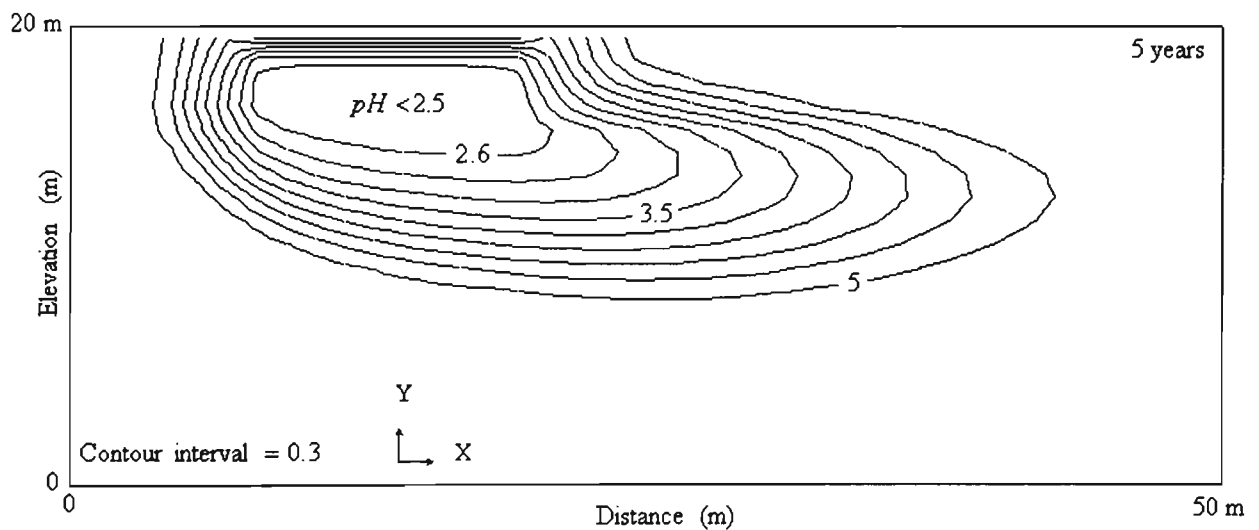
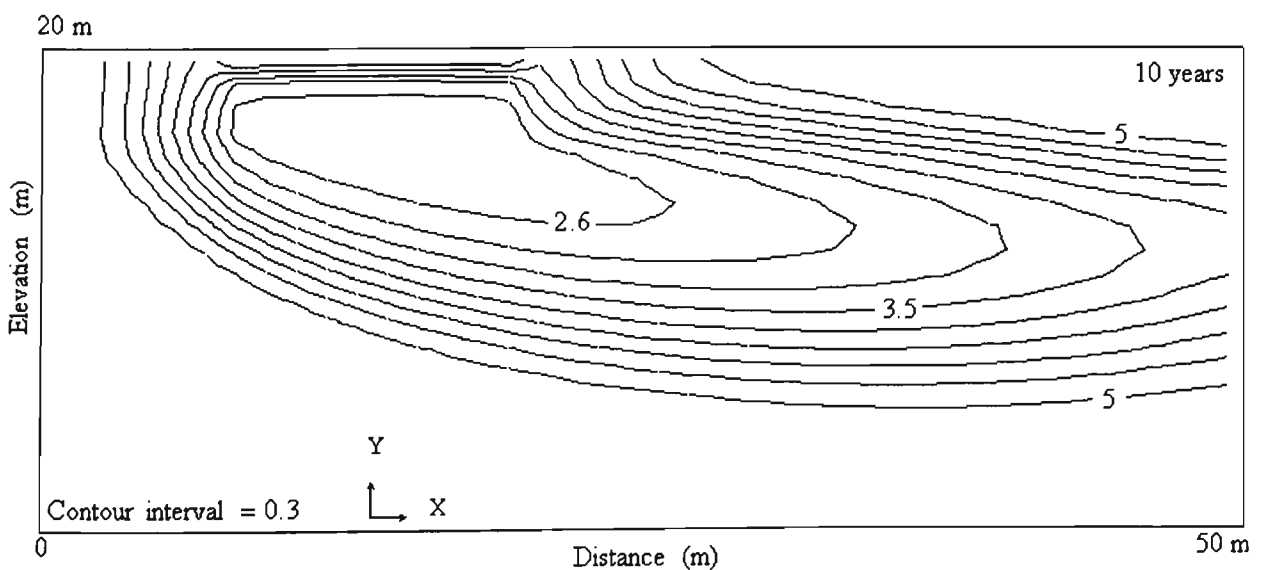


Figure 9.9. Temperature rise after: (a) 5 years; (b) 10 years of the simulation.

$pH$  is the principle factor controlling the quality of the open cut coalmine discharge water. Figures 9.10.a and 9.10.b show  $pH$  variations after 5 and 10 years of simulations. No  $pH$  neutralisation process was considered in this case. The initial  $pH$  change occurred in the unsaturated zone where the oxidation reactions take place and then spread into the saturated groundwater flow system. The  $pH$  dropped to less than 2.5 at the shallow unsaturated zone where the oxygen reacts with pyrite and hydrogen ions are released. The  $pH$  increased to its background value in the direction of groundwater flow.



(a)



(b)

Figure 9.10.  $pH$  after: (a) 5 years; (b) 10 years of simulation.

Figures 9.11.a and 9.11.b show the concentration of sulphate for time periods of 5 and 10 years. The  $SO_4^{2-}$  peak occurs in the unsaturated zone where oxygen is present; in this zone  $SO_4^{2-}$  increased from its background concentration ( $50 \text{ mol/m}^3$ ) to  $54 \text{ mol/m}^3$ . In this case because oxygen is the only oxidant, no considerable amount of  $SO_4^{2-}$  was produced.

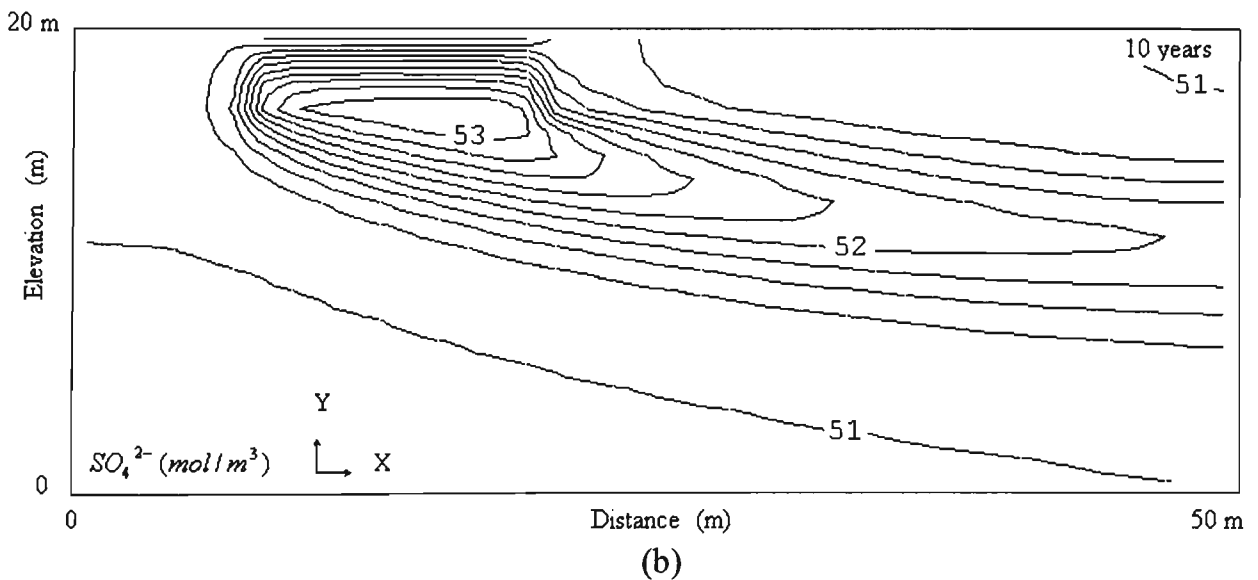
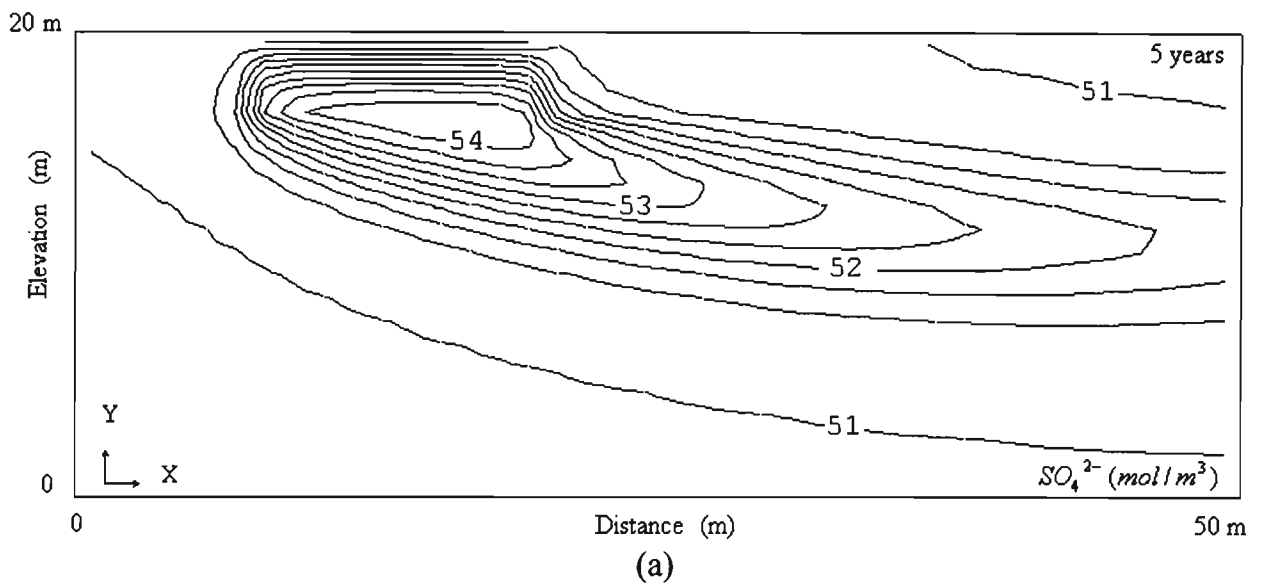


Figure 9.11.  $SO_4^{2-}$  concentrations after: (a) 5; (b) 10 years of simulation.

Ferric iron concentrations are shown in Figures 9.12 and 9.13. In Figures 9.12.a and 9.12.b, the simulation time is 5 years while in Figures 9.13.a and 9.13.b the ferric concentrations are given for a time period of 10 years.

In Figures 9.12.b and 9.13.b the effects of the ferric precipitation are included. In Case 2D-1, because the chemical oxidation of ferrous iron is the main source of ferric iron generation no significant ferric iron was generated. Therefore, the role of  $Fe^{3+}$  in pyrite oxidation was insignificant. The concentrations of ferric iron are mainly restricted to the unsaturated zone where oxygen is diffused through the pore space of the spoil. As illustrated in Figures 9.12.b and 9.13.b, the precipitation reaction removed ferric iron from the solution phase in the direction of the groundwater flow where the  $pH$  is above 3.

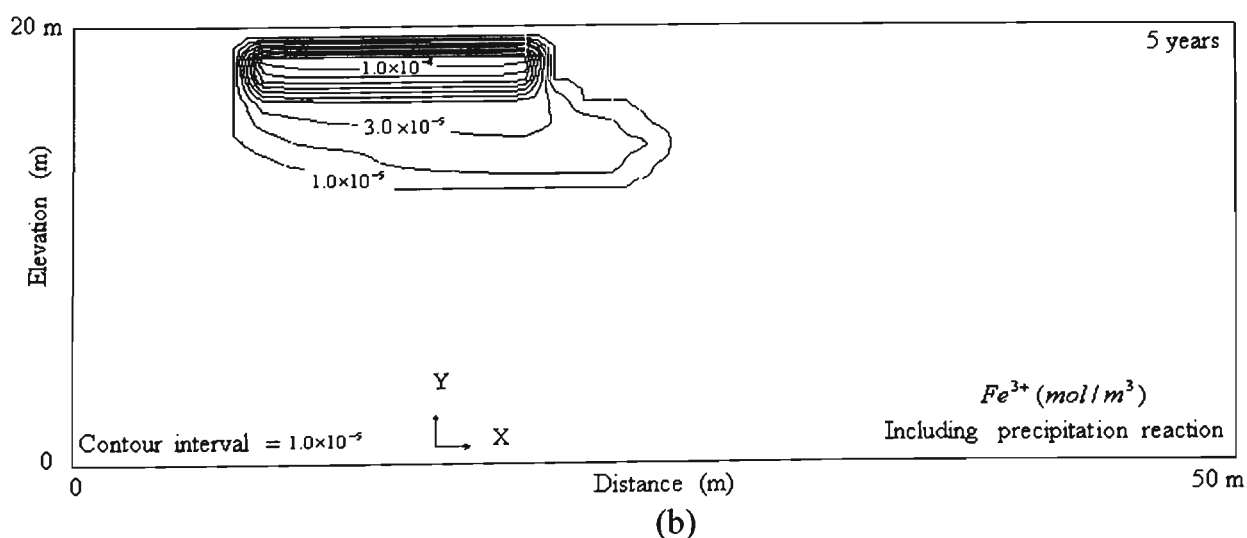
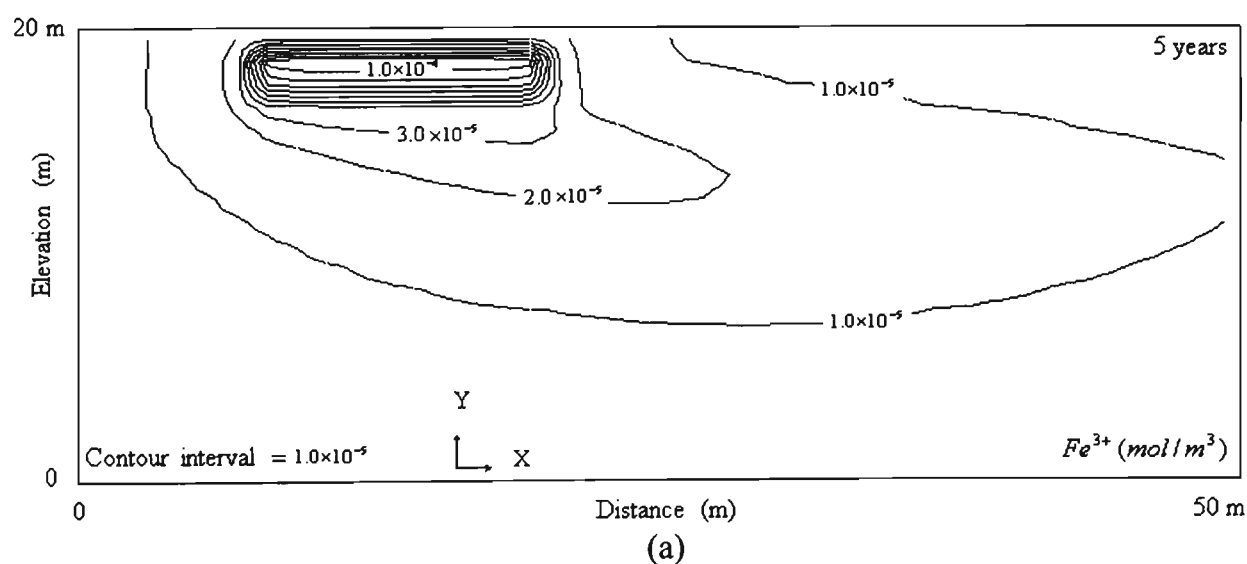


Figure 9.12.  $Fe^{3+}$  after 5 years of simulation: (a) without precipitation reaction; (b) including precipitation reaction.

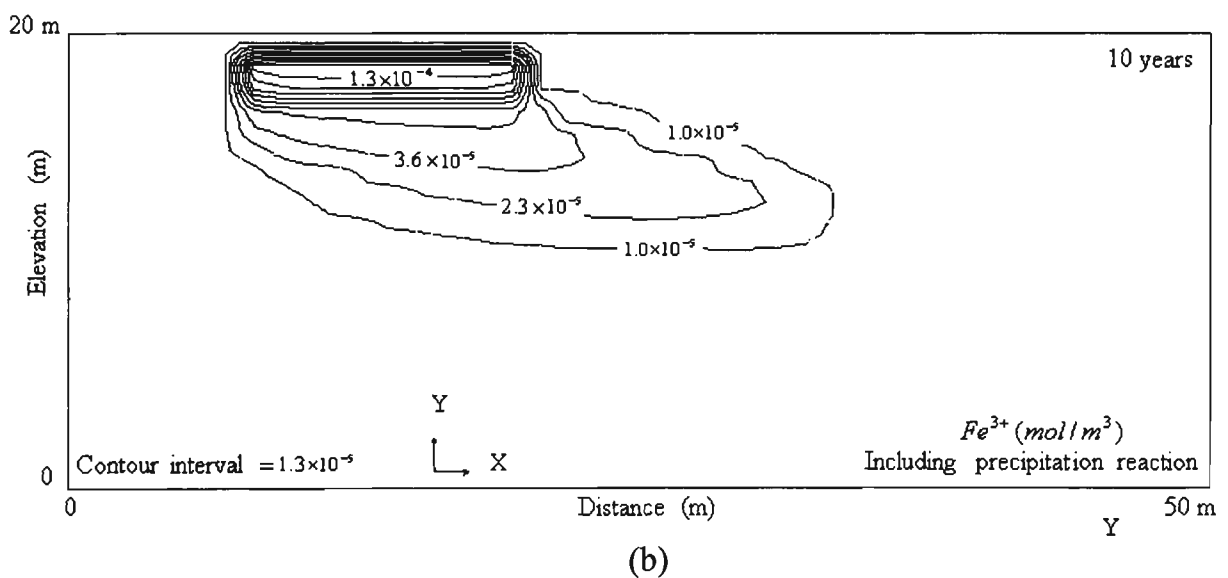
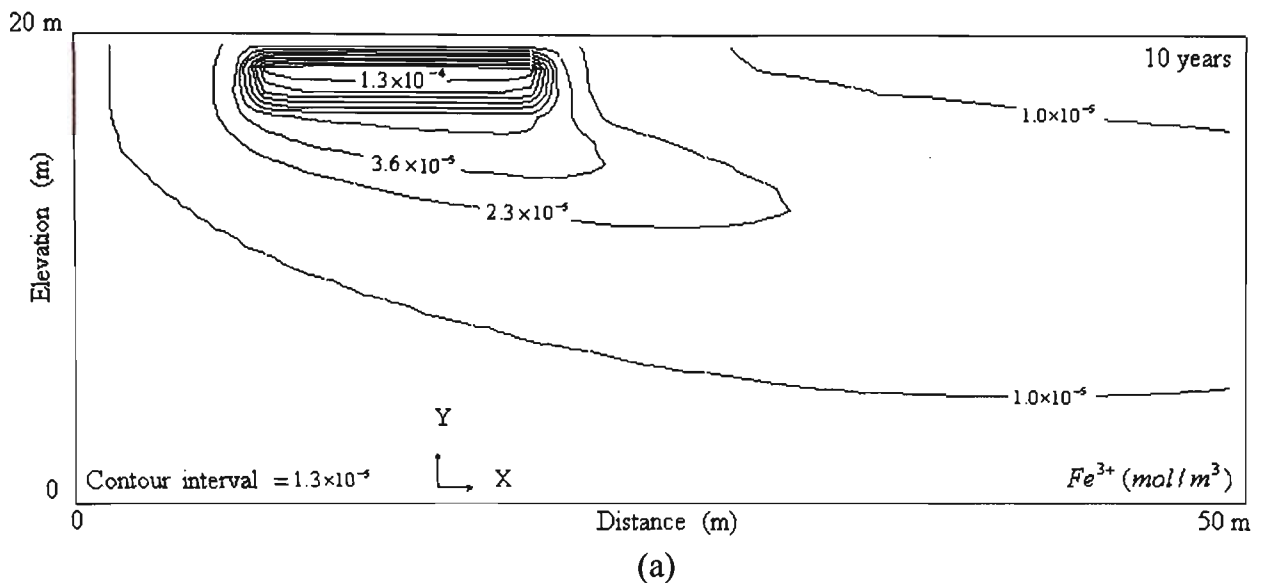


Figure 9.13.  $Fe^{3+}$  after 10 years of simulation: (a) without precipitation reaction; (b) including precipitation reaction.

Figures 9.14.a and 9.14.b show ferrous iron concentrations for simulation times of 5 and 10 years. A peak concentration (above  $2.5 \text{ mol/m}^3$ ) occurred in the unsaturated zone at 5 years due to the presence of oxygen and some  $Fe^{2+}$  penetrated to the saturated zone by surface recharge. Ultimately  $Fe^{2+}$  in the saturated zone was transported in the direction of groundwater flow (Figures 9.14.b). In Case 2D-1, because no bacteria were active and the chemical oxidation of ferrous iron is too slow, no significant ferrous iron was removed and converted to ferric iron.  $Fe^{2+}$  concentration was mainly attenuated by physical transport processes in the direction of groundwater flow.

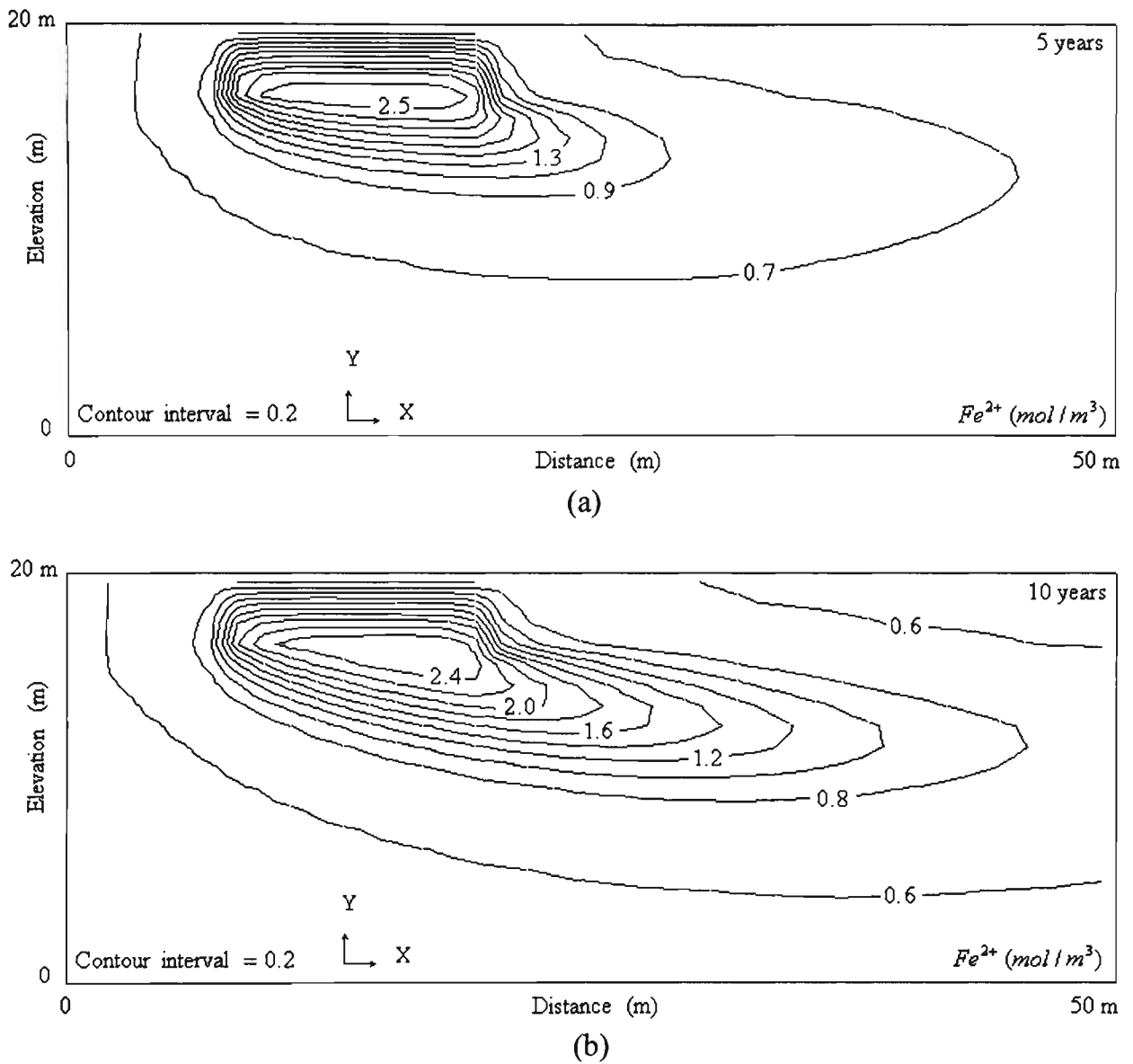


Figure 9.14.  $Fe^{2+}$  concentration after: (a) 5 years; (b) 10 years of simulation.

**(b) Case 2D-2, without ion-exchange process, incorporating acid neutralisation, bacteria are present**

In Case 2D-2, bacteria were allowed to be active and also the interactions between  $H^+$  produced by the oxidation processes and the spoil were considered. In this case the  $pH$  of the system was not allowed to drop below 2.5. The interaction between  $H^+$  and the spoil and also maintaining the  $pH$  closer to the optimum  $pH$  required for the maximum activity of the iron-oxidising bacteria ( $\approx 3$ ), caused more ferric iron to be produced by the bacterially mediated oxidation of ferrous iron. Consequently more pyrite was oxidised.

Figure 9.15 shows the oxygen concentration for a 5-year-period of the simulation. In the segment where chemical reactions take place, more oxygen was consumed due to bacterial activity.

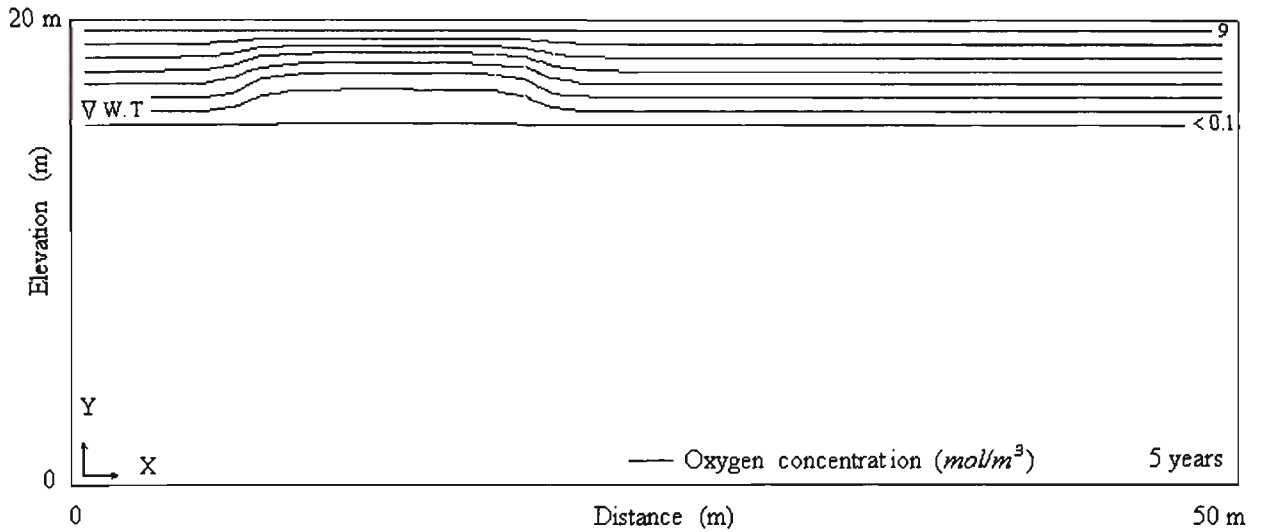


Figure 9.15. Oxygen concentration after 5 years of simulation.

Although not shown, at early times,  $Fe^{2+}$  concentration is relatively large in the unsaturated zone whereas the ferric iron concentrations are very small. This is because at the very beginning of the simulations,  $pH$  is high (more than 4) and is not favourable for the bacterial activity to convert ferrous iron to ferric iron.

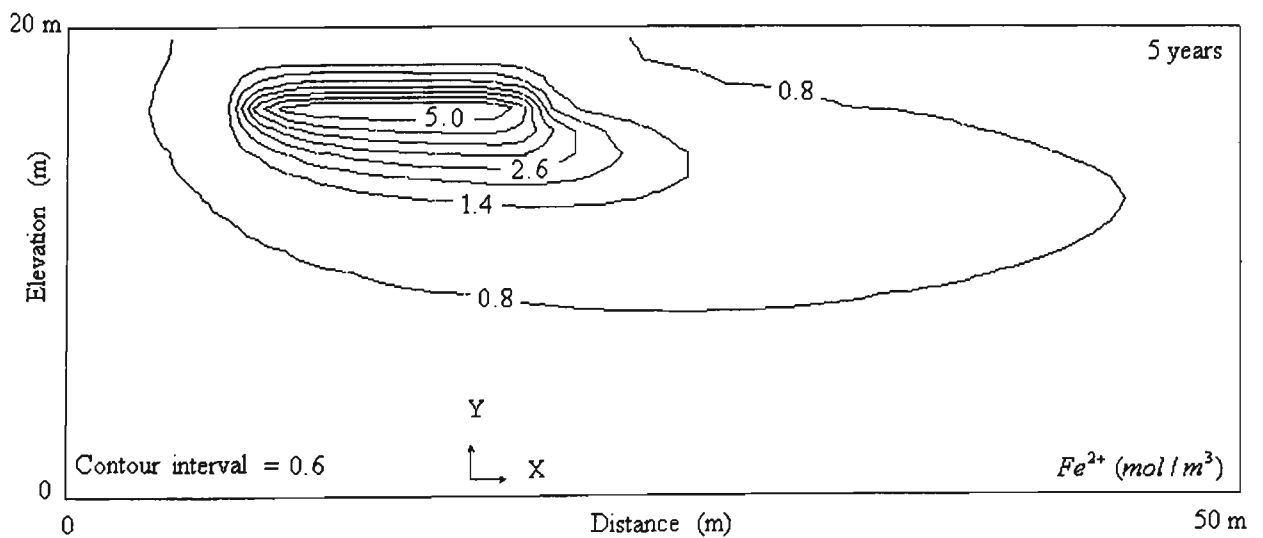


Figure 9.16.  $Fe^{2+}$  after 5 years of simulation.

The ferrous iron concentrations for simulation times of 5 and 10 years were illustrated in Figures 9.16 and 9.17. After 5 years of the simulation (Figure 9.16),  $pH$  reached about 3; a favourable  $pH$  required for bacterial activity. The bacteria catalysed the ferrous iron oxidation reaction and more  $Fe^{2+}$  converted to  $Fe^{3+}$ . Therefore, ferrous iron concentration decreased in the unsaturated zone whereas the ferric iron concentrations increased considerably in this zone.

After 10 years of the simulation (Figure 9.17),  $pH$  is still in the range that it is favourable for bacterial activity; therefore, low concentrations of ferrous iron are seen in the unsaturated zone where the ferric concentration is dominant and a peak  $Fe^{2+}$  concentration is seen in the saturated zone.

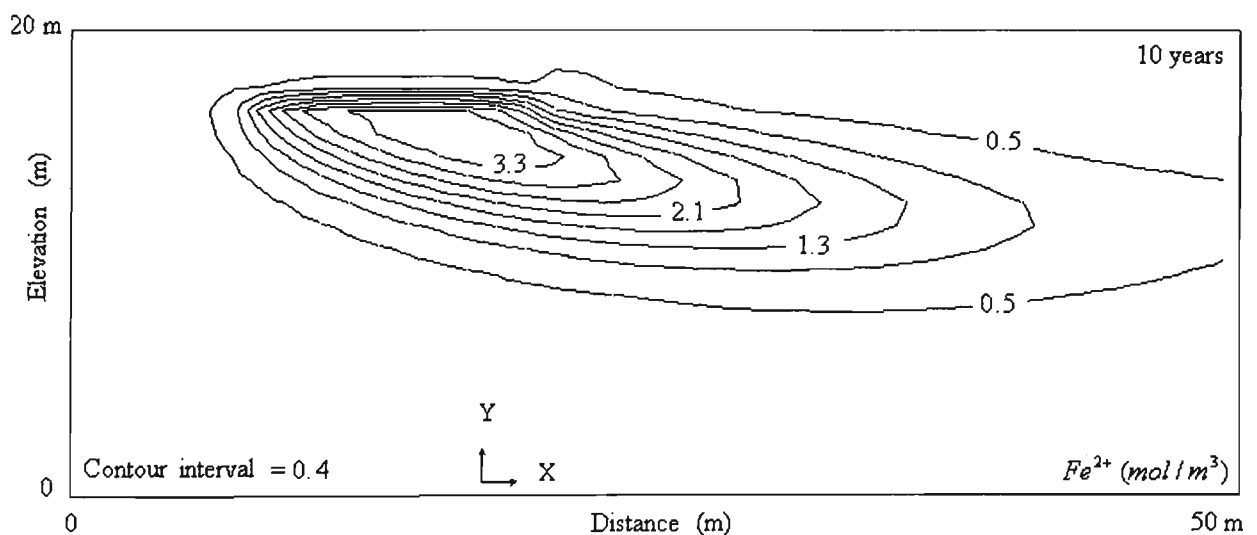


Figure 9.17.  $Fe^{2+}$  after 10 years of simulation.

Figures 9.18.a And 9.18.b show the solution  $pH$  for simulation times of 5 years and 10 years respectively. As pyrite oxidation takes place the  $pH$  dropped significantly (average  $pH$  is 3 in the unsaturated zone) but unlike Case 2D-1, the  $pH$  did not drop below about 2.5 due to the neutralisation reactions and also taking into account the reaction between the spoil and  $H^+$ . By 10 years the average  $pH$  is about 3.5 in the unsaturated zone due to the transport of hydrogen ions downward by the water flow.

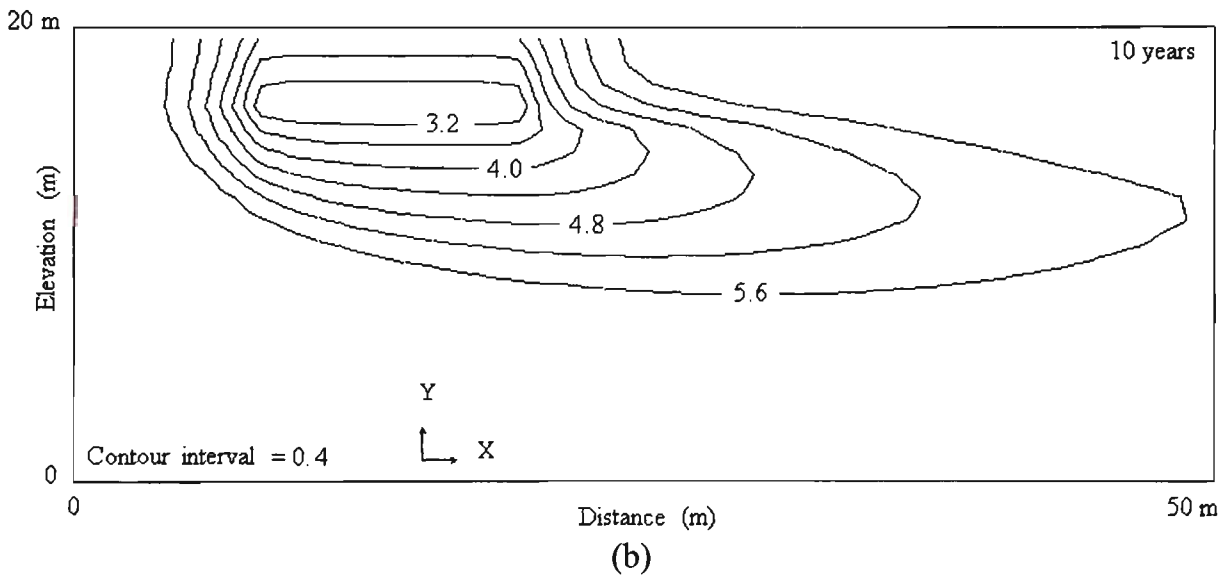
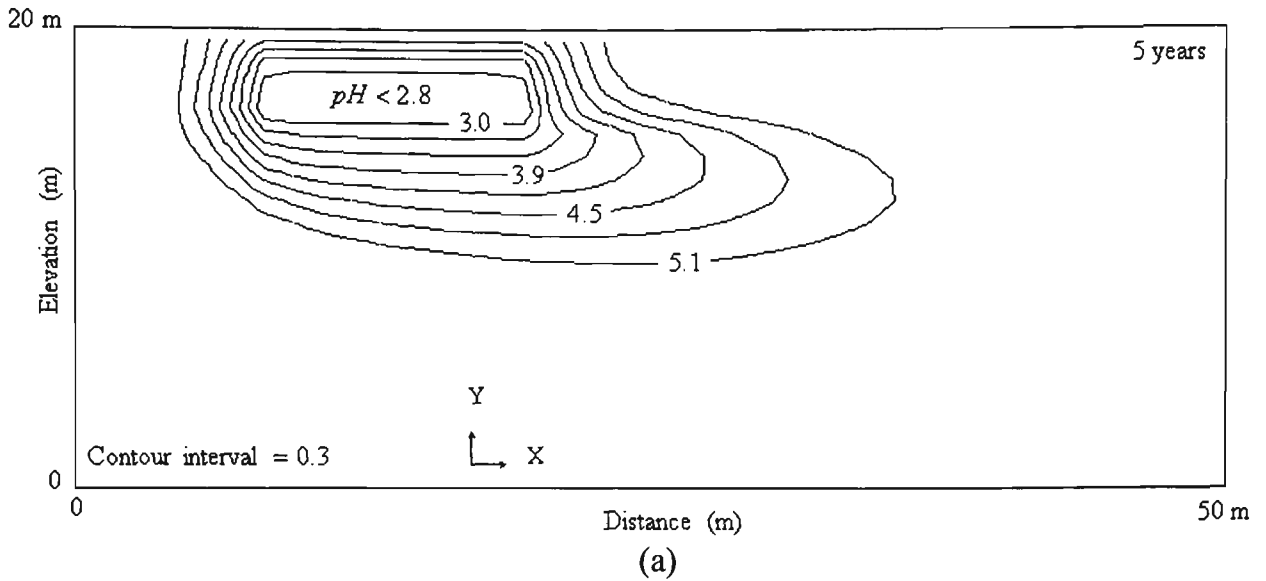
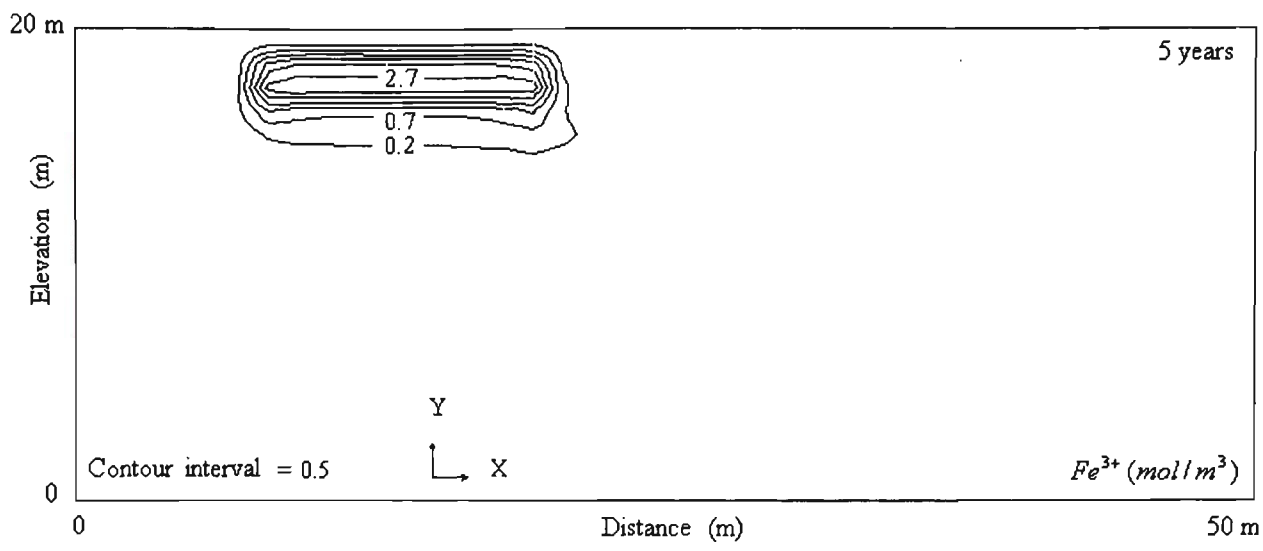
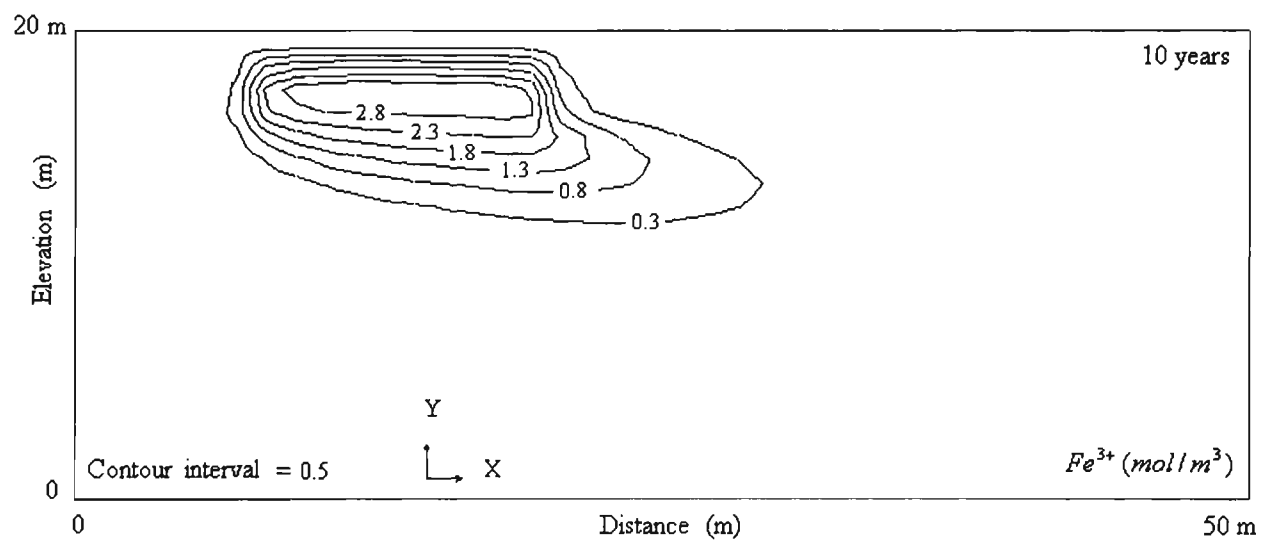


Figure 9.18.  $pH$  after: (a) 5 years; (b) 10 years of simulation.

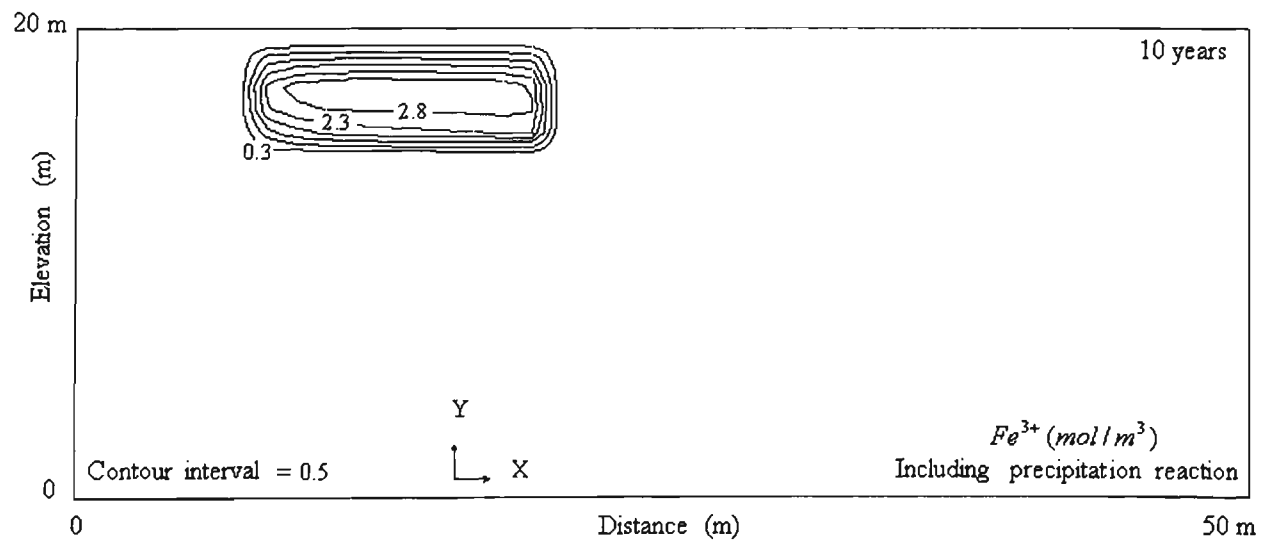
Figure 9.19.a shows the ferric iron concentration after 5 years of simulation. The concentrations of  $Fe^{3+}$  are high in the unsaturated zone where oxygen is available and the conditions for maximum bacterial activity are favourable. The ferric concentrations are limited to the unsaturated zone, but as time progresses (Figure 9.19.b) some is being transported below the water table. In the case where pyrite is present below the water table,  $Fe^{3+}$  is converted back into  $Fe^{2+}$  through the  $Fe^{3+}$  - pyrite reaction. By incorporating the ferric iron precipitation reaction (Figure 9.19.c), aqueous ferric iron was removed from the solution phase in the saturated zone where the  $pH$  is greater than 3.5.



(a)



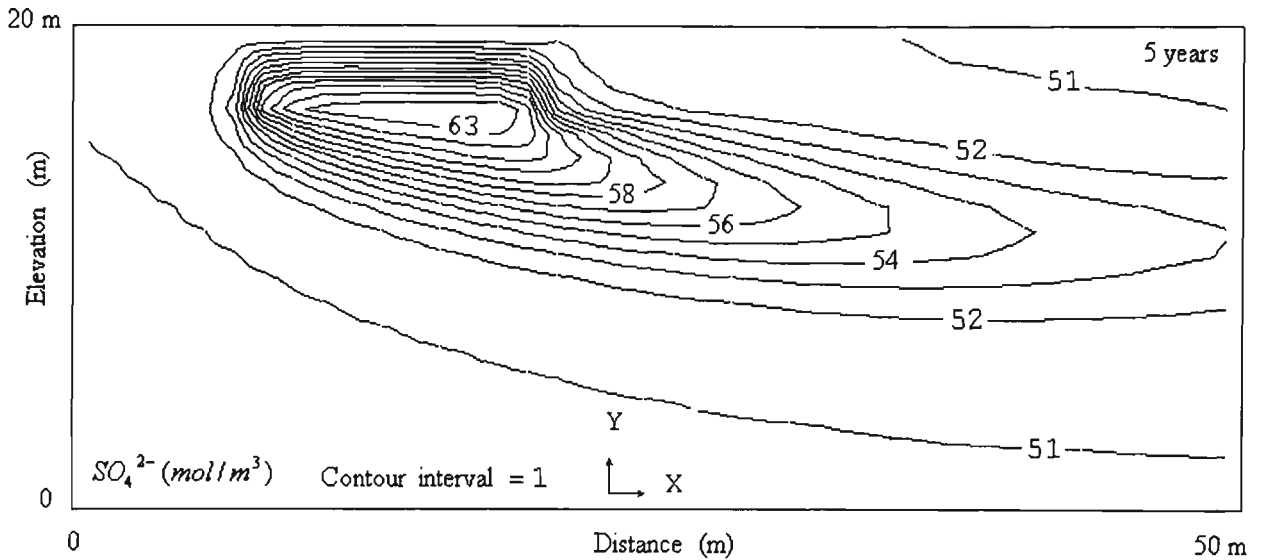
(b)



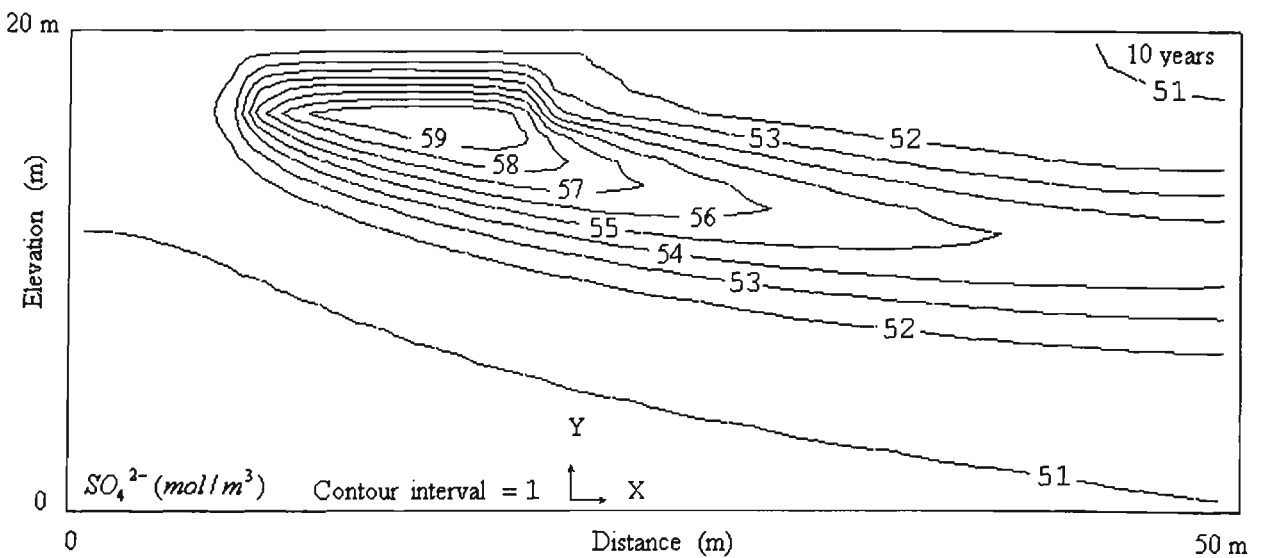
(c)

Figure 9.19.  $Fe^{3+}$  concentration after: (a) 5 years; (b) 10 years (without precipitation reaction); (c) 10 years (including precipitation reaction) of simulation.

Figures 9.20.a and 9.20.b show  $SO_4^{2-}$  concentrations for time periods of 5 and 10 years. Unlike Case 2D-1, in Case 2D-2 considerable amounts of  $SO_4^{2-}$  were produced due to the fact that both oxygen and  $Fe^{3+}$  react with pyrite and higher  $SO_4^{2-}$  concentrations are produced.



(a)



(b)

Figure 9.20.  $SO_4^{2-}$  concentration after: (a) 5 years; (b) 10 years of simulation.

Although not illustrated, early in the simulation the  $SO_4^{2-}$  peak occurs in the unsaturated zone. Pyrite-oxygen reaction is recognised to be the only important source for  $SO_4^{2-}$  production at the beginning of the simulation.

At 5 years (Figure 9.20.a), an  $SO_4^{2-}$  peak (greater than  $63 \text{ mol/m}^3$ ) occurred in the saturated zone due to a downward recharge water flow. In the saturated zone,  $SO_4^{2-}$  spreads by groundwater flow. By 10 years (Figure 9.20.b), the  $SO_4^{2-}$  peak moved further down into the saturated zone to about 6 metre depth, whereas  $SO_4^{2-}$  concentrations in the unsaturated zone began to decrease. No significant concentrations of  $SO_4^{2-}$  were produced in the saturated zone by the reaction between ferric iron and pyrite, because, for two-dimensional simulations, it was considered that only pyrite in a 12.5-m-wide segment of the unsaturated zone participates in the oxidation reaction.

**(c) Case 2D-3, incorporating ion-exchange process, without acid neutralisation process, bacteria are absence**

Case 2D-3 is similar to Case 2D-1 but ion exchange reactions were allowed to take place between the ions  $Fe^{2+}$ ,  $Ca^{2+}$ ,  $Mg^{2+}$ , and  $Na^+$ . A cation exchange capacity of  $0.1 \text{ meq/gr}$  was used for the simulations. The selectivity coefficients used here are listed in Table 9.6. Figure 9.21 shows the evolution of  $Fe^{2+}$  over 10 years of simulation. Due to flowing groundwater, some  $Fe^{2+}$  is removed from the solution phase due to substitution by  $Na^+$ .

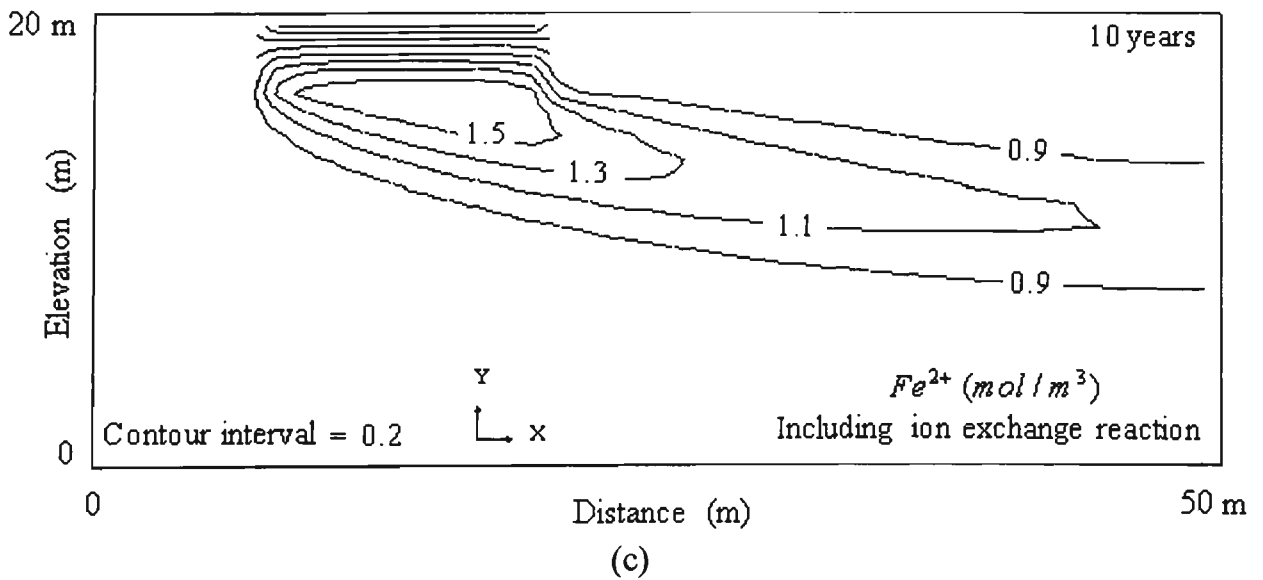
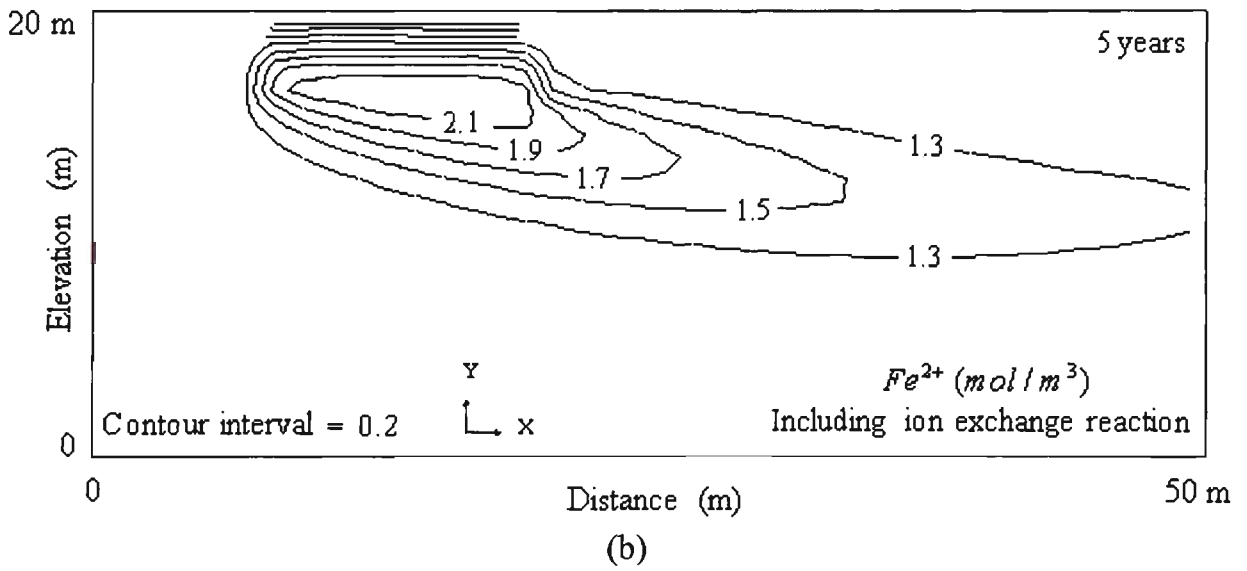
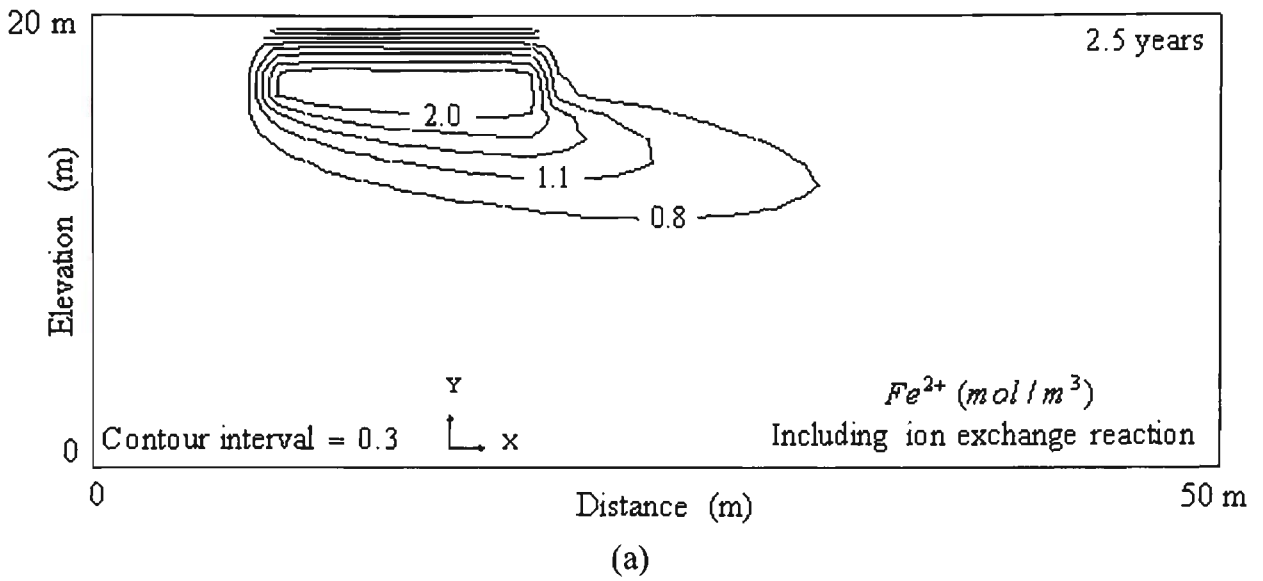


Figure 9.21. Evolution of  $Fe^{2+}$  concentrations at: (a) 2.5; (b) 5; and (c) 10 years of simulation.

## 9.10 Conclusions

This chapter briefly discussed the main processes of mass transport. The details of these processes are provided in Appendices D through K. One-dimensional models were used to simulate various cases of nonlinear ion exchange processes and these models were validated with analytical, numerical models and field monitored data, suggesting that the finite volume model using PHOENICS package is suitable for the reactive transport of the pyrite oxidation products through groundwater flow relating to backfilled open cut mines. Unlike rate-controlling reactions which are very slow such as the pyrite oxidation reaction and the chemical oxidation of ferrous iron, for those chemical reactions which are relatively fast, such as precipitation and ion exchange reactions, a local equilibrium was assumed.

The results of the two-dimensional simulations are also given in this chapter. These results show how contaminants spread into groundwater systems and how the physical and chemical processes influence the transport of the pyrite oxidation products. The results of the 2-D simulations can be used for designing effective site remediation programs in order to minimise environmental effects arising from abandoned backfilled open cut coalmines.

The results of 2-D simulations indicate:

- Bacterial activity caused a sharp depletion of oxygen in vadose zone
- The oxidation of only small fraction of pyrite is enough to generate acid mine drainage load. Considerable pyrite creates a long-term source of acid mine drainage that if no action is taken to reduce the acid generation and pollutant leaching, the receiving environments and water resources will be seriously damaged.

- The lowering of  $pH$  in the range between 2.5 to 3.5, the bacterial oxidation of pyrite is enhanced. Subsequently the bacterial action produces more  $Fe^{3+}$ ,  $SO_4^{2-}$ ,  $H^+$ , and  $Fe^{2+}$ .
- The results of 2-D simulations clearly indicate that dissolved ferric iron remain above water table while ferrous iron peak appears below it, in saturated zone.
- Sulphate generated by initially pyrite-oxygen reaction and subsequent production from  $Fe^{3+}$  - pyrite reaction due to bacterial action mainly has peak below the water table

## **CHAPTER TEN**

### **GENERAL CONCLUSIONS AND RECOMMENDATIONS**

## CHAPTER TEN

### GENERAL CONCLUSIONS AND RECOMMENDATIONS

#### 10.1 Summary

The hydrogeological systems affected by mining operations and subsequent pollution potential emanating from the spoil of the open cut coalmines have been comprehensively investigated during the course of this research work. The thesis presents a computer-based methodology that enables:

- (i) Quantifying the amount of groundwater inflow taking place during open cut mine advancement.
- (ii) Predicting post-mining hydrogeological response resulting from disturbances made during mining operations in order to obtain the pre-mining equilibrium regime.
- (iii) Predicting long-term pollution problems after abandonment of mining operations.
- (iv) Evaluating, assessing, quantifying and better understanding the processes involved in pollutant generation, and
- (v) Identifying important factors in a real environment that are most sensitive to the variations of pollution potential associated with open cut coalmines.

The purpose of this thesis was to study groundwater flow systems influenced by backfilled open cut coal mining during mine advancement and after the mining

operation has ceased, to assist in the prediction of long-term pollution generation. To achieve these goals, a comprehensive numerical model was used. The amount of pollutants generated in a backfilled open cut mine site can be effectively reduced by the use of efficient reclamation methods. A numerical model can help in the design and optimisation of the performance of site remediation and land reclamation projects. A result of the development of a numerical model would be to facilitate the formation of a mine rehabilitation and environmental management strategy during the feasibility stage of designing an open cut mining operation.

In order to evaluate the accuracy of the model, attempts were made to validate the modelling performance. For this purpose, field monitored data taken from the literature, analytical solutions as well as published modelling results were used. Comparison of the present modelling output with those results obtained from field measurements, analytical equations and existing numerical models showed an average error of less than 5 %, suggesting that the model can be reliably used by mining engineers and environmental specialists. The main aims followed throughout the thesis were:

- (i) Prediction of groundwater inflow into a mining excavation during mining extension in order to propose during the mine designing stage a cost-effective dewatering and drainage scheme and attendant storage facilities.
- (ii) Prediction of both the configuration of the phreatic surface and the height of the seepage face on the highwalls of mining excavations providing the information necessary for slope stability analysis.

- (iii) Prediction of post-mining groundwater rebound giving significant information for assessing the long-term impact of mining operations on local and regional hydrologic systems.
- (iv) Simulation of post-mining water table recovery within the mine spoil providing important information for appropriate and sufficient addition of alkalinity to the backfill and special re-handling techniques in order to minimise pollution potential.
- (v) To achieve sufficient data from the simulation of post-mining groundwater rebound for use in predicting backfill settlement.
- (vi) Prediction of most of the important hydrological parameters affecting the quantity of water inflow into mining excavations and those characteristics influencing groundwater rebound after mine closure.
- (vii) Simulation of long-term pyrite oxidation and pollution generation providing potential for a useful tool for evaluating the effectiveness of a rehabilitation plan to reduce pollutant production within the spoil of an open cut mine containing pyrite.
- (viii) Simulating transportation of oxidation products through groundwater flow systems and incorporating the effects of boundary values such as surface recharge and evaporation gives the distribution of pollutants at each position and time. This information is necessary for designing appropriate site remediation programs.

## 10.2 General Conclusions

This research work which was carried out to present a numerical model for predicting groundwater inflow, post-mining rebound and pollution potential associated with open cut coalmines for designing an appropriate dewatering system and sufficient control of pollution. The conclusions from the study are summarised below:

Although analytical solutions used in this thesis provide quick predictions of groundwater inflow, post-mining rebound and solute transport for use in a field test, in particular, during the beginning stage of mine development, they are, however, restricted to some specific assumptions that limit their capability under difficult mining situations.

For appropriate use of an inflow and post-mining rebound model the following data are required:

- Pre-mining groundwater table elevation for an unconfined aquifer and the thickness of the confined aquifer.
- Rainfall data.
- Geological and hydrogeological characteristics of the aquifer such as hydraulic conductivities, porosity, and transmissivity.
- Surface mining excavation geometry.
- Hydraulic parameters of open cut mine spoil such as permeability and transmissivity, porosity and groundwater velocity.

Among the problems associated with open cut coalmines, acid mine drainage is recognised to be a source of great concern affecting the quality of surface water bodies, groundwater resources and having a detrimental impact on aquatic life. A study of the quality and quantity of mine drainage is necessary for modelling verification purposes. This also provides valuable information for a site remediation program.

The following major factors influence oxidation processes and pollution generation at open cut coalmines:

- The form of the sulphide mineral.
- The size of spoil particles containing the sulphide minerals.
- The availability of oxygen.
- *pH* and *Eh* conditions.
- Sulphide mineral content in spoil particles.
- Temperature.
- The role of iron-oxidising bacteria.
- The role of buffering minerals.

A model describing pyrite oxidation and the pollutant generation mechanism in the spoil of an open cut coalmine should take into account the role of iron-oxidising bacteria. The following major characteristics affect the rate of bacterially mediated oxidation reactions in open cut coalmines:

- *pH*.
- Oxygen concentration.
- Temperature.
- Bacterial populations.
- Pressure and light.
- Nutrients.
- Mineralogical factors.
- Secondary mineral formation.
- Carbon dioxide content.
- Nitrate concentration.

A comprehensive model of pyrite oxidation and pollution prediction should take into consideration the following major characteristics:

- The model should incorporate an enthalpy balance so as to predict the temperature rise due to pyrite oxidation processes within the spoil of open cut coalmines since any change of temperature affects bacterial activity in the spoil.
- Gaseous diffusion processes govern the oxygen supply to the reaction site within the spoil where pyrite oxidation takes place.
- Ferric iron produced by the bacterially catalysed oxidation of ferrous iron cooperates with oxygen in pyrite oxidation and leaching generation.
- Pyrite oxidation process is adequately described by a core-shrinking model.
- In the absence of iron-oxidising bacteria, oxygen plays an important role in oxidising pyrite and the oxidation rate is significantly controlled by the effective diffusion coefficient for oxygen within the pore spaces in the spoil.
- Combined pyrite oxidation and subsequent transportation model should incorporate the acid neutralisation reaction, complexation and precipitation reactions and ion exchange processes.
- Ion exchange, precipitation and complexation reactions are relatively fast and a local equilibrium model was assumed for these reactions.
- Pyrite oxidation and chemical oxidation of ferrous iron are very slow and are assumed to be rate-controlling reactions.

The results of two-dimensional simulation of pyrite oxidation and pollutant prediction associated with backfilled open cut coalmines indicated that at beginning of simulation of the oxidation processes when  $pH$  is high enough to prevent bacterial activity, ferrous iron

concentration is high in the unsaturated zone while the ferric iron concentration is very low. After 5 years of the simulation,  $pH$  dropped to a range between 2.5 to 3.5 causing an enhancement in the bacterial oxidation of pyrite and conversion of ferrous iron to ferric iron. Therefore ferrous iron concentration decreased in the vadose zone while the ferric iron concentration increased considerably in this zone. At 10 years of the simulation the  $pH$  is still favourable for the bacterial activity while ferrous iron depleted in the unsaturated zone whereas the ferric concentration is dominant in this zone. Sulphate generated by both initially oxygen-pyrite reaction and subsequent generation by the bacterial action showed a peak below the water table.

Although the applications of the PHOENICS package in the mining industry was not well recognised, in this research work it was found that PHOENICS is a versatile and reliable commercial package for simulating many mining related problems.

### **10.3 Capabilities of inflow and post-mining rebound models**

The main capabilities and features of the inflow and post-mining rebound models using the SEEP/W package are summarised as follows:

- (i) Simulating both saturated and unsaturated flow; this feature is required to obtain realistic results.
- (ii) Predicting the configuration of the phreatic surface and the height of the seepage face on mining excavation highwalls.
- (iii) Definition of hydraulic conductivity and volumetric water content as a function of pore-water pressure in saturated-unsaturated flow systems.
- (iv) Simulating heterogeneous hydraulic properties in a heterogeneous flow system.

This feature of the model is very important for simulating inflow and post-

mining rebound associated with open cut backfilled mines where the hydraulic characteristics of the backfilled materials are different from those of the solid strata and unexcavated rocks.

- (v) Various boundary conditions such as head boundary condition and recharge flux boundary conditions, flow and no-flow boundary conditions and infinite boundary conditions can be easily specified in the model.
- (vi) Simulating unconfined flow by assuming a zero-water pressure contour within the flow system in order to simulate the position of the water table. Due to this capability in dealing with unconfined flow, downward flow of recharge water within the unsaturated zone is adequately incorporated.

#### **10.4 Capabilities of pyrite oxidation and solute transport model using finite volume method**

The main capabilities and features of the model for describing long-term pyrite oxidation and the subsequent pollutant leaching model incorporating the finite volume technique and using PHOENICS as a computational fluid dynamic package are listed below:

- (i) The fundamentals of the finite volume method are easy to understand and apply.
- (ii) The finite volume method is particularly strong on coarse non-uniform meshes.
- (iii) One important advantage of using the finite volume method over other numerical methods is its strong capability in implementing specific source terms, in particular, those source terms which make the transport equation non-linear.
- (iv) Different boundary conditions can be easily set in the pre-processing module of the PHOENICS model.
- (v) For those very complicated and non-linear source terms, the necessary FORTRAN coding needs to be supplied to the model via an easily accessed subroutine named

GROUND. This subroutine is called by the PHOENICS solver in the course of the solution process.

- (vi) The capability and user-friendly feature of the post-processing module of the PHOENICS package allows easy comparison of the PHOENICS output with field measurements or analytical predictions. The output results can be presented in different ways such as vector and contour plots and graphs.

### **10.5 Modelling studies and evaluation of the results**

A two-dimensional finite element model called SEEP/W was modified to predict the groundwater inflow into surface mining excavations. This model was evaluated with analytical equations and existing numerical models to ensure that the simulation algorithm and the modelling performance is correct using the SEEP/W model. After verification, it was used to predict groundwater inflow to an open cut mine. For comparison purposes, analytical equations again were used. The results of numerical simulation of inflow quantity are in agreement with the inflow predicted by two analytical equations (presented in Singh et al., 1985; and McWhorter, 1981) during pit elongation. Once the maximum elongation was made, both analytical methods and the numerical model showed a decrease in inflow by time, but they are not fully in agreement.

The results of a numerical simulation of post-mining rebound were evaluated with analytical solutions, an existing numerical model (developed for groundwater recovery in open pit mines) and field measurements obtained by other researchers and close agreement was achieved. The error analysis showed that the maximum error never exceeded to 5 % except in two measurement points at site 'A' in the East Midlands area in the UK ( $P_1$ , error = 5.33 %;  $P_4$ , error = 6.61 %).

The close agreement between the simulating results, field data and those results obtained using analytical solutions suggests that the Galerkin finite element method is useful for prediction of inflow and post-mining rebound processes.

The ability of the finite element model of inflow and the post-mining rebound using the SEEP/W package to simulate saturated/unsaturated flow conditions, height of the seepage face on pit highwalls, heterogeneous hydraulic properties, and also simulating unconfined flow conditions taking into consideration hydraulic conductivity and water content as a function of pore-water pressure, makes it a quick and cost-effective method for designing new drainage control systems.

A numerical model has been developed for describing long-term pyrite oxidation and pollutant generation from backfilled open cut coalmines. The modelling was performed using the PHOENICS package incorporating a finite volume technique. The one-dimensional modelling results were verified with those results which were obtained by an existing numerical model and good agreement was obtained.

Simulating the transport of oxidation products through groundwater flow systems was carried out and the model was verified in a one-dimensional case. The following methods were used for verification of the reactive transport model:

- An analytical model was used, incorporating convection, diffusion and linear ion exchange reactions.
- Existing numerical finite element model was used incorporating physical transport processes and non-linear ion exchange reactions.
- A field results obtained by another researcher

The agreement was very close between present modelling results and those results obtained from above listed methods.

Based on the verification made for a one-dimensional simulation, a two-dimensional model has been also developed to take into account the oxygen diffusion model, enthalpy balance, and pyrite oxidation and subsequent transportation of pyrite oxidation products. Although reasonable results were obtained from the two-dimensional simulations the model should be further verified and validated to prove its accuracy.

Based on the above findings, it can be concluded that these numerical models can be reliably used to simulate groundwater inflow, post-mining rebound as well as long-term pyrite oxidation and subsequent pollution generation from backfilled open cut coalmines. Such results can be used for designing site remediation plans in order to minimise environmental side-effects and to provide a sustainable environment for the further use of abandoned mining areas.

#### **10.6 Recommendation for further research**

This study has provided a comprehensive computer-based methodology for mine drainage prediction and designing a mine dewatering system and has also promoted advances in better understanding of the physical, chemical and biological processes involved in long-term pyrite oxidation and pollution generation in backfilled open cut coalmines. However there is still scope for further research in this area and some of these factors are given below:

- (i) The model is limited to two-dimensions. A significant improvement can be made on inflow and post-mining groundwater rebound results by applying this simulation to

three-dimensions (3-D) rather than two-dimensional cross sections, taking into account that flow behaviour in coupled spoil and solid strata is three-dimensional and realistic results can be obtained if simulations are performed in this direction.

- (ii) Although simulation of long-term pyrite oxidation and pollution prediction can be described by one and two-dimensional analysis, the proposed two-dimensional model using the PHOENICS package can be easily modified to perform three-dimensional simulations. Therefore, there is still scope for further research to expand the model. To accomplish this task sufficient data should be available.
- (iii) The present model has the capability to take into account the role of sulphate reduction bacteria. In the present model the role of these bacteria was ignored due to lack of input data and it is recommended that this be incorporated where such bacteria are active.
- (iv) A two-dimensional analysis was performed based on the calibration and verification made on one-dimensional simulations of pyrite oxidation, oxygen diffusion, and subsequent reactive transport of oxidation products. This model should be further validated with actual field measurements.
- (v) The present proposed model for pyrite oxidation and pollution prediction can only be applied to coalmines or to where pyrite is the main reactive sulphide mineral. This model can be easily modified to take into consideration oxidation reactions and metal leaching processes from metallic sulphide mines. Therefore there is a need to expand the model for describing the processes which take place in metal sulphide mines.

- (vi) The rate of pyrite oxidation, acid generation and pollutant loading can be reduced significantly by avoiding an exposure of the pyritic material to the air. This can be achieved by completely sealing off the pyritic material to the atmosphere. If the covering layer also contains clay, the seal will additionally reduce water recharge and further reduce the effect of leaching.

## REFERENCES

- Adam, K., Kourtis, A., Gazea, B. and Kontopoulos, A. (1997). Evaluation of static tests used to predict the potential for acid drainage generation at sulphide mine sites. Transactions of the Institution of Mining and Metallurgy, Section A, Mining Industry, 106, A1-50.
- American Forests (1992). A solution to mine drainage ? (manmade swamp as filter for acid mine drainage)(watershed wars) Soc Clay, 98(7-8), pp. 42-44.
- Arkesteyn, G.J.M.W. (1980). Pyrite oxidation in acid sulphate soils: The role of microorganisms. Plant Soil, 54 (12), p.119-134.
- Atkins, A.S., and Pooley, F.D. (1982). The effects of bio-mechanisms on acidic mine drainage in coal mining. International Journal of Mine Water, No. 1, pp.31-44.
- Atkinson, T. (1982). Surface mining-past, present and future. Journal of mines, metals and fuels, special number on surface mining- Techniques and practices, pp.241-253
- Atkinson, T. (1976), Surface mining, an abridged version of a paper presented in 1976 at Delft University of Technology, 11p.
- Azrag, E.A., Ugorets, V.I. and Atkinson, L.C. (1998). Use of a finite element code to model complex mine water problems. Symposium on International Mine Water Association, Mine Water and Environmental Impacts, proceedings volume 1, Marlin Press C C, Johannesburg, South Africa.
- Balusu, S.R. (1993). Design and development of a multi-scrubber dust control system for longwall faces: Experimental and modelling studies. Ph.D. Thesis, University of Wollongong, pp.188-246.
- Banks, D. (1994). The abandonment of the Killingdal sulphide mine, Norway: a Saga of acid mine drainage and radioactive waste disposal. Mine Water and the Environment, 13, pp.35-48.
- Berner, R.A. (1964). An idealized model of dissolved sulfate distribution in recent sediments. Geochimica et Cosmochimica Acta, 28 (9), pp.1497-1503.
- Binning, P. and Celia, M.A. (1996). A finite volume Eulerian-Lagrangian localized adjoint method for solution of the contaminant transport equations in two-dimensional multiphase flow systems. Water Resources Research, 32 (1), pp.103-114.
- Blowes, D.W., Ptacek, C.J., Frind, E.O., Johnson, R.H., Robertson, W.D., and Molson, J.W. (1994). Acid neutralization reactions in inactive mine tailings impoundments and their effect on the transport of dissolved metals. Proceedings of the Third International Conference on the Abatement of Acidic Drainage, Pittsburgh, PA, April 24-29, 1, pp.429-438.

Bohnet, E.L. and Kunze, L. (1990). Waste disposal-planning and environmental protection aspects. *Surface Mining*, 2<sup>nd</sup> edition, B. A. Kennedy (Ed.), Society for Mining, Metallurgy and Exploration Inc., AIME, Colorado, pp. 485-494.

Bowell, R.J., Barta, J., Gringrich, M., Mansanares, W. and Parshley, J. (1998). Geological controls on pit lake chemistry: Implications for the assessment of water quality in inactive open pits. *Symposium on Mine Water and Environmental Impacts*, P.J. Norton and M. Veselic (Eds.), Proceedings Volume 2, Johannesburg, South Africa, pp. 375-386.

Bridwell, R.J. and Travis, B.J. (1995). Numerical simulation of acid mine drainage (AMD) in a fully-coupled 3-D ground water flow and chemical transport model: part I, field example and validation. *Proceedings, Conference on mining and the environment*, Sudbury, Ontario, Canada, pp.775-784.

Brown, A. (1979). Simple mine inflow evaluation for underground oil shale mines. *Proceedings of the first International Mine Drainage Symposium*, Denver, Colorado, pp.528-551.

Bucyrus-Erie Company (1977). *Surface mining supervisory training program*, South Milwaukee, Wisconsin.

Castro, J.M., Wielinga, B.W., Gannon, J.E. and Moore, J.N. (1999). Stimulation of sulfate-reducing bacteria in lake water from a former open-pit mine through addition of organic wastes. *Water Environment Research*, 71(2), pp. 218-223.

Cathles, L.M. (1979). Predictive capabilities of a finite difference model of copper leaching in low grade industrial sulfide waste dumps. *Mathematical Geology*, 11 (2), pp.175-191.

Cathles, L.M. and Apps, J.A. (1975). A model of the dump leaching process that incorporates oxygen balance, heat balance and air convection. *Metallurgical Transactions B. Volume 6B*, pp.617-624.

CHAM (2000). *The PHOENICS On-Line Information System*,  
[http://www.cham.co.uk/phoenics/d\\_polis/polis.htm](http://www.cham.co.uk/phoenics/d_polis/polis.htm)

Chen, M., Soulsby, C. and Younger, P.L. (1999). Modelling the evolution of mine water pollution at Polkemmet Colliery, Almond catchment, Scotland. *Quarterly Journal of Engineering Geology*, 32(4), pp. 351-362.

CRC, *Handbook of chemistry and physics*, D.R., Lide (Editor-in-chief), 78<sup>th</sup> edition, CRC press LLC, Boca Roton, New York, 1997-1998.

Davis, A.D. and Zabolotney, G.A. (1996). Ground-water simulations for the determination of post mining recharge rates at the Belle Ayr Mine, *Mining Engineering*, 48 (11), pp.80-83.

Davis, G.B. (1983). Mathematical modelling of rate-limiting mechanisms of pyritic oxidation in overburden dumps. Ph.D. Thesis, University of Wollongong, Australia, 159p.

Davis, G.B. and Ritchie, A.I.M. (1986a). A model of oxidation in pyritic mine wastes: part 1: Equations and approximate solution. *Applied Mathematical Modelling*, 10 (5), pp.314-322.

Davis, G.B., Doherty, G. and Ritchie, A.I.M. (1986b). A model of oxidation in pyritic mine wastes: part 2: Comparison of numerical and approximate solutions. *Applied Mathematical Modelling*, 10, pp.323-329.

Department of Resources and Energy (1983). Water 2000, Consultants Report No. 7 Water Quality Issues, Australian Government Publishing Service (AGPS), Canberra.

Desai, C.S. (1974). Finite element methods for flow in porous media. International symposium on finite element methods in flow problems, University of Swansea, finite element method in flow problems, J.T. Oden, O.C. Zienkiewicz, R.H. Gallagher and C. Taylor (Eds.), UAH press, University of Alabama, Huntsville, Alabama.

Destouni, G., Malmstrom, M., Berglund, S., and Lindgren, M. (1998). Modelling of acid mine drainage from waste rock and mill tailings. Technical Report, Division of Water Resources Engineering, Department of Civil and Environmental Engineering, Royal Institute of Technology, Stockholm, Sweden, ISSN 1400-1306, ISBN 91-7170-361-6, 25p.

Diz, H.R. (1998). The selective oxide system: Acid drainage treatment that avoids the formation of sludge. *Mine Water and the Environment*, 17(1), pp. 1-7.

Domenico, P.A. and Schwartz, F.W. (1990). Physical and chemical hydrogeology, 1<sup>st</sup> edition, John Wiley & Sons, Inc., New York, 824 p.

Drury, W.J. (2000). Modelling of sulfate reduction in anaerobic solid substrate bioreactors for mine drainage treatment. *Mine Water and the Environment*, 19 (1), pp.19-29.

Dudgeon, C.R. (1985). Unconfined non-Darcy flow near open-pit mines. Proceedings of the Second International Congress of the International Mine Water Association, Granada, Spain, pp.443-454.

Edwards, J.S., Ren, T.X. and Jozefowicz, R. (1995). Using computational fluid dynamics (CFD) to solve mine safety and health problems. APCOM xxv 1995, Technical Proceedings, Application of Computers and Operations Research in the Minerals Industries, Brisbane, Australia, 9-14 July 1995, pp.41-47.

Elberling, B., Nicholson, R.V. and Scharer, J.M. (1994). A combined kinetic and diffusion model for pyrite oxidation in tailings: a change in controls with time. *Journal of Hydrology*, 157(1), pp.47-60.

Environment Australia (1997). Managing sulphidic mine wastes and acid drainage. One booklet in a series on best practice environmental management in mining, Commonwealth of Australia.

Erickson, P.M., Kleinmann, R.L.P., Posluszny, E.T. and Leonard-Mayer, P.J. (1982). Hydrogeochemistry of a large mine pool. Proceedings of the First International Mine Water Congress of the International Mine Water Association (IMWA), April 19-24, 1982, Budapest, Hungary, pp.27 -42.

Eriksson, N. and Destouni, G. (1997). Combined effects of dissolution kinetics, secondary mineral precipitation, and preferential flow on copper leaching from mining waste rock. *Water Resources Research*, 33 (3), pp.471-483.

Ezeigbo, H.I. And Ezeanyim, B.N. (1993). Environmental pollution from coal mining activities in the Enugu areas, Anambka State, Nigeria. *Mine Water and the Environment*, 12, pp. 53-62.

Fang, H.Y. (1997). *Introduction to Environmental Geotechnology*, CRC Press LLC, Boca Roton, 652p.

Fetter, C.W. (1988). *Applied hydrogeology*, Merrill publishing company, Columbus, Ohio, U.S.A, 592p.

Freeze, R.A. and Cherry, J.A. (1979). *Groundwater*, Prentice-Hall, Inc., Englewood Cliffs, New Jersey, 604p.

Frind, E.O. and Verge, M.J. (1978). Three-dimensional modelling of groundwater flow systems. *Water Resources Research*, 14 (5), pp.844-856.

Gardner, L.R. and Lerche, I. (1987). Simulation of sulfate-dependent sulfate reduction using Monod kinetics. *Mathematical Geology*, 19 (3), pp.219-239.

GEO-SLOPE International, Ltd. (2002). SEEP/W for finite element seepage analysis, <http://www.geo-slope.com/products/seepw.asp>

Govil, P.K., Reddy, G.L.N. and Gnaneswara R.T. (1999). Environmental pollution in India: Heavy metals and radiogenic elements in Nacharam Lake. *Journal of Environmental Health*, 61, i8, pp.23-28.

Gray, N.F. (1998). Acid mine drainage composition and the implications for its impact on lotic systems. *Water Resources*, 32(7), pp. 2122-2134.

Gray, W.G. and Pinder, G.F. (1974). Galerkin approximation of the time derivative in the finite element analysis of groundwater flow. *Water Resources Research*, 10 (4), pp.821-828.

Green, S.R. and Clothier, B.E. (1994). Simulation water and chemical movement into unsaturated soils. *The PHOENICS Journal of Computational Fluid Dynamics & Its Applications*, 7(1), pp.76-92.

Grove, D.B. (1977). The use of Galerkin finite-element methods to solve mass-transport equations. U.S. geological survey, water resources division, Denver federal center, Denver, Colorado.

Guedes de Carvalho, R.A., Gonzalez Bega, C.G., Martins Sampaio, M.N., Neves, O. and Sol pereira, M.C. (1986). A study of the drainage of the pyrite mines of Aljustrel (Portugal). *International Journal of Mine Water*, 5(2), pp. 43-56.

Hamilton, Q.U.I., Lamb, H.M., Hallett, C. and proctor, J.A. (1999). Passive treatment systems for the remediation of acid mine drainage at Wheal Jane, Cornwall. *Journal of the Institution of Water & Environmental Management*, 13(2), pp. 93-103.

Hammack, R.W., de Vegt, A.L. and Schoeneman, A.L. (1998). The removal of sulfate and metals from mine waters using bacterial sulfate reduction: Pilot plant results. *Journal of Mine Water and The Environment*, 17 (1), pp.8-27.

Hanna, T.M., Azrag, E.A. and Atkinson, L.C. (1994). Use of an analytical solution for preliminary estimates of groundwater inflow to a pit, *Mining Engineering*, 46 (2), pp.149-152.

Hawkins, J.W. (1995). Impacts on ground-water hydrology from surface coal mining in Northern Appalachia. *Proceedings on Water Resources at Risk*, W.R. Hotckkiss, J.S. Downey, E.D. Gutentag and J.E. Moore (Eds.), American Institute of Hydrology, pp.32-43.

Hawkins, J.W. (1998). Hydrogeologic characteristics of surface-mine spoil. In: *Coal Mine Drainage Prediction and Pollution Prevention in Pennsylvania*, Chapter 3. K.B.C. Brady, M.W. Smith and J. Schueck (Eds.), Department of Environmental Protection, Harrisburg, Pennsylvania, USA, pp.3\_1-3\_11.

Hawkins, J.W. and Aljoe, W.W. (1990). Hydrological characterization and modelling of a heterogeneous acid-producing surface coal mine spoil, Upshur County, WV, *proceedings, 1990 National symposium on mining*, University of Kentucky, pp.43-52.

Hellier, W.W. (1998). Abatement of acid mine drainage by capping a reclaimed surface mine with fluidized bed compustion ash. *Mine Water and the Environment*, 17 (1), pp. 28-40.

Henton, M.P. (1981). The problem of water table rebound after mining activity and its effect on ground and surface water quality. *Quality of groundwater*, *Proceedings of an International Symposium*, Noordwijkethout, The Netherlands, W. Van Duijvenbooden, P. Glasbergen and H. Van Lelyveld (Eds.), studies in environmental science, Vol. 17, Elsevier scientific publishing company, Netherlands.

Herbert Jr., R.B. (1994). Metal transport in groundwater contaminated by acid mine drainage. *Nordic Hydrology*, 25, pp.193-212.

Herbert Jr., R.B., Benner, S.G. and Blowes, D.W. (1998). Reactive barrier treatment of groundwater contaminated by acid mine drainage: Sulphur accumulation and sulphide

formation. International Association of Hydrological Sciences (IahS), No.250, pp. 451-457.

Hofedank, R.H. (1979). Computation of and experience on lignite opencast mine drainage. Proceedings of the First International Mine Drainage Symposium, Denver, Colorado, pp.383 -408.

Hoffmann, M.R., Faust, B.C., Panda, F.A., Koo, H.H., and Tsuchiya, H.M. (1981). Kinetics of the removal of iron pyrite from coal by microbial catalysis. Applied and Environmental Microbiology, 42 (2), pp.259-271.

Hoth, N., Hafner, F. and Boy, S. (1998). Modelling of groundwater contamination caused by lignite mining in eastern Germany. Symposium on Mine Water and Environmental Impacts, IMWA Symposium, Johannesburg, pp. 223-233.

Hounslow, A.W. (1995). Water quality data, analysis and interpretation, Lewis Publishers, CRC Press, U.S.A, 397p.

Hromadka II, T.V. (1992). A review of groundwater contaminant transport modelling techniques. Environmental Modeling, P. Melli and P. Zannetti (Eds.), Computational Mechanics Publications, Elsevier Applied Science, UK, pp.35-53.

Hughson, D.L. and Codell, R. (2001). Comparison of numerical and analytical models of unsaturated flow around underground openings. Mining Engineering, 53(12), pp. 45-48.

Hummel, J., Fischer, R., Luckner, L., Kaden, S. (1985). Submodels of water quality for the analysis of regional water policies in open-pit Lignite mining areas. Proceedings of the Second International Congress of the International Mine Water Association, Granada, Spain, Volume 2, pp.673-684.

Huyakorn, P.S., Springer, E.P., Guvanasen, V. and Wadsworth, T.D. (1986). A three-dimensional finite-element model for simulating water flow in variably saturated porous media. Water Resources Research, 22 (13), pp.1790-1808.

Isles, P.T., Hagan, T.N. and Smith, G.H. (1986). Strip mining, Australasian coal mining practice, Monograph 12, The Australian Institute of Mining and Metallurgy, pp.189-202.

Jaynes, D.B. (1983). Atmosphere and temperature within a reclaimed coal-stripmine and a numerical simulation of acid mine drainage from stripmined lands. Ph.D. dissertation, Pa. State Univ., University Park, pp.161-170.

Jaynes, D.B., Rogowski, A.S. (1983). Applicability of Fick's law to gas diffusion. Soil Science Society of America Journal, 47 (3), pp.425-430.

Jaynes, D.B., Rogowski, A.S. and Pionke, H.B., (1984a). Acid mine drainage from reclaimed coal strip mines, 1, Model description. Water Resources Research, 20 (2), pp.233-242.

Jaynes, D.B., Rogowski, A.S. and Pionke, H.B., (1984b). Acid mine drainage from reclaimed coal strip mines, 2, Simulation results of model. *Water Resources Research*, 20 (2), pp.243-250.

Jennings, A.A., Kirkner, D.J. and Theis, T.L. (1982). Multicomponent equilibrium chemistry in groundwater quality models. *Water Resources Research*, 18 (4), pp.1089-1096.

Kennedy, B.A. (1990). *Surface mining*, Littleton, Colo.: Society for Mining, Metallurgy, and Exploration, AIME, 2<sup>nd</sup> edition, 1194p.

Kleinmann, R.L.P. (1990). Acid mine water treatment using engineered wetlands. *International Symposium on Acid Mine Water in Pyritic Environments*, P.J. Norton (Ed.), Proceedings, Lisbon, Portugal, September 16-19, pp.269-276.

Krabbenhoft, D.P., Anderson, M.P. and Bowser, C.J. (1990). Estimating groundwater exchange with lakes, 2. Calibration of a three-dimensional solute transport model to a stable Isotope plume. *Water Resources Research*, 26 (10), pp.2455-2462.

Kruseman, G.P. and De Ridder, N.A. (1979). Analysis and evaluation of pumping test data, Bulletin 11, International Institute for Land Reclamation and Improvement, The Netherlands, 200p.

Kukla, G.T., Buffier, M.J., Balks, R.J. and Farnell, G.K. (1986). *Open pit mining. Australasian coal mining practice*, Monograph 12, The Australian Institute of Mining and Metallurgy, pp. 203-215.

Lefebvre, R. and Gelinas, P.J. (1995). Numerical modelling of AMD production in waste rock dumps. *Conference on Mining and the Environment, Proceedings*, Sudbury, Ontario, pp.869-878.

Lerman, A. (1979). *Geochemical processes: water and sediment environments*, John Wiley, New York, 481p.

Levenspiel, O. (1972). *Chemical reaction engineering*, John Wiley, New York, 578p.

Lewis, R.L. (1999). Predicting the steady-state water quality of pit lakes. *Mining Engineering*, 51 (10), pp.54-58.

Malouf, E.E. and Prater, J.D. (1961). Role of bacteria in the alteration of sulfide minerals. *Journal of Metals*, 13 ( 5), p.353-356.

Marinelli, F. and Niccoli, W.L. (2000). Simple analytical equations for estimating ground water inflow to a mine pit. *Ground Water*, 38 (2), p.311-314.

McKnight, D.M., Kimball, B.A. and Runkel, R.L. (2001). pH dependence of iron photoreduction in a rocky mountain stream affected by acid mine drainage. *Hydrological Processes*, 15, p.1979-1992.

- McNab Jr., W.W. and Narasimhan, T.N. (1994). Modelling reactive transport of organic compounds in groundwater using a partial redox disequilibrium approach. *Water Resources Research*, 30(9), pp. 2619-2635.
- McWhorter, D.B. (1981). Predicting groundwater response to disturbance by mining-selected problems. *Symposium of Surface Mining, Hydrology, Sedimentology and Reclamation*, pp.89-95, University of Kentucky, Lexington, Kentucky, U.S.A.
- Merrington, G. and Alloway, B.J. (1993). Leaching characteristics of heavy metals from three historical Pb–Zn mine tailings heaps in the united kingdom, *Mining Industry*, 102, pp. 71-152.
- Middelburg, J.J. (1989). A simple rate model for organic matter decomposition in marine sediments. *Geochimica et Cosmochimica Acta*, 53, pp.1577-1581.
- Miller, C.W. and Benson, L.V. (1983). Simulation of solute transport in a chemically reactive heterogeneous system: Model development and application. *Water Resources Research*, 19 (2), pp.381-391.
- Mirabediny, H. (1998). A dragline simulation model for strip mine design and development, Ph.D. Thesis, University of Wollongong, 327p.
- Mittel, H.K. and Singh, J. (1993). Effect of water harvesting structure on groundwater recharge – A case study. *Environmental Management, Geo-Water and Engineering Aspects*, R.N. Chowdhury and M. Sivakumar (eds), Balkema, Rotterdam, pp.461-465.
- Modis, K., Adam, K., Panagopoulos, K. and Kontopoulos, A. (1998). Development and validation of a geostatistical model for prediction of acid mine drainage in underground sulphide mines. *Transaction of the Institution of Mining and Metallurgy, Section A, Mining Industry*, 107, A63-108.
- Moolick, R.T. and O'Neill, J.E. (1968). Strip methods, including advanced stripping, surface mining (1<sup>st</sup> edn), E.P. Pfeleider (Ed.), *The American Institute of Mining, Metallurgical, and Petroleum Engineers, Inc., AIME*, New York, pp. 166-183.
- Naugle, G.D. and Atkinson, L.C. (1993). Estimating the rate of post-mining filling of pit lakes, *Mining Engineering*, 45(4), pp. 402-404.
- National Coal Board (1982). *Technical management of water in the coal mining industry*, the national coal board, London, 129p.
- Neuman, S.P. (1972). Theory of flow in unconfined aquifers considering delayed response of the water table, *Water Resources Research*, 8 (4), pp.1031-1045.
- Neuman, S.P. (1974). Galerkin approach to unsaturated flow in soils. *International Symposium on Finite Element Methods in Flow Problems*, University of Swansea, J.T. Oden, O.C. Zienkiewicz, R.H. Gallagher and C. Taylor (Eds.), UAH press, University of Alabama, Huntsville, Alabama.

Ngah, S.A. (1985). Hydrogeological aspects of surface coal mine dewatering, M. Phil Thesis, University of Nottingham, 288p.

Nordstrom, D.K. and Southam G. (1997). Geomicrobiology of sulfide mineral oxidation. In: Reviews in mineralogy: Geomicrobiology: interactions between microbes and minerals, Banfield J.F. and Nealson K.H. (Eds), Mineral Association of Canada, 35, pp.361-390.

Norton, P.J. (1983). A study of groundwater control in British surface mining, Ph.D. Thesis, Nottingham University, 460p.

Norton, P.J. (1992). The control of acid mine drainage with wetlands. *Mine Water and the Environment*, 11(3), pp. 27-34.

Norton, P.J. (1995). The impact of mine closures on groundwater and the environment: A UK lesson for all countries, *Proceedings on Water Resources at Risk*, W.R. Hotchkiss, J.S. Downey, E.D. Gutentag and J.E. Moore (Eds.), American Institute of Hydrology, pp. IMWA (85-91).

Pankow, J.F. (1991). *Aquatic chemistry concepts*, Lewis Publishers, Chelsea, Mich., 673p.

Parkhurst, D.L., and Appelo, C.A.J. (2002). User's guide to PHREEQC (Version 2) – A computer program for speciation, batch-reaction, one-dimensional transport, and inverse geochemical calculations”  
[http://wwwbrr.cr.usgs.gov/projects/GWC\\_coupled/phreeqc/html/final.html](http://wwwbrr.cr.usgs.gov/projects/GWC_coupled/phreeqc/html/final.html)

Patankar, S. . (1980). *Numerical heat transfer and fluid flow*, Taylor&Francis, USA, 197p.

Pearce, P.F. and Ries, E.R. (1982). Protection of environmental resources by effective mine water management. *Proceedings of the First International Mine Water Congress of the International Mine Water Association (IMWA)*, April 19-24, 1982, Budapest, Hungary, pp.80-95.

Pentreath, R.J. (1994). The discharge of waters from active and abandoned mines. *Issues in Environmental Science and Technology, Mining and its Environmental Impact*, R.E. Hester and R.M. Harrison (Eds.), The Royal Society of Chemistry, Cambridge, pp.121-131.

Perry, A. and Kleinmann, R.L.P. (1991). The use of constructed wetlands in the treatment of acid mine drainage. *Natural Resources Forum*, 15 (3), pp.178-184.

Pickens, J.F. and Lennox, W.C. (1976). Numerical simulation of waste movement in steady groundwater flow systems. *Water Resources Research*, 12 (2), pp.171-180.

Pinder, G.F. (1973). A Galerkin-finite element simulation of groundwater contamination on Long Island, New York. *Water Resources Research*, 9 (6), pp.1657-1669.

Pinder, G.F. and Frind, E.O. (1972). Application of Galerkin's procedure to aquifer analysis. *Water Resources Research*, 8 (1), pp.108-120.

Pinder, G.F., Frind, E.O. and Papadopoulos, S.S. (1973). Functional coefficients in the analysis of groundwater flow. *Water Resources Research*, 9(1), pp.222-226.

Putti, M. and Yen, W.W.-G. and Mulder, W.A. (1990). A triangular finite volume approach with high-resolution upwind terms for the solution of groundwater transport equations. *Water Resources Research*, 26 (12), pp.2865-2880.

Rabbani, M.G. (1994). Direct-formulation finite element (DFFE) method for groundwater flow modelling: Two-dimensional case. *SIAM Journal on Applied Mathematics*, a Publication of the Society for Industrial and Applied Mathematics, 54 (3), pp.674-687.

Rabbani, M.G. and Warner, J.W. (1994). Shortcomings of existing finite element formulations for subsurface water pollution modelling and its rectification: One-dimensional case. *SIAM Journal on Applied Mathematics*, A publication of the society for industrial and applied mathematics, 54 (3), PP.660-673.

Reddi, L.N. and Inyang, H.I. (2000). *Geoenvironmental engineering, principles and applications*, Marcel Dekker, Inc., New York, 494p.

Reed, S.M. (1986). Groundwater recovery problems associated with opencast mine Backfills. Ph.D. Thesis, University of Nottingham, 332p.

Reed, S.M., McLean, A. and Singh R.N. (1987). Aspects of opencast mine backfill compaction. *Compaction technology*, Proceeding of the Conference Organized by New Civil Engineer and held in London, T. Telford (Ed.), pp.163-171.

Reed, S.M. and Singh R.N. (1986). Groundwater recovery problems associated with opencast mine backfills in the United Kingdom. *International Journal of Mine Water*, 5 (3), pp.47-74.

Ricca, V.T. and Schultz, R.R. (1979). Acid mine drainage modelling of surface mining. *Mine Drainage*, Proceedings of The First International Mine Drainage Symposium, G.O. Argall, Jr. C.O. Brawner (Eds.), Miller Freeman Publications, Inc., U.S.A, pp. 651-670.

Robb, G.A. and Robinson, J.D.F. (1995). Acid drainage from mines, *The Geographical Journal*, 161(1), pp.47-54.

Robins, R.G. (1991). Chemical interactions in sulfide mineral tailings. *International Conference on Mining and the Environment, Waste Disposal and Pollution Control*, Section 6, Bandung, Indonesia, Paper 3.1.

Rogowski, A.S., Pionke, H.B., and Broyan, J.G. (1977). Modelling the impact of strip mining and reclamation processes on quality and quantity of water in mined areas: A review. *Journal of Environmental Quality*, 6 (3), pp.237-244.

Rogowski, A.S. and Weinrich, B.E. (1981). Modeling water flux on strip-mined land. *Transactions of the American Society of Agricultural Engineers*, 24 (4), pp.935-940.

Rose, A.W. and C.A. Cravotta III (1998). Geochemistry of coal mine drainage. In: *Coal Mine Drainage Prediction and Pollution Prevention in Pennsylvania*, Chapter 1. K.B.C. Brady, M.W. Smith and J. Schueck (Eds.), Department of Environmental Protection, Harrisburg, Pennsylvania, USA, pp.1\_1-1\_22.

Rossi, G. (1990). *Biohydrometallurgy*, McGraw-Hill Book Company GmbH, Hamburg, 609p.

Rubin, J. (1983). Transport of reacting solutes in porous media: relation between mathematical nature of problem formulation and chemical nature of reactions. *Water Resources Research*, 19 (5), pp.1231-1252.

Rubin, J. and James, R.V. (1973). Dispersion-affected transport of reacting solutes in saturated porous media: Galerkin method applied to equilibrium-controlled exchange in unidirectional steady water flow. *Water Resources Research*, 9 (5), pp.1332-1356.

Rubio, R.F. and Del Olmo, A.G. (1995). Mining drainage and water supply under sustainable constraints. *Proceedings on Water Resources at Risk*, W.R. Hotchkiss, J.S. Downey, E.D. Gutentag and J.E. Moore (Eds.), May 14-18, Denver, American Institute of Hydrology, pp.23-32.

Rubio, R.F. and Lorca, D.F. (1993). Mine water drainage. *Journal of Mine Water and the Environment*, 12, pp.107-130.

Serrat, E., Jezequel, D. and Sarazin, G. (2000). Determination of sulfate reduction kinetics in Aydat lake sediments, ASLO 2000, Copenhagen-Denmark, June 5-9.

Saharan, M.R., Gupta, K.K., Jamal, A. and Sheoran, A.S. (1995). Management of acidic effluents from tailing dams in metalliferous mines. *Mine Water and the Environment*, 14, pp. 85-94.

Salmon, S.U.J. (1999). Overview of models for biogeochemical modelling of acid mine drainage. Division of Water Resources Engineering, Department of Civil and Environmental Engineering, Royal Institute of Technology, Stockholm, Sweden.

Sasaki, K., Tsunekawa, M., Ohtsuka, T. and Konno, H. (1998). Role of sulfur – oxidizing bacteria *Thiobacillus Thiooxidans* in pyrite weathering. *Colloids & Surface A-Physicochemical & Engineering Aspects*, 133(3), pp. 269-278.

Scharer, J.M., Nicholson, R.V., Halbert, B. and Snodgrass W.J. (1994a). A computer program to assess acid generation in pyritic tailings. In *Environmental Geochemistry of Sulfide Oxidation*, Alpers C.N. and Blowes D.W. (Eds), ACS Symposium Series 550, pp.132-152.

Scharer, J.M., Pettit, C.M., Chambers, D.B., Kwong, E.C. (1994b). Mathematical simulation of a waste rock heap. *Proceedings of the International Land Reclamation and*

Mine Drainage Conference and the Third International Conference on the Abatement of Acidic Drainage, Pittsburg, PA, April 1994, p.30-39.

Schnaitman, C.A., Korczynski, M.S. and Lundgren, D.G. (1969). Kinetic studies of iron oxidation by whole cells of *Ferrobacillus ferrooxidans*. *Journal of Bacteriology*, 99 (2), 552-557.

Schnoor, J.L. (1996). Environmental modelling, fate and transport of pollutants in water, air and soil, John Wiley & sons, U.S.A, 682p.

Shaw, E.M. (1983). *Hydrology in Practice*, Van Nostrand Reinhold, U.K, 569p.

Sheng, D. and Smith, D.W. (1997). Analytic solutions to the advective contaminant transport equation with non-linear sorption, Research report No. 158.12.1997, ISBN 0 7259 10194, Department of civil, surveying and environmental engineering, The Univ of Newcastle, Australia.

Shevenell, L. (2000). Analytical method for predicting filling rates of mining pit lakes: example from the Getchell Mine, Nevada. *Mining Engineering*, 52(3), p.53-60.

Singer, P.C. and Stumm, W. (1970). Acidic mine drainage: The rate determining step. *Science*, 167, pp.1121-1123.

Singh, R.N. (1998). *Mine water*, University Press, Wollongong, Australia, 290p.

Singh R.N., and Atkins A.S. (1984). Application of analytical solutions to simulate some mine inflow problems in underground coal mining. *International Journal of Mine Water*, 3(4), pp.1-27.

Singh, R.N. and Atkins, A.S. (1985a). Application of idealised analytical techniques for prediction of mine water inflow. *Mining Science and Technology*, 2, Elsevier science publishers B. V., Amsterdam, Netherlands, pp.131-138.

Singh, R.N. and Atkins, A.S. (1985b). Analytical techniques for the estimation of mine water inflow. *International Journal of Mining Engineering*, 3, pp.65-77.

Singh, R.N., Ngah, S.A. and Atkins, A.S. (1985). Applicability of current groundwater theories for the prediction of water inflows to surface mining excavations. *Proceedings of the Second International Congress of the International Mine Water Association*, Granada, Spain, pp.553-571.

Singh, R.N. and Reed, S.M. (1987). Estimation of pumping requirements for a surface mining operation. *Pumps and Pumping*, two day Symposium at East Midlands Conference Centre, Marylebone press limited, University of Nottingham, England, pp.1-24.

Silver, M. (1989). Control of acid mine drainage including coal pile and ash pond seepage: 42a Biology and chemistry of generation, prevention and abatement of acid mine drainage. *Constructed wetlands for wastewater treatment: municipal, industrial and agricultural*, D.A. Hammer (Ed.), Lewis publishers, Inc., USA, pp.753-760.

- Skousen, J. (2000). Acid mine drainage treatment. Division of Plant and Soil Science, College of Agriculture and Forestry, <http://www.wvu.edu/~research/acidminedrainage.html>
- Skousen, J. (2002). Overview of passive systems for treating acid mine drainage. West Virginia University, center for agriculture, natural resources, and community development, 20 December 2002. <http://www.wvu.edu/~agexten/landrec/passtrt/passtrt.htm>
- Soderberg, A. and Rausch, D.O. (1968). Pit planning and layout, surface mining (1<sup>st</sup> edn), E.P. Pfeleider (Ed.). The American Institute of Mining, Metallurgical and Petroleum Engineers, Inc., AIME, New York, pp.141-165.
- Spalding, D.B. (1981). A general purpose computer program for multi-dimensional one- and two-phase flow. *Mathematics and Computers in Simulation*, 23(3), pp.267-276.
- Stiefel R.C. and Busch, L.L. (1983). Surface water quality monitoring. *Surface Mining Environmental Monitoring and Reclamation Handbook*, L.V.A. Sendlein, H. Yazicigil and C.L. Carlson (Eds.), Elsevier Science Publishing Co., Inc., New York, pp. 189-212.
- Stokstand, P. (1998). Structuring a reclamation program for abandoned non-coal mine. *Ecology Law Quarterly*, 25(1), pp. 121-165.
- Stumm, W. and Morgan, J. (1996). *Aquatic chemistry: chemical equilibria and rates in natural waters*, John Willey, New York, 1022p.
- Svensson, U. (1997). Modelling groundwater flow on a regional scale. *The PHOENICS Journal: Computational Fluid Dynamics and its Applications*, 10 (4), pp. 442-450.
- Todd, D.K. (1959). *Groundwater hydrology*, John Wiley & Sons, Inc., New York, 336p.
- Toit, I., Jansen, H. and Johnstone, A. (1998). Assessing groundwater quality trends after mine closure- the South African situation. *Symposium on Mine Water and Environmental Impacts*, P.J. Norton and M. Veselic (Eds.), *Proceedings Volume2*, Johannesburg, South Africa, pp.359-365.
- Tsukamoto, T.K. and Miller, G.C. (1999). Methanol as a carbon source for microbiological treatment of acid mine drainage, *Water Resources*, 33(6), pp. 1365-1370.
- U.S. Environmental Protection Agency (1994). Acid mine drainage prediction. Technical document, office of solid waste, special waste branch, EPA530-R-94-036, NTIS, PB94-201829, 48p.
- Valocchi, A.J., Street, R.L. and Roberts, P.V. (1981). Transport of ion-exchanging solutes in groundwater: Chromatographic theory and field simulation. *Water Resources Research*, 17 (5), pp.1517-1527.
- Vandersluis, G.D., Straskraba, V. and Effner, S.A. (1995). Hydrogeological and geochemical aspects of lakes forming in abandoned open pit mines. *Proceedings on*

Water Resources at Risk, W.R. Hotchkiss, J.S. Downey, E.D. Gutentag and J.E. Moore (Eds.), American Institute of Hydrology, pp.162-177.

Venburg, L.G. (1979). Dewatering of mines – A practical analysis. Proceedings of the First International Mine Drainage Symposium, Denver, Colorado, pp.219-232.

Versteeg, H.K. and Malalasekera, W. (1995). An introduction to computational fluid dynamics, the finite volume method, Prentice Hall, UK, 257p.

Walter, A.L., Frind, E.O., Blowes, D.W., Ptacek, C.J. and Molson, J.W. (1994a). Modelling of multicomponent reactive transport in groundwater, 1, Model development and evaluation. Water Resources Research, 30(11), pp.3137-3148.

Walter, A.L., Frind, E.O., Blowes, D.W., Ptacek, C.J. and Molson, J.W. (1994b). Modelling of multicomponent reactive transport in groundwater, 2, Metal mobility in aquifers impacted by acidic mine tailings discharge. Water Resources Research, 30(11), pp.3149-3158.

Walton, W.C. (1970). Groundwater resource evaluation, McGraw-Hill, Kogakusha Ltd., 664p.

Wang, H.F. and Anderson, M.P. (1982). Introduction to groundwater modelling, finite difference and finite element methods, W. H. Freeman and company, San Francisco, 237p.

Watson, I. And Burnett, A.D. (1993). Hydrology an Environmental approach, Buchanan Books, Cambridge, Ft. Lauderdale, 702p.

Williams, R.E. (1975). Waste production and disposal in mining, milling, and Metallurgical industries, Miller-Freeman Publishing Company, San Francisco, California, 489p.

Williams, R.E., Baldwin, J. and Ralston, D.R. (1979). Coping with mine drainage regulations. Proceedings of the First International Mine Drainage Symposium, Denver, Colorado, pp.184 -218.

Williams, R.E., Winter, G.V., Bloomsburg, G.L. and Ralston, D.R. (1986). Mine Hydrology, Society of Mining Engineers, Inc., Port city press, Inc, Littleton, Colorado, 169p.

Wunderly, M.D., Blowes, D.W., Frind, E.O. and Ptacek, C.J. (1996). Sulfide mineral oxidation and subsequent reactive transport of oxidation products in mine tailings impoundments: A numerical model. Water Resources Research, 32 (10), pp.3173-3187.

Xavier, A.G. (1990). Environmental-biochemical aspects of heavy metals in acid mine water. International Symposium on Acid Mine Water in Pyritic Environment, Lisbon, Portugal, pp. 43-55.

Yakowitz, S. and Szidarovszky, F. (1989). An introduction to numerical computations, second edition, Macmillan, New York, 462p.

## APPENDIX A

### FINITE ELEMENT DISCRETISATION OF THE GROUNDWATER FLOW EQUATION

Equation 4.9 (Chapter 4, Page 124) may be rewritten as:

$$L(h) = \frac{\partial}{\partial x} \left( K_x \frac{\partial h}{\partial x} \right) + \frac{\partial}{\partial y} \left( K_y \frac{\partial h}{\partial y} \right) - C_{uw} \frac{\partial h}{\partial t} + W = 0 \quad (\text{A.1})$$

where,

$L$  = differential operator defined in the flow region.

To solve  $L(h) = 0$  by the Galerkin approach a trial solution is assumed:

$$h \approx \hat{h}(x, y, t) = \sum_{i=1}^n h_i(t) N_i(x, y) \quad (\text{A.2})$$

where,

$h_i(t)$  = hydraulic head at node  $i$ ;

$n$  = total number of nodes in the problem domain;

$N_i(x, y)$ , ( $i = 1, 2, \dots, n$ ) = a set of pre-selected functions known as shape functions or basis functions that satisfy the boundary conditions imposed on Equation A.1.

The functions  $N_i$  are considered to be linearly dependent and to represent the first  $n$  functions of a system of functions  $N_i(x, y)$ , ( $i = 1, 2, \dots, n$ ) which is complete in the flow region.

It should be mentioned that the functions  $h_i(t)$  are undetermined coefficients that are considered to be the solution of Equation A.1 at the  $n$  nodal points in domain  $D$ . Substituting the trial solution into Equation A.1 results in a residual, or error  $R$  defined by Equation A.3.

$$L[\hat{h}(x, y, t)] = R \quad (\text{A.3})$$

The exact solution is obtained when the residual could be made zero for all nodal points on the domain. Mathematically this is expressed as:

$$\int_D R W_i dD = 0 \quad i = 1, 2, \dots, n \quad (\text{A.4})$$

where,

$W_i$  = weighting functions over domain  $D$

In the Galerkin approach the weighting functions  $W_i$  are set equal to the basis functions  $N_i$ , which define the trial solutions. Thus  $L(\hat{h})$  is set orthogonal to all the basis functions  $N_i(x, y)$ .

This can be expressed as:

$$\iint_D L[\hat{h}(x, y, t)] N_i(x, y) dx dy = 0 \quad i = 1, 2, \dots, n \quad (\text{A.5})$$

The basis functions  $N_i$  are selected to have a value of unity at node  $i$  and zero at all other nodes in the domain, hence,  $h_i(t)$  is equal to the required function  $\hat{h}$  at the  $n$  node points (Pickens and Lennox, 1976).

Substituting Equation A.2 into Equation A.5 yields Equation A.6.

$$\iint_D L \left( \sum_{j=1}^n h_j(t) N_j(x, y) \right) N_i(x, y) dx dy = 0 \quad i = 1, 2, \dots, n \quad (\text{A.6})$$

By substituting Equations A.1 and A.2 into Equation A.6, the Equation A.7 can be obtained:

$$\iint_D \left\{ \left[ \frac{\partial}{\partial x} \left( K_x \frac{\partial}{\partial x} \right) + \frac{\partial}{\partial y} \left( K_y \frac{\partial}{\partial y} \right) \right] \sum_{j=1}^n h_j N_j - C_{uw} \frac{\partial}{\partial t} \sum_{j=1}^n h_j N_j + W \right\} N_i dx dy = 0,$$

$$i = 1, 2, \dots, n \quad (\text{A.7})$$

To eliminate the second derivatives in Equation A.7, which impose unnecessary continuity restrictions between elements in domain D, Green's theorem can be applied in the form given in Equation A.8 (Pinder and Frind, 1972; Pinder et al., 1973; Gray and Pinder, 1974; Frind and Verge, 1978; and Rabbani, 1994):

$$\iint_D \lambda \frac{\partial^2 \varphi}{\partial x^2} + \lambda \frac{\partial^2 \varphi}{\partial y^2} dx dy = - \iint_D \frac{\partial \lambda}{\partial x} \frac{\partial \varphi}{\partial x} + \frac{\partial \lambda}{\partial y} \frac{\partial \varphi}{\partial y} + \int_{\beta} \lambda \left[ \frac{\partial \varphi}{\partial x} l_x + \frac{\partial \varphi}{\partial y} l_y \right] d\beta$$

$$(\text{A.8})$$

where,

$\beta$  = boundary of the problem domain;

$l_x$  and  $l_y$  = direction cosines of the normal to the boundary.

By introducing Green's theorem into Equation A.7, the following equation can be obtained:

$$\iint_D \sum_{j=1}^n \left( K_x \frac{dN_i}{dx} \frac{dN_j}{dx} + K_y \frac{dN_i}{dy} \frac{dN_j}{dy} \right) h_j dx dy + \iint_D C_{uw} N_i \sum_{j=1}^n N_j \frac{dh_j}{dt} dx dy - \iint_D W N_i dx dy -$$

$$\int_{\beta} N_i \sum_{j=1}^n \left[ K_x \frac{dN_j}{dx} l_x + K_y \frac{dN_j}{dy} l_y \right] h_j d\beta = 0$$

$$i = 1, 2, \dots, n \quad (\text{A.9})$$

In matrix form Equation A.9 can be written as:

$$[A]\{h\} + [B]\left\{\frac{dh}{dt}\right\} + \{C\} = 0 \quad (\text{A.10})$$

where  $[A]$  and  $[B]$  are  $n$  by  $n$  matrices in which

$$A_{ij} = \iint_D \left[ K_x \frac{dN_i}{dx} \frac{dN_j}{dx} + K_y \frac{dN_i}{dy} \frac{dN_j}{dy} \right] dx dy \quad (\text{A.11})$$

$$B_{ij} = \iint_D C_{iw} N_i N_j dx dy \quad (\text{A.12})$$

and  $\{C\}$  is the flux vector in which

$$C_i = -\iint_D W N_i dx dy - \int_{\beta} N_i \sum_{j=1}^n \left[ K_x \frac{dN_j}{dx} l_x + K_y \frac{dN_j}{dy} l_y \right] h_j d\beta \quad (\text{A.13})$$

The last term in Equation A.13 incorporates the Neumann boundary condition in the form

$$\int_{\beta} N_i q d\beta \quad (\text{A.14})$$

where  $q$  is the flux of water and can be expressed as

$$q = K \frac{dh}{dn} \quad (\text{A.15})$$

This term is formed only when groundwater flux is nonzero along the edge of a boundary element.

Equation A.10 is the general finite element equation for a transient groundwater flow in porous media. For a steady-state flow, the head is independent of time and consequently

Equation A.10 can be reduced to:

$$[A]\{h\} + \{C\} = 0 \quad (\text{A.16})$$

The integrals that appear in the matrices of Equation A.10 are evaluated using numerical methods. A Gaussian quadrature scheme can be used to perform integrations (Pinder and Frind, 1972; Wang and Anderson, 1982).

An exact solution can be obtained using this scheme (Pinder, 1973). Integrations are performed in the local coordinate system, with limits of integration of  $-1$  and  $+1$  (see Chapter 4, Figure 4.3 and Table 4.2, Page 131).

The  $x$  and  $y$  coordinates anywhere in the element are related to the local coordinates and to the  $x$ - $y$  coordinates of the nodes by the following equations:

$$x = N_i \{X\} \quad (\text{A.17})$$

$$y = N_i \{Y\} \quad (\text{A.18})$$

or

$$x = N_1 x_1 + N_2 x_2 + N_3 x_3 + N_4 x_4 \quad (\text{A.19})$$

$$y = N_1 y_1 + N_2 y_2 + N_3 y_3 + N_4 y_4 \quad (\text{A.20})$$

where,

$N_i$  = a vector of interpolating shape functions;

$\{X\}$  and  $\{Y\}$  = global  $x$ - $y$  coordinates of the element nodes.

Therefore, once a set of local coordinates  $(\xi, \eta)$  have been specified, the corresponding global coordinates can be obtained by the Equations A.17 and A.18.

## Interpolating Functions

The interpolating functions in terms of local coordinates  $\xi$  and  $\eta$  for quadrilateral elements are defined as follows:

$$N_1 = \frac{1}{4}(1+\xi)(1+\eta) \quad (\text{A.21})$$

$$N_2 = \frac{1}{4}(1-\xi)(1+\eta) \quad (\text{A.22})$$

$$N_3 = \frac{1}{4}(1-\xi)(1-\eta) \quad (\text{A.23})$$

$$N_4 = \frac{1}{4}(1+\xi)(1-\eta) \quad (\text{A.24})$$

The head distribution model for each element is defined as:

$$h^e = N_i \{h\} \quad (\text{A.25})$$

or

$$h^e = N_1 h_1 + N_2 h_2 + N_3 h_3 + N_4 h_4 \quad (\text{A.26})$$

where,

$h$  = head at any local coordinate;

$N_i$  = vector of interpolation function;

$\{h\}$  = vector of heads at the nodes.

The interpolating functions are written in terms of local coordinates  $\xi$  and  $\eta$ . The derivatives can consequently be determined by the chain rule of differentiation, as given in Equations A.27 and A.28:

$$\frac{\partial N_i}{\partial \xi} = \frac{\partial N_i}{\partial x} \frac{\partial x}{\partial \xi} + \frac{\partial N_i}{\partial y} \frac{\partial y}{\partial \xi} \quad (\text{A.27})$$

$$\frac{\partial N_i}{\partial \eta} = \frac{\partial N_i}{\partial x} \frac{\partial x}{\partial \eta} + \frac{\partial N_i}{\partial y} \frac{\partial y}{\partial \eta} \quad (\text{A.28})$$

The interpolating function derivatives can be written as:

$$\begin{Bmatrix} \frac{\partial N_i}{\partial \xi} \\ \frac{\partial N_i}{\partial \eta} \end{Bmatrix} = [J] \begin{Bmatrix} \frac{\partial N_i}{\partial x} \\ \frac{\partial N_i}{\partial y} \end{Bmatrix} \quad (\text{A.29})$$

where  $[J]$  is the Jacobian matrix and is defined as follows:

$$[J] = \begin{bmatrix} \frac{\partial x}{\partial \xi} & \frac{\partial y}{\partial \xi} \\ \frac{\partial x}{\partial \eta} & \frac{\partial y}{\partial \eta} \end{bmatrix} \quad (\text{A.30})$$

From Equations A.17 and A.18, elements of  $[J]$  reduce to Equations A.31 through A.34.

$$\frac{\partial x}{\partial \xi} = \frac{\partial N_i}{\partial \xi} \{X\} \quad (\text{A.31})$$

$$\frac{\partial x}{\partial \eta} = \frac{\partial N_i}{\partial \eta} \{X\} \quad (\text{A.32})$$

$$\frac{\partial y}{\partial \xi} = \frac{\partial N_i}{\partial \xi} \{Y\} \quad (\text{A.33})$$

$$\frac{\partial y}{\partial \eta} = \frac{\partial N_i}{\partial \eta} \{Y\} \quad (\text{A.34})$$

Substituting Equations A.31 through A.34 into Equation A.30, the  $[J]$  matrix reduces to:

$$[J] = \begin{bmatrix} \frac{\partial N_1}{\partial \xi} & \frac{\partial N_2}{\partial \xi} & \frac{\partial N_3}{\partial \xi} & \frac{\partial N_4}{\partial \xi} \\ \frac{\partial N_1}{\partial \eta} & \frac{\partial N_2}{\partial \eta} & \frac{\partial N_3}{\partial \eta} & \frac{\partial N_4}{\partial \eta} \end{bmatrix} \begin{bmatrix} x_1 & y_1 \\ x_2 & y_2 \\ x_3 & y_3 \\ x_4 & y_4 \end{bmatrix} \quad (\text{A.35})$$

where,

$x_1, x_2, \dots$  and  $y_1, y_2, \dots$  = nodal coordinates.

The Jacobian matrix is a  $2 \times 2$  matrix:

$$[J] = \begin{bmatrix} J_{11} & J_{12} \\ J_{21} & J_{22} \end{bmatrix} \quad (\text{A.36})$$

The inverse of Jacobian matrix is:

$$[J]^{-1} = \frac{1}{\det[J]} \begin{bmatrix} J_{22} & -J_{12} \\ -J_{21} & J_{11} \end{bmatrix} \quad (\text{A.37})$$

The determinant of  $[J]$  is:

$$\det[J] = (J_{11} J_{22} - J_{21} J_{12}) \quad (\text{A.38})$$

The following relationship (Equation A.39) is required to perform the necessary integrations in the local coordinate rather than global coordinate system (Pinder and Frind, 1972):

$$\partial x \partial y = \det[J] \partial \eta \partial \xi \quad (\text{A.39})$$

The limits of integration must be changed to  $-1$  and  $+1$  by applying the above transformations Equation A.11 for example can be rewritten as:

$$A_{ij} = \int_{-1}^1 \int_{-1}^1 \left[ K_x \frac{\partial N_i}{\partial x} \frac{\partial N_j}{\partial x} + K_y \frac{\partial N_i}{\partial y} \frac{\partial N_j}{\partial y} \right] \det[J] \partial \eta \partial \xi \quad (\text{A.40})$$

Similar forms are developed for the Equations A.12 and A.13 and given in Equations A.41 and A.42:

$$B_{ij} = \int_{-1}^1 \int_{-1}^1 C_{uvw} N_i N_j \det[J] \partial\eta \partial\xi \quad (\text{A.41})$$

and

$$C_i = - \int_{-1}^1 \int_{-1}^1 W N_i \det[J] \partial\eta \partial\xi - \int_{\beta} N_i \sum_{j=1}^n \left[ K_x \frac{dN_j}{dx} l_x + K_y \frac{dN_j}{dy} l_y \right] h_j d\beta \quad (\text{A.42})$$

## APPENDIX B

### DERIVATION OF THE PYRITE OXIDATION MODEL BASED ON A SHRINKING CORE MODEL

#### B.1 Pyrite oxidation model

Pyrite oxidation (Reactions 2.8 and 2.10, Chapter 2, Section 2.5.3, Page 50) was categorised in the class of heterogeneous reactions (Levenspiel, 1972). In this reaction an aqueous component or gas may react with the pyrite and transforms it into products. If the oxidant is simply shown by  $A$  and the pyrite is represented by  $B$ , the oxidation reaction may be represented by (Levenspiel, 1972):



where,

$b$  = stoichiometric ratio of pyrite to oxidant consumption.

A mathematical model is needed to describe the pyrite oxidation reaction based on the shrinking-core model (Levenspiel, 1972). The model takes into account the following assumptions:

- The effects of both surface reaction kinetics and the rate of oxidant diffusion into the particle
- Particles containing pyrite are spherical

The reaction rates, which they have been developed by Levenspiel (1972) and a complete derivation of the pyrite oxidation model, are given below.

### B.1.1 Chemical reaction controls

Considering that the oxidation reaction is controlled by a chemical reaction and also the rate of pyrite oxidation is first order with respect to oxidant concentration and the available surface area of pyrite, for a spherical particle containing pyrite as shown in Figure B.1,

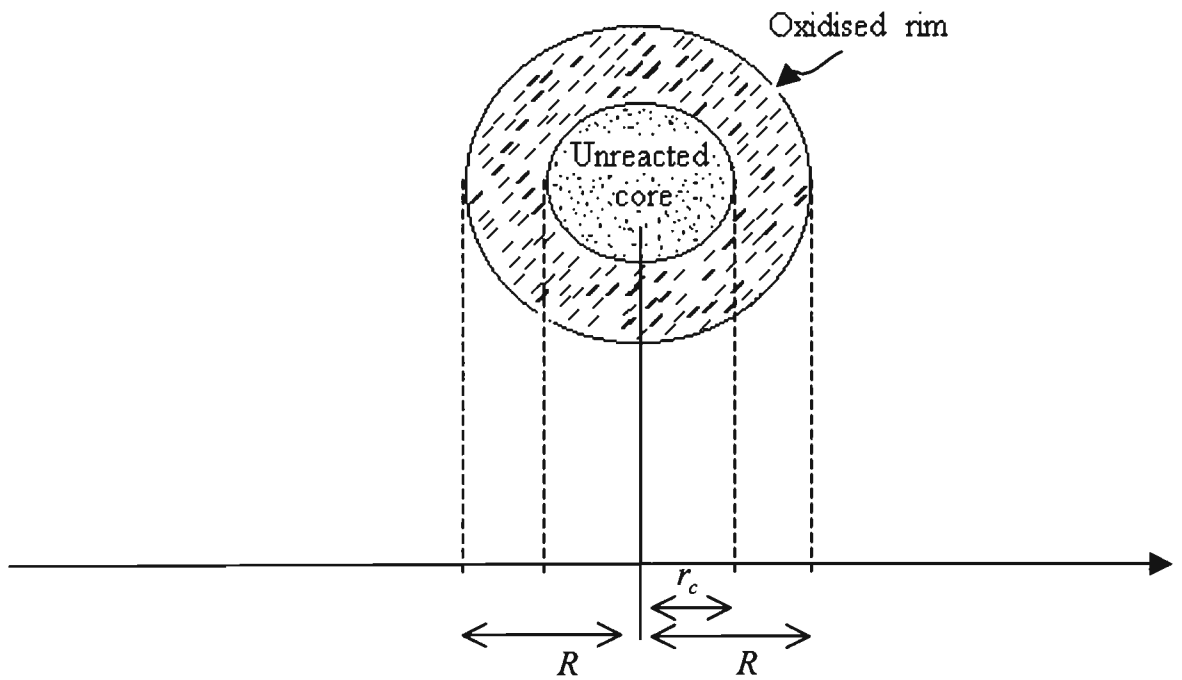


Figure B.1. Illustration of a partially oxidised particle when chemical reaction controls the rate of reaction.

the reaction rate is expressed by (Levenspiel, 1972):

$$-\frac{1}{4\pi r_c^2} \frac{dN_B}{dt} = -\frac{b}{4\pi r_c^2} \frac{dN_A}{dt} = bK_S C_{AS} \quad (\text{B.2})$$

where,

$K_S$  = first-order surface reaction rate constant.

Noting that

$$N_B = \rho_B V \quad (\text{B.3})$$

where,

$\rho_B$  = molar density of  $B$  in the solid;

$V$  = volume of a particle;

$N_B$  = amount of  $B$  within a particle.

Taking into account the stoichiometry of reaction B.1, and further noting the Equation B.3, the following expression can be written:

$$dN_B = b dN_A = \rho_B dV = \rho_B d\left(\frac{4}{3}\pi r_C^3\right) = 4\pi \rho_B r_C^2 dr_C \quad (\text{B.4})$$

Replacing Equation B.4 in Equation B.2 yields:

$$-\frac{1}{4\pi r_C^2} \rho_B 4\pi r_C^2 \frac{dr_C}{dt} = -\rho_B \frac{dr_C}{dt} = bK_S C_{AS} \quad (\text{B.5})$$

Integrating over Equation B.5 gives:

$$\int_R^{r_C} -\rho_B dr_C = \int_0^t bK_S C_{AS} dt$$

or

$$-\rho_B \int_R^{r_C} dr_C = bK_S C_{AS} \int_0^t dt$$

or

$$t = \frac{\rho_B}{bK_S C_{AS}} (R - r_C) \quad (\text{B.6})$$

According to Equation B.6, the time  $\tau_C$  required for fully oxidation is obtained when

$r_C = 0$ , then

$$\tau_C = \frac{\rho_B R}{bK_S C_{AS}} \quad (\text{B.7})$$

Combining Equations B.6 and B.7 gives:

$$\frac{t}{\tau_C} = 1 - \frac{r_C}{R} = 1 - X^{\frac{1}{3}} \quad (\text{B.8})$$

where,

$X$  = fraction of pyrite remaining within a particle.

### B.1.2 Diffusion controls

To develop a relationship between the particle radius and time when the diffusion of oxidant through the oxidised rim controls the rate of reaction, a partially reacted particle as illustrated in Figure B.2 is considered.

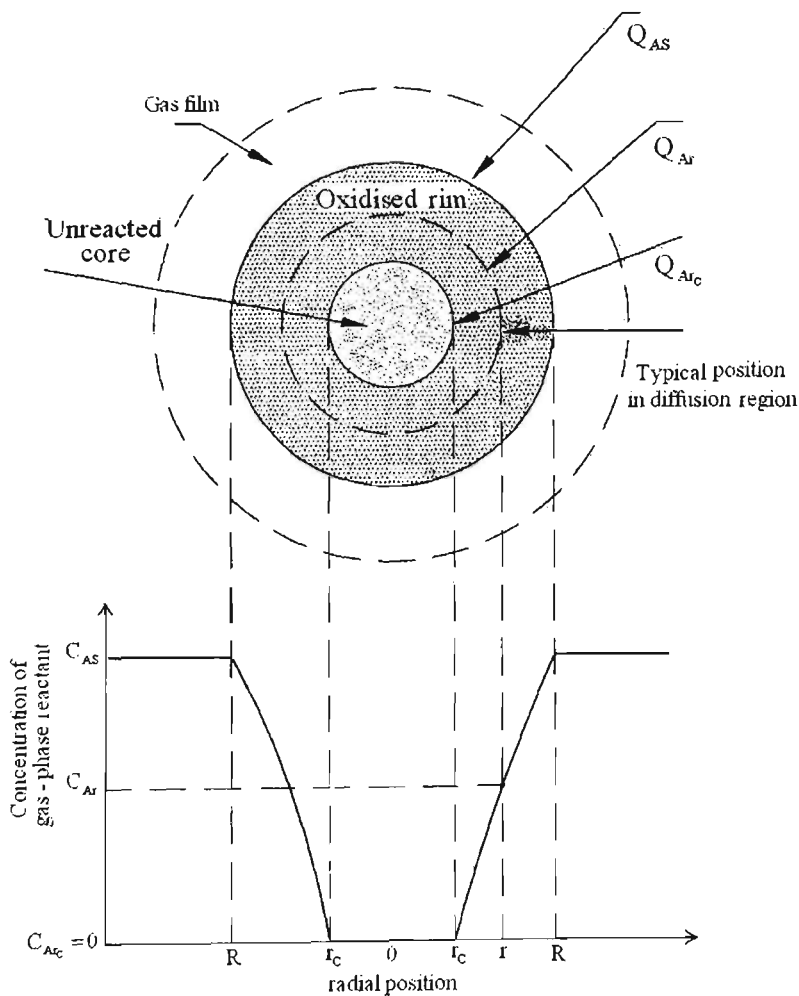


Figure B.2. Illustration of a partially leached particle when diffusion of oxidant through oxidised rim controls the rate of reaction (after Levenspiel, 1972).

As Figure B.2 shows the oxidant diffuses from the surface of the particle through the porous oxidised rim toward the unleached core of the particle. According to Levenspiel (1972), the boundary of the unreacted core moves inward and the radius of the

unreacted core reduces as the oxidation reaction progresses, while the thickness of the oxidised rim increases. The oxidant concentration gradient between the particle surface and the unreacted core of the particle is responsible for the transport of the oxidant into the particle as shown in Figure B.2.

According to Levenspiel (1972), the rate at which the unreacted core of the particle shrinks is about 1000 times slower than the flow rate of oxidant in the particle; it is equivalent to the ratio of solid density to gas density. Thus, it allows the assumption that the reaction front is stationary with regard to the oxidant concentration gradient between the particle surface and the unreacted core of the particle. Therefore, within the depleted coating, the oxidant concentration decreases linearly. Levenspiel (1972) noted that this steady-state assumption allows simplification in the derivation of the consumption term for the oxidant. Taking into consideration this simplification, the rate at which oxidant  $A$  reacts with the particle at any time is obtained by its rate of diffusion toward the reaction surface (Levenspiel, 1972):

$$-\frac{dN_A}{dt} = 4\pi r^2 Q_{Ar} = 4\pi R^2 Q_{AS} = 4\pi r_c^2 Q_{Ar_c} = C.T.E \quad (B.9)$$

where,

$Q_{Ar}$  = flux of oxidant  $A$  through surface of particle when radius is  $r$ ;

$Q_{AS}$  = flux of oxidant  $A$  through outside of particle;

$Q_{Ar_c}$  = flux of oxidant  $A$  through reaction surface.

Considering that the flux of oxidant  $A$  through the oxidised rim is governed by Fick's law:

$$Q_{Ar} = D_{e[OX]} \frac{dC_{Ar}}{dr} \quad (B.10)$$

where,

$D_{e[OX]}$  = diffusion coefficient of the oxidant  $A$  within the particle.

From Equations B.9 and B.10, it can be found for any  $r$ :

$$-\frac{dN_A}{dt} = 4\pi r^2 D_{e[OX]} \frac{dC_{Ar}}{dr} = C.T.E \quad (B.11)$$

Rearranging Equation B.11 gives:

$$-\frac{dN_A}{dt} \frac{dr}{r^2} = 4\pi D_{e[OX]} dC_{Ar} \quad (B.12)$$

Integrating Equation B.12 over thickness of oxidised rim yields:

$$-\frac{dN_A}{dt} \left( \frac{1}{r_C} - \frac{1}{R} \right) = 4\pi D_{e[OX]} C_{AS} \quad (B.13)$$

Equation B.13 contains three variables  $N_A$ ,  $r_C$  and  $t$ . One must be eliminated.  $N_A$  can be eliminated if it is written in terms of  $r_C$  according to Equation B.4.

$$-\frac{1}{b} 4\pi \rho_B r_C^2 dr_C \left( \frac{1}{r_C} - \frac{1}{R} \right) = 4\pi D_{e[OX]} C_{AS} dt \quad (B.14)$$

or

$$-\rho_B \left( \frac{1}{r_C} - \frac{1}{R} \right) r_C^2 dr_C = b D_{e[OX]} C_{AS} dt \quad (B.15)$$

Integrating Equation B.15 gives:

$$-\rho_B \int_R^{r_C} \left( \frac{1}{r_C} - \frac{1}{R} \right) r_C^2 dr_C = b D_{e[OX]} C_{AS} \int_0^t dt \quad (B.16)$$

or

$$t = \frac{\rho_B R^2}{6b D_{e[OX]} C_{AS}} \left[ 1 - 3 \left( \frac{r_C}{R} \right)^2 + 2 \left( \frac{r_C}{R} \right)^3 \right] \quad (B.17)$$

The time required for complete leaching of a particle is obtained by assigning  $r_C = 0$  in

Equation B.17:

$$\tau_D = \frac{\rho_B R^2}{6bD_{e[OX]} C_{AS}} \quad (\text{B.18})$$

Dividing Equation B.17 by Equation B.18 gives:

$$\frac{t}{\tau_D} = 1 - 3 \left( \frac{r_C}{R} \right)^2 + 2 \left( \frac{r_C}{R} \right)^3 \quad (\text{B.19})$$

Equation B.19 can be written in terms of the fractional remaining within the particle,  $X$ ,

$$\frac{t}{\tau_D} = 1 - 3X^{\frac{2}{3}} + 2X \quad (\text{B.20})$$

Rearranging Equations B.8 and B.20 yields:

$$t = \left( 1 - X^{\frac{1}{3}} \right) \tau_C \quad (\text{B.21})$$

and

$$t = \left( 1 - 3X^{\frac{2}{3}} + 2X \right) \tau_D \quad (\text{B.22})$$

Taking into consideration that both the chemical reaction and diffusion through the oxidised rim participate in the leaching of the particle the total time will be:

$$t_{tot} = \left( 1 - 3X^{\frac{2}{3}} + 2X \right) \tau_D + \left( 1 - X^{\frac{1}{3}} \right) \tau_C \quad (\text{B.23})$$

Integrating Equation B.23 gives:

$$dt = \left( -2X^{-\frac{1}{3}} + 2 \right) \tau_D dX - \frac{1}{3} X^{-\frac{2}{3}} \tau_C dX \quad (\text{B.24})$$

or

$$dt = \left[ \left( \frac{-2}{X^{\frac{1}{3}}} + 2 \right) \tau_D - \frac{\tau_C}{3X^{\frac{2}{3}}} \right] dX \quad (\text{B.25})$$

Rearranging Equation B.25 yields:

$$\frac{dX}{dt} = \frac{1}{\left(\frac{-2}{X^{\frac{1}{3}}} + 2\right) \tau_D - \frac{\tau_C}{3X^{\frac{2}{3}}}} = \frac{1}{\tau_D \left(\frac{-6X^{\frac{1}{3}} + 6X^{\frac{2}{3}}}{3X^{\frac{2}{3}}}\right) - \tau_C} \quad (\text{B.26})$$

or

$$\frac{dX}{dt} = \frac{-3X^{\frac{2}{3}}}{6\tau_D X^{\frac{1}{3}} \left(1 - X^{\frac{1}{3}}\right) + \tau_C} \quad (\text{B.27})$$

Equation B.27 is called the shrinking core model, which describes the leaching of a spherical particle when both the chemical reaction and diffusion control the pyrite oxidation rate.

## APPENDIX C

### A REVIEW OF PYRITE OXIDATION MODELS

#### C.1 Waste dump leaching process model

Cathles and Apps (1975) described a one-dimensional, unsteady-state model for oxidation and leaching of sulphide-bearing fragments. The model relates the three elements: oxygen balance, heat balance and air convection assuming air convection as the main mechanism of oxygen movement. The model assumes that the waste dump is composed of an aggregate of rock particles containing non-sulphide copper minerals and the sulphide minerals such as pyrite and chalcopyrite. The sulphide minerals are oxidised primarily by ferric iron where the ferric ions are maintained as a constant concentration by bacterial activities. The model predicts the rate of copper recovery depending on the parameters such as the dump height, sulphide in particular, pyrite concentrations and dump permeability. Schematic diagrams showing elements of the model are illustrated in Figures C.1 and C.2.

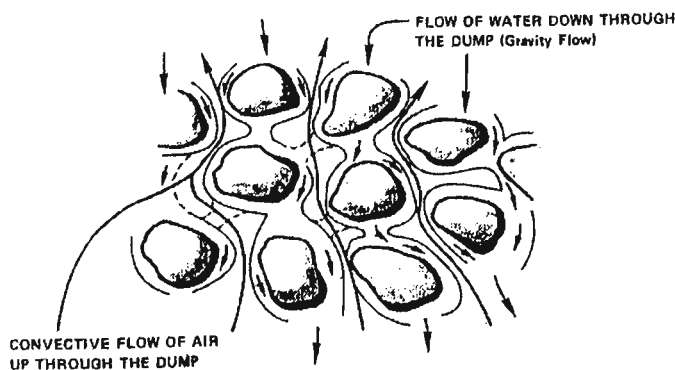


Figure C.1. Schematic diagram showing flow of air and water through a leach dump (after Cathles and Apps, 1975).

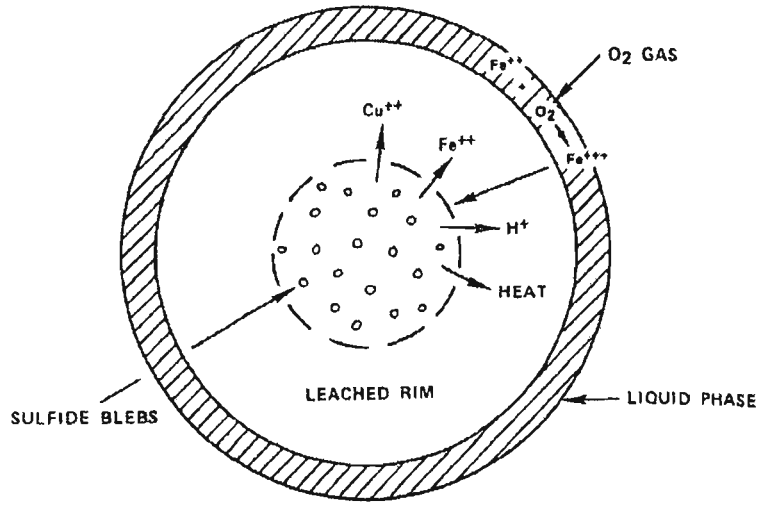


Figure C.2. Schematic diagram representing leaching of a single waste particle (after Cathles and Apps, 1975).

The rate at which copper is leached from the waste dump was given by:

$$R_{Cu} = \rho_R (1 - \phi) \left( G_S \frac{dX_S}{dt} + G_{NS} \frac{dX_S}{dt} \right) \quad (C.1)$$

Similarly the rate of oxygen consumption,  $R_{O_2}$ , and the rate of heat generation,  $R_A$ , were expressed from the following expressions:

$$R_{O_2} = \rho_R (1 - \phi) G_S \frac{dX_S}{dt} (1.75 + 1.91FPY) \quad (C.2)$$

and

$$R_A = \rho_R (1 - \phi) G_S \frac{dX_S}{dt} (2.89 + 5.41FPY) \quad (C.3)$$

where,

$R_{Cu}$ ,  $R_{O_2}$  and  $R_A$  = rate of leaching of copper, the rate of oxygen consumption, and the rate of heat generation, respectively;

$\phi$  = inter-block porosity of the dump;

$\rho_R$  = density of waste materials;

$G_S$  = initial copper sulphide grade of dump;

$G_{NS}$  = initial copper nonsulphide grade of dump;

$X_S$  = fraction of initial sulphide copper remaining in the dump after some leaching;

$FPY$  = moles of pyrite leached per mole of sulphide copper leached.

A well-known shrinking core model was used to describe the leaching process in the dump as expressed by Equations C.4 and C.5:

$$\frac{dX_S}{dt} = \frac{-3X_S^{\frac{2}{3}}}{6\tau_{DS}X_S^{\frac{1}{3}}(1-X_S^{\frac{1}{3}}) + \tau_{CS}} \quad (C.4)$$

$$\frac{dX_{NS}}{dt} = \frac{-3X_{NS}^{\frac{2}{3}}}{6\tau_{DNS}X_{NS}^{\frac{1}{3}}(1-X_{NS}^{\frac{1}{3}}) + \tau_{CNS}} \quad (C.5)$$

where,

$\tau_D$  = time for full oxidation a particle when the process is controlled by the diffusion;

$\tau_C$  = time required for complete leaching a waste particle when the process is controlled by the shrinking surface area.

$\tau_D$  and  $\tau_C$  are calculated by:

$$\tau_D = \frac{T_R^L a^2 K}{6[OX]D'_{OX}\phi_R^L} \quad (C.6)$$

$$\tau_C = \frac{K a}{k_{OX} a_{Sulf}^R \delta [OX]} \quad (C.7)$$

where,

$T_R^L$  = tortuosity of diffusion pathways;

$a$  = waste particle radius;

$K$  = oxidant required for leaching a unit volume of waste particle;

$[OX]$  = oxidant concentration ( $Fe^{+++}$ ) in leaching solution;

$D'_{OX}$  = diffusion coefficient of ferric ions in water;

$\phi_R^L$  = porosity of waste particles;

$k_{OX}$  = first order rate constant for the oxidation of pyrite by  $Fe^{+++}$ ;

$a_{Sulf}^R$  = surface area of sulphide mineral per unit volume of waste;

$\delta$  = reaction skin depth.

The reaction skin depth is a measure of the distance into the particle containing sulphide mineral with a significant chemical reaction. The following mathematical expression may be used to compute the reaction skin depth:

$$\delta = \sqrt{\frac{D'_{OX} \phi_R^L}{k_{OX} T_R^L a_{Sulf}^R}} \quad (C.8)$$

The heat balance for a one-dimensional dump with a vertical flow of air and water was reduced to:

$$\rho_T C_T \frac{dT}{dt} = (\rho_l C_l V_l - \rho_g C_g V_g) \frac{dT}{dz} + R_A + K_T \frac{d^2 T}{dz^2} \quad (C.9)$$

where,

$\rho$  = density of the total dump (subscript T), the liquid (subscript  $l$ ) and gas (subscript  $g$ ) phase of the dump;

$C$  = heat capacity for the total dump (subscript T), the liquid (subscript  $l$ ) and gas (subscript  $g$ ) phase of the dump;

$K_T$  = thermal conductivity of the dump;

$T$  = temperature of the dump;

$z$  = depth of the dump;

$V_l$  = Darcy velocity for the liquid phase;

$V_g$  = Darcy air velocity through the dump.

In a one- dimensional case,  $V_g$  is obtained by:

$$V_g = \frac{k_{AVE} \Delta P}{\mu_g H} \quad (C.10)$$

where,

$H$  = height of the dump;

$\mu_g$  = viscosity of air;

$\Delta P$  = pressure drop across the dump;

$k_{AVE}$  = average permeability of the waste dump.

For a known depth of a dump, the oxygen concentration is given by:

$$[\overline{O_2}]^g = 1 - \frac{R_{O_2} Z_i}{V_g [O_2]_{STP}^g} \quad (C.11)$$

where,

$Z_i$  = depth;

$[O_2]_{STP}^g$  = oxygen concentration in atmosphere under standard conditions;

$[\overline{O_2}]^g$  = normalised concentration of oxygen in gas phase of dump defined by:

$$[\overline{O_2}]^g = [O_2]^g / [O_2]_{STP}^g \quad (C.12)$$

where,

$[O_2]^g$  = concentration of oxygen in gas phase of dump.

Equations C.9 through C.11 define a model for oxidation and leaching processes of a waste dump.

The percent copper leached per month and the cumulative percentage leached are given by:

$$\frac{\text{Fraction Cu}}{\text{month}} = 2.68 \times 10^6 \sum_{\text{dump}} \frac{(G_{NS} \frac{dX_{NS}^i}{dt} + G_S \frac{dX_S^i}{dt})}{N(G_S + G_{NS})} \quad (\text{C.13})$$

The cumulative percentage leached,  $(1 - X_{Tot})$  is defined:

$$\text{Fraction Cu leached} = 1 - \frac{(G_{NS} X_{NS} + G_S X_S)}{G_{NS} + G_S} \quad (\text{C.14})$$

where,

$N$  = number of layers of dump;

$X_S^i$  = fraction of sulphide copper remaining in the  $i^{\text{th}}$  layer of the dump.

Figure C.3 compares the observed and predicted leaching process of the Midas test dump (Cathles and Apps, 1975).

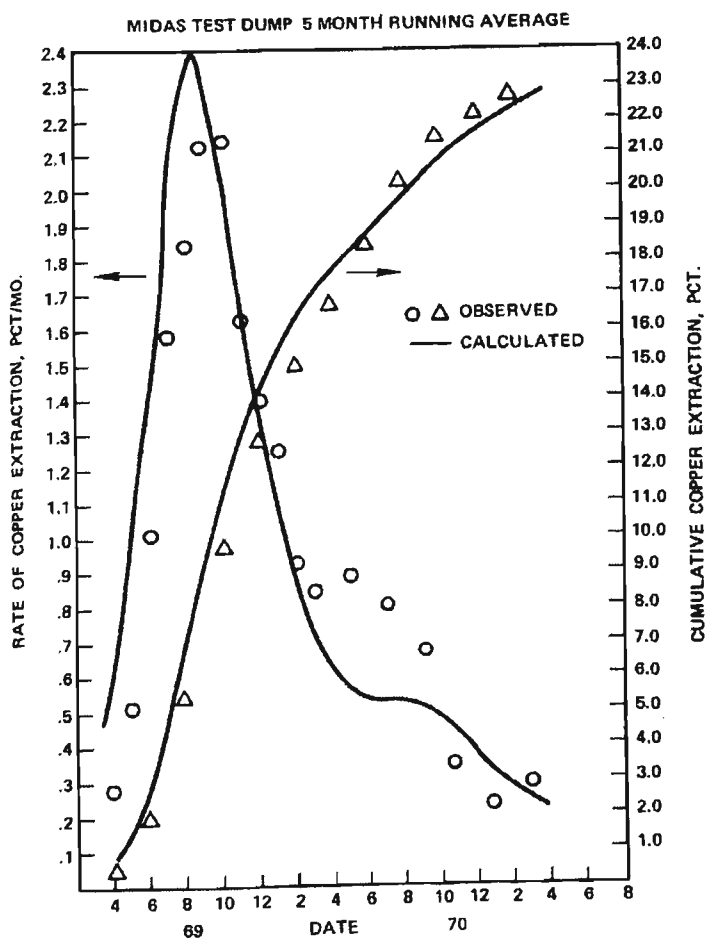


Figure C.3. Comparison of observed and predicted copper leaching process in Midas test waste dump (after Cathles and Apps, 1975).

Cathles and Apps (1975) concluded that air convection plays an important part in both oxygen movement and the dump oxidation and leaching process. Furthermore the sulphide minerals were oxidised primarily by  $Fe^{+++}$ , with a constant concentration of ferric ions maintained by bacterial activity. These conditions are reasonable for the very coarse copper-waste dumps. According to Jaynes et al. (1984a) such conditions could not be applied well to reclaimed open cut coalmines where diffusion is a dominant process and the role of iron-oxidising bacteria in the oxidation reaction is unclear.

## C.2 POLS

Jaynes et al. (1984a, b) developed a mathematical model for simulation of the long-term oxidation of pyrite and leachate generation from reclaimed coal strip mines. The model takes into account pyrite oxidation by both direct-oxygen and ferric iron within spoil. The model combined chemical kinetics and oxygen diffusion with the activity of *T. ferrooxidans* to mediate pyrite oxidation rate. The bacterial activity depends on the *pH*, temperature, and oxygen. A schematic diagram of the model is presented in Figure C.4.

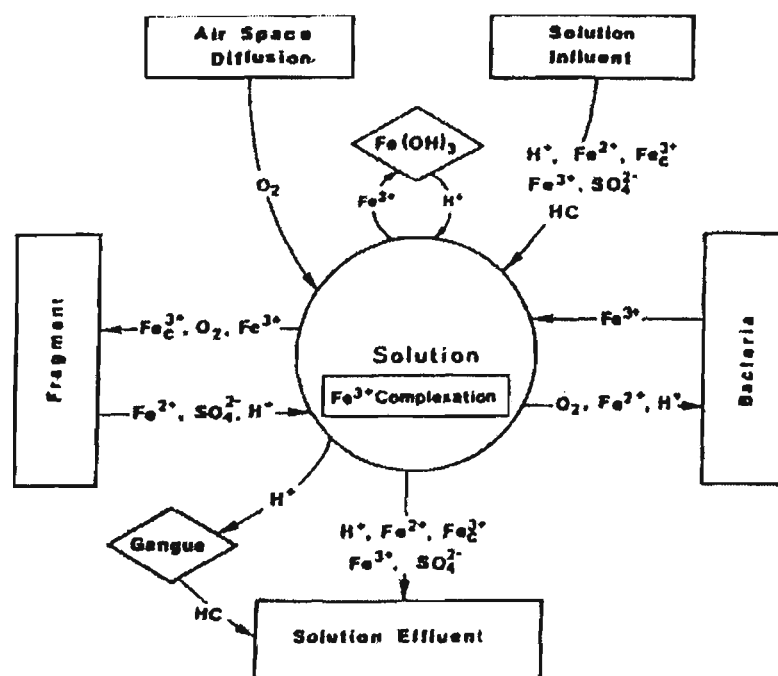


Figure C.4 Schematic diagram of acid mine drainage model (POLS) presented by Jaynes et al. (1984a).

The pyrite oxidation process was determined by use of the shrinking core model, assuming that the fragments containing pyrite were thin plates. The rate of pyrite oxidation per unit area of pyrite within a fragment was reduced to:

$$\frac{dX}{dt} = \frac{-1}{2t_D(1-X) + t_C} \quad (\text{C.15})$$

where,

$X$  = fraction of pyrite remaining in a fragment;

$t$  = time;

$t_D$  = total time required for complete oxidation of pyrite within a fragment when the diffusion processes control the oxidation rate;

$t_C$  = total time required for full leaching of pyrite where the chemical reactions were the rate controlling process.

$t_D$  can be computed from the following equation:

$$t_D = \frac{\sigma_f l^2}{2bD_C C_0} \quad (\text{C.16})$$

where,

$\sigma_f$  = molar density of pyrite within the fragment;

$l$  = one-half thickness of a thin plate fragment;

$b$  = stoichiometric ratio that relates pyrite and oxidant consumption;

$D_C$  = effective diffusion coefficient of oxidant in water;

$C_0$  = oxidant concentration at fragment surface.

$t_C$  is obtained from:

$$t_C = \frac{\sigma_f l}{bK_S C_0 \partial \alpha} \quad (\text{C.17})$$

where,

$K_s$  = first-order surface reaction rate constant per unit surface area of pyrite;

$\partial$  = effective thickness of the fragment in which pyrite is oxidised;

$\alpha$  = surface area of pyrite per unit volume of fragment.

According to Jaynes et al. (1984a) for  $t_c \leq t_D$  diffusion processes will control the reaction rate and for  $t_c \geq t_D$ , the chemical reactions will become the rate controlling process.

When both oxygen and ferric iron act as reactant, the total oxidation rate will be the sum of the rates of each of them and Equation C.15 is modified to Equation C.18:

$$\frac{dX}{dt} = \frac{-1}{t_{D(O_2)}(1-X) + t_{C(O_2)}} + \frac{-1}{t_{D(Fe^{3+})}(1-X) + t_{C(Fe^{3+})}} \quad (C.18)$$

The model assumes that the diffusion process is the main mechanism for oxygen transport from the spoil surface to the fragment surface. The governing equation for this process reduces to:

$$\phi_a \frac{d}{dt} (\sigma_a Y_0) = \frac{P}{R} \frac{d}{dz} \left[ \frac{D_0 \phi_a dY_0}{T \tau dz} \right] + Q_o \quad (C.19)$$

where,

$\phi_a$  = air-filled porosity;

$\sigma_a$  = molar density of air;

$Y_0$  = mole fraction of oxygen in gas;

$P$  = atmospheric pressure;

$R$  = gas constant;

$T$  = temperature;

$\tau$  = tortuosity of diffusion channels;

$Q_o$  = oxygen consumption term. The term  $Q_o$  could be partitioned into three components:

$$Q_o = Q_p + Q_A + Q_C \quad (C.20)$$

where,

$Q_p$  = rate of oxygen consumption by the oxygen-pyrite reaction;

$Q_C$  = oxygen consumption rate due to chemical oxidation of ferrous iron;

$Q_A$  = consumption term for oxygen by bacteria while oxidising ferrous iron.

The model also takes into account the complexation and precipitation reactions of ferric iron. Jaynes et al. (1984a) noted that ferric iron forms strong complexes with hydroxides and sulphates, which can raise total dissolved ferric iron concentration. Thus the complexation reactions of ferric iron must be incorporated in the model.

Furthermore, the ferric iron produced by the oxidation of ferrous iron may precipitate as described in Chapter 2 (Reaction 2.11, Section 2.5.3, Page 50). The ferric iron precipitation reaction removes the  $Fe^{3+}$  ions and raises the  $H^+$  concentration. Therefore, the precipitation reaction must be also incorporated in the model.

The model termed POLS also takes into account the acid neutralisation reaction taking place within the spoils of the strip mine. Acid generated by pyrite oxidation is consumed or transformed into reserve forms of acidity by reaction with the spoil matrix. The effect of acid neutralisation reaction was expressed by a simple empirical equation.

Jaynes et al. (1984b) assessed the sensitivity of the POLS model by simulating a series of eight cases for two magnitudes of pore space tortuosity, and air-filled porosity, in the presence of iron-oxidising bacteria as well as  $H^+$  - gangue interactions. They found that

for systems without iron-oxidising bacteria, oxygen is the only important oxidant for pyrite oxidation. In conditions where there is an unconstrained oxygen supply the pyrite oxidation rate by the iron-oxidising bacteria increases. The model predicts that  $pH$  neutralisation reactions are important in maintaining the  $pH$  of the solution in the range where both the bacterial activity and the solubility of ferric iron are reasonably high ( $2.0 < pH < 3.0$ ). In this  $pH$  range, the pyrite oxidation rate is increased by ferric iron produced by bacterial oxidation of ferrous iron. Jaynes et al. (1984b) also concluded that the rate of pyrite oxidation decreased by a reducing the air-filled pore space and an increase in pore space tortuosity.

### **C.3 Model developed by Davis and Ritchie (1986a) and Davis et al. (1986b)**

Davis and Ritchie (1986a) and Davis et al. (1986b) developed a model for pyrite oxidation within the White's overburden dump at Rum Jungle, Australia. The model assumed that oxygen transport is the rate-limiting step in the oxidation of pyrite and that oxygen transport is taking place by gaseous diffusion through the pore space of the dump. Oxygen is supplied by a diffusion process to oxidation sites within the particles in the dump. Figure C.5 shows a schematic diagram of the model described by Davis and Ritchie (1986a). The dump was modelled as a porous slab with the surface open to the atmosphere while the base of the dump was assumed impermeable to oxygen transport.

The model assumed that pyrite is uniformly distributed throughout the particles of the dump. Further, the model ignores the roles of bacteria in the oxidation process.

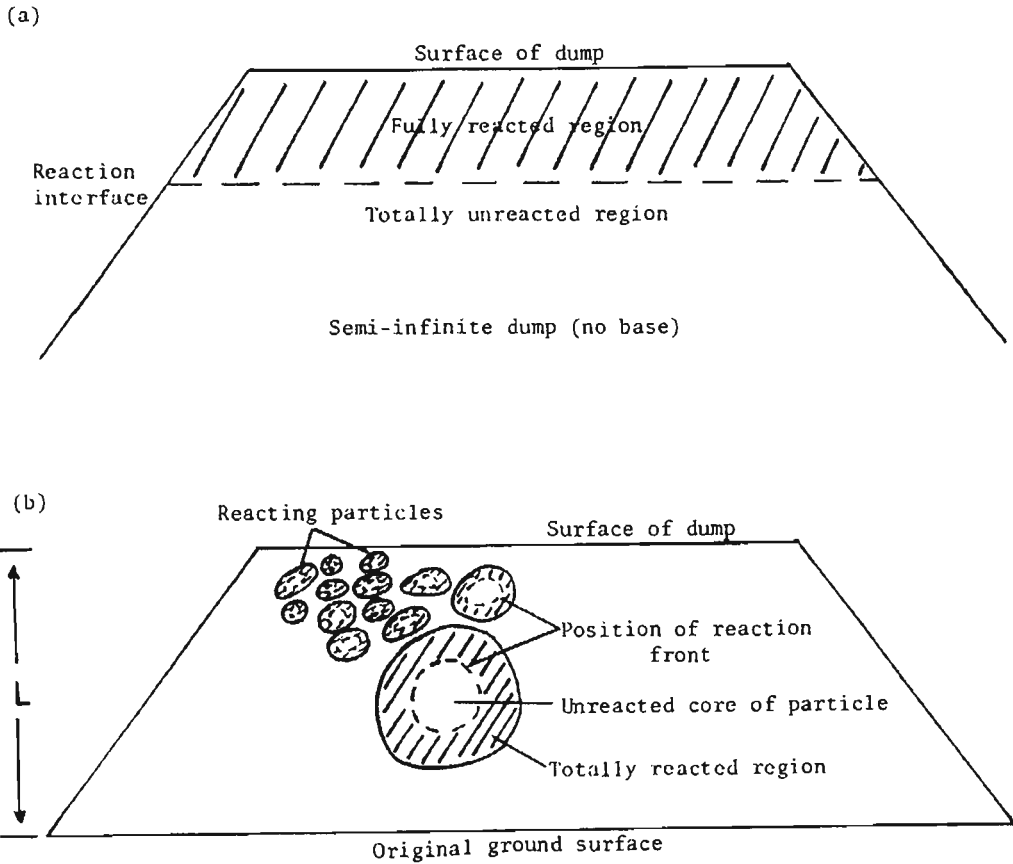


Figure C.5. Pyrite oxidation model within waste rock dump. (a) simple homogeneous slab model (b) model proposed by Davis and Ritchie (1986a).

The equation governing oxygen diffusion into the pore space of the dump was given by:

$$P \frac{\partial u^*}{\partial t^*} = D_1 \frac{\partial^2 u^*}{\partial x^{*2}} - q^* , \quad 0 < x^* < L \quad (\text{C.21})$$

where,

$u^*$  = oxygen concentration within the pore space of the dump;

$q^*$  = volumetric consumption of oxygen from the pore space of the dump;

$P_1$  = porosity of the dump;

$L$  = height of the dump;

$D_1$  = effective diffusion coefficient of oxygen within the pore space of the dump;

$x^*$  = vertical coordinate;

$t^*$  = time.

The following boundary conditions were specified for the model:

- 1) The top surface of the dump was assigned a first-type boundary with the oxygen concentration equal to its atmospheric concentration:

$$u^*(0, t^*) = u_0 \quad (\text{C.22})$$

- 2) A no-flow boundary condition was maintained at the base of the dump:

$$\frac{\partial u^*}{\partial x^*}(L, t^*) = 0 \quad (\text{C.23})$$

- 3) The dump contained initially no oxygen concentration:

$$u^*(x^*, 0) = 0 \quad (\text{C.24})$$

The particles of the dump were assumed spherical and all particles have equal size.

The volumetric consumption term was given by:

$$q^*(x^*, t^*) = \nu D_2 4\pi a^2 \frac{\partial v^*}{\partial r^*}(a, x^*, t^*) \quad (\text{C.25})$$

where,

$v^*(r^*, x^*, t^*)$  = concentration of oxygen within a particle of the dump;

$r^*$  = radial distance within a particle;

$a$  = radius of the particle;

$D_2$  = diffusion coefficient of oxygen in water;

$\nu$  = number of particles per unit volume of the dump.

For spherical particles the constant  $\nu$  was given by:

$$\nu = \frac{3(1-P)}{4\pi a^3} \quad (\text{C.26})$$

Combining Equations C.25 and C.26, gives the oxygen consumption term  $q^*$ :

$$q^*(x^*, t^*) = \frac{3(1-P)D_2}{a} \frac{\partial v^*}{\partial r^*}(a, x^*, t^*) \quad (\text{C.27})$$

The partial differential equation of oxygen transport within the particle reduces to:

$$\frac{\partial v^*}{\partial t^*}(r^*, x^*, t^*) = D_2 \left( \frac{\partial^2 v^*}{\partial r^{*2}}(r^*, x^*, t^*) + \frac{2}{r^*} \frac{\partial v^*}{\partial r^*}(r^*, x^*, t^*) \right) \quad (C.28)$$

For  $R^*(x^*, t^*) < r^* < a$

where,

$R^*(x^*, t^*)$  = location of the reaction front within particles of the dump. It depends on time and depth in the dump.

As the rate of the reaction proceeds as quick as oxygen can transport from the dump surface, the oxygen concentration at the reaction front is zero, i.e.

$$v^*(R^*, x^*, t^*) = 0 \quad (C.29)$$

A partial differential equation for oxygen transport within particle to the moving reaction front is given by:

$$\frac{\partial R^*}{\partial t^*} = \frac{(1-P)}{\epsilon \rho_s} \left( D_2 \frac{\partial v^*}{\partial r^*}(R^*, x^*, t^*) + v^*(R^*, x^*, t^*) \frac{\partial R^*}{\partial t^*} \right) \quad (C.30)$$

By combining Equations C.29 and C.30 give the following relationship:

$$D_2 \frac{\partial v^*}{\partial r^*}(R^*, x^*, t^*) = - \frac{\epsilon \rho_s \partial R^*}{(1-P) \partial t^*} \quad (C.31)$$

where,

$\epsilon$  = mass of oxygen used per mass of sulphur in the oxidation reaction;

$\rho_s$  = density of sulphur in the dump.

The initial condition is given by:

$$R^*(x^*, 0) = a \quad (C.32)$$

According to Davis and Ritchie (1986a), the model still needs another boundary condition at just outside the particle to link oxygen concentration in the pore spaces

of the dump with those within the particle. For this purpose, the Henry's law and the gas law were used:

$$v^*(a, x^*, t^*) = \gamma u^*(x^*, t^*) \quad (C.33)$$

where,

$\gamma$  = a constant and was set 0.03.

The equations written above define a model of the waste dump.

The major chemical reaction for oxidation of pyrite was given as below to determine the ratio of the mass of oxygen to sulphur consumed during the oxidation process:

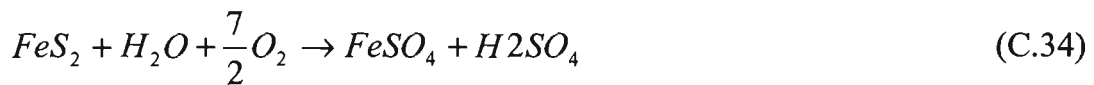


Figure C.6 shows oxygen concentration profile in the pore spaces of the dump and

Figure C.7 illustrates the rate of sulphate generation as a function of time.

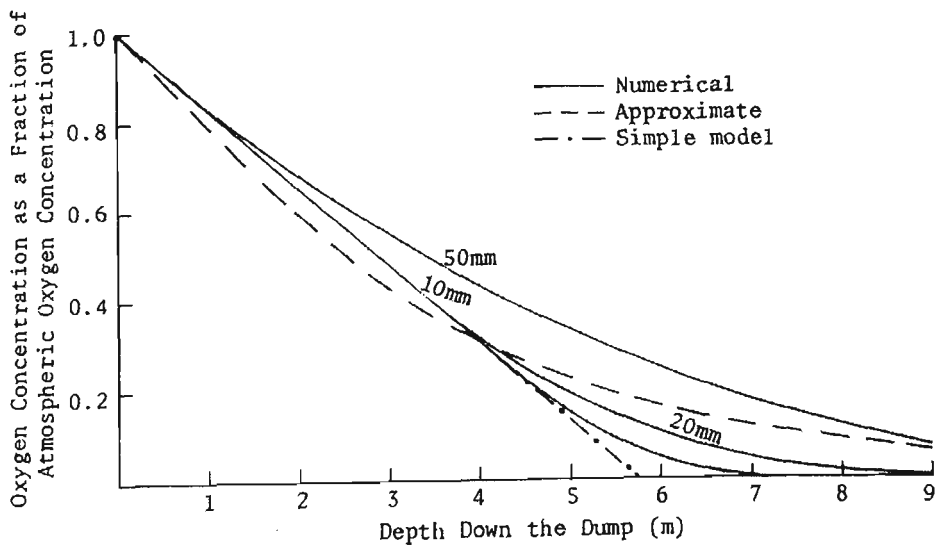


Figure C.6. Normalised oxygen concentration as a function of depth for various particle sizes (after Davis et al., 1986b).

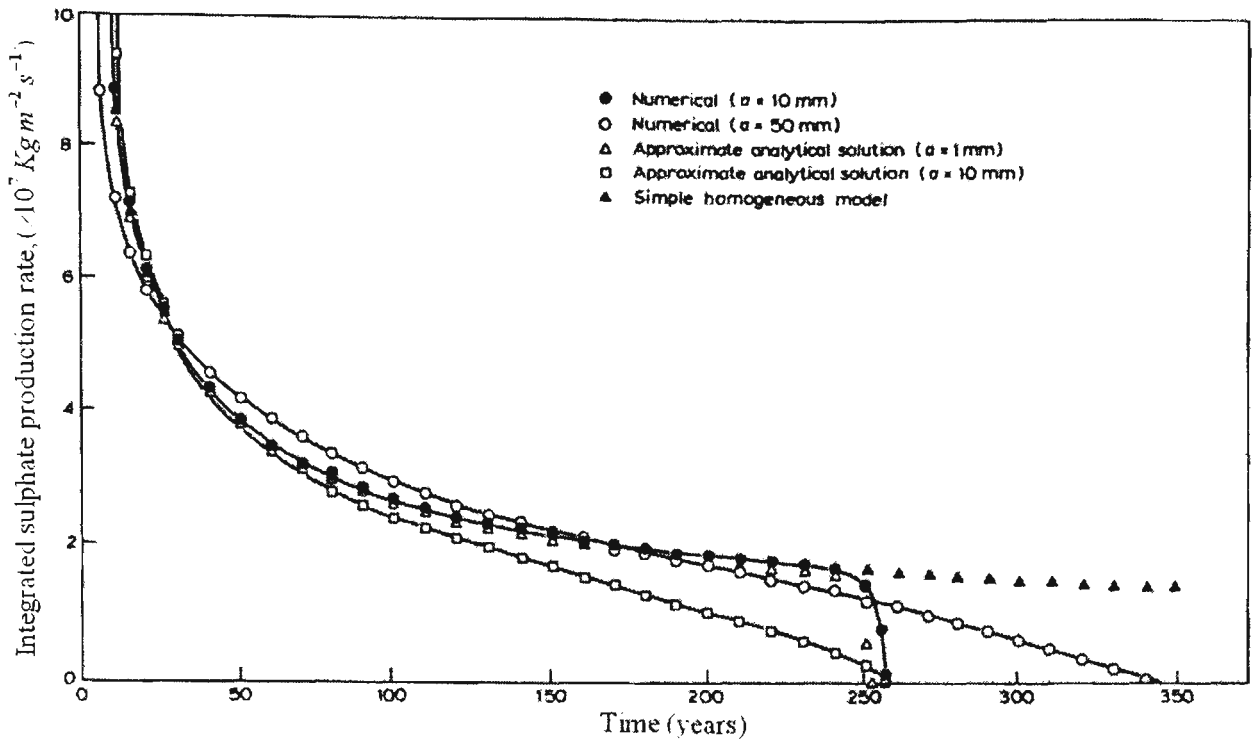


Figure C.7. Total sulphate production rate as a function of time  
(after Davis et al., 1986b).

#### C.4 Numerical model developed by Elberling et al. (1994)

Elberling et al. (1994) developed a numerical model for the simulation of the pyrite oxidation in tailings. The model was formulated by combining the effect of oxygen diffusion to a depth where oxidation takes place with first-order kinetics with respect to oxygen. The rate of pyrite oxidation in the model is based on the continuity relationship for oxygen with both oxygen transport through the tailings and the consumption of oxygen at the surface of the sulphide minerals grains. The model assumes that the transport of oxygen takes place through the molecular diffusion and it can be modelled by Fick's first law as follows:

$$J_D = -D_e \frac{dC}{dz} \quad (\text{C.35})$$

where,

$J_D$  = diffusive flux of oxygen in the gas phase;

$D_e$  = effective diffusion coefficient within pore space of the tailings which is assumed to be constant with time and depth above the water table;

$C$  = oxygen concentration in the gas phase;

$z$  = depth.

One-dimensional diffusion of oxygen into the tailings is given by:

$$\frac{dC}{dt} = D_e \frac{d^2C}{dz^2} - G \quad (\text{C.36})$$

where,

$G$  = volumetric rate of oxygen consumption by the oxygen-pyrite reaction.

Elberling et al. (1994) reported that although several sulphide minerals consist of pyrite, pyrrhotite, chalcopyrite, sphalerite and arsenopyrite can generate acidic drainage, but pyrite is assumed to be the major sulphide mineral in mine tailings reacting with oxygen. Furthermore, it was assumed that oxygen is the only oxidant causing pyrite oxidation and particles containing pyrite are equal in diameter. As the particles of pyrite react, they shrink in size resulting in smaller surface areas. As a consequence, the oxygen consumption term from the pyrite-oxygen reaction decreases with time. The reaction kinetics for pyrite oxidation is given by:

$$\frac{-d[FeS_2]}{dt} = -\frac{4}{15} \frac{d[O_2]}{dt} = KSC^n \quad (\text{C.37})$$

where,

$K$  = first order rate constant;

$S$  = surface area per unit volume of particle;

$C$  = oxygen concentration.

Using the assumption that the pyrite oxidation reaction is approximated by first-order kinetics ( $n = 1$ ) at low concentrations of oxygen, and using experimentally obtained data for the rate constant,  $K$ , the consumption of oxygen due to the oxidation of pyrite is given by:

$$-\frac{dC}{dt} = 22.1 \times 10^{-10} C_z / C_0 \quad (\text{C.38})$$

where,

$C_z$  = concentration of oxygen at the depth,  $z$ , where the oxidation takes place;

$C_0$  = concentration of oxygen at the surface.

The equation used to govern oxygen diffusion with first-order kinetics at steady-state conditions is as follows:

$$D_e \frac{d^2 C}{dz^2} - KC = 0 \quad (\text{C.39})$$

Since the pyrite surface area reduces with time, the  $K$  value should be recalculated for each time-step. The reduction in pyrite surface area  $S$  is approximated to a radial shrinkage rate equal to the oxidation rate  $\frac{d[FeS_2]}{dt}$  for one time-step over the molar

density  $D_{Py}$  using the following equation:

$$S_t = S_{t-1} - K_x dt / D_{Py} \quad (\text{C.40})$$

The length of the time-step was noted to be an important factor for given purposes:

- To ensure that the change in surface area is unimportant in the selected time-step;
- To establish the steady-state condition for the concentration of oxygen.

A time-step of one month was set in the model developed by Elberling et al. (1994).

One of the important features of the model proposed by Elberling et al. (1994) was that they assessed the sensitivity of the model against physical parameters related to the mine tailings, such as pyrite fraction, particle size, and the effective diffusion coefficient

using a series of simulation runs. The tailings were initially assumed unoxidised. They investigated that at the beginning of oxidation reaction, an oxidation front develops from the ground surface to a depth that depends on the effective diffusion coefficient for a specific rate constant  $K$ . As time progresses, the oxidation front shifts downward, causing a lower oxygen concentration to be available for the pyrite-oxygen reaction and a higher diffusion distance. As a consequence, the rate of pyrite oxidation decreases with time. The results obtained showed that, although pyrite oxidation rate was significant for small-sized particles at early time (a few years) after beginning of the simulation but the overall oxidation rate was considerably independent of the grain size and the pyrite content after a long period (Figure C.8). Figure C.9 shows the pyrite oxidation rate as a function of time using a series of simulation runs.

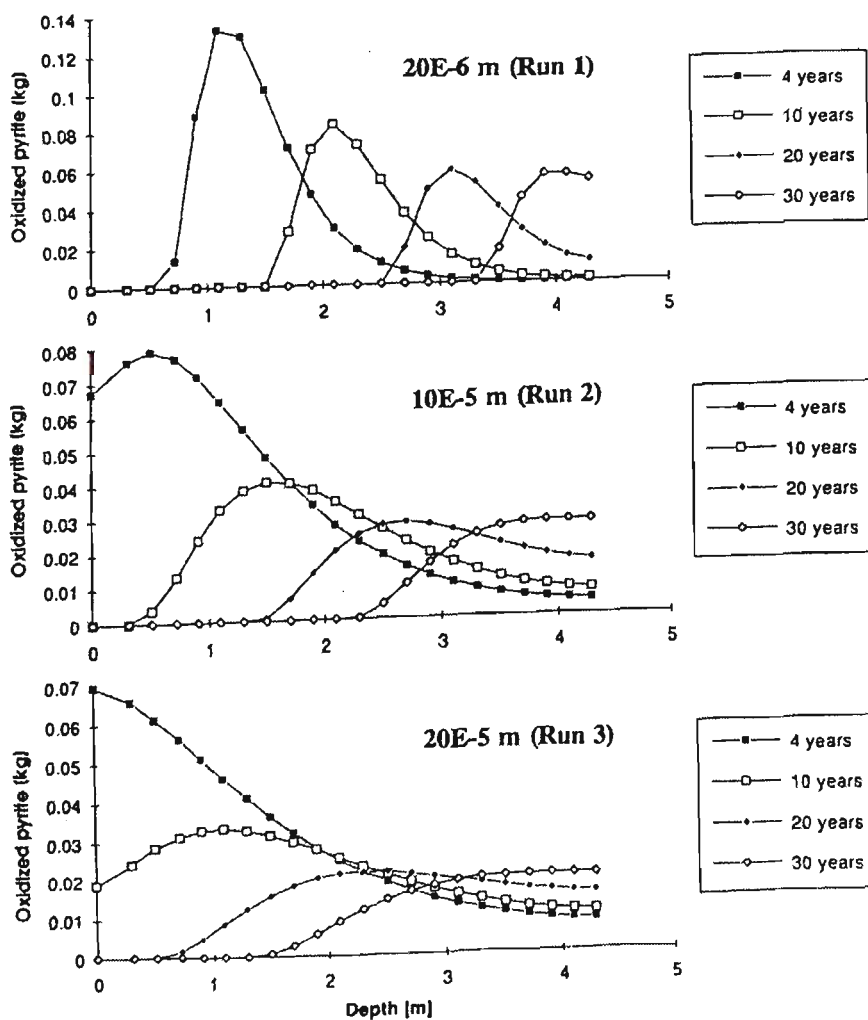


Figure C.8. Pyrite oxidation rate as a function of depth shown for different particle diameters (after Elberling et al., 1994).

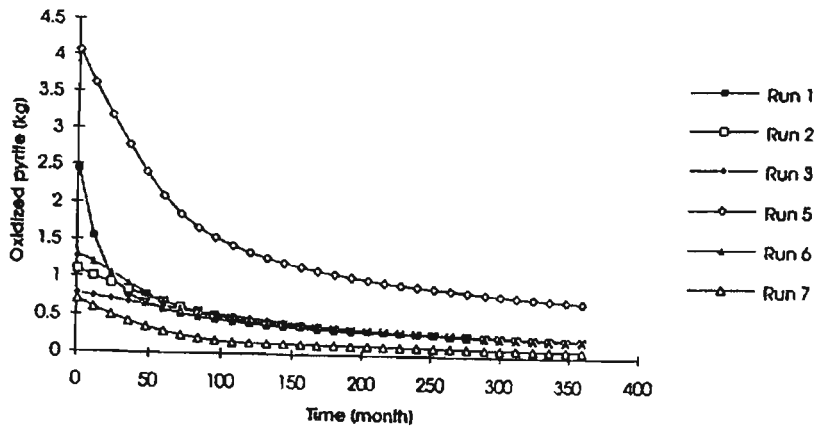


Figure C.9. Pyrite oxidation rate as a function of time (after Elberling et al., 1994).

The pyrite oxidation rate was very sensitive to the effective diffusion coefficient. As demonstrated in Figure C.10, the highest oxidation rate resulted from high diffusion coefficients, although the effect is reduced by time.

Results showed that the oxygen concentration was most sensitive to the effective diffusion coefficient. As shown in Figure C.11 lower  $D_e$  values cause steeper gradients in oxygen concentration profiles.

Elberling et al. (1994) concluded that for the sulphide mine tailings, after a few years the overall rate of oxidation is mostly controlled by the effective diffusion coefficient of oxygen in the tailings. Consecutively, the effective diffusion coefficient is mostly determined by the degree of saturation as well as the particle size of the tailings. According to Elberling et al. (1994) the high diffusion rate resulted from low saturation and coarse particle size in the tailings. In some tailings where the saturated thickness is important and consequently the effective diffusion coefficient is low, hence the rate of pyrite oxidation and acid generation are significantly reduced.

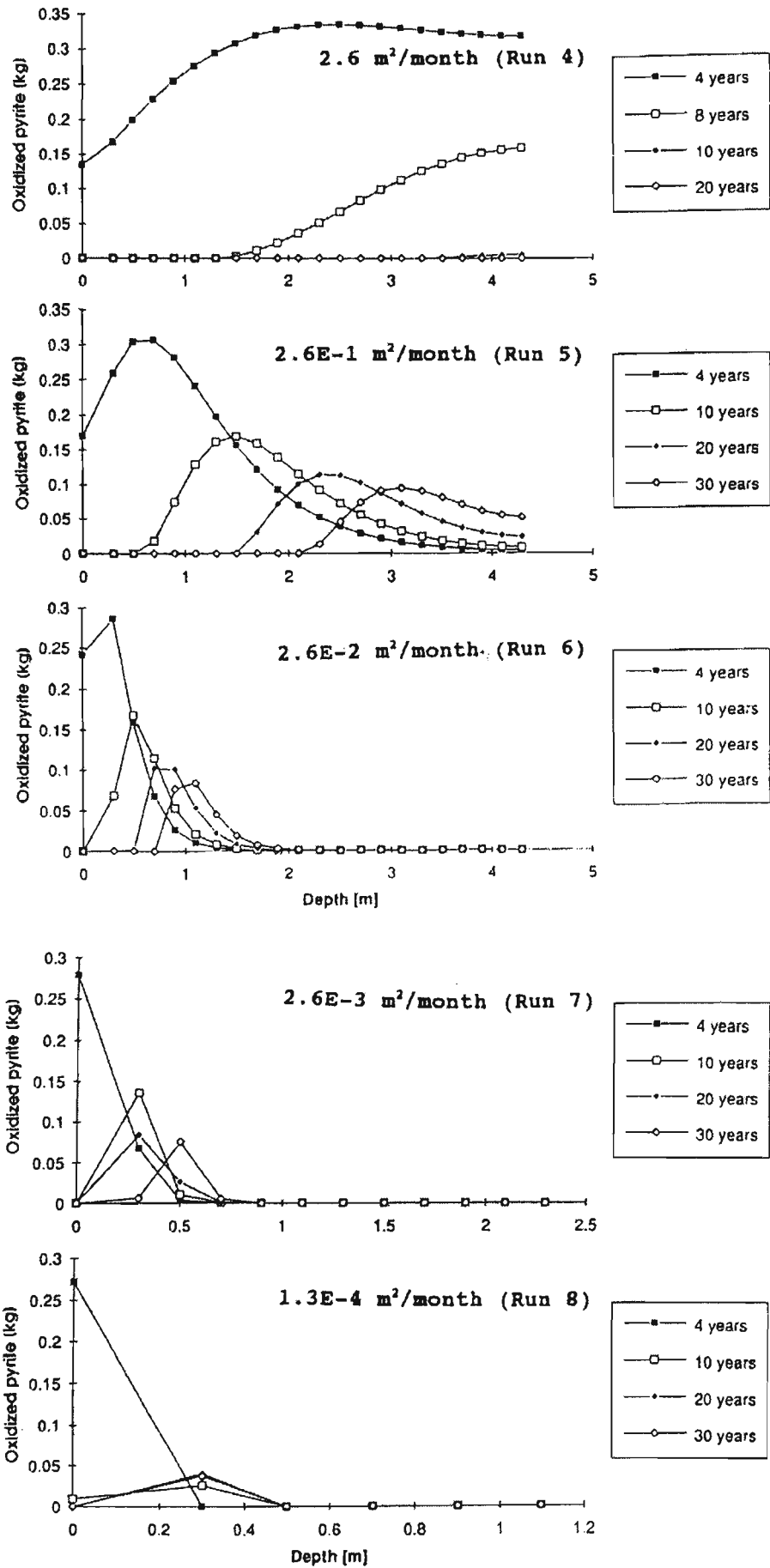


Figure C.10. Pyrite oxidation rate as a function of depth shown for different effective diffusion coefficients (after Elberling et al., 1994).

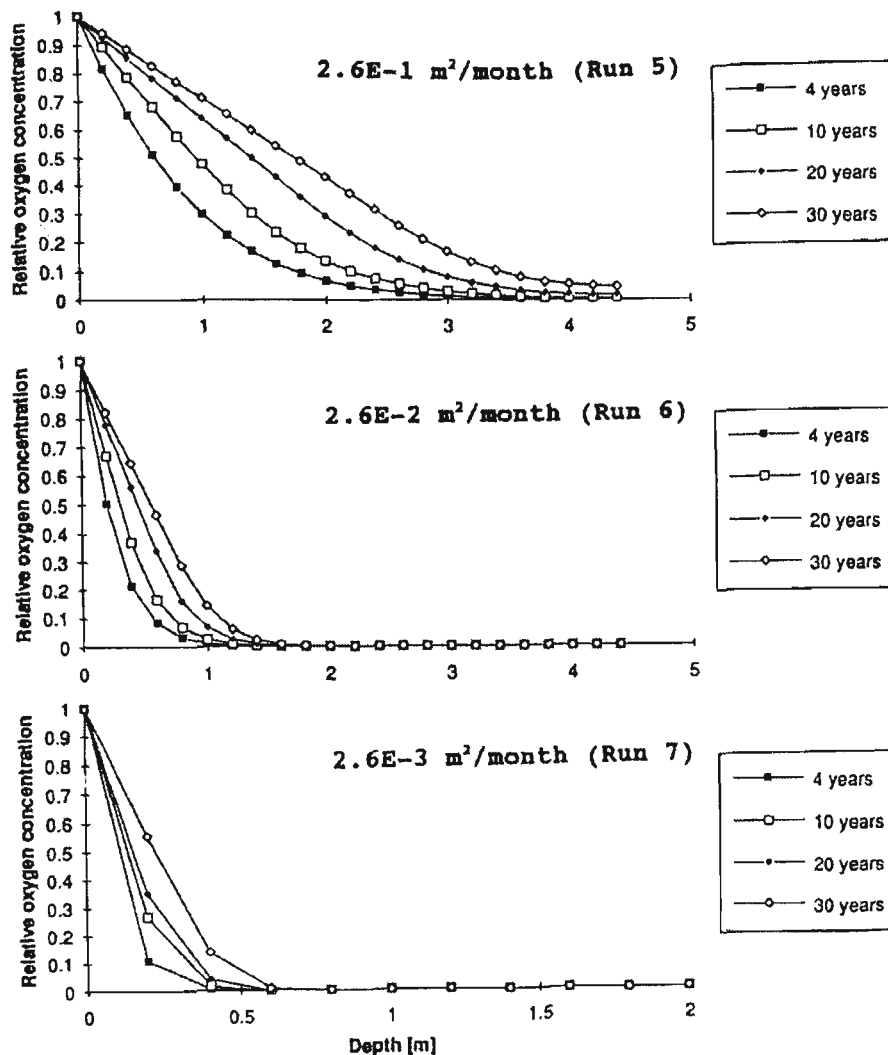


Figure C.11. Oxygen concentration profiles as a function of depth shown for different effective diffusion coefficient (after Elberling et al., 1994).

### C.5 TOUGH AMD

Lefebvre and Gelinas (1995) developed a numerical model for the simulation of acid mine drainage generation in waste rock dumps. The major processes incorporated in the model are hydrology, gas and heat transfer, geochemistry and mass transport process. The important features of the model were that it was multi-component, multiphase and non-isothermal and it was called a TOUGH AMD model. A reaction core model was used to take into account the rate of oxidation of pyrite within the waste rock dumps. Based on field observations made at La Mine Doyon, a zonation appears within waste rock blocks with the following characteristics:

- Exterior zone in which pyrite is completely depleted.
- Interior core where pyrite remained unreacted

According to Lefebvre and Gelinas (1995) the whole pyrite within a particle is not oxidised simultaneously because the oxidation reaction is restricted by the rate of diffusion of oxygen within the blocks. Furthermore, a reaction core model must also take into consideration the concentration and surface area of pyrite exposed within waste rocks. The reaction core model applied by Lefebvre and Gelinas (1995) presumes that oxygen is the only effective pyrite oxidant. In addition since the model does not directly take into account ferric iron as an oxidant, thus the leachate speciation was avoided. Similar to the works done by Levenspiel (1972); Jaynes et al. (1984a, b); and Elberling et al. (1994), the reaction core model takes into consideration the effects of both the surface reaction kinetics and the rate of oxygen diffusion. Lastly, high temperatures limited the bacterial activity.

The reaction core model for pyrite oxidation was presented by:

$$Q_{OX} = -K_{OX} X_T X_{WO} \rho_{OX}^{air} f(X) \quad (C.41)$$

where,

$K_{OX}$  = overall volumetric kinetic constant (1/s);

$X_T$  = temperature kinetic factor (between 0 and 1);

$X_{WO}$  = kinetic factor of oxygen in the liquid phase (between 0 and 1);

$\rho_{OX}^{air}$  = oxygen concentration in the air ( $kg / m^3$ );

$f(x)$  = a geometric factor depending on the fraction of pyrite remaining, X (0 to 1).

The volumetric kinetic constant  $K_{OX}$  was given by the following expression:

$$K_{OX} = \frac{3(1-n)k_{OX} a_{Py}^{rock} \gamma \delta}{R} \quad (C.42)$$

where,

$n$  = porosity;

$k_{OX}$  = surface reaction kinetic constant ( $m/s$ );

$a_{Py}^{rock}$  = surface area of pyrite per unit volume of waste rock ( $m^{-1}$ );

$\gamma$  = conversion factor between the concentrations of oxygen in the gas and liquid phases;

$\delta$  = thickness of the rock block in which pyrite oxidation occurs ( $m$ );

$R$  = radius of waste particle ( $m$ ).

The geometric factor  $f(x)$  which takes into consideration the relative effects of surface reaction kinetics and oxygen diffusion into the waste rock blocks was given by:

$$f(x) = \frac{X^{\frac{2}{3}}}{6\tau_d / \tau_c X^{\frac{1}{3}}(1 - X^{\frac{1}{3}}) + 1} \quad (C.43)$$

where,

$$\tau_c = \frac{\rho_{Py}^{rock} R}{b k_{OX} a_{Py}^{rock} \delta \gamma \rho_{OX}^{air}} \quad (C.44)$$

$$\tau_d = \frac{\rho_{Py}^{rock} R^2}{6b D_e \gamma \rho_{OX}^{air}} \quad (C.45)$$

where,

$X$  = fraction of pyrite remaining in waste rock blocks;

$\tau_c$  = total time required for complete oxidation of pyrite in waste rock particles if the oxidation process is only controlled by surface reaction ( $s$ );

$\tau_d$  = total time required for full oxidation of pyrite in waste rock blocks if the oxidation reaction is only limited by oxygen diffusion into the waste rock blocks (s);

$\rho_{Py}^{rock}$  = density of pyrite within the blocks ( $kg/m^3$ );

$b$  = stoichiometric ratio between the masses of oxygen and pyrite consumed;

$D_e$  = effective diffusion coefficient of oxygen within the rock blocks ( $m^2/s$ ).

According to Lefebvre and Gelinias (1995), the reaction core model and the stoichiometric ratio between the masses of oxygen and pyrite can be used to calculate the volumetric oxygen consumption rate  $Q_{ox}$  ( $kg/m^3s$ ) in a unit volume of waste rocks.

It was concluded that the air convection process controlled the rate of the contaminant generation. A study of acid mine drainage is necessary for a better understanding and assessment of the processes involved in acid mine drainage generation.

### **C.6 PYROX-MINTRAN-MINTOX model**

Wunderly et al. (1996) developed a numerical model referred to as PYROX that couples one-dimensional oxygen diffusion and sulphide mineral oxidation to simulate pyrite oxidation in the vadose zone (unsaturated zone) of mine tailings. For the simulation, a shrinking-core model and a finite element numerical approach were used to simulate the transport of oxygen and the oxidation of pyrite particles. Figure 8.12 represents a schematic diagram of the model.

The PYROX model has been coupled with a two-dimensional finite element reactive transport model, MINTRAN, for contaminant transport and MINTEQA2 to solve the equilibrium geochemistry. The chemical reactions considered in the model are based on a local equilibrium assumption. The resulting model has been called MINTOX. A two-

step equilibrium approach has been used for the simulation. In this approach, the solution is divided into the two separate parts:

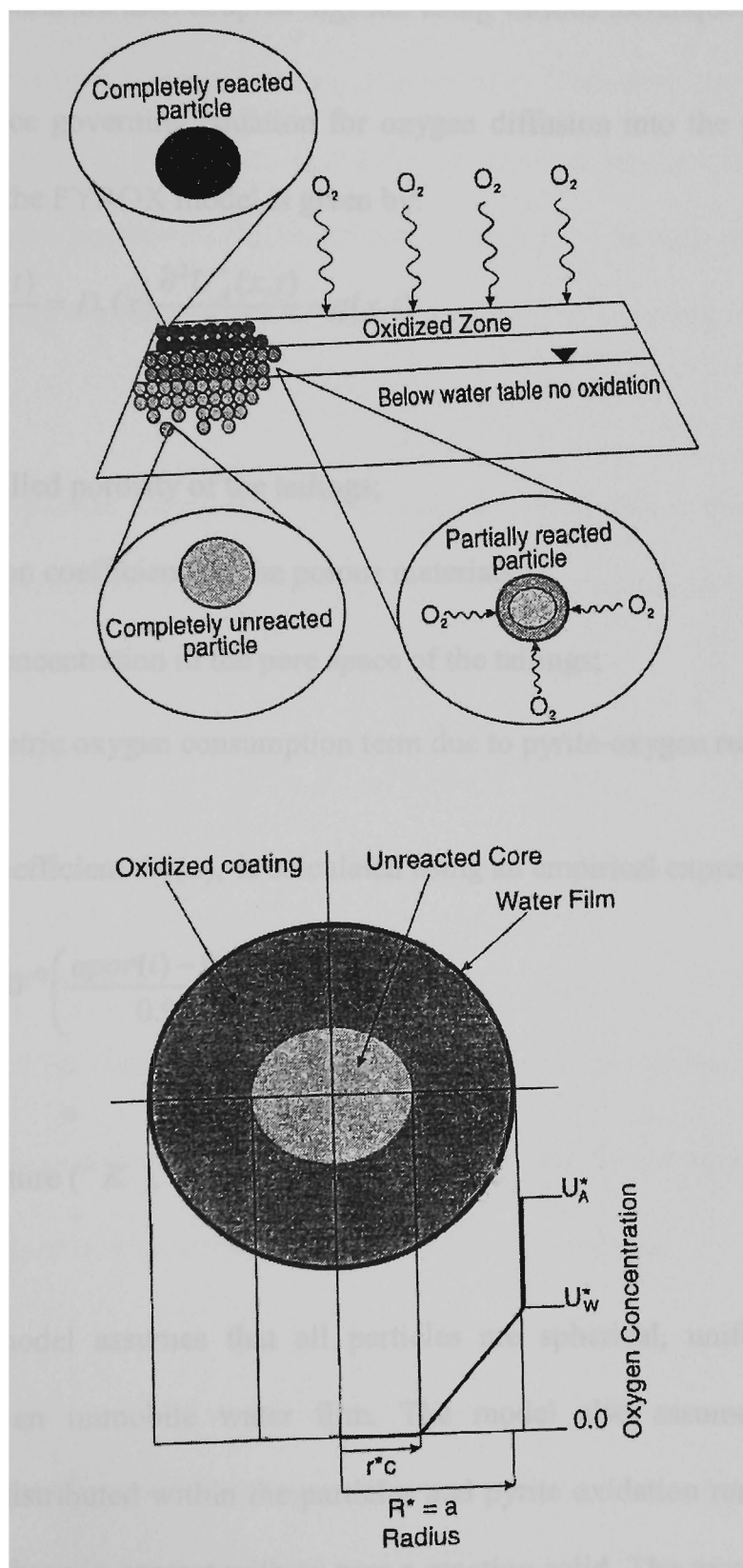


Figure C.12. Schematic diagram representing the model developed by Wunderly et al. (1996).

a) Advection-dispersion transport and

b) Chemical equilibrium

These separate parts are then coupled together using various techniques.

The mass balance governing equation for oxygen diffusion into the pore space of the tailings used in the PYROX model is given by:

$$apor(x) \frac{\partial U_A^*(x,t)}{\partial t} = D_1(x) \frac{\partial^2 U_A^*(x,t)}{\partial x^2} - q(x,t) \quad (C.46)$$

where,

$apor(x)$  = air-filled porosity of the tailings;

$D_1(x)$  = diffusion coefficient for the porous materials;

$U_A^*$  = oxygen concentration in the pore space of the tailings;

$q(x,t)$  = volumetric oxygen consumption term due to pyrite-oxygen reaction.

The diffusion coefficient  $D_1(x)$ , is calculated using an empirical expression:

$$D_1(x) = 3.98 \times 10^{-9} \left( \frac{apor(i) - 0.05}{0.95} \right)^{1.7} \times (temp)^{1.5} \quad (C.47)$$

where,

$temp$  = temperature ( $^{\circ} K$ ).

The PYROX model assumes that all particles are spherical, uniform in size and surrounded by an immobile water film. The model also assumes that pyrite is homogeneously distributed within the particles and pyrite oxidation reactions take place in the aqueous phase in contact with or near a reacting solid. The oxygen diffuses from the outside of particle through the porous oxidised rim of the particle towards the unleached core of the particle where the oxidation reaction takes place. As the pyrite

oxidation reaction develops in the particles, the radius of the unreacted core will decrease while the thickness of the oxidised zone increases. According to Wunderly et al. (1996), the rate of shrinkage of the unoxidised core is approximately 1000 times slower than the flux of oxygen within the particle. Therefore the reaction front is immobile with regard to the oxygen concentration gradient between the outer surface of the particle and the reaction front and the concentration of oxygen within the oxidised rim of the particles decreases linearly from the outside of the particle to the unreacted core boundary.

Considering the pseudo steady-state assumption described above, the sink term in the mass balance equation for oxygen representing oxygen consumption by pyrite oxidation within a unit volume of tailings,  $q(x, t)$  has been calculated by:

$$q(x, t) = \frac{3(1 - por(x))}{R^{*3}} D_2 \left( \frac{R^* r_c^*(x)}{R^* - r_c^*(x)} \right) U_w^*(x, t) \quad (C.48)$$

where,

$R^*$  = radius of the particle;

$r_c^*(x)$  = radius of the reaction front or the radius of the unreacted core;

$U_w^*$  = oxygen concentration in the water film surrounding the particle;

$D_2$  = diffusion coefficient for the oxidised coating of the particle.

By combining Equations C.46 and C.48, Equation C.49 describes oxygen diffusion into tailings with the consumption term represented as shrinking core particles:

$$apor(x) \frac{\partial U_A^*(x, t)}{\partial t} = D_1(x) \frac{\partial^2 U_A^*(x, t)}{\partial x^{*2}} - \frac{3(1 - por(x))}{R^{*3}} D_2 \left( \frac{R^* r_c^*(x, t)}{R^* - r_c^*(x, t)} \right) U_w^*(x, t) \quad (C.49)$$

Equation C.49 describes the mass balance for oxygen diffusion into the pore space of the tailings incorporating the volumetric consumption of oxygen to the particles. Equation C.49 contains two variables,  $U_A^*(x,t)$  and  $r_c^*(x,t)$ . To attain a unique solution, another equation linking  $U_A^*(x,t)$  and  $r_c^*(x,t)$  was essential. This equation determines the radius of the reaction front within the tailings particles as follows:

$$\frac{\partial r_c^*}{\partial t} = \frac{D_2(1-por)}{\varepsilon\rho_s r_c^{*2}} \left( \frac{R^* r_c^*(x)}{R^* - r_c^*(x)} \right) U_W^*(x,t) \quad (C.50)$$

where,

$\varepsilon$  = mass ratio of oxygen to sulphur;

$\rho_s$  is obtained using the following equation:

$$\rho_s = \rho_b \times \text{fraculf}(x) \quad (C.51)$$

where,

$\rho_b$  = bulk density of the tailings ( $kg / m^3$ );

$\text{fraculf}(x)$  = fraction of sulphur in the tailings materials ( $kg/kg$ )

The dimensionless forms of Equations C.49 and C.50 were developed and solved using the Galerkin finite element method for the variable  $U_A^*(x,t)$  and a Newton-Raphson technique for the variable  $r_c^*(x,t)$ .

The model was modified to take into account the speciation of iron into  $Fe^{++}$  and  $Fe^{+++}$ , which is dependent on the geochemical conditions at each node of the finite element mesh in the simulation. The oxygen concentration calculated in PYROX is dependent on the speciation of iron. The following expression was derived based on the equilibrium assumption:

$$\log\left(\frac{a_{Fe^{3+}}}{a_{Fe^{2+}}}\right) = \log(K_{eq}) + \frac{1}{4}\log(P_{O_2}) - pH \quad (C.52)$$

where,

$a_{Fe^{3+}}$  and  $a_{Fe^{2+}}$  = activities of ferric and ferrous iron respectively;

$K_{eq}$  = equilibrium constant for iron.

The total amount of iron produced is given by:

$$Fe^{total} = Fe(ferric) + Fe(ferrous) \quad (C.53)$$

The PYROX model was linked with the reactive transport model MINTRAN. The resulting model was called MINTOX. MINTOX was capable of running either a one-dimensional or a two-dimensional simulation, while oxygen transport was assumed to occur only in the vertical direction. As the simulation by MINTOX is performed, the rate of pyrite oxidation occurring within the current time step is determined. The concentration of pyrite oxidation products such as  $H^+$ ,  $SO_4^{2-}$ ,  $Fe^{2+}$  and  $Fe^{3+}$  are estimated at each node in the finite element grid within the unsaturated zone and then added to the equivalent spatial node in the reactive transport part of the model. Dissolved chemical species are transported individually and a new chemical condition is equilibrated at each node before moving on to the next time step and pyrite oxidation continues. When the pyrite at any node is completely depleted, the program computes a zero concentration increase at that node for all the oxidation products.

In order to assess the MINTOX model, Wunderly et al. (1996) ran a one-dimensional simulation using field data monitored in the Nordic Main tailings impoundment near Elliot Lake, Ontario.

MINTOX was validated by Wunderly et al. (1996) with field-monitored data. A simulation for the effects of 12 years of pyrite oxidation was performed based on physical and chemical data collected at the site.

The general trends predicted in the one-dimensional simulation results report by Wunderly et al. (1996) matched closely with field data monitored at the above-mentioned site. Figure C.13 shows the normalised oxygen concentration versus depth profile and Figure C.14 shows the normalised pyrite content versus depth profile for the modelled output and field data. Furthermore, The results of one-dimensional simulation are given in Figures C.15 and C.16.

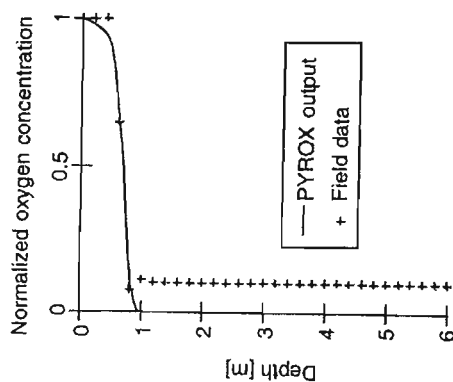


Figure C.13. Normalised oxygen concentration for the model and field data from Elliot Lake, Ontario (after Wunderly et al., 1996).

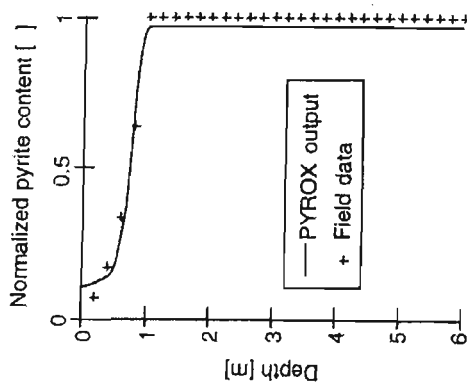


Figure C.14. Normalised pyrite content for the simulation results and field data from Elliot Lake, Ontario (after Wunderly et al., 1996).

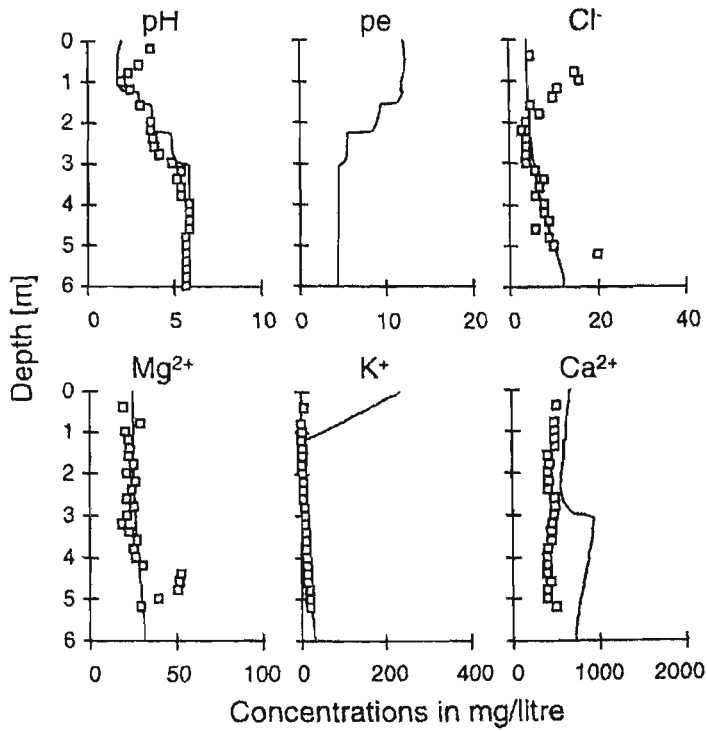


Figure C.15. One-dimensional modelling results in comparison to field data from Elliot Lake, Ontario (after Wunderly et al., 1996).

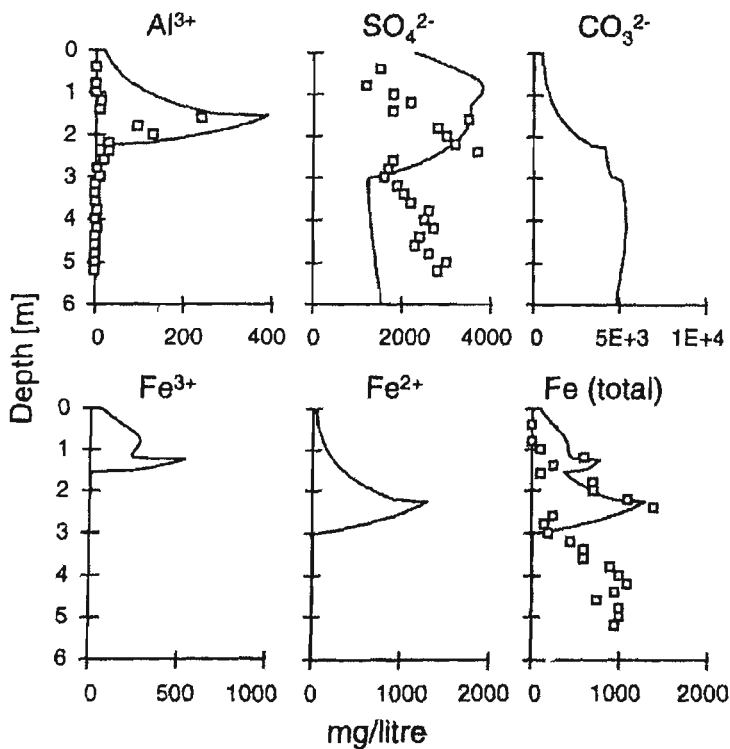


Figure C.16. One-dimensional simulation results in comparison to field data from Elliot Lake, Ontario (continued) (after Wunderly et al., 1996).

Wunderly et al. (1996) also performed a two-dimensional simulation to describe the capability of the MINTOX model to simulate physical and chemical changes enforced upon the tailings and demonstrate that these changes may have basic roles on the rate of acid and contaminant generation and subsequent leaching of contaminants caused by the oxidation of sulphide minerals, mainly pyrite. Furthermore, the results obtained from numerical simulation suggested that PYROX may be appropriate to predict the long-term sulphide mineral oxidation and leaching of the oxidation products such as  $H^+$ ,  $SO_4^{2-}$  and  $Fe^{2+}$  to the pore waters of sulphide rich tailings.

## APPENDIX D

### MASS TRANSPORT MECHANISMS

#### D.1 Physical mechanisms of mass transport

##### D.1.1 Dispersion

The process of dispersion causes dilution of the contaminant and lowers its concentration. The dispersion process consists of two components. One component is an apparent mixing and another is molecular diffusion. As a contaminant moves through a groundwater system, it will mix with uncontaminated water resulting in dilution of the contaminant. This mixing component is often called mechanical dispersion and it arises from groundwater velocity variations in the porous media. These variations may occur on a microscopic scale due to the friction between the particles of medium and the fluid and also due to curvatures in the flow path as shown in Figure D.1.

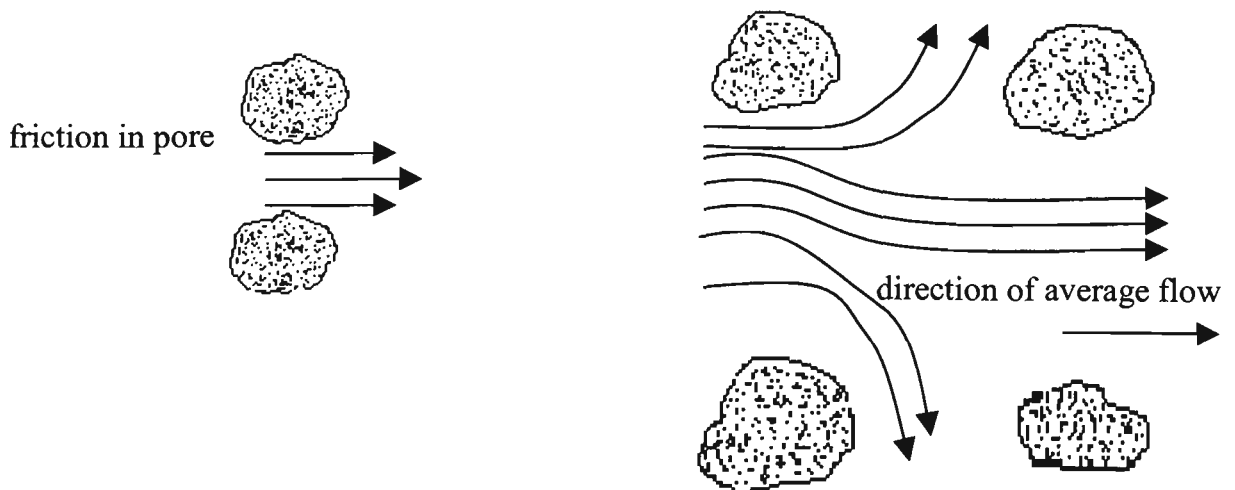


Figure D.1. Factors causing mechanical dispersion.

The mechanical dispersion is equal to the product of the average linear velocity and a factor named the dispersivity:

$$D_m = \alpha v \quad (D.1)$$

where,

$D_m$  = mechanical dispersion ( $m^2 / s$ );

$\alpha$  = dispersivity ( $m$ );

$v$  = linear velocity ( $m/s$ ).

### D.1.2 Diffusion

Molecular diffusion results in the spreading of contaminant due to concentration gradients. By this process, both ionic and molecular species dissolved in groundwater move from areas of higher concentration to areas of lower concentration. The role of diffusion processes is to cause the solute to spread out in all directions in response to these concentration gradients.

Diffusion processes can be mathematically formulated using Fick's laws. Fick's first law of diffusion describes the flux of a contaminant under steady-state conditions and can be written as follows:

$$F = -D_1 \frac{\partial C}{\partial x} \quad (D.2)$$

where,

$D_1$  = diffusion coefficient ( $L^2 T^{-1}$ );

$F$  = mass flux of contaminant per unit area per unit time ( $ML^{-2}T^{-1}$ );

$C$  = contaminant concentration ( $ML^{-3}$ );

$\frac{\partial C}{\partial x}$  = concentration gradient which is negative in the direction of diffusion.

For the major cations and anions in groundwater such as  $Na^+, K^+, Mg^{2+}$ ,  $Ca^{2+}, Cl^-, HCO_3^-$  and  $SO_4^{2-}$ , the diffusion coefficient ranges from  $1 \times 10^{-9}$  to  $2 \times 10^{-9} \text{ m}^2 / \text{s}$  at  $25^\circ \text{C}$  (Freeze and Cherry, 1979).

For systems where the solute concentrations may vary with time, Fick's second law can be applied:

$$\frac{\partial C}{\partial t} = D_1 \frac{\partial^2 C}{\partial x^2} \quad (\text{D.3})$$

where,

$$\frac{\partial C}{\partial t} = \text{change in concentration with time.}$$

In porous media, the diffusion coefficient for an ion is smaller than that in water because the ion must travelling a longer path around the mineral particle. To take this into consideration, an effective diffusion coefficient  $D^*$  can be calculated in solids as given below:

$$D^* = \omega D_1 \quad (\text{D.4})$$

where,

$\omega$  = an empirical constant ranging from 0.5 to 0.01 (Fetter, 1988).

### D.1.3 Hydrodynamic dispersion

The combined effect of diffusion and mechanical dispersion is named hydrodynamic dispersion and can be formulated as:

$$D_L = \alpha_L v_x + D_{dif} \quad (\text{D.5})$$

$$D_T = \alpha_T v_y + D_{dif} \quad (\text{D.6})$$

where,

$D_L$  and  $D_T$  = longitudinal and transverse dispersion coefficients respectively;

$\alpha_L$  and  $\alpha_T$  = longitudinal and transverse dispersivities of porous medium;

$v_x$  and  $v_y$  = average linear velocities in the  $x$  and  $y$  directions;

$D_{dif}$  = molecular diffusion coefficient.

Dispersivity varies spatially with changes in the lithology of the porous medium. In laboratory studies using relatively homogeneous porous media, the longitudinal dispersion coefficient ( $D_L$ ) was reported (Pickens and Lennox, 1976) to be greater than the transverse dispersion coefficient ( $D_T$ ) by a factor of 5-20.

It should be noted that in systems where groundwater velocities are low, contaminant attenuation is mainly governed by molecular diffusion whereas at higher velocities mechanical dispersion (mixing) is dominant.

#### **D.1.4 Advection**

Advection is the process of transport of a contaminant due to motion of the groundwater.

The velocities are derived from the potential (flow) equation using Darcy's law. The

advection flux is given by:

$$F_1 (\text{advection}) = v_{x_j} n C \quad (\text{D.7})$$

where,

$v_{x_j}$  = linear groundwater velocity and is a vector with components  $v_x$  and  $v_y$  in a two-

dimensional case;

$n$  = porosity.

Coupling advection and dispersion, the mass fluxes in the two directions become:

$$F_x = v_x n C - n D_x \frac{\partial C}{\partial x} \quad (\text{D.8})$$

$$F_y = v_y n C - n D_y \frac{\partial C}{\partial y} \quad (\text{D.9})$$

where,

$v_x n C$  and  $v_y n C$  = advection fluxes in  $x$  and  $y$  directions.

### D.1.5 The advection-diffusion equation

For systems with groundwater movement, mass transport can be described by both advection and diffusion. The equation incorporating these processes is called the advection-diffusion equation. The one-dimensional form of this equation can be written as:

$$n \frac{\partial C}{\partial t} = n D_{dif} \frac{\partial^2 C}{\partial x^2} - n v_x \frac{\partial C}{\partial x} \quad (\text{D.10})$$

or,

$$\frac{\partial C}{\partial t} = D_{dif} \frac{\partial^2 C}{\partial x^2} - v_x \frac{\partial C}{\partial x} \quad (\text{D.11})$$

The first term on the right describes mass transport by advection and the second describes mass transport by diffusion.

### D.1.6 The advection-dispersion equation

Diffusion alone does not fully account for mixing during contaminant transport. Hence, mechanical dispersion is considered to be important in many systems. The hydrodynamic

dispersion takes into account both the mechanical mixing and diffusion. The one-dimensional equation incorporating hydrodynamic dispersion reduces to:

$$\frac{\partial C}{\partial t} = D_L \frac{\partial^2 C}{\partial x^2} - v_x \frac{\partial C}{\partial x} \quad (\text{D.12})$$

where,

$D_L$  = longitudinal dispersion coefficient;

$v_x$  = average ground water velocity in the x-direction;

$C$  = contaminant concentration;

$t$  = time.

## D.2 Mass transport with reaction

Contaminant passage in a porous medium is diluted by chemical reactions taking place during transport. These reactions can occur between the solute and the porous media or between the solute mass and the pore fluid. A contaminant is produced or removed by chemical processes during the course of transport. Therefore, the mass transport equation has to be modified to incorporate the suitable source or sink terms. In the case of one-dimensional transport, the conservation equation becomes:

$$\frac{\partial C}{\partial t} = D_x \frac{\partial^2 C}{\partial x^2} - v_x \frac{\partial C}{\partial x} \pm \frac{r}{n} \quad (\text{D.13})$$

where,

$r$  = mass produced or consumed per unit volume per unit time ( $\text{mol} / \text{m}^3 \text{s}$ ).

According to Reddi and Inyang (2000), the mass transport mechanisms are categorised into two groups:

- abiotic processes
- biotic processes

Abiotic processes occur independent from biological activities. The biotic processes include those processes in which micro-organisms consume the mass of chemicals. The major abiotic processes are acid-base reactions, oxidation-reduction reactions, complexation, precipitation and dissolution, radioactive decay and sorption.

The process of sorption is considered to be a dominant process in attenuating the transport of dissolved species in groundwater. Sorption is the phase-transfer process responsible for the transfer of contaminants from liquid to solid state.

Sorption includes absorption, adsorption and ion exchange processes. In absorption processes the contaminant is included into the solid, but the adsorption process is responsible for the attraction of solutes to the solid surface. Ion exchange is the process at which the cations are substituted into the solids.

## APPENDIX E

### CHEMICAL REACTIONS AND THE LAW OF MASS ACTION

#### E.1 Chemical reactions

Two principal chemical reactions that often take place in solute transport problems are as follows:

##### (i) Irreversible kinetically controlled reactions

Kinetically controlled reactions refer to the rates and mechanisms by which chemical reactions occur. Rate-controlling reactions are relatively slow. The examples of the kinetic reaction are the first-order decay of a radioactive species, biodegradation (Domenico and Schwartz, 1990), pyrite oxidation and ferrous iron oxidation (Jaynes et al., 1984a).

##### (ii) Equilibrium-controlled reactions/ reversible reactions

Reversible reactions are characterised by a mixture of products and reactants remaining at chemical equilibrium. An equilibrium-controlled reaction is relatively fast. Ion-exchange reactions, complexation, precipitation or dissolution, are considered to be equilibrium processes (Rubin and James, 1973; Jennings et al., 1982; Miller and Benson, 1983; Jaynes et al., 1984a; Walter et al., 1994a, b; and Schnoor, 1996).

#### E.2 Law of mass-action

Based on the law of mass action, a reversible chemical reaction will attempt to reach equilibrium (Fetter, 1988). In the law of mass action, the rate of a chemical reaction is proportional to the product of the concentration of each dissolved species participating in the reaction raised to the power of its stoichiometric coefficients (Schnoor, 1996). Consider a general reversible chemical reaction:



If the rate expression can be given by the following expressions:

$$\text{Rate of the forward reaction} = K_f [M]^m [N]^n \quad (\text{E.2})$$

$$\text{Rate of the reverse reaction} = K_r [O]^o [P]^p \quad (\text{E.3})$$

Then, overall rate of reaction reduces to:

$$R_o = K_f [M]^m [N]^n - K_r [O]^o [P]^p \quad (\text{E.4})$$

If the reaction reaches chemical equilibrium, the rate of the forward reaction becomes equal to the rate of the reverse reaction, i.e.

$$K_f [M]^m [N]^n = K_r [O]^o [P]^p \quad (\text{E.5})$$

The ratio of the forward rate constant ( $K_f$ ) divided by the reverse rate constant ( $K_r$ ) of a chemical equilibrium is defined as the equilibrium constant:

$$K_{eq} = \frac{K_f}{K_r} = \frac{[O]^o [P]^p}{[M]^m [N]^n} \quad (\text{E.6})$$

In general, the mass-action expression can be written as:

$$K_i = [A_i] \prod_{m=1}^{N_{aq}} [A_m]^{-\alpha_{i,m}} \quad (\text{E.7})$$

where,

$K_i$  = equilibrium constant;

$\alpha_{i,m}$  = stoichiometric coefficient of dissolved species  $m$  in species  $i$ ;

$N_{aq}$  = total number of aqueous species;

[ ] = activities in solution.

The activities can be related to the concentrations of dissolved species using the following equation (Miller and Benson, 1983; Fetter, 1988; and Walter et al., 1994a, b):

$$[A_m] = \gamma_m C_m \quad (\text{E.8})$$

where,

$C_m$  = concentration of dissolved species;

$\gamma_m$  = activity coefficient.

The activity coefficients of the dissolved species are functions of pressure, temperature and chemical composition (Miller and Benson, 1983). They can be calculated using the Davies equation (Miller and Benson, 1983; Jaynes, et al., 1984a; and Fetter, 1988).

$$\gamma_m = \exp \left[ -0.5 Z_m^2 \left( \frac{I^{\frac{1}{2}}}{1 + I^{\frac{1}{2}}} - 0.3I \right) \right] \quad (\text{E.9})$$

where,

$Z_m$  = charge of aqueous species  $m$  ;

$I$  = ionic strength of the solution defined as (Fetter, 1988):

$$I = \frac{1}{2} \sum_{m=1}^{N_{aq}} C_m Z_m^2 \quad (\text{E.10})$$

where,

$C_m$  = concentration of  $m^{th}$  aqueous species;

$Z_m$  = charge of  $m^{th}$  species.

## APPENDIX F

### THE COMPLEMENT OF THE ERROR FUNCTION

The error function ‘*erf*’ can be used to calculate its complement ‘*erfc*’ which in turn is used in analytical equations of solute transport (Equation 9.3, Chapter 9, Section 9.4, Page 266). The complement of the error function is given in terms of its argument  $\beta$  as follows (Freeze and Cherry, 1979; Reddi and Inyang, 2000):

$$erfc(\beta) = 1 - erf(\beta) = 1 - \left( \frac{2}{\sqrt{\pi}} \right) \int_0^{\beta} e^{-u^2} du \quad (F.1)$$

Values for the error function ( $erf(\beta)$ ) and its complement ( $erfc(\beta)$ ) for different values of the argument  $\beta$  are given in Table F.1 which does not show the negative values of the argument  $\beta$ . It may be calculated using the following expression:

$$erfc(-\beta) = 1 + erf(\beta) \quad (F.2)$$

The following useful relationships in Equations F.3 and F.4 can also be applied (Domenico and Schwartz, 1990):

$$erf(-\beta) = -erf(\beta) \quad (F.3)$$

$$erfc(\beta) = 1 - erf(\beta) \quad (F.4)$$

Table F.1. Values of  $erf(\beta)$  and  $erfc(\beta)$  (quoted in Domenico and Schwartz, 1990).

$\beta$	$erf(\beta)$	$erfc(\beta)$
0	0.000000	1.000000
0.05	0.056372	0.943628
0.1	0.112463	0.887537
0.15	0.167996	0.832004
0.2	0.222703	0.777297
0.25	0.276326	0.723674
0.3	0.328627	0.671373
0.35	0.379382	0.620618
0.4	0.428392	0.571608
0.45	0.475482	0.524518
0.5	0.520500	0.479500
0.55	0.563323	0.436677
0.6	0.603856	0.396144
0.65	0.642029	0.357971
0.7	0.677801	0.322199
0.75	0.711156	0.288844
0.8	0.742101	0.257899
0.85	0.770668	0.229332
0.9	0.796908	0.203092
0.95	0.820891	0.179109
1.0	0.842701	0.157299
1.1	0.880205	0.119795
1.2	0.910314	0.089686
1.3	0.934008	0.065992
1.4	0.952285	0.047715
1.5	0.966105	0.033895
1.6	0.976348	0.023652
1.7	0.983790	0.016210
1.8	0.989091	0.010909
1.9	0.992790	0.007210
2.0	0.995322	0.004678
2.1	0.997021	0.002979
2.2	0.998137	0.001863
2.3	0.998857	0.001143
2.4	0.999311	0.000689
2.5	0.999593	0.000407
2.6	0.999764	0.000236
2.7	0.999866	0.000134
2.8	0.999925	0.000075
2.9	0.999959	0.000041
3.0	0.999978	0.000022

## APPENDIX G

### DERIVATION OF THE OPERATIONAL PARTIAL DIFFERENTIAL EQUATIONS FOR DIFFERENT CASES OF ION-EXCHANGE REACTIONS

#### G.1 Assumptions

For the derivation of the transport equations incorporating ion exchange reactions the following assumptions were made (Rubin and James, 1973):

(i) The activities of adsorbed species is assumed to be equal to their equivalent mole fraction:

$$\bar{C}_i^* = \frac{\bar{C}_i}{\bar{C}_T} \quad (\text{G.1})$$

where,

$\bar{C}_i$  = concentration of species  $i$  on the surface phase;

$\bar{C}_i^*$  = equivalent mole fraction of species  $i$  in the sorbed phase;

$\bar{C}_T$  = cation exchange capacity (CEC) of the medium which is given by:

$$\bar{C}_T = \sum_{i=1}^{n_c} \bar{C}_i \quad (\text{G.2})$$

where,

$n_c$  = number of dissolved species participating in the ion exchange reactions.

The mass action Equation 9.9 (Chapter 9, Page 270) can now be rewritten as:

$$K_i^j = \left( \frac{\bar{C}_j^*}{\bar{C}_j} \right)^{n_j} \left( \frac{\bar{C}_i}{\bar{C}_i^*} \right)^{n_i} \quad (\text{G.3})$$

It should be noted that cation exchange capacity describes the quantity of exchangeable cations sorbed on the surface (Domenico and Schwartz, 1990). It varies considerably depending on the type of clay mineral.

(ii) A local chemical equilibrium exists for ion exchange reaction at any point of the system. Among the  $n_c$  exchanging species in the system, there are  $n_c + 1$  equations with  $2n_c$  unknown functions or dependent variables. Hence,  $n_c - 1$  independent equilibrium relationships are required of the form of Equation G.3. One additional algebraic equation may be considered when the following conditions are met:

(a) The total concentration ( $C_T$ ) of the species participating in the exchange reactions in the influx boundary remains constant with time and is defined by Equation G.4.

$$\sum_{i=1}^{n_c} C_{i_{\text{influx}}} = C_{T_{\text{influx}}} \quad (\text{G.4})$$

where,

$C_{i_{\text{influx}}}$  = influx concentration of  $i^{\text{th}}$  dissolved species;

$C_{T_{\text{influx}}}$  = influx total concentration of the aqueous species.

(b) At all points of the system, the initial total concentration of the aqueous species involving in the exchange process is given by:

$$C_{T_{\text{init}}} = \sum_{i=1}^{n_c} C_{i_{\text{init}}} \quad (\text{G.5})$$

where,

$C_{i_{\text{init}}}$  = initial concentration of  $i^{\text{th}}$  dissolved species;

$C_{T_{\text{init}}}$  = initial total concentration of the aqueous species.

$C_{T_{mi}}$  may also equals to  $C_{T_{influx}}$ .

(c) The total concentration of pore fluid species  $C_T$  can be defined as:

$$C_T = \sum_{i=1}^{n_c} C_i \quad (G.6)$$

This means that total concentration of the dissolved species may be not changed by the exchange reaction alone. Equation G.6 can be applied to eliminate one of the variables  $C_i$  from the set of  $n_c$  partial differential equation presented by Equation 9.2 (Chapter 9, Section 9.2, Page 264). Hence, the new set of equations consists of  $n_c - 1$  partial differential equations.

## G.2 Method

The following technique of Rubin and James (1973) is used to derive the operational partial differential equations for the general case of a non-linear ion exchange.

The following set of equations is solved:

$$\phi \frac{\partial C_i}{\partial t} + \rho_b \frac{\partial \bar{C}_i}{\partial t} = D \frac{\partial^2 C_i}{\partial x_j^2} - q_j \frac{\partial C_i}{\partial x_j} + q_{re} C_i \pm S \quad (G.7)$$

$$K_j^i = \left( \frac{\bar{C}_i}{C_i} \right)^{P_j} \left( \frac{C_j}{\bar{C}_j} \right)^{P_i} \quad (G.8)$$

$$\sum_{i=1}^{n_c} \bar{C}_i = \bar{C}_T \quad (G.9)$$

where,

$K_j^i$  = a constant and  $i = 1, 2, 3, \dots, n_c$ ,  $j = 2, 3, 4, \dots, n_c$

For any given  $i^{th}$  species,  $\bar{C}_i$  may be eliminated from the derivatives of Equation G.7.

Equation G.8 can be rewritten in the following form:

$$f_j^i = K_j^i C_i^{P_j} \bar{C}_j^{P_i} - \bar{C}_i^{P_j} C_j^{P_i} = 0 \quad (G.10)$$

Differentiating Equation G.10 with respect to  $t$  and dividing by  $\frac{\partial f_j^i}{\partial \bar{C}_j}$  gives:

$$\frac{\partial f_j^i / \partial C_i}{\partial f_j^i / \partial \bar{C}_j} \frac{\partial C_i}{\partial t} + \frac{\partial f_j^i / \partial \bar{C}_i}{\partial f_j^i / \partial \bar{C}_j} \frac{\partial \bar{C}_i}{\partial t} + \frac{\partial f_j^i / \partial C_j}{\partial f_j^i / \partial \bar{C}_j} \frac{\partial C_j}{\partial t} + \frac{\partial \bar{C}_j}{\partial t} = 0 \quad (G.11)$$

where,  $\partial f_j^i / \partial \bar{C}_j \neq 0$

Equation G.9 yields:

$$\sum_{j=1}^{n_s} \frac{\partial \bar{C}_j}{\partial t} = -\frac{\partial \bar{C}_i}{\partial t}, \quad j \neq i \quad (G.12)$$

For a given  $i$ , the following expression can be derived:

$$\frac{\partial \bar{C}_i}{\partial t} = \frac{1}{g_i} \left( f_{ii} \frac{\partial C_i}{\partial t} - \sum_{\substack{j=1 \\ j \neq i}}^{n_s} f_{ij} \frac{\partial C_j}{\partial t} \right) \quad (G.13)$$

where,

$$g_i = 1 - \sum_{\substack{j=1 \\ j \neq i}}^{n_s} \frac{\partial f_j^i / \partial \bar{C}_i}{\partial f_j^i / \partial \bar{C}_j} \quad (G.14)$$

$$f_{ii} = \sum_{\substack{j=1 \\ j \neq i}}^{n_s} \frac{\partial f_j^i / \partial C_i}{\partial f_j^i / \partial \bar{C}_j} \quad (G.15)$$

$$f_{ij} = -\frac{\partial f_j^i / \partial C_j}{\partial f_j^i / \partial \bar{C}_j} \quad (G.16)$$

Substituting Equation G.13 into Equation G.7 yields the following operational equation:

$$\left( \phi + \frac{\rho_b}{g_i} f_{ii} \right) \frac{\partial C_i}{\partial t} - \frac{\rho_b}{g_i} \sum_{\substack{j=1 \\ j \neq i}}^{n_c} f_{ij} \frac{\partial C_j}{\partial t} = D \frac{\partial^2 C_i}{\partial x^2} - q_j \frac{\partial C_i}{\partial x} + q_{re} C_i \pm S \quad (\text{G.17})$$

where,  $i = 1, 2, 3, \dots, n_c$

Given appropriate initial and boundary conditions, the non-linear partial differential Equation G.17 is solved using the finite volume method. For any given  $i$ , Equation G.8 gives:

$$\bar{C}_j = (K_i^j)^{1/P_i} \left( \frac{\bar{C}_i}{C_i} \right)^{P_j/P_i} C_j \quad (\text{G.18})$$

where,  $j = 1, 2, 3, \dots, n_c$  and  $j \neq i$

For all the values of  $j$  and considering Equation G.9,  $\bar{C}_i$  can be calculated from the following equation:

$$\bar{C}_i = \bar{C}_T - \sum_{\substack{j=1 \\ j \neq i}}^{n_c} (K_i^j)^{1/P_i} \left( \frac{\bar{C}_i}{C_i} \right)^{P_j/P_i} C_j \quad (\text{G.19})$$

Based on the general Equation G.17 the governing equations can be developed for various cases of ion exchange reactions as given below:

### G.2.1 Binary homoivalent exchange

Binary homoivalent exchange is noted to be the simplest case of two-species ( $n_c = 2$ ,  $P_1 : P_2 = 1 : 1$ ) exchange (Valocchi, et al., 1981). The general transport equations are developed for a one-dimensional problem, in both cases of constant  $C_T$  and varying  $C_T$ .

**(a) Constant  $C_T$**

In this case the feed solution has the same concentration as the background solution.  $C_T$  is constant. This simplification reduces the binary exchange problem to the well-known single ion adsorption problem (Rubin and James, 1973; and Valocchi, et al., 1981). The following set of the equations describe this problem:

$$C_1: \left( \phi + \frac{\rho_b}{g} f_1 \right) \frac{\partial C_1}{\partial t} - \frac{\rho_b}{g} f_2 \frac{\partial C_2}{\partial t} = D \frac{\partial^2 C_1}{\partial x^2} - q_x \frac{\partial C_1}{\partial x} + q_{re} C_1 \pm S \quad (G.20)$$

$$C_2: \left( \phi + \frac{\rho_b}{g} f_2 \right) \frac{\partial C_2}{\partial t} - \frac{\rho_b}{g} f_1 \frac{\partial C_1}{\partial t} = D \frac{\partial^2 C_2}{\partial x^2} - q_x \frac{\partial C_2}{\partial x} + q_{re} C_2 \pm S' \quad (G.21)$$

$$K_2^1 = \left( \frac{\bar{C}_1}{C_1} \right)^1 \left( \frac{C_2}{\bar{C}_2} \right)^1 \quad \text{or} \quad K_2^1 C_1 (\bar{C}_T - \bar{C}_1) - \bar{C}_1 C_2 = 0 \quad (G.22)$$

$$\bar{C}_T = \bar{C}_1 + \bar{C}_2 \quad (G.23)$$

$$g = K_2^1 C_1 + C_2 \quad (G.24)$$

$$f_1 = K_2^1 (\bar{C}_T - \bar{C}_1) \quad (G.25)$$

$$f_2 = \bar{C}_1 \quad (G.26)$$

$$C_T = Cte; \quad \frac{\partial C_1}{\partial t} = -\frac{\partial C_2}{\partial t} \quad (G.27)$$

In this case  $\bar{C}_1$  is:

$$\bar{C}_1 = \frac{K_2^1 C_1 \bar{C}_T}{K_2^1 C_1 + C_2} \quad (G.28)$$

Because  $C_T$  is constant, thus,

$$g \frac{\partial \bar{C}_1}{\partial t} = f_1 \frac{\partial C_1}{\partial t} + f_2 \frac{\partial C_1}{\partial t} \quad (G.29)$$

The partial differential equations for species  $C_1$  and  $C_2$  become,

$$\left(\phi + \frac{\rho_b}{g} f_1\right) \frac{\partial C_1}{\partial t} + \frac{\rho_b}{g} f_2 \frac{\partial C_1}{\partial t} = D \frac{\partial^2 C_1}{\partial x^2} - q_x \frac{\partial C_1}{\partial x} + q_{re} C_1 \pm S \quad (\text{G.30})$$

$$\left(\phi + \frac{\rho_b}{g} f_2\right) \frac{\partial C_2}{\partial t} + \frac{\rho_b}{g} f_1 \frac{\partial C_2}{\partial t} = D \frac{\partial^2 C_2}{\partial x^2} - q_x \frac{\partial C_2}{\partial x} + q_{re} C_2 \pm S' \quad (\text{G.31})$$

With rearranging above equations in a 'PHOENICS equivalent' the following equations can be obtained:

$$\frac{\partial C_1}{\partial t} = D \frac{\partial^2 C_1}{\partial x^2} - q_x \frac{\partial C_1}{\partial x} + (1 - \phi) \frac{\partial C_1}{\partial t} - \left(\frac{\rho_b}{g} [f_1 + f_2]\right) \frac{\partial C_1}{\partial t} + q_{re} C_1 \pm S \quad (\text{G.32})$$

$$\frac{\partial C_2}{\partial t} = D \frac{\partial^2 C_2}{\partial x^2} - q_x \frac{\partial C_2}{\partial x} + (1 - \phi) \frac{\partial C_2}{\partial t} - \left(\frac{\rho_b}{g} [f_1 + f_2]\right) \frac{\partial C_2}{\partial t} + q_{re} C_2 \pm S' \quad (\text{G.33})$$

### (b) Varying $C_T$

In a general case where the total concentration of exchangeable species,  $C_T$  is different between the background and feed solutions, the transport equations for two species  $C_1$  and  $C_2$  are as follows:

$$\frac{\partial C_1}{\partial t} = D \frac{\partial^2 C_1}{\partial x^2} - q_x \frac{\partial C_1}{\partial x} + (1 - \phi) \frac{\partial C_1}{\partial t} - \frac{\rho_b}{g} f_1 \frac{\partial C_1}{\partial t} + \frac{\rho_b}{g} f_2 \frac{\partial C_2}{\partial t} + q_{re} C_1 \pm S \quad (\text{G.34})$$

$$\frac{\partial C_2}{\partial t} = D \frac{\partial^2 C_2}{\partial x^2} - q_x \frac{\partial C_2}{\partial x} + (1 - \phi) \frac{\partial C_2}{\partial t} - \frac{\rho_b}{g} f_2 \frac{\partial C_2}{\partial t} + \frac{\rho_b}{g} f_1 \frac{\partial C_1}{\partial t} + q_{re} C_2 \pm S' \quad (\text{G.35})$$

## G.2.2 Binary heterovalent exchange

In this case, the selectivity coefficient is assumed to be constant, and  $C_T$  may vary. The non-linear ion exchange reaction taking place involves two species of unequal valence,  $C_1 (P_1 = 1)$  and  $C_2 (P_2 = 2)$ . The chemical reaction describing the problem is:

$$2C_1 + \bar{C}_2 \Leftrightarrow 2\bar{C}_1 + C_2^2 \quad (\text{G.36})$$

The selectivity relationship is given by the following equation:

$$K_2^1 = \left( \frac{\bar{C}_1}{C_1} \right)^2 \left( \frac{C_2}{\bar{C}_2} \right)^1 \quad (\text{G.37})$$

Using relationships  $C_T = \sum_{i=1}^{n_c} C_i$  and  $\bar{C}_T = \bar{C}_1 + \bar{C}_2$ , Equation G.37 can be rewritten as a

quadratic equation for  $\bar{C}_1$  as follows:

$$K_2^1 C_1 (\bar{C}_T - \bar{C}_1) - \bar{C}_1^2 C_2 = 0 \quad \text{or} \quad C_2 \bar{C}_1^2 + K_2^1 C_1^2 \bar{C}_1 - K_2^1 C_1^2 \bar{C}_T = 0 \quad (\text{G.38})$$

The solution of the above quadratic equation gives the following expression for  $\bar{C}_1$ .

$$\bar{C}_1 = \frac{-K_2^1 C_1^2 \pm C_1 \left( K_2^1 C_1^2 + 4K_2^1 C_2 \bar{C}_T \right)^{1/2}}{2C_2} \quad (\text{G.39})$$

Only one of the two roots in Equation G.39 will give physically meaningful  $\bar{C}_1$ .

The values of  $f_1$ ,  $f_2$  and  $g$  are given as follows:

$$f_1 = 2K_2^1 C_1 (\bar{C}_T - \bar{C}_1) \quad (\text{G.40})$$

$$f_2 = \bar{C}_1^2 \quad (\text{G.41})$$

$$g = K_2^1 C_1^2 + 2C_2 \bar{C}_1 \quad (\text{G.42})$$

The operational partial differential equations for the case of the binary heterovalent exchange, for  $C_T$  as a constant or  $C_T$  as a variable can be expressed as follows:

**(a)  $C_T$  as a constant**

If  $C_T = Cte$ , then  $\frac{\partial C_1}{\partial t} = -\frac{\partial C_2}{\partial t}$

$$\frac{\partial C_1}{\partial t} = D \frac{\partial^2 C_1}{\partial x^2} - q_x \frac{\partial C_1}{\partial x} + (1-\phi) \frac{\partial C_1}{\partial t} - \left( \frac{\rho_b}{g} [f_1 + f_2] \right) \frac{\partial C_1}{\partial t} + q_{re} C_1 \pm S \quad (G.43)$$

$$\frac{\partial C_2}{\partial t} = D \frac{\partial^2 C_2}{\partial x^2} - q_x \frac{\partial C_2}{\partial x} + (1-\phi) \frac{\partial C_2}{\partial t} - \left( \frac{\rho_b}{g} [f_1 + f_2] \right) \frac{\partial C_2}{\partial t} + q_{re} C_2 \pm S' \quad (G.44)$$

### (b) $C_T$ as a variable

If  $C_T \neq Cte$ ,

$$\frac{\partial C_1}{\partial t} = D \frac{\partial^2 C_1}{\partial x^2} - q_x \frac{\partial C_1}{\partial x} + (1-\phi) \frac{\partial C_1}{\partial t} - \frac{\rho_b}{g} f_1 \frac{\partial C_1}{\partial t} + \frac{\rho_b}{g} f_2 \frac{\partial C_2}{\partial t} + q_{re} C_1 \pm S \quad (G.45)$$

$$\frac{\partial C_2}{\partial t} = D \frac{\partial^2 C_2}{\partial x^2} - q_x \frac{\partial C_2}{\partial x} + (1-\phi) \frac{\partial C_2}{\partial t} - \frac{\rho_b}{g} f_2 \frac{\partial C_2}{\partial t} + \frac{\rho_b}{g} f_1 \frac{\partial C_1}{\partial t} + q_{re} C_2 \pm S' \quad (G.46)$$

### G.2.3 Ternary homoivalent exchange

A system with a ternary ion exchange ( $n_c = 3, P_1 : P_2 : P_3 = 1:1:1$ ) has the following partial differential equations for transport of  $C_1, C_2$  and  $C_3$ .

$$\frac{\partial C_1}{\partial t} = D \frac{\partial^2 C_1}{\partial x_j^2} - q_j \frac{\partial C_1}{\partial x_j} + (1-\phi) \frac{\partial C_1}{\partial t} - \frac{\rho_b}{\tilde{g}_1} \tilde{f}_{11} \frac{\partial C_1}{\partial t} + \frac{\rho_b}{\tilde{g}_1} \tilde{f}_{12} \frac{\partial C_2}{\partial t} + \frac{\rho_b}{\tilde{g}_1} \tilde{f}_{13} \frac{\partial C_3}{\partial t} + q_{re} C_1 \pm S \quad (G.47)$$

$$\frac{\partial C_2}{\partial t} = D \frac{\partial^2 C_2}{\partial x_j^2} - q_j \frac{\partial C_2}{\partial x_j} + (1-\phi) \frac{\partial C_2}{\partial t} - \frac{\rho_b}{\tilde{g}_2} \tilde{f}_{22} \frac{\partial C_2}{\partial t} + \frac{\rho_b}{\tilde{g}_2} \tilde{f}_{23} \frac{\partial C_3}{\partial t} + \frac{\rho_b}{\tilde{g}_2} \tilde{f}_{21} \frac{\partial C_1}{\partial t} + q_{re} C_2 \pm S' \quad (G.48)$$

$$\frac{\partial C_3}{\partial t} = D \frac{\partial^2 C_3}{\partial x_j^2} - q_j \frac{\partial C_3}{\partial x_j} + (1-\phi) \frac{\partial C_3}{\partial t} - \frac{\rho_b}{\tilde{g}_3} \tilde{f}_{33} \frac{\partial C_3}{\partial t} + \frac{\rho_b}{\tilde{g}_3} \tilde{f}_{31} \frac{\partial C_1}{\partial t} + \frac{\rho_b}{\tilde{g}_3} \tilde{f}_{32} \frac{\partial C_2}{\partial t} + q_{re} C_3 \pm S'' \quad (G.49)$$

where,

$$K_2^1 = \frac{\bar{C}_1}{C_1} \frac{C_2}{\bar{C}_2} \quad (G.50)$$

$$K_3^1 = \frac{\bar{C}_1}{C_1} \frac{C_3}{\bar{C}_3} \quad (\text{G.51})$$

$$\bar{C}_T = \bar{C}_1 + \bar{C}_2 + \bar{C}_3 \quad (\text{G.52})$$

$$\tilde{g}_1 = C_1 + K_1^2 C_2 + K_1^3 C_3 \quad (\text{G.53})$$

$$\tilde{g}_2 = C_2 + K_2^3 C_3 + K_2^1 C_1 \quad (\text{G.54})$$

$$\tilde{g}_3 = C_3 + K_3^1 C_1 + K_3^2 C_2 \quad (\text{G.55})$$

$$\tilde{f}_{11} = \bar{C}_2 + \bar{C}_3, \quad \tilde{f}_{12} = K_1^2 \bar{C}_1, \quad \tilde{f}_{13} = K_1^3 \bar{C}_1 \quad (\text{G.56})$$

$$\tilde{f}_{22} = \bar{C}_3 + \bar{C}_1, \quad \tilde{f}_{23} = K_2^3 \bar{C}_2, \quad \tilde{f}_{21} = K_2^1 \bar{C}_2 \quad (\text{G.57})$$

$$\tilde{f}_{33} = \bar{C}_1 + \bar{C}_2, \quad \tilde{f}_{31} = K_3^1 \bar{C}_3, \quad \tilde{f}_{32} = K_3^2 \bar{C}_3 \quad (\text{G.58})$$

Considering Equations G.18 and G.19, for a ternary exchange,  $\bar{C}_1$ ,  $\bar{C}_2$  and  $\bar{C}_3$  can be expressed as follows:

$$\bar{C}_1 = \frac{C_1 \bar{C}_T}{(C_1 + K_1^2 C_2 + K_1^3 C_3)} \quad (\text{G.59})$$

$$\bar{C}_2 = \frac{C_2 \bar{C}_T}{(C_2 + K_2^1 C_1 + K_2^3 C_3)} \quad (\text{G.60})$$

and

$$\bar{C}_3 = \bar{C}_T - (\bar{C}_1 + \bar{C}_2) \quad (\text{G.61})$$

#### G.2.4 Ternary heterovalent exchange

The main chemical mechanism involved is the heterovalent ion exchange of  $C_1, C_2$  and  $C_3$ . It is assumed that species  $C_1$  is monovalent while species  $C_2$  and  $C_3$  are

divalent ( $n_c = 3, P_1 : P_2 : P_3 = 1 : 2 : 2$ ). In such case, the following system of equations are to be solved as follows:

$$\phi \frac{\partial C_i}{\partial t} + \rho_b \frac{\partial \bar{C}_i}{\partial t} = D \frac{\partial^2 C_i}{\partial x_j^2} - q_j \frac{\partial C_i}{\partial x_j} + q_{re} C_i \pm S, \quad i = 1, 2, 3 \quad (G.62)$$

$$K_2^1 = \left( \frac{\bar{C}_1}{C_1} \right)^2 \left( \frac{C_2}{\bar{C}_2} \right) \quad (G.63)$$

$$K_3^1 = \left( \frac{\bar{C}_1}{C_1} \right)^2 \left( \frac{C_3}{\bar{C}_3} \right) \quad (G.64)$$

$$\bar{C}_T = \bar{C}_1 + \bar{C}_2 + \bar{C}_3 \quad (G.65)$$

As for the ternary homovalent exchange, the partial differential equations are obtained as follows:

$$\frac{\partial C_1}{\partial t} = D \frac{\partial^2 C_1}{\partial x_j^2} - q_j \frac{\partial C_1}{\partial x_j} + (1 - \phi) \frac{\partial C_1}{\partial t} - \frac{\rho_b}{g_1} f_{11} \frac{\partial C_1}{\partial t} + \frac{\rho_b}{g_1} f_{12} \frac{\partial C_2}{\partial t} + \frac{\rho_b}{g_1} f_{13} \frac{\partial C_3}{\partial t} + q_{re} C_1 \pm S \quad (G.66)$$

$$\frac{\partial C_2}{\partial t} = D \frac{\partial^2 C_2}{\partial x_j^2} - q_j \frac{\partial C_2}{\partial x_j} + (1 - \phi) \frac{\partial C_2}{\partial t} - \frac{\rho_b}{g_2} f_{22} \frac{\partial C_2}{\partial t} + \frac{\rho_b}{g_2} f_{23} \frac{\partial C_3}{\partial t} + \frac{\rho_b}{g_2} f_{21} \frac{\partial C_1}{\partial t} + q_{re} C_2 \pm S' \quad (G.67)$$

$$\frac{\partial C_3}{\partial t} = D \frac{\partial^2 C_3}{\partial x_j^2} - q_j \frac{\partial C_3}{\partial x_j} + (1 - \phi) \frac{\partial C_3}{\partial t} - \frac{\rho_b}{g_3} f_{33} \frac{\partial C_3}{\partial t} + \frac{\rho_b}{g_3} f_{31} \frac{\partial C_1}{\partial t} + \frac{\rho_b}{g_3} f_{32} \frac{\partial C_2}{\partial t} + q_{re} C_3 \pm S'' \quad (G.68)$$

where,

$$f_{11} = \frac{2\bar{C}_2}{C_1} + \frac{2\bar{C}_3}{C_1} \quad (G.69)$$

$$f_{12} = \frac{\bar{C}_1^2}{K_2^1 C_1^2} \quad (\text{G.70})$$

$$f_{13} = \frac{\bar{C}_1^2}{K_3^1 C_1^2} \quad (\text{G.71})$$

$$g_1 = 1 + \frac{2C_2 \bar{C}_1}{K_2^1 C_1^2} + \frac{2C_3 \bar{C}_1}{K_3^1 C_1^2} \quad (\text{G.72})$$

$$f_{22} = \frac{\bar{C}_1}{2C_2} + \frac{\bar{C}_3}{C_2} \quad (\text{G.73})$$

$$f_{21} = \frac{\bar{C}_2 C_1}{K_1^2 C_2 \bar{C}_1} \quad (\text{G.74})$$

$$f_{23} = \frac{\bar{C}_2^2 C_3}{K_3^2 C_2^2 \bar{C}_3} \quad (\text{G.75})$$

$$g_2 = 1 + \frac{C_1^2}{2K_1^2 C_2 \bar{C}_1} + \frac{C_3^2 \bar{C}_2}{K_3^2 C_2^2 \bar{C}_3} \quad (\text{G.76})$$

$$f_{33} = \frac{\bar{C}_1}{2C_3} + \frac{\bar{C}_2}{C_3} \quad (\text{G.77})$$

$$f_{31} = \frac{\bar{C}_3 C_1}{K_1^3 C_3 \bar{C}_1} \quad (\text{G.78})$$

$$f_{32} = \frac{\bar{C}_3^2 C_2}{K_2^3 C_3^2 \bar{C}_2} \quad (\text{G.79})$$

$$g_3 = 1 + \frac{C_1^2}{2K_1^3 C_3 \bar{C}_1} + \frac{C_2^2 \bar{C}_3}{K_2^3 C_3^2 \bar{C}_2} \quad (\text{G.80})$$

$$\bar{C}_1 = \frac{-C_1^2 \pm \sqrt{C_1^4 + 4(\bar{C}_7 C_1^2)(K_1^2 C_2 + K_1^3 C_3)}}{2(K_1^2 C_2 + K_1^3 C_3)} \quad (\text{G.81})$$

$$\bar{C}_2 = \frac{\{2\bar{C}_T C_2 (C_2 + [K_2^3]^{1/2} C_3) + K_2^1 C_1^2 C_2\} \pm D^{1/2}}{2(C_2 + [K_2^3]^{0.5} C_3)^2} \quad (\text{G.82})$$

where,

$$D = \{2\bar{C}_T C_2 (C_2 + [K_2^3]^{1/2} C_3) + K_2^1 C_1^2 C_2\}^2 - 4\bar{C}_T^2 C_2^2 (C_2 + [K_2^3]^{1/2} C_3)^2 \quad (\text{G.83})$$

and

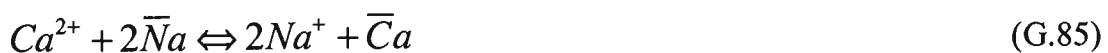
$$\bar{C}_3 = \bar{C}_T - (\bar{C}_1 + \bar{C}_2) \quad (\text{G.84})$$

Only one of the two roots in Equations G.81 and G.82 will give physically meaningful values of  $\bar{C}_1$  and  $\bar{C}_2$ .

One of the most important examples of such a ternary heterovalent exchange reaction is the nonlinear ion exchange of  $Mg^{2+}$ ,  $Ca^{2+}$ , and  $Na^+$  which has been modelled by Valocchi et al. (1981) and the model validated using field experiment data observed in the Palo Alto Baylands, California. The data measured in this field experiment was also used for the validation of the present model as discussed in Chapter 9, Section 9.7.2 (a), Page 275. For detailed information related to this field test, the readers are referred to Valocchi et al. (1981); Miller and Benson (1983); and Walter et al. (1994a, b).

### G.2.5 Quaternary heterovalent ion exchange

Another important example of the ion exchange process (Domenico and Schwartz, 1990) in groundwater flow systems is represented by the following reactions:





Groundwater with relatively high concentrations of ions  $Ca^{2+}, Mg^{2+}$  and other ions such as  $Fe^{2+}$  changes its composition as it flows into the clay or shale with  $Na^+$  species on the exchange reaction sites. As the groundwater moves,  $Ca^{2+}, Mg^{2+}$  as well as  $Fe^{2+}$  are removed from the solution due to replacement by  $Na^+$ .

In such cases the following general equations can be solved ( $n_c = 4, P_1 : P_2 : P_3 : P_4 = 1 : 2 : 2 : 2$ ).

$$\phi \frac{\partial C_i}{\partial t} + \rho_b \frac{\partial \bar{C}_i}{\partial t} = D \frac{\partial^2 C_i}{\partial x_j^2} - q_j \frac{\partial C_i}{\partial x_j} + q_{re} C_i \pm S, \quad i = 1, 2, 3, 4 \quad (G.88)$$

$$K_2^1 = \left( \frac{\bar{Na}}{Na^+} \right)^2 \left( \frac{Mg^{2+}}{\bar{Mg}} \right) \quad (G.89)$$

$$K_3^1 = \left( \frac{\bar{Na}}{Na^+} \right)^2 \left( \frac{Ca^{2+}}{\bar{Ca}} \right) \quad (G.90)$$

$$K_4^1 = \left( \frac{\bar{Na}}{Na^+} \right)^2 \left( \frac{Fe^{2+}}{\bar{Fe}} \right) \quad (G.91)$$

$$\bar{C}_r = \bar{C}_1 + \bar{C}_2 + \bar{C}_3 + \bar{C}_4 \quad (G.92)$$

The partial differential equations describing transport of species  $Na^+, Ca^{2+}, Mg^{2+}$  and  $Fe^{2+}$  are given as:

$$\frac{\partial [Na^+]}{\partial t} = D \frac{\partial^2 [Na^+]}{\partial x_j^2} - q_j \frac{\partial [Na^+]}{\partial x_j} + (1-\phi) \frac{\partial [Na^+]}{\partial t} - \frac{\rho_b}{g_1} f_{11} \frac{\partial [Na^+]}{\partial t} + \frac{\rho_b}{g_1} f_{12} \frac{\partial [Mg^{2+}]}{\partial t} + \frac{\rho_b}{g_1} f_{13} \frac{\partial [Ca^{2+}]}{\partial t} + \frac{\rho_b}{g_1} f_{14} \frac{\partial [Fe^{2+}]}{\partial t} + q_{re} [Na^+] \pm S \quad (G.93)$$

$$\frac{\partial[Mg^{2+}]}{\partial t} = D \frac{\partial^2[Mg^{2+}]}{\partial x_j^2} - q_j \frac{\partial[Mg^{2+}]}{\partial x_j} + (1-\phi) \frac{\partial[Mg^{2+}]}{\partial t} - \frac{\rho_b}{g_2} f_{22} \frac{\partial[Mg^{2+}]}{\partial t} + \frac{\rho_b}{g_2} f_{21} \frac{\partial[Na^+]}{\partial t} + \frac{\rho_b}{g_2} f_{23} \frac{\partial[Ca^{2+}]}{\partial t} + \frac{\rho_b}{g_2} f_{24} \frac{\partial[Fe^{2+}]}{\partial t} + q_{re}[Mg^{2+}] \pm S'$$

(G.94)

$$\frac{\partial[Ca^{2+}]}{\partial t} = D \frac{\partial^2[Ca^{2+}]}{\partial x_j^2} - q_j \frac{\partial[Ca^{2+}]}{\partial x_j} + (1-\phi) \frac{\partial[Ca^{2+}]}{\partial t} - \frac{\rho_b}{g_3} f_{33} \frac{\partial[Ca^{2+}]}{\partial t} + \frac{\rho_b}{g_3} f_{31} \frac{\partial[Na^+]}{\partial t} + \frac{\rho_b}{g_3} f_{32} \frac{\partial[Mg^{2+}]}{\partial t} + \frac{\rho_b}{g_3} f_{34} \frac{\partial[Fe^{2+}]}{\partial t} + q_{re}[Ca^{2+}] \pm S''$$

(G.95)

$$\frac{\partial[Fe^{2+}]}{\partial t} = D \frac{\partial^2[Fe^{2+}]}{\partial x_j^2} - q_j \frac{\partial[Fe^{2+}]}{\partial x_j} + (1-\phi) \frac{\partial[Fe^{2+}]}{\partial t} - \frac{\rho_b}{g_4} f_{44} \frac{\partial[Fe^{2+}]}{\partial t} + \frac{\rho_b}{g_4} f_{41} \frac{\partial[Na^+]}{\partial t} + \frac{\rho_b}{g_4} f_{42} \frac{\partial[Mg^{2+}]}{\partial t} + \frac{\rho_b}{g_4} f_{43} \frac{\partial[Ca^{2+}]}{\partial t} + q_{re}[Fe^{2+}] \pm S'''$$

(G.96)

where,

$$g_1 = 1 + \frac{2C_2\bar{C}_1}{K_2^1 C_1^2} + \frac{2C_3\bar{C}_1}{K_3^1 C_1^2} + \frac{2C_4\bar{C}_1}{K_4^1 C_1^2}$$

(G.97)

$$g_2 = 1 + \frac{C_1^2}{2K_1^2 C_2 \bar{C}_1} + \frac{C_3^2 \bar{C}_2}{K_3^2 C_2^2 \bar{C}_3} + \frac{C_4^2 \bar{C}_2}{K_4^2 C_2^2 \bar{C}_4}$$

(G.98)

$$g_3 = 1 + \frac{C_1^2}{2K_1^3 C_3 \bar{C}_1} + \frac{C_2^2 \bar{C}_3}{K_2^3 C_3^2 \bar{C}_2} + \frac{C_4^2 \bar{C}_3}{K_4^3 C_3^2 \bar{C}_4}$$

(G.99)

$$g_4 = 1 + \frac{C_1^2}{2K_1^4 C_4 \bar{C}_1} + \frac{C_2^2 \bar{C}_4}{K_2^4 C_4^2 \bar{C}_2} + \frac{C_3^2 \bar{C}_4}{K_3^4 C_4^2 \bar{C}_3}$$

(G.100)

$$f_{11} = \frac{2\bar{C}_2}{C_1} + \frac{2\bar{C}_3}{C_1} + \frac{2\bar{C}_4}{C_1}$$

(G.101)

$$f_{12} = \frac{\bar{C}_1^2}{K_2^1 C_1^2}$$

(G.102)

$$f_{13} = \frac{\bar{C}_1^2}{K_3^1 C_1^2}$$

(G.103)

$$f_{14} = \frac{\bar{C}_1^2}{K_4^1 C_1^2}$$

(G.104)

$$f_{22} = \frac{\bar{C}_1}{2C_2} + \frac{\bar{C}_3}{C_2} + \frac{\bar{C}_4}{C_2} \quad (\text{G.105})$$

$$f_{21} = \frac{\bar{C}_2 C_1}{K_1^2 C_2 \bar{C}_1} \quad (\text{G.106})$$

$$f_{23} = \frac{\bar{C}_2^2 C_3}{K_3^2 C_2^2 \bar{C}_3} \quad (\text{G.107})$$

$$f_{24} = \frac{\bar{C}_2^2 C_4}{K_4^2 C_2^2 \bar{C}_4} \quad (\text{G.108})$$

$$f_{33} = \frac{\bar{C}_1}{2C_3} + \frac{\bar{C}_2}{C_3} + \frac{\bar{C}_4}{C_3} \quad (\text{G.109})$$

$$f_{31} = \frac{\bar{C}_3 C_1}{K_1^3 C_3 \bar{C}_1} \quad (\text{G.110})$$

$$f_{32} = \frac{\bar{C}_3^2 C_2}{K_2^3 C_3^2 \bar{C}_2} \quad (\text{G.111})$$

$$f_{34} = \frac{\bar{C}_3^2 C_4}{K_4^3 C_3^2 \bar{C}_4} \quad (\text{G.112})$$

$$f_{44} = \frac{\bar{C}_1}{2C_4} + \frac{\bar{C}_2}{C_4} + \frac{\bar{C}_3}{C_4} \quad (\text{G.113})$$

$$f_{41} = \frac{\bar{C}_4 C_1}{K_1^4 C_4 \bar{C}_1} \quad (\text{G.114})$$

$$f_{42} = \frac{\bar{C}_4^2 C_2}{K_2^4 C_4^2 \bar{C}_2} \quad (\text{G.115})$$

$$f_{43} = \frac{\bar{C}_4^2 C_3}{K_3^4 C_4^2 \bar{C}_3} \quad (\text{G.116})$$

$$\bar{C}_1 = \frac{-C_1^2 \pm \sqrt{D}}{2(K_1^2 C_2 + K_1^3 C_3 + K_1^4 C_4)} \quad (\text{G.117})$$

$$D = C_1^4 + 4(\bar{C}_T C_1^2)(K_1^2 C_2 + K_1^3 C_3 + K_1^4 C_4) \quad (\text{G.118})$$

$$\bar{C}_2 = \frac{\{2\bar{C}_T C_2 (C_2 + [K_2^3]^{1/2} C_3 + [K_2^4]^{1/2} C_4) + K_2^1 C_1^2 C_2\} \pm D_1^{1/2}}{2(C_2 + [K_2^3]^{1/2} C_3 + [K_2^4]^{1/2} C_4)^2} \quad (\text{G.119})$$

where,

$$D_1 = \{2\bar{C}_T C_2 (C_2 + [K_2^3]^{1/2} C_3 + [K_2^4]^{1/2} C_4) + K_2^1 C_1^2 C_2\}^2 - 4\bar{C}_T^2 C_2^2 (C_2 + [K_2^3]^{1/2} C_3 + [K_2^4]^{1/2} C_4)^2 \quad (\text{G.120})$$

$$\bar{C}_3 = \frac{\{2\bar{C}_T C_3 (C_3 + [K_3^2]^{1/2} C_2 + [K_3^4]^{1/2} C_4) + K_3^1 C_1^2 C_3\} \pm D_2^{1/2}}{2(C_3 + [K_3^2]^{1/2} C_2 + [K_3^4]^{1/2} C_4)^2} \quad (\text{G.121})$$

where,

$$D_2 = \{2\bar{C}_T C_3 (C_3 + [K_3^2]^{1/2} C_2 + [K_3^4]^{1/2} C_4) + K_3^1 C_1^2 C_3\}^2 - 4\bar{C}_T^2 C_3^2 (C_3 + [K_3^2]^{1/2} C_2 + [K_3^4]^{1/2} C_4)^2 \quad (\text{G.122})$$

and

$$\bar{C}_4 = \bar{C}_T - (\bar{C}_1 + \bar{C}_2 + \bar{C}_3) \quad (\text{G.123})$$

## APPENDIX H

### ACID NEUTRALISATION REACTIONS

$H^+$  released by pyrite oxidation may be neutralised by carbonates or transformed into weaker acids by reaction with the spoil matrix or gangue material in the pyritic reaction sites (Rogowski et al., 1977; and Jaynes et al., 1984a) or with acid neutralisation reactions in the aquifer materials below the reaction site (Walter et al., 1994a, b). Neutralisation of  $H^+$  when acid reacts with carbonate minerals is an important means of moderating acid generation (U.S Environmental Protection Agency, 1994). The most common carbonates are calcite ( $CaCO_3$ ), dolomite ( $CaMg(CO_3)_2$ ) or siderite ( $FeCO_3$ ). Carbonates may occur as layers of limestone or dolomite in the overburden above the coal seam or as cement in sandstone or shale. The  $pH$  of the drainage waters will generally rise with a corresponding increase in  $Ca^{2+}$ ,  $Mg^{2+}$ , or possibly the  $Fe^{2+}$  concentration, unless the  $Ca^{2+}$  content exceeds the solubility of  $CaSO_4$ , or unless the  $Fe^{2+}$  is oxidised and exceeds the solubility of the  $Fe^{3+}$  compounds (Rogowski et al., 1977).

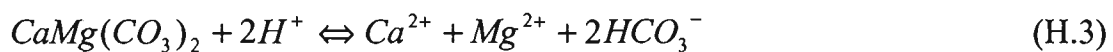
Blowes et al. (1994) found that the  $H^+$  released by sulphide oxidation in inactive mine waste at the Nordic uranium tailings impoundment near Elliot lake, is neutralised by a series of mineral dissolution reactions. These are carbonate mineral dissolution, hydroxide mineral dissolution, and alumina silicate mineral dissolution. The authors also reported that acid consuming reactions that occur along the groundwater flow path affect the mobility of dissolved metals as they are transported through the mine wastes and through underlying aquifers. According to Destouni et al. (1998), reactions that tend to buffer the pore-water  $pH$  are therefore essential in decreasing or delaying the

transport of oxidation products. The initial reaction with an acid solution is given below:

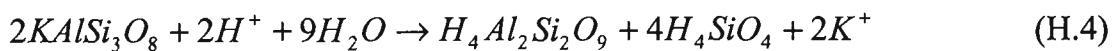


Here, calcite is an  $H^+$  neutralising mineral.

Upon further neutralising acidic drainage with carbonates such as calcite and dolomite to  $pH$  values above 6-6.3 (see Blowes et al., 1994), the product is bicarbonate ( $HCO_3^-$ ).



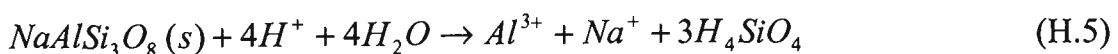
Silicate minerals, however, can buffer the  $pH$ . In this reaction, the transformation of  $H^+$  are relatively very slow such as clay mineral transformation in the formation of kaolinite (Jaynes et al., 1984a):



(Orthoclase)

(Kaolinite)

Or, the acidic dissolution of albite (Herbert, 1994) can transform  $H^+$  through the following reaction:



(albite)

This reaction releases  $Al$ ,  $Na$ , and silicate acid. Where  $Al$  may be subsequently removed from solution by substitution in the goethite mineral lattice or by precipitation as  $Al$  oxides, basic  $Al$  sulphates, or secondary alumina silicates such as kaolinite. The  $H^+$  transformation may be more rapid if there are considerable amount of clay minerals ( $X$ ) present, with an exchange capacity of kaolinite or greater (Rogowski et al., 1977)

for which the exchange complex is predominantly saturated with  $Ca$  and/or  $Mg$ , according to the following reaction:



where,

$X$  = clay mineral.

Jaynes et al. (1984a) reported that in situ neutralisation reactions are important in strip mine sites studied in Pennsylvania. They noted that acid neutralisation and transformation to reserve forms of acidity of mostly aluminum species were observed in small column-leaching studies of sulphidic material. Therefore,  $H^+$  neutralisation processes must be included in the model. All acid neutralisation due to reactions with carbonates, buffering and exchange reactions produce material which is called acidity. Changes in solution  $pH$  caused by the spoil would depend on the mineralogy of the spoil material and the initial  $pH$  of the solution. Jaynes et al. (1984a) described a simple empirical expression in order to account for  $H^+$  neutralisation reactions taking place in coal strip mine sites. This relationship divides the  $H^+$  generated into active solution  $H^+$  and the combined neutralised or reserve  $H^+$ . The expression is:

$$\frac{H^+}{H_{Gen}^+} = \{1.0 - EXP(G_A - pH)\} \quad (H.7)$$

where,

$H^+$  = actual increase of hydrogen ion in solution ( $mol / m^3$ );

$H_{Gen}^+$  =  $H^+$  generated through chemical reactions ( $mol / m^3$ );

$G_A$  = an empirical constant that defines the buffer system.

Based on Equation H.7, when solution  $pH$  reaches the empirical constant  $G_A$ , all the  $H^+$  produced is consumed by surrounding spoil materials, and the  $pH$  remains

constant. The increase in the acidity term  $A_T$  (Jaynes et al., 1984a) is then represented as:

$$A_T = H_{Gen}^+ - H^+ \quad (\text{H.8})$$

Rearranging Equation H.7 may yield the  $H^+$  consumption per cubic meter of spoil per time and:

$$\frac{\partial H^+}{\partial t} = -\frac{H_{Gen}^+}{\Delta t} \exp(G_A - pH) \quad (\text{H.9})$$

where,

$\Delta t$  = simulation time step (s).

The equation H.9 was incorporated as a sink term in governing transport equation of hydrogen ion.

## APPENDIX I

### MINERAL PRECIPITATION AND DISSOLUTION REACTIONS

Mineral precipitation and dissolution reactions are described by the mass action law for a solid and the reacting ions. The general form of the dissolution reaction of a solid is



where,

(*aq*) = aqueous phase

(*s*) = solid phase

The reaction above is described by a solubility product of the form

$$\frac{[C]^c [D]^d}{[C_c D_d]} = K_{sp} \quad (I-2)$$

where,

$K_{sp}$  = solubility product which is an equilibrium constant specific to a solid.

The left-hand side of Equation I-2 is called the ion activity product (*IAP*). For a pure solid,

$$[C_c D_d] = 1.$$

When a system is at equilibrium, then,

$$K_{sp} = IAP$$

If system is not at equilibrium, the degree of disequilibrium can then be given by the following expression (Walter et al., 1994a, b):

$$SI = \log \left( \frac{IAP}{K_{sp}} \right) \quad (I-3)$$

where,

$SI$  = saturation index.

- (i) In the case of supersaturation,  $SI > 0$ , the mineral tends to precipitate;
- (ii) When  $SI = 0$ , the mineral and the solution are in equilibrium;
- (iii) When  $SI < 0$ , the solution is under saturation and mineral tends to dissolve.

It should be mentioned that the dissolution and precipitation of minerals are two of the important chemical reactions in terms of their control on chemistry of groundwater that affect solute transport (Domenico and Schwartz, 1990). These processes have significant effects on the mass transfer taking place in groundwater systems (Reddi and Inyang, 2000). Dissolution reaction supplies dissolved material into the pore water whereas a precipitation process removes it from pore water (Lerman, 1979; Reddi and Inyang, 2000). Hence, these reactions must be considered in the model.

### **I.1 Precipitation reaction for $Fe^{3+}$ species**

In strip mine spoil the only important source of  $Fe^{3+}$  is the in situ oxidation of ferrous iron (Reaction 2.9, Chapter 2, Section 2.5.3, Page 50).  $Fe^{3+}$  formed by this reaction may react with pyrite to produce additional  $Fe^{2+}$ ,  $SO_4^{2-}$ , and  $H^+$ . Alternatively, the  $Fe^{3+}$  released may be hydrolysed and precipitated as amorphous ferrihydrite (Jaynes et al., 1984a, Walter et al., 1994a, b) according to Equation 2.11 (Chapter 2, Section 2.5.3, Page 50) as again given below:



### **I.2 Modelling of precipitation reactions**

All reactions will be assumed to be relatively fast so that local chemical equilibrium always exists at every point of the system (Rubin and James, 1973).

The solubility product for Equation I.4 may be expressed as:

$$K = [Fe^{3+}] / [H^+]^3 \quad (I-5)$$

where,

$K$  = solubility product of amorphous ferrihydrite based on the stoichiometric relationship (I-4).

The rate of dissolution or precipitation of a solid phase can be estimated by the rate of change of concentration in pore fluid  $\left(\frac{\partial C}{\partial t}\right)$  (Lerman, 1979). Thus to incorporate an equilibrium precipitation-dissolution reaction, the following transport equations can then be written to describe the system in question:

$$\phi \frac{\partial [Fe^{3+}]}{\partial t} + \frac{\partial \bar{C}_{fh}}{\partial t} = D \frac{\partial^2 [Fe^{3+}]}{\partial x_j^2} - q_j \frac{\partial [Fe^{3+}]}{\partial x_j} \pm [Source\ terms]_{[Fe^{3+}]} \quad (I-6)$$

$$\phi \frac{\partial [H^+]}{\partial t} - \frac{\partial \bar{C}_{fh}}{\partial t} = D \frac{\partial^2 [H^+]}{\partial x_j^2} - q_j \frac{\partial [H^+]}{\partial x_j} \pm [Source\ terms]_{[H^+]} \quad (I-7)$$

where,

$\bar{C}_{fh}$  = amount of precipitated ferrihydrite per bulk volume of solids;

$\phi$  = porosity;

[ ] = concentration operator.

It is assumed that the precipitate occurs as very thin layers on non-reacting surfaces, thus not affecting the other processes or the groundwater flow (Rubin, 1983; and Eriksson and Destouni, 1997).

Adding Equations I-6 and I-7 and rearranging the new equation gives:

$$\phi \frac{\partial[\psi]}{\partial t} = D \frac{\partial^2[\psi]}{\partial x_j^2} - q_j \frac{\partial[\psi]}{\partial x_j} \pm [\text{Source terms}]_{[Fe^{3+}]} \pm [\text{Source terms}]_{[H^+]} \quad (I-8)$$

where,

$$[\psi] = [Fe^{3+}] + [H^+] \quad (I-9)$$

Equation I-8 now can be solved by defining the appropriate initial and boundary conditions.

The required  $[Fe^{3+}]$  and  $[H^+]$  concentrations can then be obtained from  $[\psi]$  by combining and rewriting Equations I-5 and I-9 as follows:

$$K [H^+]^3 + [H^+] - [\psi] \quad (I-10)$$

$$[Fe^{3+}] = [\psi] - [H^+] \quad (I-11)$$

### I.3 Initial and boundary conditions

The following initial and boundary conditions can be specified for problem at hand:

$$\begin{aligned} t = 0 \quad , \quad x_j \geq 0 \quad , \quad [\psi] &= [Fe^{3+}]_{init} + [H^+]_{init} \\ t \geq 0 \quad , \quad x_j = 0 \quad , \quad [\psi] &= q_{re} \left( [Fe^{3+}] + [H^+] \right)_{influx} \\ t \geq 0 \quad , \quad x_j = \infty \quad , \quad [\psi] &= [Fe^{3+}]_{init} + [H^+]_{init} \end{aligned} \quad (I-12)$$

The nonlinear Equation I-10 was first solved for  $[H^+]$  using the Secant method (Yakowitz and Szidarovszky, 1989). The ferric iron concentrations were then calculated from Equation I-11. The calculation were done with FORTRAN language and supplied in group 19 of GROUND subroutine (Appendix M).

## APPENDIX J

### FERRIC IRON COMPLEXATION REACTIONS

Complexation involves reaction between simple cations (usually metallic), and anions called ligands (Reddi and Inyang, 2000). Complexation facilitates the transport of potentially toxic metals such as cadmium, chromium, copper, lead, uranium, or plutonium. Such reaction also influences some types of surface reactions.

A complex is an ion that forms by combining simpler cations, anions, and sometimes molecules. The ligand includes many of the common inorganic species found in groundwater such as  $OH^-$ ,  $Cl^-$ ,  $F^-$ ,  $Br^-$ ,  $SO_4^{2-}$ ,  $PO_4^{3-}$  and  $CO_3^{2-}$ . The ligand might also comprise various organic molecules such as amino acids. It should be noted that  $OH^-$  is a very important ligand in aqueous solutions (Pankow, 1991). The simplest complexation reaction involves the combination of a metal and ligand as follows:



Examples of such reactions are:



A more complicated case of complexation reaction is the reaction series that forms when complexes themselves combine with ligands. An example is the hydrolysis reaction of

$Cr^{3+}$ :





The metal is distributed among at least three complexes. Such series involve not only hydrolysis reactions but also other ligands such as  $Cl^-$ ,  $F^-$  and  $Br^-$  (Domenico and Schwartz, 1990).

Complexation reactions are important in studying the transport of metals in the subsurface. In assessing the total metal concentration in the pore fluid, the complexes must be considered in addition to the free metal ion concentration. Because of the complexation reactions the actual quantities of metal transported downstream in the pore fluid might be more than the concentrations of metal ions alone might indicate (Reddi and Inyang, 2000).

### J.1 Stability of complexes and speciation modelling

Most inorganic reactions involving complexes are kinetically fast. Thus, equilibrium concepts can be used to examine these reactions quantitatively. For example, the mass-law relationships for Reactions J.4 to J.6 may be expressed as:

$$K_{Cr(OH)^{2+}} = \frac{[Cr(OH)^{2+}]}{[Cr^{3+}][OH^-]}, \quad K_{Cr(OH)_2^+} = \frac{[Cr(OH)_2^+]}{[Cr(OH)^{2+}][OH^-]}, \quad K_{Cr(OH)_3^0} = \frac{[Cr(OH)_3^0]}{[Cr(OH)_2^+][OH^-]} \quad (J.7)$$

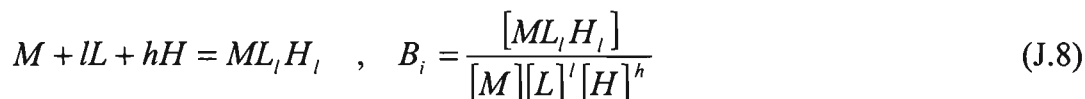
where,

$K$  = stability constant.

Calculation of the distribution of metals among various complexes involves the solution of a series of mass-action equations.

## J.2 Mononuclear complexation reactions

Mononuclear complexation reactions have the following general form:



where,

$M$  = a metal;

$L$  = a ligand;

$H$  = a hydrogen ion.

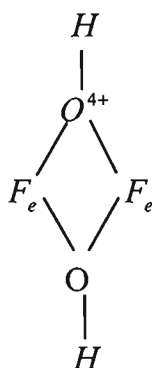
The stability constants  $B_i$ , for the reaction determine the strength of the complex. Large values of  $B_i$  are associated with stronger or more stable complexes. Stability constants are related to the equilibrium constants for the series of reactions. The stability constants for a series of metal ligand reactions provide the basic information necessary to determine how the total concentration of a metal in solution  $(M)_T$  is distributed as a metal ion and various complexes.

## J.3 Polynuclear hydroxide complexes

A Polynuclear complex is a complex containing more than one metal centre. The most important polynuclear complexes are those involving the ligand  $OH^-$  together with high-oxidation state metals like  $Fe^{3+}$ ,  $Cr^{3+}$ , and  $Al^{3+}$ .

For  $Fe^{3+}$ , the most important polynuclear  $Fe^{3+}$  species is  $Fe_2(OH)_2^{4+}$ . Like most other  $M(III)$  polynuclear species,  $Fe_2(OH)_2^{4+}$  is characterised by  $OH$  bridges between the

metal centres. When  $H_2O$  ligand molecules surrounding the  $Fe$  (III) centres are neglected, the  $Fe_2(OH)_2^{4+}$  species may be represented as:



#### J.4 Ferric iron complexation reactions

One of the most important metals, which forms relatively strong complexes with ligands of  $OH^-$  (hydroxides) and  $SO_4^{2-}$  is ferric iron. Ferric complexation raises the total dissolved concentration of  $Fe^{3+}$  a hundred to a thousand times in particular at  $pH \approx 5$  (Jaynes et al., 1984a). Therefore, the ferric complexation reaction is noted to be an important reaction, which affects transport of dissolved ferric iron and must be considered in the present model. Furthermore, total dissolved ferric iron in the aqueous phase is used to determine the rate of pyrite oxidation, hence the calculation of the actual values of ferric ions is necessary. Table J.1 shows the ferric iron complexes, their mass action and equilibrium constants included in this model (Jaynes et al., 1984a; Pankow, 1991; Walter et al., 1994a, b; Stumm and Morgan, 1996; and Wunderly et al., 1996).

Instantaneous equilibrium is assumed for all of these  $Fe^{3+}$  complexation reactions according to the appropriate mass action expressions. In the case of non-equilibrium, kinetic expressions may be substituted for any reaction by adding terms to the differential rather than algebraic equation set (Jennings et al., 1982).

The mole balance equation for  $(Fe)_T$  is:

$$(Fe)_T = \{Fe^{3+}\} + \{Fe(OH)^{2+}\} + \{Fe(OH)_2^+\} + \{Fe(OH)_3^0\} + \{Fe(OH)_4^-\} + 2\{Fe_2(OH)_2^{4+}\} + \{FeSO_4^+\} + \{Fe(SO_4)_2^-\} \quad (J.9)$$

By substitution of the appropriate mass action equations, the concentrations of all complex species may be eliminated as follows:

$$(Fe)_T = \{Fe^{3+}\} + \frac{{}^*K_1\{Fe^{3+}\}}{\{H^+\}^1} + \frac{{}^*\beta_2\{Fe^{3+}\}}{\{H^+\}^2} + \frac{{}^*\beta_3\{Fe^{3+}\}}{\{H^+\}^3} + \frac{{}^*\beta_4\{Fe^{3+}\}}{\{H^+\}^4} + \frac{2\{Fe^{3+}\}^2 {}^*\beta_{22}}{\{H^+\}^2} + \{SO_4^{2-}\}\{Fe^{3+}\}K_1 + \{SO_4^{2-}\}^2\{Fe^{3+}\}K_2 \quad (J.10)$$

where,

${}^*K_1, K_1, K_2, {}^*\beta_2, {}^*\beta_3, {}^*\beta_4,$  and  ${}^*\beta_{22}$  = stability constants for  $Fe^{3+}$  complexes.

Equation J.10 can be rearranged as follows:

$$(Fe)_T = \{Fe^{3+}\} \left\{ 1 + \frac{{}^*K_1}{\{H^+\}^1} + \frac{{}^*\beta_2}{\{H^+\}^2} + \frac{{}^*\beta_3}{\{H^+\}^3} + \frac{{}^*\beta_4}{\{H^+\}^4} + \frac{2\{Fe^{3+}\} {}^*\beta_{22}}{\{H^+\}^2} + \{SO_4^{2-}\}K_1 + \{SO_4^{2-}\}^2 K_2 \right\} \quad (J.11)$$

Now consider the following mass transport partial differential equation:

$$R_f \frac{\partial C_i}{\partial t} = D \frac{\partial^2 C_i}{\partial x_j^2} - u_j \frac{\partial C_i}{\partial x_j} + q_{re} C_i \pm S, \quad i = 1, 2, \dots, n_c \quad (J.12)$$

Substitution of Equation J.11 into the mass transport equation for  $C_i = Fe^{3+}$  yields:

---

\* Noted that a factor of 2 is included since there are two  $Fe^{3+}$  in each  $Fe_2(OH)_2^{4+}$  species

$$\begin{aligned}
L_{Fe^{3+}}(\{Fe^{3+}\}, \{SO_4^{2-}\}) &\equiv R_f \frac{\partial \{Fe^{3+}\}}{\partial t} = D \frac{\partial^2 \{Fe^{3+}\}}{\partial x_j^2} - u_j \frac{\partial \{Fe^{3+}\}}{\partial x_j} + q_{re} \{Fe^{3+}\} \pm \left(\frac{1}{A}\right) (S) \\
&- \left(\frac{1}{A}\right) \{Fe^{3+}\} (K_1 + K_2 \{SO_4^{2-}\}) \frac{\partial \{SO_4^{2-}\}}{\partial t} + \left(\frac{1}{A}\right) D \{Fe^{3+}\} (K_1 + K_2 \{SO_4^{2-}\}) \frac{\partial^2 \{SO_4^{2-}\}}{\partial x_j^2} \\
&- \left(\frac{1}{A}\right) \{Fe^{3+}\} (K_1 + K_2 \{SO_4^{2-}\}) u_j \frac{\partial \{SO_4^{2-}\}}{\partial x_j} \quad (J.13)
\end{aligned}$$

where,

$$A = \left[ 1 + \frac{{}^*K_1}{\{H^+\}^1} + \frac{{}^*\beta_2}{\{H^+\}^2} + \frac{{}^*\beta_3}{\{H^+\}^3} + \frac{{}^*\beta_4}{\{H^+\}^4} + \frac{2\{Fe^{3+}\}^* \beta_{22}}{\{H^+\}^2} + \{SO_4^{2-}\} K_1 + \{SO_4^{2-}\}^2 K_2 \right] \quad (J.14)$$

Table (J.1). Ferric iron complexes, Log of the equilibrium constants and their mass action expressions (Jaynes et al., 1984a; Pankow, 1991; Walter et al., 1994a, b; Stumm and Morgan, 1996; and Wunderly et al., 1996).

	Reaction	$\log K$	Mass action
1	$Fe^{3+} + H_2O \Leftrightarrow Fe(OH)^{2+} + H^+$	-2.2	${}^*K_1 = \frac{\{Fe(OH)^{2+}\} \{H^+\}}{\{Fe^{3+}\}}$
2	$Fe^{3+} + 2H_2O \Leftrightarrow Fe(OH)_2^+ + 2H^+$	-5.7	${}^*\beta_2 = \frac{\{Fe(OH)_2^+\} \{H^+\}^2}{\{Fe^{3+}\}}$
3	$Fe^{3+} + 3H_2O \Leftrightarrow Fe(OH)_3^0 + 3H^+$	-13.6	${}^*\beta_3 = \frac{\{Fe(OH)_3^0\} \{H^+\}^3}{\{Fe^{3+}\}}$
4	$Fe^{3+} + 4H_2O \Leftrightarrow Fe(OH)_4^- + 4H^+$	-21.6	${}^*\beta_4 = \frac{\{Fe(OH)_4^-\} \{H^+\}^4}{\{Fe^{3+}\}}$
5	$2Fe^{3+} + 2H_2O \Leftrightarrow Fe_2(OH)_2^{4+} + 2H^+$	-2.9	${}^*\beta_{22} = \frac{\{Fe_2(OH)_2^{4+}\} \{H^+\}^2}{\{Fe^{3+}\}^2}$
6	$Fe^{3+} + SO_4^{2-} \Leftrightarrow FeSO_4^+$	3.92	$K_1 = \frac{\{FeSO_4^+\}}{\{Fe^{3+}\} \{SO_4^{2-}\}}$
7	$Fe^{3+} + 2SO_4^{2-} \Leftrightarrow Fe(SO_4)_2^-$	5.42	$K_2 = \frac{\{Fe(SO_4)_2^-\}}{\{Fe^{3+}\} \{SO_4^{2-}\}^2}$

### J.5 Modified transport equation of $SO_4^{2-}$

Because the ligand  $SO_4^{2-}$  is involved in ferric complexation reaction, modification must be made to take this into account in the transport equation of  $SO_4^{2-}$ . By assumption that the ligand  $SO_4^{2-}$  only forms complexes with ferric iron (Table J.1, Reactions 6 and 7), the mole balance equation for  $(SO_4)_T$  will be:

$$(SO_4)_T = \{SO_4^{2-}\} + \{FeSO_4^+\} + \{Fe(SO_4)_2^-\} \quad (J.15)$$

Substitution of mass action equations into Equation J.15 yield:

$$(SO_4)_T = \{SO_4^{2-}\} \left( 1 + K_1 \{Fe^{3+}\} + K_2 \{Fe^{3+}\} \{SO_4^{2-}\} \right) \quad (J.16)$$

Substitution of Equation J.16 into the mass transport Equation J.12 gives:

$$\begin{aligned} L_{SO_4^{2-}}(\{Fe^{3+}\}, \{SO_4^{2-}\}) &\equiv R_f \frac{\partial \{SO_4^{2-}\}}{\partial t} = D \frac{\partial^2 \{SO_4^{2-}\}}{\partial x_j^2} - u_j \frac{\partial \{SO_4^{2-}\}}{\partial x_j} + q_{re} \{SO_4^{2-}\} \pm \left( \frac{1}{C} \right) (S) \\ &- \left( \frac{1}{C} \right) \{SO_4^{2-}\} (K_1 + K_2 \{SO_4^{2-}\}) \frac{\partial \{Fe^{3+}\}}{\partial t} + \left( \frac{1}{C} \right) D \{SO_4^{2-}\} (K_1 + K_2 \{SO_4^{2-}\}) \frac{\partial^2 \{Fe^{3+}\}}{\partial x_j^2} \\ &- \left( \frac{1}{C} \right) \{SO_4^{2-}\} (K_1 + K_2 \{SO_4^{2-}\}) u_j \frac{\partial \{Fe^{3+}\}}{\partial x_j} \end{aligned} \quad (J.17)$$

where,

$$C = \left[ 1 + \{Fe^{3+}\} K_1 + \{SO_4^{2-}\} \{Fe^{3+}\} K_2 \right] \quad (J.18)$$

## APPENDIX K

### THE ROLE OF BACTERIA

#### K.1 Iron-oxidising bacteria

Chemical reactions that involve certain types of bacteria play an important role in the oxidation processes taking place in pyritic environments. Literature considering the influence of microbiological activities on the sulphide oxidation processes include Malouf and prater (1961); Schnaitman et al. (1969); Singer and stumm (1970); Cathles and Apps (1975); Cathles (1979); Arkesteyn (1980); Hoffmann et al. (1981); Jaynes et al. (1984a, b); Rossi (1990); Scharer et al. (1994a, b); Nordstrom and Southam (1997); Sasaki et al. (1998); Salmon (1999); and McKnight et al. (2001). Bacteria may accelerate the rate of pyrite oxidation and subsequently the rate of acid generation by increasing the ferric iron concentration in accordance with the stoichiometric Equations 2.9 and 2.10 (Chapter 2, Section 2.5.3, Page 50) (Hoffmann et al., 1981).

##### K.1.1 Bacterial model used in this study

In this thesis the approach presented by Jaynes et al. (1984a, b) was used to determine the rate at which bacteria oxidise  $Fe^{2+}$ . In this method the rate at which bacteria oxidise ferrous iron and consume oxygen is represented by  $K_B$ . Between the upper and lower limits of  $K_B$  (described in Chapter 8, Page 242), the value of  $K_B$  is determined by the bacterial activity, which in turn depends on the energy available to the bacteria and the quality of their environment.

This bacterial model incorporated the bacterial kinetics of indirect oxidation. In this approach there is no need to know the exact bacterial population size or metabolic kinetics. Energy available from the environment and inhibition factors were used to

calculate the activity which yields the rate of ferric iron production. The bacterial activity was expressed as being dependant on  $pH$ , temperature, and oxygen concentration. The effects of these factors were determined empirically based on experimental data. Except in the early stages of the bacterial reaction when the bacteria grow and extend more rapidly than the environmental factors would indicate, the bacterial activity was considered to be in dynamic equilibrium with the bacterial environment. It was observed that in those parts of the spoil where the oxygen is readily available, bacterial activity can greatly increase the rate of pyrite oxidation.

### K.1.2 The value of $K_B$

In the case where iron oxidising bacteria are active, the value of  $K_B$  must be calculated.

The ferric/ferrous ratio can be predicted in the spoil solution from the following equation (Jaynes et al., 1984a):

$$\frac{[Fe^{3+}]}{[Fe^{2+}]} = \frac{\gamma_{Fe^{2+}} \gamma_{H^+}}{\gamma_{Fe^{3+}}} [H^+] Y_O^{\frac{1}{4}} \exp\left(\frac{0.46 - E_{M'}}{8.6 \times 10^{-5} T}\right) \quad (K.1)$$

where,

$T$  = absolute temperature ( $^{\circ}K$ );

$\gamma_{Fe^{3+}}$ ,  $\gamma_{Fe^{2+}}$ , and  $\gamma_{H^+}$  = activity coefficients for  $Fe^{3+}$ ,  $Fe^{2+}$ , and  $H^+$  respectively;

$Y_O$  = mole fraction of oxygen;

$E_{M'}$  = energy per mole of electrons oxidised used by the bacterial population.

The bacterial system is assumed to be in dynamic equilibrium with the oxidising pyrite, the rates at which the two systems consume and produce  $Fe^{2+}$  and  $Fe^{3+}$  must be predicted if the condition in Equation K.1 is met.

$K_B$  essentially needs to be found iteratively by adjusting its magnitude until the condition in Equation K.1 is met. In the model this was done iteratively by estimating the magnitude of  $K_B$  at the next time step, running the model to find the predicted  $Fe^{3+} / Fe^{2+}$  ratio and adjusting the value of  $K_B$  until this ratio is in agreement with Equation K.1. For a full description of the bacterial activity model, the reader is referred to Jaynes et al. (1984a).

## K.2 Sulphate reduction bacteria

Mine drainage containing relatively low  $SO_4^{2-}$  concentration could be caused by sulphate reduction, which involves the reaction of acid mine water with bacteria (Rose and Cravotta III, 1998). Sulphate reduction plays an important role in *pH* neutralisation and sulphate and toxic metals removal (Drury, 2000). Bacterial sulphate reduction produces approximately two moles of alkalinity per mole of sulphate that is reduced, according to Reaction 2.12 (Chapter 2, Section 2.5.3, Page 50). Sulphate and acidity in the solution are consumed by this reaction (Hammack et al., 1998). Evidence for sulphate reduction is the fact that  $H_2S$  or similar sulphur containing gases can be smelled at some mine sites. According to Reaction 2.12, one mole of sulphide is generated per mole of sulphate reduction and the sulphide may precipitate heavy metals with low metal sulphide solubility products (Hammack et al., 1998):



where,

$M^{2+}$  = a divalent heavy metal.

Reaction 2.12 (Chapter 2, Section 2.5.3, Page 50) may take place in wetlands and other natural environments where  $SO_4$  bearing water encounters organic matter. In most acid

mine drainage, the  $H_2S$  will react immediately with iron to precipitate  $FeS$ . Because most AMD originates from pyrite oxidation containing more  $S$  than  $Fe$ , it is unlikely that  $SO_4$  reduction will form an effluent with low  $SO_4$  and high  $Fe$ . However, any unreacted  $H_2S$  can be oxidised to form  $H_2SO_4$  where oxygen is available (Rose and Cravotta III, 1998).

Some research work taking into account the role of sulphate reduction bacteria is presented by Berner (1964); Gardner and Lerche (1987); Middelburg (1989); Drury (2000); and Serrat et al. (2000).

According to Drury (2000) in his development of a model for bacterial sulphate reduction, the effects of substrate degradability, temperature and hydraulic retention time should be taken into account.

Gardner and Lerche (1987) reported that the dependence of the rate of sulphate reduction on sulphate concentration can be described accurately by the Monod equation.

The amount of sulphate reduction by bacteria depends on the availability of an electron donor at a low oxidation-reduction potential to deliver electrons to the sulphate (Drury, 2000).

The rate of degradation of organic matter via sulphate reduction can be modelled using simple first-order kinetics (Berner, 1964; Gardner and Lerche, 1987; Middelburg, 1989; and Drury, 2000):

$$\frac{dG}{dt} = -k(t)G(t) \tag{K.3}$$

where,

$G$  = concentration of organic carbon;

$k$  = time-dependent first-order rate parameter.

$k(t)$  will decrease with time because as time progresses, the remaining organic carbon will be less biodegradable and will therefore decay more slowly than at earlier times. Consequently, bacterial sulphate reduction will decrease with time. According to Drury (2000), Equation K.3 can predict the electrons released over time, in carbon equivalents.

The rate of biodegradation of the original organic matter can be better described by incorporating an apparent initial age 'a' in the expression of  $k(t)$  (Middelburg, 1989; and Drury, 2000):

$$k(t) = b(a + t)^m \quad (\text{K.4})$$

where,

$b$  and  $m$  = empirical coefficients (0.16 and -1 respectively, Middelburg, 1989; and Drury, 2000).

Gardner and Lerche (1987) developed a model using the Monod kinetics for the sulphate reduction process. The non-dimensional equations of the model are given below:

$$-\frac{\partial T}{\partial Z} - \frac{\alpha T \theta}{K + \theta} = 0 \quad (\text{K.5})$$

$$\frac{\partial^2 \theta}{\partial Z^2} - \frac{1}{\alpha} \frac{\partial \theta}{\partial Z} - \frac{T \theta}{K + \theta} = 0 \quad (\text{K.6})$$

Dimensionless parameters  $Z$ ,  $T$ ,  $\theta$ , and  $\alpha$  are obtained from the following equations:

$$Z = \sqrt{\frac{k}{D_s}} z \quad (\text{K.7})$$

$$T = \frac{fG}{S_0} \quad (\text{K.8})$$

$$\theta = \frac{S}{S_0} \quad (\text{K.9})$$

$$\alpha = \frac{\sqrt{D_s k}}{w} \quad (\text{K.10})$$

where,

$S_0$  = concentration of  $SO_4$  at  $Z = 0$  ;

$D_s$  = diffusion coefficient for sulphate ion;

$f$  = stoichiometric coefficient that relates degradation of organic carbon to consumption of sulphate. Based on Reaction 2.12 (Chapter 2, Section 2.5.3, Page 50),  $f$  is set equal to 0.5 (Berner, 1964);

$w$  = pore water velocity;

$S$  = sulphate concentration;

$z$  = depth;

The boundary conditions for Equations K.5 and K.6 are:

$$\begin{aligned} T &= T(0) & \text{at} & \quad Z = 0 \\ \theta &= 1 & \text{at} & \quad Z = 0 \\ \theta &\rightarrow 0 & \text{at} & \quad Z \rightarrow \infty \end{aligned} \quad (\text{K.11})$$

In this present study the Monod model was used to describe sulphate reduction process. Therefore, the rate of decay of organic matter and the overall rate for sulphate reduction can be expressed as:

$$\frac{dG}{dt} = -b(a+t)^m G(t) \frac{[SO_4^{2-}]}{K_s + [SO_4^{2-}]} \quad (\text{K.12})$$

$$\frac{dS}{dt} = -f \beta \eta b(a+t)^m G(t) \frac{[SO_4^{2-}]}{K_s + [SO_4^{2-}]} \quad (\text{K.13})$$

where,

$K_s$  = concentration at which rate of reduction is half of maximum reduction rate ( $mol/m^3$ ). Serrat et al. (2000) found  $K_s$  values of 0.25-0.37  $mol/m^3$  in Aydat Lake sediments.

$\eta$  = conversion factor accounts the number of electrons released by organic carbon decay to those electrons actually used in sulphate reduction process. Drury (2000) used an  $\eta$  of 0.75 in the model;

$\beta$  = ratio of solid volume to water volume is given by:

$$\beta = \frac{1 - \phi}{\phi} \quad (K.14)$$

where,

$\phi$  = porosity.

Incorporating Monod model into transport equation of sulphate ion yields:

$$\phi \frac{\partial [SO_4^{2-}]}{\partial t} + \rho_b \frac{\partial \overline{SO_4}}{\partial t} = D \frac{\partial^2 [SO_4^{2-}]}{\partial x_j^2} - q_j \frac{\partial [SO_4^{2-}]}{\partial x_j} + q_{rech} [SO_4^{2-}] - f \beta \eta b (a+t)^m G(t) \frac{[SO_4^{2-}]}{K_s + [SO_4^{2-}]} \pm S = 0$$

(K.15)

In order to show the capability of the present finite volume model using the PHOENICS package for the simulation of Monod kinetics, the non-dimensional model developed by Gardner and Lerche (1987) (Equations K.5 and K.6) was run with the same parameter values shown in Figure 1, page 228 (Gardner and Lerche, 1987), i.e.,  $T(0)=10$ ,  $K=0.05$ ,  $\alpha = 0.1, 0.2, 0.5, 1.0, 2.0, 2.5, 3.0, \text{ and } 5.0$ . The agreement was very close. Such comparisons are presented in Figure K.1.

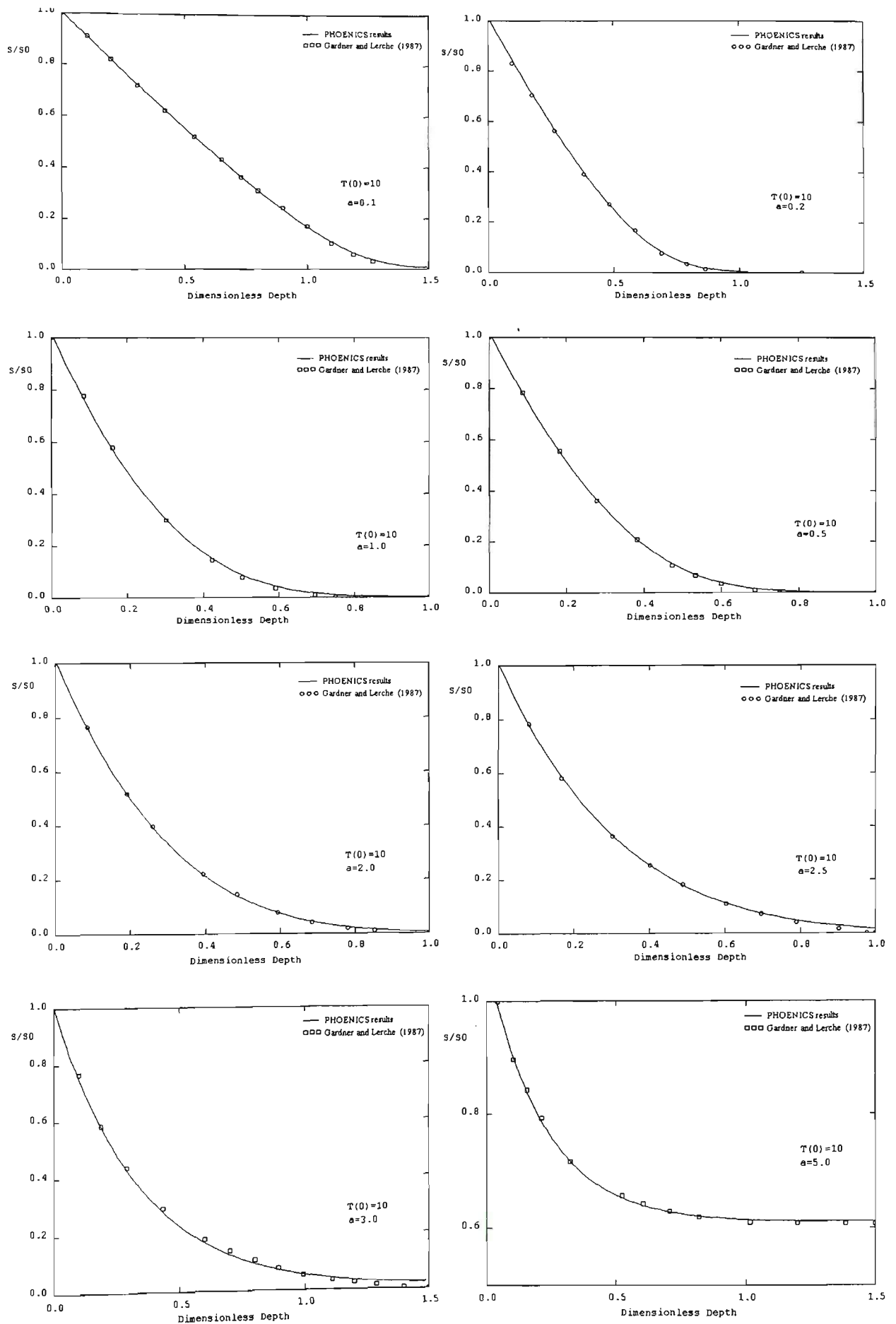


Figure K.1. Model profiles of the dimensionless  $SO_4^{2-}$  concentration vs. dimensionless depth for various values of parameter  $\alpha$  with a dimensionless initial organic matter concentration  $T(0)$  and a saturation constant  $K$  of 0.05 using Monod model.